UNIVERSITÉ DU LUXEMBOURG

PhD-FSTM-2025-039
The Faculty of Science, Technology and Medicine

DISSERTATION

Defence held on 28/03/2025 in Esch-sur-Alzette

to obtain the degree of

DOCTEUR DE L'UNIVERSITÉ DU LUXEMBOURG

EN BIOLOGIE

by

Cristian ANGELI
Born on 29 May 1995 in Guastalla (RE) (Italy)

HIGH-THROUGHPUT DRUG DISCOVERY FOR NRAS-MUTANT MELANOMA: LEVERAGING ADVANCED PRECLINICAL CO-CULTURE MODELS

Dissertation defence committee

Prof. Dr. Stephanie Kreis
Université du Luxembourg

Prof. Dr Elisabeth Letellier, Chairman
Université du Luxembourg

Prof. Dr. Jochen Sven Utikal
University Medical Center Mannheim, Germany

Prof. Dr. Lionel Larue
Institut Curie, France

Dr. Bassam Janji
Luxembourg Institute of Health, Luxembourg

A dissertation by

Cristian ANGELI

University of Luxembourg

The Faculty of Science, Technology and Medicine (FSTM)

Department of Life Sciences and Medicine (DLSM)

Doctoral School in Systems and Molecular Biomedicine

High-Throughput Drug Discovery for NRAS-Mutant Melanoma: Leveraging Advanced Preclinical Co-Culture

Supervisor: Prof. Dr. Stephanie Kreis (University of Luxembourg, Luxembourg)

CET committee:

- Prof. Dr. Stephanie Kreis (University of Luxembourg, Luxembourg)
- Dr. Johannes Meiser (Luxembourg Institute of Health, Luxembourg)
- Prof. Dr. Jochen Sven Utikal (University Medical Center Mannheim, Germany)

Dissertation Defence Committee:

- **Supervisor:** Prof. Dr. Stephanie Kreis (University of Luxembourg, Luxembourg)
- **Chair of committee**: Prof. Dr Elisabeth Letellier (Université du Luxembourg, Luxembourg)
- **Committee member**s:
    - Prof. Dr. Jochen Sven Utikal (University Medical Center Mannheim, Germany)
    - Prof. Lionel Larue (Institut Curie, France)
    - Dr. Bassam Janji (Luxembourg Institute of Health, Luxembourg)

Statement of originality / Affidavit

Last name: Angeli

First name: Cristian

Title of Thesis: High-Throughput Drug Discovery for NRAS-Mutant Melanoma: Leveraging Advanced Preclinical Co-Culture

Supervisor(s) name: Prof. Dr. Stephanie Kreis

I declare that this thesis:

- is the result of my own work. Any contribution from any other party, and any use of generative artificial intelligence technologies have been duly cited and acknowledged;
- is not substantially the same as any other that I have submitted, and;
- is not being concurrently submitted for a degree, diploma or other qualification at the University of Luxembourg or any other University or similar institution except as specified in the text.

With my signature I furthermore confirm the following:

- I have adhered to the rules set out in the University of Luxembourg's Code of Conduct and the Doctoral Education Agreement, in particular with regard to research integrity.
- I have documented all methods, data, and processes truthfully and fully.
- I have mentioned all the significant contributors to the work.
- I am aware that the work may be screened electronically for originality.

Luxembourg, 28th of March 2025 Cristian Angeli

Acknowledgments

Above all, I wish to extend my heartfelt gratitude to my supervisor, **Prof. Dr. Stephanie Kreis**, for her unwavering guidance, encouragement, and support throughout my research journey. I am deeply thankful for the opportunity she provided me to grow both academically and personally under her supervision. Additionally, I sincerely appreciate her patience, dedication, and willingness to offer valuable feedback and insightful advice. I am especially grateful for the profound lessons she has imparted, which have helped me evolve not only as a future researcher but also as an individual. Her enthusiasm, support as a mentor, and continuous motivation and belief in my work have been truly inspiring and kept me driven throughout my PhD, ultimately leading to the successful completion of this important milestone in my life. Hence, Grazie Mille!

In addition to my thesis supervisor, Prof. Dr. Stephanie Kreis, I would like to extend my gratitude to the members of my dissertation defense committee, **Prof. Dr. Jochen Sven Utikal**, **Prof. Lionel Larue**, **Dr. Bassam Janji**, and **Prof. Dr. Elisabeth Letellier** for kindly agreeing to review and assess my PhD thesis. Moreover, I am also thankful to Prof. Dr. Stephanie Kreis, Prof. Dr. Jochen Sven Utikal, and **Dr. Johannes Meiser** for monitoring my PhD progress and providing valuable feedback throughout my studies.

A huge thank you to all the members of the Signal Transduction Group! First and foremost, I am incredibly grateful to **Dr. Joanna Wroblewska** for her immense support throughout this project. Her expertise and experience have guided my work from the very beginning. Even though we had a few moments of disagreement along the way, she remained exceptionally supportive and provided immeasurable emotional encouragement, which was essential for me to continue my studies. I also want to express my heartfelt gratitude to **Demetra Philippidou**, whose vast experience greatly contributed to the development and completion of this project. Beyond her scientific support, I truly appreciate the fun and joyful moments we shared in the lab. A special thanks go to **Eliane Klein** for her tremendous help in the lab, performing essential experiments for this project, and to **Dr. Christiane Margue** for her kindness, valuable contributions, and insightful reviews of manuscripts and my thesis.

I would like to sincerely thank my colleagues and friends **Daniela "Danielita" Vega Gutierrez**, **Dzeneta "Jennifer" Halilovic**, **Sagarika "Sagaraki" Ghosh**, and **Antonieta "Anto" Bravo Iglesias** for their unwavering support throughout this journey. I am also grateful for all the fun and joyful moments we shared, both inside and outside the lab. But please, no Frappuccino! Finally, my deepest gratitude goes to my former PhD fellows and friends, **Dr. Vincent Gureghian**, **Dr. Jasmine Preis**, and **Dr. Tijana Randic**.

Then, I would like to thank the kind **Catherine Rolvering** who tried to teach me German over the years. Additionally, I would like to thank **Prof. Dr. Iris Behrmann, Dr. Claude Haan, Milène Tetsi, Odile Lecha, Dr. Fabrice Tolle, Dr. Mélanie Kirchmeyer,** and **Dr. Sabrina Brechard.**

Furthermore, I would like to extend my gratitude to our external collaborators. First, I would like to thank **Dr. Meritxell B. Cutrona** and the DMSP platform for conducting the high-throughput drug screening. I also sincerely appreciate Prof. Dr. Jochen Sven Utikal for providing crucial melanoma patient samples and for always being available to answer our clinical questions related to melanoma. Many thanks to **Dr. Anthoula Gaigneaux** for her guidance and support in helping me

navigate the best statistical analyses for my results, as well as to **Dr. Aurélien Ginolhac** for his fantastic explanations of the fascinating world of R.

I would like to express my deepest gratitude to **Prof. Dr. Dagmar Kulms** from the University of Dresden for hosting me in her lab for three incredible months. She gave me the opportunity to learn a variety of new techniques and work on exciting projects. Her expertise, guidance, and inspiring temperament had a profoundly positive impact on my career. Additionally, I am truly grateful to **Prof. Dr. Mitchell Levesque** from the University of Zurich for welcoming me into his outstanding lab and melanoma biobank. His guidance, along with the support of his wonderful team, taught me how to properly work with melanoma patient tumors, an experience that greatly enriched my scientific journey.

I would like to thank Prof. Dr. Stephanie Kreis for funding my PhD position, the MelCol project (FNR), and the Vera Nijs & Jens Erik Rosborg Foundation. Also, I am grateful to Fondation du Pelican to have founded my research visit to Prof. Dr. Mitchell Levesque's Lab.

Lastly, I would like to profoundly thank my girlfriend Silvia, my father Rossano, my mother Vania, my sister Valentina, my acquired brother Riccardo, my best friends Luca and Davide, and my grandmas, uncles, and cousins whom they always believed in my potential and endlessly supported me along each step of my life. **Vi voglio bene!**

Dedications

I want to dedicate this PhD to the most important people in my life: my girlfriend Silvia, my father Rossano, my mother Vania, my sister Valentina, and my acquired brother Riccardo.

A special dedication goes to my beloved grandfathers Franco and Romano who have been the reason I decided to dedicate my life to fighting cancer.

Voglio dedicare questo dottorato alle persone più importanti della mia vita e che mi hanno sempre supportato: la mia fidanzata Silvia, mio padre Rossano, mia madre Vania, mia sorella Valentina, e il mio fratello acquisito Riccardo.

Una dedica speciale va ai miei amati nonni Franco e Romano i quali sono stati il motivo della scelta di dedicare la mia vita alla lotta contro in cancro.

List of abbreviations

ACTH: adrenocorticotropin hormone
AKT: Protein Kinase B or PKB or Ak strain transforming
ALM: acral lentiginous melanoma
ANGPT: Angiopoietin 1
AP-1: Activator protein-1
APC: Adenomatous polyposis coli
ARAF: A-Raf proto-oncogene serine/threonine kinase
AXL: AXL receptor tyrosine kinase
BAP1: BRCA1 Associated Deubiquitinase 1
BCC: basal cell carcinoma
BRAF: V-Raf Murine Sarcoma Viral Oncogene Homolog B
CAF: Cancer-associated fibroblast
CCND1: Cyclin D1
CD28: Cluster of differentiation 28
CD31/PECAM-1: Platelet endothelial cell adhesion molecule
CD4/CD8: Cluster of differentiation 4/8
CD80/CD86: Cluster of differentiation 80/86
CD99: Cluster of differentiation 99
CDK4/6: Cyclin-dependent kinase 4/6
CDKN2A: Cyclin-Dependent Kinase Inhibitor 2A
c-MYC: Cellular myelocytomatosis oncogene
COT: Cancer Osaka thyroid or Mitogen-Activated Protein Kinase Kinase Kinase 8 or MAP3K8
CR: Complete response
CRAF: C-Raf proto-oncogene serine/threonine kinase
CREB: cAMP responsive element binding protein
CSC: Cancer stem cells
CSD: Chronic Sun Damage
CTLA-4: Cytotoxic T-lymphocyte-associated protein 4
DC: Dendritic cells
DCT: Dopachrome tautomerase
DH: Daunorubicin HCl
DOPA: dihydroxyphenylalanine
DQ: dopaquinone
DTP: Drug tolerant persister
DUSP: Dual-specificity phosphatase
ECM: Extracellular matrix
EGFR: Epidermal growth factor receptor
ERK: Extracellular signal-regulated kinase
FAP: Fibroblast Activation Protein
FGF-2: Fibroblast growth factor 2
FSP1: Fibroblast-specific protein 1
GAP: GTPase-activating protein
GEF: Guanine nucleotide exchange factor
GM-CSF: Granulocyte-macrophage colony-stimulating factor
GNA11: Guanine nucleotide-binding protein subunit alpha-11
GNAQ: Guanine nucleotide-binding protein G(q) subunit alpha
GRB2: Growth factor receptor-bound protein 2
HA: Hyaluronic acid

HGFR: Hepatocyte growth factor receptor
HIF: Hypoxia-inducible factor
HSV-1: herpes simplex virus 1
HTS: High throughput screening
IC50: Inhibitory concentration 50
ICAM-1: Intercellular adhesion molecule 1
ICI: Immune Checkpoint Inhibitors
IDO: Indoleamine 2,3-dioxygenase
IGF-1: Insulin growth factor 1
IL: Interleukin
JARID1B: Jumonji/ARID domain-containing protein 1B
JNK: c-Jun amino (N)-terminal kinase
KDM5A: Lysine demethylase 5A
KIT: KIT Proto-Oncogene, Receptor Tyrosine Kinase
LAG-3: Lymphocyte activation gene 3 protein
LMM: lentigo maligna melanoma
LOF: Loss-of-function
MAF: Melanoma-associated fibroblast
MAGE A-3: Melanoma-associated antigen 3
MAPK: Mitogen-Activated Pathway Kinase
MC1R: melanocortin 1 receptor
MDCS: Myeloid-derived suppressor cell
MDM2: Mouse double minute 2 homolog
MEK: Mitogen-activated protein kinase kinase
MHC: Major histocompatibility complex
MITF: microphthalmia-associated transcription factor
MLANA/MART-1: Melanoma antigen recognized by T cells 1
MM: mucosal melanoma
MMP: Matrix metalloproteinase
MMS: Melanoma multicomponent spheroid
MRD: Minimal residual disease
mTOR: Mammalian target of rapamycin
NEC: Normal endothelial cell
NF1: Neurofibromin 1
NM: nodular melanoma
Non-CSD: non-chronic sun damage
NRAS: Neuroblastoma RAS viral oncogene homolog
NSCS: Neural Crest Stem Cells
NY-ESO-1: New York esophageal squamous cell carcinoma 1
OS: Overall Survival
PAX3: Paired Box 3
PD1/PD-L1: Programmed cell death protein 1/ Programmed death-ligand 1
PDGFR: Platelet-derived growth factor receptor
PDK1: Phosphoinositide-dependent kinase 1
PEG: Polyethylene glycol
PFS: Progression-Free Survival
PI3K: Phosphoinositide 3-kinase
PIP2: Phosphatidylinositol 4,5-bisphosphate
PIP3: Phosphatidylinositol (3,4,5)-trisphosphate
PKA: protein kinase A
PMEL: Premelanosome protein

POMC: proopiomelanocortin
POT1: Protection of telomeres protein 1
PP: Pyrvinium pamoate
PTEN: Phosphatase and tensin homolog
PTPN11: Protein tyrosine phosphatase non-receptor type 11
RAC1: Ras-related C3 botulinum toxin substrate 1
RASGRF10: Ras-specific guanine nucleotide-releasing factor 1
RGD: Arginyl-glycyl-aspartic acid
RGP: Radial Growth Phase
ROS: Reactive Oxygen Species
RTK: Receptor Tyrosinase Kinase
S6: Ribosomal protein S6
SCC: squamous cell carcinoma
SCF: stem cell factor
SHIP 1/2: Phosphatidylinositol-3,4,5-trisphosphate 5-phosphatase
SOS1: Son of sevenless homolog 1
SOX10: SRY-Box Transcription Factor 10
SSM: superficial spreading melanoma
T: Trametinib
TAM: Tumor-associated macrophage
TEC: Tumor endothelial cell
TERT: Telomerase reverse transcriptase
TGF-β: Transforming growth factor beta
TIM-3: T-cell immunoglobulin and mucin domain 3
TMB: Tumor mutational burden
TME: Tumor microenvironment
TOP1: Topoisomerase I
TOP2: Topoisomerase II
TP53: Tumor protein P53
TPTE: Putative tyrosine-protein phosphatase
T-VEC: Talimogene laherparepvec
TYR: tyrosinase
TYRP1/2: tyrosinase-related protein 1 and 2
UV: uveal melanoma
UVR: Ultraviolet Ray
VCAM-1: Vascular cell adhesion protein 1
VEGF: Vascular endothelial growth factor
VGP: Vertical Growth Phase
α-MSH: Alpha-melanocyte stimulating hormone
α-SMA: Alpha smooth muscle actin
γH2AX: Phosphorylated histone H2AX

List of Publications

1. **Cristian Angeli**, Joanna Patrycja Wroblewska, Demetra Philippidou, Eliane Klein, Sagarika Ghosh, Fizza Irfran, Christiane Margue, Bruno Santos, Meritxell Cutrona, Stephanie Kreis: High-throughput screening of advanced multicomponent pre-clinical 3D melanoma models identify potential first-line targeted therapies for NRAS mutant melanoma, **in preparation**. **Cell Death&Disease**. (Submission before defence in March)

2. **Cristian Angeli**, Joanna Patrycja Wroblewska, Eliane Klein, Christiane Margue, and Stephanie Kreis; Protocol to generate scaffold-free, multicomponent 3D melanoma spheroid models for preclinical drug testing; **STARprotocols (CellPress)**, 2024, DOI: 10.1016/j.xpro.2024.103058.

3. Luise Dunsche, Nikita Ivanisenko, Shamala Riemann, Sebastian Schindler, Stefan Beissert, **Cristian Angeli**, Stephanie Kreis, Mahvash Tavassoli, Inna Lavrik and Dagmar Kulms; **Cell Death and Disease**; 2023, DOI: 10.1038/s41419-023-06360-4.

4. Vincent Gureghian, Hailee Herbst, Ines Kozar, Katarina Mihajlovic, Noël Malod-Dognin, Gaia Ceddia, **Cristian Angeli**, Christiane Margue, Tijana Randic, Demetra Philippidou, Milène Tetsi Nomigni, Ahmed Hemedan, Leon-Charles Tranchevent, Joseph Longworth, Mark Bauer, Apurva Badkas, Anthoula Gaigneaux, Arnaud Muller, Marek Ostaszewski, Fabrice Tolle, NatašaPržulj, and Stephanie Kreis; A multi-omics integrative approach unravels novel genes and pathways associated with senescence escape after targeted therapy in NRAS mutant melanoma; **Cancer Gene Therapy**; 2023, DOI: 10.1038/s41417-023-00640-z.

Several Figures from publications 1. and 2. are shown in this thesis.

Contribution by others

The following figures contain data that were generated by or with the contribution of the following people:

- Dr. Joanna Wroblewska, postdoc, (DLSM) generated the data presented in Figures 38 B, 57, and 64;
- Eliane Klein, R&D specialist, (DLSM) generated the data presented in Figures 34, 36, 37, and Suppl. Fig. 8; and contributed to generating the data presented in Figures 55, 59 B-E, and 60;
- Demetra Philippidou, research support engineer, (DLSM) generated the data presented in Figures 54 E-G and 59 A; contributed to generating the data presented in Figure 62; and developed the blots (western blots) in Figure 58 and Suppl. Figure 9;
- Sagarika Ghosh, PhD student (DLSM): contributed to the generation of Figure 58 B-D, Fig. 58 F-H, Suppl. Figure 9 B-D and F-H ;
- Dr. Christiane Margue, research scientist, (DLSM) generated the data presented in Figure 59 A;
- Fizza Irfran (former Master's student): Co-supervised by me, she supported the visual inspection of the HTS spheroid pictures and literature research of the selected hit drugs listed in Table 3.
- Dr. Bruno Santos, postdoc, (LCSB, LIH) generated the data presented in Figures 48 and 49, and the high-throughput screening and DRCs data using the DMSP platform (LCSB, LIH);
- ChatGPT was solely used to edit text passages written by me to correct for grammar and spelling mistakes and to improve the readability of the text. AI tools were not used to generate original content in any way.

Abstract

Significant therapeutic advancements have been achieved in the treatment of advanced $BRAF^{mut}$ melanoma through the approval of combined targeted therapies (BRAFi+MEKi) and immunotherapies (anti-PD1/PD-L1 and anti-CTLA4). However, patients with $NRAS^{mut}$ and wild-type (WT) melanoma continue to face limited therapeutic options, relying on immune checkpoint inhibitors and off-label treatments such as MEKi, with over 50% experiencing disease progression due to primary and acquired resistance. A critical challenge in developing effective therapies lies in the limitations of conventional pre-clinical models, which fail to adequately replicate the physiological complexity of the tumor microenvironment (TME). This doctoral thesis addresses these gaps through the development of advanced multicomponent 3D melanoma models and their application in the evaluation of compound efficacy identified by 3D high-throughput drug screening.

Advanced *in vitro* 3D melanoma models were established, incorporating co-cultures of melanoma cells with endothelial cells and fibroblasts, simulating the metastatic niches of skin, lung, and liver. 3D models were also integrated into a 3D high-throughput drug screening platform, enabling the evaluation of over 1300 compounds in $NRAS^{mut}$ and WT melanoma spheroids. Promising hits were identified and two compounds, Daunorubicin HCl and Pyrvinium pamoate, underwent detailed validation. Both compounds demonstrated potent anti-melanoma activity in advanced 3D co-culture models and zebrafish *in vivo* models, with Pyrvinium pamoate notably having cytotoxic effects in $NRAS^{mut}$ melanoma cells. Comparative studies revealed Pyrvinium pamoate's superior efficacy over Trametinib, the standard MEKi used off-label or for disease control in clinics for $NRAS^{mut}$ melanoma, particularly in 3D models. Furthermore, combinatory treatments with Trametinib showed additive effects on cell proliferation and viability, while both compounds exhibited substantial efficacy in MEKi-resistant $NRAS^{mut}$ and WT melanoma cell lines.

In conclusion, this thesis presents a robust pipeline for pre-clinical melanoma drug evaluation through physiologically relevant 3D models, addressing critical challenges in the development of effective first-line therapies for $NRAS^{mut}$ and WT melanoma. These findings highlight a potential interest in Pyrvinium pamoate as a first-line therapeutic candidate for the treatment of $NRAS^{mut}$ melanoma patients.

Table of Contents

1. Introduction

1.1. Melanoma

1.1.1. Etiology

Melanoma arises from the malignant transformation of melanocytes, cells physiologically programmed to produce melanin. Cutaneous melanoma is an aggressive type of skin cancer that accounts for thousands of deaths every year with an increasing number of cases mostly in Caucasians (1,2). An important risk factor for skin cancer is exposure to UV radiation, especially UV-B which is also the main cause of photoaging (3). Moreover, another important risk factor for melanoma is the number of melanocytic nevi. In this regard, although melanoma arises sporadically from healthy skin in 70 % of the cases, approximately 30 % develop from pre-existing nevi (4). Mutations and inherited factors such as a CDKN2A gene mutation account for 5% to 10% of melanoma (5). During the initial phase of illness, melanoma development is marked by a radial growth phase (RGP). As the disease advances, malignant melanocytes transition to the vertical growth phase (VGP), penetrate through the basement membrane into the dermis and subcutaneous tissue, and ultimately infiltrate lymph nodes and blood vessels, leading to metastasis formation (6–8) (Fig. 1).

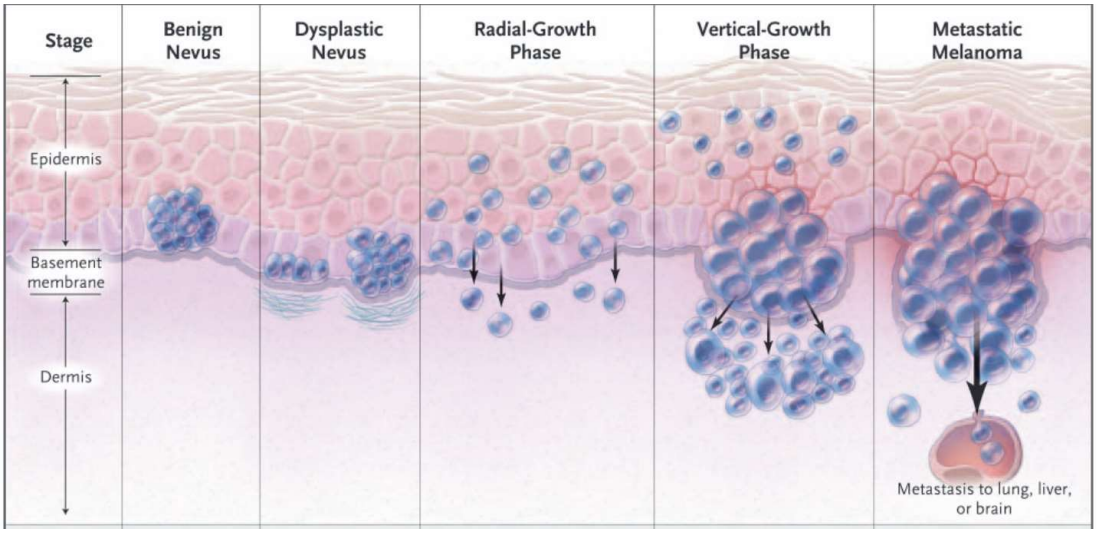

Figure 1: Representation of melanoma progression underlining important melanoma progression phases as radial growth phase (RGP), vertical growth phase (VGP) and metastatic event *(Arlo J. Miller & Martin C. Mihm, 2006)*

Constitutive activation of the MAPK pathway is the major driver of melanoma cell proliferation and survival, due to mutations in key proteins such as BRAF and NRAS. Cutaneous melanoma is classified into chronic (CSD) and non-chronic sun damage (non-CSD). The BRAF V600E mutations

usually occurs on proximal extremities and the trunk in younger individuals (<55 years old), while NRAS mutations of the head and neck region occur in older patients (9) (Fig. 2).

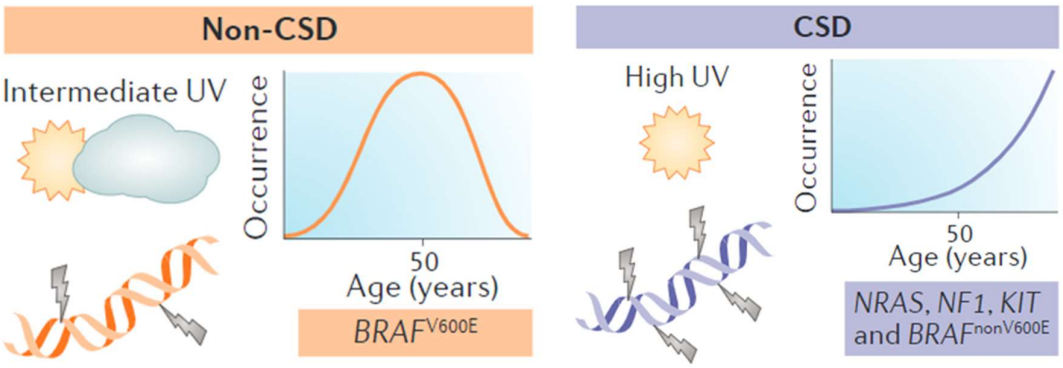

Figure 2: CSD and non-CSD melanoma characteristics. Non-CSD melanoma originates from intermediate UV exposure, has a higher occurrence in younger subjects, and bears BRAF V600E mutations. CSD melanoma originates from high UV ray exposure, has a higher occurrence in older subjects, and bears NRAS and other non-BRAF V600E mutations *(Shain & Bastian, 2016, modified)*

1.1.2. Melanoma precursor cells: Melanocytes

The melanocytic lineage originates from neural crest stem cells (NSCSs), which during embryonic development delaminate from the neural tube through a migration process called epithelial-to-mesenchymal transition (10,11). Afterward, NCSCs start to differentiate into melanoblasts, which are the precursors of melanocytes (11). Melanocytes are slow-dividing cells (12) and their differentiation is mainly driven by the master transcription factor microphthalmia-associated transcription factor (MITF) whose activation is synergistically sustained by two other important transcription factors: Paired Box 3 (PAX3) and SRY-Box Transcription Factor 10 (SOX10) (10). Melanocytes are located in the skin in the stratum basale of the epidermis, but they are also present in other anatomical locations such as mucosal membranes and the middle layer of the uvea (13).

The main role of melanocytes is to provide photoprotection to the skin against UV radiation via the production of the pigment melanin (14). UVB directly binds to the DNA, inducing damage (in the form of the characteristic UVR fingerprint mutation, which is a C->T substitution at dypirimidine sites while UVA indirectly induces DNA damage (mainly DNA single-strand breaks) through the production of reactive oxygen species (ROS), such as hydrogen peroxide and singlet oxygen (15). Melanin production is induced by paracrine and autocrine hormonal signaling through a

communication network between melanocytes, keratinocytes, and Langerhans cells (each basal layer melanocyte is connected to about 36 keratinocytes and 1 Langerhans cell).

Melanin synthesis takes place in specialized organelles called melanosomes (16), which are transferred from melanocytes to keratinocytes through filopodia and nanotubule fusion (17). Two main types of melanin are produced: brown/dark eumelanin and yellow/red pheomelanin. Both melanin types arise from the enzymatic transformation of tyrosine into the intermediate dihydroxyphenylalanine (DOPA) and dopaquinone (DQ) (Fig. 3).

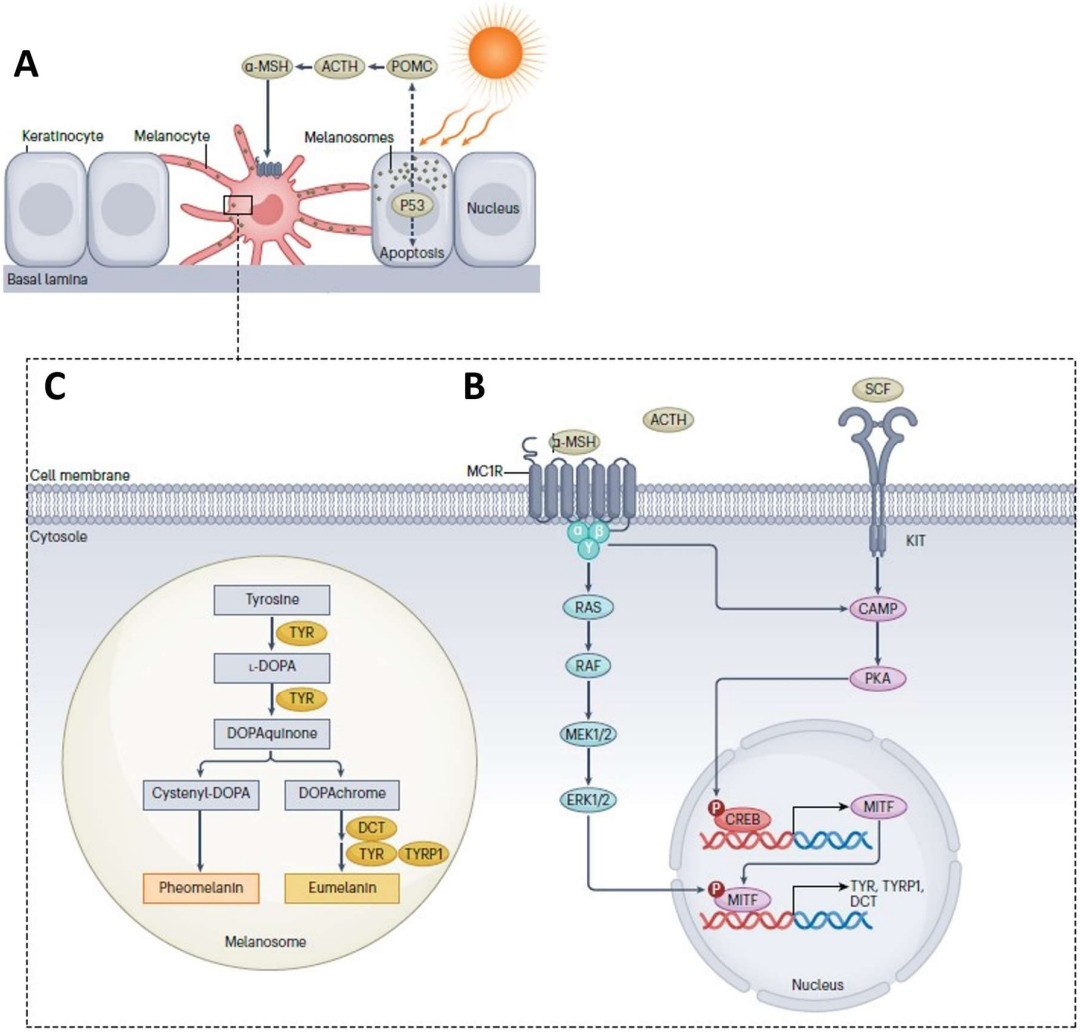

Figure 3: Molecular processes of induction of melanin production. A) UV rays stimulate keratinocytes to produce α-MSH in a p53-dependent manner. B) α-MSH binds to the MC1R receptor on melanocytes and triggers the MAPK pathway. Moreover, SCF binds to the KIT receptor by activating PKA. ERK1/2 and PKA phosphorylate CREB and MITF, stimulating the transcription of key targets for melanin production. C) Enzymatic cascade utilizes Tyrosinase as the main substrate to produce two types of melanin (eumelanin and pheomelanin) passing through intermediate substrates such as DOPA and DOPAquinone. (1)

1.1.3. Classification and Staging

Cutaneous melanoma (CM) has been historically classified by Dr. Wallace Clark (and further updated in 2006 by the WHO) based on its histopathological features, in four major subtypes: superficial spreading (SSM), nodular (NM), acral lentiginous (ALM), lentigo maligna (LM) (18,19). Following the work of Bastian in 2014 (20), this classification was further updated in 2018 ("blue book"), to include the degree of cumulative sun damage (CSD).

Superficial spreading melanoma (SSM) (Fig. 4A) is the most common type of CM and occurs in younger individuals (18). It accounts for almost 70% of all melanoma cases and is characterized by extensive intra-epidermal RGD spreading along the skin. This melanoma subtype may emerge spontaneously or in pre-existing nevi, and it is commonly linked to sun-exposed skin, frequently appearing in areas such as the back, trunk, or extremities. The lesions undergo an initial flat phase, exhibiting alterations in size, shape or color (21,22). The BRAF V600E mutation is commonly found in SSM, which is also associated with a high mutational burden and a strong UV mutation signature (23).

Nodular melanoma (NM) comprises 15% of all melanomas. (Fig. 4B) It frequently exhibits non-pigmented symmetrical nodules which rapidly enlarge and elevate. NM often presents BRAF mutations, and it tends to occur more frequently in the elderly, especially in men and in the in the head and neck region. Moreover, this subtype has a remarkable VGP (20,21,24).

Lentigo maligna melanoma (LMM) (Fig. 4C) also accounts for ~15% of CM, and it is prevalently observed in elderly individuals and in outdoor workers underlining the strong association of LMM with prolonged sun exposure. Clinically, it presents as large and flat structures with dark color and uneven borders. Histologically, LMM is characterized by the proliferation of cells situated in the basal layers of the epidermis (25,26). Genetically, LMM presents mutations in BRAF (non-V600E), NF1, NRAS and, less frequently, KIT (23).

Acral lentiginous melanoma (ALM) (Fig. 4D) accounts for 5% of all melanomas and is often recognized for appearing in areas not exposed to the sun, primarily localizing on glabrous skin such as palms and soles. Higher incidence is identified in elderly individuals and in particular in females (26). Usually, as a depigmented spot extends over the course of several years before initiating VGP (27). ALM frequently exhibits multiple amplifications of genes, including CCND1, KIT, and TERT, while BRAF and NRAS mutations are rare (only in 10-15% of AML cases) (23).

Further aggressive melanoma subtypes have been reported with low frequency (rare subtypes), such as **uveal melanoma** (UV) (Fig. 4F) (28), frequently mutated in guanine-nucleotide proteins GNAQ and GNA11 (29), and **mucosal melanoma** (MM) (Fig. 4E) which arises from mucosal body sites (23) with mutations in the tumor suppressor PTEN and in KIT, CCND1 and CDK4 (29). A**melanotic melanoma** is characterized by the absence of or minimal pigmentation (30).

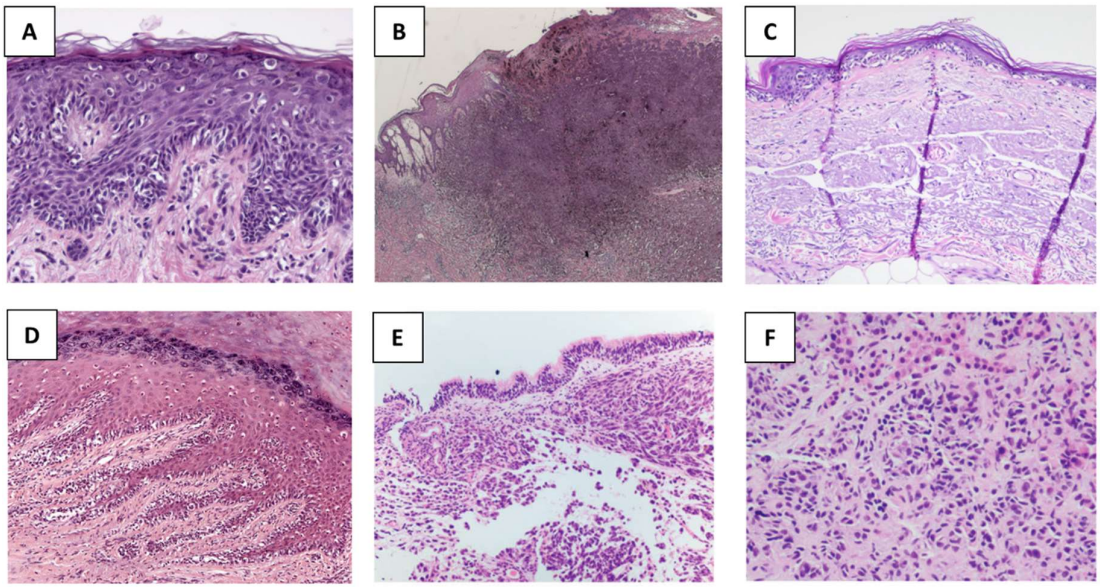

Figure 4: Histology sections of the different malignant melanoma subtypes. A) Superficial spreading melanoma (SSM); B) Nodular melanoma (NM); C) Lentigo maligna melanoma (LMM); D) Acral lentiginous melanoma (ALM); E) Mucosal melanoma (MM); F) Uveal melanoma (UM). Figure created from (23,29)

Early melanoma detection is crucial for patient survival, suspicious pigmented lesions are analyzed using the **"ABCDE"** concept: asymmetry (A), border irregularities (B), colour heterogeneity (C), diameter (D), and (E) evolution of the lesion's growth (31,32). The 8th edition of the American Joint Committee on Cancer (AJCC) serves as a widely used international manual for staging melanoma. The **TNM staging system** comprises three categories: primary tumor (T) based on Breslow tumor thickness, regional lymph node involvement (N), and the presence of distant metastasis (M) (31,33).

According to the TNM system, melanoma is classified in five stages (0, I, II, III, and IV) further subclassified based on the severity (I A/B, II A/B/C, III A/B/C). Stage 0 is also called melanoma *in situ* in which cancer cells only grow in the epidermis with no dermis invasion. In stage I, melanoma cells remain confined to the epidermis but have reached a thickness of around 2mm.

By stage II, the melanoma extends to both the epidermis and dermis, with a thickness of approximately 4mm. In stage III, malignant cells have infiltrated deeper layers of the skin, and they are found in lymph nodes (34). Finally, stage IV melanoma has disseminated and formed metastases in distant organs such as liver, lung, and brain (34,35) .

1.1.4. Prognosis

Among the different aspects that influence the survival of melanoma patients, the two main features are the stage at diagnosis and, as melanoma has a great ability to disseminate, the organ to which it metastasized. Melanoma has a 5-year OS (overall survival) of 99% for patients diagnosed at stage I-II, 68% at stage III while it dramatically drops to less than 30% at stage IV (36). Melanomas metastasize to different organs where the main sites are skin, lung, lymph nodes, brain, and liver. Stage IV patients with skin and lymph node metastasis experience an OS at 5 years of about 23%, while it is lower for patients with lung (17%), brain, and liver metastasis (less than 10% each) (37). Furthermore, metastatic melanoma patients with high levels of LDH (lactate dehydrogenase) have significantly lower OS (38).

1.1.5. Melanoma Epidemiology

Overall, CM continues to be a tumor with a high societal impact due to its growing incidence (39). Worldwide, melanoma ranked 17th for incidence and 22nd for mortality in 2022 and accounted for 3.2% of all cancers diagnosed and 0.53% of all cancer-related deaths, whereas other non-melanoma skin cancers, such as squamous cell carcinoma (SCC) and basal cell carcinoma (BCC), accounted for 10.4% and 0.59% of all cancers diagnosed, respectively (40,41). The age-standardized incidence for males and females shows a rate of 3.8/100,000 and 3.0/100,000, while the mortality sees a rate of 0.7/100,000 and 0.4/100,000, respectively. The highest incidence of melanoma is recorded in regions of the world with high UV radiation combined with mostly White and/or Caucasian populations, such as in Australia, New Zeland, and Northen Europe (36) (Fig. 5).

In Europe, almost 20,000 people per year die with a huge disparity between the West and East, where the East sees higher mortality (39,42). In Luxembourg, in 2022, melanoma ranked 5th for incidence and 17th for mortality among all cancers (43).

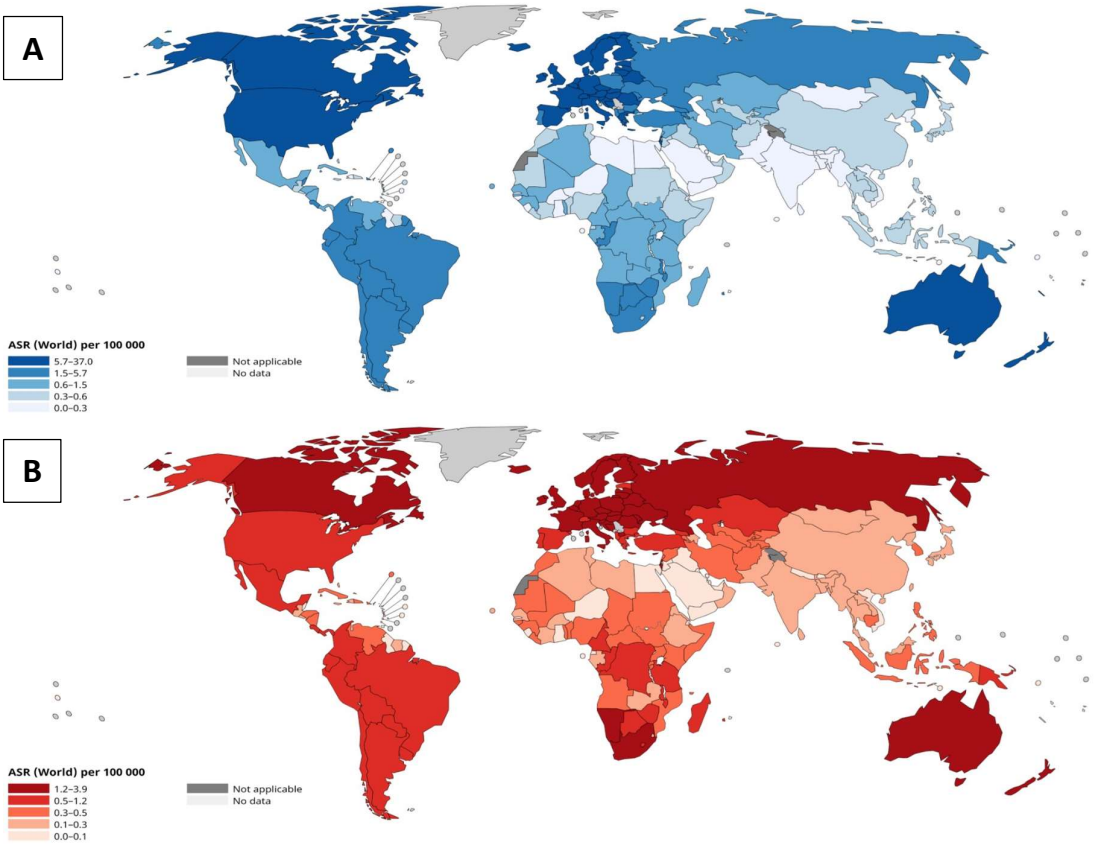

Figure 5: A) incidence and B) mortality of melanoma in different countries. Females and males are together, and age-standardized *(Globocan. 2022)*.

1.2. Genomic subtypes and pathways involved in melanoma development.

1.2.1. The MAPK pathway

The mitogen-activated protein kinase (MAPK) pathway, also referred to as the Ras/Raf/MEK/ERK pathway, is a signaling cascade responsible for transmitting signals from the cell membrane to the nucleus through successive phosphorylation events. This pathway encompasses a family of serine/threonine kinases, known as MAPK, which play roles in regulating cell growth, differentiation and apoptosis (44–46). Enzyme activity within this pathway is initiated by the activation of membrane receptors, mainly receptor tyrosine kinases (RTK), prompted by ligand binding-induced conformational changes. These changes facilitate interactions between the receptor and intracellular adaptor proteins (such as Shc, GRB2 and others), which then engage with guanine nucleotide exchange factors (such as SOS) to relay signals to small GTP-binding proteins (such as RAS) (47).

Subsequently, activated RAS triggers RAF (also called MAPKinase-Kinase-Kinase or MAPKKK), the initial intracellular kinase in the cascade, which includes the different RAF isoforms, ARAF, BRAF, and CRAF. Once activated, RAF phosphorylates MEK (also called MAPKinase-Kinase or MAPKK), leading to the activation of extracellular signal-regulated kinase (ERK or MAPK) (48). Moreover, MEK phosphorylates other important MAPKs: p38 and c-Jun amino (N)-terminal kinases 1/2 (JNK), which are important kinases involved in the control of differentiation, proliferation, and apoptosis (49). ERK 1/2, once activated, has the ability to phosphorylate various nuclear and cytoplasmatic substrates involved in proliferation and differentiation. These substrates include effectors essential for cell cycle progression such as CCND1 (cyclin D1) and the cellular master regulator of cell cycle entry and proliferative metabolism (c-MYC) as well as inhibitors that downregulate MAPK pathway signaling such as dual specificity phosphatase (DUSP) (50,51). The signaling pathway's complexity is exemplified by the existence of multiple isoforms of RAS, RAF, MEK and ERK and alterations at different points in the pathway can result in uncontrolled cell growth and proliferation, contributing to the development of various cancers, including melanoma. In melanoma, the MAPK pathway undergoes significant deregulation, with mutations in genes encoding key players resulting in its constitutive activation independent of external signals (52,53) (Fig. 6).

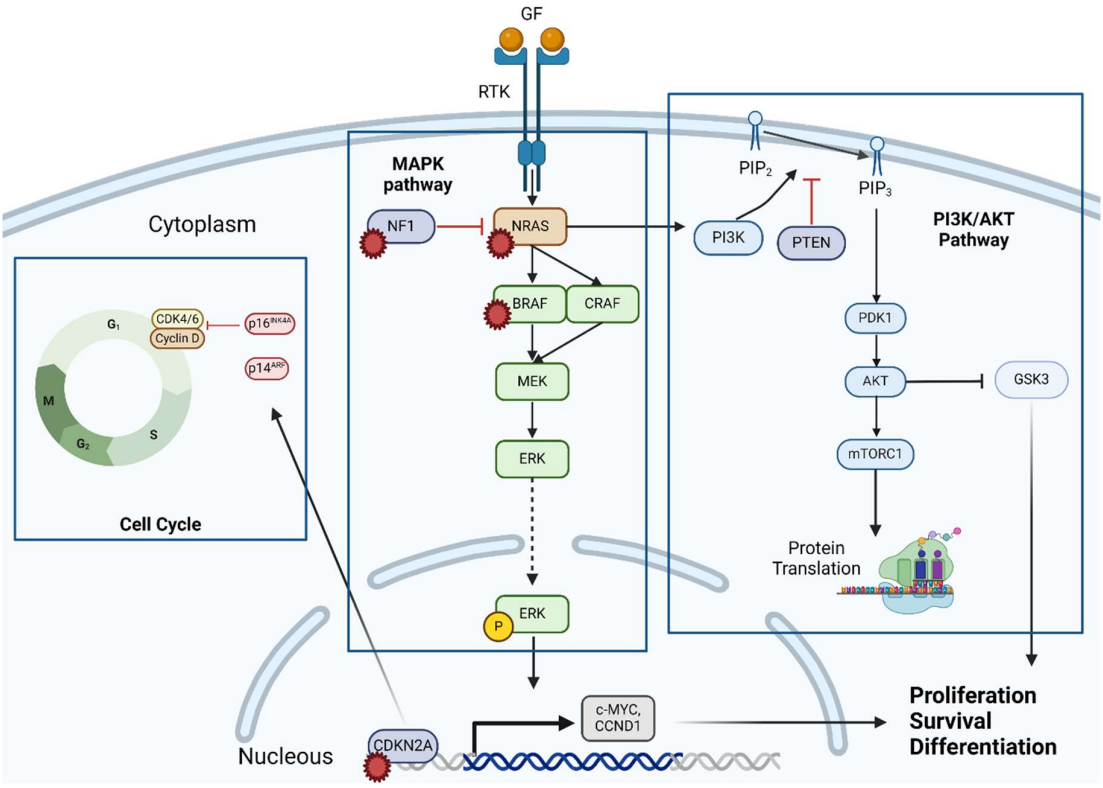

Figure 6: Key pathways involved in melanoma proliferation, survival, and differentiation. From the left, the first panel represents the cell cycle and important interphase checkpoint modulators such as CDK4/6 and cyclin D. Familiar melanoma often bears a CDKN2A gene deletion, leading to a lack of expression of the important cell cycle inhibitors p16 and p14. The central panel represents the most deregulated pathway in melanoma: the MAPK pathway. On the right the PI3K/AKT signaling pathway, involved in protein translation regulation and metabolism through mTOR complex 1 and GSK3, is depicted. Red stars indicate main mutated proteins in melanoma.. (Figure created using Biorender.com).

The pathway's importance for melanoma is underscored by the genomic classification introduced by Akbani R. et al in 2015 in which the analysis of hundreds of patient data stored in The Cancer Genome Atlas (TCGA) have identified four distinct melanoma genomic subtypes: BRAF-mutant melanoma (mutation presents in ~50% of patients), NRAS-mutant melanoma (~25% of patients), NF1-mutant melanoma (occurring in about 15% of the cases), and the triple-wild type (WT) melanoma (with lack hotspot mutations in BRAF, NRAS and NF1 genes) (54) (Fig. 7).

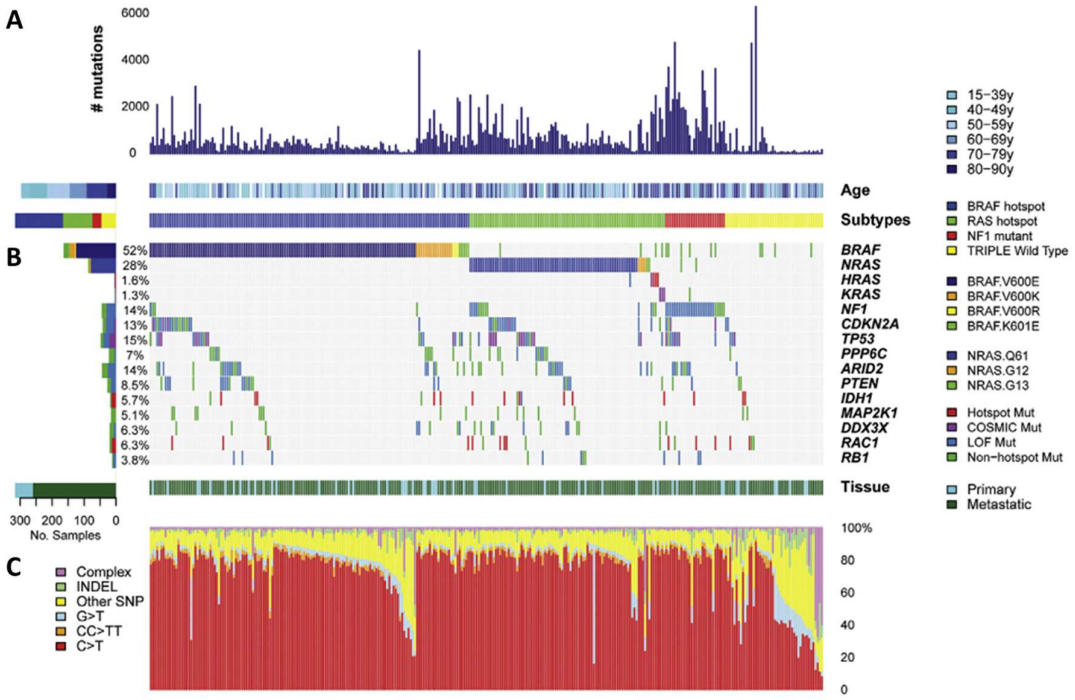

Figure 7: Landscape of driver mutations in melanoma. Identification of the four genomic subtypes in melanoma: mutant BRAF, NRAS, NF1, and triple wild type (WT). A) Plot showing the number of mutations, age at melanoma excision, and associated genomic subtype. B) Color-coded matrix reporting individual mutations and sample type (primary or metastatic). C) Waterfall plot representing the mutation spectra for all samples (Akbani et al., 2015).

1.2.2. The BRAF mutation

As previously described, the V-Raf Murine Sarcoma Viral Oncogene Homolog B (BRAF) gene is frequently mutated in benign nevi and cutaneous melanoma, driving the constitutive activation of the MAPK pathway resulting in increased melanoma cell proliferation. The BRAF gene, located on chromosome 7q34, is a proto-oncogene encoding a 766 amino acids cytoplasmatic serine/threonine kinase responsible for transmitting mitogenic signals from the cell membrane to the nucleus (55,56). Numerous mutations in BRAF have been identified in melanoma, with the majority occurring within the P-loop and activation segments of the protein. These mutations are believed to disrupt the inactive conformation, leading to continuous kinase activity and pathway overactivation (56). The most common BRAF mutation is the V600E mutation, localized on exon 11, which results in an aminoacidic substitution of a valine (V) for a glutamic acid (E) (57).

Mutations in the BRAF oncogene are also frequently detected in benign nevi (>80%) (58), suggesting that melanoma cells have acquired additional mutations, which trigger increased proliferative and metastatic features. The most common mutations alongside BRAF, affect TERT and tumor suppressor genes such as CDKN2A, PTEN, and TP53 (59–62) (Fig. 8).

BRAF mutations are present in similar proportions in primary and metastatic melanomas, suggesting that BRAF mutations occur before tumor dissemination and their frequency remains constant during tumor progression (63).

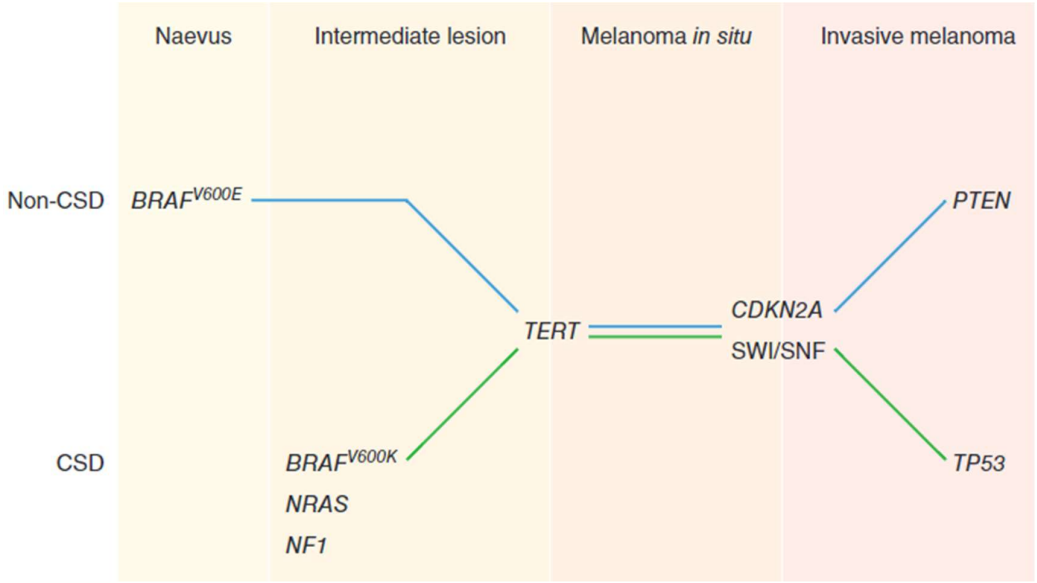

Figure 8: Melanoma progression model. Melanoma cells acquire new mutations during their development. The BRAF V600E mutation by itself is not enough for melanoma development, as this mutation is also found in benign nevi. Hence, melanoma cells need to acquire additional mutations such as in key tumor suppressor proteins such as TERT, CDKN2A, PTEN and or TP53. Moreover, chromatin remodeling complexes as SWI/SNF can be mutated, contributing to melanoma progression (60).

1.2.3. The NRAS mutation

The neuroblastoma ras viral oncogene homolog (NRAS) was initially identified as the first melanoma oncogene in 1984. Presently, mutations in NRAS, KRAS, or HRAS are detected in approximately 25%, 2% and 1% of tested melanoma, respectively (64). The predominant oncogenic alteration observed in over 80% of NRAS mutations involves a point mutation leading to the substitution of glutamine with leucine at position 61 (Q61L), while mutations at positions 12 and 13 occur less frequently.

The NRAS (Q61) mutation disrupts RAS's GTPase activity, keeping it in an active state, while NRAS (G12 or G13) mutations impact the P-loop of the protein, reducing its sensitivity to GTPase-accelerating proteins (Fig. 9) (64–68). Additionally, NRAS mutations are rarely detected in benign melanocytic nevi, except for congenital nevi (64). The presence of NRAS mutations in melanoma carries prognostic significance, with affected patients typically older than 55 years and exhibiting a chronic pattern of UV exposure (CSD) (9).

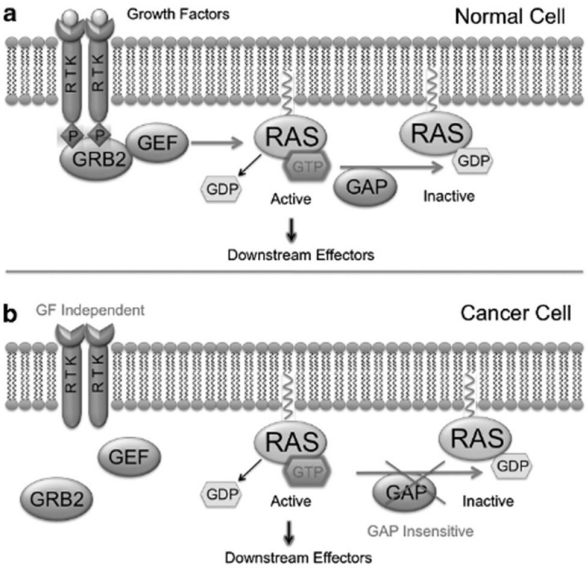

Figure 9: Physiological and constitutive GTPase active status of mutated RAS. A) NRAS-wt oscillates between active (GTP-bound) to inactive (GDP-bound) states in an RTK-dependent way. B) NRAS-mutated remains constitutively bound to GTP (active state) in an RTK-independent way (67)

Physiologically, RAS proteins function as small intracellular GTPases, exhibiting both active (GTP-bound) and inactive (GDP-bound) states in normal human melanocytes (69). Active RAS forms play pivotal roles in various cellular processes including proliferation and survival (70). NRAS activation is triggered by RTK signaling, facilitated by guanine nucleotide exchange factors (GEFs) such as SOS1/2 and RASGRF10, along with adaptor molecules such as growth factor receptor-bound protein 2 (GRB2). Hydrolysis, catalyzed by GTPase-activating proteins (GAPs), leads to RAS reverting to its inactive form. RAS-mediated signaling primarily activates two main pathways: the MAPK and the phosphoinositide-3-kinase (PI3K)/protein kinase B (AKT) cascade (67,70,71). NRAS, particularly in non-malignant cells, strongly binds to BRAF, favoring MAPK pathway activation over other RAF isoforms like CRAF, culminating in ERK1/2 phosphorylation that, after its nuclear translocation, regulates numerous transcription factors such as AP-1, which in turn, induce the expression of cyclin D, inducing the cell cycle transition from G1 to S phase (67,72) (Fig. 6). Additionally, RAS activates the PI3K/AKT pathway, which also plays a role in cell cycle progression, survival, and metabolic processes.

In melanoma, mutated NRAS activates the MAPK pathway primarily through CRAF rather than BRAF, and the PI3K/AKT/mTOR pathway through PI3K phosphorylation. The intersection between these two pathways is carried by the phosphorylation of the ribosomal protein S6, which in turn increases the expression of cyclin D1 (69).

While early detection and surgical excision of cutaneous melanoma enhances patient survival rates, managing metastatic melanoma still poses significant challenges, often leading to a bleak prognosis for many patients (32,73). Compared to BRAF-mutant or triple wt subtypes, NRAS-mutant melanomas exhibit a more aggressive nature, contributing to a reduced median OS (74,75).

1.2.4. Other mutations in melanoma

Cutaneous melanoma presents different other mutations that occur less frequently in key oncogenes and tumor suppressor genes, but that can influence aggressiveness and resistance to treatments, such as mutations of NF1 (classified as the third genomic subtype), CDKN2A, PTEN, TP53, and TERT (76).

NF1 (neurofibromin 1), is a cytoplasmatic protein highly expressed in various cell types, including neurons (77). It acts as a tumor suppressor in the RAS pathway by inhibiting RAS activity as a GTPase-activating protein (GAP), converting active RAS-GTP into inactive RAS-GDP. Mutations in NF1 lead to a loss of loss-of-function of its tumor suppressor ability (78,79). NF1 mutation is particularly prevalent in wt BRAF and NRAS melanomas, especially in older or CSD patients, and

often in combination with mutations in other genes such as PTPN11 (important non receptor protein tyrosine phosphatase), enhancing its role in melanoma genesis (80). The NF1 melanoma genomic subtype has been associated with poorer overall survival (80,81), and loss of NF1 in BRAF V600E mutated melanomas leads to higher RAS-GTP activity and resistance to BRAF inhibitors (82).

The **CDKN2A** gene encodes two protein variants through alternative splicing, namely p16INK4A and p14ARF, both acting as inhibitors of G1/S cell cycle progression through distinct mechanisms. P16INK4A impedes G1 progression by binding to CDK4 and CDK6 (Fig. 6), thus preventing their interaction with cyclin D and the subsequent phosphorylation of Retinoblastoma protein (RB). On the other hand, p14ARF binds to MDM2, which targets p53 for ubiquitination and degradation, indirectly influencing G1 progression (83–85). TCGA data analysis showed that p16 and p14 are inactivated in ~67% and ~27% of melanomas respectively, and almost 40%-70% of melanomas show CDKN2A inactivation (86).

TP53 is a tumor suppressor gene known as the guardian of the genome. It plays a vital role in halting cell division and promoting apoptosis upon DNA damage (87,88). TP53 is the most frequently mutated gene in all human cancers (more than 50%) (89). In melanoma, 10% of cases carry TP53 mutations (90) conferring enhanced resistance to treatment (91). LOF of p53 is typically not observed in early-stage and *in situ* melanomas but tends to occur as a late event in melanoma development (62) (Fig. 8).

The **TERT** gene, responsible for encoding a catalytic subunit of telomerase, plays a crucial role in maintaining telomere length ensuring chromosomal stability (92,93). Many human cancers present mutations in the TERT promoter allowing cancer cells to replicate rapidly and avoiding telomere shortening; work conducted by Huang et al. found that 71% of melanomas analyzed had the TERT promoter mutated (94). TERT promoter mutations in melanoma are associated with increasing metastatic behavior and poor patient outcome. Moreover, it tends to co-occur with BRAF and CDKN2A mutations and in CSD sites (95).

1.2.5. The PI3K/AKT pathway

Under physiological conditions, the PI3K/AKT plays a crucial role in controlling various cellular functions such as proliferation, survival, and metabolism (96). Activation of PI3K by RTKs and RAS proteins triggers the generation of PIP_3 (PI 3,4,5-trisphosphate) from PIP_2 (PI 4,5-bisphosphate), which recruits AKT for phosphorylation by mTOR complex 2 (mTORC2) and PDK1. Activated AKT phosphorylates numerous targets thus inhibiting GSK3 and activating mTOR resulting in the inhibition of apoptosis and stimulating cell proliferation (97,98) (Fig. 6).

Phosphatases such as PTEN and SHIP1/2 counteract PI3K activity by dephosphorylating PIP3, thus negatively regulating AKT activity (99,100).

In melanoma, the PI3K/AKT pathway is activated through various mechanisms, and one of the most common is the mutation and subsequent LOF of PTEN. PTEN is a tumor suppressor gene that encodes a phosphatidyl-inositol-3,4,5-triphosphate 3-phosphatase, which acts as a negative regulator of the PI3K/AKT pathway (101,102). Consequently, the deletion or inactivation of PTEN leads to continuous AKT activation (103,104). PTEN LOF has been observed in various human cancers, and in about 8.5% of melanomas (54) resulting in poorer survival (105). Cooperation between BRAF mutations and PTEN LOF in melanoma development indicates that both MAPK and PI3K/AKT pathways may be necessary for melanoma progression (76,106). Specific mutations in PIK3CA (gene that encodes the catalytic subunit of PI3K) (107), are infrequent in melanoma, with a prevalence of 3%-5%, while mutations in AKT are even rarer (approximately 2%) (96,108).

1.3. Therapeutic options for melanoma

In the past, advanced melanoma had a dismal prognosis and the main therapeutic options were surgical resection and/or chemotherapy. Nowadays, the implementation of targeted therapies and immune checkpoint inhibitors (ICI) have altered the trajectory of the illness, allowing for lasting responses. Moreover, the evolution of novel therapies such as oncolytic viruses and mRNA vaccine-based therapy is enhancing the treatment of advanced melanoma patients. Nevertheless, surgical resection remains the key procedure for early-stage melanoma.

1.3.1. Targeted therapy

The first approved targeted therapy (2011) for advanced melanoma relied on BRAF inhibitor (BRAFi) monotherapy with **Vemurafenib** (PLX4032), which was followed by two other BRAF inhibitors named **Dabrafenib** (GSK2118436) and the second-generation **Encorafenib** (LGX818) (109,110). These therapies demonstrated improved survival outcomes compared to standard chemotherapy in the frontline metastatic setting (111,112). BRAFi monotherapy effectively inhibits the constitutively active BRAF V600 (class I) mutated monomer but fails to prevent signaling of other BRAF mutations (class II and III) and wt BRAF homo- and -heterodimers, leading to paradoxical downstream MAPK pathway activation in non-BRAF-mutated tissues (113). This paradoxical activation can also result from activated RAS mutations or increased RTK signaling. Consequently, BRAFi use has been associated with the development of cutaneous squamous cell

carcinoma (SCC) due to rapid reactivation of the MAPK signaling in wt BRAF cells (114). This adverse event was more prevalent with Vemurafenib than with Dabrafenib or Encorafenib (115). To address paradoxical downstream activations and to target the MAPK pathway more effectively in parallel, BRAFi and MEKi were combined and used to treat BRAF V600 mutated melanoma patients (Fig. 10 A) (113,116–118). The addition of **Cobimetinib** (MEK inhibitor) to Vemurafenib prolonged PFS and OS compared with Vemurafenib alone (coBRIM phase III trial), with a tolerable safety profile and fewer secondary skin tumors (119,120). Similarly, the COMBI-V (NCT01597908) trial showed a significant improvement in OS and PFS with the combination of Dabrafenib and **Trametinib** (MEKi) compared with Vemurafenib as first-line therapy in patients with advanced BRAF-mutated melanomas (121,122). The COLUMBUS trial (NCT01909453) illustrated safety and benefits in terms of OS and PFS with the combination of Encorafenib and **Binimetinib** (MEKi), consistent with other double combinations (123,124) (Fig. 11). BRAFi/MEKi combinations are now considered the standard of care first-line treatment for BRAF V600 mutated melanoma patients, showing prolonged OS with a good safety profile.

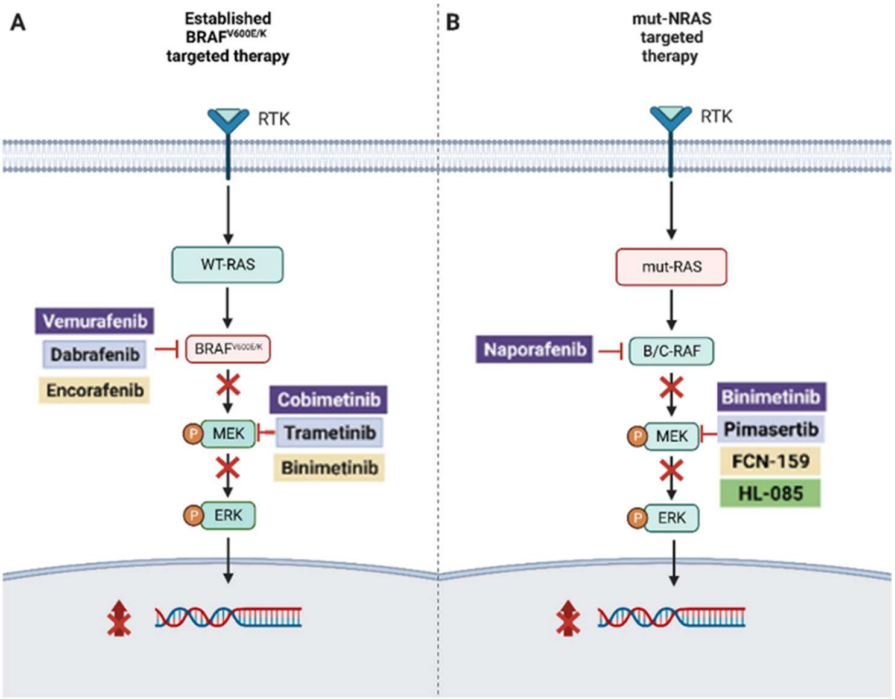

Figure 10: Targeted therapeutic strategies for BRAF V600E/K and NRAS mutated melanoma patients. A) Patients with BRAF V600E/K mutated melanoma have approved combinatorial therapies composed of BRAFi (Vemurafenib, Dabrafenib, and Encorafenib) combined with MEKi (Cobimetinib, Trametinib, and Binimetinib respectively). B) NRAS-mutated melanomas are still therapeutically challenging, and the main targeted therapeutic options are represented by pan-BRAF inhibition (Naporafenib and Belvarafenib) and MEKi using novel and more potent inhibitors. (118).

Efforts to directly target mutant NRAS have faced significant challenges. Due to the difficulty to directly target NRAS, therapeutic strategies for NRAS mutant melanoma have concentrated on inhibiting downstream MAPK pathway signaling (Fig. 10 B). Binimetinib (MEKi) was studied as a therapeutic option for advanced NRAS-mutant melanoma patients in the NEMO trial (NCT01763164). Despite an improvement in PFS, no differences were reported in OS between Binimetinib and dacarbazine (refer to Chapter 1.3.3)-treated patients, showing a non-significant improved efficacy of MEKi in NRAS-mutant patients (125) (Fig. 11). Trametinib (MEKi) is actually used as an off-label inhibitor and is currently only studied in combination with other agents for NRAS-mutant melanoma patients. Non-selective RAF inhibitors, including Naporafenib and Belvarafenib, which bind to both CRAF and BRAF, have shown potential to inhibit signaling downstream on mutated NRAS melanomas. Interesting clinical trials aim to evaluate the effect of these pan-RAF inhibitors in combination with ERKi, MEKi, and CDK4/6i in unresectable melanoma (phase II, NCT04417624) and in NRAS-mutated melanoma patients (phase I b, NCT04835805), respectively. Interestingly, Naporafenib demonstrated encouraging activity when combined with MEKi and ERKi, albeit with significant skin toxicity. MEK 1/2 and ERK 1/2 inhibitors have also been used as monotherapy but have shown limited efficacy in NRAS mutant melanoma patients (118).

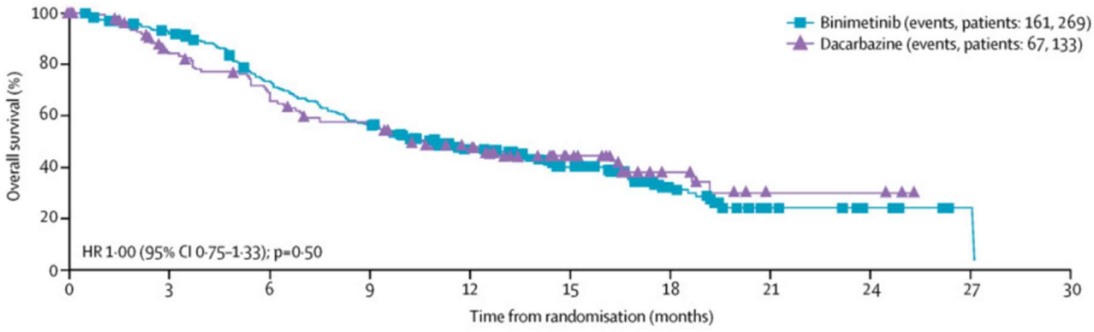

Figure 11: Graph shows the OS of NEMO clinical trial of Binimetinib vs. Dacarbazine in patients with NRAS-mutant melanoma (125).

Despite extensive efforts to explore various therapeutic options and the emergence of immunotherapy (discussed in Chapter 1.3.2), no targeted therapy or combination thereof is currently approved for patients with $NRAS^{mut}$, $NF1^{mut}$, and WT melanoma. Presently, MEK inhibitors are utilized as an off-label treatment for treating these patients, but the outcomes have been limited. Therefore, the development of novel or combinatorial therapies is urgently needed.

1.3.2. Immunotherapy

Apart from the early development of targeted therapies, melanoma has also served as a poster child for the development of immune therapies for cancer treatment. This is partly due to the high mutational burden seen in melanomas, which enhances their immunogenicity and immune cell infiltration into tumors compared to other cancer types. As the tumor progresses, it accumulates numerous genetic and epigenetic alterations, some of which contribute to tumor cell immunogenicity and immune infiltration (Kalaora et al., 2022; Passarelli et al., 2017).

Interferon-α2b was the first FDA-approved adjuvant immune therapy in 1995, showing limited efficacy in reducing disease recurrence and death in high-risk patients. In 1998, interleukin-2 (IL-2) became the first immunotherapy agent approved for advanced metastatic melanoma, albeit limited by significant toxicity and low efficacy (128).

In 2011, the FDA approved the first Cytotoxic T lymphocyte-associated protein **(CTLA-4)** immune checkpoint inhibitor (ICI), **ipilimumab**, for treating advanced metastatic melanoma (129). CTLA-4 is a cell surface receptor similar to CD28, expressed on both regulatory and conventional T cells, and its expression increases after T-cell activation. When it binds to B7 (CD80/86) on dendritic cells, it triggers inhibitory signaling leading to suppression of T-cell functions (Fig. 12 A). CTLA-4 plays a crucial role in immune tolerance, and its inhibition with ipilimumab enhances T cell activation and immune recognition of cancer cells (130–132) (Fig. 12 C). In the first clinical studies, Ipilimumab, in combination with dacarbazine, demonstrated longer OS compared to dacarbazine alone (11.2 vs. 9.1 months) but was associated with a high rate of high-grade adverse events (133).

The programmed cell death protein **(PD-1)** receptor, expressed on lymphocytes, binds to its ligand PD-L1 on tumor cells, also leading to decreased T-cell activity and promoting self-tolerance (Fig. 12 B).

Figure 12: Key mechanisms that regulate immune cell activity. A) In lymph nodes, fundamental steps are required for T-cell priming and activation against specific tumor antigens. First, the interaction between TCR and antigen-MHC complex is associated with co-stimulatory signals mediated by CD28. On the other hand, CTLA-4 binds to CD80/86 providing inhibitory signals that suppress T cells. B) During the effector phase, mostly in the TME, T-cells engage cancer cells through TCR-MHC binding. PD-1 is expressed by T-cells and after the interaction with its ligand PD-L1 expressed in cancer cells, T-cell activity is inhibited. C) Anti-CTLA-4 antibodies and anti-PD-1 antibodies are currently used to block inhibitory T cell signaling, enhancing CD4+ and CD8+ effector cells and inhibiting the activity of immune suppressive cells such as T reg cells (134,135) (Modified).

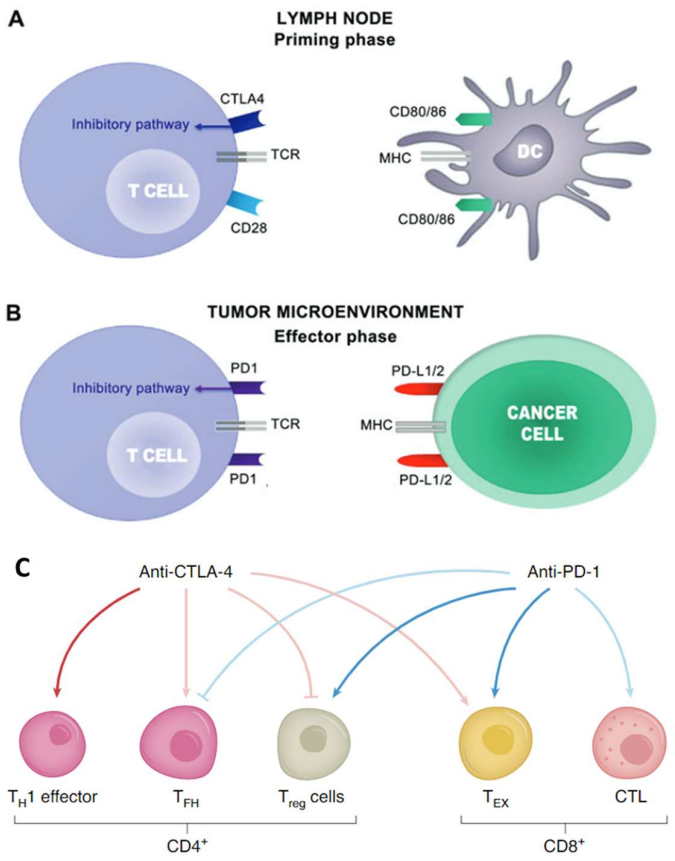

PD-L1 overexpression on tumors, including melanoma, fosters immune evasion; inhibition of PD-1 enables the restoration of a competent immune reaction against cancer cells (135,136) (Fig. 12 C). Two PD-1 inhibitors have been approved: **pembrolizumab and nivolumab**. Pembrolizumab showed improved outcomes compared to ipilimumab with less toxicity (137). Nivolumab also demonstrated superior OS and PFS compared to dacarbazine (138).

The combination of ipilimumab and nivolumab has synergistic effects on the immune response against advanced melanoma, surpassing the efficacy of single agents. This combination received FDA approval based on improved PFS compared to ipilimumab or nivolumab alone (139–141) (Fig. 13).

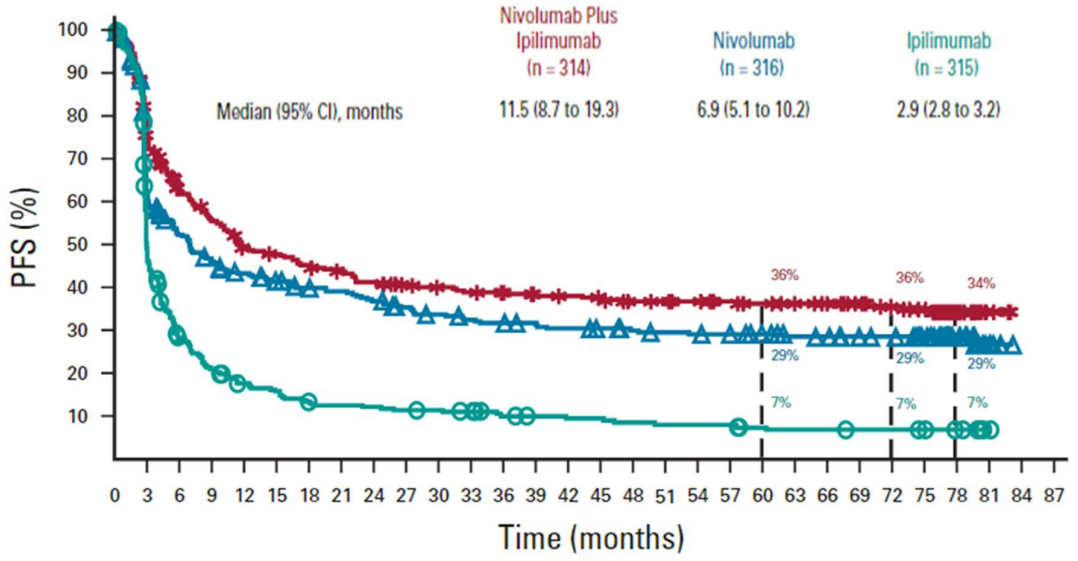

Figure 13: PFS in patients who received combinatorial immune therapy nivolumab plus ipilimumab, versus nivolumab or ipilimumab alone. Patients with combinatorial therapy experienced the longest PFS. OS showed the same trend (Wolchok et al., 2021, modified)

Despite the obvious survival benefits, approximately half of the patients treated with combination ICIs experience high-grade adverse effects (142,143).

Relatlimab, a new ICI approved in 2022, targets lymphocyte-activation gene 3 **(LAG-3)** expressed on T-cells, enhancing T-cell activation and growth. Combinatorial ICI treatment of relatlimab and nivolumab improved PFS compared to nivolumab alone in advanced metastatic melanoma patients (128).

For advanced melanoma patients harboring a targetable BRAF mutation, combined BRAF/MEK inhibitors and ICIs are potential front-line therapies. However, a retrospective analysis suggests a survival benefit for patients when ICI is given first followed by BRAF/MEK inhibitors (142). Furthermore, other therapeutical options have been explored. The IMspire150 clinical trial (NCT02908672) explored the impact of a three-drug combination involving atezolizumab (anti-PD-L1 antibody), vemurafenib (BRAFi), and cobimetinib (MEKi) in advanced BRAF-mutated melanoma. Patients receiving all three agents experienced 15.1 months of PFS compared to 10.6 months in the control group treated with vemurafenib, cobimetinib, and placebo. This triple combination demonstrated superior efficacy, safety, and tolerability as a first-line therapy than previous combination regimens. In 2020, the FDA approved this triple combination for therapeutic use in BRAF V600-mutated melanoma (117,144)

Currently, NRAS-mutant melanoma patients received as first-line therapy the ICIs (anti-PD-1/CTLA-4), unfortunately showing a poorer response compared with wt NRAS patients (116,145,146).

1.3.3. Other therapies

Advanced melanoma therapy has seen major advancements in the last decades thanks to the approval of targeted therapies and immunotherapies with ICIs. Other therapeutic options are available for melanoma patients ranging from "classical" chemotherapy to oncolytic virus therapy and the most recent mRNA vaccines.

Among the chemotherapeutic agents, FDA approved only dacarbazine for the treatment of advanced melanoma patients. **Dacarbazine** is an alkylating agent that works by damaging DNA through the introduction of alkyl groups to guanine bases, leading to cell death. Dacarbazine has a low response rate of about 10% to 20% and a PFS of approximately 3 to 6 months (147)

Talimogene laherparepvec (T-VEC) is a modified herpes simplex virus 1 (HSV-1). The virus infiltrates and reproduces specifically within tumor cells, leading to the breakdown of infected melanoma cells. The release of epitopes attracts antigen-presenting cells and increases the production of granulocyte macrophage-colony-stimulating factor (GMCSF). T-VEC is injected directly into lesions in the skin and lymph nodes close to the lesion in melanoma patients following initial surgery. T-VEC was the first oncolytic viral immunotherapy to receive FDA approval in 2015 for localized treatment of unresectable metastatic stage IIIB/C and IV melanoma (148,149). Interestingly, Ribas et al. demonstrated that the combination of T-VEC and pembrolizumab has a high overall response and complete response rate in some metastatic melanoma patients (150).

mRNA vaccines facilitate antigen presentation by dendritic cells, which take up the vaccine and present the cancer antigens on their surface. This process triggers the activation of cytotoxic CD8+ and helper CD4+ cells, along with an increase in the release of inflammatory mediators. This approach shows promise in delivering genetic information to immune cells without disrupting the structure of nuclear DNA or permanently altering cellular protein expression, as mRNA does not enter the cell nucleus, thereby reducing the risk of harmful mutations. The development of lipid nanoparticles as mRNA carriers has enabled the safe transportation of mRNA into the cytoplasm, where they remain stable and undergo endocytosis without affecting the functionality of the loaded mRNA. The discovery of neoantigens is a key step for the development of effective personalized mRNA vaccines against melanoma (151,152).

Melanoma neoantigens such as NY-ESO-1, Tyrosinase, MAGE A-3 and TPTE (153) are used in several clinical trials where mRNA vaccines are administered to patients with advanced melanoma. An interesting phase IIb clinical trial (NCT03897881) shows increased recurrence-free survival in patients receiving combination of pembrolizumab and mRNA vaccine compared to pembrolizumab alone (154)

With the development of targeted and immune therapies, melanoma patients experience a dramatic survival improvement and enhanced quality of life. Moreover, combinatorial therapies and novel technologies such as personalized mRNA vaccines aim to foster melanoma patients' prognosis. Despite these major efforts, a relevant fraction of patients do not respond or tolerate the current treatments, develop resistance after an initial response, or belong to genomic subtypes (such as NRAS-mutated) where there are limited or no treatment options available, posing an important challenge in the field.

1.4. Drug resistance mechanisms in melanoma

The effectiveness of melanoma therapy can be impaired by the occurrence of genetic and epigenetic resistance mechanisms, which are categorized as either intrinsic or acquired (155,156). **Intrinsic or primary resistance** denotes a pre-existing insensitivity to drugs, affecting either the entire cancer cell population or only a subset, which then becomes more prevalent due to natural selection during drug exposure. This often happens due to the absence of the targeted mutation or independence from the inhibited pathway due to alternative active pathways (156,157). Conversely, **acquired resistance** refers to cancer cells initially responsive to the drugs but eventually adapting to become resistant. This can occur through a stepwise selection for increasingly resistant cells with a genetically or epigenetically-mediated resistance profile, starting from a pool where some rare cells are already drug-resistant in a stochastic and dynamic manner (157,158). Moreover, increasing evidence indicates that a subset of residual cells called drug-tolerant persister (DTP) cells, which exhibit a reversible phenotype characterized by diminished sensitivity to drugs and reduced cell growth, sustains minimal residual disease (MRD) and could function as a reservoir for resistant cells (159). (Fig. 14)

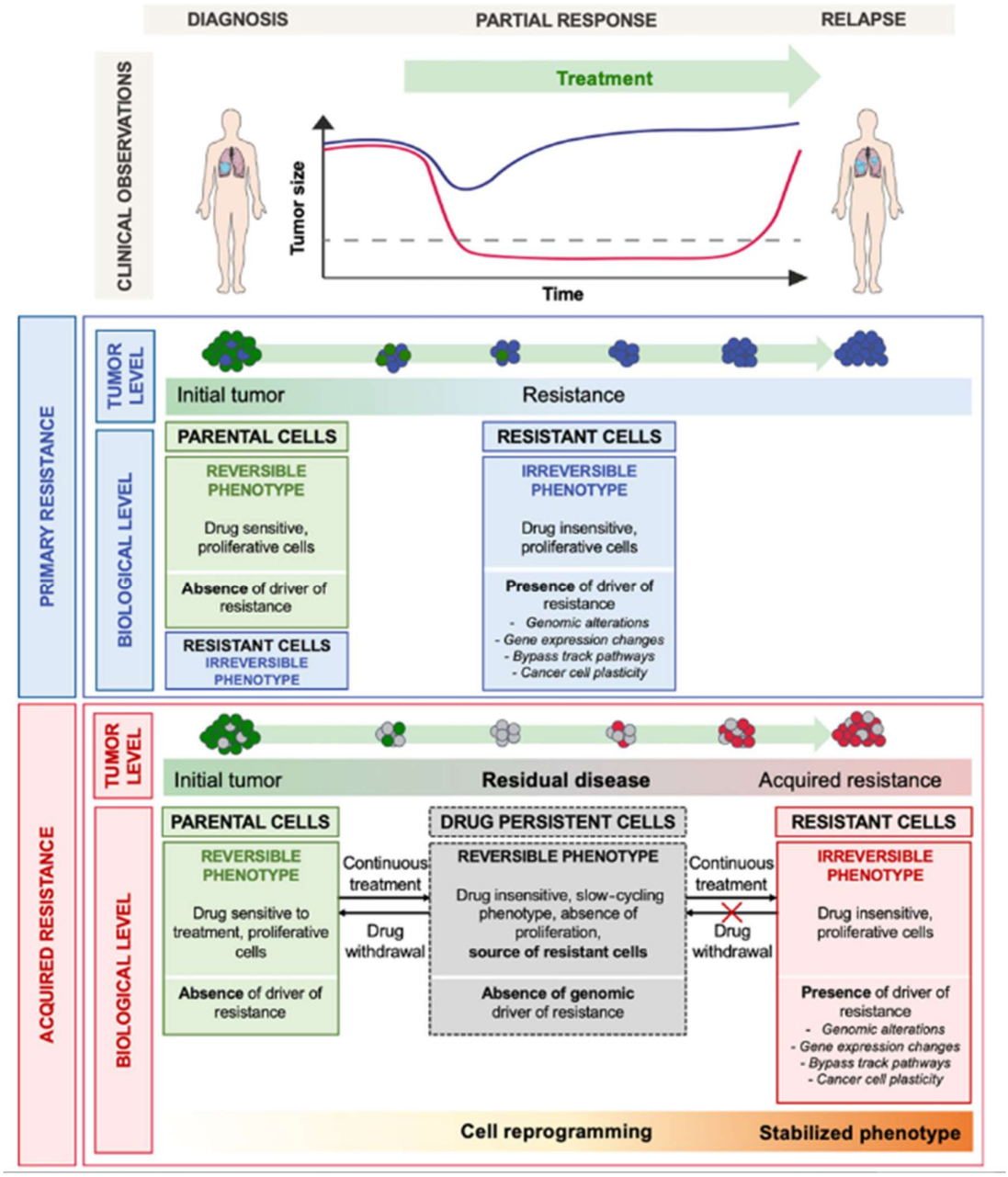

Figure 14: Schematic representation of tumor dynamics in patients after administration of systemic therapy. Primary resistance (blue) presents a fast progression upon treatment, often established by pre-existing resistant clones in the naïve population bearing an irreversible phenotype. Before the development of acquired resistance (red), patients respond to treatment with an effective eradication of sensitive cells, but a reversible subpopulation of cells persists during the treatment (drug persistent cells) establishing minimal residual disease. The fate of persistent cells is decided by the treatment itself. Discontinuation brings to the re-establishment of the initial sensitive population, while continuous treatment leads to an irreversible resistant phenotype. (159)

Although the current therapies have led to a dramatic improvement in OS of metastatic melanoma patients, the development of resistance poses a significant obstacle to long-term survival outcomes.

1.4.1. Targeted therapy resistance mechanisms

One of the primary mechanisms of resistance to targeted therapies in melanoma is **the reactivation of the MAPK signaling pathway** (160). This can occur through various mechanisms, such as amplification of the mutated BRAF allele, leading to increased BRAF protein expression and spontaneous dimerization of the mutated BRAF V600E protein, reactivating ERK (113). BRAF splicing variants can form dimers independently of NRAS activity, bypassing BRAF inhibitors (Amaral et al., 2017a., Corcoran et al., 2010; Manzano et al., 2016). BRAF inhibitors target V600E monomers, but due to the high tumor heterogeneity in melanoma, cells expressing both BRAF wt and V600E coexist. This coexistence can stabilize BRAF wt-CRAF heterodimers, paradoxically reactivating the MAPK pathway (162,163). Melanoma cells can also switch to other RAF isoforms during combinatorial BRAFi/MEKi treatment, such as ARAF and CRAF (162).

Furthermore, MAPK reactivation can occur via secondary mutations in MEK1/2 and COT (MAP3K8) kinases, with COT activating the MAPK pathway independently of RAF (162,164,165). Of note, BRAF and NRAS mutations are typically mutually exclusive in treatment-naïve patients (166), but after patients become resistant to BRAF inhibitors, new RAS oncogenic mutations trigger CRAF hyperactivation and downstream reactivation of ERK (113,167–169). Loss of function of NF1 and PTEN can contribute to MAPK inhibitor resistance by constitutively activating MAPK and **PI3K/AKT pathways**, respectively.

Moreover, mutations in RAC1, a small GTPase, also contribute to targeted therapy resistance by activating PAK and AKT (164,167,170). Blocking MAPK signaling activity can also cause compensatory overactivation of PI3K/AKT signaling, counteracting BRAF inactivation and leading to acquired resistance to BRAF inhibitors. Additionally, mutations activating PI3K or AKT can enhance AKT signaling, amplifying antiapoptotic signals and upregulating key genes involved in survival and proliferation (171–174). (Fig. 15) Finally, aberrant growth factor receptor-mediated signaling through **HGFR (or cMET) and EGFR** has also been connected to resistance to targeted therapies (161,175,176).

Figure 15: Resistance mechanisms to targeted therapy in melanoma. Reactivation of the MAPK pathway, activation of alternative pathways such as PI3K/AKT signaling, and involvement of the tumor microenvironment mainly through the secretion of growth factors, are the main resistance mechanisms used by melanoma cells to overcome targeted therapy (160)

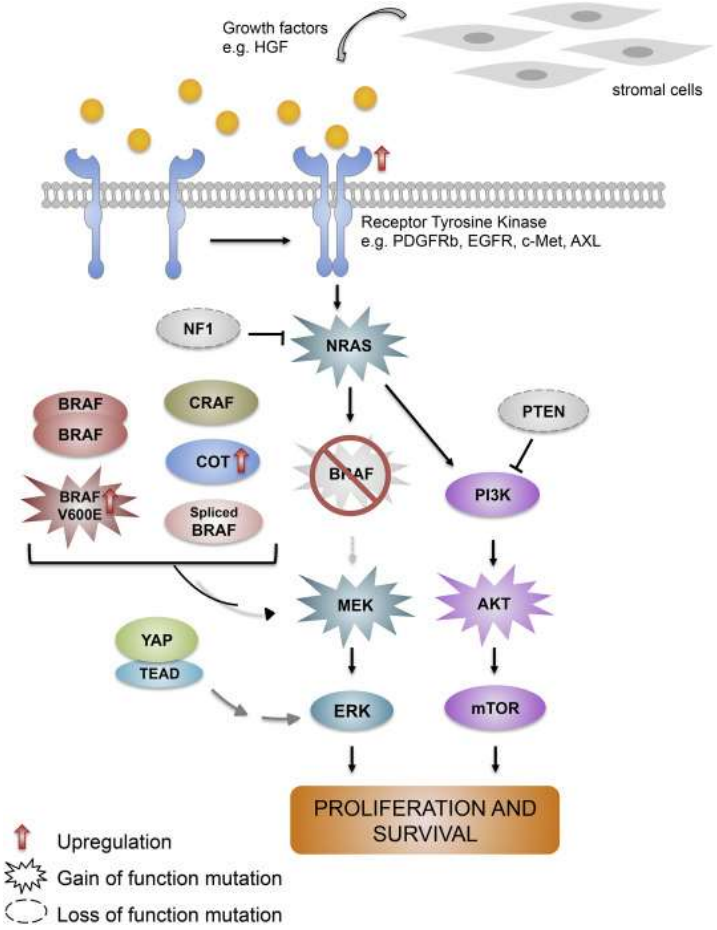

1.4.2. Resistance against Immunotherapy

In response to therapy and when cancer cells die, cancer-associated neoantigens are released into the microenvironment where they are recognized by antigen-presenting cells (APCs), such as dendritic cells in the skin. APCs then migrate to tumor-draining lymph nodes and present the tumor antigen to naïve T cells, leading to their priming and maturation into effector T cells. Next, activated T cells infiltrate the tumors and destroy malignant cells, primarily through the action of cytotoxic CD8+ T cells (177).

Approximately 50% of melanoma patients develop resistance to ICI treatment within 5 years of treatment (178,179). Mechanisms driving the resistance are still poorly understood, but tumor mutational burden (TMB), the immune microenvironment, and activation of alternative inhibitory receptors (179), have been discussed.

TMB is the number of somatic mutations in the cancer genomes. Tumors with higher TMB, such as melanoma, are associated with higher neo-tumor-associated antigen expression and better T-cell priming and immunogenicity: higher CD8+ T-cell infiltration ("hot tumors) (180,181) correlating with a better prognosis for patients receiving ICIs. Conversely, low TMB predicts poorer response to ICIs (182,183). Under immunotherapy, melanoma moves from a "hot" to a "cold" status, which is characterized by reduced immune cell infiltration exhibiting weaker responses to treatment (184).

Dendric cells (DCs) play an important role as tissue-resident APCs and activation of T cells CD8+, and their maturation is essential for effector T-cell activation, so DC maturation impairment decreases ICI sensitivity (185,186). Melanoma cells are able to impair DCs activity through several factors: by secretion of interleukin-6 (IL-6), IL-10 (187), and by vascular growth factor (VEGF), which foster the production of disorganized tumor vasculature in which T cell trafficking through the endothelium is impaired (188,189). Finally, melanoma cells can modify the composition of the immune cell pool, creating a more immune-tolerant environment by recruiting immunosuppressive cells such as regulatory T cells (Tregs), tumor associated macrophages (TAMs), and myeloid-derived suppressor cells (MDCSs) (190) all contributing to emerging resistance to ICIs. (Fig. 16)

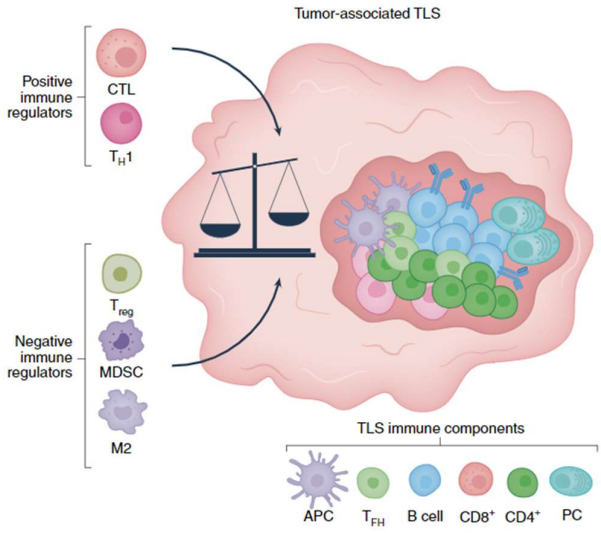

Figure 16: Immune cell infiltration in melanoma forms aggregates called tertiary lymphoid structures (TLS). These infiltrates are composed of positive immune regulators such as cytotoxic T-cells and T-helper cells. Upon immunotherapy, melanoma cells can immunomodulate the infiltrate composition by reducing the number of positive immune cells and increasing the number of negative immune regulators such as T regs, MDCSs and TAMs (M2). *(135)*

Finally, another important mechanism of immune evasion of melanoma cells treated with ICIs is the expression of ligands for other inhibitory receptors on effector T-cells, such as lymphocyte activation gene 3 (LAG-3) (191) and T-cell immunoglobulin and mucin domain 3 (TIM-3) (192).

1.5. Melanoma plasticity

Melanoma is characterized by a high degree of intrinsic heterogeneity, leading to phenotypic plasticity, one of the key elements that induce resistance to currently available treatments (193–195), and a hallmark of cancer (196). Gene expression analyses have identified two predominant transcriptional programs characterized by "proliferative" or "invasive" phenotypes. Identification of distinct expression patterns of key transcriptional regulators such as MITF is indicative of the proliferative phenotype, and expression of the RTK AXL is characteristic of the invasive phenotype. Consequently, these markers were used to classify these two distinct phenotypes: **MITF^{high}/AXL^{low} (proliferative)** and **MITF^{low}/AXL^{high} (invasive)** (197–202). The "rheostat model" hypothesizes that high MITF levels promote differentiation and reduce proliferation, intermediate MITF levels enhance proliferation and glycolytic metabolism, while MITF levels lead to a dedifferentiated state with low proliferation, senescence, and increased invasiveness (203–205) . Molecularly, low MITF expression correlates with high levels of p27 (cell cycle inhibitor) and arrest in G1, while high MITF expression shows upregulated targets involved in melanoma differentiation and pigmentation such as MLANA, PMEL, DCT, and TYRP (203,206–208).

Relapse, even after complete response (CR), is frequently linked to a pool of cells, which are able to survive drug treatment, modulate the immune system and serve as a reservoir for future relapses and spreading metastasis. Such cells giving rise to **Minimal Residual Disease (MRD)** typically share genetic and phenotypic similarities with the original tumor cells (209,210). The so-called **Drug-Tolerant Persister (DTP)** cells are slow-proliferative and reversibly drug-resistant: upon drug removal, the phenotype mainly driven by non-genetic modifications reverts back to a drug-sensitive state (211). In 2010, studies by Sharma et al. and Roesch et al. identified slow-proliferating DTP cells in NSCLC and melanoma, respectively. Sharma et al. found that NSCLC DTP cells, driven by enhanced IGF-1 signaling, histone demethylase KDM5A, and CSC-like signature, could survive high-dose EGFR inhibitor treatment and regenerate the sensitive population after a period of drug holiday (212).

Similarly, Roesch et al. highlighted the role of chromatin remodeling via H3K4 demethylase (JARID1B) in melanoma DTP cells, emphasizing epigenetic mechanisms in DTP cell survival (213).

The origin of DTP cells remains under debate, with two main theories: they either pre-exist in a heterogeneous population and are selected under stress ("Darwinian") or emerge through gradual adaptation to treatment ("Lamarckian") (211,214–218) (Fig. 17). Single-cell RNA sequencing of melanoma MRD cells from PDX models treated with BRAFi and MEKi identified multiple co-existing DTP states with distinct transcriptional programs, expanding the MITF rheostat model (202). These states include nutrient deprived cells reliant on fatty-acid β-oxidation (starved melanoma cells or SMCs), neural crest-like cells (NGFR^{high}), invasive/dedifferentiated cells (AXL^{high}), and hyperpigmented (MITF^{high}) (202,219–221).

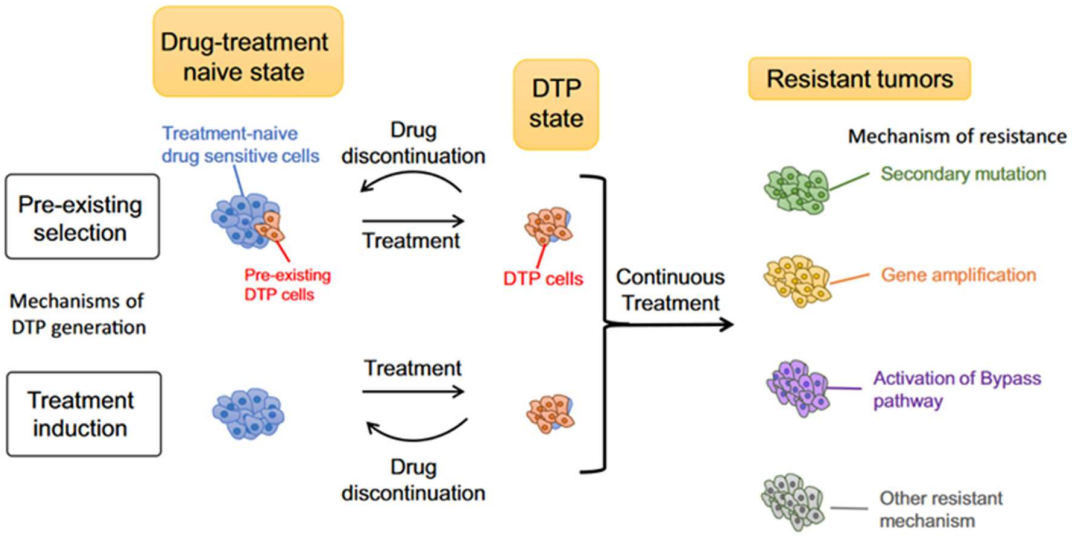

Figure 17: DTP cell generation and evolution hypothesis. It is hypothesized that DTP cells might be pre-existing in naïve tumors and selected in a "Darwinian" fashion upon treatment, or that the treatment induces the DTP state in a subpopulation of cancer cells. DTPs can revert to the initial sensitive population when drugs are withdrawn but can also serve as a major reservoir for fully resistant cells when the treatment is maintained (Mikubo et al., 2021).

In conditions of stress driven by microenvironmental conditions such as hypoxia, lack of nutrients, and immune pressure, proliferative melanoma cells might phenotypically switch to invasive cells shifting the expression patterns and presenting a more undifferentiated/dedifferentiated phenotype allowing the cells to "escape" the pressure by moving away from unfavorable environments (223) (Fig. 18).

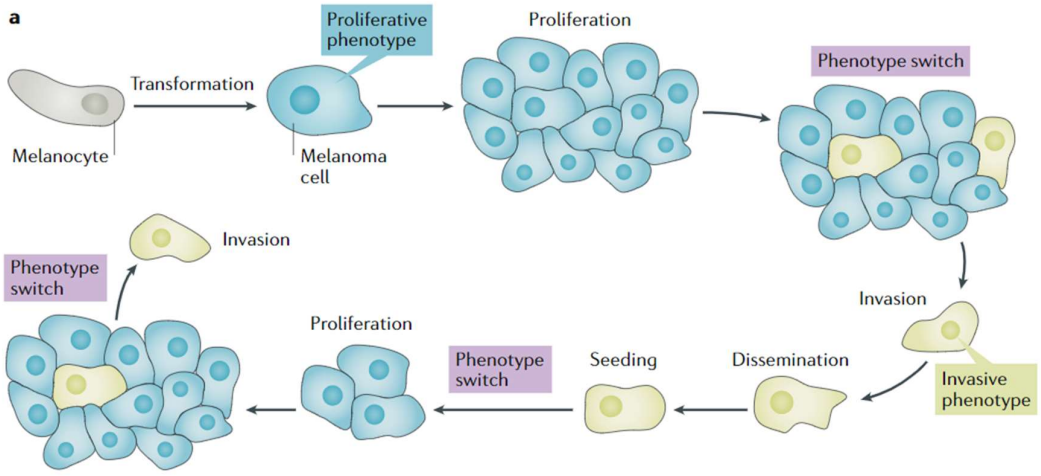

Figure 18: The melanoma phenotype-switch model. Melanoma cells are plastic cells and are able to switch from a "proliferative" to an "invasive" phenotype and vice versa, upon stress *(200)*.

While phenotype switching bears a resemblance to epithelial-to-mesenchymal transition (EMT), it is inappropriate to characterize this process in melanoma using the EMT terminology, as melanocytes are non-epithelial cells. Rather, this process is called EMT-like and plays an important role in migration of neural crest stem cells during embryonal development. Of note, invasive melanoma cells express genes associated with EMT, including SNAI1, ZEB1, SERPINE1, or SOX9. All of these molecular features contribute to their high invasiveness, ability to modulate the ECM, and the development of drug tolerance and resistance (224).

1.6. The Tumor Microenvironment and its role in melanoma

1.6.1. Cancer-associated fibroblasts (CAFs)

Fibroblasts are the major cellular component of the stroma, playing essential roles in synthesizing the extracellular matrix (ECM), modulating the inflammatory response and the wound healing process (recently recognized as an important process involved in cancer progression) (225). When closely interacting with cancer cells, either by cell-to-cell interaction or via soluble factors, fibroblasts undergo differentiation into so called "**cancer-associated fibroblasts" (CAFs)** (226–228). Specific markers have been described to distinguish CAFs from normal fibroblasts such as α-SMA (alpha smooth muscle actin), fibroblast activation protein (FAP), fibroblast specific protein (FSP1), elevated levels of vimentin and platelet-derived growth factor receptors (PDGFR) α and β.

CAFs have been described in solid cancers to participate in numerous cellular processes, encompassing ECM remodeling, angiogenesis, and intercellular interactions (226,227,229,230). Melanoma cells, when co-cultured with CAFs (called melanoma-associated fibroblasts or MAFs), display higher invasion and migration abilities, representing a crucial step in melanoma metastasis formation (231) (Fig. 19).

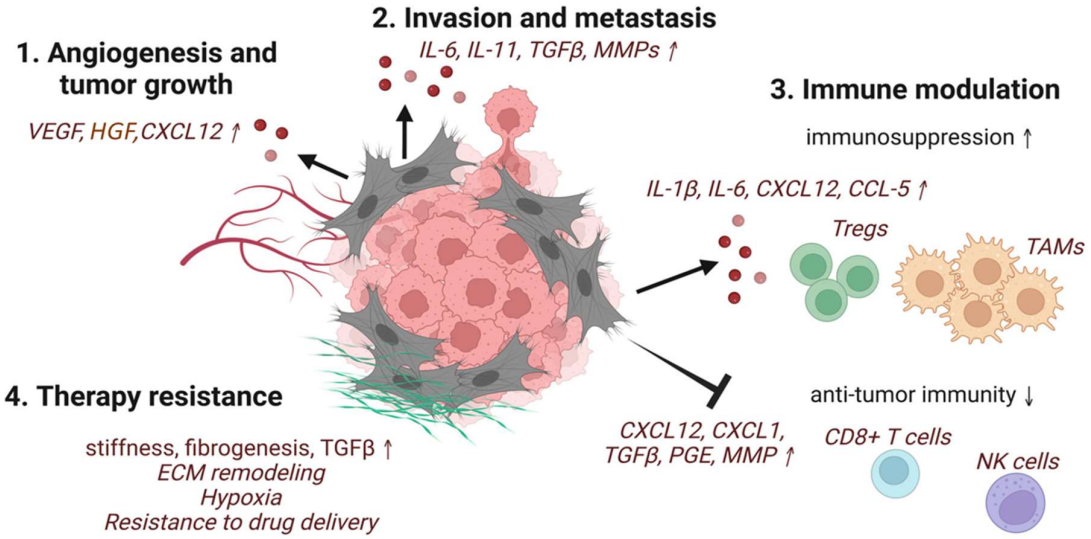

Figure 19: The pro-tumorigenic functions of cancer-associated fibroblasts (CAFs). Through secretion of specific cytokines such as TGF-β, VEGF, and HGF, a variety of pro-angiogenetic and immune-suppressive interleukins such as IL-6 and IL-1, and chemokines such as CXCL12, CAFs modulate the TME fostering tumor growth and metastasis, angiogenesis, and immunomodulation. Moreover, CAFs hijack the ECM by secreting metalloproteinases (MMPs) and ECM components such as collagen and fibronectin. These CAF characteristics play key roles in conferring therapeutic resistance to cancer cells (Glabman et al., 2022 *modified).*

Mechanistically, HGF, secreted by MAFs, is able to trigger the activation of MAPK and PI3K/AKT pathways in melanoma cells through the interaction with its receptor tyrosine kinase MET, consequently fostering resistance to BRAF inhibition (233). The BRAF inhibitor vemurafenib induces increased production of TGF-β by melanoma cells and subsequently, TGF-β triggers the activation of MAFs enhancing ECM remodeling through fibronectin production, further contributing to BRAF inhibitor (234) and ICI resistance. TGF-β released by MAFs promotes a phenotype switch in melanoma cells from the "proliferative" and immunogenic $MITF^{high}/AXL^{low}$ to the "invasive" and immune tolerant $MITF^{low}/AXL^{high}$ phenotype (235).

1.6.2. Tumor endothelial cells (TECs)

Solid tumor growth increases the distance of tumor cells from blood vessels, causing lack of nutrients and oxygen, finally inducing hypoxia. Subsequently, tumor cells find themselves in an inadequate environment to sustain proliferation and begin to increase the expression of important angiogenic factors such as HIF (hypoxia-inducible factor), VEGF (vascular endothelial growth factor), PDGF (platelet-derived growth factor), ANGPT (angiopoietin), and FGF-2 (fibroblast growth factor 2) along with other pro-angiogenic chemokines to promote neo-angiogenesis (236–238).

Tumor endothelial cells (TECs) exhibit phenotypic differences compared to their normal counterparts (normal endothelial cells or NECs). Morphologically, TECs display irregular surfaces, extensive fenestrated cell walls, and loose intercellular junctions with pericytes, and they are usually characterized by higher proliferation rates than NECs (236,239). Physiologically, NECs play a crucial role in leukocyte migration to the tumor site. Expression of selectins (such as P-selectin and E-selectin), integrin ligands (such as VCAM-1 and ICAM-1), and adhesion molecules (such as glycosaminoglycans) facilitate leukocyte adhesion, while immune cell migration involves adhesion molecules such as CD31 (also known as PECAM-1) and CD99. Upon arrival in the tumor, leukocytes extravasate passing through fenestrated NECs, base membranes and pericyte sheaths (240).

In metastatic melanoma, TECs reduce the expression of adhesion molecules, impeding the migration and extravasation of immune cells toward the tumor site (241), and increasing tumor cell intravasation (236) (Fig. 20). TECs are also able to influence the immunogenicity of the TME of multiple solid cancers, including melanoma, by up-regulating various inhibitory molecules such as PD-L1, PD-L2 and TIM-3 which inhibit T cell activation at the vessel site (242).

Figure 20: Role of TECs in tumor cell spread and metastasis. Cancer cells induce the transformation of endothelial cells from NEC to TEC through the secretion of angiocrine factors and specific cytokines such as VEGF, PDGF, and TGF-β, interleukins, and molecules such as biglycan and NOTCH1. TECs have deregulated expression of adhesion molecules such as PECAM-1 and E-cadherin, which creates leaking blood vessel walls and increases cancer cell intravasation. Moreover, TECs bind to circulating tumor cells preventing anoikis. TECs also sustain the creation of tertiary lymphoid structures (TLS). (236).

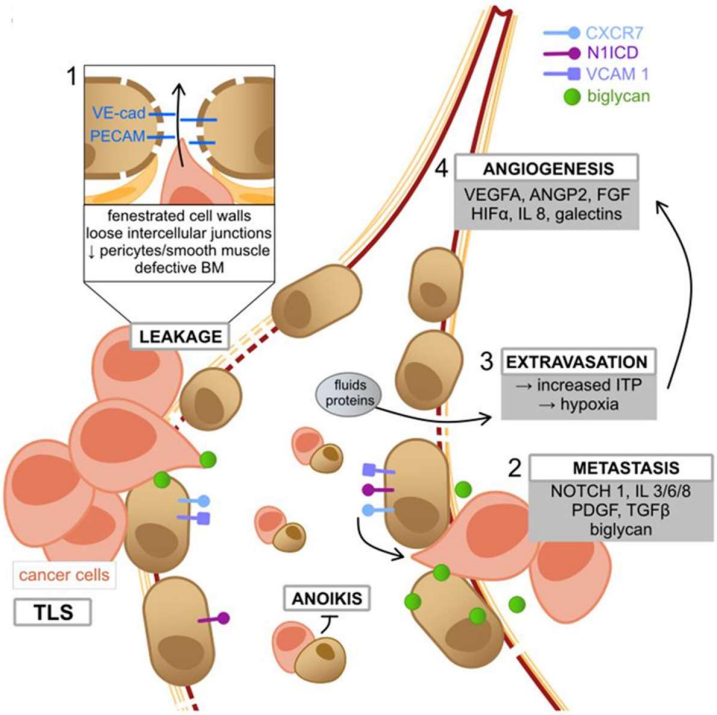

1.6.3. Immune cells

Melanoma is known to shape its own TME towards a pro-tumoral environment. The evasion of melanoma cells from immune surveillance is governed by a process called **"immune editing"**, which primarily relies on an intricate network of intra- and extracellular signals (243). Lymphocytes, mostly CD4+ T helper cells and CD8+ T cytotoxic cells, are key players in tumor immune surveillance (244–246). (Fig. 21).

The accumulation of immune suppressive cells in the melanoma TME, such as tumor-associated macrophages (TAMs), regulatory T-cells (Tregs), and myeloid-derived suppressor cells (MDSCs), constitutes an additional mechanism that impairs cytotoxic T-cells (247). Finally, melanoma cells create an immune suppressive TME through the release of specific cytokines that are able to inhibit T cells, such as TGF-β, VEGF, indoleamine 2,3-dioxygenase (IDO), and also through the reduced expression of MHC I and II (major histocompatibility complex) (248,249).

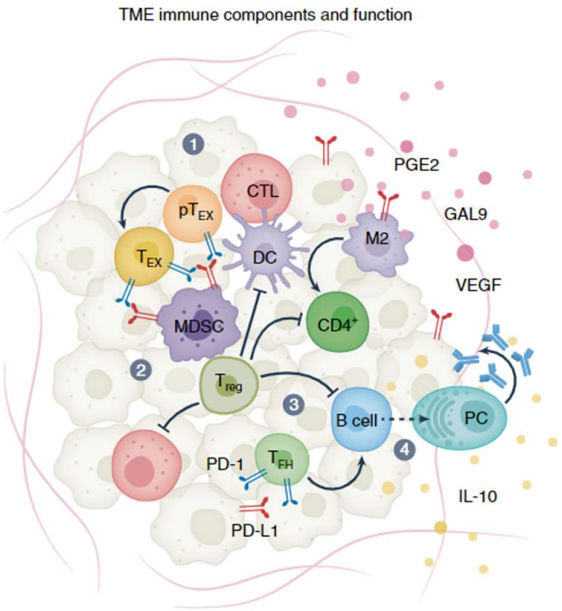

Figure 21: Representation of the main immune elements in melanoma. The anti-tumorigenic immune compartment is represented by antigen-presenting cells such as dendritic cells (DC), cytotoxic T-cells (CTL, CD8+), helper T-cells (CD4+), and B cells important for the anti-cancer antibodies production transforming into plasma cells (PC). On the other hand, the pro-tumoral immune compartment is characterized by myeloid-derived suppressor cells (MDSCs), M2-polarized macrophages, and regulatory T-cells (T-reg). Moreover, cytokines such as VEGF and IL-10 play a fundamental immune regulatory role. *(135)*

1.6.4. Extracellular Matrix (ECM)

The extracellular matrix (ECM) represents the acellular element found in all tissues. In cancer, the ECM often shows significant disorganization and imbalance, which is recognized as a hallmark of solid cancers (250). Melanoma progression and therapeutic resistance are also affected by certain ECM characteristics; important pro-survival processes are activated by the interaction of transmembrane receptors, such as integrins, with ECM molecules. Of note, fibrillar collagen I (major component of most tissues), non-fibrillar collagen IV (predominantly presents in basement membranes), and fibronectin contribute significantly to melanoma cell adhesion and migration, thus facilitating invasion and metastasis formation (251,252). Melanoma cell motility can be triggered by direct interaction of collagen IV with integrins α2β1 and α3β1, which also stimulate the activation of metalloproteinases (MMP) 2 and 9 (251). MMPs are zinc-dependent proteins specialized in ECM degradation and are generally recognized as key elements for cancer progression (253). Prognostically, higher expression of collagen I is associated with poor prognosis and higher melanoma invasiveness (254,255).

An important ECM feature that promotes melanoma survival is increased ECM stiffness, which through the activation of mechanosensory pathways (such as the integrin β1/FAK/Src axis) fosters therapy resistance, invasion and reduces T cell infiltration (256,257).

As presented in the previous chapters, what is known about the melanoma TME, involves all types and cancer-cells-specific signaling and mechanisms to evade control by the immune system and therapies. However, we are still far from understanding all the complexities of the tumor and its TME, and much needs to be done regarding better therapies for melanoma patients, irrespective of their genomic subtype. In the following, new *in vitro* approaches will be presented.

1.7. 3D cancer models

1.7.1. From monolayer culture (2D) to three-dimensional (3D) culture

The most common method of cultivating cancer cells involves 2D adherent cultures, in which cells usually grow on a plastic surface. Albeit easy and cheap, 2D culture lacks the complexity of a real tissue or tumor with cell-cell and cell-ECM interactions, nutrient/waste exchanges, and oxygen gradients. Preclinical drug tests are typically conducted using animal models, such as mice, which effectively enable representation of tumor cellular complexity within a living organism. However, these models present major drawbacks such as a lack of human cell origin (or lack of a functional immune system), high cost, not suitable for high-throughput screenings, and significant ethical concerns. In the last decade, more interest has been placed in developing 3D culture approaches, that better mimic tissue architecture and cell interactions, bridging between 2D and animal models. Yet, challenges of reproducibility and high-throughput applicability compared to 2D models remain and conditions still need to be optimized. Especially, in basic cancer research as well as for drug screening and drug testing studies, 3D model systems are increasingly used (Fig. 22).

Figure 22: Representation of 3D cancer models ordered according to the cellular complexity. 3D models, as well as 2D models, can be generated using established cell lines or patient-derived material. A plethora of 3D models bridge the gap between 2D culture and *in vivo* tumors, ranging from spheroids, organoids, chips, and respectively co-culture with other cellular components (258).

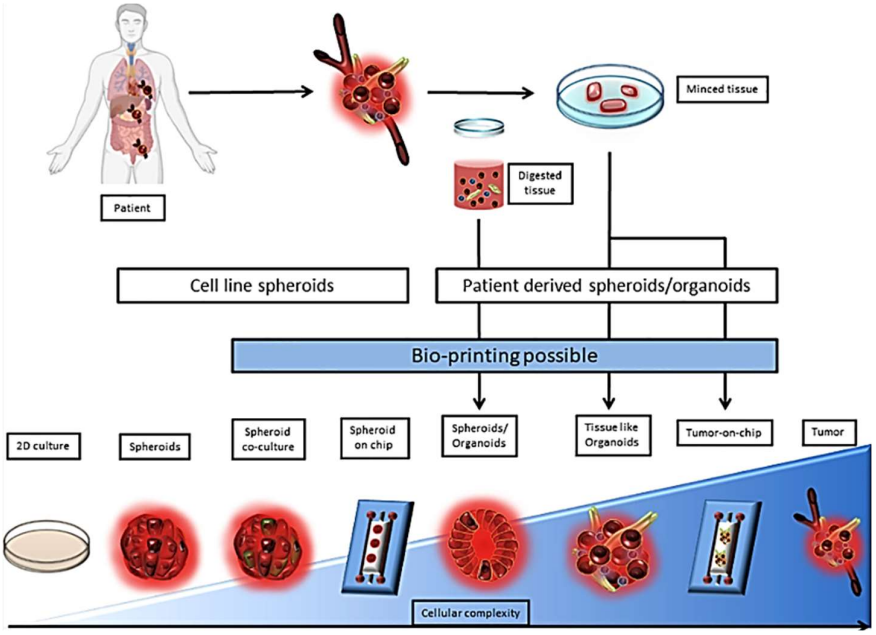

1.7.2. Spheroids

Spheroids are small cell aggregates that closely resemble solid tumors in terms of cellular architecture, signaling pathways, and interaction with the ECM; as such they provide an effective representation of oxygen, nutrients, soluble factors, or drug diffusion and exchange (259,260). Spheroids larger than 500 µm in diameter develop distinct layers, with increasing quiescence, waste products towards the core and necrosis, and decreasing oxygen and nutrient concentration, while maintaining a proliferative outer layer (261,262) (Fig. 23).

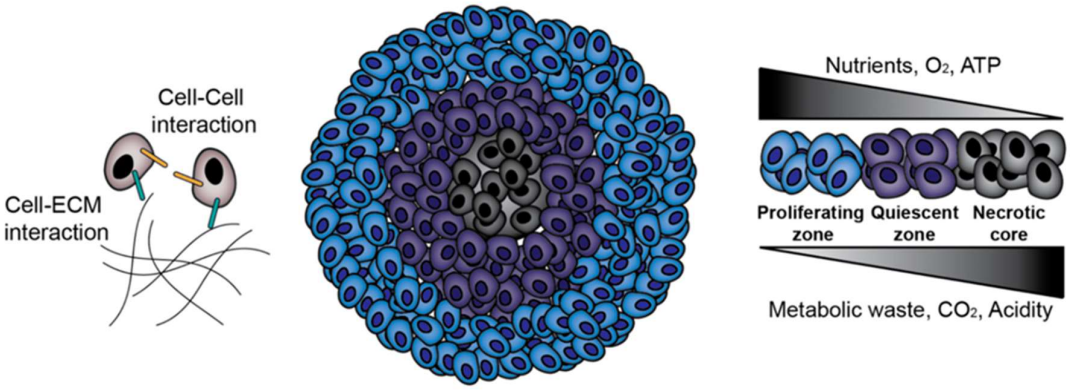

Figure 23: Spheroid architecture. The outer spheroid layer is characterized by high cellular proliferation, availability of nutrients, and oxygen. Moving toward the spheroid core, cells become quiescent and apoptotic/necrotic due to the accumulation of waste products and lack of important supplies (259).

Various methods exist for generating tumor spheroids, that can be categorized into scaffold-free and scaffold-based system (263). In **scaffold-free** approaches, spheroids form when cells are pushed to interact more with each other than with the surface, leading to spontaneous aggregation. Common methods include the liquid overlay technique, where cells are seeded on a culture plate (usually with U- or -V shape wells) coated with an inert substrate, or the "hanging drop" method, where cells grow in suspension in a drop of medium on the lid of a dish (264–266). Bioreactors can also generate large quantities of spheroids, though uniformity in size may vary (267). **Scaffold-based** systems rely on spheroids formed in matrices or hydrogels, which mimic the cell-ECM interactions. These systems are also valuable for studying tumor progression and invasion, and for testing drug efficacy on cell migration by embedding spheroids on Collagen I (265).

As discussed, the interactions of cancer cells with stromal cells belonging to the TME, modify the response to and the effectiveness of anti-cancer compounds. In this regard, the co-culture of cancer cells with stromal cells can be adapted to a spheroid-forming culture system better mimicking physiological conditions. Different scaffold-free 3D spheroid co-culture methods have been explored. Yakavets et al. showed that classical "simultaneous" seeding, in which cancer cells are seeded together with fibroblasts, does not allow prolonged fibroblast survival and equal distribution of cell types in the sphere. Adopting an alternative "sequential seeding" method, in which fibroblasts are added 24 hours after the formation of the tumor sphere, allows the infiltration of fibroblasts into the tumor sphere, prolonging their survival and displaying a more homogeneous distribution (268). Interestingly, melanoma cells co-cultured with fibroblasts and keratinocytes in a 3D spheroid system showed increased resistance to targeted therapies, and it can also be used as a model to study early melanoma cell invasion into the dermal compartment (269,270).

1.7.3. Hydrogel-embedded cultures and skin reconstructs

One of the main challenges in 3D cancer models is to recreate as close as possible the TME, in which cancer cells reside in actual tumors. In this regard, the co-culture of cancer cells with stromal cells such as fibroblasts, endothelial, and immune cells **embedded in ECM** is the key for *in vitro* mimicking the *in vivo* tumor environment (Nii et al., 2020; Vitale et al., 2022). As mentioned in previous chapters, CAFs, endothelial cells, immune cells, and the ECM can increase the aggressiveness and survival of cancer cells, and foster drug resistance through different

mechanisms, hence the choice of stromal cells and the ECM type (Fig. 24) needs to be made in view of the objectives of co-culture experiments (272).

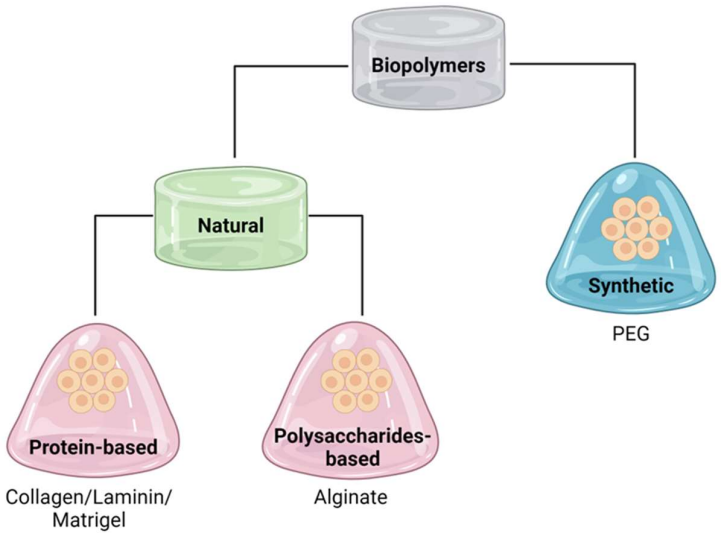

Figure 24: Biomaterials used to generate 3D hydrogel co-cultures. There are two main families of biopolymers: natural, represented by protein-based (such as collagen and laminin) and polysaccharide-based (such as alginate and chitosan) hydrogels, and synthetic hydrogels (such as polyethylene-glycol or PEG). (Figure created using Biorender.com).

The choice of cellular ratios, matrix, and culture medium are key elements for a functional hydrogel-embedded co-culture. For instance, vascular engineering techniques necessitate suitable scaffolds that facilitate the transportation of growth factors or cells and offer a 3D matrix for the growth and development of blood vessels (273–276). Pericytes and mesenchymal stem cells, together with important growth factors such as VEGF and FGF-b, were observed to be necessary for sprouting and tubule formation of endothelial cells cultured in PEG-based synthetic hydrogels (277–280). It is still under debate whether natural matrices, such as collagen I, Matrigel (consisting of 60% laminin, 30% collagen IV, and 10% of other ECM components and growth factors), fibrin, or laminin, or semi-synthetic/synthetic matrices, such as hyaluronic acid (HA) or polyethylene glycol (PEG) are more suitable for co-cultures. Natural matrices are very often animal-derived, with high batch-to-batch variability, and an ill-defined composition, which makes customization difficult (272,281). On the other hand, synthetic matrices allow for personalized tailoring, for instance by the bioconjugation of important adhesion and matrix-degradation peptides such as RGD (arginyl glycyl aspartic acid, found in fibronectin) and MMP cleavable sites (282–284) or by the modulation of matrix stiffness (285,286), which is particularly important when studying tumor cell migration and invasion.

In melanoma, the best characterized matrix-embedded co-culture systems are represented by **organotypic skin models** (260,287). This method involves the co-culture of primary human cutaneous cells (such as dermal fibroblasts, keratinocytes, and endothelial cells) with melanoma cells within an ECM (such as collagen I), which allows to investigate cell-cell interactions and the influence of the TME on tumor progression, invasion, and drug responses (265). These constructs consist of a bottom layer containing fibroblasts and endothelial cells embedded in ECM mimicking the dermis, overlaid by an upper layer of differentiated keratinocytes mimicking the epidermis. Melanoma cells are seeded on the surface of the construct to establish a dynamic environment for melanoma development (288–290). Vörsmann et al. developed an organotypic full skin equivalent containing melanoma tumor spheroids of specific sizes, which can be used as functional models for drug testing (291). Interestingly, Bourland et al. reconstructed organotypic skin in which fibroblasts, stimulated by ascorbic acid, produced natural ECM in which fully functional blood and lymphatic vessels developed. The addition of melanoma cells allowed for the testing of drugs in a skin-equivalent environment (292) (Fig. 25).

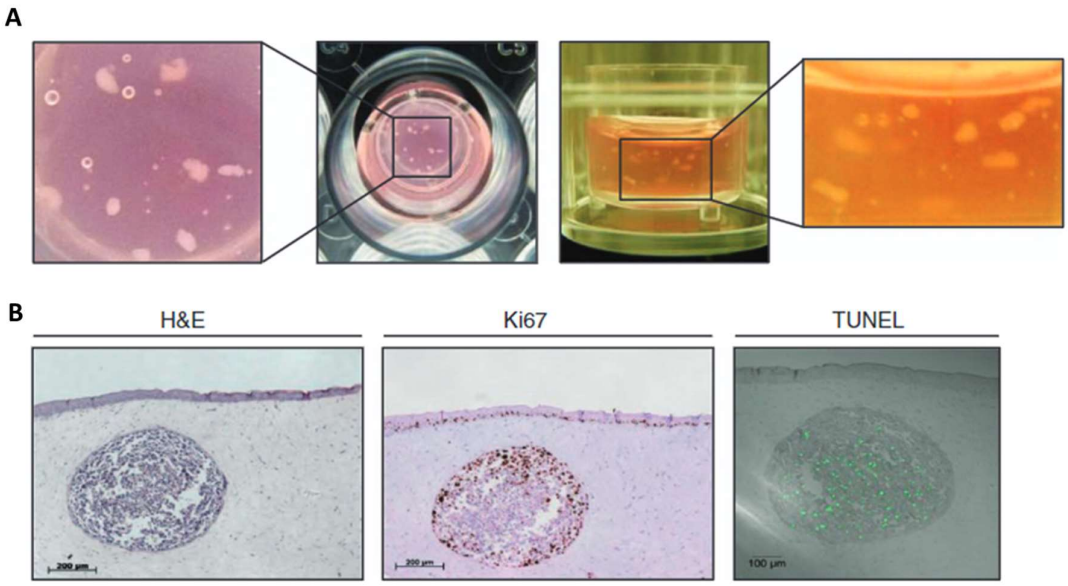

Figure 25: Organotypic skin with melanoma spheroids embedded, resembling melanoma skin metastasis. A) Different points of view show the full-thickness organotypic skin with collagen-embedded metastatic melanoma spheroids (white clusters in zoomed pictures). B) FFPE sections stained for hematoxylin and eosin (H&E), Ki67 (proliferation marker), and apoptotic cells (TUNEL assay). Figure modified from (291).

1.7.4. Organoids and Microfluidic chips

Organoids and microfluidics chips represent advanced 3D culture system for cancer research, offering complementary advantages.

Organoids originate from cells with stemness properties that autonomously propagate and self-organize into 3D structures resembling native tissue, containing autologous cell populations such as tissue-resident immune cells, fibroblasts and endothelial cells (293–295). The models enable high-throughput drug testing and mirror patient-specific tumor characteristics more closely than traditional cell lines, although challenges include the need for specific isolation protocols, tailored media, and matrix compositions, along with limitations in cellular heterogeneity and vascularization (258,296). Efficient organoid cultures have been established for a variety of solid cancers, including melanoma (297). However, the number of organoid studies on melanoma is still limited.

Microfluidic chips, on the other hand, offer a "tumor-on-a-chip approach, more precisely replicating the tumor microenvironment, including multicellular architecture, chemical gradients, and mechanical forces (262,264). These systems enable continuous perfusion, mimicking vascular flow and shear forces, which are critical for tumor growth and metastasis studies (298). For melanoma specifically, innovations like the "skin-on-a-chip" simulate the 3D structural organization of skin, providing a physiological platform for long-term studies (260,265).

1.8. Drug repurposing

Traditional drug discovery is a multi-stage process that requires a wide set of skilled experts, the application of advanced technologies, and enormous time and economic investments. Approximately 2.8 billion dollars are spent over a period of 12 to 15 years before approval of a specific drug (299). In brief, large drug screenings identify promising disease-related compounds, which undergo further preclinical tests through *in vitro* assays and animal models to assess efficacy and safety profiles. Drug candidates move across three phases of human clinical trials (phase I, II, and III) where dosage, efficacy, and toxicity are assessed. If the candidate drug proves efficacious across all three phases, it proceeds to regulatory registration, paving the way for the market (300,301). (Fig. 26)

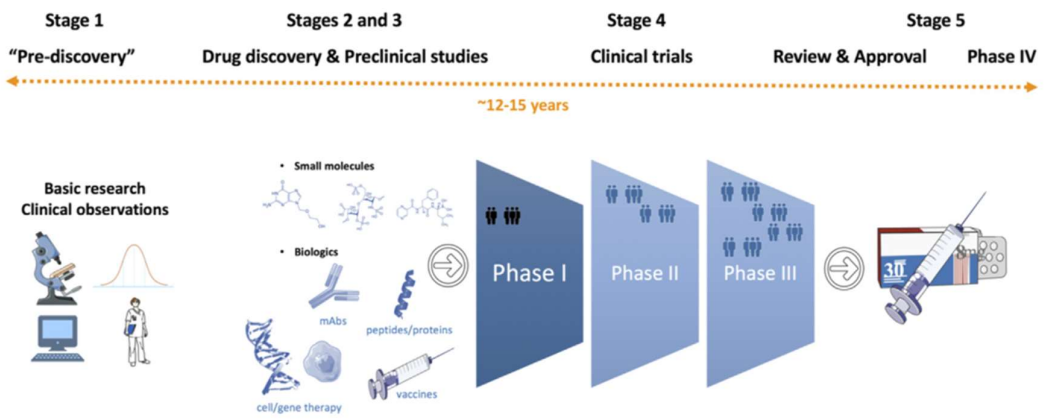

Figure 26: Main stages of classical drug discovery and development (299).

Drug repurposing involves the identification of novel therapeutic applications for existing drugs, whether approved or investigational, beyond the original purpose (302). This approach offers several advantages compared to the traditional drug discovery process. The risk of failure is reduced as repurposed drugs have already been tested in safety trials, potentially decreasing the safety-related problems. Timewise, drug repurposing has shorter development times since much of the pre-clinical and clinical testing may already be completed. Furthermore, fewer investments are required due to significantly simpler pre-clinical and phase I/II clinical trials (303). Drugs that have already received FDA (Food and Drug Administration) or EMA (European Medicines Agency) approval, can be tested in different diseases with a shorter timeline.

1.8.1. High-throughput screening (HTS)

Nowadays, high-throughput screening is recognized as a key strategy in the identification of new potential compounds for cancer therapy and it has become a standard method in the pharmaceutical industry. Relevant features of HTS are its sensitivity, robustness, and cost-effectiveness (304). In brief, HTS is a process in which large numbers of compounds (from hundreds to thousands), usually belonging to pre-defined libraries, are being tested simultaneously on specific cancer cells of interest (305).

Multiple assays can be used to assess the efficacy of drugs in an HTS setting, such as cell viability assays, which rely on the measurement of ATP content, usually assessed by luciferase- or fluorescence-based assays (306,307). Interestingly, a popular method to assess cell viability is through high-content imaging applied to HTS, using high-throughput microscopy.

The instruments automatically capture and analyze optical fluorescent images of cells grown in multi-well plates, providing quantitative data through image analysis tools (308). A general scheme of HTS-driven drug identification is as follows: in primary screenings, drugs are typically tested once or twice (often at different concentrations). An essential step in this process is evaluating the robustness of the assay through metrics such as the Z' factor (309).

Hits can be computationally identified by analyzing quantitative data, setting a threshold, and declaring hits for values beyond this threshold, or by visually identifying compounds based on their effects deviating from bulk measurements and background (310). Following the primary screening, hits undergo further validation. They are tested at multiple concentrations to generate dose-response curves (DRCs) and to determine the half-maximal inhibitory or effective concentration (IC50 or EC50) (305,309,311). Of note, HTS is also applied to 3D culture systems.

An interesting study, conducted by Kota et al., described 3D spheroid-based HTS with a library of 1280 compounds in KRAS mutated pancreatic cell lines, revealing differences in drug response mechanisms between cells cultured in 3D compared to 2D (312). However, despite their potential, 3D models in HTS present challenges, notably in the limited methods available for high-throughput analysis of cells in a 3D context compared to the 2D counterpart (271,313,314).

In conclusion, while several therapeutic options for BRAF-mutated melanoma patients exist, the emergence of resistance underscores the urgent need for novel treatments, particularly for other melanoma genomic subtypes, such as NRAS-mutated melanoma. The introduction of advanced 3D models in pre-clinical phases offers promise in identifying more effective anti-melanoma compounds. Nevertheless, further advancements are needed to fully replicate the complexity of patient tumors. Using 3D models, such as spheroids in HTS drug repurposing approaches, enhances the accuracy and efficiency of drug testing, representing a crucial step forward in fighting melanoma.

2. Aims of the Thesis

In recent decades, significant therapeutic advancements have been achieved for the treatment of advanced $BRAF^{mut}$ melanoma, leading to the approval of combined targeted therapies (BRAFi + MEKi) and immunotherapies (anti-PD1/PD-L1 and anti-CTLA-4). Despite these advancements, $NRAS^{mut}$ and wild-type (WT) melanoma patients still lack specific, approved therapies. Currently, these patients are treated with off-labeled inhibitors such as MEK inhibitors or immune checkpoint inhibitors, but over 50% experience disease progression due to primary or acquired resistance. Therefore, there is an urgent need for more effective therapies for $NRAS^{mut}$ and WT melanoma patients, along with advanced models that better replicate the tumor microenvironment (TME). One critical challenge in developing effective cancer therapies lies in the limitations of current preclinical models. Conventional models lack the physiological relevance of 3D cancer environments, leading to the exclusion of potentially promising compounds during drug screening and the inclusion of many drugs ineffective in the patient settings.

This doctoral thesis addresses these needs through four main objectives:

1. **Development of Advanced 3D Melanoma Models**: These models will be designed to more accurately mimic melanoma cell interactions with other crucial components of the TME, enhancing the physiological relevance for the tested drugs;
2. **Establishment of a 3D High-Throughput Drug Screening workflow**: This workflow will allow to culture melanoma cells as 3D spheroids, enabling the testing of thousands of drugs within a model that better represents physiological conditions;
3. **Identification of Novel Drug Candidates**: Using the 3D high-throughput screening workflow, this objective aims to identify promising drug candidates specifically for $NRAS^{mut}$ and WT melanoma patients;
4. **Validation of Novel Drug Candidates**: Drugs identified in Objective 3 will undergo efficacy and characterization testing against $NRAS^{mut}$ melanoma cells within the advanced 3D models established in Objective 1, allowing for an in-depth assessment of their therapeutic potential.

In summary, this thesis aims to propose novel, effective therapies for $NRAS^{mut}$ and WT melanoma patients by leveraging advanced 3D cancer *in vitro* models to improve drug screening relevance and therapeutic precision.

3. Material & Methods

The methods detailed in the manuscript "Protocol to generate scaffold-free, multicomponent 3D melanoma spheroid models for preclinical drug testing" (315) are included in Appendix 4, with several techniques utilized in this thesis for subsequent studies. The following methods were applied specifically in the development of the manuscript:

1. The generation and characterization of multicomponent melanoma models (MMSs) co-cultured with PBMCs, analyzed via flow-cytometry;
2. Histological analysis of MMSs using formalin-fixed paraffin-embedded (FFPE) sections;
3. Assessment of cell death and apoptosis in MMSs following treatment, performed through flow cytometry.

3.1. Cell lines and culture

Information regarding the source and mutational background of the melanoma cell lines used in these studies is shown in Table 1.

Cell line	NRAS mutation	Other mutations	Source	Reporter
SKmel147	Q61R	CDKN2A (P114L)	Prof. Dr. Jochen Utikal (University Medical Center Mannheim, Germany)	
SKmel147-mCherry	Q61R	CDKN2A (P114L)	Prof. Dr. Jochen Utikal (University Medical Center Mannheim, Germany)	rLV.EF1.mCherry-9
SKmel30	Q61K	CDKN2A (P114L) TP53 (T284fs*21, deletion-frameshift) TERT (C228T)	DSMZ (Leibniz Institut, Germany)	
SKmel30-mCherry	Q61K	CDKN2A (P114L) TP53 (T284fs*21, deletion-frameshift) TERT (C228T)	DSMZ (Leibniz Institut, Germany)	rLV.EF1.mCherry-9
M160915	Q61R	BRAFwt	Prof. Mitchell Levesque (University of Zurich Hospital, Switzerland)	
M161022	Q61K	BRAFwt, cKITwt	Prof. Mitchell Levesque (University of Zurich Hospital, Switzerland)	
M161022	Q61K	BRAFwt, cKITwt	Prof. Mitchell Levesque (University of Zurich Hospital, Switzerland)	rLV.EF1.mCherry-9
624mel	/	BRAF (V600E) TP53 (C275W)	Dr. Ruth Halaban (Yale, United States)	
624mel-iRFP	/	BRAF (V600E) TP53 (C275W)	Dr. Ruth Halaban (Yale, United States)	pLenti6.2_miRFP670
624mel-mCherry	/	BRAF (V600E) TP53 (C275W)	Dr. Ruth Halaban (Yale, United States)	rLV.EF1.mCherry-9
WM3918	/	CDKN2A (deletion)	Tebu-bio (Rockland)	
WM3918-mCherry	/	CDKN2A (deletion)	Tebu-bio (Rockland)	rLV.EF1.mCherry-9

Table 1: Human melanoma cell lines.

SKmel147, SKmel30, 624mel and WM3918 were cultured in RPMI 1640 enriched with GlutaMAX (Gibco Thermo Fisher Scientific), supplemented with 10% FCS (Fetal Calf Serum, Gibco Thermo Fisher Scientific) and with 0.1 mg/mL Normocin (InvivoGen). M160915 and M161022 were cultured in RPMI 1640 (Gibco Thermo Fisher Scientific), supplemented with 10% FCS, 1mM Sodium Pyruvate (Gibco Thermo Fisher Scientific), 4mM L-Glutamine (Gibco Thermo Fisher Scientific), and with 0.1 mg/mL Normocin. Trametinib (MEKi)-resistant SKmel30 and WM3918 cell lines were generated by continuous drug exposure of parental-drug sensitive cell lines to 5xIC50 and 1xIC50 concertation, respectively, for approximately 3 months.

Normal Human Dermal Fibroblasts (NHDF) were purchased from Promocell (C-12300), Human Fetal Lung Fibroblasts (MRC-5) were purchased from ATCC (CCL-171), Hepatic Stellate Cells (LX-2) were purchased from Merk (SCC064), Human Microvascular Endothelial Cells (HMEC-1) were purchased from ATCC (CRL-3243). NHDF, MRC-5, and LX-2 were cultured in DMEM enriched with GlutaMAX (Gibco Thermo Fisher Scientific), supplemented with 10% FCS, 2.5% of HEPES buffer 1M (Gibco Thermo Fisher Scientific), and with 0.1 mg/mL Normocin. HMEC-1 were cultured in MCDB131 (Gibco Thermo Fisher Scientific), supplemented with 10% FCS, 1 µg/mL Hydrocortisone (Sigma-Aldrich), 10mM L-Glutamine, 0.1 mg/mL Normocin, and 10 ng/mL recombinant human EGF (PeproTech). Leukopacks for PBMC isolation were obtained from Croix Rouge Luxembourg under ethical approval. NHDF, MRC-5, and LX-2 were transduced with pLenti-C-mGFP-P2A-Puro to stably express GFP, while HMEC-1 was transduced with either LV-iRFP-P2A-Puro to express iRFP or with pLV-Bsd-CMV>tagBFP to express BFP. Transduced cell lines were cultured in the same medium as the parental cells.

Cell growth was maintained at 37°C in a humidified atmosphere comprising 5% CO_2. All cell lines were regularly examined for mycoplasma contamination.

3.2. Lentiviral transduction for stable fluorescent protein expression

All cell lines were transduced with Multiplicity of Infection (MOI) 3 of lentiviral vectors carrying reporter genes, for stable fluorescent protein expression. SKmel147 and SKmel30 were transduced with rLV.EF1.mCherry-9; NHDF, MRC-5 and LX-2 were transduced with pLenti-C-mGFP-P2A-Puro.; HMEC-1 were transduced with pLV-Bsd-CMV>tagBFP. After transduction, cells were subjected to antibiotic selection (either Puromycin or Blasticidin) and FACS sorted using a BD FACSMelody™ Cell Sorter (BD Bioscences, USA). Cell line transduction was performed by Dr. Joanna Wroblewka and Demetra Philippidou.

3.3. 3D Mono- and Multi-component melanoma spheroid models

Mono-component spheroids were generated in 384 well ULA U-bottom plate as follows. Melanoma cells were seeded at a density of 0.5-1 × 10^3 cells/well in 80 µL of RPMI. The plate was centrifuged 500 x g for 5 minutes and incubated at 37°C and 5% CO2 for 96 hours.

Multi-component spheroids were generated as described before (315). Melanoma cells, fibroblasts or hepatic stellate cells, and endothelial cells were seeded at a cellular ratio of 1:3:3 in 384-well black/clear round bottom ultra-low attachment spheroid microplates (Corning®). In brief, melanoma cells and HMEC-1 were seeded together at densities of 0.5 × 10^3 cells/well and 1.5 × 10^3 cells/well, respectively, in 40 µL of RPMI. The plate was centrifuged 500 x g for 5 minutes and incubated. After 24 hours of incubation, either NHDF, MRC-5, or LX-2 were seeded at densities of 1.5 × 10^3 cells/well in a further 40 µL of RPMI, on top of the preformed spheroids, the plate was then centrifuged 500 x g for 5 minutes and incubated at 37 37°C and 5% CO2 for 72 hours.

3.4. Immunofluorescence of frozen sections of spheroids

Cells were seeded in a 96-well plate ULA U-bottom plate at a density of 0.5 × 10^3 cells/well in 200 µL of RPMI. The plate was centrifuged 500 x g for 5 minutes and incubated at 37 37°C and 5% CO2. After 4-, 7-, 10- and 14-day spheroids were collected. After washing, spheroids were embedded in a cryo embedding matrix (Leica) and snap-frozen in liquid nitrogen. Frozen sections of 7 µm thickness were generated using a cryotome (Leica) and posed on slides. Sections were fixed using 4% PFA and permeabilized using 0.3% Triton X. After washing, sections were blocked with 10% FBS for 1 hour at RT and incubated with primary antibodies overnight at 4 degrees. Ki67 (1:200 Rabbit, Abcam), cPARP (1:400 Rabbit, Cell Signaling). Sections were incubated at RT for 1 hour with a secondary antibody conjugated with fluorochromes (anti-Rabbit Alexa 647, 1:500) and DAPI for nuclei counterstaining. Slides were mounted using a cover glass and fluoromount (Thermo). Fluorescent pictures were acquired using Cytation 5 (BioTek, Winooski, VT).

3.5. Generation of primary melanoma cell lines

Melanoma samples were collected at the University Clinic in Mannheim by Prof. Utikal with existing ethical approval. Samples were taken after obtaining informed written consent from the patients and ensuring their consent for the use of their tumor biopsies in the proposed research project. The tumor samples were pseudonymized and further processed in Luxembourg. The Regional Ethical Committee (REC) approved tissue collection, biobank storage of tumor biopsies, as well as development and use of cell lines (REC Approvals 2013/720 and 2020/65185).

The protocol that was followed to generate primary cell lines was first published by Prof. Mitchell Levesque group (316). In brief, tumors were first cleaned from all the identifiable non-cancerous material, such as epidermis, dermis, and fat tissue, by following the melanotic edges of the tumor. Afterward, tumors were cut into pieces of approximately 3x3 or 5x5 millimeters, and 2 to 3 pieces were disposed into a cryovial with FBS supplemented with 10% DMSO for preservation at -80°C for about a week and then moved into liquid nitrogen for long storage periods ("slow frozen biopsies"). Subsequently, a cryovial containing slow-frozen biopsies was quickly thawed, and specimens were placed into a Petri dish with pre-warmed RPMI with no FBS and fine cut into pieces as small as possible. The content was moved into a Falcon tube and a 1:1 solution of Dispase II (Roche, Switzerland) and RPMI (without FBS) was added and incubated at 37°C on a shaker for 1 to 4 hours, depending on the size of the pieces. The solution was centrifuged, the Dispase II solution removed, and a Collagenase (Merk, Germany) solution was added and incubated at 37°C on a shaker for up to 45 minutes. After centrifugation, the Collagenase solution was removed and complete RPMI was added and the cell solution was passed through a strainer to create a homogeneous single-cell solution. After a few more washings with complete RPMI, the cell solution was either directly placed into an adherent plate (first method), or cultured for about a week in an ultra-low adherent plate with complete RPMI supplemented with 50 ng/mL of EGF (Peprotech), 0.5 µM of A83-01 (STEMCELL Technologies), and 10 µM Thiazovivin (STEMCELL Technologies), and then placed in adherent plate in complete RPMI (second method). Differential trypsinization can be applied when the fibroblast population appears abundant. Briefly, cells are trypsinized and detached from the plate surface, then replated and incubated for 30 minutes, allowing primarily fibroblasts to adhere. The supernatant, which contains the majority of melanoma cells, is then collected and transferred to a new plate.

3.6. Immunofluorescence of adherent cells

Cells were seeded in multi-chamber slides (Ibidi, Germany) at a density of 10-20 x 10^3 cells/chamber in 300 µL of medium/chamber and incubated at 37°C and 5% CO2 overnight. Cells were fixed in 4% PFA for 10 minutes at RT and permeabilized with 0.3% Triton X solution for 10 minutes at RT. Afterward, cells were washed with PBS and incubated in a blocking solution (10% FCS) for 1 hour. Primary antibodies were added and incubated at 4°C overnight. MLANA/MART-1 (1:500, Rabbit, Cell Signalling®), Anti-Melanoma antibody (1:50, Mouse, Abcam), TE-7 (1:100, Mouse, Merk), α-SMA (1:200, Rabbit, Cell Signalling®). Secondary antibodies conjugated with fluorophore and DAPI (1:1000) were added and incubated for 1 hour in RT. Alexa Fluor 488 (goat

anti-mouse, 1:1000, Thermo), Alexa Fluor 647 (donkey anti-rabbit, 1:1000, Thermo). Confocal images were acquired using Cytation 10 with 20x objective, and with GFP and CY5 filter cubes.

3.7. High-throughput screening (HTS)

3.7.1. Drug libraries

Two libraries were selected for HTS:

1) The Prestwick Chemical library® (PCL) composed of 1267 compounds with over 85% marketed drugs, and all compounds at 10mM concentration (Appendix 2);

2) The "Melanoma drug library" (MDL) composed of 54 compounds selected for this study based on literature for their effects on the different melanoma genomic subtypes and further discussed with our clinical partner Prof. Jochen Utikal (Appendix 3). Additionally, 7 well-known anti-melanoma compounds were added: Vemurafenib (BRAFi), Dabrafenib (BRAFi), Encorafenib (BRAFi), Cobimetinib (MEKi), Trametinib (MEKi), Binimetinib (MEKi), and Palbociclib (CDK4/6i). All MDL compounds were at a 10 mM concentration, and the library was generated by Selleckchem;

Selected HIT drugs were purchased individually from Prestwick® and dispensed in a specific ready-to-use source plate. Foretinib (multi-target tyrosine kinase inhibitor, Selleckchem) was used as a positive control at a concentration of 30 µM, and 0,1% DMSO was used as a vehicle/negative control. For cell stimulations outside the HTS workflow: Trametinib (#S2673; Selleckchem, Germany), Daunorubicin HCl (#S3035; Selleckchem, Germany), Pyrvinium Pamoate (#S5816; Selleckchem, Germany).

3.7.2. Optimized HTS workflow

The semi-automated HTS platform, "Disease Modelling and Screening Platform" of LIH/LCSB, Luxembourg was used to perform the HTS assays. The platform is equipped with two liquid handler workstations (Biomek NXp and Biomek FXp (Beckman Coulter)), two integrated incubators, an acoustic droplet ejector Echo 550 (Labcyte Inc.), a multimode plate reader SpectraMax i3 (Molecular Devices), a confocal high-content microscope CV8000 (Yokogawa) equipped with solid lasers (wavelengths: 405/488/561 nm) and emission filters (445/45 nm, 525/50 nm, 600/37 nm), and an integrated robotic arm. Cells were seeded in 384-well U-bottom ULA black plates (Corning®) at cell-line specific densities of 5 x 10^3 cells/well for SKmel147, 10 x 10^3 cells/well for WM3918, and 0.5 x 10^3 cells/well for 624mel in 20 µL/well, centrifuged at 500 *x g* for 5 minutes and incubated for 72 hours at 37°C and 5% CO_2. The compounds from the PLC and MDL libraries were dispensed (one well per compound) using the acoustic droplet ejector, a further 40 µL/well of the medium was

added and spheroids were incubated for 5 days at 37°C and 5% CO_2. Every compound was dispensed at a final concentration of 10 µM and 1 µM, each of them in duplicate (on two separate plates), with a final DMSO concentration of 0.1%. Side wells were dedicated to positive (Foretinib 30 µM) and negative controls (DMSO 0.1%), and the first and last row and columns of the plate were excluded to reduce edge effects. The plate layout is shown in Fig. 27A. Cell viability was assessed using Calcein AM (Cayman Chemical). Calcein AM was added 4X concentrated in 20 µL/well (80 µL is the total volume per well) and incubated for 2 hours. Confocal images were acquired using a 10x objective, 488 nm laser 525/50 nm emission filter, and Z-stack acquisition mode.

A mock test was run before each HTS to check the quality of the cells and assay, following the same seeding and timing procedures and including a drug response performed using a 3-fold dilution series of Foretinib (positive ctrl) starting at 10 µM.

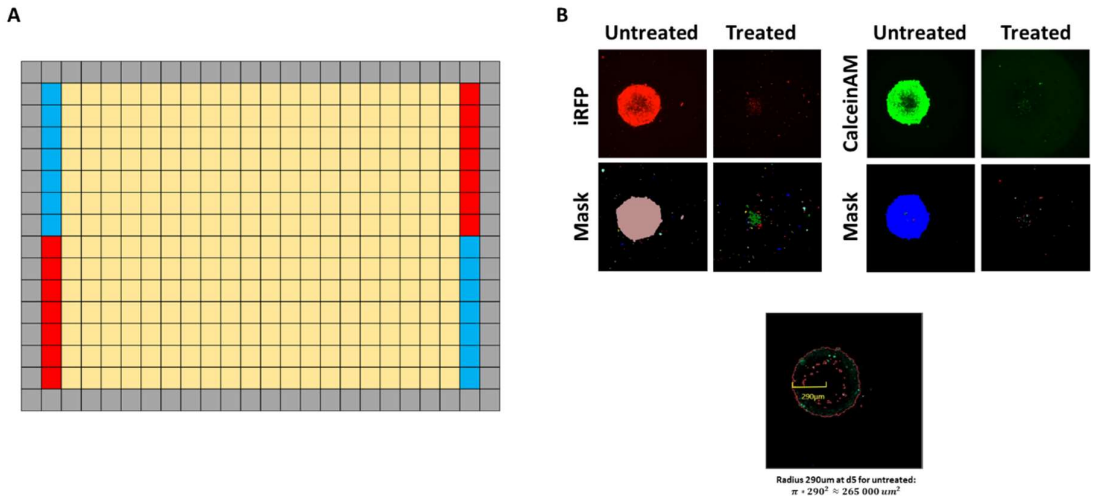

Figure 27: A) **Plate layout adopted for HTS assays**. In grey are the wells excluded to reduce edge effects; in blue are the wells dedicated to the negative control (DMSO 0.1%); in red are the wells dedicated to the positive control (Foretinib 30 µM); in yellow are the wells dedicated to the library compounds (1 well/drug). The Prestwick Library was divided into 4 plates, while the MDL into only 1 plate. B) Segmentation analysis to calculate the total spheroid area following iRFP or Calcein AM signal.

3.7.3. Data analysis and hit selection

Z-stack pictures for each well were transformed into a unique picture per well by maximum intensity projection (MIP). CellPathFinder® was used to analyze MIP figures and extract the total area/well. In brief, following the Calcein AM green-fluorescent signal, a segmentation mask was

created and allowed for the calculation of the radius and area segments (Fig. 27 B). Next, the software summed all the area's segments outputting a total Calcein AM area per well (μm^2). The application of a statistical test (Grubb's test), followed by visual confirmation, removed outliers from the analysis. Importantly, the Z'-factor and coefficient of variation (CV) were calculated for each screened plate as a quality control step. Raw area/well was used to mathematically set a plate-specific threshold for determining hit drugs, by applying the following formula: averageDMSO - (3 x standard_deviationDMSO) (310). Drugs were taken into consideration if their total area was below the set threshold in both duplicates. Afterward, data were normalized for their DMSO control and placed as the percentage of cell viability. Only drugs below 50% of cell viability in both duplicates and previously mathematically below the set threshold, were entereing a more stringent selection. Finally, visualization of the MIP pictures to further confirm the drug effect and exclude false positives given by the plate edge effect and application of additional conditions such as literature research, led us to generate a list of hit drugs. Rstudio was used for the statistical/mathematical analysis and the creation of relative plots.

3.7.4. Hits validation

Drug-response curves with relative IC50 values were generated for each selected HIT drug. The DMSP platform was set as for HTS (described in chapter 3.4.2). Drugs were dispensed in duplicate using a 3-fold dilution series from the dedicated source plate, starting from 10µM with 10 dilutions. As a further internal quality control, Foretinib was dispensed in duplicate using a 3-fold dilution series from the dedicated source plate, starting from 10µM with 10 dilutions. Extrapolation of the total area/well of MIP Calcein AM pictures, Z'-factors, and CV values was performed as described in Chapter 3.7.3. Data were normalized by the DMSO control. GraphPad Prism® (10.0.0) was used to analyze the data. A non-linear regression (four parameters) analysis was used to extrapolate IC50 and R^2 values for each tested compound.

3.8. 2D and 3D drug response curve (DRC) and IC50 determination

Outside the DMSP platform, we generated DRCs for melanoma and additional non-cancerous cell lines. Generation of DRCs and determination of IC50 values of drugs tested in non-cancerous cells (NHDF, MRC-5, LX-2, and HMEC-1) in 2D was performed as follows: cells were seeded at a density of 5×10^3 cells/well in 100 µL of cell line-specific medium. Drugs were diluted in a 3-fold dilution series for 8 dilutions, with starting amounts for Daunorubicin HCl and Pyrvinium Pamoate of 10 µM. Cell viability was determined with the CellTiter-Glo® 3D Cell Viability Assay (Promega).

Upon 5 days of treatment, a microplate reader Cytation 5 Cell Imaging Multi-Mode Reader (BioTek, Winooski, VT) was used for measurements of luminescence. The IC50 experiments were performed in technical and biological triplicates. Dose-response curves and IC50 values were generated with GraphPad Prism 10 and determined with the non-linear log (inhibitor) vs response-variable slope (four parameters) equation.

For selected melanoma cell lines, the determination of IC50 values of drugs tested was performed in 3D as follows: cells were seeded in 384-well U-bottom ULA plates (S-bio®) at densities of 0.5-1 x 10^3 cells/well in 80 µL/well, centrifuged at 500 x g for 5 minutes, and incubated for 4 days at 37°C and 5% CO2. Drugs were diluted in a 3-fold dilution series for 10 dilutions, with starting amounts for Daunorubicin HCl of 10 µM and Pyrvinium Pamoate of 1 µM. Before drug and cell viability reagent dispensations, spheroid observation utilizing a bench-top microscope was executed as a quality control step. Cell viability was determined with the CellTiter-Glo® 3D Cell Viability Assay (Promega). Upon 5 days of treatment, a microplate reader Cytation 5 Cell Imaging Multi-Mode Reader (BioTek, Winooski, VT) was used for luminescence measurements. The IC50 experiments were performed in technical and biological triplicates. Dose-response curves and IC50 values were generated with GraphPad Prism 10 and determined with the non-linear log (inhibitor) vs response-variable slope (four parameters) equation.

3.9. 3D Synergy Assay

SKmel30 and SKmel147 cells were seeded at a density of 500 cells/well in 384-well ULA plates (SBio) and spheres were allowed to form for 3 days before addition of drugs. They were treated for 5 days with either single drugs or combinations of Trametinib and either Pyrvinium Pamoate or Daunorubicin HCl in a matrix format at a fixed 1:2 dilution range. Drug concentrations were pre-determined based on each inhibitor's IC50 value. Cell viability was assessed with the CellTiter-Glo® 3D Cell Viability Assay (Promega). Synergy scoring was determined using the "inhibition readout" (calculated as "100 - Cell Viability") on the online SynergyFinder software version 3.0 (https://synergyfinder.fimm.fi) and implementing the ZIP calculation method as published before (317). Zero Interaction Potency (ZIP) scores <−10 and >10 correspond to antagonist and synergistic effects, respectively.

3.10. 3D spheroids drug efficacy assessment: kinetic and end-point assays

Kinetic (time-lapse microscopy) and endpoint cell proliferation (cell viability assay), upon drug treatments, were evaluated as described before (315). In brief, either mono- or -multi-component spheroids were generated utilizing labeled cells to allow the kinetic tracking of the cells.

After the incubation period, 40 µL were removed from each well and replaced with 40 µL supplemented with 2 times concentrated tested compounds and controls. The plate was centrifuged at 500 x g for 5 minutes and placed in the live-cell incubator (BioSpa8, BioTek, Winooski, VT) linked with an automated microplate reader (Cytation 10, BioTek, Winooski, VT). A robotic arm placed the plates into the reader for time-lapse microscopy in which images were acquired every 12 hours for 5 days using a 4X magnification object and 590 nm LED and a Texas Red filter cube (Excitation 586/15 nm, Emission 647/57 nm) were employed for tracking melanoma fluorescence changes over time. On day 5, spheroid cell viability was determined using the CellTiter-Glo® 3D Cell Viability Assay (Promega). A microplate reader Cytation 5 Cell Imaging Multi-Mode Reader (BioTek, Winooski, VT) was used for luminescence measurements. Kinetic and end-point cell proliferation data were analyzed and plotted with GraphPad Prism 10.

3.11. Confocal microscopy of 3D Multi-component spheroids

Confocal images of 3D multi-component spheroids were acquired using a Cytation 10 (BioTek, Winooski, VT) confocal microscope with spinning disk technology. The instrument is equipped with a laser combiner (spectral range 398–643 nm) and a DAPI filter cube (Excitation 390/40 nm, Emission 442/42 nm), a GFP filter cube (Excitation 472/ 30 nm, Emission 520/35 nm), and a TRITC filter cube (Excitation 556/20 nm, Emission 600/37 nm). Pictures were acquired using a 20X magnification object.

3.12. 3D spheroid apoptosis and cell death assay using confocal microscopy

Melanoma cells were seeded in 384-well black U-bottom ULA microplate (Corning®) at densities of 0.5 x 10^3 cells/well in 80 µL/well of the medium, centrifuged at 500 x g for 5 minutes, and incubated for 2 days at 37°C and 5% CO2. Upon removal of 40 µL/well of the medium, drugs were dispensed 2 times concentrated in 40 µL/well of the medium, centrifuged at 500 x g for 5 minutes, and incubated for 5 days at 37°C and 5% CO2. CellEvent™ Caspase-3/7 Detection Reagent (Invitrogen, Thermo) and SYTOX™ Blue Dead Cell Stain (Invitrogen, Thermo) were added and incubated at 37°C for at least 2 hours. Cytation 10 was used to was used to acquire multiple images in z-stack modality using DAPI, GFP, and TRITC filter cubes and a 20X magnification object. Brightfield pictures were also acquired using a 20x magnification object. Maximum intensity projected images were analyzed using Gen5 (Agilent). Total fluorescence intensity (TFI) signals emitted by CellEvent™ and SYTOX™ Blue positive cells were extracted. For mCherry-expressing melanoma cell lines, mCherry signal was used to measure the total tumor mass, while for non-labeled melanoma cells, brightfield images were used to measure the total tumor mass. Then, TFI was normalized by the total tumor mass.

3.13. Western blot analysis

Cells were seeded in 6-well Aggrewell plates (StemCell) at densities of 0.5-1 x 10^3 cells/well in 5 mL of medium, centrifuged at 100 x g for 5 minutes, and incubated for 4 days at 37°C and 5% CO2. Drugs were dispensed and incubated for further 1, 3, and 5 days. Cell lysis was performed on ice with cold lysis buffer (RIPA 1X plus Complete phosphates inhibitor), Protein content was determined using Pierce™ BCA Protein Assay Kits (Thermo), and protein lysates were further analyzed by SDS-PAGE. The detection of enhanced chemiluminescence signals was performed as previously described (318,319). Primary antibodies used in the study were: Topoisomerase 2α (1:1000, Rabbit, CellSignaling®), γH2AX (1:1000, Mouse, CellSignaling®), β-catenin (1:1000, Rabbit, CellSignaling®), GAPDH (1:5000, Rabbit, Sigma®), ERK (1:1000, Rabbit, CellSignaling®), pERK (1:1000, Rabbit, CellSignalling®), AKT (1:1000, Mouse, CellSignalling®), pAKT (Ser473) (1:1000, Rabbit, CellSignalling®). All primary and HRP-conjugated secondary antibodies were purchased from Cell Signalling Technology (Boston, MA, USA). Blots were developed by Demetra Philippidou.

3.14. Hydrogel-embedded melanoma co-cultures

Melanoma-TME hydrogel encapsulation co-cultures were generated as follows. A multi-arm (8) STAR poly-ethylene-glycol (PEG), bioconjugate with RGD and adhesion MMP cleavable sites and cross-linkable with transglutaminase (Factor XIII) hydrogel (ECTICA technologies, Switzerland) was used as a scaffold for the encapsulation. mCherry-expressing melanoma cells at a density of 2-4 x 10^4/100µL were mixed with either NHDF, MRC-5, or LX-2 expressing GFP a density of 20 x 10^4/100µL and with HMEC-1 expressing BFP at a density of 20 x 10^4/100µL, were centrifuged at 300 x g for 3 minutes and supernatant was removed. For 100 µL of hydrogel solution, 45 µL of RPMI and 43 µL of PEG were added and gently mixed to dissolve the cellular pellet. Then, 12 µL of Factor XIII (ECTICA technologies, Switzerland) was added and the solution was gently mixed without introducing bubbles. 5 µL of solution was dispensed in each well in a black 96 well plate (µClear Greiner®) in order to create homogeneous domes and incubated at RT for 5 minutes until complete polymerization. 200 µL/well of RPMI supplemented with 10ng/mL of VEGF (Peprotech) was dispensed in each well and incubated for 3 days at 37°C and 5% CO2. 2x concentrated drugs were added in 100µL/well of fresh medium, upon removal of 100 µL/well of the old medium, and further incubated for 5 days at 37°C and 5% CO2. Confocal microscope Cytation 10 (BioTek, Winooski, VT) was used to acquire multiple images in z-stack modality using DAPI, GFP, and TRITC filter cubes and 20X magnification object, selecting 4 ROIs per well. Maximum intensity projected images were analyzed using ImageJ (Fiji).

3.15. 3D Collagen assay

This assay was performed by Dr. Joanna Wroblewka. Melanoma cell lines SKmel147 and M160915 were seeded in ultra-low attachment BIOFLOAT™ 96-Well plates (Facellitate, Mannheim, Germany) in densities of 2,5 x 10^3 and 5 x 10^3, respectively. After 72h of formation, spheres were embedded between two layers of collagen type I solution, containing 2mg/ml Collagen type I (MercMillipore, Darmstadt, Germany), 1x RPMI (Gibco Thermo Fisher Scientific, MA, USA), 1% of Fetal Calf Serum (Fetal Calf Serum, Gibco Thermo Fisher Scientific, MA, USA). The pH of the collagen solution was adjusted to 7.4 using 1M NaOH. Fifty microliters per well of collagen I solution were pipette into an optically clear, black-walled 96 well plate (µClear Greiner®) and let to polymerize for 5 minutes at 37°C. Next, one spheroid per well was transferred on top of the collagen layer and immediately covered with 50 µL of collagen solution and polymerized for 15 minutes at 37°C. Immediately after, 200 µl of medium containing either 0,5% DMSO (negative control) or 2x IC50 concentration of drugs of interest was added on top of the collagen layer. For each experimental condition, 8 spheroids were used. Pictures were taken on day 0 (immediately after embedding) and after 72 hours of incubation, using Cytation 10 (BioTek, Winooski, VT) manual mode and 4x magnification. The area of cellular migration/invasion was analyzed using ImageJ software (Fiji).

3.16. Zebrafish husbandry and xenograft

Zebrafish xenograft experiments were performed by Dr. Joanna Wroblewka in collaboration with Prof. Natascia Tiso at the zebrafish facility (University of Padova, Italy), and Dr. Maria Lorena Cordero Maldonado from the Aquatic Platform (LCSB, University of Luxembourg), under the authorization 407/2015-PR (OPBA). All procedures complied with the European Legislation for the Protection of Animals used for Scientific Purposes (Directive 2010/63/EU). Embryos were obtained from the natural spawning of adults of nacre/mitfa background. In prior injections, doses of Trametinib, Daunorubicin HCl and Pyrvinium Pamoate were determined as Maximum Tolerated Doses (MTD). Briefly, uninfected nacre/mitfa 2dpf larvae were treated with serial dilution of drugs of interest, to determine the highest tolerated and non-toxic dose. Larvae viability and development was monitored daily during drug treatment. The cut-off of 20% mortality and no developmental defect was set to determine MTD. Two days after fertilization, embryos were manually dechorionated and anesthetized with a solution of tricaine (80 mg/l, Sigma-Aldrich). SKmel147-mCherry cell line was detached using phenol red-free TryplE reagent (Gibco Thermo Fisher Scientific) and resuspended in PBS at a concentration of 2 x 10^5 cell/ µL.

The cells were injected into the yolk of larvae as a single droplet (around 100 cells per embryo) using a World Precision Instrument (Sarasota, FL, USA) or FemtoJet 4i (Eppendorf, Hamburg, Germany) microinjectors. PBS with Phenol red was injected as a vehicle control. After 24h, larvae were assessed for successful yolk injections and subjected to drug treatment with 12 nM Trametinib, 1 µM Daunorubicin HCl, 111 nM of Pyrvinium Pamoate for 3 days. Larvae viability was monitored daily. After 3 days, larvae were anesthetized as described above and photos of xenografts were taken using an M165 FC microscope with DFC7000T camera (Leica Camera, Wetzlar, Germany) or Nikon SMZ25 fluorescent microscope (Nikon Instruments, Japan). Data were analyzed based on fluorescence intensity to measure xenograft area and number of cells.

3.17. Statistical analysis

Statistical analysis was performed using GraphPad 10.3.1 software (GraphPad, Boston, MA, USA). Data following Gaussian distribution was analyzed using Ordinary one-way ANOVA with Dunett's multiple comparison test. Data not following Gaussian distribution was analyzed using ordinary Kruskal-Wallis with Dunn's multiple comparison test. Data with untreated controls set at 100 were analyzed using One sample T-test.

4. Results

This thesis focuses on four key objectives: i) creating advanced 3D melanoma models that better reflect tumor microenvironment interactions; ii) establishing a high-throughput screening workflow for 3D melanoma spheroids; iii) identifying novel drug candidates for $NRAS^{mut}$ and WT melanoma patients; iv) validating promising compounds against $NRAS^{mut}$ melanoma.

4.1. Establishment of Multi-component 3D melanoma spheroid (MMS) models for preclinical drug testing

To establish more physiological melanoma models allowing for testing drug candidates in *vitro* models, we first established **spheroid-based co-culture models** composed of melanoma cells with key cell types that mostly represent the tumor microenvironment in the skin or different melanoma-specific metastatic sites (lung, liver), with endothelial cells, fibroblasts, and PBMCs. Moreover, specific assays were established to evaluate drug efficacy.

4.1.1. Co-culture methods

Before establishing advanced melanoma spheroid systems with several different cell types, key parameters had to be optimized for mono-component spheroid cultures, such as spheroid size, viability, structure, and duration of culture. First, we seeded 624mel cells at different **cell numbers** per well (500, 1000, 1500, 2000, and 2500) and followed the spheroid growth for 7 days by measuring the diameter or area of the spheroids (Fig. 28 A). At all seeding densities, melanoma cells grew exponentially. A diameter of 250-300 µm for spheroids represents a good size model to mimic nutrient, oxygen, waste, and drug perfusion without necrosis in the inner core (259,260). Above 500 µm in diameter, spheroids are described to have a thin proliferative outer cellular layer and an inner apoptotic and necrotic core (261,262). **Histological evaluation** through Hematoxylin and Eosin (H&E) and immunofluorescence (IF) of cryo-sections was used to assess the architectural structure, viability, and apoptosis of 624mel spheroids seeded at a density of 500 cells/well and collected after 4, 7, 10, and 14 days of culture. H&E staining revealed a time-dependent decellularization toward the inner core. Spheroids collected after 4 days of culture, presented high cellular proliferation and absence of apoptosis, while those collected after 7 days showed an onset of decellularization in the core with a reduction of the Ki67 signal and an increase in cleaved PARP indicating apoptosis. After 10 days, the inner spheroid core presented higher apoptosis levels and a thinning of the outer proliferative layer, until the loss of spheroid structure on day 14 (Fig. 28 B).

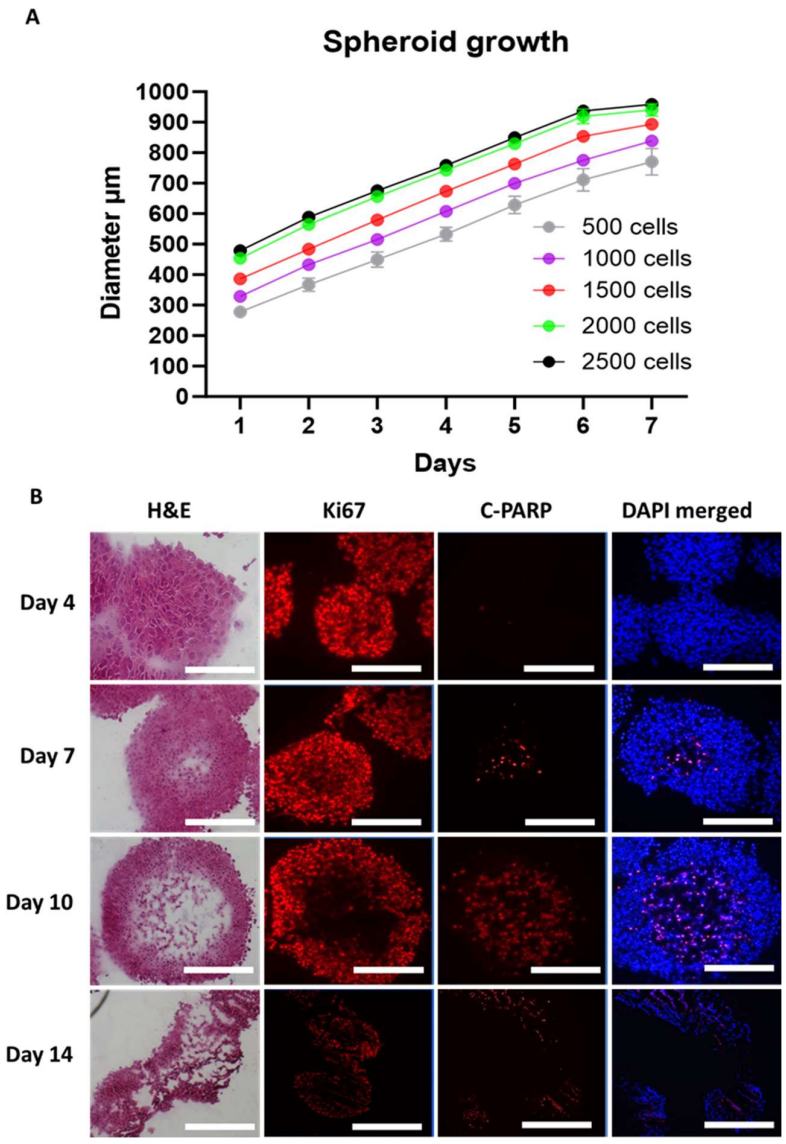

Figure 28: **Spheroid culture in the setup phase.** A) The plot represents 624mel spheroid diameters during a growth period of 7 days in which cells were seeded at different densities. Data shows the mean ± SD of *n* = 2 independent biological replicates. B) Cryo-sections of 624mel spheroids collected after 4, 7, 10, and 14 days of culture were stained for H&E, Ki67 (proliferation marker), cleaved PARP (apoptosis marker), and DAPI (nucleus staining). Scale bar = 300 µm.

Based on these results, we used a 500 cells/well seeding density for highly proliferative melanoma cells for most of the following assays. Given the spheroid size ranges and the absence of cell death, we chose to take as drug-treatment starting time point at day 4, without exceeding day 10 as the treatment end time point. Several melanoma $BRAF^{mut}$, $NRAS^{mut}$, and WT melanoma cell lines were tested for their sphere formation capacity and growth as spheroids by Demetra Philippidou (research support engineer) and Christiane Margue (research scientist) (Suppl. Fig. 1 A and B).

Afterwards, we specifically selected four NRAS^{mut} melanoma cell lines (two well-studied cell lines, SKmel147 and SKmel30, and two primary metastatic melanoma cell lines, M160915 and M161022) and assessed the growth at 4 and 9 days after seeding, showing growth in all 4 cell lines (Fig.29 A and B). SKmel147, SKmel30 and M160915 demonstrated a high sphere formation capacity, while M161022 showed a lower spheroid formation capacity, forming a compact 3D cellular aggregate.

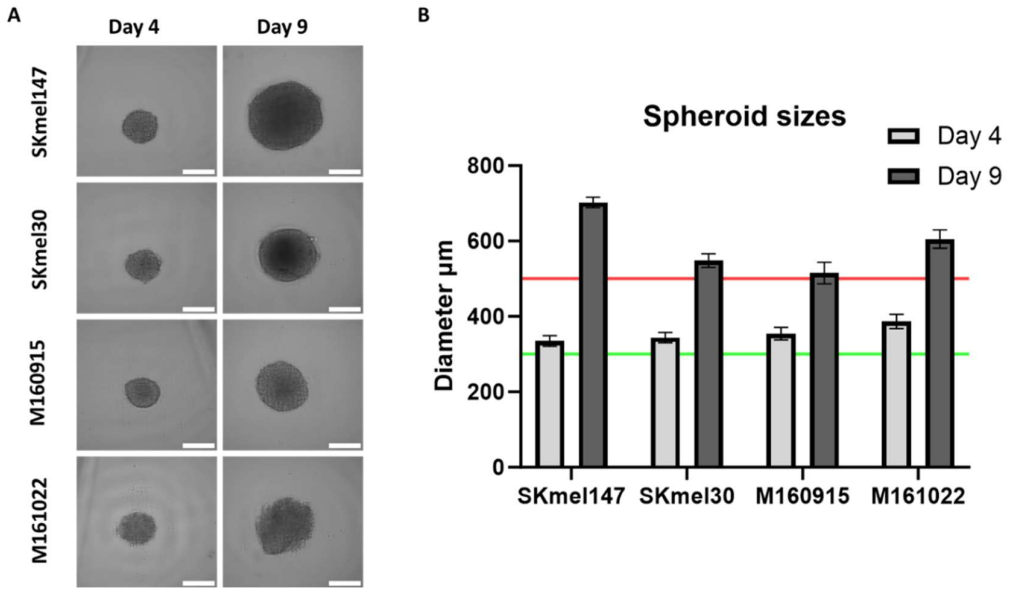

Figure 29: **Melanoma cell lines cultured as spheroids**. A) Spheroid morphology of the four NRAS-mutated melanoma cell lines after 4 and 9 days of culture. B) Two established (SKmel147 and SKmel30) and two primaries metastatic (M160915 and M161022) melanoma cell lines reached a spheroid diameter of >300 µm and >500 µm after 4 and 9 days respectively of culture. Scale bar = 300 µm. Data are mean ± SD of *n* = 3 independent biological replicates.

One of the most common methods of co-culture is the **simultaneous seeding** of cancer cells with other cell types of interest. First, the simultaneous seeding method was tested by co-seeding 624mel-iRFP and NHDF-GFP in ULA microplates at a 1:3 ratio and assessed the behavior of fibroblasts after 72 hours of culture by tracking the fluorescent signal constitutively expressed by both cell types. In line with previous observations (268), after only 24 hours of co-culture, NHDFs rapidly concentrated in the inner core of the spheroids (Fig. 30 A), which is known to be highly hypoxic, and lacking nutrients. To overcome these issues emphasized by the simultaneous seeding approach, alternative seeding and culture methods were tested to confer a more equal distribution of fibroblasts thus allowing longer survival and improved interaction with melanoma cells. Hence, we tested a **sequential seeding** approach, where melanoma cells are seeded first and incubated

for 24 hours allowing them to form spheroids before fibroblasts are added on top and incubated for another 24 hours. Live cell imaging revealed a more equal cellular distribution through the whole spheroid, without the concentration of fibroblasts in the inner core (Fig 30 B). These observations are in line with the work of Yakavets et al. who observed that MRC-5 fibroblasts, co-cultured with breast cancer cells, concentrated in the core of the spheroid after a short time in culture (268). Furthermore, spheroids after the sequential method were slightly bigger than after simultaneous seeding (Fig 30 C). To check whether the co-culture of fibroblasts had any advantageous effect on melanoma growth, we tracked over time the fluorescence signal of 624mel constitutively expressing iRFP in monoculture or co-cultured with NHDF. We observed that melanoma cells seem to grow more when co-cultured with fibroblasts (Fig 30 D) in line with what was observed in literature where the interaction of melanoma cells with fibroblasts increases the proliferation and survival of melanoma cells (231,233).

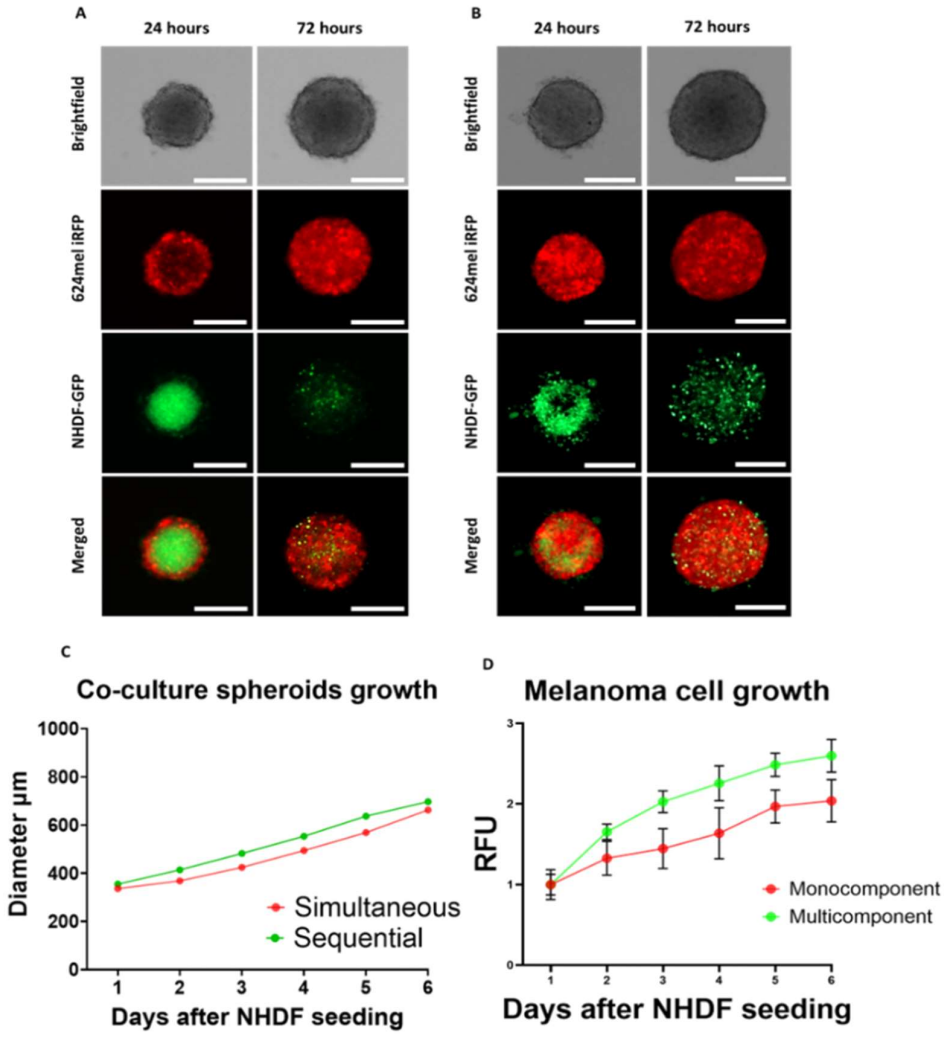

Figure 30: **Simultaneous and sequential seedings for spheroid melanoma-NHDF co-culture**. Live-cell imaging of melanoma (624mel-iRFP, red) and fibroblast (NHDF-GFP, green) co-culture spheroids generated by adopting the A) simultaneous seeding method and B) the sequential seeding method. Pictures show spheroids 24 and 72 hours after seeding. Scale bar = 250 µm. C) Spheroid growth (diameter) compared for the two different generation methods. D) Melanoma-specific fluorescent signal (iRFP) was tracked for 6 days to evaluate melanoma cell growth in mono- and co-culture systems. RFU was normalized by Day 1. Data are mean ± SD of *n* = 2 independent biological replicates.

Finally, I tested different melanoma cell densities (500, 1000, 1500, 2000, and 2500 cells/well) co-cultured with NHDF at a 1:3 ratio and tracked spheroid diameter and melanoma-specific fluorescent signal. An **optimal size range** (Fig. 31 A) and more **linear melanoma growth** (Fig. 31 B) were observed when 500 melanoma cells were seeded. Interestingly, we observed that RFU values for all seeding conditions were very similar on day 5, while only spheroids seeded with 1000 and 500 melanoma cells/well experienced a growth in fluorescence intensity. It is hypothesized that in conditions seeded with a higher cell density likely reached maximum saturation by day 5, after which continued growth may have led to signal oversaturation, resulting in a reduction of fluorescence intensity. This observation highlights the critical importance of careful optimization during the setup phase for 3D culture assays.

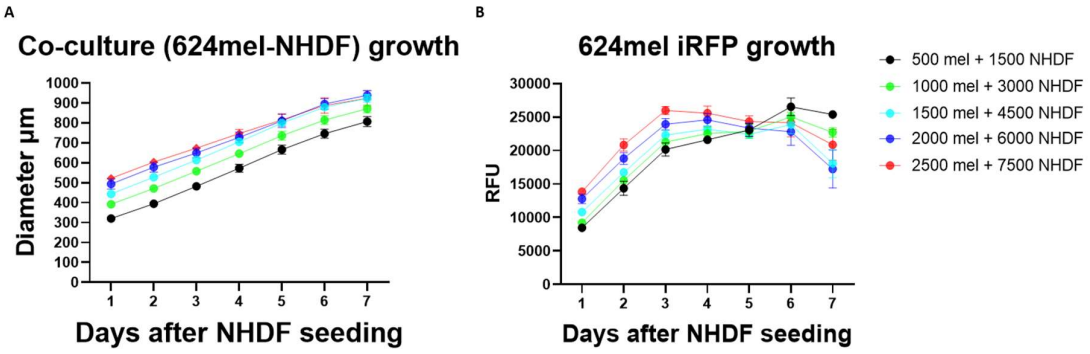

Figure 31: **Different cell densities in co-culture melanoma-NHDF spheroids**. A) The spheroid's diameters were measured daily for 7 days. B) The fluorescent melanoma-specific signal was tracked for 7 days to evaluate melanoma cell growth. Data are mean ± SD of *n* = 2 independent biological replicates.

4.1.2. Characterization of Multi-component Melanoma Spheroids (MMSs)

Next, the complexity of our 3D models was further enriched by adding endothelial cells represented by the HMEC-1 cell line. Moreover, to mimic other main melanoma metastatic sites, besides the skin, such as the lung and the liver, we also included lung fibroblasts (MRC-5) or hepatic stellate cells or HSC (LX-2) instead of NHDFs.

As seen before, cellular ratios are an important aspect of an efficient co-culture setting. We tested different ratios by co-culturing melanoma cells with different genomic backgrounds (624mel ($BRAF^{mut}$), SKmel147 ($NRAS^{mut}$), WM3918 (WT), (see Table 1) with HMEC-1, and either NHDF or MRC-5 or LX-2. **MMS-skin** corresponds to melanoma cells co-cultured with HMEC-1 and NHDF, **MMS-lung** corresponds to melanoma cells co-cultured with HMEC-1 and MRC-5, and **MMS-liver** corresponds to melanoma cells co-cultured with HMEC-1 and LX-2.

Different cell types were added following the **sequential seeding protocol** introduced in 4.1.1 to a constant 500 melanoma cells in the following ratios: 1:1:1, 1:3:1, 1:3:3, 1:3:10. Three melanoma cell lines belonging the main melanoma genomic subtypes were tested. Spheroids were grown for 7 days after the seeding of fibroblast/HSC, and no major differences were observed in the spheroid area between the different ratios (Fig. 32 A-C). Using melanoma cell lines stably expressing fluorescent mCherry, a similar effect was observed also for the different ratios in melanoma-specific growth by tracking their fluorescent signal (Suppl. Fig.2.). Given the lack of overall significant differences in whole spheroid growth and specific melanoma cell growth in all the tested ratios, we decided to adopt for all following experiments the **cellular ratio of 1:3:3** (melanoma:endothelial:fibroblasts/HSC).

To visualize the morphology and distribution of live cells over time in MMS, **high-resolution confocal imaging** was performed. SKmel147 ($NRAS^{mut}$) melanoma cells stably expressing mCherry, dermal/lung fibroblasts and HSC expressing GFP, and endothelial cells expressing BFP allowed for tracking the different cell components of MMSs (Fig.33) (see also the Materials & Methods section). Imaging demonstrated consistent growth of melanoma cells across all MMS models, indicating a favorable environment for melanoma cell proliferation within this system. Non-cancerous cell types, specifically NHDF and MRC-5 cells, displayed similar viability, sustaining survival until day 3 post fibroblast seeding within the spheroid structure, after which they were increasingly overgrown by the highly proliferative melanoma cells.

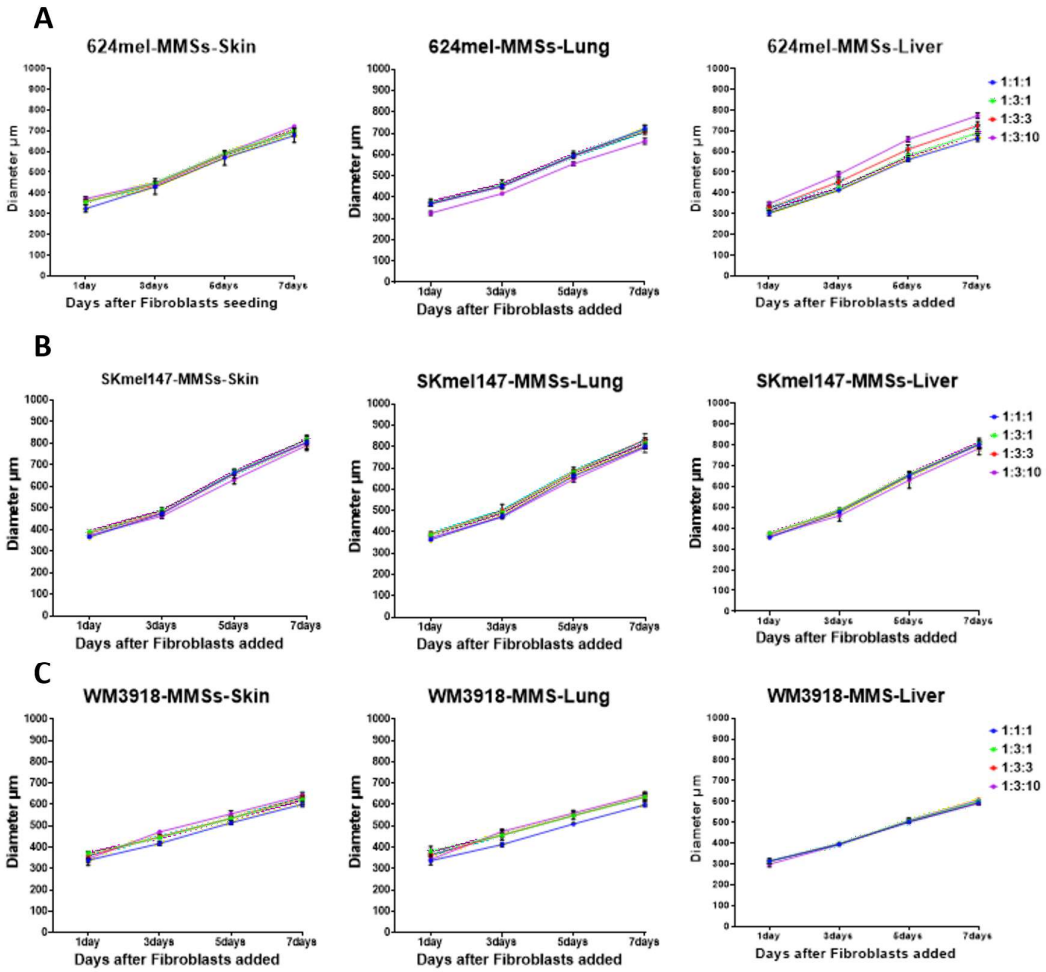

Figure 32: **Multicomponent melanoma spheroid growth (spheroid area µm²) generated using different cellular ratios of melanoma, endothelial, and fibroblast cells**. Three melanoma cell lines of different genetic backgrounds were used to create MMSs-Skin (melanoma, HMEC-1, and NHDF), Lung (melanoma, HMEC-1, and MRC-5), and Liver (melanoma, HMEC-1, and LX-2): A) 624mel B) SKmel147, and C) WM3918. Data are mean ± SD of *n* = 2 independent biological replicates.

This outcome aligns with our expectations and reflects the typical development and cellular composition of melanoma metastases. Liver (LX-2) cells were found in the outer layer of the MMS, displaying a totally different behavior from NHDF and MRC-5 cells which migrated inside the MMSs. Regardless of the MMS and the melanoma cell types, HMEC-1 cells mostly reside in the inner core of the MMS, following the same fate as NHDF and MRC-5 (Fig. 33 A-D, Suppl. Fig. 3 A-B).

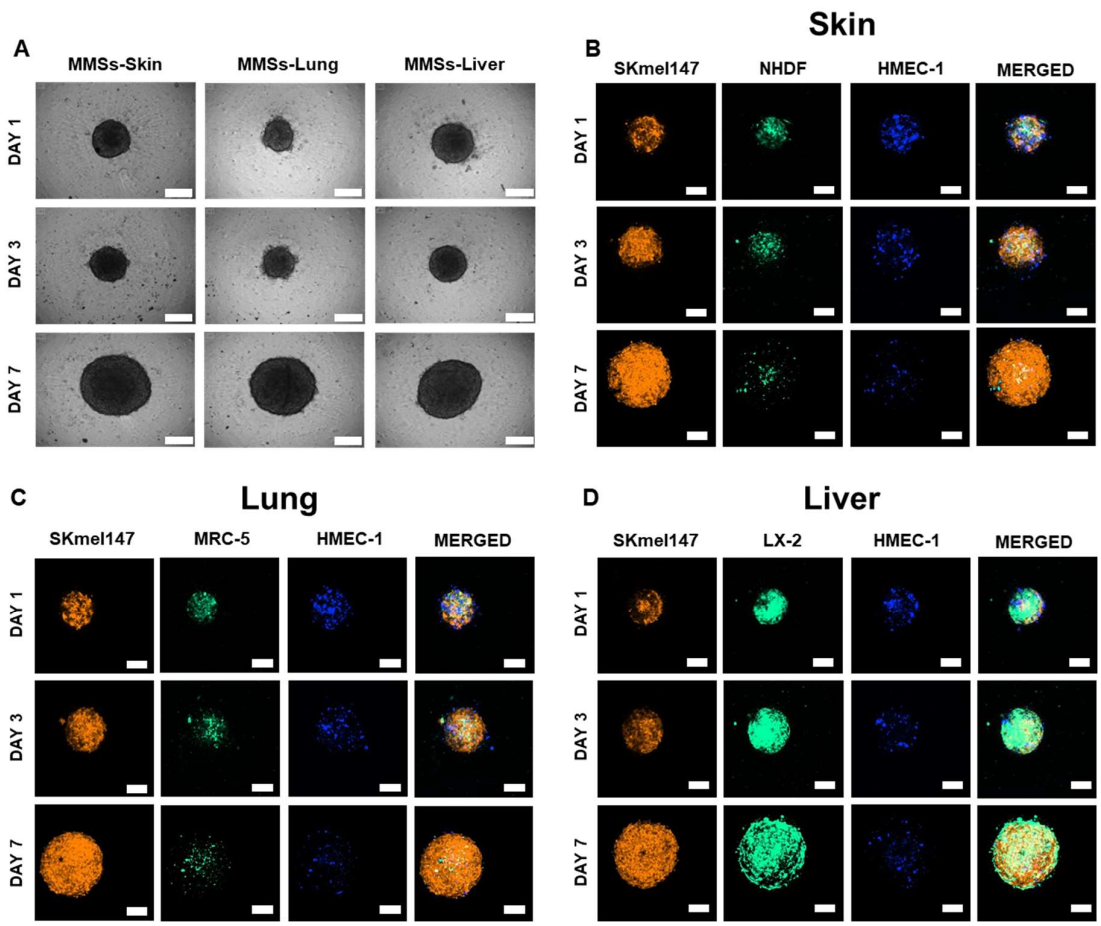

Figure 33: **Live-cell imaging of MMSs**. (A) Brightfield pictures of whole MMSs at day 1, 3 and 7 of culture (days after fibroblast/HSC seeding). (B-D) Cell lines constitutively expressing fluorescent proteins: Fluorescently labelled SKmel147 (orange-mCherry), HMEC-1 (blue-BFP), and either NHDF (B), or MRC-5(C) or LX-2 (D) (green-GFP). Confocal images were taken at maximum intensity projections of multiple z-stacks. Scale bar = 200 µm.

Finally, **histological staining** was performed to study spheroid structure and architecture, cell proliferation and apoptosis. FFPE sections of MMS-skin, -lung, and -liver were stained using hematoxylin and eosin (H&E) to show the whole spheroid structure and cellular architecture (Fig. 34 A). Moreover, immunofluorescence staining of the sections assessed cell proliferation with an antibody against Ki67, a key proliferation marker (Fig. 34 B). Antibodies against cell type-specific markers were used for the histological identification of the different cell types within the MMSs: CD31, for endothelial cells (Fig. 34 C), S100A4, for melanoma cells (Fig. 34 D), and α-smooth muscle actin (α-SMA), a specific activated-fibroblast marker (Fig. 34 E).

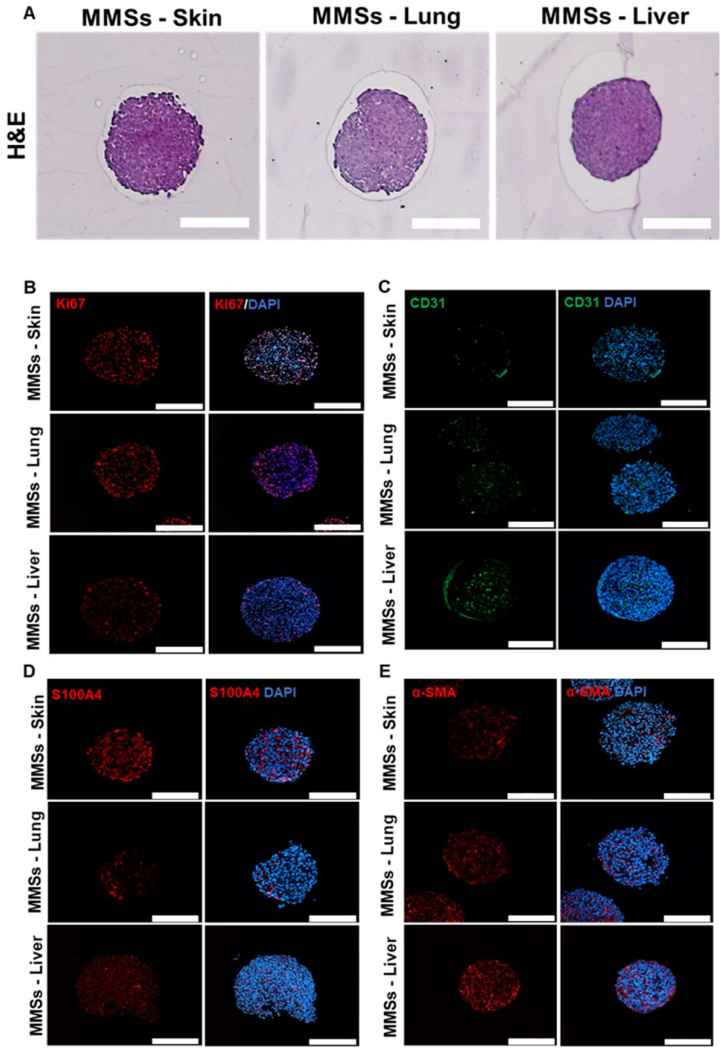

Figure 34: **Histological evaluation of MMSs-skin, -lung, and –liver**, generated using SKmel147 as melanoma cell line. Shown are MMSs collected after 3 days from NHDF/MRC-5/LX-2 seeding. A) Hematoxylin & Eosin staining for the evaluation of the structure and cellular architecture. Immunofluorescence staining: (B) Ki67 for cell proliferation, (C) CD31/PECAM-1 for endothelial cells, (D) S100A4 for melanoma cell identification, and (E) α-Smooth Muscle Actin (α-SMA) as a marker for fibroblasts/HSCs activation. Scale bar = 200 µm.

Taken together, our 3D multicomponent melanoma models provide increased biological complexity of spheroids models, showing efficient growth, and retention of cell-specific markers and allowing for mimicking the TME of melanoma-specific metastatic sites. To further increase the physiological relevance of the models we next included immune cells.

4.1.3. Characterization of MMSs co-cultured with PBMCs

The immune system plays an important role in tumor control and, in the last decades, immune therapies represented a major groundbreaking step forward in cancer therapy, especially in melanoma. 3D models capable of mimicking the interaction of cancer cells with immune cellular compartments are needed to test novel immune therapeutic agents efficiently and at the same time limiting animal experiments. In this regard, we also included immune cells in our MMS models, by co-culturing MMSs with **peripheral blood mononuclear cells** (PBMCs).

MMSs were generated as previously described (see: 4.1.2.Characterization of MMSs) and after 3 days after the fibroblasts/HSC seeding, PBMCs (isolated from healthy donors) were added in a 1:10 ratio (1:10 ratio of MMS total cells to PBMCs) and cultured for further 3 days. (Fig. 35) Anti-CD28 antibody was added to the medium to ensure the necessary co-stimulatory signals to activate immune cells.

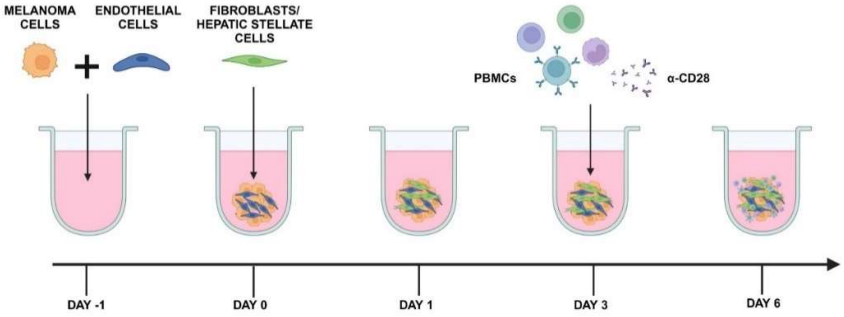

Figure 35: **Sequential seeding protocol for Melanoma Multicomponent Spheroid (MMS) generation including PBMCs.** On Day -1, melanoma and endothelial cells are seeded at a 1:3 ratio. One day later (Day 0), 3 parts of fibroblasts or HSCs are added on top (final ratio: 1:3:3). After 3 days of culture, MMSs can be co-cultured with PBMCs at a 1:10 ratio. Anti-CD28 antibody is added for co-stimulatory signals for activation of immune cells. Created with Biorender.com.

To determine whether or not immune cellular fractions had infiltrated the MMSss, the supernatant and MMSs were collected separately, dissociated, stained with a **specific panel of antibodies** and analyzed by flow cytometry (Fig. 36). Identification through flow cytometry of the different PBMC populations co-cultured with MMSs was performed by Eliane Klein (R&D specialist in our group).

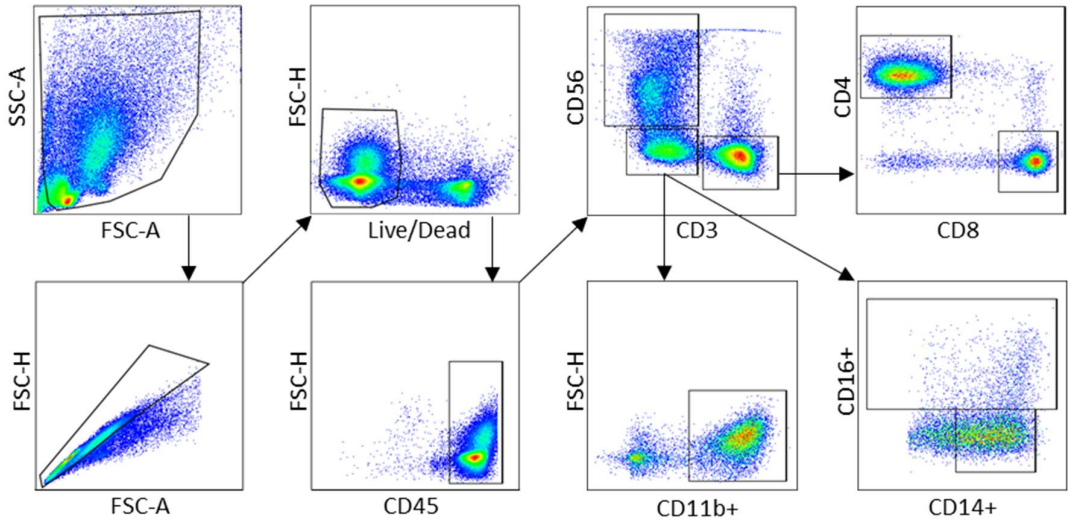

Figure 36: **Flow-cytometry gating strategy for identification of different immune cell populations** using a specific panel of antibodies. Arrows indicate in which order the gating was performed.

Major fractions of alive CD45+ cells were still present in the supernatant, while less than 50% had infiltrated the MMSs with the highest infiltration in MMS-liver models (Fig. 37 A). Among CD45+ cells, CD3+ lymphocytes were the largest infiltrative population compared to CD56+ natural killer (NK) cells, and CD11b+ and CD14+ monocytes (Fig. 37 B). ICI therapies mostly rely on the activation of lymphocytes, especially of cytotoxic T-cells, which efficiently kill cancer cells. Given the predominant infiltrative presence of CD3+ cells, discrimination between CD8+ and CD4+ cells revealed relevant levels for both cell types with a higher presence of CD4+ cells (Fig. 37 C). The panel of antibodies also included specific markers for tumor-associated macrophages (TAMs) such as CD163 and CD206. Given the polarization of macrophages to TAMs, the expression of CD163 and CD206 was evaluated by median fluorescence intensity depicting a higher expression of CD163 (Fig. 37 D).

To conclude, the efficient **co-culture of immune cells with our MMS models** illustrates the employability of such models even for immune therapeutic agent screenings. Further refinements of immune cells co-cultured with MMSs are currently ongoing.

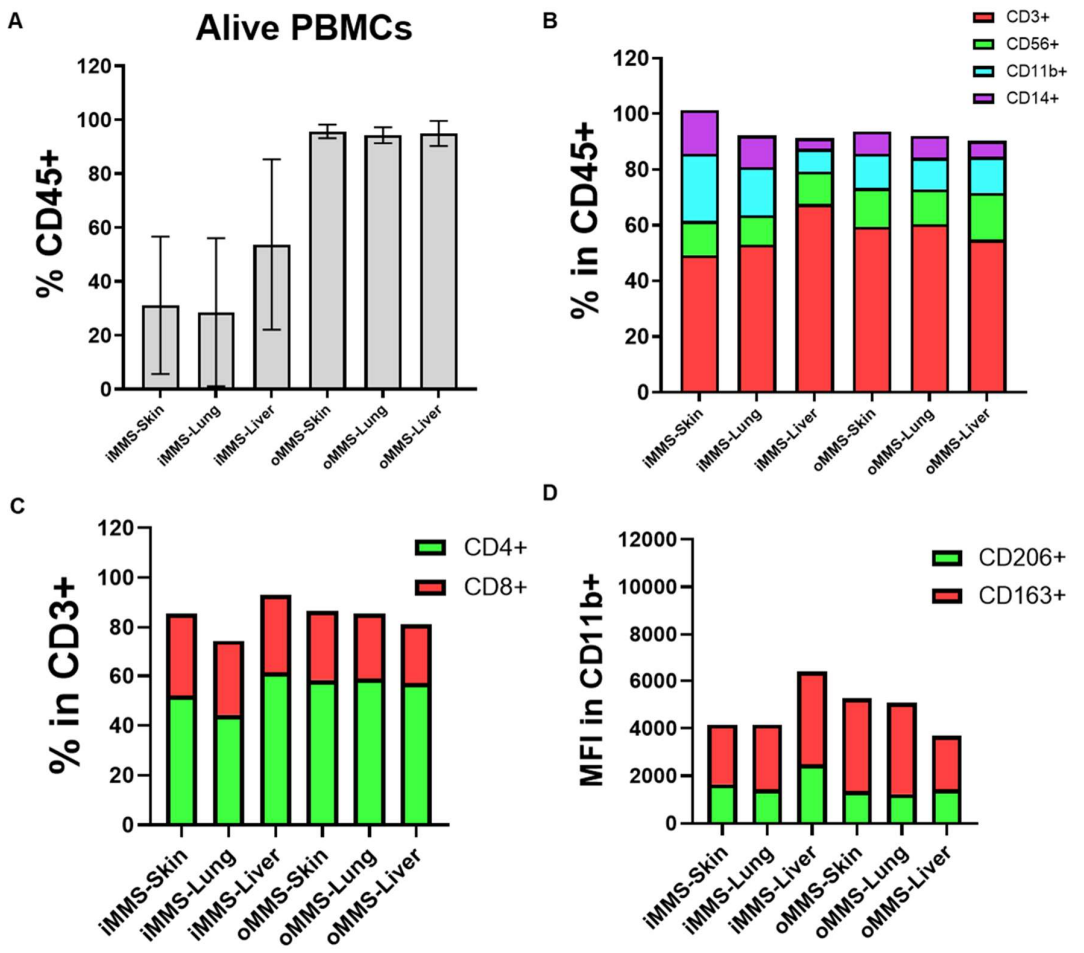

Figure 37: **Quantification of PBMC populations able to interact/infiltrate the MMSs (iMMS) or remaining in the supernatant (oMMS)**. Data are mean of *n* = 3 independent biological replicates. A) The PBMC populations in the supernatant remain stable across the three MMS types (skin, lung, and liver), while the interacting/infiltrating fractions show heterogeneity across the MMS types. (B) Immune cell fractions for iMMSs and oMMSs identified CD3+ lymphocytes, CD56+ Natural Killer cells and CD11b+ and CD14+ monocytes. (C) CD8+ and CD4+ T-cell fractions within the CD3+lymphocyte population. C) Median Fluorescence Intensity (MFI) is depicted to assess tumor-associated macrophages (CD163 and CD206).

4.1.4. Assays to assess drug efficacy

A major application of the developed multi-component melanoma spheroid models is their use in drug screening facilitating more efficient evaluation of novel anti-melanoma compounds. To establish different readout assays for assessing drug efficacy, we selected a potent MEKi (Trametinib) used off-label in $NRAS^{mut}$ and WT melanoma treatment. The following assays were performed on MMSs in the absence of PBMC co-culture.

Cell viability assay: Trametinib (500nM) was added on day 3 of MMS formation (Fig. 35) and after 4 days, the viability of the whole spheroid was assessed by measuring the ATP content (Cell-Titer Glo 3D Cell Viability Assay). As expected, SKmel147 ($NRAS^{mut}$) and WM3918 (BRAF/NRAS wt) showed high sensitivity to Trametinib (Fig. 38 and Suppl.Fig. 4 A). At the same time, 624mel ($BRAF^{mut}$) cells were less sensitive to the MEKi (Suppl.Fig. 4 B). In this drug-response assay, no particular differences were seen between the MMS models. Likely, the test of more specific compounds utilizing a tailored cancer-specific concentration (for instance IC50 values), can result in different drug responses given the interaction of cancer cells with different stromal cell types.

Cell death assay: Induction of cellular death, specifically early and late apoptosis is an important aspect to assess anti-cancer compound efficacy. After 4 days of treatment with Trametinib, MMSs were dissociated, stained with a combination of fluorogenic substrates for caspase 3 and caspase 7 activity (early apoptosis) and propidium iodide (late apoptosis, necrosis), and analyzed by flow cytometry. Trametinib-treated MMS-Skin and -Lung had similar features with a high presence of late-apoptotic cells. At the same time, MMS-Liver still presented a remarkable fraction of early-apoptotic cells, displaying differences in drug response depending on the MMS model (Fig. 38 B).

Kinetic cell proliferation: The kinetic evaluation of drug response is a valuable assay to determine when the drug starts to have an impact specifically in targeted cancer cells. We used SKmel147 stably expressing mCherry fluorescent protein to generate MMS models and followed the fluorescent signal over 4 days of treatment. MEK inhibition showed a similar kinetic profile among the MMS models (Fig. 38 C).

In conclusion, with these methods, a versatile set of read-out assays had been established allowing to efficiently analyze drug response in advanced 3D models. The described methodology has been published in STARprotocols (CellPress) in 2024: "**Protocol to generate scaffold-free, multicomponent 3D melanoma spheroid models for preclinical drug testing**". Refer to Appendix 4.

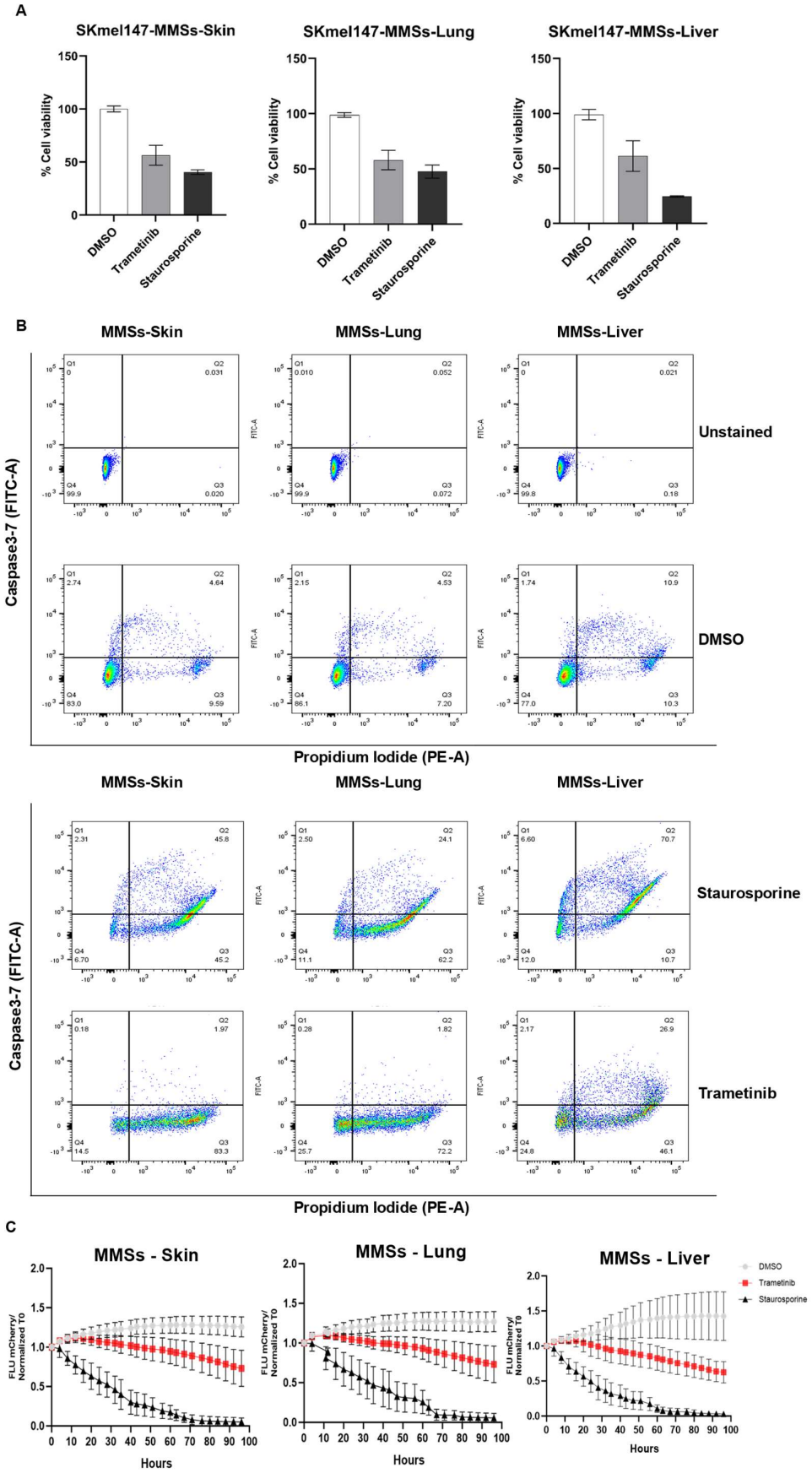
A
SKmel147-MMSs-Skin
SKmel147-MMSs-Lung
SKmel147-MMSs-Liver
% Cell viability
DMSO
Trametinib
Staurosporine
B
MMSs-Skin
MMSs-Lung
MMSs-Liver
Unstained
DMSO
Staurosporine
Trametinib
Caspase3-7 (FITC-A)
Propidium Iodide (PE-A)
C
MMSs - Skin
MMSs - Lung
MMSs - Liver
FLU mCherry/ Normalized T0
Hours
DMSO
Trametinib
Staurosporine

Figure 38: **Assays evaluating drug efficacy in MMS models.** Trametinib was used at 500 nM concentration, DMSO at 0.1%. A) MMS cell viability is assessed using an end-point luminescence-based assay measuring cellular ATP content (3D Cell Titer Glo®) after 96 hours. The tested compound (Trametinib), vehicle, and positive control (Staurosporine 1µM) are represented for MMSs-skin, -lung, and -liver. Data are mean ± SEM of *n* = 3 independent biological replicates. B) Representative dot plots of an apoptosis assay. Cells were treated with Trametinib for 4 days or 1 µM Staurosporine (positive control) for 24h. DMSO was used as a vehicle control. Double staining with Caspase 3-7 and propidium iodide allows us to determine the ratio of early apoptotic (positive for Caspase), late apoptotic (positive for both markers), and necrotic cells (positive for propidium iodide). C) The fluorescent signal emitted by labeled melanoma cells is captured every four hours for the kinetic evaluation of drug efficacy. Plotted is the kinetic profile of MMSs-skin, -lung, and -liver treated for 96 hours with Trametinib, DMSO, and Staurosporine 200 nM. Data are mean ± SD of *n* = 3 independent biological replicates.

4.2. Generation of primary metastatic melanoma cell lines derived from patient samples

To enhance the translational relevance of our models, we aimed to establish and cultivate **primary cell lines derived from melanoma metastases** provided by our clinical collaborator, Prof. Jochen Utikal (University Medical Center Mannheim, Germany). Through the support of the Pelican Grant (2023), which facilitates international research exchanges for doctoral students, I had the opportunity to undertake a research visit to Prof. Mitchell Levesque's laboratory and melanoma biobank at the University Hospital of Zurich, Switzerland. During this period, I acquired expertise in processing whole metastatic biopsies for **slow-freezing preservation and in generating primary metastatic melanoma cell lines**. We received several specimens from our clinical collaborator; however, due to delivery challenges and the highly necrotic nature of the metastasis (Fig. 39 A-D) highlighted by the prominent presence of necrotic fluid, extracting viable cells from these samples proved difficult. In a next attempt, we successfully **established a primary cell line from a BRAF^{V600E} mutated melanoma** breast and lymph node metastasis (Fig. 39 E and Fig. 40), which we have designated as MelLux19.

To establish this cell line, **two distinct methodologies** previously described by Levesque's group were tested (316). These approaches were specifically designed to enhance the purity of melanoma cells and effectively eliminate fibroblasts, which are notoriously challenging to remove during the generation of primary cancer cell lines.

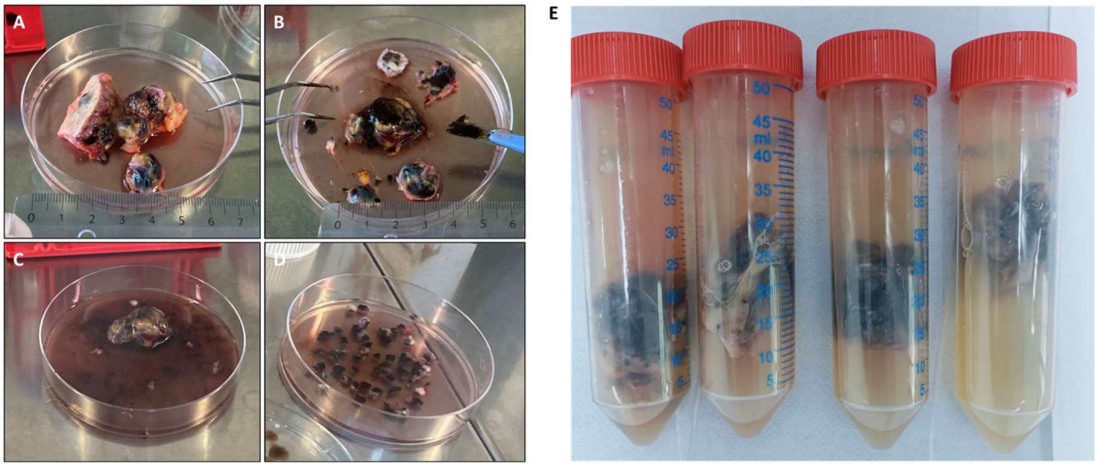

Figure 39: **Melanoma patient metastasis samples**. A-D) An $NRAS^{mut}$ (Q61K) subcutaneous melanoma metastasis, which we first removed all the non-cancerous tissue by following the melanotic edges (A-B) and then chopped it in 3-millimeter pieces for frozen preservation (C-D). Cutting of metastasis released a huge amount of necrotic and melanotic fluid (C). E) MelLux19, a $BRAF^{mut}$(V600E) breast melanoma metastasis, which was processed as for MelLux18, and successfully generated a primary melanoma cell line.

Initially**,** the patient's metastatic tissue was processed by carefully **excising non-cancerous regions**, guided by the melanotic edges of the tumor. The tumor was then sectioned into fragments approximately 3 millimeters in diameter and preserved in cryovials containing FBS supplemented with 10% dimethyl sulfoxide (DMSO), subsequently stored in liquid nitrogen as **"slow-frozen biopsies"**. A subset of these tumor fragments was **enzymatically dissociated** using a combination of Dispase II and Collagenase. The resulting cell suspension was filtered to obtain a single-cell solution for further processing. A portion of the cell suspension was utilized for the **first method of primary cell line generation**, as described by Raaijmakers et al. (316). In this approach, the solution was **directly plated into an adherent flask**, allowing cells to attach over a period of several days. During the initial phase, the medium was exchanged infrequently (approximately once a week or every two weeks) to create a nutrient-deprived environment. This strategy was aimed at selectively starving fibroblasts while allowing melanoma cells, which are more resilient under such conditions, to survive. When necessary, **differential trypsinization** was employed to further reduce fibroblast contamination. After several weeks of culture, the melanoma cell population appeared morphologically homogeneous (Fig. 40 A), although the cells displayed low pigmentation levels (Fig. 40 B). **Immunofluorescence** analysis revealed weak expression of key melanoma markers, including MLANA-MART-1, HMB45, and tyrosinase, (included in "melanoma antibody cocktails").

Furthermore, fibroblast contamination remained evident, as confirmed by positive staining for fibroblast markers such as α-SMA and TE-7 (an antibody for stromal cell identification specifically used for fibroblast identification) (Fig. 41 A).

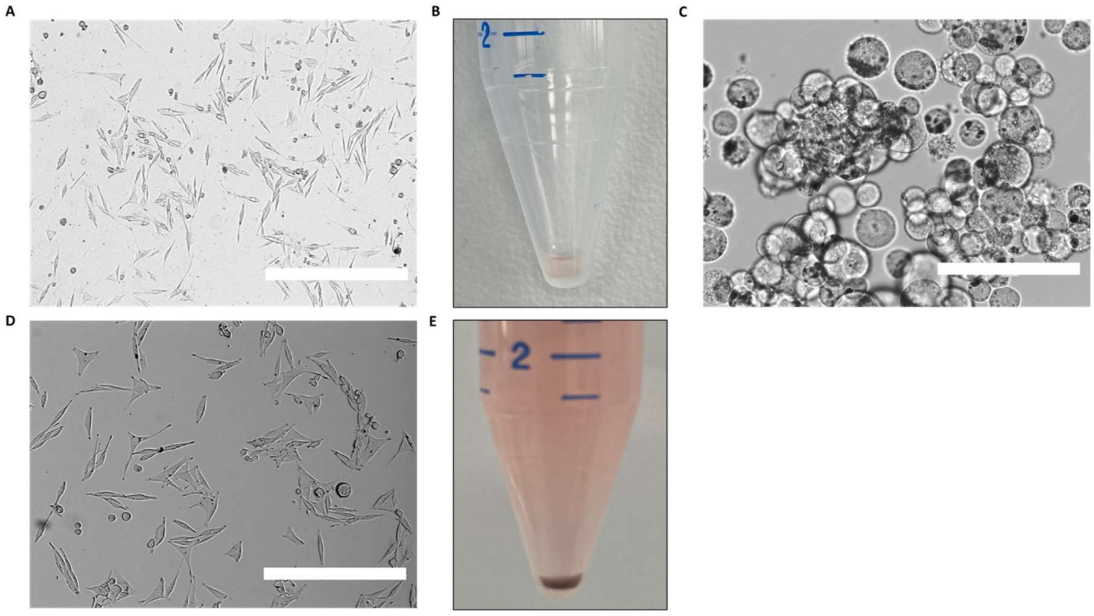

Figure 40: **Two methods were tested to generate MelLux19 primary cell line.** A) The image shows MelLux 19 after 20 days from the tumor dissociation and directly seeded in an adherent plate. B) Pellet of MelLux 19 after 20 days of culture. C) The image shows MelLux19 in the ULA plate after 7 days from the tumor dissociation. D) MelLux 19 after 13 days from the initial 7 days of non-adherent culture treatment (second method). E) A pellet of MelLux 19 after 20 days was generated using the second method. Images: brightfield, 4X objective, scale bar = 1000 µm.

Conversely, the second fraction of the single-cell solution obtained from the enzymatic dissociation of the tumor was used for a **different primary cell line generation method**. In this approach, the cells were cultured for approximately one week in an **ultra-low attachment (ULA) plate** (Fig. 40 C) with RPMI medium supplemented with factors commonly used in organoid culture (320). These included RHO/ROCK pathway inhibitors (Thiazovivin), to minimize Anoikis (a type of programmed cell death triggered by the loss of cell contact) and increase stemness and self-renewal (321,322), TGF-β receptor inhibitor (A83-01), to reduce SMAD-driven apoptosis (323); and EGF, to enhance cell proliferation and survival. After this initial culture phase (approximately 7 days), the floating cells were **transferred to an adherent flask**. This method resulted in a highly homogeneous melanoma cell population with typical melanoma morphology (Fig. 40 D) and pronounced pigmentation (Fig. 40 E), closely resembling the original tumor (Fig. 39 B).

Furthermore, the resulting cell population exhibited a higher enrichment of melanoma-specific markers, with no detectable positivity for fibroblast-specific markers (Fig. 41 B). In conclusion, for this case study, the pre-culture of dissociated cells in ULA plates with medium supplemented with factors commonly used in organoid culture proved to be a more effective method for generating melanoma primary cell lines with minimal or no fibroblast contamination, in a shorter period of time. However, the study's limitations include the small number of samples tested, necessitating the evaluation of a larger sample set to confirm the superior efficacy of this approach.

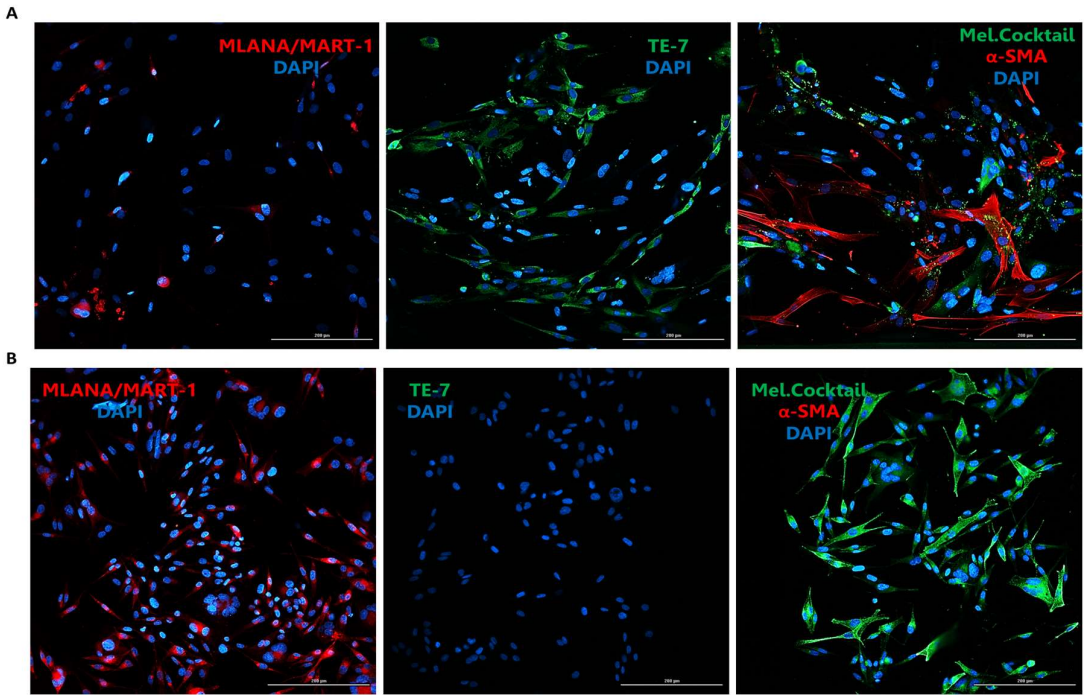

Figure 41: **Melanoma cell purity in MelLux19 cell population by immunofluorescence**. A) MLANA-MART-1 and an antibody cocktail ("melanoma cocktail") were used to identify the melanoma-specific population, while α-SMA and TE-7 were specifically used to identify fibroblastic populations in MelLux19 obtained with the first primary cell line generation method. B) Melanoma- and fibroblast-specific markers used to identify the two cell types within MelLux19 cell population were obtained using the second primary cell line generation method. Images: Confocal microscope, 20X objective, scale bar = 200µm.

4.3. Generation of Xeno-free Hydrogel-Embedded melanoma co-cultures for preclinical drug testing

Incorporation of **extracellular matrix (ECM)** is critical for enhancing the physiological relevance of preclinical 3D melanoma *in vitro* models, as it enables the replication of cell behavior in a tissue-like environment. To explore this, we **encapsulated** melanoma cells (624mel) and fibroblasts (NHDF), which were stably transduced to express iRFP and GFP, respectively, within various ECM types. The tested matrices included animal-derived and synthetic options: 1) Matrigel® (a matrix predominantly composed of 60% laminin, 30% Collagen IV, and 10% of other basal membrane components, derived from Engelbreth-Holm-Swarm (EHS) mouse sarcoma cells), 2) PeptiGel® (a hydrogel formed by self-assembling oligo-peptides 3D fibrillar structures), and 3) ECTICA™ (a hydrogel based on polyethylene glycol).

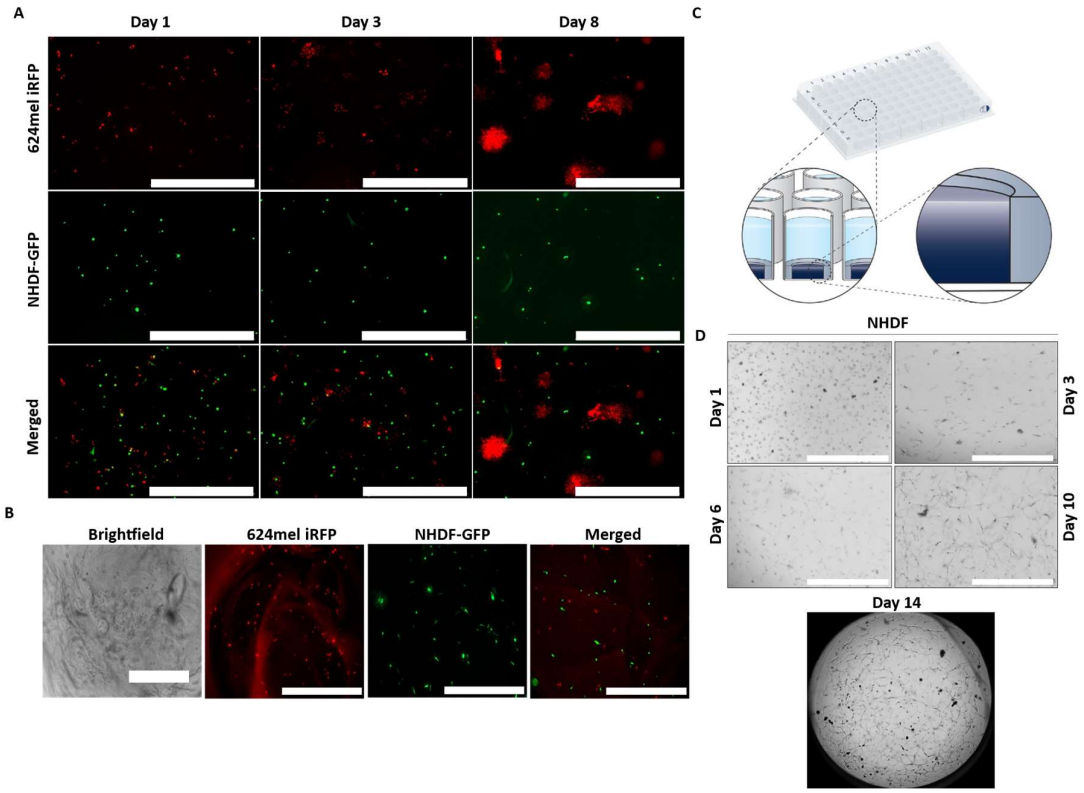

Figure 42: **Tested matrices for the encapsulation of melanoma and TME cells co-culture**. A) Melanoma cells (624mel iRFP, red) co-cultured for 8 days with fibroblasts (NHDF-GFP, green) and embedded in Matrigel®. B) Melanoma cells (624mel iRFP, red) co-cultured for 8 days with fibroblasts (NHDF-GFP, green) and embedded in PeptiGel®. C) ECTICA™ 3DProSeed™ technology with a PEG-based hydrogel pre-casted using an in-depth cross-linking density gradient (low density at the top and high density at the bottom) in a 96-well plate format plate. D) NHDF cultured in 3DProSeed™ plates for a total of 14 days. Images: widefield microscope, 4X objective, scale bar = 1000 µm.

The co-culture embedded in Matrigel® (Fig. 42 A) exhibited melanoma tumoroid-like growth within 3 days of culture, with this effect becoming more pronounced after 8 days. However, the **fibroblasts showed no significant growth or characteristic morphology** (spindle shape), suggesting Matrigel® may not be suitable for fibroblast proliferation. In contrast, **PeptiGel®** (Fig. 42 B) **demonstrated even poorer performance**; neither melanoma cells nor fibroblasts exhibited growth or proper morphology after 3 days of culture. Additionally, PeptiGel® presented **technical challenges**, including difficulties in handling and polymerization, as evidenced in the brightfield image in Figure 42 B. To address the limitations of previous matrices and promote proper growth of both melanoma cells and fibroblasts, we tested a **polyethylene glycol (PEG)**-based hydrogel bioconjugate with **RGD** (arginyl-glycyl-aspartic acid, a key cell adhesion motif found in fibronectin and recognized by integrins (324)) and **matrix metalloproteinase (MMP)-cleavable sites**. The hydrogel was cross-linked with transglutaminase (Factor XIII) and pre-casted using an in-depth cross-linking density gradient (low density at the top and high density at the bottom) in a 96-well plate format plate (3DProSeed^{TM}), provided by ECTICA Technologies (Zurich, Switzerland) (Fig. 42 C). NHDF were seeded at a density of $10x10^3$ cells on top of the hydrogel and cultured for 14 days. By day 3, **fibroblasts began adopting a proper 3D morphology**, elongating through the hydrogel gradient, and achieved full development after 10-14 days of culture (Fig. 42 D). After confirming the suitability of fibroblasts to grow in the synthetic hydrogel matrix, I extended the analysis to evaluate the growth and behavior of a **panel of melanoma cell lines** representing various genomic subtypes cultured in this animal-free synthetic hydrogel. The selected panel included 3 commercially available melanoma cell lines: 624mel ($BRAF^{mut}$), SKmel147 ($NRAS^{mut}$), and WM3918 ($BRAF^{wt}$/$NRAS^{wt}$); as well as two treatment naïve (BE) and two treatment resistant (AF) primary melanoma cell lines for each genomic subtype. Among the **$BRAF^{mut}$ melanoma cell lines**, 3/5 showed growth over time (Fig. 43 A), exhibiting diverse phenotypes such as tumoroid-like structures (624mel) or more dispersed, single-cell proliferation (BE-2 and AF-6) (Fig. 43 B). For **$NRAS^{mut}$ melanoma cell lines**, 5/5 demonstrated growth (Fig. 43 C), characterized by varied growth patterns, including single-cell proliferation (SKmel147 and BE-1), aggregates (AF-5 and AF-6), and tumoroid-like structures (BE-2) (Fig. 43 D). A similar trend was observed in **WT primary melanoma cell lines**, all of which grew over time (Fig. 43 E) with distinct phenotypes, such as tumoroid-like growth (WM3918 and BE-1), single-cell proliferation (BE-2), and aggregate formation (AF-5 ad AF-6) (Fig. 43 F). These findings highlight the **hydrogel's suitability not only for fibroblast culture** but also for supporting the growth of a wide range of melanoma cell lines, thereby offering a promising platform for developing efficient melanoma co-culture hydrogel models. However, certain melanoma cell lines, particularly those forming tumoroid-like structures, faced challenges in deeply

penetrating the full thickness of the hydrogel. These cells were prone to removal or damage during medium exchange required for long-term culture. To address these challenges, we opted to utilize the same PEG-based hydrogel matrix but **encapsulated the cell co-culture in dome-shaped constructs** (Fig 44 A). To evaluate the feasibility of a co-culture model using this PEG-based hydrogel as the matrix, we co-cultured SKmel147-mCherry melanoma cells with fibroblasts or hepatic stellate cells (HSCs) stably labeled with GFP, seeding $1x10^3$ melanoma cells and $3x10^3$ fibroblasts per dome. This setup mirrored key melanoma metastatic sites by incorporating NHDF (dermal fibroblasts), MRC-5 (lung fibroblasts), and LX-2 (HSCs), previously used in Melanoma Multicomponent Spheroid (MMS) model generation. Over 10 days, melanoma cells demonstrated efficient growth (Fig. 44 B and C) accompanied by increased melanin production (Fig. 44 D) across all co-culture conditions.

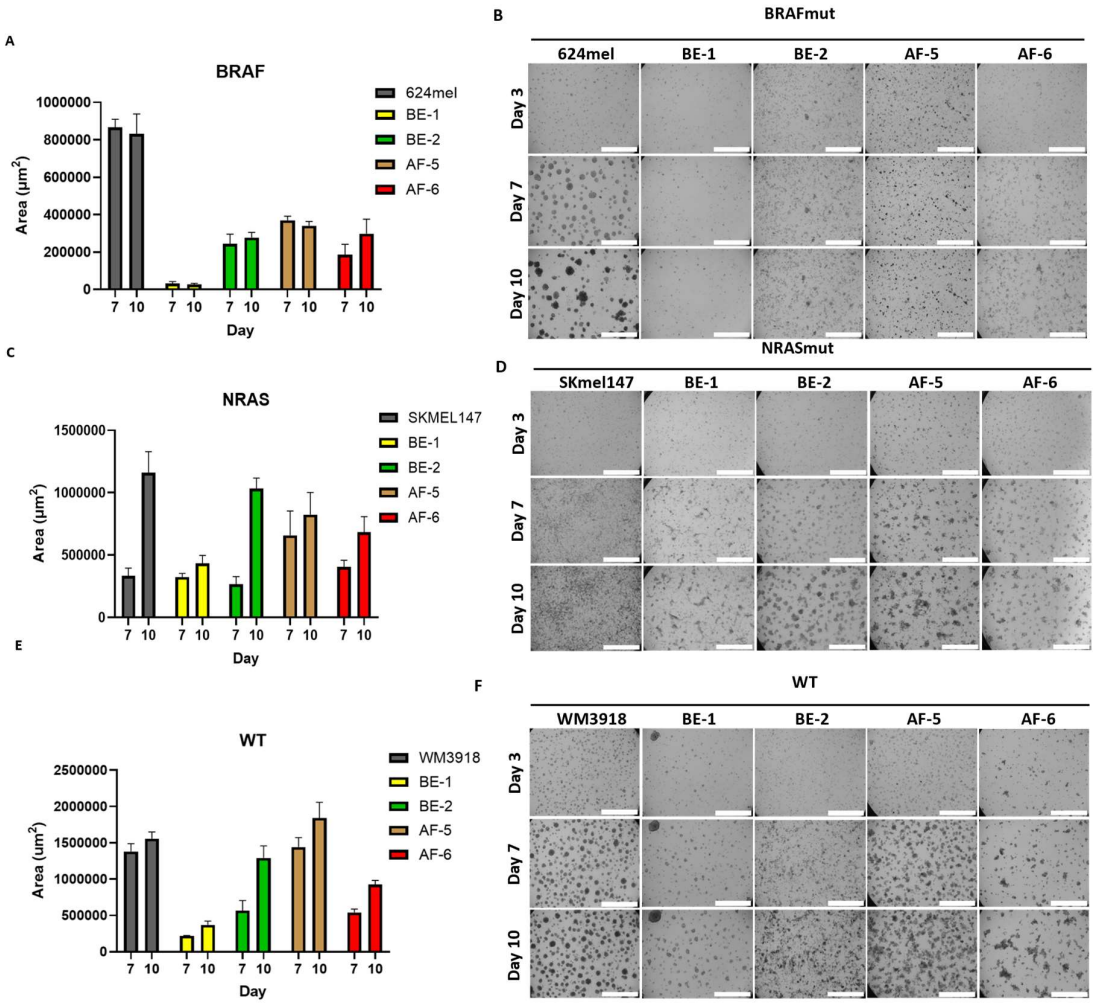

Figure 43: **Panel of commercially available and primary melanoma cell lines cultured in PEG-hydrogel**. A) BRAF^{mut} melanoma cell growth was measured by the area covered by cells after 7 and 10 days of culture. B) Images showing the BRAF^{mut} melanoma cells after 3, 7, and 10 days of culture. C) Calculated area covered by NRAS^{mut} melanoma cells after 7 and 10 days of culture. D) Images showing the NRAS^{mut} melanoma cells after 3, 7, and 10 days of culture. E) Calculated area covered by WT melanoma cells after 7 and 10 days of culture. F) Images showing the WT melanoma cells after 3, 7, and 10 days of culture. Images: brightfield, 4X objective, scale bar = 1000 µm. Data are mean ± SD of *n* = 2 independent biological replicates.

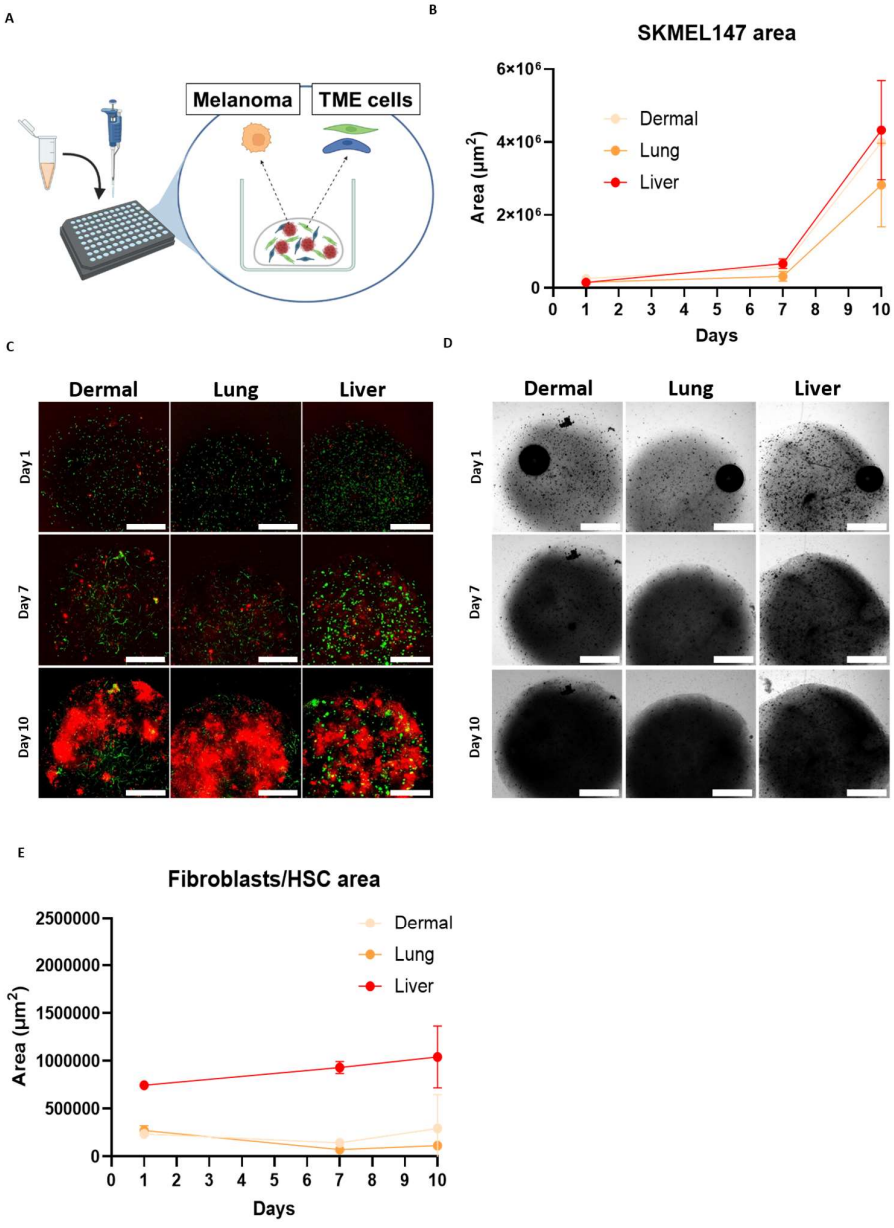

Figure 44: **Embedding of melanoma-fibroblast/hepatic stellate cell (HSC) co-culture in PEG hydrogel domes**. A) Schematic representation of melanoma-TME cells co-culture embedded in PEG hydrogel and seeded as domes in 96 well plates. B) Skmel147-mCherry proliferation co-cultured with NHDF (dermal), MRC-5 (lung), and LX-2 (liver) calculating the area covered by the fluorescent signal emitted by melanoma cells after 1, 7, and 10 days of culture. C) The panel represents the three types of melanoma co-culture models after 1, 7, and 10 days of culture. In red, SKmel147-mCherry. In green, either NHDF (dermal), MRC-5 (lung), and LX-2 (liver), expressing GFP. D) Melanin production among the different models along a 10-day culture period. E) Area covered over time by the GFP signal emitted by NHDF, MRC-5, and LX-2 co-cultured with melanoma cells in the three models. Images: widefield microscope (brightfield and fluorescence), 4X objective, scale bar = 1000 µm. Data are mean ± SD of *n* = 2 independent biological replicates.

Fibroblasts (NHDF and MRC-5) initially exhibited a slight reduction in growth by day 7, followed by a recovery by day 10, while HSCs (LX-2) maintained consistent proliferation throughout the experiment (Fig. 44 E). Based on image analysis, we hypothesized that the observed temporary reduction of the fibroblast area resulted from a minor fraction of cells dying due to the encapsulation process, after which the surviving majority resumed proliferation, adopting a physiological spindle-shaped morphology and expanding their coverage area. To enhance the biological complexity of the melanoma-fibroblast co-culture models, **endothelial cells (HMEC-1) were incorporated** into the models.

The aim was to recreate a tissue-like architecture by increasing the stromal cell density, by seeding $10x10^3$ fibroblasts and endothelial cells, and $1x10^3$ melanoma cells (due to their high proliferative features). Given the need for extensive optimization to establish suitable culture conditions for three cell types, NHDF was selected as the reference fibroblastic cell type for these initial experiments. **Encapsulation in hydrogel domes of SKmel147-mCherry melanoma cells with NHDF-GFP fibroblasts and HMEC-1-BFP endothelial cells** demonstrated significant melanoma cell proliferation and moderate fibroblast growth, but a decline in HMEC-1 viability (Fig. 45 A-B). This reduction was likely due to the absence of essential factors in the medium to support endothelial cell survival. To address this, varying concentrations of **vascular endothelial growth factor (VEGF)**, a key cytokine for endothelial cell proliferation, survival, and sprouting (325), were tested.

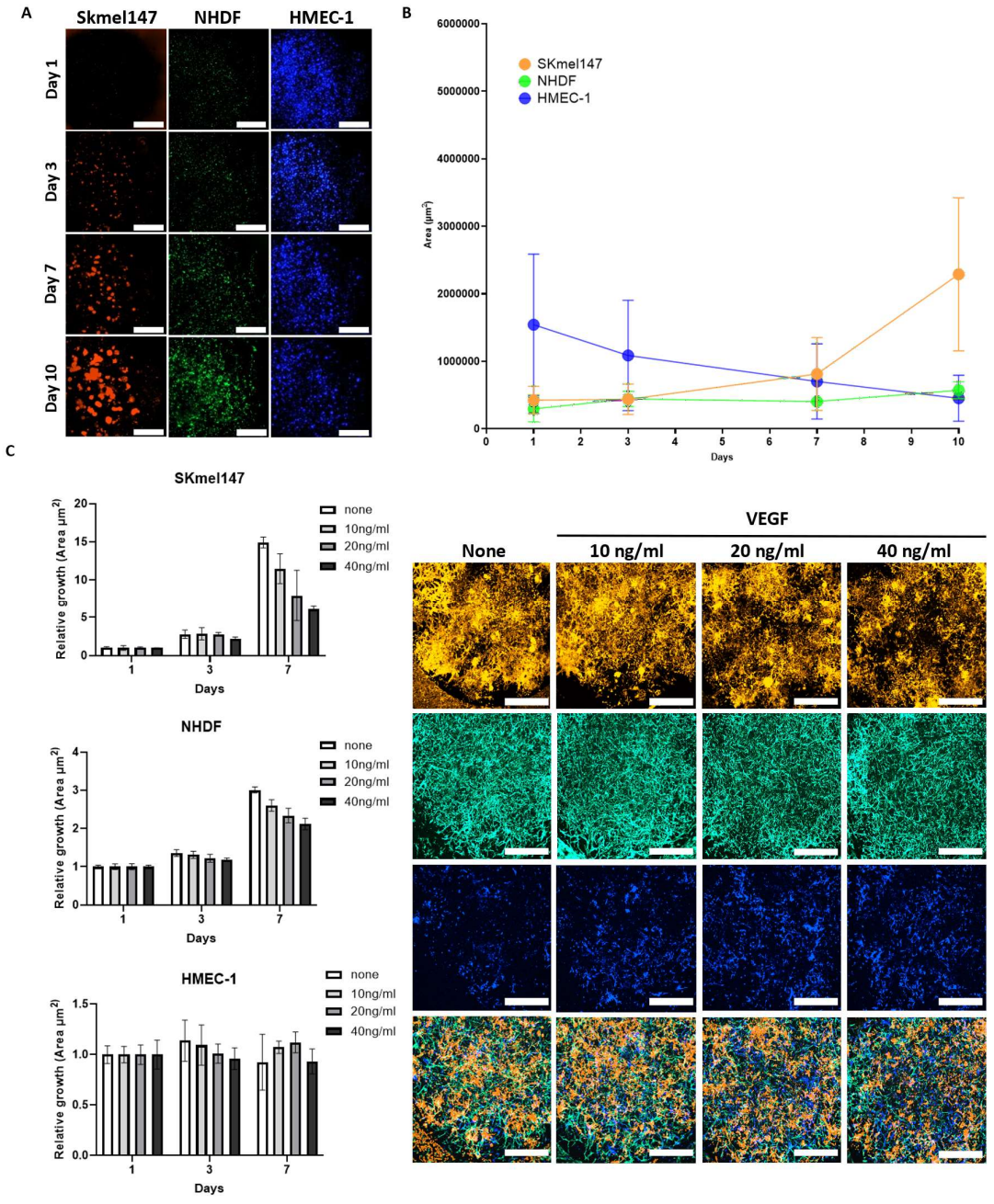

Figure 45: **Hydrogel-embedded triple melanoma co-culture**. A) Panel represents SKmel147-mCherry (red) co-cultured with NHDF-GFP (green) and HMEC-1-BFP (blue) embedded in PEG-based hydrogel domes over 10 days. Images: widefield microscope, 4X objective, scale bar = 1000 µm. B) Calculated Area by following the fluorescent signal of every cell type in the co-culture system until day 10 of culture. C) Time-lapse confocal microscopy showed the proliferation of co-cultured cells in the presence of different concentrations of VEGF supplemented in the medium. Images: confocal microscope, 4X objective, scale bar = 300 µm. Data are mean ± SD of *n* = 2 independent biological replicates.

It was crucial to monitor the behavior of fibroblasts and melanoma cells to ensure their normal growth was not adversely impacted by VEGF. Time-lapse confocal microscopy over a 7-day culture period confirmed that the addition of 10 ng/mL of VEGF to the medium improved HMEC-1 survival compared to the VEGF-free medium while minimally affecting the physiological growth of melanoma cells and fibroblasts (Fig. 45 C).

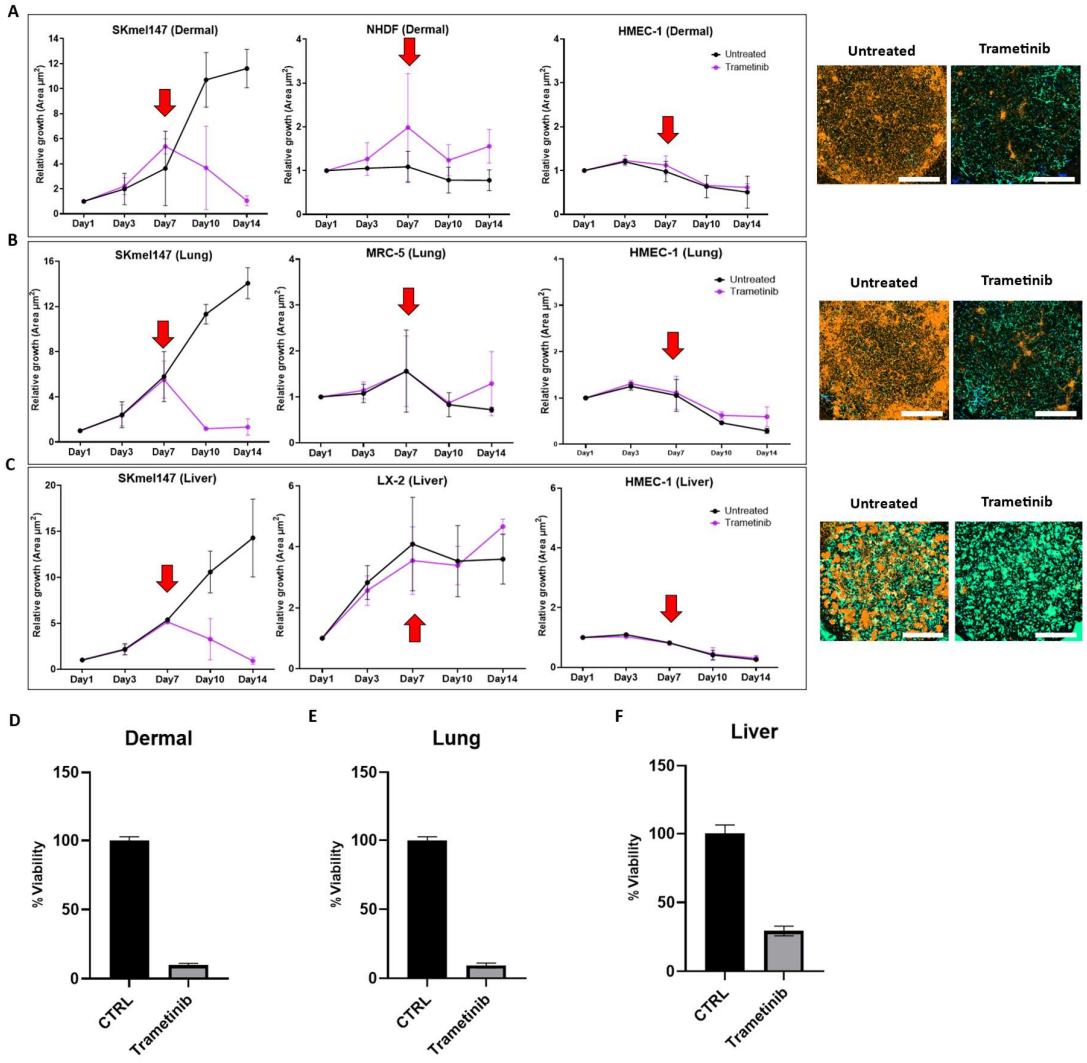

Figure 46: **Assessment of drug treatment in hydrogel melanoma co-culture models**. A) On the left, is the relative growth of each cell type used in the dermal hydrogel co-culture model, before and after drug treatment. The area was evaluated by following the different fluorescent signals emitted by the cells. The red arrows indicate the onset of the treatment. On the right, confocal pictures of the untreated and treated dermal co-cultures after 14 days. Images: confocal microscope, 4X objective, scale bar = 300 µm B) Relative growth of each cell type used in the lung hydrogel co-culture model, before and after drug treatment. C) Relative growth of each cell type used in the liver hydrogel co-culture model, before and after drug treatment. D) Cell viability was assessed after 7 days of treatment on untreated (CTRL) and treated (Trametinib) dermal melanoma models. E) Cell viability was assessed after 7 days of treatment on lung melanoma models. F) Cell viability was assessed after 7 days of treatment on liver melanoma models. Data are mean ± SD of *n* = 2 independent biological replicates.

The primary goal of developing these advanced *in* vitro 3D models is to utilize them as **pre-clinical platforms** for more effective validation of novel anti-melanoma drugs. To achieve this, we implemented **kinetic and cell viability assays** to evaluate the efficacy of various drugs. Using confocal time-time lapse microscopy, the behavior of various cell types in hydrogel-embedded models was followed using the constitutive expression of different fluorescent proteins.

In this experiment, SKmel147-mCherry was co-cultured with HMEC-1-BFP, along with either NHDF-GFP (dermal), MRC-5 (lung), or LX-2 (liver) cells (Fig. 46). After 7 days of co-culture, the models were treated with a high dosage of Trametinib (MEKi), 10-times the IC50 value for SKmel147, for an additional 7 days. As anticipated, melanoma cells exhibited a significant response to the treatment, with a clear reduction in the mCherry area. Interestingly, stromal cells demonstrated higher survival at day 14 in most of the models compared to the untreated controls. This may be attributed to the reduced pressure from melanoma cells, which proliferate faster than the other components of the tumor microenvironment (TME) (Fig. 46 A-C). In addition, we evaluated the cell viability of the entire co-culture system at the endpoint (day 14) using an ATP-luciferase-based assay (CellTiter-Glo® 3D Cell Viability Assay, Promega). While treated models exhibited significantly lower cell viability compared to untreated controls (Fig 46 D-E), further tests are necessary to confirm proper reagent penetration through the hydrogel matrix and effective cellular lysis.

Finally, we investigated whether the hydrogel-embedded co-culture models could accommodate **patient-derived primary melanoma cells**. Preliminary findings, illustrated in Figure 47, demonstrated that MelLux19, a $BRAF^{mut}$ primary melanoma cell line (previously described in Chapter 4.3) and transiently labeled with a near-infrared fluorescent dye, successfully co-cultured for 10 days with NHDF-GFP and HMEC-1-BFP (Fig. 47 A-B). Furthermore, immunofluorescence analysis revealed substantial **deposition of type I Collagen**, a primary component of the ECM (Fig. 47 C). This phenomenon was likely attributed to the degradation of PEG via MMP-cleavable sites and the subsequent deposition of ECM components synthesized by the encapsulated cells, enhancing the physiological relevance of the models.

In conclusion, we successfully established animal-free, matrix-embedded co-culture melanoma models, providing a robust platform for advanced preclinical *in* vitro studies to evaluate the efficacy of novel therapeutic compounds. However, further experiments are required to enhance the model's characterization and to improve the vascularization potential of endothelial cells. Additionally, optimizing co-culture conditions for freshly derived patient melanoma cells remains a critical area for future investigation.

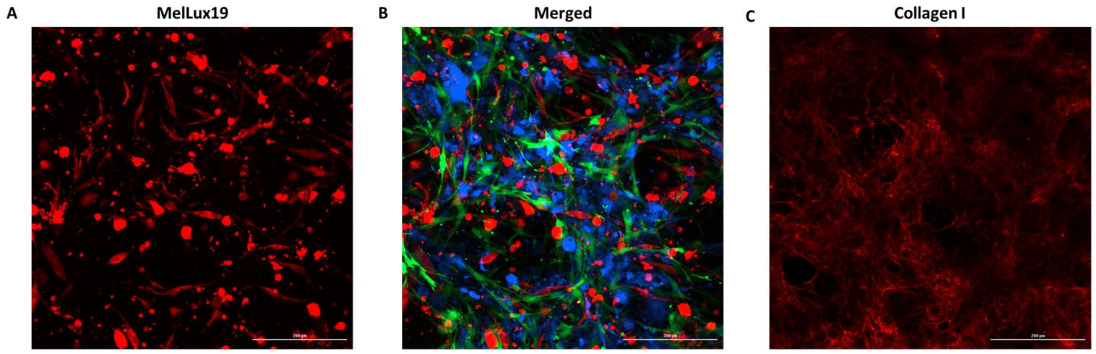

Figure 47: **Hydrogel-embedded MelLux19 co-culture dermal model**. A) MelLux19 transiently labeled with near-IR dye. B) Merged picture of MelLux19 (red) with NHDF-GFP (green) and HMEC-1-BFP (blue), after 10 days of culture. C) Collagen I fibrils (red) into the hydrogel co-culture after 10 days and identified by immunofluorescence. Images: confocal microscope, 20X objective, scale bar = 200 µm

4.4. High-throughput Drug Screening (HTS) for the identification of novel drugs for NRAS^{mut}, BRAF^{wt}/NRAS^{wt}, and BRAF^{mut} melanoma

Currently, late-stage melanoma patients bearing BRAF mutations have effective approved first-line treatments mostly represented by combinations of targeted therapies and immune checkpoint inhibitors, while such therapies are not available for other melanoma genomic subtypes such as NRAS^{mut} and BRAF^{wt}/NRAS^{wt}. Moreover, a significant fraction of patients **develop resistance** to available therapies, underscoring the urgent need for novel therapeutic approaches. To address this, we conducted **high-throughput screening (HTS)** using **3D spheroid cultures** to improve the reliability of drug effects. Many of the tested compounds were already FDA-approved for other diseases, thus positioning them as potential **repurposed treatments** for melanoma.

4.4.1. High-throughput screening assay development

A **semi-automated robotic platform**, referred to as "Disease Modelling and Screening Platform" (DMSP) installed at the LCSB in the University of Luxembourg, was utilized to conduct high-throughput drug screening (HTS). Prior to screening the selected drug libraries, preliminary studies were undertaken to establish the complete HTS workflow.

For the screening, three melanoma cell lines representing the key genomic subtypes were chosen: 624mel (BRAF^{mut}), SKmel147 (NRAS^{mut}), and WM3918 (BRAF^{wt}/NRAS^{wt}).

The 624mel-iRFP ($BRAF^{mut}$) cell line was initially selected to **establish the HTS workflow**, as it was the most extensively studied in the laboratory and demonstrated the highest capacity for sphere formation. However, given the need for new therapies targeting $NRAS^{mut}$ and WT melanoma, we subsequently prioritized screening and validating novel compounds for $NRAS^{mut}$ and WT melanoma. **Optimizing the culture volume** was an important first step, as incorrect volumes can hinder proper cell growth and yield inaccurate drug response data. To enhance throughput, we utilized 384 well-format plates for the HTS. Cells were initially seeded at a density of 500 cells/well (see chapter 4.1.1) in a volume of 80 µL/well, and after 3 days, 60 µL/well of the medium was replaced with fresh media. However, we observed that the medium exchange process resulted in the unintended removal of multiple spheroids from the wells (Fig. 48 A), which poses a significant challenge for future HTS experiments, as each drug library compound is associated with a specific well.

To prevent the loss of spheroids during the medium exchange, we adopted a **"no-exchange approach"**, where all subsequent steps involved the addition of solutions without replacing the medium. Cells were seeded in a volume of 20 µL/well, and after 3 days, a dilution series of Foretinib as a positive control, potentially inducing cell death, along with an additional 40 µL/well was added. To ensure that reducing the seeding medium volume did not affect normal spheroid growth, we monitored spheroids over 3 days. No significant difference was observed between the two initial volume conditions (Fig. 48 B). Additionally, a 5-day treatment period was identified as the optimal endpoint for the assay, as it provided the best **Z'-factor** (Fig. 48 C), the most consistent Foretinib dose-response curve (DRC) (Fig. 48 D), and a robust **coefficient of variation (CV)** of less than 15% across all the conditions.

Lastly, we evaluated various **cell densities** for the SKmel147-mCherry and WM3918-mCherry (0.5 x 10^3, 1 x 10^3, 2.5 x 10^3, 5 x 10^3, and 10 x 10^3 cells/well). Based on spheroid growth over an 8-day period, and using the growth of 624mel as a reference, we identified 5 x 10^3 cells/well as the optimal initial density for SKmel147 (Fig. 49 A), and 10 x 10^3 cells/well for WM3918 (Fig. 49 B).

Our goal was to develop an HTS workflow suitable for cells directly derived from melanoma patients. However, primary cells are not ideal for stable transduction with fluorescent proteins because of low transduction efficacy. To address this, we selected **Calcein AM as a live-cell staining** reagent to assess cell viability, tracking the green fluorescent signal emitted by viable cells (Fig. 49 C) for subsequent high-content imaging analysis (Fig. 27 B).

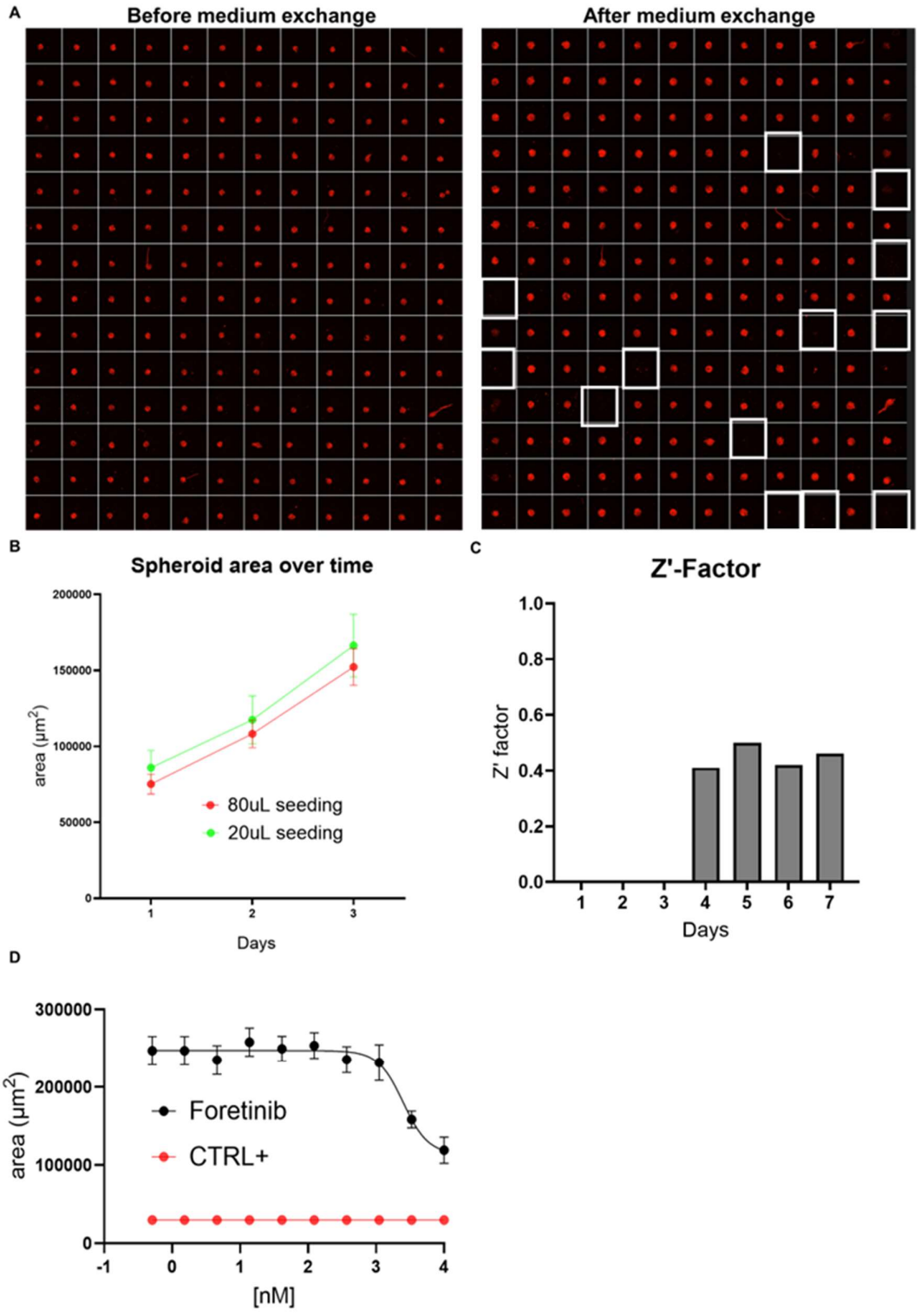

Figure 48: **HTS assay development**. A) Images represent 624mel-iRFP cultured as spheroids before and after the medium exchange. White boxes highlight wells where spheroids were removed due to the medium exchange process. B) Area followed over 3 days to evaluate the growth of spheroids cultured in two different culture volumes. C) Z'-factor of the tested plate over a period of 7 days. D) Dose-response curve of Foretinib generated as assay control quality step. CTRL+ is Foretinib used at 30µM.

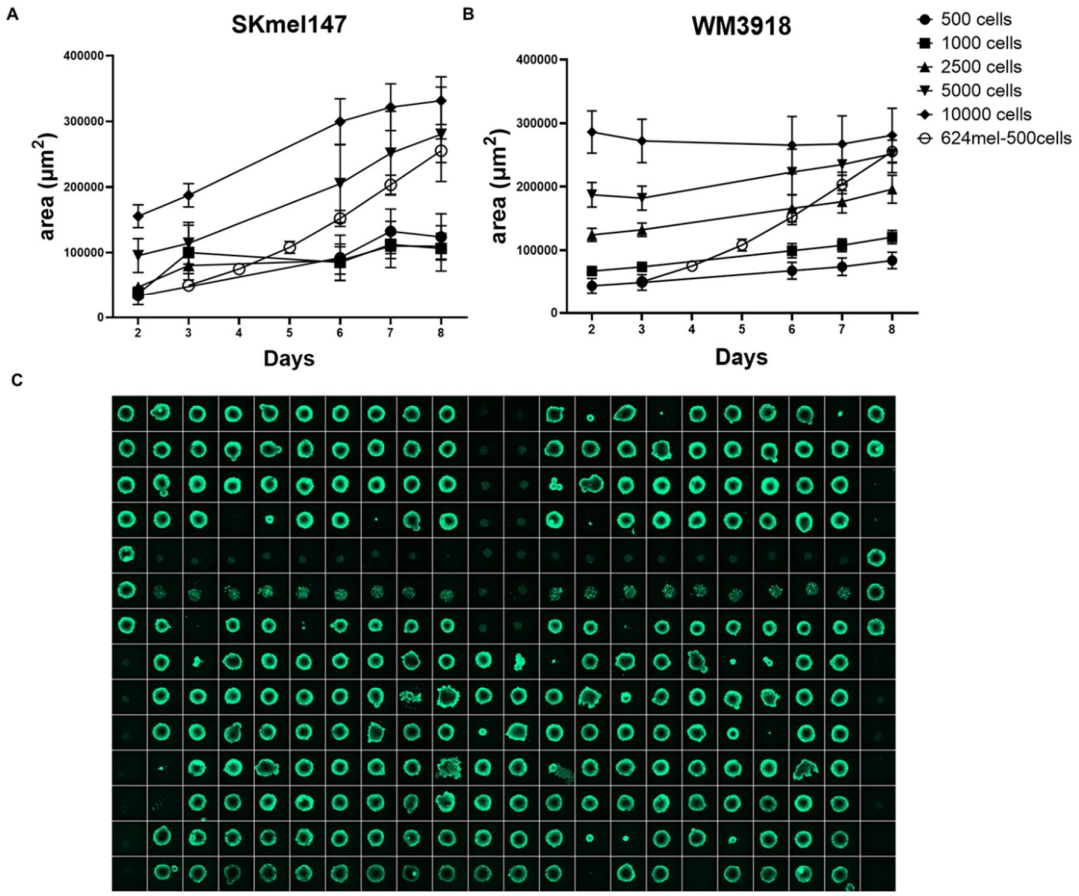

Figure 49: **Spheroid growth of NRAS^{mut} and BRAF^{wt}/NRAS^{wt} melanoma cell lines selected for the screening**. A) Area of SKmel147 spheroids measured following mCherry signal over a period of 8 days, and B) WM3918 cell line. C) Representative full-plate maximum intensity projected pictures of Calcein AM stained spheroids.

With this, we successfully developed a **semi-automated high-throughput drug screening workflow** that enables the testing of thousands of compounds on 3D spheroid cancer models.

4.4.2. High-throughput screening

Following the establishment of a **robust and reproducible HTS workflow**, we proceeded to evaluate **two drug libraries** (Prestwick Chemical Library® and Melanoma Drug Library, detailed in chapter 3.3.1 and Annex 1) focusing on the two melanoma genomic subtypes with limited approved therapeutic options: **SKmel147 (NRAS^{mut})** and **WM3918 (BRAF^{wt}/NRAS^{wt}).** Additionally, we conducted HTS on 624mel (BRAF^{mut}).

Drug libraries (1328 compounds in total) were tested at two concentrations: 10 µM, which corresponds to a standard concentration in HTS and 1 µM to also have concentrations where off-target effects are less significant.

Before analyzing the HTS data for hit drug identification, essential quality control steps were conducted. The **Z'-factor**, a statistical metric assessing HTS assay quality, was utilized. The Z'-factor ranges between 0 and 1, where a score of zero indicates overlapping negative and positive controls, suggesting poor assay quality, while a score of 1 signifies well-separated controls, reflecting an ideal assay (326). DMSP set a Z'-factor standard of >0.3, though our assays exceeded this with a Z'-factor above 0.5, indicating excellent assay quality (Fig. 50 A). Another important metric, the coefficient of variation (CV), quantifies data dispersion relative to the mean. With DMSP's standard set below 15%, our assays maintained a CV below 10%, demonstrating robustness (Fig. 50 B).

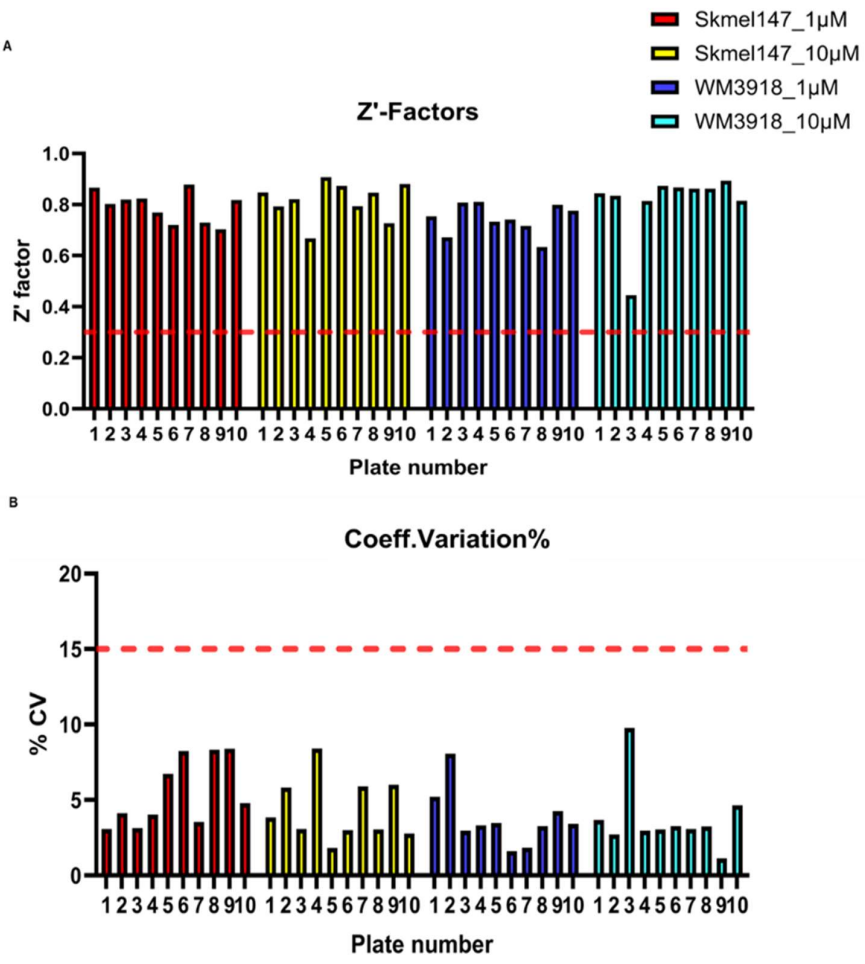

Figure 50: **Quality control steps for HTSs**. A) Z'-factor for each screened plate. The quality assay acceptance threshold is >0.3. B) Coefficient of variation (%) referred to DMSO control for each screened plate. The quality assay acceptance threshold is <15%.

Hit drug identification was a multi-step process designed to select promising drugs for further validation:

1) A **statistical model** based on the three-sigma rule was applied to analyze the raw total Calcein AM area of spheroids, as obtained by **image segmentation**. Only those measurements that deviated by at least three standard deviations from the mean of the DMSO control (cut-off) in both duplicates were selected for the next selection step (Fig. 51 A).

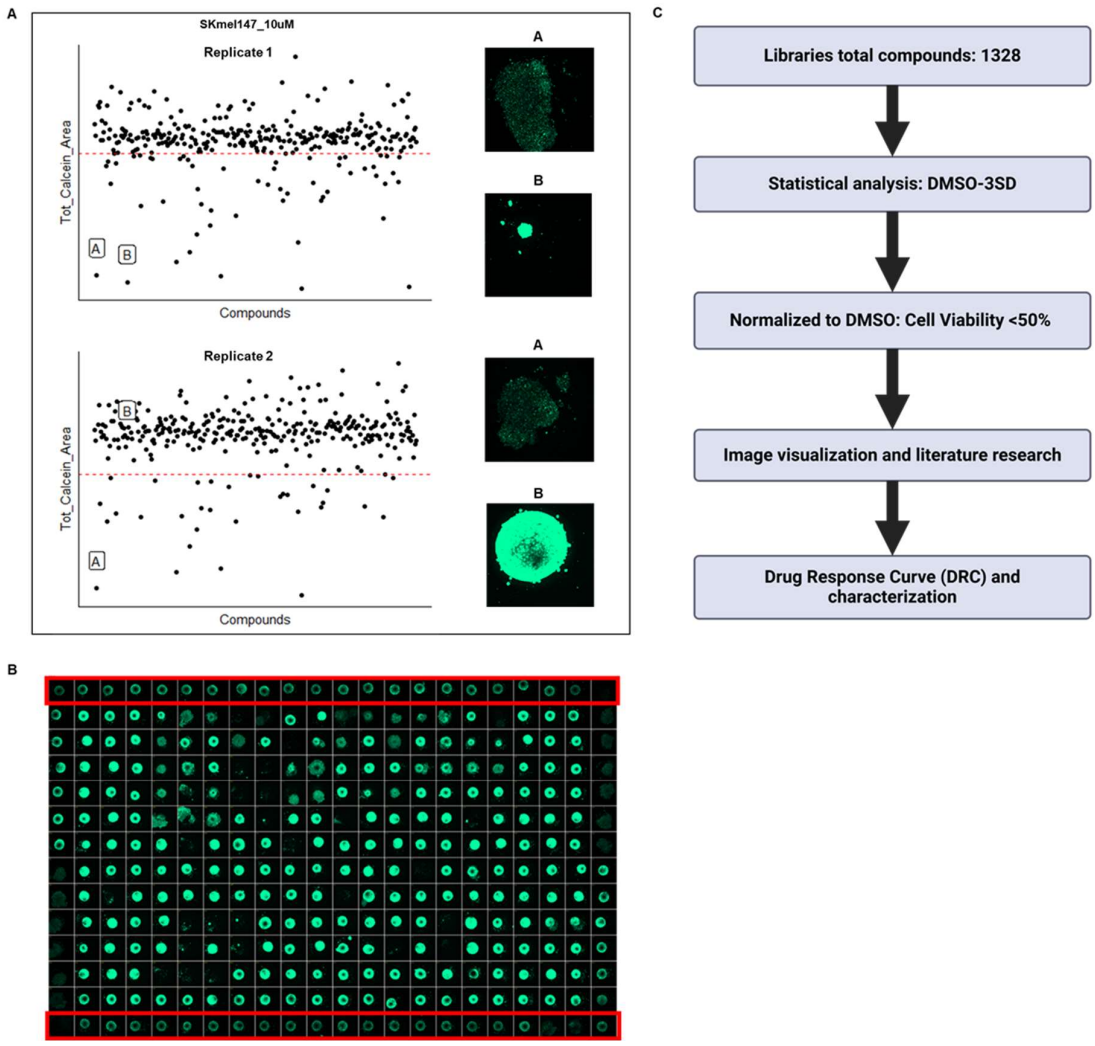

Figure 51: **Hit drugs selection process**. A) Scatter plots represent the duplicates for a screened set of drugs. Red dashed lines indicate the plate-specific statistical threshold below which compounds are selected for further steps. Examples of compounds A and B are highlighted; compound A was selected for further evaluation, while compound B, which was only effective in one of the two tested duplicates, was not chosen for further consideration. B) Calcein AM stained HTS plate. Red boxes highlight the plate edge effect. C) Scheme of the multi-step selection process is represented.

2) After **normalizing the data** to the DMSO control for compounds identified in step 1, only those that showed cell viability below 50% in both duplicates were selected. The number of compounds identified at each step is detailed in Table 2. To assess reproducibility between the biological replicates, we calculated Pearson's correlation coefficients, with values above 0.5 for SKmel147 (0.67 for 10 µM and 0.5 for 1 µM) (Suppl.Fig. 5 A-B), and values slightly below 0.5 for WM3918 (0.43 for 10 µM and 0.44 for 1 µM) (Suppl.Fig. 5 C-D). These results align with expectations given the increased heterogeneity inherent in 3D culture systems compared to 2D culture methods (327).

	SKmel147 1µM	SKmel147 10µM	Common for 1-10µM
First	55	152	53
Second	15	52	15

	WM3918 1µM	WM3918 10µM	Common for 1-10µM
First	122	147	64
Second	40	39	19

Table 2: **Number of drugs identified for the first two steps** of the selection process for both cell lines and tested compound concentrations.

3) Confirmation of the effect of the identified compounds by **manually inspecting images** of Calcein AM-stained spheroids was performed. Despite removing external wells from the plate to minimize the "edge effect', several wells were still affected, leading to the exclusion of various compounds, as exemplified in Fig. 51 B. Moreover, we conducted further **literature research** on each compound, including FDA status, information on potential toxicity, and information on concluded, terminated, or ongoing clinical trials in melanoma or other cancers, as well as the published support of each compound to the targetable pathway. This third selection step was supported by a Master's student (Fizza Irfran), who was co-supervised by me.

A schematic representation of the selection process is shown in Figure 51 C. Ultimately, **20 hit drugs** (Table 3) were selected for further validation through DRC generation.

Drug	Target	FDA approved	Cell line specificity	Therapeutic effect	Targeted pathway
Albendazole	Beta tubulin	YES	WM3918	Antihelmintic	Cytoskeleton
AZD6738	ATR	NO	SKMEL147	Antineoplastic	DNA synthesis
Camptothecine	Topoisomerase I	NO	SKMEL147	Antineoplastic	DNA synthesis
CHIR-124	CHK1	NO	SKMEL147	Antineoplastic	Cell cycle
Cladribine	Ribonucleotide reductase	YES	SKMEL147	Antineoplastic	DNA synthesis
Daunorubicin hydrochloride	Topoisomerase II	YES	BOTH	Antibacterial	DNA synthesis
Entinostat	HDAC	NO	SKMEL147	Antineoplastic	Epigenetic
Epirubicin hydrochloride	Topoisomerase II	YES	SKMEL147	Antineoplastic	DNA synthesis
Irinotecan hydrochloride trihydrate	Topoisomerase I	YES	SKMEL147	Antineoplastic	DNA synthesis
Itopride	D(2) dopamine receptor	NO	WM3918	Antipsychotic	Neurotransmission
Lanatoside C	Plasma membrane Na+/K+ ATPase	NO	SKMEL147	Cardiotonic	Molecular pump
Obatoclax	Bcl-2	NO	BOTH	Antineoplastic	Apoptosis
PD0325901	MEK	NO	SKMEL147	Antineoplastic	MAPK
Proscillaridin A	Plasma membrane Na+/K+ ATPase	NO	SKMEL147	Antiarrhythmics	Molecular pump
Pyrvinium pamoate	CK1α	YES	BOTH	Antihelmintic	WNT
TAK-733	MEK	NO	SKMEL147	Antineoplastic	MAPK
Thioridazine hydrochloride	Dopaminergic D1 and D2 receptors	YES	WM3918	Antipsychotic	Neurotransmission
Topotecan	Topoisomerase I	YES	BOTH	Antineoplastic	DNA synthesis
Ulixertinib	ERK	NO	SKMEL147	Antibacterial	MAPK
XL888	HSP90	NO	SKMEL147	Antineoplastic	Epigenetic

Table 3: The table reports information about the main targets, FDA status, screened cell-line specificity and the therapeutic effect type and targeted pathway of the **20 selected hit drugs**.

The majority of the selected compounds were specific to SKmel147, which aligns with our intended focus on $NRAS^{mut}$ melanoma. The most common targets among these compounds were **topoisomerase I and II**, which are usually complexes involved DNA synthesis of highly proliferative cells (328). SKmel147 presents a CDKN2A mutation, lacking important cell cycle inhibitors such as p14 and p16. Hence, we also selected a **checkpoint kinase 1 (CHK1)** inhibitor (CHIR-124). In the last decades, melanoma drug resistance has been linked to the reprogramming of epigenetic mechanisms (329,330), increased expression of chaperone proteins (331), and anti-apoptotic proteins (332). Consequently, we selected inhibitors targeting **histone deacetylase (HDAC)** (Entinostat), **heat-shock protein 90 (HSP90)** (XL888), and **BCL-2** (Obatoclax). We included **cardiac glycosides** (Lanatoside C and Proscillaridin A), which primarily inhibit the plasma membrane Na+/K+ ATPase (ATP1) pump activity. This class of compounds has garnered attention as a potential novel cancer treatment (333–335), including melanoma (336–338). Furthermore, we selected promising **MEK inhibitors** (PDO325901 and TAK-733) and **ERK inhibitors** (Ulixertinib). For WM3918, we chose **dopamine receptor antagonists** (Itopride and Thioridazine hydrochloride), which have shown notable anticancer properties and effectiveness against multi-drug resistant cancer cells (339,340), as well as a **β-tubulin inhibitor** (Albendazole), given that β-tubulin alterations are recognized as a hallmark of cancer and play a role in melanoma progression (341,342). We identified compounds that were effective across both cell lines: Topotecan (topoisomerase I poison), Daunorubicin hydrochloride (Topoisomerase II poison), and Pyrvinium Pamoate (**CK1α agonist and Respiratory Complex I inhibitor**).

We also conducted HTS on the $BRAF^{mut}$ melanoma cell line, 624mel. The HTS for 624mel exhibited lower assay quality, with a reduced Z'-factor and higher CV, with some plates showing CVs greater than 15%, compared to the previously screened melanoma cell lines (Fig. 52 A). Given our primary focus on $NRAS^{mut}$ and $BRAF^{wt}$/$NRAS^{wt}$ melanoma cells, we did not perform an extensive hit drug selection analysis for 624mel; instead, we conducted basic data normalization to provide a general overview of drug responses (Fig. 52 B). This analysis revealed increased drug sensitivity in 624mel compared to SKmel147 and WM3918, with many compounds reducing cell viability by more than 50% at both tested concentrations (Fig. 52 C and D). These data may serve as a foundation for future studies on $BRAF^{mut}$ melanoma.

In conclusion, we successfully performed HTS testing of over a thousand compounds using 3D melanoma spheroids. Through a sequential drug selection process, we identified promising candidates specifically targeting $NRAS^{mut}$ and $BRAF^{wt}$/$NRAS^{wt}$ melanoma cells for further validation.

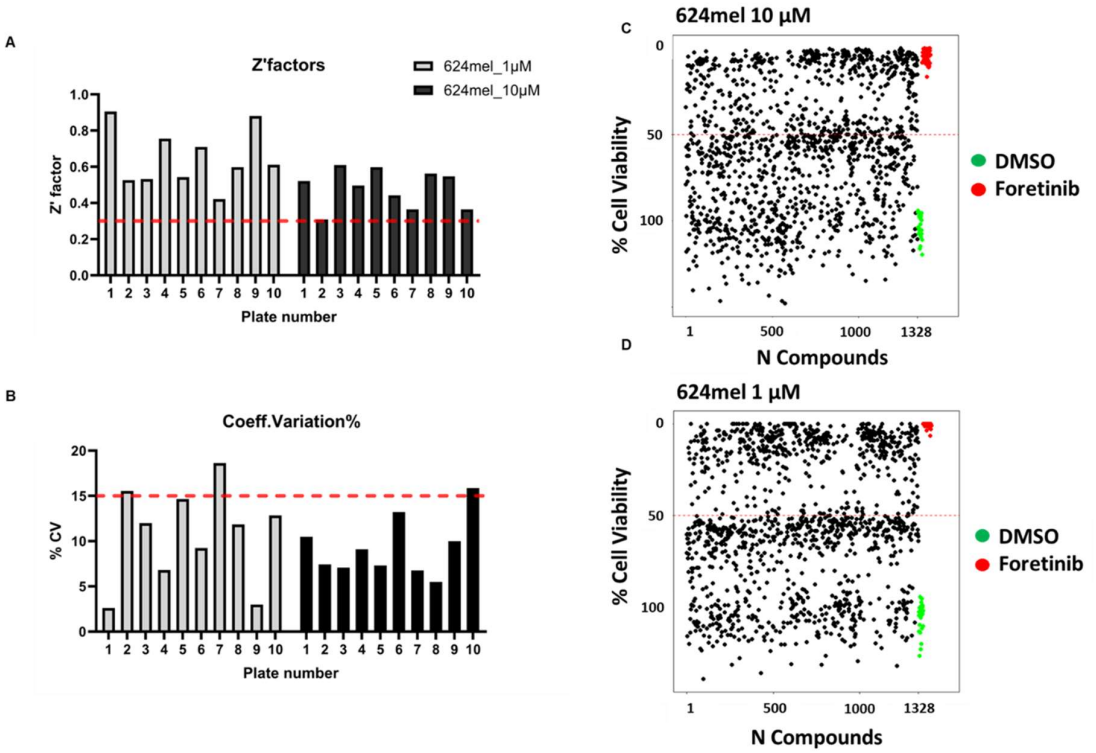

Figure 52: **Analysis of 624mel HTS**. A) Z'-factor for each screened plate, and B) coefficient of variation for each screened plate. Overall, a generally lower quality assay was observed for this melanoma cell line compared to the previously two screened cell lines. Scatter plots show the % cell viability (DMSO-normalized) of each screened compound at C) 10 µM and D) 1 µM.

4.4.3. Drug response curve (DRC) of selected compounds

The cytotoxic effect of the selected hit drugs (Table 3) was further investigated in dose-response assays by the **generation of IC50 values** on the DMSP. Assay quality control steps included Z'-factor and positive control DRC with Foretinib. All the plates presented a Z'-factor bigger than 0.4 and a robust DRC curve (Fig. 53 A and B).

Selected compounds were tested in both cell lines. IC50 values of the hit drugs are reported in Table 4 and respective curves in Suppl. Fig 6 and 7. Trametinib was added as an internal control given its proven high sensitivity in both cell lines. Tested compounds showed IC50 values ranging from 2 nM to more than 7 µM, displaying **a higher sensitivity in SKmel147 than in WM3918**, confirming HTS results. 15/20 tested compounds showed strong activity in SKmel147, with IC50 values below 300 nM.

High sensitivity was mostly given by the compounds targeting DNA stability and replication such as Cladribine, Topotecan, Irinotecan, and Daunorubicin HCl having IC50 values lower than 50 nM. On the other hand, these four compounds showed heterogeneous efficacy in WM3918, with Cladribine and Daunorubicin HCl having IC50 values below 100 nM, while Topotecan and Irinotecan had IC50 values higher than 4 µM and 7 µM, respectively.

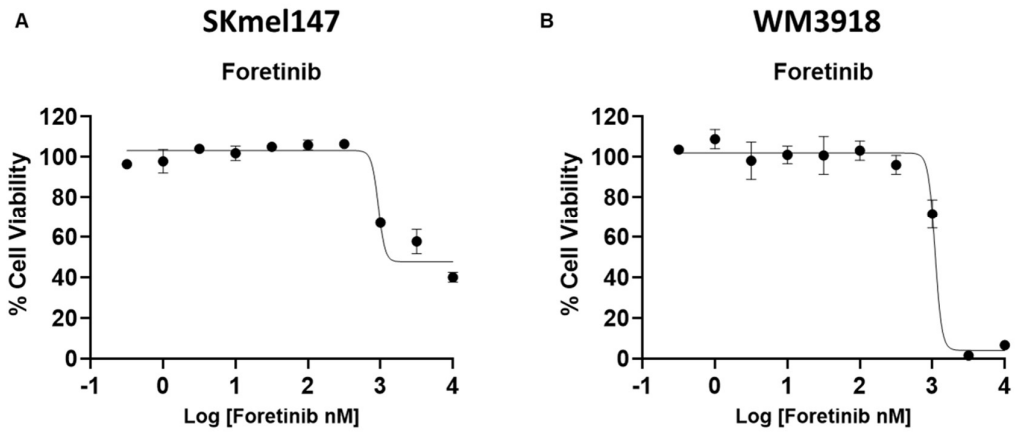

Figure 53: **Drug response curves for Foretinib executed before the validation screening to test the robustness of the assays**. A) Foretinib DRC for SKmel147. B) Foretinib DRC for WM3918.

	IC50 [nM]		R squared	
Compounds	**SKmel147**	**WM3918**	**SKmel147**	**WM3918**
Albendazole	2.79	126	0.99	0.95
Camptothecine (S+)	n.d.	n.d.	n.d.	n.d.
Cladribine	1.737	42.8	0.97	0.98
Daunorubicin hydrochloride	42.83	93.58	0.99	0.97
Entinostat	291.5	n.d.	0.97	n.d.
Epirubicin hydrochloride	n.d.	n.d.	n.d.	n.d.
Irinotecan hydrochloride trihydrate	20.07	7412	0.98	0.91
Lanatoside C	92.57	102.3	0.99	0.99
Obatoclax	1500	2223	0.97	0.90
Proscillaridin A	16.7	19.77	0.95	0.95
Pyrvinium pamoate	195.2	635.5	0.99	0.93
TAK-733	n.d.	n.d.	n.d.	n.d.
Thioridazine hydrochloride	168.9	231.3	0.98	0.96
Topotecan	4.505	4395	0.96	0.91
Ulixertinib	n.d.	n.d.	n.d.	n.d.
XL888	66.33	438.3	0.99	0.68
Itopride	295.8	1085	0.98	0.87
Trametinib	2.495	51.38	0.99	0.83
AZD6738	66.54	1733	0.97	0.96
PD0325901	171.5	n.d.	0.98	n.d.
CHIR-124	n.d.	n.d.	n.d.	n.d.

Table 4**: IC50 values and R squared of hit drugs** tested on SKmel147 and WM3918 cell lines, respectively.

Other topoisomerase inhibitors such as Camptothecine (S+) (both cell lines) and Entinostat (WM3918) had no significant effect. Moreover, compounds specifically selected to be tested in WM3918 were efficient in SKmel147, such as Albendazole, Itopride, and Thioridazine hydrochloride with IC50 values of 2 nM, 296 nM, and 169 nM, respectively. On the other hand, those compounds presented a slightly lower sensitivity in WM3918 with higher IC50 values (126 nM, 1085 nM, and 231 nM, respectively) but still within the clinically relevant range. Cardiac glycosides had an interesting effect on both cell lines, among the most sensitive compounds for WM3918.

Other compounds such as Pyrvinium Pamoate, and XL888 were efficiently effective in both cell lines. Following the high cell line specificity, AZD6738 and PD0325901 had significantly lower IC50 values in SKmel147 than in WM3918 (the IC50 value for PD0325901 was not determined). Unexpectedly, potent MAPK pathway inhibitors such as TAK-733 and Ulixertinib and cell cycle inhibitors such as CHIR-124 did not show relevant cytotoxicity.

In conclusion, we generated dose-response curves on the DMSP validating the efficacy of all selected hit drugs, and highlighting the possibility of repurposing several compounds for the treatment of $NRAS^{mut}$ and $BRAF^{wt}$/$NRAS^{wt}$ melanoma.

4.5. Characterization of selected re-purposed drugs in 3D-preclinical melanoma models for $NRAS^{mut}$ melanoma

$NRAS^{mut}$ melanoma represents an aggressive melanoma subtype characterized by poor patient prognosis (75,343). Current therapeutic options, including chemotherapy, targeted therapies such as MEK inhibitors (MEKi), and immunotherapies such as immune checkpoint inhibitors (ICI), exhibit lower efficacy compared to treatments for $BRAF^{mut}$ melanoma, leading to shorter progression-free survival due to primary or acquired resistance (69,344,345).

This underscores the **urgent need for novel first- and second-line** therapies tailored to $NRAS^{mut}$ patients. Utilizing 3D high-throughput drug screening followed by dose-response curve (DRC) validation of identified hits, we prioritized two candidate compounds. Subsequent experiments were conducted to further characterize and validate their potential as novel therapeutic options for $NRAS^{mut}$ melanoma.

4.5.1. NRAS^{mut} melanoma cells are highly sensitive to selected compounds

In our focus on NRAS^{mut} melanoma, we selected two candidate compounds for further validation. The first compound, **Daunorubicin HCl (DH)**, a topoisomerase II poison, was identified within the major fraction of targeted pathways among the selected hit drugs, specifically within the "DNA synthesis" category (Fig. 54 A).

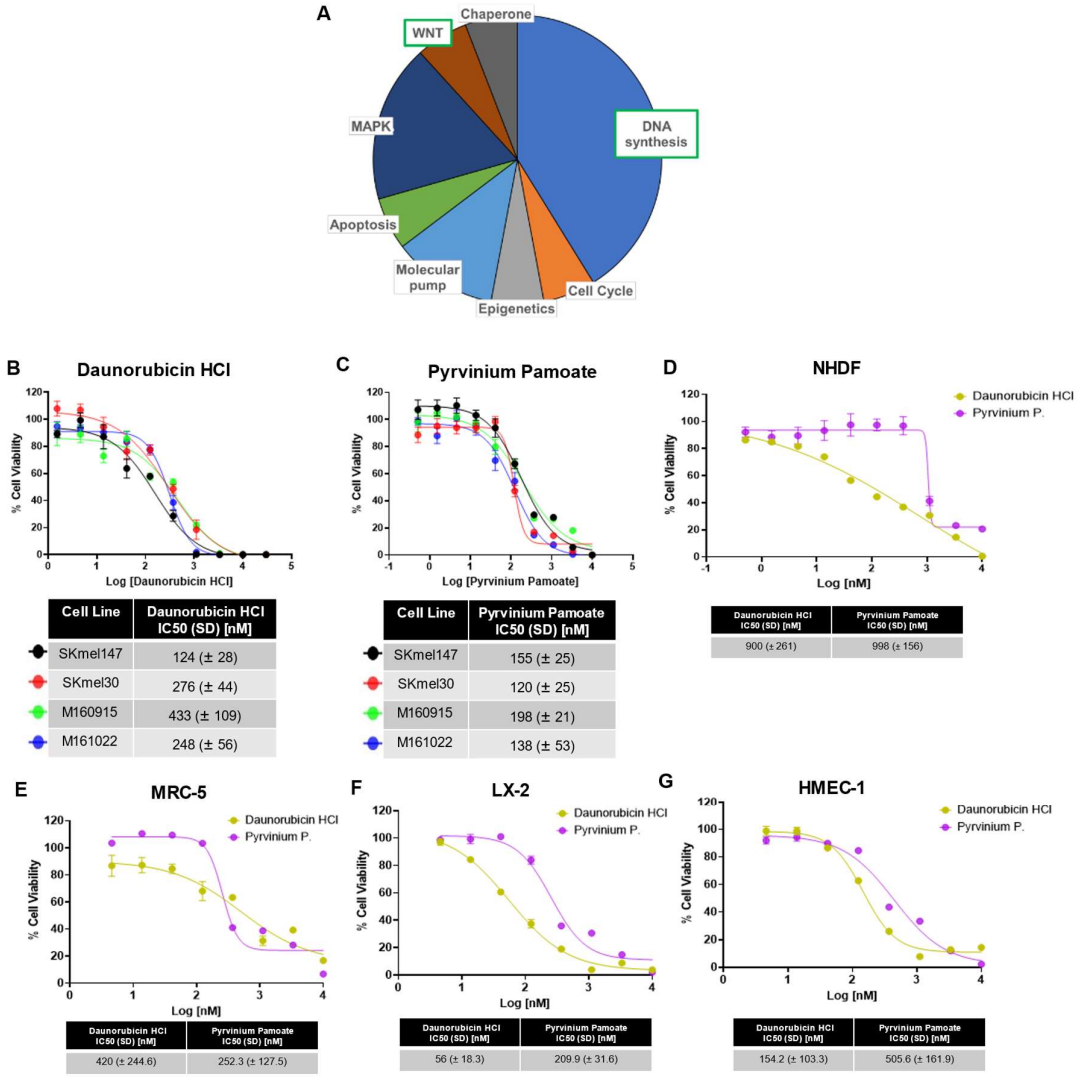

Figure 54: **Daunorubicin HCl and Pyrvinium pamoate DRCs in additional melanoma and non-cancerous cell lines**. A) Pie chart representing the fractions of targeted pathways which the 20 selected compounds belong to. B-C) Representative drug-response curves of Daunorubicin HCl and Pyrvinium Pamoate tested on four NRAS-mutated melanoma cell lines. Tables below the graphs report the respective cell line-specific IC50 values. N=3. D-G) Representative DRCs of Daunorubicin HCl and Pyrvinium pamoate tested in non-cancerous cell lines: NHDF (D), MRC-5 (E), LX-2 (F), and HMEC-1 (G). Tables below the graphs report the respective cell line specific IC50 values. N=3.

The second compound, **Pyrvinium Pamoate (PP)**, was chosen for its ability to target the canonical WNT pathway, a well-known driver of drug resistance, survival, and metastasis in melanoma and other cancers (346–349). Both DH and PP are FDA-approved drugs, currently employed for the treatment of specific conditions: acute myeloid leukemia (AML) (350) and pinworm infections (351), respectively. To assess the sensitivity of $NRAS^{mut}$ melanoma cells to the two compounds, we evaluated their effects on four $NRAS^{mut}$ melanoma cell lines, two commercially available lines, and two primary cell lines, cultured as mono-component spheroids. It is important to note that one of the two primary cell lines used, M161022, did not form rounded and compact spheroids but instead developed into a dense 3D cell aggregate.

DRCs were generated, and the corresponding IC50 values were determined. Both compounds demonstrated generally low IC50 values, depicting **high sensitivity of melanoma cells** (Fig 54 B and C). Notably, **PP exhibited greater potency**, emphasizing the high sensitivity of this $NRAS^{mut}$ melanoma cell line panel to these compounds. Additionally, DRCs were conducted on **non-cancerous cell lines**, including NHDF (Fig. 54 D), MRC-5 (Fig. 54 E), LX-2 (Fig. 54 F), and HMEC-1 (Fig. 54 G), to evaluate their selectivity. NHDF and MRC-5 cells showed low sensitivity to DH, whereas sensitivity was observed in LX-2 and HMEC-1 cells. MRC-5 and HMEC-1 cells displayed slightly higher sensitivity to PP compared to NHDF and LX-2, but lower than melanoma cells.

In conclusion, Daunorubicin HCl and Pyrvinium pamoate demonstrated significant efficacy, exhibiting remarkable sensitivity across a panel of $NRAS^{mut}$ melanoma cell lines cultured as 3D spheroids. Their lower impact on non-cancerous cell lines than melanoma cells further underscores their potential therapeutic safety, as reflected by their FDA-approved status.

4.5.2. Characterization of the drug's effects on $NRAS^{mut}$ melanoma cells

To further investigate the **mode of action** of DH and PP in $NRAS^{mut}$ melanoma cells, we conducted **kinetic analyses** using time-lapse microscopy. The **proliferation** of three melanoma cell lines constitutively expressing mCherry fluorescent protein, cultured as mono-component spheroids, was monitored. Trametinib (MEKi), a clinically used compound, and Staurosporine, a well-established apoptosis inducer, were included as controls. The fluorescent signal emitted by melanoma cells was used to measure spheroid size over time, providing a dynamic assessment of compound effects in cellular proliferation.

From this point onward, **we adopted the IC50 values** determined for each melanoma cell line for Daunorubicin HCl and Pyrvinium pamoate as the primary feature for comparison.

The IC50 values for Trametinib, previously determined in our laboratory, were as follows: 5 nM for SKmel147, 2 nM for SKmel30, 8 nM for M160915, and 1 nM for M161022. Unfortunately, M160915 could not be included in this assay due to culture issues following transduction for the induction of mCherry fluorescent protein expression.

Pyrvinium pamoate, along with Trametinib, exhibited a **strong reduction** in melanoma spheroid and 3D aggregates proliferation across all tested cell lines (Fig. 55 A-C). **Daunorubicin HCl** showed a comparable inhibitory effect to these compounds in SKmel147 and M161022 (a primary melanoma cell line), but its **effect was weaker** in SKmel30. We hypothesized that this diminished effect of Daunorubicin HCl on SKmel30 may be attributed to the cell line's differential capacity to manage DNA damage, potentially due to a TP53 mutation (gene deletion, Cellosaurus.com). In contrast, Pyrvinium pamoate demonstrated the most pronounced reduction in proliferation in SKmel30 (Fig. 55 B). Additionally, this proliferation assay revealed that all compounds exhibited the onset of a marked effect between 60 and 72 hours after treatment initiation.

To validate the inhibitory effect on spheroid proliferation observed through time-lapse microscopy, we evaluated **cell viability** following a 5-day treatment period. SKmel147 exhibited **significant strong reductions** in cell viability across all compounds compared to the untreated controls (Fig. 55 D). SKmel30 showed a significant sensitivity to PP and a reduced response to Daunorubicin HCl, consistent with the proliferation assay results, although the effect remained significant relative to the untreated control (Fig. 55 E). Similarly, M161022 demonstrated a significant reduction in cell viability for all compounds, with a significant reduction of cell viability upon PP treatment. Interestingly, the reduction was more pronounced with Daunorubicin HCl and Pyrvinium pamoate than with Trametinib (Fig. 55 F).

Based on the results of these assays, the compounds **appeared to exert predominantly cytostatic effects**. To confirm this, **we assessed cell death and apoptosis** by measuring nucleic acids for dead cells and activation of effector caspases (caspase 3 and 7), respectively, after a 5-day treatment period using the cell-line specific IC50 values of the drugs (Fig. 56 A-C).

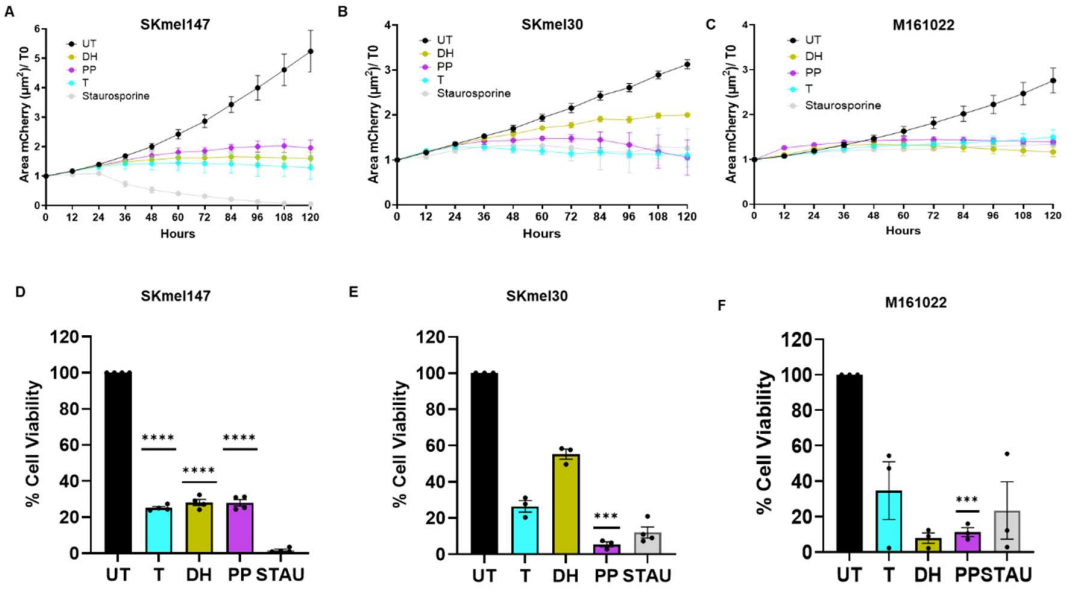

Figure 55: **Effect of Daunorubicin HCl and Pyrvinium pamoate on melanoma spheroids proliferation and cell viability**. **A)** The graph represents the fluorescent spheroid areas of kinetic responses to drug stimulations of SKmel147-mCherry treated for 5 days. Fluorescent images were acquired every 12 hours. **B)** The graph represents the fluorescent spheroid areas of kinetic responses to drug stimulations of SKmel30-mCherry treated for 5 days. **C)** The graph represents the fluorescent spheroid areas of kinetic responses to drug stimulations of M161022-mCherry treated for 5 days. **D)** Cell viability assay assessed after 5 days of drug treatment on SKmel147 spheroids. **E)** Cell viability assay assessed after 5 days of drug treatment on SKmel30 spheroids. **F)** Cell viability assay assessed after 5 days of drug treatment on M161022 spheroids. Staurosporine was used as positive control in both assays at 200 nM in SKmel147 and M161022, and at 400 nM in SKmel30. Data are normalized by the untreated control. For proliferation assays: (n=3. mean±SD). For cell viability assay: (n=3. mean±SD;***p≤0.001 ****p≤0.0001).

The level of **apoptosis and cell death** induction was associated with the tumor mass of the spheroid or cell aggregate on day 5 of treatment. Intrinsic levels of apoptosis and cell death were observed in the inner core of untreated spheroids, which is consistent with the innate architecture of 3D tumor formations (259). SKmel147 exhibited the **highest sensitivity** to all three compounds, showing strong spheroid shrinkage and significant levels of apoptosis and cell death upon the treatments (Fig. 56 A and B), in line with the strong reduction in cell viability (Fig. 55 D). SKmel30 presented high resistance to T and DH. Moreover, Staurosporine induced the lowest level of apoptosis and cell death in SKmel30, underlining an intrinsic resistance to apoptosis in the SKmel30 cell line. On the other hand, **PP induced a remarkable cytotoxic effect on SKmel30** highlighted by a significant increase in apoptosis and cell death (Fig. 56 C and D).

The primary melanoma cell lines M161022 and M160915 displayed similar levels of cytotoxicity across the three compounds, with PP presenting the highest levels (Fig. 56 E-H).

Furthermore, signals from activated caspase 3 and 7 (green) and nucleic acids of dead cells (blue) largely overlapped. The nuclear presence of activated effector caspases indicated that the cells had already reached a late stage of apoptosis, during which PARP and other nuclear components are cleaved (352,353).

The inhibitory effect of Daunorubicin HCl, Pyrvinium pamoate, and Trametinib on the **migratory and invasive capacities** of melanoma cells was assessed in SKmel147 and M160916 spheroids embedded in a type I Collagen matrix, following 3 days of drug treatment. SKmel30 was excluded from this assay due to its lack of motility in the Collagen I matrix, while M161022 was not tested because of its 3D cellular aggregate formation, which posed technical challenges for this analysis. In SKmel147, significant inhibition of migration and invasion was observed only with Trametinib, while Daunorubicin HCl and Pyrvinium pamoate elicited only slight reductions in cell motility (Fig. 57 A). On the other hand, in the primary melanoma cell line M160916, all three compounds **significantly inhibited migratory and invasive activity** (Fig. 57 B). These findings underscore the potential of Daunorubicin HCl and Pyrvinium pamoate to impair melanoma cell motility, particularly in primary melanoma cells.

Lastly, we wanted to investigate how those drugs affected their **main molecular targets** and the regulation of key proteins involved in proliferation, survival, and drug resistance in melanoma, and that are downstream targets commonly activated by mutant NRAS, such as ERK, which belongs to the MAPK pathway, and AKT, which belongs to the PI3K/AKT pathway (see Chapter 1.2.3). Following the outcomes of the kinetic assay, we collected and extracted protein samples from SKmel147 and SKmel30 cultured as spheroids after 3 and 5 days of treatment with IC50 concentrations of either T, DH, or PP.

TOP2α and β-catenin were selected as the main deregulated targets based on existing literature on DH and PP, respectively (350,351). Additionally, **γH2AX** was included as a marker of DNA damage due to the ability of DH to induce double-strand breaks (DSBs); however, we did not observe any expression within the expected weight-related band of 15 kDa. Instead, only an unspecific band above 20 kDa was detected (Fig. 58 A and E; Suppl. Fig. 9 A and E).

We performed Western blot followed by densitometric analyses of the detected bands across all biological replicates, which primarily guided the interpretation of the results.

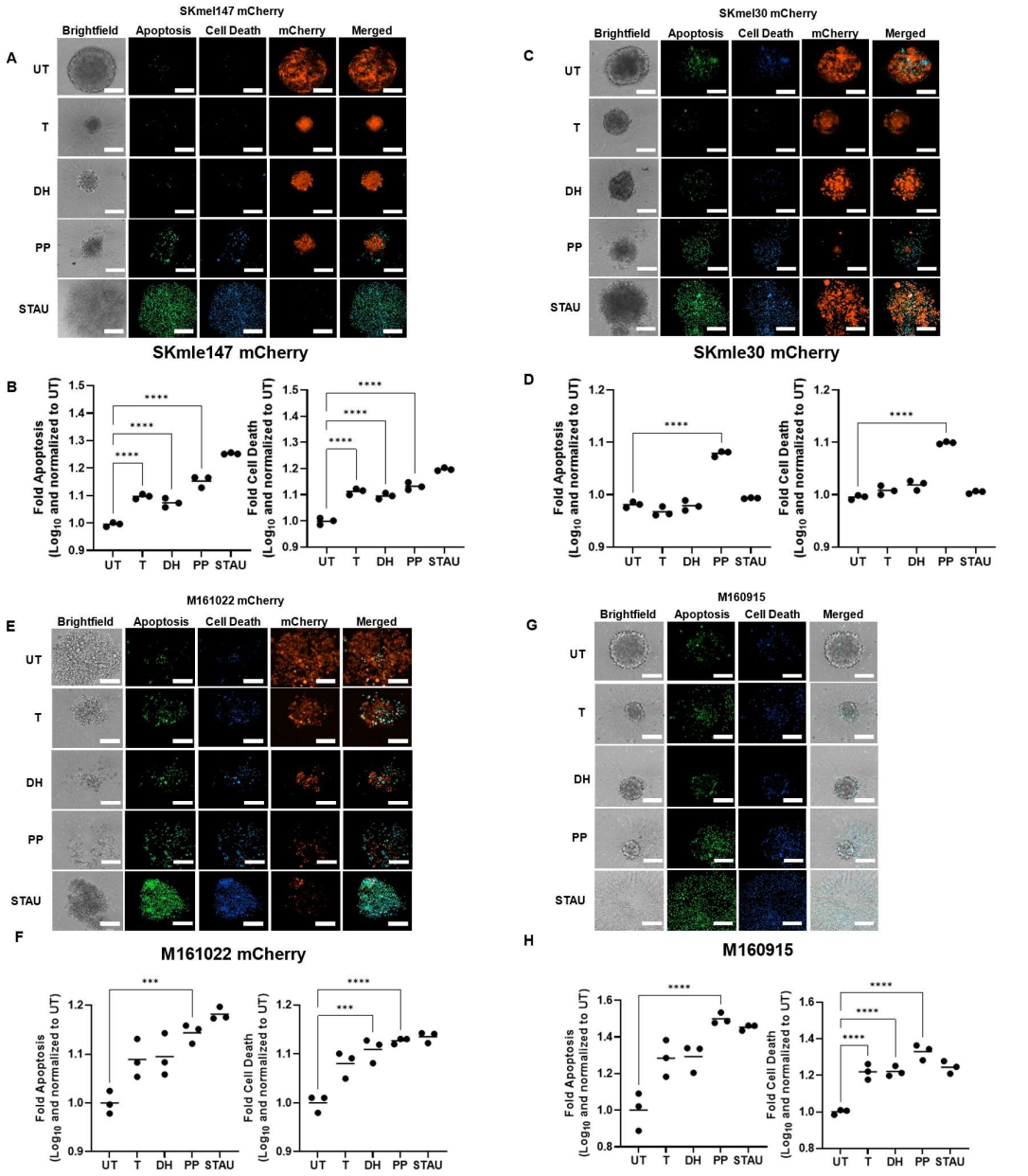

Figure 56: **Apoptosis and cell death induction in treated 3D NRAS^{mut} cell melanoma cell lines**. A) Skmel147-mCherry spheroid apoptosis and cell death assessed after 5 days of treatment. B) Quantification of apoptosis and cell death for each compound used to treat SKmel147 mCherry for 5 days. C) SKmel30-mCherry spheroid apoptosis assessed after 5 days of treatment. D) Quantification of apoptosis and cell death of treated SKmel30 mCherry for 5 days. E) M161022-mCherry 3D aggregate apoptosis assessed after 5 days of treatment. F) Quantification of apoptosis and cell death of treated M161022 mCherry for 5 days. F) M160915 spheroid apoptosis assessed after 5 days of treatment. F) Quantification of apoptosis and cell death of treated M160915 for 5 days. Staurosporine was used as positive control at 1µM 24 hours prior to the end of the assay. Confocal images (objective 20x) of single spheroids are shown. (n=3. Mean is represented by a line and dots represent the values of the independent biological replicates; ***p≤0.001, ****p≤0.0001).

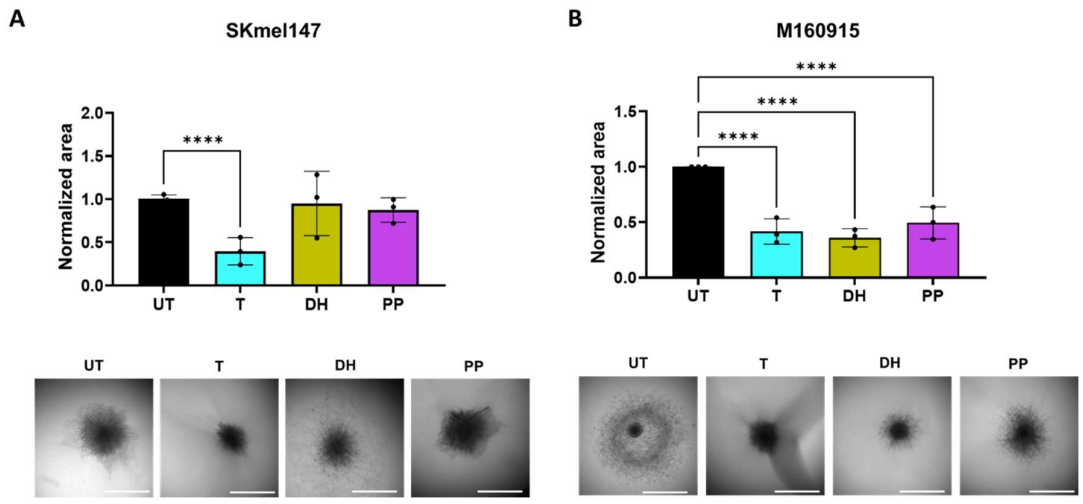

Figure 57: **Effect of Daunorubicin HCl and Pyrvinium pamoate on migration and invasion**. **A)** Bar graph shows the area covered by migratory/invasive SKmel147 cells encapsulated as spheroids in Collagen I matrix (3D Collagen I assay). **B)** Bar graph shows the normalized area covered by migratory/invasive M160915 cells encapsulated as spheroids in Collagen I matrix. Drug stimulation was applied for 3 days. Brightfield images (objective 4x) are shown. (n=3. mean±SD; **p≤0.01, ***p≤0.001, ****p≤0.0001).

TOP2α expression was reduced following all three treatments in SKmel147 (Fig. 58 A-B), while in SKmel30, a small reduction was observed upon 5 days of T and PP treatment (Fig. 58 E-F) without evidence of DH-specific deregulation. Similarly, **β-catenin** did not exhibit significant deregulation upon PP treatment in either cell line, but a slight increase was detected after 5 days in SKmel30 (Fig. 58 B and F). Interestingly, T induced an upregulation of β-catenin in SKmel147 (Fig. 58 A-B).

ERK and its phosphorylated form showed no expression changes upon T treatment in SKmel147, consistent with the low or absent inhibition of its phosphorylated form. A slight increase in pERK was observed in SKmel147 treated with DH. In contrast, PP exhibited an interesting inhibitory effect on ERK phosphorylation after three days of exposure, which returned to levels similar to the untreated control by day five (Fig. 58 B-C). In SKmel30, ERK and pERK levels were consistently reduced at both time points following T treatment, while DH and PP treatments did not induce strong changes compared to untreated controls (Fig. 58 F-G). Interestingly, a marked reduction in **AKT** and its phosphorylated form (Ser473) was observed in SKmel147 (Fig. 58 B and D), whereas the opposite trend was noted in SKmel30 (Fig. 58 F-H).

Deregulation of selected targets was further analyzed in two primary cell lines (Suppl. Fig. 9 A and E). M160915 exhibited increased TOP2α levels upon DH treatment (Suppl. Fig. 9 B), an effect not observed in M161022 (Suppl. Fig. 9 F).

Notably, PP strongly reduced TOP2α in both cell lines (Suppl. Fig. 9 B and F). β-catenin deregulation was detected only after 3 days of PP treatment in M160915 (Suppl. Fig. 9 B), suggesting that PP does not strongly promote β-catenin degradation in these models. Consistent with findings in SKmel147, PP reduced AKT and pAKT levels in both cell lines (Suppl. Fig. 9 B and D, F and H), **reinforcing the hypothesis that PP targets AKT**, though further investigation is needed to determine its mechanism of inhibition. As expected, T reduced pERK (Suppl. Fig. 9 C and G). However, pAKT showed opposite effects in T-treated cells: an increase in M160915 (Suppl. Fig. 9 D) and a decrease in M161022 compared to untreated controls (Suppl. Fig. 9 G). ERK protein levels remained largely unchanged across treatments (Suppl. Fig. 9 B and F). Interestingly, DH increased AKT activation after 3 days in M161022 (Suppl. Fig. 9 H) and after 5 days in M160915 (Suppl. Fig. 9 D).

Overall, none of the selected DH- or PP-specific targets showed significant deregulation in either cell line. Experimentally, considerable variability was observed in certain conditions across the three biological replicates, particularly in SKmel30, as indicated by the large standard deviation bars in the plots. The underlying cause of this variability remains unclear. Additionally, during the first tests with M160915 and M161022, we observed that protein concentrations for primary cell lines after 5 days of treatment with PP yielded a remarkably low amount of protein. In line with this, we increased considerably the amount of material collected for each biological replicate, resulting unfortunately still insufficient (Suppl. Fig. 9 A and E). On the other hand, this might further confirm the strong sensitivity of the cell lines to PP.

In conclusion, Daunorubicin HCl and Pyrvinium pamoate effectively reduced the proliferation and cell viability of $NRAS^{mut}$ melanoma spheroids over time, with effects comparable to those of MEK inhibitor (Trametinib). Notably, Pyrvinium pamoate induced a significant cytotoxic effect, providing a stronger rationale for its potential as a promising drug candidate. At the molecular level, significant deregulation of selected drug-specific targets was not observed, hypothesizing for the deregulation of alternative targets. While PP showed a remarkable inhibitory effect on AKT levels in most of the cell lines posing the deregulation of this kinase as one of the possible triggers of PP's cytotoxic effect.

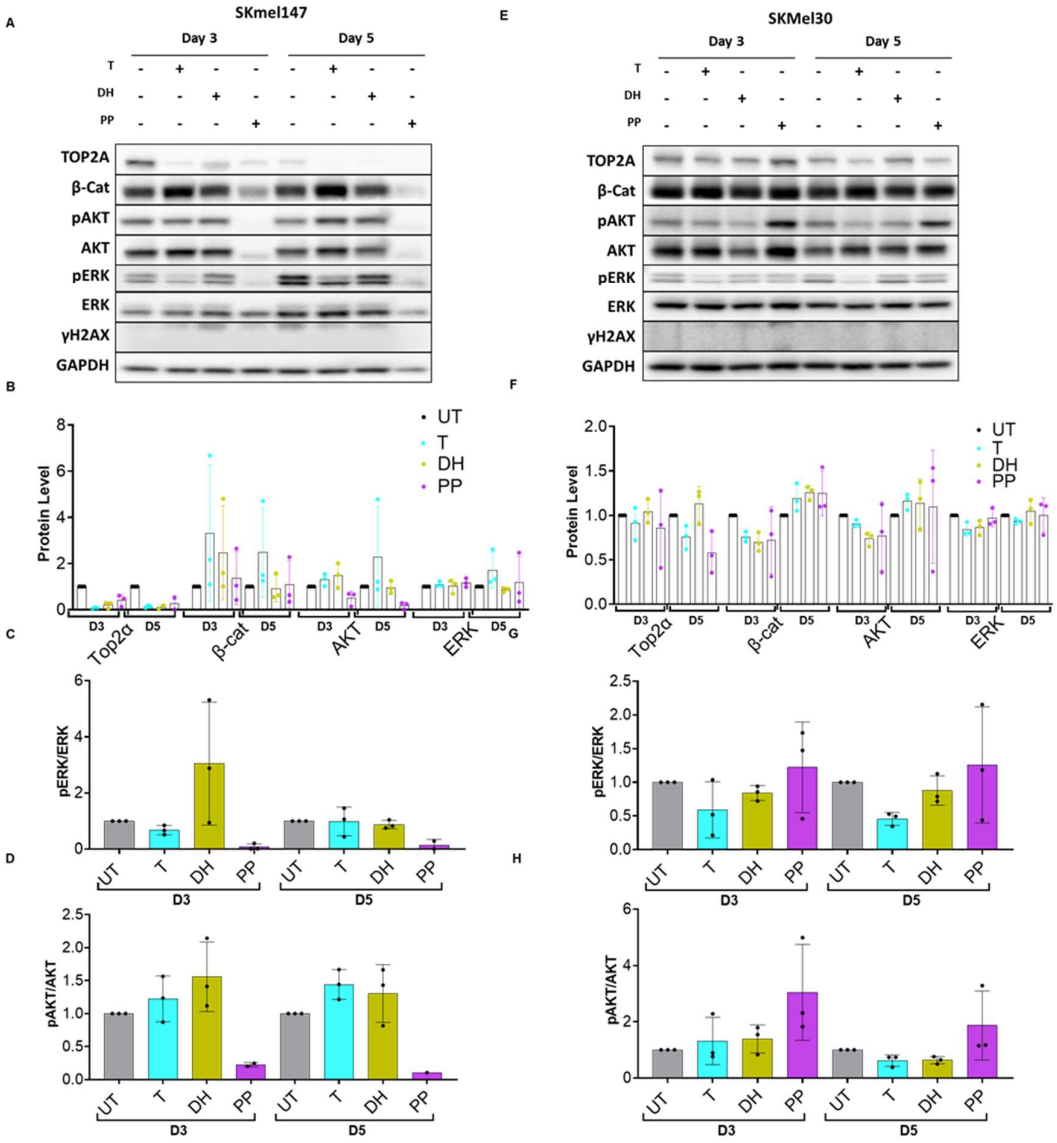

Figure 58: **Effect of Daunorubicin HCl and Pyrvinium Pamoate on drug-specific targets and key melanoma survival and proliferation kinases**. A) Representative Western blots of SKmel147 treated for 3 and 5 days with cell-line specific IC50 values of T, DH, and PP. B) Quantification of the protein levels in SKmel147, normalized to the untreated control. C) pERK/ERK ratio analyzed as quotient of pERK versus ERK, in SKmel147. D) pAKT/AKT ratio analyzed as quotient of pAKT versus AKT, in SKmel147. E) Representative Western blots of SKmel30 treated for 3 and 5 days with cell-line specific IC50 values of T, DH, and PP. F) Quantification of the protein levels in SKmel30, normalized to the untreated control. G) pERK/ERK ratio analyzed as quotient of pERK versus ERK, in SKmel30. D) pAKT/AKT ratio analyzed as quotient of pAKT versus AKT, in SKmel30. γH2AX was excluded from the analysis. GAPDH was used as loading control; representative blots of three biological replicates are shown. (n=3. mean±SD). Blots were developed by Demetra Philippidou and densitometry was performed by Sagarika Ghosh.

4.5.3. Combinatorial treatment with Trametinib (MEKi)

After evaluating the effects of Daunorubicin HCl and Pyrvinium pamoate on a panel of $NRAS^{mut}$ melanoma cell lines, we sought to investigate their **potential in combinatorial treatments** with Trametinib. This approach was motivated by the well-documented adaptability of melanoma to monotherapies, as exemplified by the rapid acquisition of resistance to Vemurafenib in $BRAF^{mut}$ melanoma, which ultimately led to the clinical approval of combination therapies involving BRAF inhibitors (BRAFi) and MEK inhibitors (MEKi). We conducted a **3D spheroid synergy assay** on two $NRAS^{mut}$ melanoma cell lines to evaluate the potential synergism between Trametinib and Daunorubicin HCl, as well as Trametinib and Pyrvinium pamoate (Fig. 59 A). The **ZIP synergy score** analysis revealed no significant overall synergistic effect (defined as ZIP synergy score > 10). However, an additive effect (defined as ZIP synergy score > -10 and < 10) was observed across all tested conditions. For further studies, we selected common drug concentrations corresponding to the region of maximum synergism: Trametinib at 0.06 nM, Daunorubicin HCl and Pyrvinium pamoate at 45 nM each. We subsequently evaluated the effects of these two drug combinations on spheroid proliferation and cell viability, in parallel with the respective single treatment, using the concentrations employed in the combinations. Despite selecting concentrations corresponding to the region of maximum synergism, **the observed effects were only additive**, with a modest reduction in both proliferation (Fig. 59 B and D) and cell viability (Fig. 59 C and E) compared to the respective single treatments. Interestingly, low concentrations of Trametinib exhibited a pro-proliferative effect in both cell lines. The drug combinations elicited greater sensitivity in SKmel147 (Fig. 59 B and C), showing a more pronounced reduction in proliferation and cell viability compared to SKmel30 (Fig. 59 D and E). We concluded that **Daunorubicin HCl and Pyrvinium pamoate do not synergize with Trametinib (MEKi) in $NRAS^{mut}$ melanoma cells**, demonstrating only additive effects. Based on these findings, we opted to focus on further characterization of the monotherapies, using advanced *in vitro* pre-clinical models.

Figure 59: **Assessment of synergy in novel combinatorial treatments exploiting 3D spheroid cultures**. A) Synergy matrices and ZIP synergy scores generated by the combinatorial treatments of Trametinib plus either Daunorubicin HCl or Pyrvinium pamoate and tested in SKmel147 and SKmel30 cultured as spheroids. White in the matrices indicates the highest synergistic area with the relative synergy score written in the boxes above. (n=3). Synergy assays were performed by Demetra P. and Dr. Christiane M. B) Line graph represents kinetic responses to drug stimulations of SKmel147-mCherry treated for 5 days. C) Cell viability assay assessed after 5 days of drug treatment on SKmel147 spheroids D) Kinetic responses to drug stimulations of SKmel30-mCherry treated for 5 days. C) Cell viability assay after 5 days of drug treatment on SKmel30 spheroids. Data are normalized by the untreated control. Staurosporine was used as positive control at 200 nM concentration for SKmel147 and 400 nM for SKmel30. T/DH/PP= drugs used at cell line specific IC50 concentrations. DH+T/PP+T= drugs used at synergistic concentrations, T = 0.06 nM and DH/PP = 45 nM. T-low, DH/PP-low = corresponding single drug synergistic concentrations. (n=3. mean±SD).

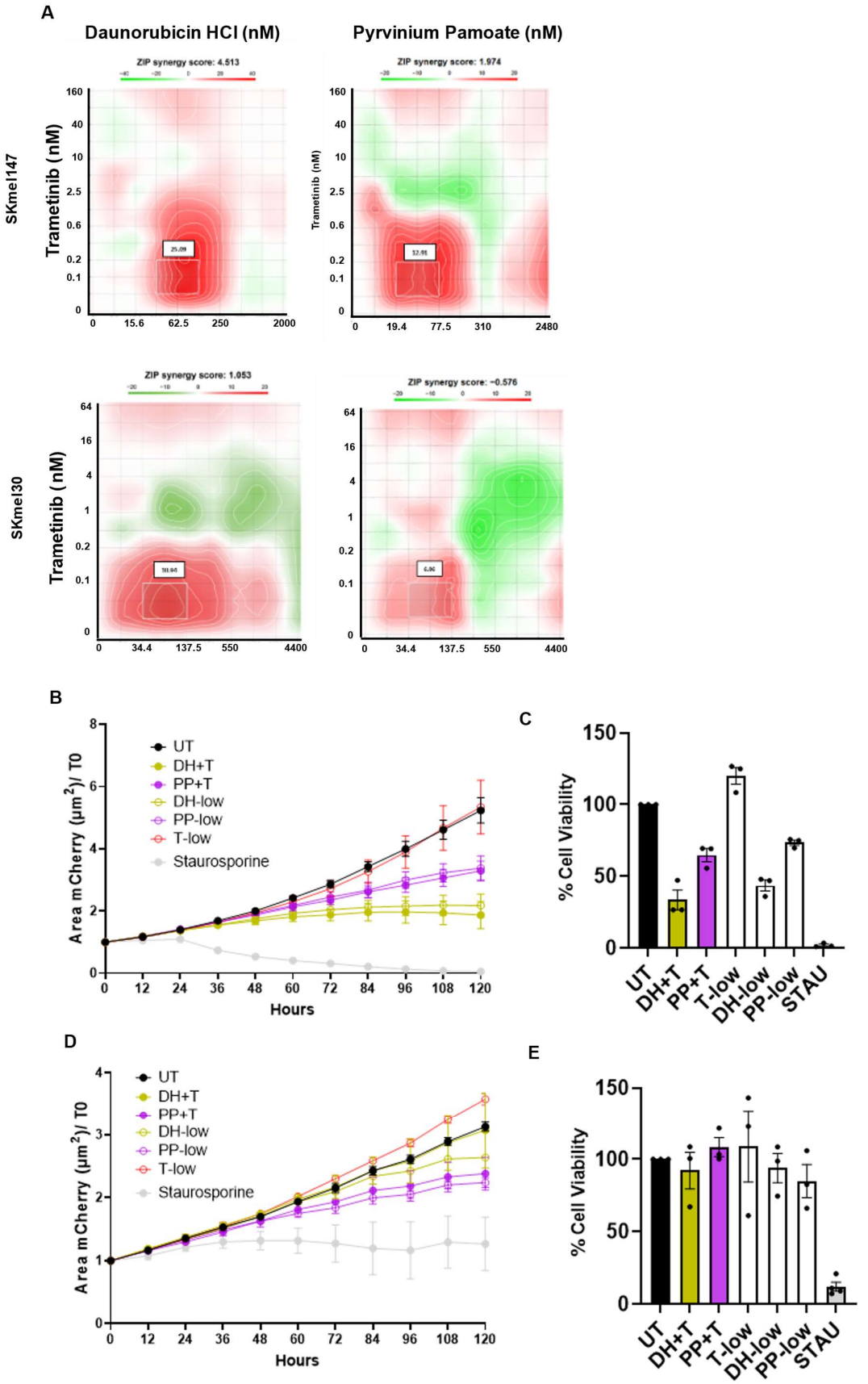
A
Daunorubicin HCl (nM)
Pyrvinium Pamoate (nM)
SKmel147
SKmel30
Trametinib (nM)
ZIP synergy score: 4.513
ZIP synergy score: 1.974
ZIP synergy score: 1.053
ZIP synergy score: −0.576
B
Area mCherry (µm²)/ T0
Hours
UT
DH+T
PP+T
DH-low
PP-low
T-low
Staurosporine
C
% Cell Viability
UT
DH+T
PP+T
T-low
DH-low
PP-low
STAU
D
E

4.5.4. Daunorubicin HCl and Pyrvinium pamoate in advanced *in vitro* 3D melanoma co-culture models

The efficacy of Daunorubicin HCl and Pyrvinium pamoate was evaluated using melanoma cells cultured as 3D spheroids, which are advanced models that mimic the architecture of real tumors. These models preserve cellular heterogeneity and are therefore more representative than traditional 2D culture systems. Over recent decades, increasing evidence has highlighted the role of non-cancerous cells within the **tumor microenvironment (TME) in supporting cancer cell survival and promoting drug resistance**. Cancer cells-TME co-culture models are valuable tools for evaluating the efficacy of anti-cancer drugs, as they allow for the simultaneous consideration of the interaction between cancer cells and surrounding cells, as well as the assessment of the drug's impact on non-cancerous cells by measuring its toxicity. To account for these features, we utilized our previously established **Multicomponent Melanoma Spheroid (MMS) models** to assess the ability of Daunorubicin HCl and Pyrvinium pamoate to impair melanoma cell proliferation and viability in the presence of direct contact with TME cells. The MMS models were designed to represent key melanoma metastatic sites: the **"dermal/skin" model**, where melanoma cells are co-cultured with HMEC-1 (endothelial cells) and NHDF (dermal fibroblasts); the **"lung" model**, where melanoma cells are co-cultured with HMEC-1 and MRC-5 (lung fibroblasts); and the **"liver" model**, where melanoma cells are co-cultured with HMEC-1 and LX-2 (hepatic stellate cells). These setups aim to **mimic melanoma metastases** to the derma, lungs, and liver, respectively. All melanoma and TME cell types used in these models were stably transduced to express distinct fluorescent proteins, enabling real-time visualization of the different cell populations within the same spheroid via live microscopy. **Time-lapse microscopy** revealed a comparable reduction in SKmel147 proliferation across all three MMS models compared to the untreated controls. DH, PP, and T exhibited **similar levels of proliferation inhibition** (Fig. 60 A) and caused a strong reduction in the total cellular mass of the co-culture (Fig. 60 B). This suggests that the remaining 30% to 40% of cell viability **was likely attributed to residual melanoma cells and the non-cancerous TME cells** that persisted after 5 days of treatment, as depicted in confocal images below the proliferation line graphs (Fig. 60 A).

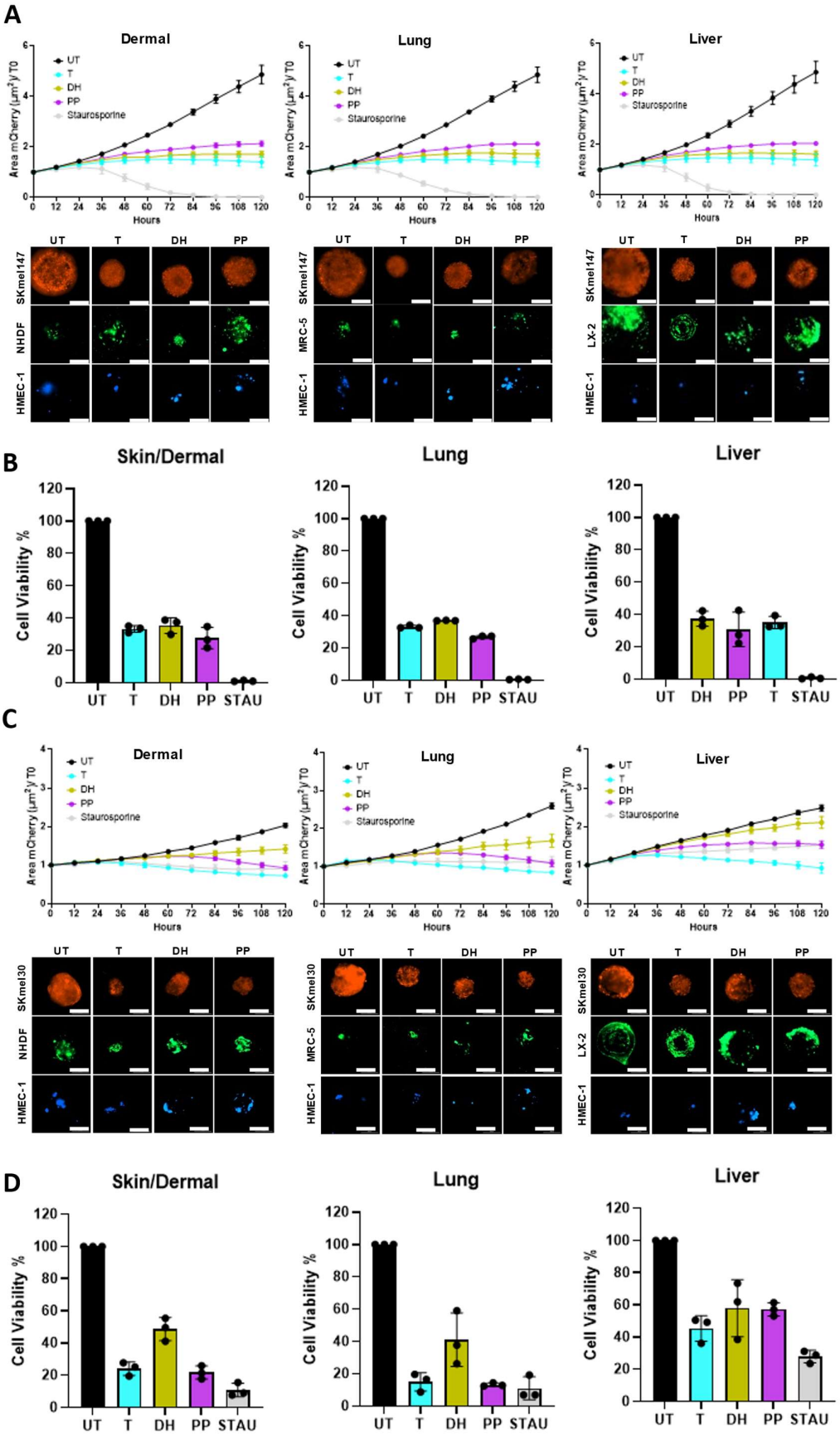
A
Dermal
Lung
Liver
UT
T
DH
PP
Staurosporine
Area mCherry (µm²) y T0
Hours
SKmel147
NHDF
HMEC-1
MRC-5
LX-2
B
Skin/Dermal
Lung
Liver
Cell Viability %
UT T DH PP STAU
C
SKmel30
D

Figure 60: **Drug efficacy tested in Melanoma Multicomponents Spheroid (MMS) models**. **A)** Line graphs represent kinetic responses to 5-day drug of SKmel147-mCherry co-cultured into three Melanoma Multicomponent Spheroid (MMS) models: "Dermal", "Lung", and Liver". Fluorescent images exciting mCherry fluorescence were acquired every 12 hours. **B)** Bar plots represent the cell viability of the three SKmel147-MMS models after 5 days of drug treatment. **C)** Line graphs represent the kinetic responses to the 5-day drug of SKmel30-mCherry co-cultured into three Melanoma Multicomponent Spheroid (MMS) models. **D)** Bar plots represent the cell viability of the three SKmel30-MMS models after 5 days of drug treatment. Data are normalized by the untreated control. Staurosporine was used as a positive control at 200 nM for SKmel147 and at 400 nM concentration for SKmel30. Confocal pictures (objective 20x) of the different cell populations composing the different MMS models after 5 days of drug stimulations are shown; SKmel30-mCherry (red), NHDF/MRC-5/LX-2 (green), HMEC-1 (blue). Scale bar = 200 µm.

Consistent with previous findings from monocomponent spheroids, DH displayed a reduced inhibitory effect in SKmel30 proliferation compared to T and PP (Fig. 60 C), which is lower than the effect observed in monocomponent spheroids (Fig. 55 B). In alignment with the proliferation assay results, cell viability across the three models co-cultured with SKmel30 also showed remarkable reductions (Fig. 60 D). Residual cell viability in these models was similarly hypothesized to result from surviving melanoma cells and TME populations. Confocal microscopy images showed the presence of non-cancerous cells in all conditions.

We also evaluated the efficacy of the compounds on one of the mCherry-expressing primary cell lines, M161022, co-cultured within the MMS models. Due to the lower proliferative capacity of this cell line compared to SKmel147 and SKmel30, the initial cellular ratio of 1:3:3 did not effectively sustain its survival, as it was gradually outcompeted by the surrounding non-cancerous cells (data not shown). Therefore, we adjusted the cellular ratio to 1:1:1, which improved the overall performance of the models. Preliminary data showed that M161022 had more heterogeneous responses among the three MMS models compared to SKmel147 and SKmel30. Preliminary data showed that T and PP similarly inhibited the proliferation of M161022 cells in Dermal and Lung models. At the same time, DH effect was potentiated in Lung models compared to Dermal models (Suppl. Fig. 8 A) and the monocomponent spheroids (Fig. 55 C). This was also captured by a strong reduction in cell viability in all three models (Suppl. Fig. 8 B). It appears that M161022 cells are not suitable for growth within the Liver model, as evidenced by their lack of proliferation over time (Suppl Fig. 8 A).

After evaluating the efficacy of DH and PP in targeting $NRAS^{mut}$ melanoma cells using advanced 3D spheroid co-culture models, we sought to further investigate their effectiveness in more complex models incorporating the extracellular matrix (ECM). To achieve this goal, I utilized the previously established **hydrogel-embedded melanoma TME co-culture models** to test the efficacy of DH and PP, in parallel with T. In these models, melanoma cells and TME cells were stably labeled with different fluorescent proteins, allowing the tracking of their growth within the models after 5 days of treatment. SKmel147 showed a **remarkable reduction** in melanoma population across all three models (Fig. 61 A-D). The three compounds demonstrated similar effects on SKmel147 in the "dermal" and "lung" models, with a reduction of slightly more than 50% of the melanoma population compared to the untreated control (Fig. 61 B and C). In the "liver" model, SKmel147 showed a higher sensitivity to T compared to DH and PP, although all treatments strongly reduced more than 50% of the melanoma population (Fig. 61 D).

Moreover, the hydrogel system allows for **the evaluation of the survival of the other TME cell populations** to assess the effect of the drugs on non-cancerous cells when co-cultured with melanoma cells. Notably, in all the models, the concentrations of the drugs used to target melanoma cells specifically had a low impact on the survival and proliferation of NHDF (Fig. 61 B), MRC-5 (Fig. 61 C), and LX-2 (Fig. 61 D), highlighting the safety and melanoma specificity of these compounds. Regarding endothelial cells, HMEC-1 overall displayed minimal reduction in the presence of DH and PP compared to melanoma cells in all three models, with the most marked effect observed in the Lung model (Fig. 61 C). Moreover, we also tested the efficacy and safety of the compounds utilizing a primary melanoma cell line labeled with mCherry fluorescent protein (M161022-mCherry) (Fig. 61 E) and we observed that DH and, in particular PP, had a **strong effect on the inhibition of melanoma growth** with a smaller impact on the other non-cancerous cells present in the different hydrogel co-culture models (Fig. 61 F-H).

Interestingly, we noted **differences in non-cancerous cell responses** to drugs when co-cultured with different melanoma cell lines, such as NHDF, MRC-5, and LX-2 growth seemed to be slightly more inhibited by DH and PP when co-cultured with M161022 primary melanoma cell line rather than with SKmel147 compared to relative untreated controls, probably given by the different drug concentrations used based on the melanoma cell line-specific IC50 values. Overall, T seems to exert the lowest impact on non-cancerous cells.

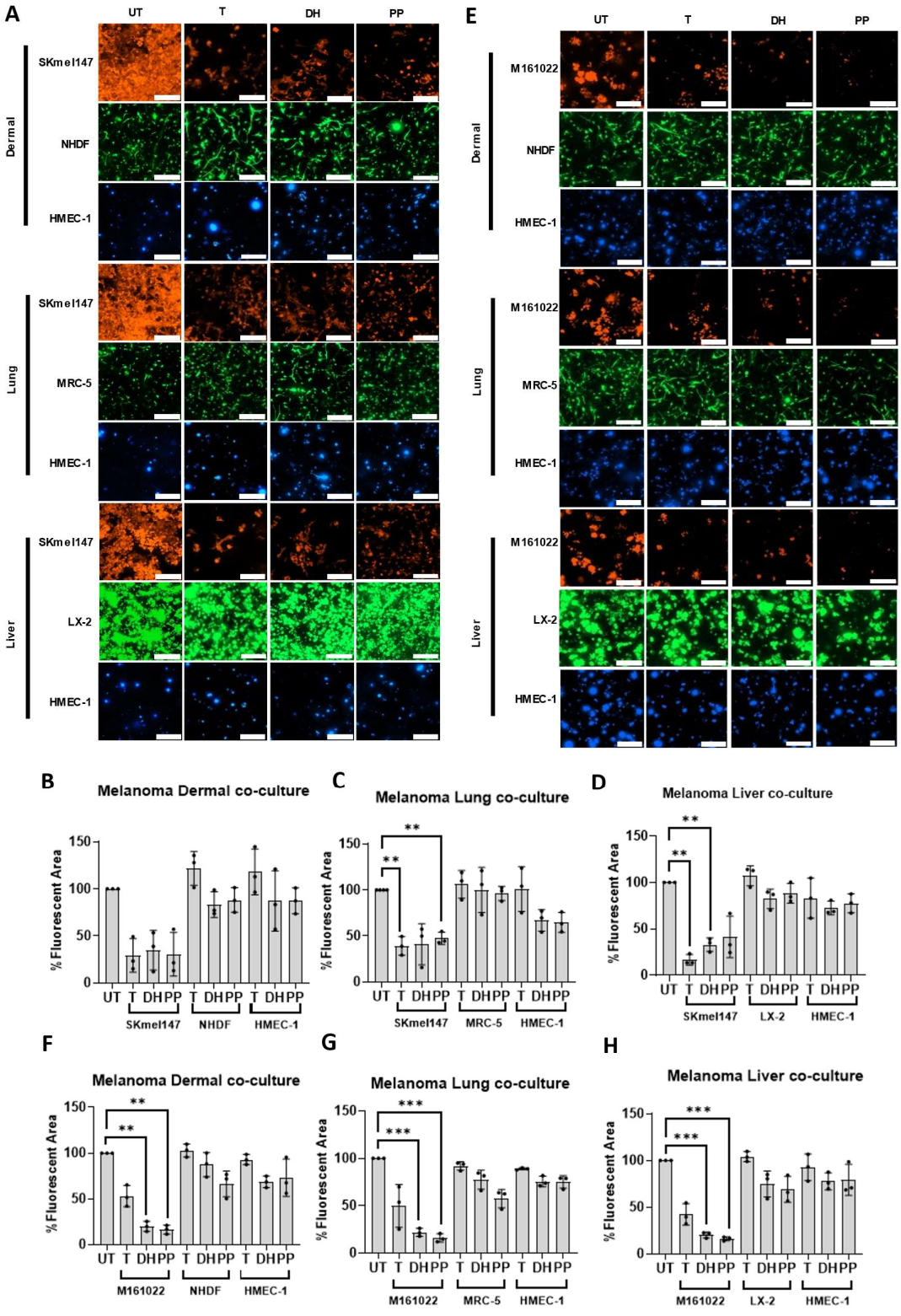
A
UT
T
DH
PP
Dermal
SKmel147
NHDF
HMEC-1
Lung
SKmel147
MRC-5
HMEC-1
Liver
SKmel147
LX-2
HMEC-1
E
UT
T
DH
PP
Dermal
M161022
NHDF
HMEC-1
Lung
M161022
MRC-5
HMEC-1
Liver
M161022
LX-2
HMEC-1
B
Melanoma Dermal co-culture
% Fluorescent Area
SKmel147
NHDF
HMEC-1
C
Melanoma Lung co-culture
% Fluorescent Area
SKmel147
MRC-5
HMEC-1
D
Melanoma Liver co-culture
% Fluorescent Area
SKmel147
LX-2
HMEC-1
F
Melanoma Dermal co-culture
% Fluorescent Area
M161022
NHDF
HMEC-1
G
Melanoma Lung co-culture
% Fluorescent Area
M161022
MRC-5
HMEC-1
H
Melanoma Liver co-culture
% Fluorescent Area
M161022
LX-2
HMEC-1

Figure 61: **Drug efficacy in hydrogel embedded melanoma-TME co-cultures**. **A)** Representative pictures of three hydrogel-embedded Skmel147-TME co-culture models ("Dermal", "Lung", and Liver") under the effect of 5-day treatment with melanoma cell line-specific IC50 concentrations of Daunorubicin HCl, Pyrvinium pamoate and Trametinib. **B-D)** Plots represent the percentage of fluorescent area of the different cell populations co-cultured into the three hydrogel co-culture models after 5 days of drug stimulation. **E) R**epresentative pictures of three hydrogel-embedded M161022-TME co-culture models at day 5 of drug treatment. **F-H)** Plots represent the percentage of fluorescent area of the different cell populations co-cultured into the three hydrogel co-culture models after 5 days of drug stimulation. Data are normalized by the untreated control of each specific cell population. (n=3. mean±SD; **p≤0.01, ***p≤0.001). Confocal pictures (objective 20x) of the different cell populations composing the different hydrogel co-culture models after 5 days of drug stimulations are shown; SKmel147-mCherry (A) or M161022-mCherry (E) (red), NHDF/MRC-5/LX-2 (green), HMEC-1 (blue). Scale bar = 200 µm.

In conclusion, Daunorubicin HCl and Pyrvinium pamoate exhibited a **significant inhibitory effect on melanoma growth**, even when melanoma cells interacted with non-cancerous cells such as fibroblasts and endothelial cells, and in the presence of ECM using a hydrogel co-culture system. Furthermore, the two compounds showed minimal effects on non-cancerous cells, highlighting their safety profile and high specificity for targeting melanoma cells. Daunorubicin HCl, and particularly Pyrvinium pamoate, demonstrated promising potential as novel candidates for first-line treatments for $NRAS^{mut}$ melanoma patients.

4.5.5. Effect of Daunorubicin HCl and Pyrvinium Pamoate on MEKi-resistant melanoma cell lines

We showed the efficacy of DH and PP in inhibiting growth and proliferation with a remarkable cytotoxic effect on treatment-naïve $NRAS^{mut}$ melanoma cells cultured as 3D spheroids and co-cultured with TME cells into advanced 3D models, elucidating their role as possible first-line therapies for $NRAS^{mut}$ melanoma patients. As melanoma rapidly becomes resistant to current therapies, we also aimed to test the efficacy of DH and PP on $NRAS^{mut}$ and WT melanoma cell lines which are **resistant to MEK inhibitors**, to propose these compounds as **second-line therapies for drug-resistant melanoma patients**. We first generated **DRC curves with specific IC50 values** for DH and PP, and in parallel also for the MEKi inhibitor Trametinib to confirm drug resistance of the cell lines.

As expected, MEKi-resistant cell lines did not produce IC50 values or showed an increase in IC50 compared to the sensitive counterparts, depicting their acquisition of resistance to the inhibitors, while the sensitive counterparts presented strong sensitivity to the relative MEKi.

Interestingly, Daunorubicin HCl and Pyrvinium pamoate showed **strong inhibitory activity** on melanoma growth in both parental and MEKi-resistant SKmel30 and WM3918 cell lines (Fig. 62 A-C).

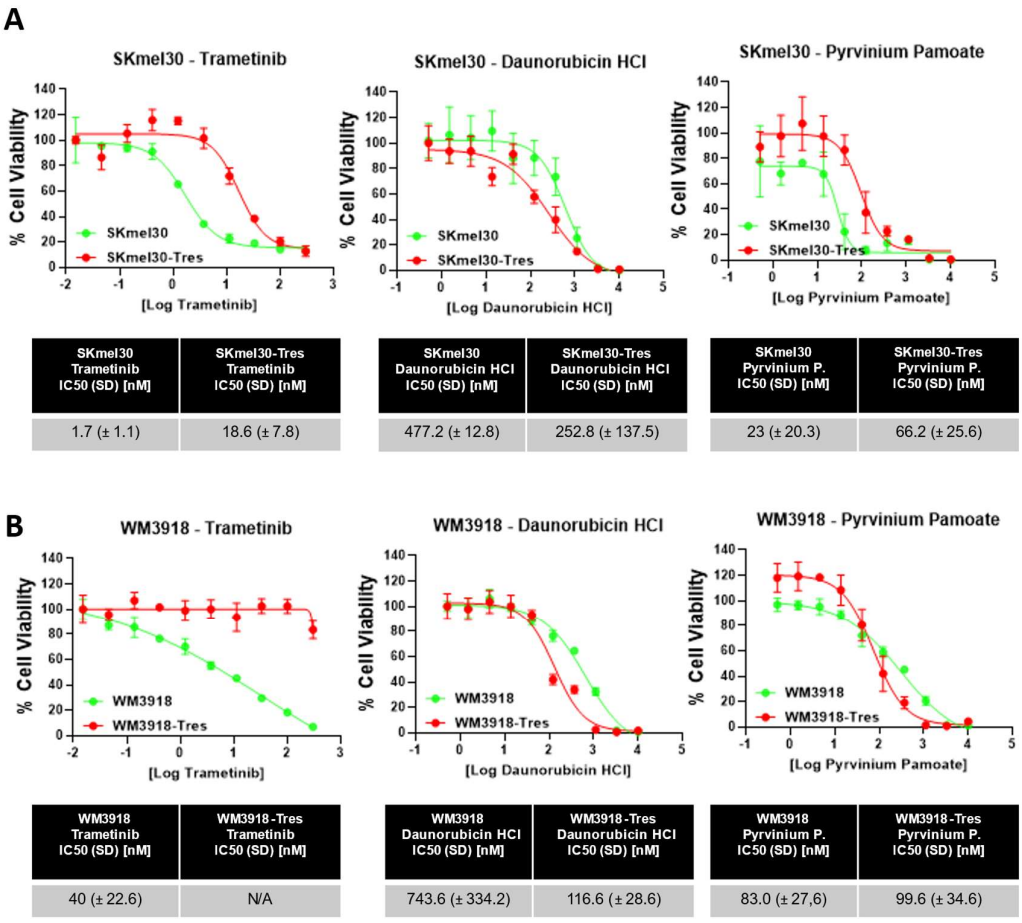

SKmel30 Trametinib IC50 (SD) [nM]	SKmel30-Tres Trametinib IC50 (SD) [nM]	SKmel30 Daunorubicin HCl IC50 (SD) [nM]	SKmel30-Tres Daunorubicin HCl IC50 (SD) [nM]	SKmel30 Pyrvinium P. IC50 (SD) [nM]	SKmel30-Tres Pyrvinium P. IC50 (SD) [nM]
1.7 (± 1.1)	18.6 (± 7.8)	477.2 (± 12.8)	252.8 (± 137.5)	23 (± 20.3)	66.2 (± 25.6)

WM3918 Trametinib IC50 (SD) [nM]	WM3918-Tres Trametinib IC50 (SD) [nM]	WM3918 Daunorubicin HCl IC50 (SD) [nM]	WM3918-Tres Daunorubicin HCl IC50 (SD) [nM]	WM3918 Pyrvinium P. IC50 (SD) [nM]	WM3918-Tres Pyrvinium P. IC50 (SD) [nM]
40 (± 22.6)	N/A	743.6 (± 334.2)	116.6 (± 28.6)	83.0 (± 27,6)	99.6 (± 34.6)

Figure 62: **Drug response curves of sensitive and MEKi-resistant cell lines**. A) Representative drug-response curves of Trametinib, Daunorubicin HCl and Pyrvinium pamoate tested in Trametinib-sensitive (green) and -resistant (red) SKmel30 ($NRAS^{mut}$) cell line cultured as spheroids. B) Representative drug-response curves of Trametinib, Daunorubicin HCl and Pyrvinium pamoate tested in Trametinib-sensitive (green) and -resistant (red) WM3918 (WT) cell line cultured as spheroids. Tables below the graphs report the respective cell line-specific IC50 values. N=3.

Cell death and apoptosis were measured using live-cell confocal microscopy. MEKi-resistant SKmel30 acquired resistance to apoptosis upon PP treatment compared to the MEKi-sensitive cell line, while inducing significant levels of cell death at day 5. Interestingly resistant SKmel30 increased the sensitivity to DH (Fig. 63 A-D).

WM3918 (WT melanoma cell line) showed significant sensitivity to DH and PP in the sensitive cell line, while DH showed a significant cytotoxic effect in MEKi-resistant cell lines, highlighting the cytotoxic effect of DH in MEKi-resistant melanoma cell lines (Fig. 63 E-H).

In conclusion, DH and PP exhibited notable effects on MEKi-resistant $NRAS^{mut}$ and WT melanoma cell lines, providing a foundation for further studies to evaluate their potential as second-line therapeutic options.

4.5.6. Strong inhibitory effect of Daunorubicin HCl and Pyrvinium pamoate in Zebrafish xenograft models

To evaluate the *in vivo* efficacy of the drugs, we used melanoma zebrafish larvae models established by Dr. Joanna Wroblewska in collaboration with Prof. Natascia Tiso (University of Padua, Italy) and Dr. Maria Lorena Cordero Maldonado (LCSB, Luxembourg). SKmel147-mCherry cells were injected into the yolks of 2-day post-fertilization zebrafish nacre/mitfa larvae. After a 24-hour incubation period, the larvae were treated with PP, DH, and T, using doses previously established as the maximum tolerated. Following 72 hours of treatment, larval survival and xenograft size were assessed. In line with the *in vitro* findings, a significant reduction in xenograft size was observed in both sensitive and resistant cell lines. Despite the highly invasive and migratory phenotype of melanoma cells, no increased migration from the initial injection site was detected (Fig. 64 A and B). A number of surviving larvae gave an indication of the toxicity of the compounds, showing a remarkably low mortality for T and DH. Some mortality was observed in groups treated with PP, despite the doses being within the previously established safe range for larval survival and development (Fig. 64 C).

Figure 63: **Apoptosis and cell death induction in MEKi sensitive- and resistant-melanoma cell lines**. A) Apoptosis and cell death, and B) relative quantifications assessed after 5 days of treatment in Trametinib-sensitive SKmel30 spheroids. C) Apoptosis and cell death, and D) relative quantification assessed after 5 days of treatment in Trametinib-resistant SKmel30 spheroids. E) Apoptosis and cell death, and F) relative quantifications assessed after 5 days of treatment in Trametinib-sensitive WM3918 spheroids. G) Apoptosis and cell death, and H) relative quantifications assessed after 5 days of treatment in Trametinib-resistant WM3918 spheroids. Staurosporine was used as positive control at 1µM concertation 24 hours prior the end of the assay. Bar graphs beneath the panels represent the Log_{10} change in apoptosis and cell death normalized with the untreated control (UT) for the 3 biological replicates (n=3. Mean is represented by a line and dots represent values of the independent biological replicates). Confocal images (objective 20x) of single spheroids are shown.

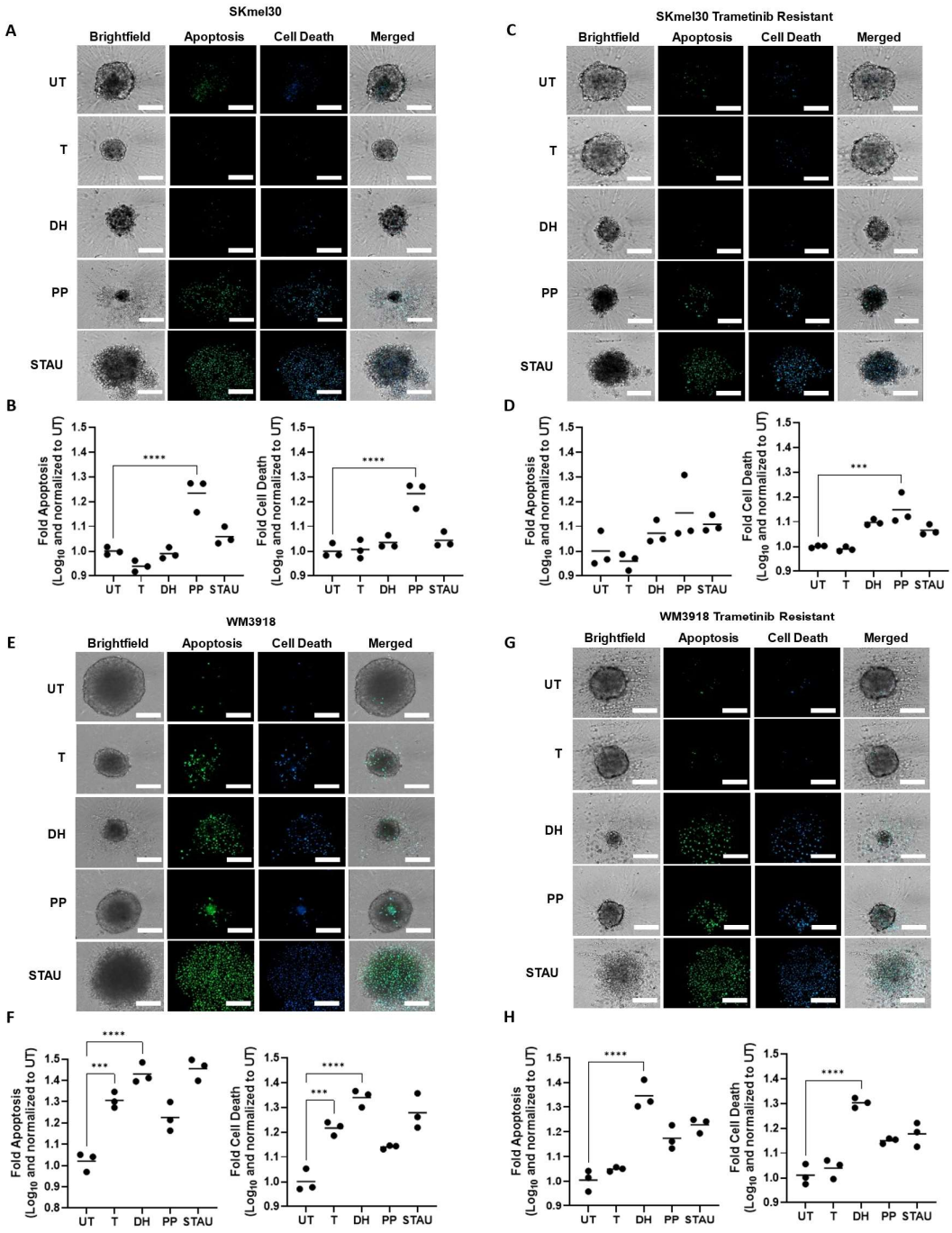
A
SKmel30
Brightfield
Apoptosis
Cell Death
Merged
UT
T
DH
PP
STAU
C
SKmel30 Trametinib Resistant
B
D
Fold Apoptosis (Log10 and normalized to UT)
Fold Cell Death (Log10 and normalized to UT)
E
WM3918
G
WM3918 Trametinib Resistant
F
H

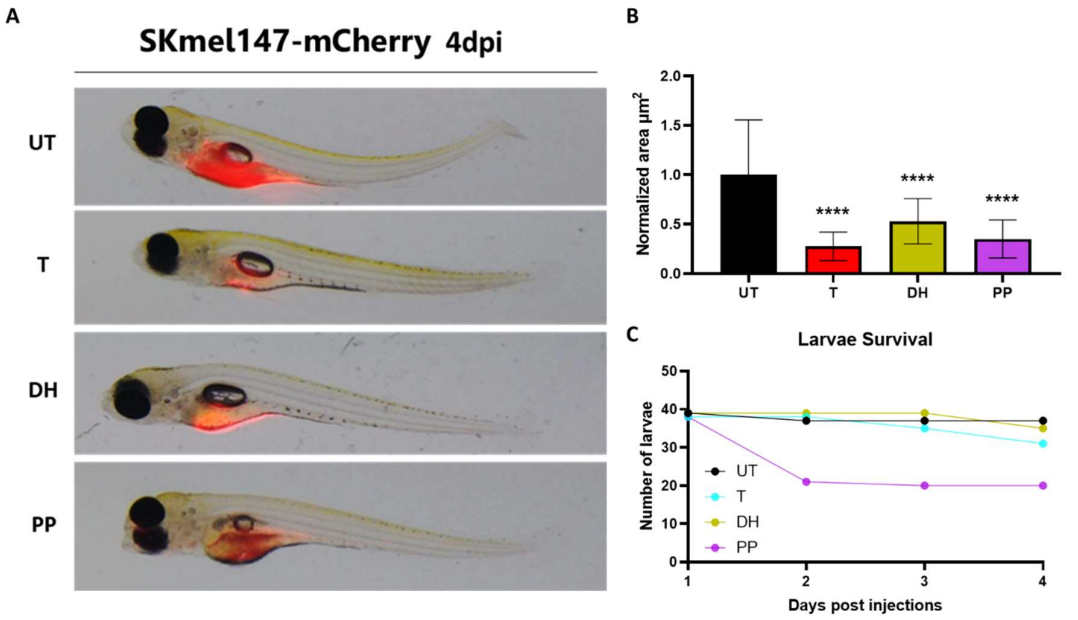

Figure 64: **Assessing the efficacy of compounds in zebrafish larvae models**. A) Pictures of zebrafish larvae 4 days post-injection, either untreated (UT) or treated with T, DH, or PP for 3 days. The tumor mass injected into the yolk is composed of SKmel147 expressing mCherry fluorescent proteins (red). B) Quantification of the tumor mass after 3 days of treatment normalized for the untreated control. (N=number of larvae quantified ±SD). C) Number of larvae survived at 4 days post injection. Day 1 the treatments started.

The results presented in Chapter 4.4 and 4.5 are being prepared for **publication to be submitted in spring 2025**.

In summary, this thesis established **advanced 3D *in vitro* co-culture melanoma models** for the discovery and characterization of novel anti-melanoma drug candidates. A **high-throughput screening** campaign tested hundreds of compounds on $NRAS^{mut}$ and WT melanoma spheroids, identifying promising candidates. Two highly effective compounds**, Daunorubicin HCl and Pyrvinium Pamoate**, were further characterized and validated using advanced 3D *in vitro* and *in vivo* melanoma models as potential first-line treatments for NRAS-mutant melanoma patients. Notably, both compounds, particularly Pyrvinium, exhibited strong efficacy against treatment-naïve NRAS-mutant melanoma cells with minimal toxicity. Additionally, Daunorubicin HCl and Pyrvinium demonstrated significant cytotoxic effects in MEK inhibitor-resistant melanoma cell lines, laying the groundwork for further investigation as potential second- or third-line therapeutic options for $BRAF^{wt}$ melanoma patients.

5. Discussion

Patients with NRAS^{mut} and WT melanoma generally experience a more aggressive disease course and have poorer prognosis than those with BRAF^{mut} melanoma. Furthermore, approved combinatorial targeted therapies and immunotherapies are available specifically for patients with BRAF^{mut} melanoma, which provide beneficial treatment options. In contrast, there are currently no approved targeted therapies for NRAS^{mut} and WT melanoma. These patients are often treated with immune checkpoint inhibitors or, as a second option with off-label with MEK inhibitors. However, these therapies typically offer only short progression-free intervals, with frequent relapses occurring shortly after treatment initiation. The scarcity of more effective therapies may partly result from a lack of highly physiological pre-clinical human cancer models. To address this gap, our project aims to develop advanced 3D *in vitro* melanoma models that better mimic physiological conditions and to use these models to identify and validate new therapeutic compounds for treating NRAS^{mut} melanoma.

5.1. The importance of advanced pre-clinical 3D *in vitro* models

Cancer research has traditionally relied on two model systems to conduct studies: *in vitro* 2D culture models, where cancer cells adhere to plastic surfaces, and *in* vivo models, predominantly using various strains of mice. However, both model systems exhibit significant limitations. 2D models fail to replicate the tumor-like architecture and lack interactions between cancer cells, non-cancerous cells comprising the tumor microenvironment (TME), and the extracellular matrix (ECM). On the other hand, *in vivo* models, particularly those involving advanced mammalian species such as mice, lack human-specific cells and microenvironmental interactions and raise substantial ethical concerns regarding their use. Over the past decade, the emergence of **3D cancer models** has provided a promising alternative, bridging the gap between traditional 2D *in vitro* and *in vivo* models. These 3D models can replicate the three-dimensional structure and architecture of actual tumors, offering the flexibility to construct various models, such as spheroids, organoids, or microfluidic chips, with or without the use of scaffolds, typically derived from ECM components or synthetic matrices (265,296,314). A **key application** of these models lies in their use as pre-clinical systems for evaluating novel anticancer agents by better mimicking real solid tumors, where important features such as drug penetration and nutrient exchanges are represented. On the other hand, this increases variability, consequently reducing reproducibility in certain cases. Additionally, 3D models allow for the identification of new mechanisms under more physiologically reliable

conditions. Moreover, 3D models allow for the integration of non-cancerous human cells, enabling the co-culture of cancer cells with their tissue-specific TME counterparts (264,354), fostering their use in melanoma research (260,355–357). Notable studies have utilized advanced 3D models incorporating melanoma cells co-cultured with TME cells. For instance, Votanopoulos et al. developed an immune-enhanced patient tumor organoid platform for personalized drug testing by co-culturing patient-derived matched melanoma cells with lymph node cells embedded in hydrogel (297). Similarly, Klicks et al. established a triple co-culture model comprising fibroblasts, keratinocytes, and melanoma cells in a spheroid-based system to investigate melanoma cell progression (270). Additionally, melanoma-TME co-culture models have been employed to explore melanoma-acquired resistance arising from interactions with stromal cells and ECM components (257,269,358,359). To date, most **melanoma-TME 3D models** primarily focus on co-cultures involving immune cells or skin-associated cells, such as dermal fibroblasts, keratinocytes, and endothelial cells. **However, scalable platforms that concurrently mimic multiple melanoma metastatic environments beyond the skin, such as the lung and liver, remain underdeveloped.**

In this context, we have established **two 3D melanoma-TME co-culture models** utilizing distinct 3D architectures: scaffold-free and matrix-embedded (scaffold-based) systems. The features of these models are discussed in detail in Chapter 1.7. The scaffold-free model is characterized by the formation of 3D melanoma spheroids cultured in a melanoma-specific medium using ultra-low attachment surfaces. Given the critical role of melanoma cell interactions with the TME in drug resistance and tumor progression, we incorporated non-cancerous cells in the models. Notably, endothelial cells were included in the models due to their ubiquitous presence in tissues as components of blood vessels. These are recognized as critical promoters of melanoma cell proliferation, survival, and drug resistance, primarily through various angiogenic sprouting and vasculogenic mechanisms, such as the *de novo* formation of blood vessels through the differentiation of progenitor cells leading to melanoma cells to reorganize and mimic the formation of blood vessels when stimulated by angiogenetic factors such as a hypoxic environment, a process named vascular mimicry (360,361). Melanoma is a highly metastatic cancer with a preference for sites such as the brain, lungs, liver, and skin. Among these, brain metastases are associated with particularly poor prognoses, followed by those in the lungs and liver (37,362–364). To replicate the microenvironments of metastatic sites, we incorporated major tissue-specific cellular components into the models, focusing on the **skin, lung, and liver**, as the brain metastatic model requires the reconstruction of a functional blood-brain-barrier to be effectively used as pre-clinical drug testing tools.

Specifically, **normal human dermal fibroblasts (NHDF)** were incorporated to mimic the interactions between melanoma cells and dermal fibroblasts in the skin. Multiple studies have demonstrated that these interactions, either by direct cell-cell contact or indirectly via the secretion of specific cytokines or secreted ECM components, can enhance melanoma progression and resistance to therapeutic agents (359,365–367). An interesting pleiotropic mechanism involves TGF-β, which has been identified as being produced by melanoma cells following BRAF inhibitor treatment. TGF-β directly promotes fibroblast activation, leading to ECM remodeling (see Chapter 1.6.1). Conversely, recent work by Loos et al. described a dose-dependent effect of TGF-β, where high doses increased sensitivity to MAPKi in MEK-resistant melanoma cells (368). To model interactions in specific environments, **MRC-5** cells were utilized to represent **lung fibroblasts** in the pulmonary microenvironment, while **LX-2** cells were included to replicate the **interplay between melanoma cells and hepatic stellate cells (HSCs)**, which are predominantly located in the liver's perisinusoidal space between endothelial cells and hepatocytes (369). Notable research by Fane et al. demonstrated that aged mice injected with mCherry overexpressing melanoma cells compared to young mice, presented higher rates lung metastasis due to the reactivated dormant melanoma cells by the secretion of sFRP1 by aged fibroblasts, a natural antagonist of WNT5, which otherwise maintains melanoma cells in a dormant state (370). Interestingly, an opposite effect was observed in aged skin where young fibroblasts were driving proliferation of primary melanoma cells, while aged fibroblasts foster melanoma phenotypic switch into more metastatic phenotype (371). Studies on melanoma-HSC interactions have primarily focused on uveal melanoma, where the liver represents the primary metastatic site (372). In contrast, fewer studies have examined these interactions in cutaneous melanoma. Of note, a study by Olaso et al. reported in hepatic metastasis, melanoma cells secreted factors and hypoxia stimulate HSC activation and subsequent VEGF production, a process further amplified under hypoxic conditions, ultimately promoting angiogenesis and tumor progression (373).

Key features for the establishment of these co-culture models include the methodologies and cell ratios used to achieve representative interactions (see Chapters 4.1.1 to 4.1.3). We systematically tested various approaches and cellular ratios for co-culturing these cell types in spheroid models, drawing on existing literature (268,374–379). We concluded that the **sequential seeding method** (268), which involves initially establishing a tumor mass consisting of melanoma and endothelial cells followed by the addition of fibroblasts or HSC the next day, worked the best. This approach was particularly effective in achieving uniform fibroblast distribution and maintaining survival of all cell types over time. No significant differences were observed among the tested ratios in terms of cell growth and proliferation, with all the ratios displaying comparable profiles. Consequently,

we selected a reference ratio consisting of one part of melanoma cells to three parts of endothelial cell and fibroblasts or HSCs as the standard for subsequent experiments. During the development of these models, only three melanoma cell lines were used, which presents a potential limitation. Specifically, using different melanoma cell lines, particularly primary cell lines, may necessitate additional optimization of cellular ratios to ensure the optimal growth of all cell types within the co-culture. Thanks to the constitutive expression of distinct fluorescent proteins, the temporal evolution of each cell type within these **Multicomponent Melanoma Spheroid (MMS)** models could be monitored. Melanoma cells exhibited efficient growth over time across all models and, owing to their highly proliferative and aggressive nature, ultimately **overgrowing the non-cancerous cells**. **This observation aligns with clinical findings**, where melanoma metastases are predominantly composed of melanoma cells, as observed in several formalin-fixed paraffin-embedded (FFPE) sections of melanoma metastasis (The Human Protein Atlas). Hence representing a versatile toolbox for different melanoma stages. Using sequential seeding, NHDF and MRC-5 cells infiltrated the tumor core, achieving a more uniform MMS distribution. In contrast, LX-2 cells localized outside the core, forming an encapsulating layer, likely due to their pericyte-like phenotype. Endothelial cells remained mainly within the spheroid's inner core. These 3D MMS models were used to investigate cell-type-specific markers via immunofluorescent staining of FFPE sections. To demonstrate this technique, we assessed classical markers like S100A for melanoma cells, α-SMA for fibroblasts, and CD31 (PECAM-1) for endothelial cells (see Chapter 4.1.2). However, a broader marker panel is needed for deeper characterization of cell activation states and phenotypes.

MMS models were developed as **preclinical tools to evaluate anti-melanoma compounds**. Efficacy was assessed using time-lapse microscopy for proliferation, ATP-luciferase assays for viability, and flow cytometry for cell death and apoptosis. These methods estimate the compounds' impact on the entire cellular system (see Chapter 4.1.4). However, further optimization or new assays are needed to better assess melanoma-specific effects and the response of non-cancerous cells during treatment.

Another key population of TME cells is represented by **immune cells**, which are particularly important in assessing the effect of ICI immunotherapies (142). In this context, we established a **co-culture system combining our MMS models with peripheral blood mononuclear cells (PBMCs)** isolated from healthy donors. A crucial step in this process was the **identification of the specific PBMC populations** capable of interacting with or infiltrating the MMSs. To achieve this, we built a panel of specific antibodies to identify immune cell subpopulations and utilized flow cytometry to distinguish between interacting/infiltrating and non-infiltrating immune cells (see Chapter 4.1.3).

Our results demonstrated varying levels of CD45-positive cells within the MMS models, with the "liver" MMS model exhibiting the highest degree of immunogenicity, likely given by the inflammatory phenotype that activated HSsC assume in a pathological environment (380). Notably, the majority of CD45-positive cells were CD3-positive lymphocytes, including a significant proportion of infiltrating CD8-positive cytotoxic T cells and CD4-positive T helper cells, both of which are critical for effective immunotherapies (381,382). This characterization highlights the successful co-culture of immune cells with our MMS models, which can now be employed to evaluate the efficacy of anti-melanoma compounds including targeted and immunotherapeutic agents.

It is worth noting that the PBMCs used in this study were isolated from healthy donors with no or minimal HLA matching. **The use of patient-derived PBMCs**, matched to the melanoma cells in the MMS model, would likely enhance the degree of immune cell infiltration and better reflect patient-specific immune interactions. Limitation of this model lies in the cultivation medium. Currently, RPMI medium is used, which primarily supports the growth of melanoma cells, while the other TME cells have been adapted to grow in different media. Additional studies are required to optimize the medium composition to better support the growth and viability of all cell types involved in the MMS models. In this context, a senior scientist in our group (Dr. Claude Haan) has extensively worked on the formulation of a more physiological medium, which better mimics the composition of human plasma (currently published in BioRxiv, DOI: https://doi.org/10.1101/2024.08.12.607529). Several melanoma cell lines are in the process to be adapted to this medium; in a next step, we will adapt MMSs to grow in a more physiological medium.

Recent studies have increasingly shifted their focus toward not only the interactions between melanoma cells and the cellular components of the TME but also **the interplay between melanoma cells and the extracellular matrix (ECM)**. It is well established that solid tumors, including melanoma, are characterized by an altered and stiffer ECM, which promotes invasion and resistance to therapies (see Chapter 1.6.4) (250). A study conducted by Miskolczi et al. demonstrated how variations in collagen abundance influence the differentiation state of melanoma cells, with a stiffer matrix promoting differentiation and a softer matrix inducing de-differentiation. This effect is mediated by TGF-β secreted by cancer-associated fibroblasts (CAFs), which suppress PAX3 and, subsequently, MITF in the differentiated phenotype, thereby driving melanoma cells into a dedifferentiated, slow-proliferative, drug resistance state (255). In contrast, research by Dilshat et al. revealed that the absence of MITF leads to an upregulation of ECM and focal adhesion gene expression (383), highlighting the critical role of ECM in the regulation of

melanoma cell behavior. In this context, I aimed to develop a more advanced 3D melanoma-TME co-culture model that incorporates an ECM, as a scaffold-based approach (263). Among the most commonly used ECM types in *in vitro* culture are animal-derived ECMs, such as type I Collagen and Matrigel. **Matrigel**, in particular, resembles the basement membrane and is primarily composed of laminin. These ECMs are foundational to 3D culture systems, such as organoids. However, **they present several significant limitations**, including high batch-to-batch variability, the presence of cytokines and growth factors, lack of tunability, ethical issues related to their animal derivation, and their non-inert nature (272,384). To enhance the models and overcome the limitations associated with animal-derived matrices, we selected an inert **polyethylene glycol (PEG)-based hydrogel**. This hydrogel polymerizes through the action of a transglutaminase enzyme (Factor XIII) and is temperature-independent, offering **greater experimental flexibility** than other temperature-dependent matrices such as Collagen and Matrigel. However, unmodified PEG lacks essential features such as focal adhesion domains and degradation sites necessary for ECM remodeling by embedded cells. To address this, the hydrogel was functionalized with **RGD** (arginyl-glycyl-aspartic acid), a key cell adhesion motif found in fibronectin and recognized by integrins (324). Additionally, matrix metalloproteinase **(MMP)-cleavable sites** were incorporated to enable embedded cells to degrade the PEG-based matrix and replace it with their own ECM production (282–284,324,385,386). This hydrogel effectively supported the culture of various commercially available and primary melanoma cell lines, which exhibited distinct phenotypes and growth patterns after 10 days of culture. Additionally, **it accommodated the growth of different TME cell types** used to model melanoma-metastatic-like sites, including NHDF (“dermal”), MRC-5 (“lung”), and LX-2 (“liver”), which were also employed in the MMS models. NHDF and MRC-5 cells displayed the characteristic elongated spindle morphology, whereas LX-2 cells assumed a more rounded shape, consistent with their distinct cellular nature as previously observed in the MMS models (see Chapter 4.1.2 and 4.3). The endothelial cell population, represented by HMEC-1, did not seem to have the same proliferation capacity as the other cells and did not show sprouting behavior, instead, it exhibited a more cytostatic behavior. This was mitigated to some extent by the **addition of VEGF**, a key cytokine critical for endothelial cell survival, proliferation, and sprouting (325). These findings align with previous studies indicating that in the absence of essential basal membrane ECM components such as laminin and collagen IV, as well as key cytokines like FGF-2 and SDF-1 and supportive mesenchymal stem cells (MSCs), endothelial cells struggle to sprout and form functional vessels within synthetic matrices (273,276,277,298). An interesting study by Taubenberger et al. developed a functional and vascularized PEG-based hydrogel system encapsulating a co-culture of breast cancer cells, mesenchymal stem cells (MSCs), and endothelial

cells (HUVEC). The PEG hydrogel was functionalized with RGD and MMP-cleavable peptides, along with collagen- and laminin-mimetic adhesion peptides. Additionally, key angiogenic cytokines, including VEGF, FGF-2, and SDF-1, were incorporated into the system, resulting in a fully functional 3D *in vitro* model. This model facilitates the study of cancer cell-TME interactions (280). However, angiogenesis and vascularization utilizing synthetic matrices remains one of the principal challenges in developing fully functional vascularized 3D cancer models (276).

As the primary objective of establishing these advanced 3D melanoma models was to use them as pre-clinical tools for drug testing, we also evaluated the **hydrogel-based co-culture models** for this purpose. Similar to the MMS models, the response of melanoma cell growth to anti-melanoma compounds could be tracked over time due to their fluorescent protein expression. Additionally, the overall viability of the entire cellular mass was assessed at the conclusion of the assay. In contrast to the MMS models, the hydrogel-based co-culture models allowed for more efficient and reliable tracking of the growth of labeled TME cells (see Chapter 4.3). This provided a unique opportunity to evaluate not only the response of melanoma cells but also the effects of the tested compounds on non-cancerous cells. Consequently, this approach **enables an estimation of the potential toxicity** of the compounds on the TME cells, thereby offering a more comprehensive evaluation of drug efficacy and safety. In summary, we developed an advanced 3D melanoma-TME co-culture model that incorporates ECM components, serving as a pre-clinical tool for evaluating the anti-melanoma efficacy of drugs while concurrently providing an estimation of the compound's toxicity to non-cancerous cells.

Importantly, as the models are intended for use in personalized drug testing, we also incorporated **melanoma cells freshly isolated from a patient's melanoma metastasis** (see Chapter 4.2) **into the hydrogel co-culture system**. Preliminary results demonstrated that these patient-derived melanoma cells successfully co-cultured with dermal fibroblasts and endothelial cells, highlighting the feasibility of utilizing these models for personalized drug testing applications. Notably, we observed the production of collagen I within the hydrogel, indicating that the cells embedded in the model were actively degrading the PEG matrix through MMP-cleavable sites and replacing it with their own synthesized ECM. This process enhanced the physiological relevance of the model by creating a microenvironment that more closely mimics native tissue conditions. Further investigations are planned to fully characterize these hydrogel models. These studies should include the identification of additional ECM components and an analysis of the matrix's physical properties (for instance through rheometric studies) after cellular remodeling to assess whether its stiffness aligns with that observed in human tissues. Figure 65 provides a graphical summary of this project part.

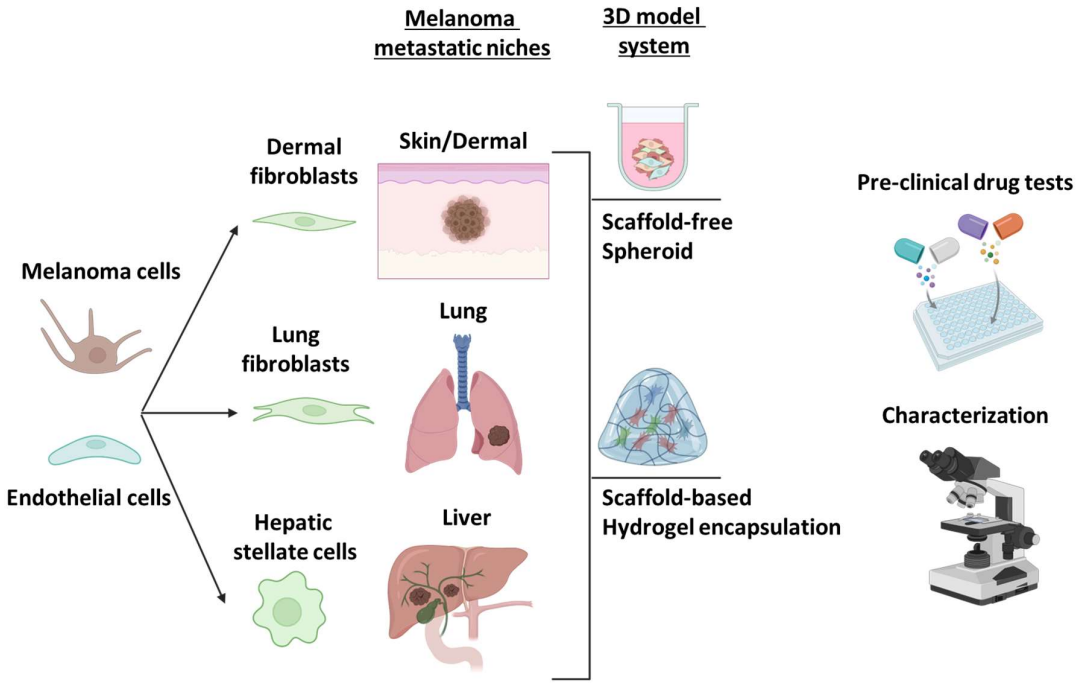

Figure 65: Established *in vitro* 3D co-culture models aim to mimic the melanoma metastatic niches found in three of the principal melanoma metastatic sites such as skin/dermal, Lung, and Liver. Two 3D model culture systems were established: a scaffold-free spheroid-based system (Melanoma Multicomponent Spheroid), and a scaffold-based hydrogel-based system (Xeno-free hydrogel embedded melanoma-TME co-culture). These models are mainly employed as platforms for pre-clinical drug tests, but they can also be employed for characterizations and investigations of melanoma molecular mechanisms.

5.2. Discovering novel compounds for NRAS^{mut} and WT melanoma through high-throughput drug screening using 3D *in vitro* models

Systemic therapy for melanoma has undergone a remarkable evolution over the past decades, marked by the approval of highly effective targeted and immune therapies, as outlined in Chapter 1.3. These therapies are primarily approved for the treatment of BRAF^{mut} melanoma. Unfortunately, and as I mentioned before, similar improvements in progression-free survival (PFS) and overall survival (OS) have not been observed in patients with other genomic subtypes, such as NRAS^{mut} and WT melanoma which are currently treated with immune checkpoint inhibitors (ICIs) as first-line therapy (116,146,387).

The NEMO clinical trial established the basis for the use of MEKi in patients with $NRAS^{mut}$ melanoma (125). This approach was further supported by findings from Salzmann et al., who demonstrated that MEKi administration in $NRAS^{mut}$ patients pre-treated with ICIs, aids in stabilizing the disease, whether subsequent or parallel initiation of alternative treatments (388). Recently, a phase II clinical trial evaluated Trametinib (MEKi) in patients with $BRAF^{V600}$/$NRAS^{Q61}$ wild-type melanoma who were refractory to ICIs. Trametinib was also combined with a low dose of dabrafenib to mitigate trametinib-induced skin toxicity. While the combination successfully reduced skin toxicity, it did not result in significant improvements in overall survival (389). Being the MEKi the only targeted drugs used in $NRAS^{mut}$ and WT patients, Trametinib (MEKi) was selected as the reference drug for comparisons with other tested compounds throughout this project.

Given the urgent need for novel therapeutic options for melanoma patients with $NRAS^{mut}$ and WT genotypes, we aimed to perform a high-throughput screening (HTS) to evaluate several compounds using the semi-automated Disease Modelling and Screening Platform (DMSP, LCSB). Traditional HTS is typically performed on cancer cells cultured on adherent surfaces, which fail to account for the influence of a 3D tumor structure on drug response, thus lacking the physiological relevance necessary to mimic the real patient tumor (390). To enhance the physiological accuracy of drug responses in our HTS, we cultured melanoma cells as 3D spheroids. It is important to note that as the complexity of the culture models increases, the complexity of the screening process also escalates (261,391). The use of 3D spheroids as a culture model for HTS is not entirely a novel approach (312,392–395), but it still represents a rarer approach than using adherent cell culture methods. This method has also been applied to melanoma research, as demonstrated in a recent study by Jordan et al., who successfully established 3D spheroids cultures utilizing a ULA 1536-well plate format. In this model, patient-derived melanoma cells and CAFs were cultured to form spheroids, enabling the testing of more than a hundred drugs (396).

Prior to conducting the screening, extensive testing and optimization were performed **to establish a robust and reliable pipeline** (see Chapter 4.4.1). This included determining the optimal cell number, volumes, and time points for each melanoma cell line used in the HTS. Additionally, various readout methods were evaluated to assess the drug effect, with **Calcein AM emerging as the most suitable option**. This led to the development of a **high-content imaging-based analysis**, utilizing high-resolution confocal microscopy to capture Calcein AM-emitted fluorescent signals, which are exclusively emitted by live cells. The technique provides a significant advantage, as it allows for the exploration of phenotypic and morphological changes in spheroids following drug treatment (397). However, it is important to note that fluorescent image-based analysis can be

influenced by the intrinsic fluorescence emitted by the drugs themselves, which might create false positive results (398).

Drug repurposing involves identifying new therapeutic applications for existing, often approved, compounds originally developed for other diseases. This strategy has gained increasing attention in recent years due to its potential to expedite the development process and reduce costs (see Chapter 1.8). In this context, we selected two drug libraries for HTS: The Prestwick Chemical Library (PCL®) and the in-house Melanoma Drug Library (MDL), together counting for 1328 compounds. These two libraries, particularly the PCL, consist of compounds and small-molecule inhibitors that have been extensively used in clinical settings for various diseases or different cancer types, with well-characterized mechanisms of action. We initially selected these libraries to repurpose existing treatments, as they could be translated into clinical applications more rapidly than entirely novel molecules, many of which have already undergone extensive clinical trials. However, numerous other libraries containing chemical or biological compounds exist, potentially revealing entirely new therapeutic options for advanced $NRAS^{mut}$ and WT melanoma. Many public and private companies have developed valuable chemical libraries for drug discovery. Notably, one of the most significant efforts in building a comprehensive repository of novel compounds is the European Lead Factory (ELF), which currently contains over 500,000 unique compounds for HTS campaigns (399,400). This should be considered in the future for conducting HTS campaigns to identify novel compounds targeting $NRAS^{mut}$ and WT melanoma.

We **conducted HTS on two melanoma cell lines** with high spheroid formation capacity and efficient growth as spheroids, SKmel147 and WM3918, representing $NRAS^{mut}$ and WT genomic melanoma subtypes, respectively. While standard drug concentration employed by the DMSP platform was 10 µM, we also included an additional screening at a lower concentration of 1 µM. This decision was based on the general principle that lower drug concentrations off-target effects (401). Key control metrics, including the **Z'-factor and the coefficient of variation (CV)**, indicated high quality for each plate screened, with values exceeding 0.5 and remaining below 15% (see Chapter 4.4.2), respectively. These parameters are critical for ensuring the reliability of the screening (309,326).

Hit drugs were identified through a **multi-step process** to maximize efficacy selection as described in Chapter 4.4.2. First, the raw Calcein AM area was analyzed using the three-sigma rule, setting a 97% confidence cut-off (µDMSO - 3σ) (309,310,402). Compounds below this threshold progressed to the next step. Second, data were normalized to plate-specific DMSO controls to minimize variability, selecting compounds with cell viability below 50%. Two biological replicates ensured reliability, with only consistent hits advancing. The final step involved comparing quantitative data

with spheroid images to eliminate false positives, often caused by reduced Calcein AM fluorescence from plate edge effects. Extensive literature research then assessed each compound's melanoma targets, resistance mechanisms, and clinical trial outcomes. Compounds withdrawn due to toxicity were flagged, while those with strong clinical potential were prioritized.

We observed a **generally weak response** of the two melanoma cell lines to the tested libraries, reflecting the inherent challenge of identifying effective targeted therapies for these two melanoma genomic subtypes. One limitation of this study is the small number of cell lines used to discover new drugs. However, considering the increased complexity of the 3D culture model, the use of a single melanoma cell line to represent each genomic subtype provided a reasonable starting point for the identification of potential candidate compounds. Additionally, a $BRAF^{mut}$ melanoma cell line was included in the screening, demonstrating generally higher sensitivity to the libraries. However, given the primary focus of this study on $NRAS^{mut}$ and WT melanoma genomic subtypes, further investigation of the $BRAF^{mut}$ melanoma cell line was not pursued at this stage. **A total of 20 hit compounds were selected for validation** through the generation of drug response curves in SKmel147 ($NRAS^{mut}$) and WM3918 (WT) melanoma cell lines. Given our primary focus on identifying effective compounds against $NRAS^{mut}$ melanoma, the majority of the selected hits were specific to SKmel147. Nonetheless, all 20 compounds were tested across both cell lines, irrespective of their initial cell line specificity, to evaluate whether these drugs exhibit plasticity in targeting different melanoma genomic subtypes. The drug selection process proved efficient, as only a limited number of compounds failed to yield IC50 values, and only a small subset exhibited IC50 exceeding 1 µM. Notably, the majority of drugs targeting DNA replication demonstrated high efficacy in both cell lines. For instance, **Daunorubicin HCl, a Topoisomerase II poison** (350), showed strong effect, consistent with the high proliferative capacity of the cell lines. Both cell lines harbor mutations in the CDKN2A/B gene (a familiar mutation in melanoma), resulting in the loss of expression of critical cell cycle inhibitors such as $p16^{INK4A}$ and $p14^{ARF}$. These inhibitors naturally suppress CDK4/6, key kinases that drive the cell cycle progression through the G1 phase and toward the S phase, where DNA replication occurs (86).

In melanoma, deregulation of the cell cycle is frequent, and therapeutic approaches targeting CDK4/6 inhibition have been investigated also in our laboratory in combination with MEKi, yielding promising results (403,404). However, the emergence of resistance to these combinations has also been reported by studies conducted in our laboratory (405,406). Furthermore, CHIR-124, despite its role in inhibiting CHK1, which is a key regulator of the cell cycle and the main downstream target of ATR following DNA damage (407), did not demonstrate effectiveness. Interestingly, a study by Zay Yar Oo et al. revealed that melanoma cells exhibit endogenous high levels of replicative stress,

both *in vitro* and *in vivo* (408). This finding may explain the heightened sensitivity of SKmel147 cells to the ATR inhibitor AZD6738, further suggesting the potential involvement of alternative downstream targets of ATR distinct from CHK1. The internal control, Trametinib (MEKi), demonstrated high efficacy in both cell lines. Surprisingly, **other MAPK inhibitors**, such as TAK-733 (MEKi) and Ulixertinib (ERKi), exhibited limited efficacy in both cell lines, whereas PDO325901 showed effectiveness exclusively in SKmel147. This reflects the intrinsic resistance of $NRAS^{mut}$ and WT melanoma to MAPKi. This resistance underscores the need for these inhibitors to be used predominantly in combination with other therapeutic agents rather than as monotherapies (76,118).

An interesting class of compounds with pronounced inhibitory effect in both cell lines was represented by **the cardiac glycosides:** Lanatoside C and Proscillaridin A, which have demonstrated strong anti-cancer activity across various cancer types (409–421). These compounds **target the Na^+/K^+ ATPase pump**, specifically binding to its α1-subunit (ATP1A1) (333,422). Interestingly, melanoma cells have been reported to exhibit high levels of ATP1A1 (338). In line with this, Soumoy et al. recently highlighted ATP1A1 as a promising target for the application of cardiac glycosides in melanoma therapy (337). Furthermore, digoxin, another cardiac glycoside, was tested in combination with Trametinib in BRAF wild-type melanoma patients, demonstrating favorable disease control and tolerability (423). A recent study by Kurzeder et al., conducted in injected mouse models alongside a prospective, open-label, proof-of-concept clinical study, demonstrated that digoxin significantly reduces the metastatic potential of breast cancer cells by decreasing the number of clustered circulating tumor cells (424).

Additional compounds targeting hallmark pathways implicated in melanoma drug resistance showed remarkable sensitivity with low IC50 values. These included those acting on epigenetic mechanisms, such as Entinostat (HDACi) and XL888 (HSP90i), and inhibitors of critical structural and signaling molecules, such as Albendazole (β-tubulin inhibitor). These compounds have previously demonstrated inhibitory effects when used in combination with MAPK inhibitors in melanoma cells (425–428). Obatoclax (BCL2i), a drug targeting anti-apoptotic pathway, was also presenting a relatively low IC50 value.

Moreover, it has been already evaluated in a clinical trial in combination with the chemotherapeutic agent Temozolomide in metastatic melanoma patients (NCT00724841), and unfortunately, terminated due to financial constraints. **Pyrvinium Pamoate, a compound known to inhibit β-catenin signaling and cellular respiratory complexes I and II** (351), exhibited significant sensitivity in both cell lines. Dopamine receptor antagonists, such as Itopride and Thioridazine

hydrochloride, demonstrated remarkable efficacy in both melanoma cell lines, irrespective of their mutational background. These compounds are recognized as effective against drug-resistant cancer cells (339,340). However, their mechanism of action in melanoma remains unknown.

Overall, **we successfully identified a group of drugs capable of efficiently inhibiting the growth of NRAS^{mut} and WT melanoma cells cultured as 3D spheroids**. These compounds warrant further investigation as potential candidates for novel melanoma therapies used as monotreatment or in combination with other compounds. We acknowledge the overall low impact of the tested compound libraries on the screened melanoma cell lines, as only 1.5% of the tested drugs were selected during the primary screening, with further reductions following the generation of dose-response curves (DRCs) (see Chapter 4.4.3). We hypothesize that this outcome may be attributed to three factors. **First**, the semi-automated high-throughput screening (HTS) protocol requires further optimization, with the most notable issue being the pronounced plate edge effect, which led to an increased number of false positives in the quantitative analysis.

Second, the three-dimensional (3D) spheroid architecture may have enhanced drug resistance by limiting drug penetration or creating a microenvironment more conducive to melanoma cell survival, thereby mimicking *in vivo* conditions.

Third, the intrinsic drug resistance of the two melanoma cell lines under investigation highlights the overall difficulties associated with targeting these melanoma subtypes efficiently.

A graphic Summary is provided in Fig. 66.

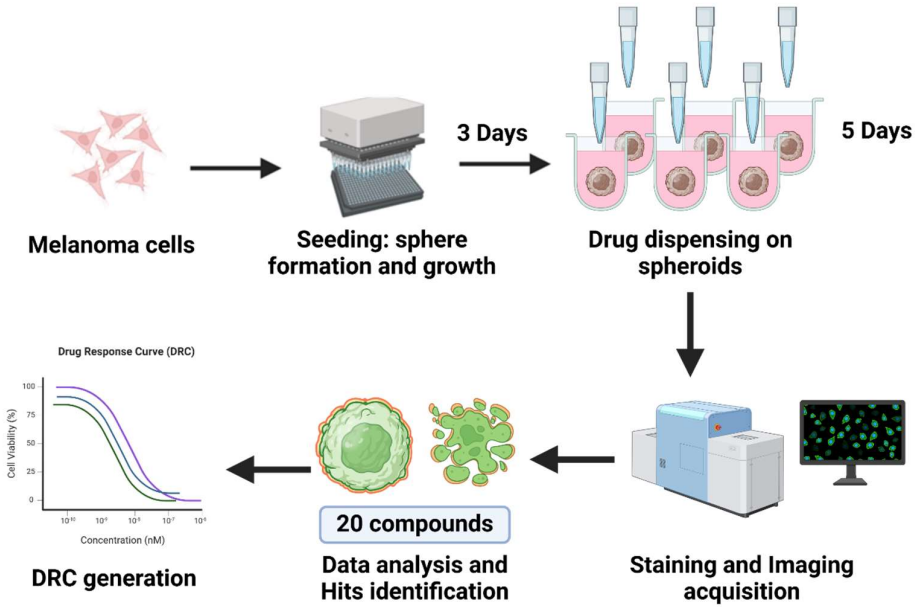

Figure 66: 3D High-throughput drug screening and hit drug identification. Melanoma cells were cultured as 3D spheroids in ultra-low attachment surface plates and after 3 days of sphere formation and growth, drugs were dispensed. After 5 days of incubation, spheroids were stained with Calcein AM. Using high-throughput confocal imaging and high-content imaging analysis, cell viability of spheroids was evaluated by the area covered by the Calcein AM signal. 20 hit drugs were selected through a multi-step analysis, and further validated by the generation of drug response curves.

5.3. Repurposing novel compounds for the treatment of NRAS^{mut} melanoma.

As described in the previous paragraphs, Daunorubicin HCl (DH) and Pyrvinium Pamoate (PP) were selected for further validation.

Daunorubicin HCl, an anthracycline antibiotic isolated from a strain of *Streptomyces* (429), is currently approved for the treatment of acute myeloid leukemia (AML) (350,430). Its main mechanism of action involves the intercalation into the major groove of DNA and binding to the minor groove, with a preference for GC base pairs. This process induces torsional stress on the DNA structure. DNA topoisomerases, enzymatic complexes responsible for maintaining the DNA topology, play critical roles in essential cellular processes such as DNA replication and RNA transcription. These enzymes operate by binding to DNA, introducing strand breaks to release torsional tension, and subsequently relegating the strands. Two types of topoisomerases have been identified: Topoisomerase I (TOP1), which induces single-strand breaks (SSNs) without ATP consumption, and Topoisomerase II (TOP2), which creates double-strand breaks (DSBs) through ATP utilization (431). **Daunorubicin exerts its cytotoxic effects by intercalating into DNA and acting as a TOP2 poison**. This intercalation stabilizes the covalent TOP2-DNA complex, preventing the enzyme from relegating the DNA strands. Consequently, DNA damage accumulates, ultimately leading to apoptosis (328,350,432). TOP2 is predominantly expressed in highly proliferative cells, including cancer cells (433–435). **In melanoma**, Mu et al. demonstrated that TOP2α, one of the most extensively studied isoforms of TOP2, is significantly more expressed in melanoma tissues compared to benign nevi (436).

Existing studies have primarily focused on its action when conjugated to peptides (437,438), incorporated into liposomes (438,439) or co-delivered via PEG-based micelles (439), rather than as a free drug. A liposomal formulation of Daunorubicin, DaunoXome® (a non-PEGylated liposomal formulation of Daunorubicin), has demonstrated improved cancer cell uptake, thereby enhancing the therapeutic index of Daunorubicin. This formulation reduces drug uptake by normal tissues,

consequently lowering toxicity and, more specifically, decreasing the conversion of Daunorubicin into its cardiotoxic metabolite, Daunorubicinol (440–442). A similar anthracycline antibiotic, Doxorubicin, which has been approved by the FDA for the treatment of acute leukemias and other solid tumors, has previously been tested in its liposomal formulation for the treatment of advanced melanoma, demonstrating limited efficacy (443). However, the effect of Daunorubicin on melanoma cells remains underexplored and there are no specific studies assessing the efficacy of this compound in $NRAS^{mut}$ melanoma.

Pyrvinium Pamoate, a cyanine dye approved as an anthelmintic drug (351), has a mechanism of action that is not yet fully elucidated. A study by Tomitsuka et al. suggested that **PP inhibits the mitochondrial electron transport chain (ETC)** in both parasitic and cancer mitochondria (444). Specifically, it blocks respiratory Complex I under normoxic conditions and inhibits Complex I and II under hypoxic conditions, a finding also observed in pancreatic cancer cells (445). Notably, Aminzadeh-Gohari et al. showed that 24-hour treatment with PP exerts a cytotoxic effect on a panel of melanoma cell lines representing various genomic subtypes. The effect is mediated by a significant reduction in mitochondrial respiration, with PP acting as an uncoupler (446). Additionally, **PP serves as an agonist of Casein Kinase 1α (CK1α)**, a component of the "destruction complex" that phosphorylates β-Catenin. This phosphorylation **promotes β-Catenin proteasomal degradation**, thereby reducing its nuclear translocation and transcription activity (351,447). This mechanism was also observed in uveal melanoma treated with PP (448). Although this specific mechanism has not been thoroughly characterized in cutaneous melanoma, we hypothesized it as a potential mode of action in our cell model and pursued further investigation. The detailed mechanisms by which DH and PP exert their effect on melanoma remain incompletely understood, warranting further exploration.

Daunorubicin HCl **(DH)** and Pyrvinium Pamoate **(PP)** were evaluated in dose-response assays on a panel of $NRAS^{mut}$ melanoma cell lines (see Chapter 4.5.1). This panel included two commercially available cell lines (SKmel147 and SKmel30) and two primary metastatic melanoma cell lines (M160915 and M161022). Both compounds demonstrated high efficacy across all four melanoma cell lines cultured as 3D spheroids. When tested on a panel of non-cancerous cell lines, they exhibited a relatively good safety profile, particularly PP, consistent with their FDA approval status. In addition, DH and PP were assessed for their ability to **kinetically inhibit the proliferation** (see Chapter 4.5.2) of melanoma cells cultured as 3D spheroids and to reduce cell viability significantly. For comparison, Trametinib (T), a potent MEK inhibitor (MEKi), was employed as a reference. MEK inhibitors are used off-label in clinical practice in or to stabilize disease in $NRAS^{mut}$ and WT melanoma patients awaiting re-challenge with immune checkpoint inhibitors (ICIs) (116,388).

Overall, despite the **significant reduction in cell viability** observed at the respective IC50 values (see Chapter 4.5.2), we hypothesized the observed effects were predominantly cytostatic. This hypothesis is supported by the dramatic reduction in spheroids cell proliferation compared to the untreated control, although proliferation did not drop below baseline levels after normalization.

All compounds demonstrated comparable effects across the three melanoma cell lines, **with the exception of SKmel30**, which exhibited higher resistance to DH. We speculate that this increased resistance to DH may be attributed to the TP53 gene deletion present in SKmel30 (Cellosaurus.org). Dysfunctional p53 has been associated with increased resistance to Doxorubicin treatment due to the upregulation of key drug transporters, such as ABCB1 (449). In melanoma, Rudolf et al. observed that a combination of the TOP1 inhibitor Camptothecin and the TOP2 inhibitor Etoposide showed reduced efficacy in melanoma cells with mutant p53 compared to wt p53 cells. They suggested that apoptosis in p53-mutant cells was driven by p53-independent mechanisms, such as mitochondrial dysfunction and the activation of stress-sensitive kinases, including (450). Furthermore, I had the opportunity to contribute to an intriguing project led by Prof. Kulms (University of Dresden, Germany), in which we demonstrated that a rare TP53 mutation (R285K) confers increased resistance to cisplatin treatment in metastatic melanoma cells. This resistance can be overcome through ferroptosis induction (91).

The time-lapse microscopy assay, which kinetically measures the proliferation of melanoma cells cultured as 3D spheroids, serves as a valuable tool for identifying the time points at which drugs begin to significantly inhibit cell proliferation. Based on this, **we determined day 3 and/or day 5 as the key time points for subsequent assay**.

To confirm that the observed effects were cytostatic or cytotoxic, **we assessed cell death and apoptosis levels** after 5 days of treatment by detecting nucleic acid of impaired cells and the activation of effector caspase 3 and 7 (see Chapter 4.5.2). **PP induced significant apoptosis and cellular death** in all the tested cell lines, highlighting its potential as an attractive candidate for first-line therapy in $NRAS^{mut}$ melanoma patients. We observed lower apoptosis induction upon T and DH treatment in the primary cell lines M160915 and M161022, particularly in SKmel30, which exhibited general resistance to apoptosis. This resistance was further evidenced by its lower cytotoxic response to Staurosporine compared to the other cell lines. This observation aligns with the fact that melanoma patients treated with anthracycline and other chemotherapeutic agents may develop resistance to these treatments through the upregulation of ABC transporters, such as ABCB5 and ABCB8, in doxorubicin-treated melanoma cells, or by the upregulation of TOP2α following Etoposide treatment (451,452).

Although DH and T induced lower levels of apoptosis than PP in the primary cell lines, a significantly higher induction of cell death was observed upon DH and T treatment. This led us to hypothesize that a higher level of apoptosis may have occurred earlier than 5 days of treatment, warranting further assessment at earlier time points. Alternatively, other programmed cell death mechanisms, such as necroptosis, may have been activated instead of apoptosis.

Necroptosis is an immunogenic form of cell death characterized by the phosphorylation of RIPK1/3 and MLKL, which leads to the formation of micropores in the cell membrane, driving the cell to death while releasing damage-associated molecular patterns (DAMPs) into the TME. These DAMPs subsequently trigger an immune response. Doxorubicin, a modified version of Daunorubicin, has also been extensively studied for its ability to induce immunogenic cell death able to boost the immune response (453,454). Therefore, further investigations into alternative cell death mechanisms should be considered.

Melanoma is a highly migratory and invasive cancer, where tumor cells exhibit vertical growth, migrating toward deeper tissues such as the dermis and subcutaneous layers by breaching the basement membrane. This process enables melanoma cells to intravasate into lymphatic and blood vessels, circulate, and extravasate into lymph nodes and distant organs, thereby metastasizing (13,455–458). To assess the potential of DH and PP in inhibiting melanoma cell motility, we tested their effects on cells cultured as spheroids and embedded in a type I collagen matrix. T inhibited invasion and migration in both melanoma cell lines, which was noteworthy given a study by Vultur et al. that showed an increase in migration and invasion potential in metastatic melanoma cell limes, but no tin non-metastatic lines, upon treatment with MEKi, using a similar 3D collagen assay (458). Interestingly, **DH and PP significantly inhibited the motility** of only the primary metastatic melanoma cell line (M160915). This suggests that these compounds may have selective inhibitory effects on motility in certain $NRAS^{mut}$ melanoma phenotypes but not for all. However, to confirm the inhibitory potential of these drugs, additional melanoma cell lines should be tested, as SKmel30 lacks motility within the Collagen matrix, and M161022 did not form sufficiently compact spheroids to withstand the experimental procedure for this assay. Furthermore, since melanoma invasion involves breaching the basement membrane, which consists of approximately 60% Laminin, 30% type IV Collagen, and 10% other glycans and proteins, the exclusive use of Collagen I, which is the main ECM component of stromal connective tissue (281,459), may not fully replicate the invasive process. Therefore, DH and PP should also be tested in melanoma cells embedded in a matrix that more closely resembles the basement membrane, as different interactions with adhesion and mechanoreceptors can activate distinct signaling pathways, potentially altering melanoma cell behavior (251,252,460).

Deregulation of drug-specific molecular targets was assessed through immunoblotting (see Chapter 4.5.2). Specifically, TOP2α was selected as a target for DH, given its ability to form complexes with TOP2, thereby inhibiting its function. Similarly, β-catenin was chosen for PP, as PP acts as CK1α, which phosphorylates β-catenin, leading to its degradation. Unfortunately, **none of the selected drug-related proteins exhibited significant deregulation** in all the treated melanoma cell lines, reinforcing the idea that **DH and PP may act on alternative targets** in these cell lines, which require further investigation. Only M160915 showed an increased level of TOP2α upon DH treatment. Additionally, CK1α expression was analyzed in spheroids treated with PP, but technical issues with antibody detection prevented reliable results (data not shown).

The only remarkable deregulation that we noted was AKT protein levels and its activation upon PP treatment in SKmel147 and the two primary cell lines, posing PP as a regulator of AKT in our melanoma cells. AKT is a well-established downstream target of mutated NRAS in melanoma and is known to be upregulated upon MAPKi treatment, contributing to resistance against targeted therapies (96). The role of PP in AKT inhibition has been previously described in cancer (461–464). Moreover, Zheng et al. demonstrated a dose-dependent effect of PP in uveal melanoma cells, where a marked reduction in pAKT/AKT led to increased GSK3β activity (a natural target of activated AKT), which subsequently promoted phosphorylation and degradation of β-catenin (448). However, this mechanism was not observed in our models, as β-catenin levels remained unchanged following PP treatment. Given the levels of apoptosis and cell death induced by PP, we hypothesize that the observed reduction in pAKT/AKT and total AKT upon PP exposure may contribute to apoptosis induction, as activated AKT is known to regulate key anti-apoptotic molecules such as BCL-2 and BCL-xL, stabilize mitochondria by reducing cytochrome-c release, and drive metabolic shifts toward oxidative metabolism (96,465). The response of SKmel30 to PP treatment remains puzzling, as we observed an increase in pAKT, which likely led to the upregulation of β-catenin. This effect may be attributed to the inhibition of GSK3β, which becomes phosphorylated by activated AKT (pAKT)This cell line exhibited strong resistance to T, DH, and even the positive control, Staurosporine, yet it was extremely sensitive to PP, which repeatedly induced pronounced apoptosis and cell death. Notably, SKmel30 showed reductions in pERK and ERK following T treatment, which resulted in minimal cytotoxicity, whereas PP treatment led to an increase in pERK/ERK and pAKT/AKT ratios while still triggering a remarkably strong cytotoxic effect. This suggests that PP may induce cell death through alternative mechanisms, potentially related to its ability to inhibit oxidative respiration and drive melanoma cells into apoptosis (446). To investigate this hypothesis, we assessed **changes in mitochondrial membrane potential (MMP)** in these cell lines using Tetramethylrhodamine, methyl ester (TMRM), A dye that emits a red

fluorescent signal upon protonation in mitochondria with functional MMP. Once the MMP is impaired due to inhibition, disruption, or uncoupling of the respiratory complexes, the signal tends to dim or disappear. The signal can then be quantified using microscopy. However, due to the spectral similarity of the reagent with PP, nonspecific signal levels increased exponentially (data not shown). Therefore, further studies are required to elucidate the underlying mechanisms.

The primary mechanism of DH is to induce DNA damage, particularly double-strand breaks (DSBs), by poisoning or inhibiting topoisomerase II activity. To assess DNA damage levels, we evaluated γH2AX expression. Phosphorylated Histone 2AX (γH2AX) is one of the most commonly used markers for detecting DNA damage in cells. Upon DNA damage, H2AX is phosphorylated by DNA-PKs (DNA protein kinases) and ATM, two key DNA damage sensors, initiating a signaling cascade that activates DNA repair mechanisms (466) However, **none of the cell lines exhibited detectable γH2AX levels following DH exposure**, nor after treatment with T or PP. Initially, we speculated that DH might be causing histone eviction in our melanoma cells, leading to a dramatic reduction in γH2AX levels. This hypothesis aligns with findings from a study by Pang et al., which demonstrated that Doxorubicin and Daunorubicin, but not Etoposide, evict histone H2AX, thereby increasing exposure to DNA damage (467). Additionally, further evaluation of antibody specificity and performance is required. This could be achieved by testing γH2AX levels in DNA damage-sensitive cell lines and employing a strong DNA damage inducer, such as radiation, to activate the γH2AX signal robustly.

Combinatorial therapies have emerged as one of the most effective strategies to overcome drug resistance mechanisms that melanoma cells acquire against single agents. For instance, the combination of BRAFi and MEKi has been employed to overcome BRAFi resistance, while the combination of anti-PD-1 and anti-CTLA-4 antibodies are used in immunotherapy to address resistance mechanisms against single-agent treatments, despite concerns regarding an increased incidence of adverse events compared to monotherapy (see Chapter 1.3). Following this approach, we tested DH and PP in combination with T to explore the potential for synergistic effects between the compounds. Unfortunately, both combinations exhibited only a strong additive effect but not a synergistic, as further confirmed by 3D melanoma spheroids proliferation and cell viability assay (see Chapter 4.5.3). In these assays, the combinations showed only a slight reduction, or similar inhibitory effects compared to the respective single compound. Surprisingly, the low concentration of T exhibited an antagonistic effect, increasing both proliferation and cell viability in melanoma spheroids, which is puzzling and needs to be investigated in more cell lines. Based on these results, we decided to proceed with further testing of the individual treatments using their respective IC50 values. The lack of significant efficacy observed with the tested combinations in this study does not

exclude the possibility that other combinations may be more effective. For instance, the combination between DH and PP, or their combination with other MAPK inhibitors (MAPKi) or immune checkpoint inhibitors (ICIs), could be explored. Notably, triple combinations of BRAFi, MEKi, and ICIs have already been tested in clinical settings, leading to the FDA approval in 2020 for the treatment of $BRAF^{mut}$ unresectable and metastatic melanoma with the combination of Vemurafenib (BRAFi), Cobimetinib (MEKi), and Atezolizumab (anti-PD-L1) (468).

The role of the TME has become increasingly critical in accurately assessing the effects of anti-cancer compounds, as extensively discussed in Chapter 1.6. Therefore, we decided to **investigate the effect of DH and PP on melanoma cells co-cultured with key stromal cells** to better mimic the main metastatic niches of melanoma. We employed the previously established Melanoma Multicomponent Spheroid (MMS) (315) and the hydrogel melanoma-TME co-culture system. First, the three mCherry-labeled $NRAS^{mut}$ melanoma cell lines were cultured in MMS models, co-cultured with endothelial cell sand either NHDF (Dermal/Skin), MRC-5 (Lung), or LX-2 (Liver) fibroblasts. These models were then treated with T, DH, and PP at cell line-specific IC50 concentrations. **The decision to co-culture $NRAS^{mut}$ melanoma cells within 3D models designed to mimic dermal/skin, lung, and liver metastatic niches proved to be highly translational**. This approach is supported by the extensive prospective study conducted by Adler et al., which demonstrated that $NRAS^{mut}$ melanoma, in addition to skin, preferentially metastasizes to the lung, liver, and brain (469). SKmel147 and SKmel30, when cultured in the Skin/Dermal and Lung models, exhibited a similar kinetic response to treatments as observed in spheroids composed solely of melanoma cells. When co-cultured in the Liver model, SKmel30 exhibited increased resistance to the proliferation-inhibitory effects of PP. This resistance was further confirmed by evaluating spheroid cell viability. Confocal images gave us important information because we could observe that non-cancerous cells were still present upon treatment (see Chapter 4.5.4, Fig. 60). The viability of the entire spheroid mass was assessed. However, questions may arise concerning the cell type specificity of the measured viability. While we acknowledge the necessity of optimizing alternative assays to specifically evaluate melanoma cell viability, we regarded the observed reduction in spheroid viability as representative of the 'entire tumor mass,' which includes contributions from both cancerous and non-cancerous cells. This approach aligns with the outcomes observed in *in vivo* assays.

We then transitioned to a **more complex 3D *in vitro* system based on melanoma co-cultures embedded in a xeno-free, inert, PEG-based matrix**. The interaction between the ECM and melanoma cells is a crucial factor that drives melanoma progression and contributes to drug resistance, as discussed in earlier chapters of this thesis. Utilizing this advanced hydrogel-based 3D

model system, DH and PP demonstrated **notable specificity in inhibiting the growth of both melanoma cell lines**, with minimal impact on non-cancerous cells across all three models (Dermal, Lung, and Liver) compared to the melanoma population. This inhibitory effect was even more pronounced than that of T in the M161022 model. Interestingly, SKmel147 displayed a differential response to the drugs when cultured in the Liver model compared to the other models (see Chapter 4.5.4, Fig. 61). The observed differences in the response to treatments of melanoma cells co-cultured with TME cells across two *in vitro* 3D model systems used in this study are particularly intriguing. These differences reflect the fact that melanoma patients can respond differently to the same treatment depending on the metastatic site, thereby contributing to variation in patient outcomes. This concept is supported by a recent study conducted by Forschner et al., which identified a negative correlation between the response to targeted therapies (TT) or ICIs and the metastatic site in patients with metastatic melanoma. Specifically, patients with skin metastases demonstrated better responses to TT, whereas patients with visceral metastasis exhibited better responses to ICIs (470). Furthermore, studies have shown that melanoma metastasis to the liver is associated with a poorer response to anti-PD-1 therapy and a lower level of CD8+ T-lymphocyte infiltration compared to other metastatic sites (471–473). Mechanistically, a study by Schmidt et al. described that liver metastases of cutaneous melanoma were characterized by high expression of RICTOR (a key subunit of mTORC2) which phosphorylates AKT and increases tumorigenicity and invasiveness of melanoma cells *in vitro* and *in vivo* utilizing a syngeneic murine splenic injection model. Interestingly, these highly motile melanoma liver metastasis cells presented activated AKT (phosphorylated in both Ser473 and Thr308 residues), which was also stimulated by HGF secreted by hepatic stellate cells (HSCs) conditioned media. These findings suggest a melanoma-promoting role of HSC. *In vivo* studies further confirmed this, showing that melanoma cells with RICTOR knockdown developed fewer liver metastases after 10 days following injections in mice (474).

Taken together, we demonstrated that **Daunorubicin HCl and Pyrvinium Pamoate are capable of efficiently inhibiting the growth of NRAS^{mut} melanoma cells co-cultured with non-cancerous cells** that mimic various metastatic melanoma niches in different in vitro 3D systems. Both compounds showed comparable, and in some cases, even greater effects on melanoma growth inhibition than Trametinib, with minimal impact on non-cancerous cells, similar to the low toxicity observed with Trametinib. Notably, while DH and T exhibited lower cytotoxic effects across all the cell lines, **PP demonstrated a more pronounced cytotoxic effect** on melanoma cells likely driven by an inhibition of AKT activity, positioning it as a **potentially more effective candidate for first-line treatment of NRAS^{mut} melanoma**.

Melanoma is a solid cancer that inherently and progressively **acquires resistance to treatments**, including targeted therapies, which often leads to patient relapse (see Chapter 1.4). Currently, $NRAS^{mut}$ melanoma patients are preferably treated with ICIs as first-line therapy, which unfortunately, almost 50% progress only after 6 months of therapy (116,475). A recent 10-year follow-up of melanoma patients treated with a combination of anti-PD-1 and anti-CTLA-4 revealed that only 59% of patients without a BRAF mutation survived three years after initiating treatment (476). Therefore, **novel second-line therapeutic options for drug-resistant melanoma patients are urgently needed**. We previously demonstrated that DH and, in particular, PP, exhibit comparable or even greater cytotoxic effects on $NRAS^{mut}$ melanoma cells than the currently clinically off-label used MEKi as a targeted therapy. It is important to highlight that while melanoma cells are known to develop resistance against MEKi, **it remains to be shown whether they can develop resistance against DH and PP**. Studies have shown that melanoma can acquire resistance to chemotherapy agents (452). Given that DH is a chemotherapeutic agent inducing lower levels of apoptosis than PP, melanoma cells may have a higher potential to develop resistance to DH compared to PP. Unfortunately, there are no studies looking into this hypothesis, and further research is needed to explore this possibility.

However, we chose to evaluate DH and PP effectiveness against an $NRAS^{mut}$ MEKi-resistant melanoma cell line (SKmel30), as well as a MEKi-resistant BRAFwt/NRASwt melanoma cell line (WM3918). We acknowledge that the **ideal experimental conditions would have involved assessing the efficacy of DH and PP on ICIs-resistant $NRAS^{mut}$ melanoma cells**, given the preferential use of ICIs as first-line therapies, also highlighted by the recent ESMO report for melanoma clinical practices (146) . However, we are currently in the process of establishing experimental models that will allow the generation of melanoma cells resistant to ICIs. Here, we opted to **generate melanoma cell lines resistant to MEK inhibitors (MEKi)** instead. Interestingly, Pyrvinium Pamoate was able to effectively inhibit the growth of MEKi-resistant melanoma cell lines. While DH exhibited even greater sensitivity compared to their respective sensitive melanoma cell line counterparts. This was also in line with the potent cytotoxic effect measured in 3D spheroids (see Chapter 4.5.5). These experiments **lay the foundation for the potential use of DH and PP as second- or third-line treatments** in melanoma patients who have developed resistance to MEK inhibitors or possibly other MAPK-targeted therapies. However, further investigations are necessary to confirm this effect, particularly by including additional MEKi- or MAPKi-resistant $NRAS^{mut}$ melanoma cell lines. A more translational approach would involve testing DH and PP in melanoma cell lines resistant to immune checkpoint inhibitors (ICIs) to better assess their clinical relevance.

By leveraging advanced *in vitro* co-culture 3D models that mimic different metastatic melanoma niches, we demonstrated the efficacy of Daunorubicin HCl (DH) and Pyrvinium Pamoate (PP) in targeting $NRAS^{mut}$ melanoma cells. These findings were further validated in **zebrafish larvae *in vivo* models,** where both compounds exhibited great tumor reduction (see Chapter 4.5.6). Given the lower cytotoxic effect of DH compared to PP, along with its innate chemotherapeutic potential to enhance immune responses, DH may serve as an alternative therapeutic option for disease control. Notably, it could be used in $NRAS^{mut}$ patients as a bridging therapy while awaiting rechallenge with other treatments. As previously mentioned, the use of chemotherapeutic agents such as DH in refractory ICI melanoma patients might serve as a viable strategy to resensitize melanoma patients to immunotherapies, given the immunogenic properties of chemotherapy (477). Supporting this approach, Haggerty et al. demonstrated that short-term treatment with Daunorubicin increased the expression of tumor antigens in melanoma cells, leading to enhanced secretion of immunogenic cytokines such as IL-2 and IFN-γ by co-cultured T-cells (478). On the contrary, **PP demonstrated notable efficiency in specifically targeting melanoma cells**, inducing significant levels of apoptosis and showing inhibitory effects on migratory and invasive melanoma cells, all while maintaining a relatively safety profile in non-cancerous human cells, while a toxic effect was observed in zebrafish larvae, warranting further investigation.

These characteristics establish PP as a promising candidate for first-line therapy in $NRAS^{mut}$ melanoma patients. Moreover, PP displayed strong efficacy in MEKi-resistant cell lines, suggesting its potential application in treating targeted therapy-resistant melanoma. One key consideration is PP's current formulation as tablets, which primarily acts locally in the gut due to its limited systemic absorption. However, Esumi et al. reported that PP can be absorbed intestinally, leading to a significant reduction in pancreatic tumor sizes in mice (479). While no studies have evaluated alternative administration routes in humans, gradual intraperitoneal administration of PP in mice demonstrated strong efficacy in tumor reduction with low toxicity (480). In this context, PP is currently being evaluated in a Phase I clinical trial (NCT05055323) to assess its safety and tolerability for the treatment of pancreatic ductal adenocarcinoma (PDAC) (481).

Overall, we successfully established a semi-automated high-throughput drug screening workflow in which cells were cultured as 3D spheroids, enhancing the translational relevance of drug responses compared to traditional 2D approaches, and identifying a small percentage of the more than 1,300 compounds tested that exhibited promising effects. While DH and PP emerged as two of the most effective drugs during the dose-response curve (DRC) validation step showing melanoma inhibitory effects in advanced 3D model systems, further evaluations are needed to reveal their clinical potential.

Despite the use of advanced human melanoma 3D *in vitro* models and melanoma zebrafish larvae in *vivo* models, a crucial step in evaluating the clinical potential of DH and PP would be to test these compounds in mammalian models, such as mice bearing NRAS-mutant melanoma (482). Nevertheless, it was encouraging to observe that PP induced a remarkable cytotoxic effect on treatment naïve $NRAS^{mut}$ melanoma cells. These findings highlight the significant challenges associated with identifying novel first- and second-line therapies for WT and $NRAS^{mut}$ melanoma patients.

A key strength and novelty of this study lies in the development and implementation of advanced human melanoma 3D co-culture systems, which uniquely integrate multiple tumor microenvironment components. These *in vitro* platforms better mimic the *in vivo* architecture and key interactions between melanoma cells and crucial TME elements, including extracellular matrices from three of the major metastatic sites of melanoma. This approach provided a more physiologically relevant context for drug testing, further reinforced by subsequent validation in a non-mammalian *in vivo* system (zebrafish larvae).

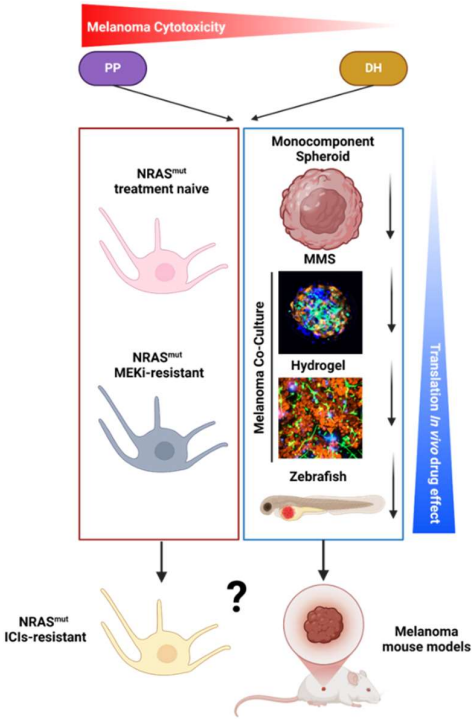

Figure 67: Characterization of Daunorubicin HCl (DH) and Pyrvinium Pamoate (PP) effects in advanced 3D melanoma co-culture models. DH and PP demonstrated potent inhibitory effects on $NRAS^{mut}$ melanoma cells cultured as spheroids, with PP inducing significant levels of apoptosis. 3D co-culture systems that mimic key melanoma metastatic sites showed that both DH and PP exert strong melanoma-specific effects, with minimal or reduced inhibitory effects on non-cancerous cells. Furthermore, the *in vivo* zebrafish larvae model corroborated the melanoma-specific action of DH and PP, revealing low toxicity. The next steps involve testing DH and PP on ICI-resistant melanoma cells and evaluating their effects in NRAS-mutant melanoma mouse models.

6. Conclusions and Perspectives

This thesis represents a comprehensive effort to establish advanced pre-clinical *in vitro* 3D melanoma models, which are suitable to explore novel therapeutic options. Here, we focused on WT and in particular $NRAS^{mut}$ melanoma, leveraging advanced 3D co-culture models to enhance the physiological relevance of preclinical drug testing for these difficult-to-treat genotypes. Through a systematic high-throughput drug screening approach, Daunorubicin HCl (DH) and Pyrvinium Pamoate (PP) emerged as promising candidates for further evaluation. These compounds demonstrated significant anti-melanoma effects in both *in vitro* 3D models and *in vivo* zebrafish larvae assays, highlighting their potential clinical relevance. PP exhibited particularly strong cytotoxic activity, efficiently targeting both naïve and MEK inhibitor (MEKi)-resistant $NRAS^{mut}$ melanoma cells while also displaying a favorable safety profile. Its ability to induce significant cytotoxic effects and inhibit melanoma cell migration and invasion positions it as a potential first-line therapeutic option. In contrast, DH showed a more moderate cytotoxic effect, suggesting its potential use as a disease control agent. Despite these promising findings, several challenges remain before these compounds can be translated into clinical applications. The limited systemic absorption of PP in its current formulation raises the need for alternative delivery strategies, and further studies are necessary to confirm its efficacy in ICI-resistant melanoma. Moreover, DH might present relevant adverse effects in patients such as cardiotoxicity, which can be mitigated utilizing different drug-delivery systems.

The future perspectives and planned activities are the following:

1. Enhancing melanoma hydrogel co-culture models by inducing vascularization and incorporating immune cells.
2. Assessing the efficacy of DH and PP in additional primary melanoma cell lines and expanding the investigation to WT melanoma cells.
3. Elucidating the mechanisms of action of DH and PP in $NRAS^{mut}$ melanoma using multi-omic and metabolism-related approaches, which are currently being explored in our laboratory.
4. Generating ICIs-resistant $NRAS^{mut}$ and WT melanoma cell lines and assessing the efficacy of DH and PP in these cell lines.
5. Exploring additional drug combinations, such as DH plus PP, and testing them alongside other compounds such as MAPK inhibitors and alternative ICIs in both sensitive and ICIs-resistant $NRAS^{mut}$ and WT melanoma cells.
6. Testing novel drug delivery systems for DH and PP, including exosomes.

7. Evaluating the efficacy and toxicity of DH and PP in $NRAS^{mut}$ melanoma mouse models.
8. Testing additional promising hit compounds that demonstrated high efficacy in the HTS campaign.

This study highlights the possibilities, opportunities but also the challenges of advanced 3D co-culture models in preclinical drug discovery. The models can enhance translational relevance while reducing reliance on animal experiments. 3D models may serve as versatile platforms for advanced preclinical studies in both academia and industry, albeit at a higher cost and requiring more complex optimization protocols than traditional 2D in vitro tissue culture. Additionally, they may be integrated into semi-automated high-throughput drug-screening (HTS), providing more physiologically relevant drug responses and thus potentially increasing the success rate of compounds progressing to clinical studies. Currently, less than 10% of compounds tested through HTS advance to preclinical studies, and less than 5% enter clinical trials (314).

Beyond drug discovery, 3D models also have important applications in basic research, offering human cancer-like characteristics that could help uncover molecular mechanisms underlying key processes that are rewired in cancer versus normal cells.

In this thesis we provide the results for 2 repurposed drugs, showing efficacy against $NRAS^{mut}$ and WT melanoma, two melanoma genomic subtypes that currently lack approved targeted therapies. By utilizing this approach, the effects of DH and PP on melanoma and various non-cancerous cells were thoroughly examined. Notably, PP exhibited promising effects, warranting further investigation in combination with other drugs targeting the MAPK signaling pathway, metabolic rewiring, epigenetic mechanisms, and other classes of inhibitors, and ultimately with ICIs, to further improve and prolong the effects of immunotherapies. Moreover, the strategic combination of repurposed, clinically approved drugs with testing them in advanced 3D human models has the potential to significantly enhance drug approval rates while at the same time accelerating the drug discovery process.

References

1. Centeno PP, Pavet V, Marais R. The journey from melanocytes to melanoma. Nature Reviews Cancer. Nature Research; 2023.

2. Schadendorf D, Fisher DE, Garbe C, Gershenwald JE, Grob JJ, Halpern A, et al. Melanoma. Vol. 1, Nature Reviews Disease Primers. 2015. p. 1–20.

3. Lee JW, Ratnakumar K, Hung KF, Rokunohe D, Kawasumi M. Deciphering UV-induced DNA Damage Responses to Prevent and Treat Skin Cancer. Vol. 96, Photochemistry and Photobiology. Blackwell Publishing Inc.; 2020. p. 478–99.

4. Pampena R, Kyrgidis A, Lallas A, Moscarella E, Argenziano G, Longo C. A meta-analysis of nevus-associated melanoma: Prevalence and practical implications. Vol. 77, Journal of the American Academy of Dermatology. Mosby Inc.; 2017. p. 938-945.e4.

5. Zocchi L, Lontano A, Merli M, Dika E, Nagore E, Quaglino P, et al. Familial melanoma and susceptibility genes: A review of the most common clinical and dermoscopic phenotypic aspect, associated malignancies and practical tips for management. Vol. 10, Journal of Clinical Medicine. MDPI; 2021.

6. Wallace H. Clark J, Lynn From, Evelina A. Bernardino, Martin C. Mihm. The Histogenesis and Biologic Behavior of Primary Human Malignant Melanomas of the Skin. Cancer Res. 1969;

7. Rahmati M, Ebrahim S, Hashemi S, Motamedi M, Moosavi MA. New insights on the role of autophagy in the pathogenesis and treatment of melanoma. Vol. 47, Molecular Biology Reports. Springer Science and Business Media B.V.; 2020. p. 9021–32.

8. Arlo J. Miller, Martin C. Mihm. Melanoma. N Engl J Med. 2006;

9. Shain AH, Bastian BC. From melanocytes to melanomas. Vol. 16, Nature Reviews Cancer. Nature Publishing Group; 2016. p. 345–58.

10. Mort RL, Jackson IJ, Patton EE, Mort RL, Jackson IJ, Patton EE. The melanocyte lineage in development and disease. Vol. 142, Development (Cambridge). 2015. p. 620–32.

11. Cichorek M, Wachulska M, Stasiewicz A, Tymińska A. Skin melanocytes: Biology and development [Internet]. Vol. 30, Postepy Dermatologii i Alergologii. 2013. p. 30–41. Available from: https://www.ncbi.nlm.nih.gov/pmc/articles/PMC3834696/pdf/PDIA-30-20287.pdf

12. Schadendorf D, van Akkooi ACJ, Berking C, Griewank KG, Gutzmer R, Hauschild A, et al. Melanoma. Vol. 392, The Lancet. 2018. p. 971–84.

13. Chopra A, Sharma R, Rao UNM. Pathology of Melanoma [Internet]. Vol. 100, Surgical Clinics of North America. Elsevier Inc; 2020. p. 43–59. Available from: https://www.sciencedirect.com/science/article/abs/pii/S0039610919301227?via%3Dihub

14. Lang D, Mascarenhas JB, Shea CR. Melanocytes, melanocyte stem cells, and melanoma stem cells. Clin Dermatol [Internet]. 2013/02/27. 2013;31(2):166–78. Available from: https://www.ncbi.nlm.nih.gov/pubmed/23438380

15. Brenner M, Hearing JV. The protective role of melanin against UV. Vol. 84, Photochem Photobiology. 2008. p. 539–49.

16. Raposo G, Marks MS. Melanosomes - Dark organelles enlighten endosomal membrane transport. Vol. 8, Nature Reviews Molecular Cell Biology. 2007. p. 786–97.

17. Alba LD', Shawkey MD. MELANOSOMES: BIOGENESIS, PROPERTIES, AND EVOLUTION OF AN ANCIENT ORGANELLE. Ancient Organelle Physiol Rev [Internet]. 2019;99:1–19. Available from: www.prv.org

18. Scolyer RA, Long G V., Thompson JF. Evolving concepts in melanoma classification and their relevance to multidisciplinary melanoma patient care. Vol. 5, Molecular Oncology. John Wiley and Sons Ltd; 2011. p. 124–36.

19. Ossio R, Roldán-Marín R, Martínez-Said H, Adams DJ, Robles-Espinoza CD. Melanoma: A global perspective [Internet]. Vol. 17, Nature Reviews Cancer. Nature Publishing Group; 2017. p. 393–4. Available from: https://www.nature.com/articles/nrc.2017.43

20. Bastian BC. The molecular pathology of melanoma: An integrated taxonomy of melanocytic neoplasia. Annual Review of Pathology: Mechanisms of Disease. 2014;9:239–71.

21. Dummer R, Siano M, Hunger RE, Lindenblatt N, Braun R, Michielin O, et al. The updated Swiss guidelines 2016 for the treatment and follow-up of cutaneous melanoma. Vol. 146, Swiss medical weekly. 2016. p. w14279.

22. Dessinioti C, Geller AC, Stergiopoulou A, Swetter SM, Baltas E, Mayer JE, et al. Nevus count associations with thinner nodular or superficial spreading melanoma. Vol. 99, Acta Dermato-Venereologica. Medical Journals/Acta D-V; 2019. p. 614–5.

23. Balch CM, Atkins MB, Garbe C, Gershenwald JE, Halpern AC, Kirkwood JM, et al. Cutaneous Melanoma Sixth Edition. 2020. 1–1508 p.

24. García-Lozano JA, Salerni G, Cuellar-Barboza A, Cárdenas-De La Garza JA, Ocampo-Candiani J. Rapid dermoscopic changes in nodular melanoma. Dermatol Pract Concept. 2020 Jan 1;10(1).

25. Matas-Nadal C, Malvehy J, Ferreres JR, Boada A, Bodet D, Segura S, et al. Increasing incidence of lentigo maligna and lentigo maligna melanoma in Catalonia. Int J Dermatol. 2019 May 1;58(5):577–81.

26. Marco Rastrelli STCRRMA. Melanoma: Epidemiology, Risk Factors, Pathogenesis, Diagnosis and Classification. In Vivo (Brooklyn). 2014;

27. Teramoto Y, Keim U, Gesierich A, Schuler G, Fiedler E, Tüting T, et al. Acral lentiginous melanoma: a skin cancer with unfavourable prognostic features. A study of the German central malignant melanoma registry (CMMR) in 2050 patients. British Journal of Dermatology. 2018 Feb 1;178(2):443–51.

28. Kaliki S, Shields CL. Uveal melanoma: Relatively rare but deadly cancer. Vol. 31, Eye (Basingstoke). Nature Publishing Group; 2017. p. 241–57.

29. Rabbie R, Ferguson P, Molina-Aguilar C, Adams DJ, Robles-Espinoza CD. Melanoma subtypes: genomic profiles, prognostic molecular markers and therapeutic possibilities. J

Pathol [Internet]. 2018/12/05. 2019;247(5):539–51. Available from: https://www.ncbi.nlm.nih.gov/pubmed/30511391

30. Gong HZ, Zheng HY, Li J. Amelanotic melanoma. Vol. 29, Melanoma Research. Lippincott Williams and Wilkins; 2019. p. 221–30.

31. Michielin O, Van Akkooi ACJ, Ascierto PA, Dummer R, Keilholz U. Cutaneous melanoma: ESMO Clinical Practice Guidelines for diagnosis, treatment and follow-up. Annals of Oncology. 2019 Dec 1;30(12):1884–901.

32. William H. Ward, Jeffrey M. Farma. CUTANEOUS MELANOMA Etiology and Therapy. 2017.

33. Gershenwald JE, Scolyer RA, Hess KR, Sondak VK, Long G V., Ross MI, et al. Melanoma staging: Evidence-based changes in the American Joint Committee on Cancer eighth edition cancer staging manual. CA Cancer J Clin [Internet]. 2017 Nov 13;67(6):472–92. Available from: https://acsjournals.onlinelibrary.wiley.com/doi/10.3322/caac.21409

34. Kozovka Z, Gabrisova V, L Kucerova L. Malignant melanoma: diagnosis, treatment and cancer stem cells. Neoplasma. 2016;63:510–7.

35. Nelson DW, Fischer TD, Graff-Baker AN, Dehal A, Stern S, Bilchik AJ, et al. Impact of Effective Systemic Therapy on Metastasectomy in Stage IV Melanoma: A Matched-Pair Analysis. Ann Surg Oncol. 2019 Dec 1;26(13):4610–8.

36. Saginala K, Barsouk A, Aluru JS, Rawla P, Barsouk A. Epidemiology of Melanoma. Vol. 9, Medical sciences (Basel, Switzerland). NLM (Medline); 2021.

37. Sandru A Panaitescu E Blidaru A VS. Survival rates of patients with metastatic malignant melanoma. 2014;

38. Palmer SR, Erickson LA, Ichetovkin I, Knauer DJ, Markovic SN. Circulating Serologic and Molecular Biomarkers in Malignant Melanoma. Mayo Clin Proc. 2011 Oct;86(10):981–90.

39. Forsea AM. Melanoma Epidemiology and Early Detection in Europe: Diversity and Disparities. Dermatol Pract Concept. 2020 Jul 14;e2020033.

40. Melanoma of the skin-Globocan. 2022.

41. Non-Melanoma of the skin-Globocan. 2022.

42. Forsea AM, Del Marmol V, De Vries E, Bailey EE, Geller AC. Melanoma incidence and mortality in Europe: New estimates, persistent disparities. British Journal of Dermatology. 2012 Nov;167(5):1124–30.

43. Melanoma of the Skin-Globocan, 2020.

44. Braicu C, Buse M, Busuioc C, Drula R, Gulei D, Raduly L, et al. A Comprehensive Review on MAPK: A Promising Therapeutic Target in Cancer. Cancers (Basel) [Internet]. 2019/10/28. 2019;11(10). Available from: https://www.ncbi.nlm.nih.gov/pubmed/31652660

45. Liu F, Yang X, Geng M, Huang M. Targeting ERK, an Achilles' Heel of the MAPK pathway, in cancer therapy [Internet]. Vol. 8, Acta Pharmaceutica Sinica B. Elsevier B.V.; 2018. p. 552–62. Available from: https://www.ncbi.nlm.nih.gov/pmc/articles/PMC6089851/pdf/main.pdf

46. Yuan J, Dong X, Yap J, Hu J. The MAPK and AMPK signalings: interplay and implication in targeted cancer therapy. J Hematol Oncol [Internet]. 2020/08/19. 2020;13(1):113. Available from: https://www.ncbi.nlm.nih.gov/pubmed/32807225

47. Katz M, Amit I, Yarden Y. Regulation of MAPKs by growth factors and receptor tyrosine kinases. Vol. 1773, Biochimica et Biophysica Acta - Molecular Cell Research. 2007. p. 1161–76.

48. Plotnikov A, Zehorai E, Procaccia S, Seger R. The MAPK cascades: Signaling components, nuclear roles and mechanisms of nuclear translocation. Vol. 1813, Biochimica et Biophysica Acta - Molecular Cell Research. 2011. p. 1619–33.

49. Cargnello M, Roux PP. Activation and Function of the MAPKs and Their Substrates, the MAPK-Activated Protein Kinases. Microbiology and Molecular Biology Reviews. 2011 Mar;75(1):50–83.

50. Roberts R. The extracellular signal-regulated kinase (ERK) pathway: a potential therapeutic target in hypertension. J Exp Pharmacol. 2012 Aug;77.

51. Maik-Rachline G, Hacohen-Lev-Ran A, Seger R. Nuclear erk: Mechanism of translocation, substrates, and role in cancer. Vol. 20, International Journal of Molecular Sciences. MDPI AG; 2019.

52. Sullivan RJ, Flaherty K. MAP kinase signaling and inhibition in melanoma. Vol. 32, Oncogene. Nature Publishing Group; 2013. p. 2373–9.

53. Inamdar GS, Madhunapantula SR V., Robertson GP. Targeting the MAPK pathway in melanoma: Why some approaches succeed and other fail. Vol. 80, Biochemical Pharmacology. 2010. p. 624–37.

54. Akbani R, Akdemir KC, Aksoy BA, Albert M, Ally A, Amin SB, et al. Genomic Classification of Cutaneous Melanoma. Cell [Internet]. 2015 Jun;161(7):1681–96. Available from: https://linkinghub.elsevier.com/retrieve/pii/S0092867415006340

55. Zaman A, Wu W, Bivona TG. Targeting oncogenic braf: Past, present, and future. Vol. 11, Cancers. MDPI AG; 2019.

56. Śmiech M, Leszczyński P, Kono H, Wardell C, Taniguchi H. Emerging braf mutations in cancer progression and their possible effects on transcriptional networks. Genes (Basel). 2020 Nov 1;11(11):1–14.

57. Ascierto PA, Kirkwood JM, Grob JJ, Simeone E, Grimaldi AM, Maio M, et al. The role of BRAF V600 mutation in melanoma [Internet]. 2012. Available from: http://www.translational-medicine.com/content/10/1/85

58. Kiuru M, Tartar DM, Qi L, Chen D, Yu L, Konia T, et al. Improving classification of melanocytic nevi: Association of BRAF V600E expression with distinct histomorphologic features. J Am Acad Dermatol. 2018 Aug 1;79(2):221–9.

59. Shain AH, Joseph NM, Yu R, Benhamida J, Liu S, Prow T, et al. Genomic and Transcriptomic Analysis Reveals Incremental Disruption of Key Signaling Pathways during Melanoma Evolution. Cancer Cell. 2018 Jul 9;34(1):45-55.e4.

60. Guterres AN, Herlyn M, Villanueva J. Melanoma. In: Encyclopedia of Life Sciences [Internet]. Wiley; 2018. p. 1–10. Available from: https://onlinelibrary.wiley.com/doi/10.1002/9780470015902.a0001894.pub3

61. Zaidi MR, Day CP, Merlino G. From UVs to metastases: Modeling melanoma initiation and progression in the mouse. Vol. 128, Journal of Investigative Dermatology. Nature Publishing Group; 2008. p. 2381–91.

62. Shain AH, Yeh I, Kovalyshyn I, Sriharan A, Talevich E, Gagnon A, et al. The Genetic Evolution of Melanoma from Precursor Lesions. New England Journal of Medicine. 2015 Nov 12;373(20):1926–36.

63. Colombino M, Capone M, Lissia A, Cossu A, Rubino C, De Giorgi V, et al. BRAF/NRAS mutation frequencies among primary tumors and metastases in patients with melanoma. Journal of Clinical Oncology. 2012 Jul 10;30(20):2522–9.

64. Muñoz-Couselo E, Adelantado EZ, Ortiz C, García JS, Perez-Garcia J. NRAS-mutant melanoma: Current challenges and future prospect [Internet]. Vol. 10, OncoTargets and Therapy. 2017. p. 3941–7. Available from: https://www.dovepress.com/getfile.php?fileID=37839

65. Heppt M V., Siepmann T, Engel J, Schubert-Fritschle G, Eckel R, Mirlach L, et al. Prognostic significance of BRAF and NRAS mutations in melanoma: a German study from routine care. BMC Cancer. 2017 Aug 10;17(1):536.

66. Grill C, Larue L. NRAS, NRAS, Which Mutation Is Fairest of Them All? Journal of Investigative Dermatology. 2016 Oct 1;136(10):1936–8.

67. Fedorenko I V., Gibney GT, Smalley KSM. NRAS mutant melanoma: Biological behavior and future strategies for therapeutic management. Vol. 32, Oncogene. 2013. p. 3009–18.

68. Grill C, Larue L. NRAS, NRAS, Which Mutation Is Fairest of Them All? Journal of Investigative Dermatology. 2016 Oct;136(10):1936–8.

69. Randic T, Kozar I, Margue C, Utikal J, Kreis S. NRAS mutant melanoma: Towards better therapies. Cancer Treat Rev [Internet]. 2021/06/08. 2021;99:102238. Available from: https://www.ncbi.nlm.nih.gov/pubmed/34098219

70. Simanshu DK, Nissley D V., McCormick F. RAS Proteins and Their Regulators in Human Disease. Vol. 170, Cell. Cell Press; 2017. p. 17–33.

71. Dumaz N, Jouenne F, Delyon J, Mourah S, Bensussan A, Lebbé C. Atypical BRAF and NRAS mutations in mucosal melanoma. Vol. 11, Cancers. MDPI AG; 2019.

72. Lim JKM, Leprivier G. The impact of oncogenic RAS on redox balance and implications for cancer development. Vol. 10, Cell Death and Disease. Springer Nature; 2019.

73. Mrazek AA, Chao C. Surviving Cutaneous Melanoma: A Clinical Review of Follow-up Practices, Surveillance, and Management of Recurrence. Vol. 94, Surgical Clinics of North America. W.B. Saunders; 2014. p. 989–1002.

74. Jakob JA, Bassett RL, Ng CS, Curry JL, Joseph RW, Alvarado GC, et al. NRAS mutation status is an independent prognostic factor in metastatic melanoma. Cancer. 2012 Aug 15;118(16):4014–23.

75. Heppt M V., Siepmann T, Engel J, Schubert-Fritschle G, Eckel R, Mirlach L, et al. Prognostic significance of BRAF and NRAS mutations in melanoma: a German study from routine care. BMC Cancer. 2017 Aug 10;17(1):536.

76. Vanni I, Tanda ET, Dalmasso B, Pastorino L, Andreotti V, Bruno W, et al. Non-BRAF Mutant Melanoma: Molecular Features and Therapeutical Implications. Vol. 7, Frontiers in Molecular Biosciences. 2020. p. 1–30.

77. Gottfried ON, Viskochil DH, Couldwell WT. Neurofibromatosis Type 1 and tumorigenesis: Molecular mechanisms and therapeutic implications. Vol. 28, Neurosurgical Focus. 2010.

78. Bergoug M, Doudeau M, Godin F, Mosrin C, Vallée B, Bénédetti H. Neurofibromin Structure, Functions and Regulation. Vol. 9, Cells. NLM (Medline); 2020.

79. Kiuru M, Busam KJ. The NF1 gene in tumor syndromes and melanoma. Vol. 97, Laboratory Investigation. Nature Publishing Group; 2017. p. 146–57.

80. Cirenajwis H, Lauss M, Ekedahl H, Torngren T, Kvist A, Saal LH, et al. NF1-mutated melanoma tumors harbor distinct clinical and biological characteristics. Mol Oncol [Internet]. 2017/03/08. 2017;11(4):438–51. Available from: https://www.ncbi.nlm.nih.gov/pubmed/28267273

81. Thielmann CM, Chorti E, Matull J, Murali R, Zaremba A, Lodde G, et al. NF1-mutated melanomas reveal distinct clinical characteristics depending on tumour origin and respond favourably to immune checkpoint inhibitors. Eur J Cancer. 2021 Dec 1;159:113–24.

82. Nissan MH, Pratilas CA, Jones AM, Ramirez R, Won H, Liu C, et al. Loss of NF1 in cutaneous melanoma is associated with RAS activation and MEK dependence. Cancer Res. 2014 Apr 15;74(8):2340–50.

83. Chen Z, Guo Y, Zhao D, Zou Q, Yu F, Zhang L, et al. Comprehensive Analysis Revealed that CDKN2A is a Biomarker for Immune Infiltrates in Multiple Cancers. Front Cell Dev Biol. 2021 Dec 23;9.

84. Smeds J, Berggren P, Ma X, Xu Z, Hemminki K, Kumar R. Genetic status of cell cycle regulators in squamous cell carcinoma of the oesophagus: the CDKN2A (p16 INK4a and p14 ARF) and p53 genes are major targets for inactivation [Internet]. Vol. 23, Carcinogenesis. 2002. Available from: http://www.gdb.org

85. Agarwal P, Sandey M, Deinnocentes P, Bird RC. Tumor suppressor gene p16/INK4A/CDKN2A-dependent regulation into and out of the cell cycle in a spontaneous canine model of breast cancer. J Cell Biochem. 2013 Jun;114(6):1355–63.

86. Kreuger IZM, Slieker RC, van Groningen T, van Doorn R. Therapeutic Strategies for Targeting CDKN2A Loss in Melanoma. Vol. 143, Journal of Investigative Dermatology. Elsevier B.V.; 2023. p. 18-25.e1.

87. Marei HE, Althani A, Afifi N, Hasan A, Caceci T, Pozzoli G, et al. p53 signaling in cancer progression and therapy. Vol. 21, Cancer Cell International. BioMed Central Ltd; 2021.

88. Aubrey BJ, Strasser A, Kelly GL. Tumor-suppressor functions of the TP53 pathway. Vol. 6, Cold Spring Harbor Perspectives in Medicine. Cold Spring Harbor Laboratory Press; 2016.

89. Chen X, Zhang T, Su W, Dou Z, Zhao D, Jin X, et al. Mutant p53 in cancer: from molecular mechanism to therapeutic modulation. Vol. 13, Cell Death and Disease. Springer Nature; 2022.

90. Box NF, Vukmer TO, Terzian T. Targeting p53 in melanoma. Vol. 27, Pigment cell & melanoma research. 2014. p. 8–10.

91. Dunsche L, Ivanisenko N, Riemann S, Schindler S, Beissert S, Angeli C, et al. A cytosolic mutp53(E285K) variant confers chemoresistance of malignant melanoma. Cell Death Dis [Internet]. 2023 Dec 14;14(12):831. Available from: https://www.nature.com/articles/s41419-023-06360-4

92. Bell RJA, Rube HT, Xavier-Magalhães A, Costa BM, Mancini A, Song JS, et al. Understanding TERT promoter mutations: A common path to immortality. Vol. 14, Molecular Cancer Research. American Association for Cancer Research Inc.; 2016. p. 315–23.

93. Dratwa M, Wysoczańska B, Łacina P, Kubik T, Bogunia-Kubik K. TERT—Regulation and Roles in Cancer Formation. Vol. 11, Frontiers in Immunology. Frontiers Media S.A.; 2020.

94. Franklin W. Huang, Eran Hodis, Mary Jue Xu, Gregory V. Kryukov, Lynda Chin, Levi A. Garraway. Highly Recurrent TERT Promoter Mutations in Human Melanoma. Science (1979). 2013 Feb 22;339(6122):953–7.

95. Heidenreich B, Nagore E, Rachakonda PS, Garcia-Casado Z, Requena C, Traves V, et al. Telomerase reverse transcriptase promoter mutations in primary cutaneous melanoma. Nat Commun. 2014;5:3401.

96. Siroy AE, Davies MA, Lazar AJ. The PI3K-AKT Pathway in Melanoma. In: Genetics of Melanoma Cancer Genetics. New York, NY.: Springer.; 2016. p. 165–80.

97. Hemmings BA, Restuccia DF. PI3K-PKB/Akt pathway. Cold Spring Harb Perspect Biol. 2012 Sep;4(9).

98. Manning BD, Toker A. AKT/PKB Signaling: Navigating the Network. Vol. 169, Cell. Cell Press; 2017. p. 381–405.

99. Malek M, Kielkowska A, Chessa T, Anderson KE, Barneda D, Pir P, et al. PTEN Regulates PI(3,4)P2 Signaling Downstream of Class I PI3K. Mol Cell. 2017 Nov 2;68(3):566-580.e10.

100. Mondal S, Subramanian KK, Sakai J, Bajrami B, Luo HR. Phosphoinositide lipid phosphatase SHIP1 and PTEN coordinate to regulate cell migration and adhesion. Mol Biol Cell. 2012 Apr 1;23(7):1219–30.

101. Lee YR, Chen M, Pandolfi PP. The functions and regulation of the PTEN tumour suppressor: new modes and prospects. Vol. 19, Nature Reviews Molecular Cell Biology. Nature Publishing Group; 2018. p. 547–62.

102. Hopkins BD, Hodakoski C, Barrows D, Mense SM, Parsons RE. PTEN function: The long and the short of it. Vol. 39, Trends in Biochemical Sciences. Elsevier Ltd; 2014. p. 183–90.

103. Álvarez-Garcia V, Tawil Y, Wise HM, Leslie NR. Mechanisms of PTEN loss in cancer: It's all about diversity. Vol. 59, Seminars in Cancer Biology. Academic Press; 2019. p. 66–79.

104. Cahuzac KM, Lubin A, Bosch K, Stokes N, Shoenfeld SM, Zhou R, et al. AKT activation because of PTEN loss upregulates xCT via GSK3β/NRF2, leading to inhibition of ferroptosis in PTEN-mutant tumor cells. Cell Rep. 2023 May 30;42(5).

105. Cabrita R, Mitra S, Sanna A, Ekedahl H, Lövgren K, Olsson H, et al. The role of PTEN loss in immune escape, melanoma prognosis and therapy response. Cancers (Basel). 2020 Mar 1;12(3).

106. Tsao H, Goel V, Wu H, Yang G, Haluska FG. Genetic Interaction Between NRAS and BRAF Mutations and PTEN/MMAC1 Inactivation in Melanoma. 2004.

107. Giovanni Ligresti, Loredana Militello, Linda S. Steelman, Andrea Cavallaro, Francesco Basile, Ferdinando Nicoletti, et al. PIK3CA mutations in human solid tumors. Landes Bioscience. 2009;

108. Samuels Y, Waldman T. Oncogenic Mutations of PIK3CA in Human Cancers. In 2010. p. 21–41.

109. Koelblinger P, Thuerigen O, Dummer R. Development of encorafenib for BRAF-mutated advanced melanoma. Vol. 30, Current Opinion in Oncology. Lippincott Williams and Wilkins; 2018. p. 125–33.

110. Swaika A, Crozier JA, Joseph RW. Vemurafenib: An evidence-based review of its clinical utility in the treatment of metastatic melanoma. Vol. 8, Drug Design, Development and Therapy. Dove Medical Press Ltd.; 2014. p. 775–87.

111. Hauschild A, Ascierto PA, Schadendorf D, Grob JJ, Ribas A, Kiecker F, et al. Long-term outcomes in patients with BRAF V600-mutant metastatic melanoma receiving dabrafenib monotherapy: Analysis from phase 2 and 3 clinical trials. Eur J Cancer. 2020 Jan 1;125:114–20.

112. Chapman PB, Robert C, Larkin J, Haanen JB, Ribas A, Hogg D, et al. Vemurafenib in patients with BRAFV600 mutation-positive metastatic melanoma: Final overall survival results of the randomized BRIM-3 study. Annals of Oncology. 2017 Oct 1;28(10):2581–7.

113. Czarnecka AM, Bartnik E, Fiedorowicz M, Rutkowski P. Targeted therapy in melanoma and mechanisms of resistance. Vol. 21, International Journal of Molecular Sciences. MDPI AG; 2020. p. 1–21.

114. Gibney GT, Messina JL, Fedorenko I V., Sondak VK, Smalley KSM. Paradoxical oncogenesis-the long-term effects of BRAF inhibition in melanoma. Vol. 10, Nature Reviews Clinical Oncology. 2013. p. 390–9.

115. Hamid O, Cowey CL, Offner M, Faries M, Carvajal RD. Efficacy, safety, and tolerability of approved combination BRAF and MEK inhibitor regimens for BRAF-mutant melanoma. Cancers (Basel). 2019 Nov 1;11(11).

116. Boutros A, Croce E, Ferrari M, Gili R, Massaro G, Marconcini R, et al. The treatment of advanced melanoma: Current approaches and new challenges. Crit Rev Oncol Hematol [Internet]. 2024 Apr;196:104276. Available from: https://linkinghub.elsevier.com/retrieve/pii/S1040842824000192

117. Boutros A, Croce E, Ferrari M, Gili R, Massaro G, Marconcini R, et al. First line treatment of BRAF mutated advanced melanoma: Does one size fit all? Vol. 99, Cancer Treatment Reviews. W.B. Saunders Ltd; 2021.

118. Fernandez MF, Choi J, Sosman J. New Approaches to Targeted Therapy in Melanoma. Cancers (Basel). 2023 Jun 17;15(12):3224.

119. Ascierto PA, McArthur GA, Dréno B, Atkinson V, Liszkay G, Di Giacomo AM, et al. Cobimetinib combined with vemurafenib in advanced BRAFV600-mutant melanoma (coBRIM): updated efficacy results from a randomised, double-blind, phase 3 trial. Lancet Oncol. 2016;17(9):1248–60.

120. Ascierto PA, Dreno B, Larkin J, Ribas A, Liszkay G, Maio M, et al. 5-year outcomes with cobimetinib plus vemurafenib in BRAFV600 mutation⇓positive advanced melanoma: Extended follow-up of the coBRIM study. Clinical Cancer Research. 2021 Oct 1;27(19):5225–35.

121. Robert C, Grob JJ, Stroyakovskiy D, Karaszewska B, Hauschild A, Levchenko E, et al. Five-Year Outcomes with Dabrafenib plus Trametinib in Metastatic Melanoma. New England Journal of Medicine. 2019 Aug 15;381(7):626–36.

122. Grob JJ, Amonkar MM, Karaszewska B, Schachter J, Dummer R, Mackiewicz A, et al. Comparison of dabrafenib and trametinib combination therapy with vemurafenib monotherapy on health-related quality of life in patients with unresectable or metastatic cutaneous BRAF Val600-mutation-positive melanoma (COMBI-v): Results of a phase 3, open-label, randomised trial. Lancet Oncol. 2015;16(13):1389–98.

123. Ascierto PA, Dummer R, Gogas HJ, Flaherty KT, Arance A, Mandala M, et al. Update on tolerability and overall survival in COLUMBUS: landmark analysis of a randomised phase 3 trial of encorafenib plus binimetinib vs vemurafenib or encorafenib in patients with BRAF V600-mutant melanoma. Eur J Cancer [Internet]. 2020/01/07. 2020;126:33–44. Available from: https://www.ncbi.nlm.nih.gov/pubmed/31901705

124. Dummer R, Flaherty KT, Robert C, Arance A, de Groot JWB, Garbe C, et al. COLUMBUS 5-Year Update: A Randomized, Open-Label, Phase III Trial of Encorafenib Plus Binimetinib Versus Vemurafenib or Encorafenib in Patients With BRAFV600–Mutant Melanoma. Journal of Clinical Oncology. 2022 Dec 20;40(36):4178–88.

125. Dummer R, Schadendorf D, Ascierto PA, Arance A, Dutriaux C, Di Giacomo AM, et al. Binimetinib versus dacarbazine in patients with advanced NRAS-mutant melanoma (NEMO): a multicentre, open-label, randomised, phase 3 trial. Lancet Oncol. 2017 Apr;18(4):435–45.

126. Kalaora S, Nagler A, Wargo JA, Samuels Y. Mechanisms of immune activation and regulation: lessons from melanoma. Vol. 22, Nature Reviews Cancer. Nature Research; 2022. p. 195–207.

127. Passarelli A, Mannavola F, Stefania Stucci L, Tucci M, Silvestris F. Immune system and melanoma biology: a balance between immunosurveillance and immune escape. Oncotarget [Internet]. 2017; Available from: www.impactjournals.com/oncotarget

128. Mutz-Rabl CG, Koelblinger P, Koch L. Immunotherapy for metastatic melanoma—from little benefit to first-line treatment. Vol. 16, Memo - Magazine of European Medical Oncology. Springer; 2023. p. 108–12.

129. Vaddepally RK, Kharel P, Pandey R, Garje R, Chandra AB. Review of indications of FDA-approved immune checkpoint inhibitors per NCCN guidelines with the level of evidence. Vol. 12, Cancers. MDPI AG; 2020.

130. Oyewole-Said D, Konduri V, Vazquez-Perez J, Weldon SA, Levitt JM, Decker WK. Beyond T-Cells: Functional Characterization of CTLA-4 Expression in Immune and Non-Immune Cell Types. Vol. 11, Frontiers in Immunology. Frontiers Media S.A.; 2020.

131. Van Coillie S, Wiernicki B, Xu J. Molecular and Cellular Functions of CTLA-4. In: Advances in Experimental Medicine and Biology. Springer; 2020. p. 7–32.

132. Buchbinder EI, Desai A. CTLA-4 and PD-1 pathways similarities, differences, and implications of their inhibition. Vol. 39, American Journal of Clinical Oncology: Cancer Clinical Trials. Lippincott Williams and Wilkins; 2016. p. 98–106.

133. Robert C, Thomas L, Bondarenko I, O'Day S, Weber J, Garbe C, et al. Ipilimumab plus Dacarbazine for Previously Untreated Metastatic Melanoma. New England Journal of Medicine. 2011 Jun 30;364(26):2517–26.

134. Stucci S, Palmirotta R, Passarelli A, Silvestris E, Argentiero A, Lanotte L, et al. Immune-related adverse events during anticancer immunotherapy: Pathogenesis and management. Vol. 14, Oncology Letters. Spandidos Publications; 2017. p. 5671–80.

135. Huang AC, Zappasodi R. A decade of checkpoint blockade immunotherapy in melanoma: understanding the molecular basis for immune sensitivity and resistance. Nat Immunol. 2022 May 1;23(5):660–70.

136. Sharpe AH, Pauken KE. The diverse functions of the PD1 inhibitory pathway. Vol. 18, Nature Reviews Immunology. Nature Publishing Group; 2018. p. 153–67.

137. Robert C, Ribas A, Schachter J, Arance A, Grob JJ, Mortier L, et al. Pembrolizumab versus ipilimumab in advanced melanoma (KEYNOTE-006): post-hoc 5-year results from an open-label, multicentre, randomised, controlled, phase 3 study. Lancet Oncol. 2019 Sep;20(9):1239–51.

138. Robert C, Long G V., Brady B, Dutriaux C, Maio M, Mortier L, et al. Nivolumab in Previously Untreated Melanoma without BRAF Mutation. New England Journal of Medicine. 2015 Jan 22;372(4):320–30.

139. Postow MA, Chesney J, Pavlick AC, Robert C, Grossmann K, McDermott D, et al. Nivolumab and Ipilimumab versus Ipilimumab in Untreated Melanoma. New England Journal of Medicine. 2015 May 21;372(21):2006–17.

140. Larkin J, Chiarion-Sileni V, Gonzalez R, Grob JJ, Rutkowski P, Lao CD, et al. Five-Year Survival with Combined Nivolumab and Ipilimumab in Advanced Melanoma. New England Journal of Medicine. 2019 Oct 17;381(16):1535–46.

141. Wolchok JD, Chiarion-Sileni V, Gonzalez R, Grob JJ, Rutkowski P, Christopher ;, et al. Long-Term Outcomes With Nivolumab Plus Ipilimumab or Nivolumab Alone Versus Ipilimumab

in Patients With Advanced Melanoma. J Clin Oncol [Internet]. 2021;40:127–37. Available from: https://doi.

142. Knight A, Karapetyan L, Kirkwood JM. Immunotherapy in Melanoma: Recent Advances and Future Directions. Vol. 15, Cancers. MDPI; 2023.

143. Kuzmanovszki D, Kiss N, Tóth B, Kerner T, Tóth V, Szakonyi J, et al. Anti-PD-1 Monotherapy in Advanced Melanoma—Real-World Data from a 77-Month-Long Retrospective Observational Study. Biomedicines. 2022 Jul 1;10(7).

144. Rager T, Eckburg A, Patel M, Qiu R, Gantiwala S, Dovalovsky K, et al. Treatment of Metastatic Melanoma with a Combination of Immunotherapies and Molecularly Targeted Therapies. Vol. 14, Cancers. MDPI; 2022.

145. Kirchberger MC, Ugurel S, Mangana J, Heppt MV, Eigentler TK, Berking C, et al. MEK inhibition may increase survival of NRAS-mutated melanoma patients treated with checkpoint blockade: Results of a retrospective multicentre analysis of 364 patients. Eur J Cancer. 2018 Jul;98:10–6.

146. Amaral T, Ottaviano M, Arance A, Blank C, Chiarion-Sileni V, Donia M, et al. Cutaneous melanoma: ESMO Clinical Practice Guideline for diagnosis, treatment and follow-up. Annals of Oncology. 2024 Jan 1;

147. Luke JJ, Schwartz GK. Chemotherapy in the management of advanced cutaneous malignant melanoma. Clin Dermatol. 2013 May;31(3):290–7.

148. Villani A, Scalvenzi M, Fabbrocini G, Ocampo-Candiani J, Ocampo-Garza SS. Looking into a Better Future: Novel Therapies for Metastatic Melanoma. Vol. 11, Dermatology and Therapy. Adis; 2021. p. 751–67.

149. Ferrucci PF, Pala L, Conforti F, Cocorocchio E. Talimogene Laherparepvec (T-VEC): An Intralesional Cancer Immunotherapy for Advanced Melanoma. Cancers (Basel). 2021 Mar 18;13(6):1383.

150. Ribas A, Dummer R, Puzanov I, VanderWalde A, Andtbacka RHI, Michielin O, et al. Oncolytic Virotherapy Promotes Intratumoral T Cell Infiltration and Improves Anti-PD-1 Immunotherapy. Cell. 2017 Sep;170(6):1109-1119.e10.

151. Bafaloukos D, Gazouli I, Koutserimpas C, Samonis G. Evolution and Progress of mRNA Vaccines in the Treatment of Melanoma: Future Prospects. Vaccines (Basel). 2023 Mar 13;11(3):636.

152. Lang F, Schrors B, Lower M, Tureci O, Sahin U. Identification of neoantigens for individualized therapeutic cancer vaccines. Nat Rev Drug Discov [Internet]. 2022/02/03. 2022; Available from: https://www.ncbi.nlm.nih.gov/pubmed/35105974

153. Sahin U, Oehm P, Derhovanessian E, Jabulowsky RA, Vormehr M, Gold M, et al. An RNA vaccine drives immunity in checkpoint-inhibitor-treated melanoma. Nature. 2020 Sep 3;585(7823):107–12.

154. Weber JS, Carlino MS, Khattak A, Meniawy T, Ansstas G, Taylor MH, et al. Individualised neoantigen therapy mRNA-4157 (V940) plus pembrolizumab versus pembrolizumab monotherapy in resected melanoma (KEYNOTE-942): a randomised, phase 2b study. The Lancet. 2024 Feb 17;403(10427):632–44.

155. Emran T Bin, Shahriar A, Mahmud AR, Rahman T, Abir MH, Siddiquee MohdFR, et al. Multidrug Resistance in Cancer: Understanding Molecular Mechanisms, Immunoprevention and Therapeutic Approaches. Front Oncol. 2022 Jun 23;12.

156. Tangella LP, Clark ME, Gray ES. Resistance mechanisms to targeted therapy in BRAF-mutant melanoma - A mini review. Biochimica et Biophysica Acta (BBA) - General Subjects. 2021 Jan;1865(1):129736.

157. Kalbasi A, Ribas A. Tumour-intrinsic resistance to immune checkpoint blockade. Nat Rev Immunol. 2020 Jan 30;20(1):25–39.

158. Bell CC, Gilan O. Principles and mechanisms of non-genetic resistance in cancer. Br J Cancer. 2020 Feb 18;122(4):465–72.

159. Leonce C, Saintigny P, Ortiz-Cuaran S. Cell-Intrinsic Mechanisms of Drug Tolerance to Systemic Therapies in Cancer. Molecular Cancer Research. 2022 Jan 1;20(1):11–29.

160. Kozar I, Margue C, Rothengatter S, Haan C, Kreis S. Many ways to resistance: How melanoma cells evade targeted therapies. Vol. 1871, Biochimica et Biophysica Acta - Reviews on Cancer. Elsevier; 2019. p. 313–22.

161. Amaral T, Sinnberg T, Meier F, Krepler C, Levesque M, Niessner H, et al. MAPK pathway in melanoma part II-secondary and adaptive resistance mechanisms to BRAF inhibition. Eur J Cancer [Internet]. 2017/02/07. 2017;73:93–101. Available from: https://www.ncbi.nlm.nih.gov/pubmed/28162869

162. Proietti I, Skroza N, Bernardini N, Tolino E, Balduzzi V, Marchesiello A, et al. Mechanisms of Acquired BRAF Inhibitor Resistance in Melanoma: A Systematic Review. Cancers (Basel). 2020 Sep 29;12(10):2801.

163. Villanueva MT. Paradox breaking. Nat Rev Cancer. 2015 Feb 23;15(2):71–71.

164. Amaral T, Sinnberg T, Meier F, Krepler C, Levesque M, Niessner H, et al. The mitogen-activated protein kinase pathway in melanoma part I - Activation and primary resistance mechanisms to BRAF inhibition. Eur J Cancer [Internet]. 2017/02/09. 2017;73:85–92. Available from: https://www.ncbi.nlm.nih.gov/pubmed/28169047

165. Johannessen CM, Boehm JS, Kim SY, Thomas SR, Wardwell L, Johnson LA, et al. COT drives resistance to RAF inhibition through MAP kinase pathway reactivation. Nature. 2010 Dec 24;468(7326):968–72.

166. Flaherty KT, Hodi FS, Fisher DE. From genes to drugs: targeted strategies for melanoma. Nat Rev Cancer. 2012 May 5;12(5):349–61.

167. Arozarena I, Wellbrock C. Overcoming resistance to BRAF inhibitors. Ann Transl Med. 2017 Oct;5(19):387–387.

168. Raaijmakers MIG, Widmer DS, Narechania A, Eichhoff O, Freiberger SN, Wenzina J, et al. Co-existence of BRAF and NRAS driver mutations in the same melanoma cells results in heterogeneity of targeted therapy resistance. Oncotarget. 2016 Nov 22;7(47):77163–74.

169. Hintzsche J, Kim J, Yadav V, Amato C, Robinson SE, Seelenfreund E, et al. IMPACT: a whole-exome sequencing analysis pipeline for integrating molecular profiles with actionable

therapeutics in clinical samples. Journal of the American Medical Informatics Association. 2016 Jul 1;23(4):721–30.

170. Monsma DJ, Cherba DM, Eugster EE, Dylewski DL, Davidson PT, Peterson CA, et al. Melanoma patient derived xenografts acquire distinct Vemurafenib resistance mechanisms [Internet]. Vol. 5, Am J Cancer Res. 2015. Available from: www.ajcr.us/

171. Perna D, Karreth FA, Rust AG, Perez-Mancera PA, Rashid M, Iorio F, et al. BRAF inhibitor resistance mediated by the AKT pathway in an oncogenic BRAF mouse melanoma model. Proceedings of the National Academy of Sciences. 2015 Feb 10;112(6).

172. Penna I, Molla A, Grazia G, Cleris L, Nicolini G, Perrone F, et al. Primary cross-resistance to BRAFV600E-, MEK1/2- and PI3K/mTOR-specific inhibitors in BRAF-mutant melanoma cells counteracted by dual pathway blockade. Oncotarget. 2016 Jan 26;7(4):3947–65.

173. Irvine M, Stewart A, Pedersen B, Boyd S, Kefford R, Rizos H. Oncogenic PI3K/AKT promotes the step-wise evolution of combination BRAF/MEK inhibitor resistance in melanoma. Oncogenesis. 2018 Sep 20;7(9):72.

174. Davies MA. The Role of the PI3K-AKT Pathway in Melanoma. The Cancer Journal. 2012 Mar;18(2):142–7.

175. Czyz M. HGF/c-MET Signaling in Melanocytes and Melanoma. Int J Mol Sci. 2018 Dec 3;19(12):3844.

176. Pastwińska J, Karaś K, Karwaciak I, Ratajewski M. Targeting EGFR in melanoma – The sea of possibilities to overcome drug resistance. Biochimica et Biophysica Acta (BBA) - Reviews on Cancer. 2022 Jul;1877(4):188754.

177. Gaudino SJ, Kumar P. Cross-Talk Between Antigen Presenting Cells and T Cells Impacts Intestinal Homeostasis, Bacterial Infections, and Tumorigenesis. Front Immunol. 2019 Mar 6;10.

178. Hassel JC, Zimmer L, Sickmann T, Eigentler TK, Meier F, Mohr P, et al. Medical Needs and Therapeutic Options for Melanoma Patients Resistant to Anti-PD-1-Directed Immune Checkpoint Inhibition. Cancers (Basel). 2023 Jun 30;15(13):3448.

179. Vukadin S, Khaznadar F, Kizivat T, Vcev A, Smolic M. Molecular Mechanisms of Resistance to Immune Checkpoint Inhibitors in Melanoma Treatment: An Update. Biomedicines. 2021 Jul 18;9(7):835.

180. Sha D, Jin Z, Budczies J, Kluck K, Stenzinger A, Sinicrope FA. Tumor Mutational Burden as a Predictive Biomarker in Solid Tumors. Cancer Discov. 2020 Dec 1;10(12):1808–25.

181. Westcott PMK, Sacks NJ, Schenkel JM, Ely ZA, Smith O, Hauck H, et al. Low neoantigen expression and poor T-cell priming underlie early immune escape in colorectal cancer. Nat Cancer. 2021 Sep 30;2(10):1071–85.

182. Wan L, Wang Z, Xue J, Yang H, Zhu Y. Tumor mutation burden predicts response and survival to immune checkpoint inhibitors: a meta-analysis. Transl Cancer Res. 2020 Sep;9(9):5437–49.

183. Moeckel C, Bakhl K, Georgakopoulos-Soares I, Zaravinos A. The Efficacy of Tumor Mutation Burden as a Biomarker of Response to Immune Checkpoint Inhibitors. Int J Mol Sci. 2023 Apr 4;24(7):6710.

184. Maleki Vareki S. High and low mutational burden tumors versus immunologically hot and cold tumors and response to immune checkpoint inhibitors. J Immunother Cancer. 2018 Dec 27;6(1):157.

185. Wang Y, Xiang Y, Xin VW, Wang XW, Peng XC, Liu XQ, et al. Dendritic cell biology and its role in tumor immunotherapy. J Hematol Oncol. 2020 Dec 3;13(1):107.

186. Ladányi A, Kiss J, Somlai B, Gilde K, Fejős Z, Mohos A, et al. Density of DC-LAMP+ mature dendritic cells in combination with activated T lymphocytes infiltrating primary cutaneous melanoma is a strong independent prognostic factor. Cancer Immunology, Immunotherapy. 2007 Sep 6;56(9):1459–69.

187. Bandola-Simon J, Roche PA. Dysfunction of antigen processing and presentation by dendritic cells in cancer. Mol Immunol. 2019 Sep;113:31–7.

188. Ott PA, Hodi FS, Buchbinder EI. Inhibition of Immune Checkpoints and Vascular Endothelial Growth Factor as Combination Therapy for Metastatic Melanoma: An Overview of Rationale, Preclinical Evidence, and Initial Clinical Data. Front Oncol. 2015 Sep 22;5.

189. Schaaf MB, Garg AD, Agostinis P. Defining the role of the tumor vasculature in antitumor immunity and immunotherapy. Cell Death Dis. 2018 Jan 25;9(2):115.

190. Fujimura T, Aiba S. Significance of Immunosuppressive Cells as a Target for Immunotherapies in Melanoma and Non-Melanoma Skin Cancers. Biomolecules. 2020 Jul 22;10(8):1087.

191. Kreidieh FY, Tawbi HA. The introduction of LAG-3 checkpoint blockade in melanoma: immunotherapy landscape beyond PD-1 and CTLA-4 inhibition. Ther Adv Med Oncol. 2023 Jan 17;15.

192. Cazzato G, Cascardi E, Colagrande A, Lettini T, Filosa A, Arezzo F, et al. T Cell Immunoglobulin and Mucin Domain 3 (TIM-3) in Cutaneous Melanoma: A Narrative Review. Cancers (Basel). 2023 Mar 10;15(6):1697.

193. Grzywa TM, Paskal W, Wlodarski PK. Intratumor and Intertumor Heterogeneity in Melanoma. Transl Oncol [Internet]. 2017/10/28. 2017;10(6):956–75. Available from: https://www.ncbi.nlm.nih.gov/pubmed/29078205

194. Ng MF, Simmons JL, Boyle GM. Heterogeneity in Melanoma. Cancers (Basel). 2022 Jun 20;14(12):3030.

195. Shannan B, Perego M, Somasundaram R, Herlyn M. Heterogeneity in Melanoma. In 2016. p. 1–15.

196. Hanahan D. Hallmarks of Cancer: New Dimensions. Cancer Discov [Internet]. 2022/01/14. 2022;12(1):31–46. Available from: https://www.ncbi.nlm.nih.gov/pubmed/35022204

197. Hossain SM, Eccles MR. Phenotype Switching and the Melanoma Microenvironment; Impact on Immunotherapy and Drug Resistance. Int J Mol Sci. 2023 Jan 13;24(2):1601.

198. Widmer DS, Hoek KS, Cheng PF, Eichhoff OM, Biedermann T, Raaijmakers MIG, et al. Hypoxia Contributes to Melanoma Heterogeneity by Triggering HIF1α-Dependent Phenotype Switching. Journal of Investigative Dermatology. 2013 Oct;133(10):2436–43.

199. Chapman A, Fernandez del Ama L, Ferguson J, Kamarashev J, Wellbrock C, Hurlstone A. Heterogeneous Tumor Subpopulations Cooperate to Drive Invasion. Cell Rep. 2014 Aug;8(3):688–95.

200. Arozarena I, Wellbrock C. Phenotype plasticity as enabler of melanoma progression and therapy resistance [Internet]. Vol. 19, Nature Reviews Cancer. Springer US; 2019. p. 377–91. Available from: https://www.nature.com/articles/s41568-019-0154-4

201. Huang F, Santinon F, Flores González RE, del Rincón S V. Melanoma Plasticity: Promoter of Metastasis and Resistance to Therapy. Vol. 11, Frontiers in Oncology. Frontiers Media S.A.; 2021.

202. Rambow F, Marine JC, Goding CR. Melanoma plasticity and phenotypic diversity: therapeutic barriers and opportunities. Genes Dev [Internet]. 2019/10/03. 2019;33(19–20):1295–318. Available from: https://www.ncbi.nlm.nih.gov/pubmed/31575676

203. Carreira S, Goodall J, Denat L, Rodriguez M, Nuciforo P, Hoek KS, et al. Mitf regulation of Dia1 controls melanoma proliferation and invasiveness. Genes Dev. 2006 Dec 15;20(24):3426–39.

204. Seberg HE, Van Otterloo E, Cornell RA. Beyond MITF: Multiple transcription factors directly regulate the cellular phenotype in melanocytes and melanoma. Pigment Cell Melanoma Res. 2017 Sep 22;30(5):454–66.

205. Ahn A, Chatterjee A, Eccles MR. The Slow Cycling Phenotype: A Growing Problem for Treatment Resistance in Melanoma. Mol Cancer Ther. 2017 Jun 1;16(6):1002–9.

206. Kido K, Sumimoto H, Asada S, Okada SM, Yaguchi T, Kawamura N, et al. Simultaneous suppression of MITF and BRAF V600E enhanced inhibition of melanoma cell proliferation. Cancer Sci. 2009 Oct 14;100(10):1863–9.

207. Hartman ML, Czyz M. MITF in melanoma: mechanisms behind its expression and activity. Cellular and Molecular Life Sciences. 2015 Apr 30;72(7):1249–60.

208. Hossain SM, Eccles MR. Phenotype Switching and the Melanoma Microenvironment; Impact on Immunotherapy and Drug Resistance. Int J Mol Sci. 2023 Jan 1;24(2).

209. Badia-Ramentol J, Linares J, Gomez-Llonin A, Calon A. Minimal Residual Disease, Metastasis and Immunity. Biomolecules [Internet]. 2021/01/28. 2021;11(2). Available from: https://www.ncbi.nlm.nih.gov/pubmed/33498251

210. Luskin MR, Murakami MA, Manalis SR, Weinstock DM. Targeting minimal residual disease: a path to cure? Nat Rev Cancer [Internet]. 2018/01/30. 2018;18(4):255–63. Available from: https://www.ncbi.nlm.nih.gov/pubmed/29376520

211. Patel RP, Somasundram PM, Smith LK, Sheppard KE, McArthur GA. The therapeutic potential of targeting minimal residual disease in melanoma. Clin Transl Med. 2023 Mar;13(3).

212. Sharma S V, Lee DY, Li B, Quinlan MP, Takahashi F, Maheswaran S, et al. A chromatin-mediated reversible drug-tolerant state in cancer cell subpopulations. Cell [Internet]. 2010/04/08. 2010;141(1):69–80. Available from: https://www.ncbi.nlm.nih.gov/pubmed/20371346

213. Roesch A, Fukunaga-Kalabis M, Schmidt EC, Zabierowski SE, Brafford PA, Vultur A, et al. A Temporarily Distinct Subpopulation of Slow-Cycling Melanoma Cells Is Required for Continuous Tumor Growth. Cell. 2010;141(4):583–94.

214. Cabanos HF, Hata AN. Emerging Insights into Targeted Therapy-Tolerant Persister Cells in Cancer. Cancers (Basel) [Internet]. 2021/06/03. 2021;13(11). Available from: https://www.ncbi.nlm.nih.gov/pubmed/34071428

215. De Conti G, Dias MH, Bernards R. Fighting Drug Resistance through the Targeting of Drug-Tolerant Persister Cells. Cancers (Basel) [Internet]. 2021/04/04. 2021;13(5). Available from: https://www.ncbi.nlm.nih.gov/pubmed/33807785

216. Shen S, Vagner S, Robert C. Persistent Cancer Cells: The Deadly Survivors. Cell [Internet]. 2020/11/14. 2020;183(4):860–74. Available from: https://www.ncbi.nlm.nih.gov/pubmed/33186528

217. Swayden M, Chhouri H, Anouar Y, Grumolato L. Tolerant/Persister Cancer Cells and the Path to Resistance to Targeted Therapy. Cells [Internet]. 2020/12/10. 2020;9(12). Available from: https://www.ncbi.nlm.nih.gov/pubmed/33291749

218. Song X, Lan Y, Zheng X, Zhu Q, Liao X, Liu K, et al. Targeting drug-tolerant cells: A promising strategy for overcoming acquired drug resistance in cancer cells. Vol. 4, MedComm. John Wiley and Sons Inc; 2023.

219. Rambow F, Rogiers A, Marin-Bejar O, Aibar S, Femel J, Dewaele M, et al. Toward Minimal Residual Disease-Directed Therapy in Melanoma. Cell [Internet]. 2018/07/19. 2018;174(4):843-855 e19. Available from: https://www.ncbi.nlm.nih.gov/pubmed/30017245

220. Marin-Bejar O, Rogiers A, Dewaele M, Femel J, Karras P, Pozniak J, et al. Evolutionary predictability of genetic versus nongenetic resistance to anticancer drugs in melanoma. Cancer Cell [Internet]. 2021/06/19. 2021;39(8):1135-1149 e8. Available from: https://www.ncbi.nlm.nih.gov/pubmed/34143978

221. Smith MP, Brunton H, Rowling EJ, Ferguson J, Arozarena I, Miskolczi Z, et al. Inhibiting Drivers of Non-mutational Drug Tolerance Is a Salvage Strategy for Targeted Melanoma Therapy. Cancer Cell. 2016 Mar 14;29(3):270–84.

222. Mikubo M, Inoue Y, Liu G, Tsao MS. Mechanism of Drug Tolerant Persister Cancer Cells: The Landscape and Clinical Implication for Therapy. J Thorac Oncol [Internet]. 2021/08/06. 2021;16(11):1798–809. Available from: https://www.ncbi.nlm.nih.gov/pubmed/34352380

223. Najem A, Soumoy L, Sabbah M, Krayem M, Awada A, Journe F, et al. Understanding Molecular Mechanisms of Phenotype Switching and Crosstalk with TME to Reveal New Vulnerabilities of Melanoma. Cells. 2022 Mar 29;11(7):1157.

224. Pedri D, Karras P, Landeloos E, Marine JC, Rambow F. Epithelial-to-mesenchymal-like transition events in melanoma. FEBS J [Internet]. 2021/05/18. 2022;289(5):1352–68. Available from: https://www.ncbi.nlm.nih.gov/pubmed/33999497

225. Swanton C, Bernard E, Abbosh C, André F, Auwerx J, Balmain A, et al. Embracing cancer complexity: Hallmarks of systemic disease. Vol. 187, Cell. Elsevier B.V.; 2024. p. 1589–616.

226. Chhabra Y, Weeraratna AT. Fibroblasts in cancer: Unity in heterogeneity. Vol. 186, Cell. Elsevier B.V.; 2023. p. 1580–609.

227. Zhao Y, Shen M, Wu L, Yang H, Yao Y, Yang Q, et al. Stromal cells in the tumor microenvironment: accomplices of tumor progression? Vol. 14, Cell Death and Disease. Springer Nature; 2023.

228. Lichtenberger BM, Kasper M. Cellular heterogeneity and microenvironmental control of skin cancer. J Intern Med [Internet]. 2020/09/26. 2021;289(5):614–28. Available from: https://www.ncbi.nlm.nih.gov/pubmed/32976658

229. Ping Q, Yan R, Cheng X, Wang W, Zhong Y, Hou Z, et al. Cancer-associated fibroblasts: overview, progress, challenges, and directions. Cancer Gene Ther [Internet]. 2021/03/14. 2021; Available from: https://www.ncbi.nlm.nih.gov/pubmed/33712707

230. Liu T, Han C, Wang S, Fang P, Ma Z, Xu L, et al. Cancer-associated fibroblasts: an emerging target of anti-cancer immunotherapy. J Hematol Oncol [Internet]. 2019/08/30. 2019;12(1):86. Available from: https://www.ncbi.nlm.nih.gov/pubmed/31462327

231. Falcone I, Conciatori F, Bazzichetto C, Ferretti G, Cognetti F, Ciuffreda L, et al. Tumor microenvironment: Implications in melanoma resistance to targeted therapy and immunotherapy. Vol. 12, Cancers. MDPI AG; 2020. p. 1–26.

232. Glabman RA, Choyke PL, Sato N. Cancer-Associated Fibroblasts: Tumorigenicity and Targeting for Cancer Therapy. Cancers (Basel). 2022 Aug 12;14(16):3906.

233. Straussman R, Morikawa T, Shee K, Barzily-Rokni M, Qian ZR, Du J, et al. Tumour micro-environment elicits innate resistance to RAF inhibitors through HGF secretion. Nature. 2012 Jul 4;487(7408):500–4.

234. Romano V, Belviso I, Venuta A, Ruocco MR, Masone S, Aliotta F, et al. Influence of Tumor Microenvironment and Fibroblast Population Plasticity on Melanoma Growth, Therapy Resistance and Immunoescape. Int J Mol Sci. 2021 May 17;22(10):5283.

235. Lee JH, Shklovskaya E, Lim SY, Carlino MS, Menzies AM, Stewart A, et al. Transcriptional downregulation of MHC class I and melanoma de- differentiation in resistance to PD-1 inhibition. Nat Commun. 2020 Apr 20;11(1):1897.

236. Nagl L, Horvath L, Pircher A, Wolf D. Tumor Endothelial Cells (TECs) as Potential Immune Directors of the Tumor Microenvironment – New Findings and Future Perspectives. Front Cell Dev Biol. 2020 Aug 19;8.

237. Potente M, Gerhardt H, Carmeliet P. Basic and Therapeutic Aspects of Angiogenesis. Cell. 2011 Sep;146(6):873–87.

238. Hida K, Maishi N, Annan DA, Hida Y. Contribution of tumor endothelial cells in cancer progression. Vol. 19, International Journal of Molecular Sciences. MDPI AG; 2018.

239. Lambrechts D, Wauters E, Boeckx B, Aibar S, Nittner D, Burton O, et al. Phenotype molding of stromal cells in the lung tumor microenvironment. Nat Med. 2018 Aug 9;24(8):1277–89.

240. Muller WA. Mechanisms of Leukocyte Transendothelial Migration. Annual Review of Pathology: Mechanisms of Disease. 2011 Feb 28;6(1):323–44.

241. Hashemi G, Dight J, Khosrotehrani K, Sormani L. Melanoma Tumour Vascularization and Tissue-Resident Endothelial Progenitor Cells. Cancers (Basel). 2022 Aug 30;14(17):4216.

242. Fang J, Lu Y, Zheng J, Jiang X, Shen H, Shang X, et al. Exploring the crosstalk between endothelial cells, immune cells, and immune checkpoints in the tumor microenvironment: new insights and therapeutic implications. Cell Death Dis. 2023 Sep 4;14(9):586.

243. Eddy K, Chen S. Overcoming Immune Evasion in Melanoma. Int J Mol Sci. 2020 Nov 26;21(23):8984.

244. Hadrup S, Donia M, thor Straten P. Effector CD4 and CD8 T Cells and Their Role in the Tumor Microenvironment. Cancer Microenvironment. 2013 Aug 16;6(2):123–33.

245. Sun L, Su Y, Jiao A, Wang X, Zhang B. T cells in health and disease. Signal Transduct Target Ther. 2023 Jun 19;8(1):235.

246. Gray JI, Farber DL. Tissue-Resident Immune Cells in Humans. 2022; Available from: https://doi.org/10.1146/annurev-immunol-093019-

247. Passarelli A, Mannavola F, Stucci LS, Tucci M, Silvestris F. Immune system and melanoma biology: a balance between immunosurveillance and immune escape. Oncotarget. 2017 Dec 1;8(62):106132–42.

248. Polak ME, Borthwick NJ, Gabriel FG, Johnson P, Higgins B, Hurren J, et al. Mechanisms of local immunosuppression in cutaneous melanoma. Br J Cancer. 2007 Jun 12;96(12):1879–87.

249. Mahmoud F, Shields B, Makhoul I, Avaritt N, Wong HK, Hutchins LF, et al. Immune surveillance in melanoma: From immune attack to melanoma escape and even counterattack. Cancer Biol Ther. 2017 Jul 3;18(7):451–69.

250. Cox TR. The matrix in cancer. Vol. 21, Nature Reviews Cancer. Nature Research; 2021. p. 217–38.

251. Popovic A, Tartare-Deckert S. Role of extracellular matrix architecture and signaling in melanoma therapeutic resistance. Front Oncol. 2022 Sep 2;12.

252. Fromme JE, Zigrino P. The Role of Extracellular Matrix Remodeling in Skin Tumor Progression and Therapeutic Resistance. Front Mol Biosci. 2022 Apr 26;9.

253. Zitka O, Kukacka J, Krizkov S, Huska D, Adam V, Masarik M, et al. Matrix Metalloproteinases. Curr Med Chem. 2010 Nov 1;17(31):3751–68.

254. van Kempen LCLT, Rijntjes J, Mamor-Cornelissen I, Vincent-Naulleau S, Gerritsen MP, Ruiter DJ, et al. Type I collagen expression contributes to angiogenesis and the development of deeply invasive cutaneous melanoma. Int J Cancer. 2008 Mar 24;122(5):1019–29.

255. Miskolczi Z, Smith MP, Rowling EJ, Ferguson J, Barriuso J, Wellbrock C. Collagen abundance controls melanoma phenotypes through lineage-specific microenvironment sensing. Oncogene. 2018 Jun 1;37(23):3166–82.

256. Diazzi S, Tartare-Deckert S, Deckert M. The mechanical phenotypic plasticity of melanoma cell: an emerging driver of therapy cross-resistance. Oncogenesis. 2023 Feb 11;12(1):7.

257. Hirata E, Girotti MR, Marais R, Sahai E, Hirata E, Girotti MR, et al. Intravital Imaging Reveals How BRAF Inhibition Generates Drug-Tolerant Microenvironments with Intravital Imaging Reveals How BRAF Inhibition Generates Drug-Tolerant Microenvironments with High Integrin b 1 / FAK Signaling. Vol. 27, Cancer Cell. The Authors; 2015. p. 574–88.

258. Boucherit N, Gorvel L, Olive D. 3D Tumor Models and Their Use for the Testing of Immunotherapies. Front Immunol [Internet]. 2020/12/29. 2020;11:603640. Available from: https://www.ncbi.nlm.nih.gov/pubmed/33362787

259. Cui X, Hartanto Y, Zhang H. Advances in multicellular spheroids formation. J R Soc Interface [Internet]. 2017/02/17. 2017;14(127). Available from: https://www.ncbi.nlm.nih.gov/pubmed/28202590

260. Nascentes Melo LM, Kumar S, Riess V, Szylo KJ, Eisenburger R, Schadendorf D, et al. Advancements in melanoma cancer metastasis models. Vol. 36, Pigment Cell and Melanoma Research. John Wiley and Sons Inc; 2023. p. 206–23.

261. Han SJ, Kwon S, Kim KS. Challenges of applying multicellular tumor spheroids in preclinical phase. Cancer Cell Int [Internet]. 2021/03/06. 2021;21(1):152. Available from: https://www.ncbi.nlm.nih.gov/pubmed/33663530

262. Rodrigues J, Heinrich MA, Teixeira LM, Prakash J. 3D In Vitro Model (R)evolution: Unveiling Tumor-Stroma Interactions. Trends Cancer [Internet]. 2020/11/22. 2021;7(3):249–64. Available from: https://www.ncbi.nlm.nih.gov/pubmed/33218948

263. Ferreira LP, Gaspar VM, Mano JF. Design of spherically structured 3D in vitro tumor models -Advances and prospects. Acta Biomater [Internet]. 2018/05/29. 2018;75:11–34. Available from: https://www.ncbi.nlm.nih.gov/pubmed/29803007

264. Manduca N, Maccafeo E, De Maria R, Sistigu A, Musella M. 3D cancer models: One step closer to in vitro human studies. Vol. 14, Frontiers in Immunology. Frontiers Media S.A.; 2023.

265. Marconi A, Quadri M, Saltari A, Pincelli C. Progress in melanoma modelling in vitro. Exp Dermatol [Internet]. 2018/04/27. 2018;27(5):578–86. Available from: https://www.ncbi.nlm.nih.gov/pubmed/29697862

266. Metzger W, Sossong D, Bachle A, Putz N, Wennemuth G, Pohlemann T, et al. The liquid overlay technique is the key to formation of co-culture spheroids consisting of primary osteoblasts, fibroblasts and endothelial cells. Cytotherapy [Internet]. 2011/05/31. 2011;13(8):1000–12. Available from: https://www.ncbi.nlm.nih.gov/pubmed/21619419

267. El Harane S, Zidi B, El Harane N, Krause KH, Matthes T, Preynat-Seauve O. Cancer Spheroids and Organoids as Novel Tools for Research and Therapy: State of the Art and Challenges to Guide Precision Medicine. Cells. 2023 Mar 24;12(7):1001.

268. Yakavets I, Francois A, Benoit A, Merlin JL, Bezdetnaya L, Vogin G. Advanced co-culture 3D breast cancer model for investigation of fibrosis induced by external stimuli: optimization study. Sci Rep [Internet]. 2020/12/06. 2020;10(1):21273. Available from: https://www.ncbi.nlm.nih.gov/pubmed/33277538

269. Flach EH, Rebecca VW, Herlyn M, Smalley KS, Anderson AR. Fibroblasts contribute to melanoma tumor growth and drug resistance. Mol Pharm [Internet]. 2011/11/10. 2011;8(6):2039–49. Available from: https://www.ncbi.nlm.nih.gov/pubmed/22067046

270. Klicks J, Masslo C, Kluth A, Rudolf R, Hafner M. A novel spheroid-based co-culture model mimics loss of keratinocyte differentiation, melanoma cell invasion, and drug-induced selection of ABCB5-expressing cells. BMC Cancer [Internet]. 2019/05/01. 2019;19(1):402. Available from: https://www.ncbi.nlm.nih.gov/pubmed/31035967

271. Nii T, Makino K, Tabata Y. Three-Dimensional Culture System of Cancer Cells Combined with Biomaterials for Drug Screening. Cancers (Basel). 2020 Sep 24;12(10):2754.

272. Caliari SR, Burdick JA. A practical guide to hydrogels for cell culture. Vol. 13, Nature Methods. Nature Publishing Group; 2016. p. 405–14.

273. Blache U, Ehrbar M. Inspired by nature: Hydrogels as versatile tools for vascular engineering. Adv Wound Care (New Rochelle). 2018 Jul 1;7(7):232–46.

274. Moon JJ, Saik JE, Poché RA, Leslie-Barbick JE, Lee SH, Smith AA, et al. Biomimetic hydrogels with pro-angiogenic properties. Biomaterials. 2010 May;31(14):3840–7.

275. Holnthoner W, Banfi A, Kirkpatrick J, Redl H. Vascularization for Tissue Engineering and Regenerative Medicine [Internet]. 2021. Available from: http://www.springer.com/series/13441

276. Dellaquila A, Le Bao C, Letourneur D, Simon-Yarza T. In Vitro Strategies to Vascularize 3D Physiologically Relevant Models. Vol. 8, Advanced Science. John Wiley and Sons Inc; 2021.

277. Blache U, Metzger S, Vallmajo-Martin Q, Martin I, Djonov V, Ehrbar M. Dual Role of Mesenchymal Stem Cells Allows for Microvascularized Bone Tissue-Like Environments in PEG Hydrogels. Adv Healthc Mater. 2016 Feb 18;5(4):489–98.

278. Martino MM, Brkic S, Bovo E, Burger M, Schaefer DJ, Wolff T, et al. Extracellular matrix and growth factor engineering for controlled angiogenesis in regenerative medicine. Vol. 3, Frontiers in Bioengineering and Biotechnology. Frontiers Media S.A.; 2015.

279. Blache U, Vallmajo-Martin Q, Horton ER, Guerrero J, Djonov V, Scherberich A, et al. Notch-inducing hydrogels reveal a perivascular switch of mesenchymal stem cell fate. EMBO Rep. 2018 Aug;19(8).

280. Taubenberger A V., Bray LJ, Haller B, Shaposhnykov A, Binner M, Freudenberg U, et al. 3D extracellular matrix interactions modulate tumour cell growth, invasion and angiogenesis in engineered tumour microenvironments. Acta Biomater. 2016 May 1;36:73–85.

281. Chang J, Chaudhuri O. Beyond proteases: Basement membrane mechanics and cancer invasion. Journal of Cell Biology. 2019 Aug 5;218(8):2456–69.

282. Ehrbar M, Rizzi SC, Hlushchuk R, Djonov V, Zisch AH, Hubbell JA, et al. Enzymatic formation of modular cell-instructive fibrin analogs for tissue engineering. Biomaterials. 2007 Sep;28(26):3856–66.

283. Simona BR, Hirt L, Demkó L, Zambelli T, Vörös J, Ehrbar M, et al. Density gradients at hydrogel interfaces for enhanced cell penetration. Biomater Sci. 2015 Apr 1;3(4):586–91.

284. Zhang N, Milleret V, Thompson-Steckel G, Huang NP, Vörös J, Simona BR, et al. Soft Hydrogels Featuring In-Depth Surface Density Gradients for the Simple Establishment of 3D Tissue Models for Screening Applications. SLAS Discovery. 2017 Jun 1;22(5):635–44.

285. Ehrbar M, Sala A, Lienemann P, Ranga A, Mosiewicz K, Bittermann A, et al. Elucidating the role of matrix stiffness in 3D cell migration and remodeling. Biophys J. 2011 Jan 19;100(2):284–93.

286. Chrisnandy A, Blondel D, Rezakhani S, Broguiere N, Lutolf MP. Synthetic dynamic hydrogels promote degradation-independent in vitro organogenesis. Nat Mater. 2022 Apr 1;21(4):479–87.

287. Rebecca VW, Somasundaram R, Herlyn M. Pre-clinical modeling of cutaneous melanoma. Nat Commun [Internet]. 2020/06/07. 2020;11(1):2858. Available from: https://www.ncbi.nlm.nih.gov/pubmed/32504051

288. Hill DS, Robinson ND, Caley MP, Chen M, O'Toole EA, Armstrong JL, et al. A Novel Fully Humanized 3D Skin Equivalent to Model Early Melanoma Invasion. Mol Cancer Ther [Internet]. 2015/09/04. 2015;14(11):2665–73. Available from: https://www.ncbi.nlm.nih.gov/pubmed/26330548

289. Pupovac A, Senturk B, Griffoni C, Maniura-Weber K, Rottmar M, McArthur SL. Toward Immunocompetent 3D Skin Models. Adv Healthc Mater [Internet]. 2018/03/16. 2018;7(12):e1701405. Available from: https://www.ncbi.nlm.nih.gov/pubmed/29542274

290. Michielon E, López González M, Stolk DA, Stolwijk JGC, Roffel S, Waaijman T, et al. A Reconstructed Human Melanoma-in-Skin Model to Study Immune Modulatory and Angiogenic Mechanisms Facilitating Initial Melanoma Growth and Invasion. Cancers (Basel). 2023 May 20;15(10):2849.

291. Vörsmann H, Groeber F, Walles H, Busch S, Beissert S, Walczak H, et al. Development of a human three-dimensional organotypic skin-melanoma spheroid model for in vitro drug testing. Vol. 4, Cell Death and Disease. 2013.

292. Bourland J, Fradette J, Auger FA. Tissue-engineered 3D melanoma model with blood and lymphatic capillaries for drug development [Internet]. Vol. 8, Scientific Reports. 2018. p. 1–13. Available from: https://www.nature.com/articles/s41598-018-31502-6.pdf

293. Drost J, Clevers H. Organoids in cancer research [Internet]. Vol. 18, Nature Reviews Cancer. Springer US; 2018. p. 407–18. Available from: https://www.nature.com/articles/s41568-018-0007-6

294. David Tuveson and HC. Cancer modeling meets human organoid technology. 2019;

295. Neal JT, Li X, Zhu J, Giangarra V, Grzeskowiak CL, Ju J, et al. Organoid Modeling of the Tumor Immune Microenvironment [Internet]. Vol. 175, Cell. Elsevier Inc.; 2018. p. 1972-

1988.e16. Available from: https://www.ncbi.nlm.nih.gov/pmc/articles/PMC6656687/pdf/nihms-1516243.pdf

296. Gunti S, Hoke ATK, Vu KP, London Jr. NR. Organoid and Spheroid Tumor Models: Techniques and Applications. Cancers (Basel) [Internet]. 2021/03/07. 2021;13(4). Available from: https://www.ncbi.nlm.nih.gov/pubmed/33669619

297. Votanopoulos KI, Forsythe S, Sivakumar H, Mazzocchi A, Aleman J, Miller L, et al. Model of Patient-Specific Immune-Enhanced Organoids for Immunotherapy Screening: Feasibility Study. Vol. 27, Annals of Surgical Oncology. Springer International Publishing; 2020. p. 1956–67.

298. Brassard-Jollive N, Monnot C, Muller L, Germain S. In vitro 3D Systems to Model Tumor Angiogenesis and Interactions With Stromal Cells. Vol. 8, Frontiers in Cell and Developmental Biology. Frontiers Media S.A.; 2020.

299. Singh N, Vayer P, Tanwar S, Poyet JL, Tsaioun K, Villoutreix BO. Drug discovery and development: introduction to the general public and patient groups. Frontiers in Drug Discovery. 2023 May 24;3.

300. Hughes J, Rees S, Kalindjian S, Philpott K. Principles of early drug discovery. Br J Pharmacol. 2011 Mar 22;162(6):1239–49.

301. Mohs RC, Greig NH. Drug discovery and development: Role of basic biological research. Alzheimer's & Dementia: Translational Research & Clinical Interventions. 2017 Nov 10;3(4):651–7.

302. Kulkarni VS, Alagarsamy V, Solomon VR, Jose PA, Murugesan S. Drug Repurposing: An Effective Tool in Modern Drug Discovery. Russ J Bioorg Chem. 2023 Apr 21;49(2):157–66.

303. Pushpakom S, Iorio F, Eyers PA, Escott KJ, Hopper S, Wells A, et al. Drug repurposing: progress, challenges and recommendations. Nat Rev Drug Discov. 2019 Jan 12;18(1):41–58.

304. Blay V, Tolani B, Ho SP, Arkin MR. High-Throughput Screening: today's biochemical and cell-based approaches. Drug Discov Today. 2020 Oct;25(10):1807–21.

305. Szymański P, Markowicz M, Mikiciuk-Olasik E. Adaptation of high-throughput screening in drug discovery-toxicological screening tests. Vol. 13, International Journal of Molecular Sciences. MDPI AG; 2012. p. 427–52.

306. An WF, Tolliday N. Cell-Based Assays for High-Throughput Screening. Mol Biotechnol. 2010 Jun 12;45(2):180–6.

307. Chiaravalli J, Glickman JF. A High-Content Live-Cell Viability Assay and Its Validation on a Diverse 12K Compound Screen. SLAS Discovery. 2017 Oct;22(9):1120–30.

308. Zanella F, Lorens JB, Link W. High content screening: Seeing is believing. Vol. 28, Trends in Biotechnology. 2010. p. 237–45.

309. Asli N. Goktug, Sergio C. Chai, and Taosheng Chen. Data Analysis Approaches in High Throughput Screening. In: Drug Discovery. InTech; 2013.

310. Malo N, Hanley JA, Cerquozzi S, Pelletier J, Nadon R. Statistical practice in high-throughput screening data analysis. Nat Biotechnol. 2006;24(2):167–75.

311. Varbanov HP, Kuttler F, Banfi D, Turcatti G, Dyson PJ. Repositioning approved drugs for the treatment of problematic cancers using a screening approach. PLoS One. 2017 Feb 1;12(2).

312. Kota S, Hou S, Guerrant W, Madoux F, Troutman S, Fernandez-Vega V, et al. A novel three-dimensional high-throughput screening approach identifies inducers of a mutant KRAS selective lethal phenotype. Oncogene. 2018 Aug 9;37(32):4372–84.

313. Nierode G, Kwon PS, Dordick JS, Kwon SJ. Cell-Based Assay Design for High-Content Screening of Drug Candidates. J Microbiol Biotechnol. 2016 Feb 28;26(2):213–25.

314. Brancato V, Oliveira JM, Correlo VM, Reis RL, Kundu SC. Could 3D models of cancer enhance drug screening? Vol. 232, Biomaterials. Elsevier Ltd; 2020.

315. Angeli C, Wroblewska JP, Klein E, Margue C, Kreis S. Protocol to generate scaffold-free, multicomponent 3D melanoma spheroid models for preclinical drug testing. STAR Protoc [Internet]. 2024 Jun;5(2):103058. Available from: https://linkinghub.elsevier.com/retrieve/pii/S2666166724002235

316. Raaijmakers MI, Widmer DS, Maudrich M, Koch T, Langer A, Flace A, et al. A new live-cell biobank workflow efficiently recovers heterogeneous melanoma cells from native biopsies. Exp Dermatol [Internet]. 2015/03/06. 2015;24(5):377–80. Available from: https://www.ncbi.nlm.nih.gov/pubmed/25739758

317. Margue C, Philippidou D, Kozar I, Cesi G, Felten P, Kulms D, et al. Kinase inhibitor library screening identifies synergistic drug combinations effective in sensitive and resistant melanoma cells [Internet]. Vol. 38, Journal of Experimental and Clinical Cancer Research. Journal of Experimental & Clinical Cancer Research; 2019. p. 1–17. Available from: https://jeccr.biomedcentral.com/track/pdf/10.1186/s13046-019-1038-x.pdf

318. Haan C, Behrmann I. A cost effective non-commercial ECL-solution for Western blot detections yielding strong signals and low background. J Immunol Methods. 2007 Jan;318(1–2):11–9.

319. Cesi G, Walbrecq G, Zimmer A, Kreis S, Haan C. ROS production induced by BRAF inhibitor treatment rewires metabolic processes affecting cell growth of melanoma cells. Mol Cancer. 2017 Dec 8;16(1):102.

320. Munro MJ, Tan ST, Gray C. Applications for Colon Organoid Models in Cancer Research. Organoids. 2023 Jan 12;2(1):37–49.

321. Wuputra K, Ku CC, Kato K, Wu DC, Saito S, Yokoyama KK. Translational models of 3-D organoids and cancer stem cells in gastric cancer research. Stem Cell Res Ther. 2021 Dec 6;12(1):492.

322. Kurosawa H. Application of Rho-associated protein kinase (ROCK) inhibitor to human pluripotent stem cells. J Biosci Bioeng. 2012 Dec;114(6):577–81.

323. Conery AR, Luo K. SMAD proteins in apoptotic and survival signaling. 2006.

324. Ludwig BS, Kessler H, Kossatz S, Reuning U. RGD-Binding Integrins Revisited: How Recently Discovered Functions and Novel Synthetic Ligands (Re-)Shape an Ever-Evolving Field. Cancers (Basel). 2021 Apr 4;13(7):1711.

325. Simons M, Gordon E, Claesson-Welsh L. Mechanisms and regulation of endothelial VEGF receptor signalling. Vol. 17, Nature Reviews Molecular Cell Biology. Nature Publishing Group; 2016. p. 611–25.

326. Lilly E, Markossian S, Grossman A, Arkin M, Auld D, Austin C, et al. Assay Guidance Manual [Internet]. 2014. Available from: https://ncats.nih.gov/expertise/preclinical/agm.

327. Edmondson R, Broglie JJ, Adcock AF, Yang L. Three-Dimensional Cell Culture Systems and Their Applications in Drug Discovery and Cell-Based Biosensors. Assay Drug Dev Technol. 2014 May;12(4):207–18.

328. Buzun K, Bielawska A, Bielawski K, Gornowicz A. DNA topoisomerases as molecular targets for anticancer drugs. Vol. 35, Journal of Enzyme Inhibition and Medicinal Chemistry. Taylor and Francis Ltd.; 2020. p. 1781–99.

329. Marine JC, Dawson SJ, Dawson MA. Non-genetic mechanisms of therapeutic resistance in cancer. Nat Rev Cancer [Internet]. 2020/10/10. 2020;20(12):743–56. Available from: https://www.ncbi.nlm.nih.gov/pubmed/33033407

330. Rubanov A, Berico P, Hernando E. Epigenetic Mechanisms Underlying Melanoma Resistance to Immune and Targeted Therapies. Cancers (Basel). 2022 Nov 28;14(23):5858.

331. Mielczarek-Lewandowska A, Hartman ML, Czyz M. Inhibitors of HSP90 in melanoma. Apoptosis. 2020 Feb 28;25(1–2):12–28.

332. Anvekar RA, Asciolla JJ, Missert DJ, Chipuk JE. Born to be Alive: A Role for the BCL-2 Family in Melanoma Tumor Cell Survival, Apoptosis, and Treatment. Front Oncol. 2011;1.

333. Kumavath R, Paul S, Pavithran H, Paul MK, Ghosh P, Barh D, et al. Emergence of cardiac glycosides as potential drugs: Current and future scope for cancer therapeutics. Vol. 11, Biomolecules. MDPI AG; 2021.

334. Schneider NFZ, Cerella C, Simões CMO, Diederich M. Anticancer and Immunogenic Properties of Cardiac Glycosides. Vol. 22, Molecules. MDPI AG; 2017.

335. Prassas I, Diamandis EP. Novel therapeutic applications of cardiac glycosides. Vol. 7, Nature Reviews Drug Discovery. 2008. p. 926–35.

336. Eskiocak U, Ramesh V, Gill JG, Zhao Z, Yuan SW, Wang M, et al. Synergistic effects of ion transporter and MAP kinase pathway inhibitors in melanoma. Nat Commun. 2016 Aug 22;7.

337. Soumoy L, Genbauffe A, Mouchart L, Sperone A, Trelcat A, Mukeba-Harchies L, et al. ATP1A1 is a promising new target for melanoma treatment and can be inhibited by its physiological ligand bufalin to restore targeted therapy efficacy. Cancer Cell Int. 2024 Dec 1;24(1).

338. Mathieu V, Pirker C, Martin de Lassalle E, Vernier M, Mijatovic T, DeNeve N, et al. The sodium pump α1 sub-unit: A disease progression-related target for metastatic melanoma treatment. J Cell Mol Med. 2009 Sep;13(9 B):3960–72.

339. Spengler G, Csonka Á, Molnár J, Amaral L. The anticancer activity of the old neuroleptic phenothiazine-type drug thioridazine. Vol. 36, Anticancer Research. International Institute of Anticancer Research; 2016. p. 5701–6.

340. Moura C, Vale N. The Role of Dopamine in Repurposing Drugs for Oncology. Vol. 11, Biomedicines. Multidisciplinary Digital Publishing Institute (MDPI); 2023.

341. Lopes D, Maiato H. The Tubulin Code in Mitosis and Cancer. Cells. 2020 Oct 26;9(11):2356.

342. Zhang J, Zhang Y, Liu J, Luo J, Yun Y, Cao Y. Identification of TUBB4A as a Prognostic Biomarker of Melanoma by Transcriptomic Data and *In Vitro* Experiments. Technol Cancer Res Treat. 2023 Jan 12;22.

343. Zablocka T, Kreismane M, Pjanova D, Isajevs S. Effects of BRAF V600E and NRAS mutational status on the progression-free survival and clinicopathological characteristics of patients with melanoma. Oncol Lett. 2023 Jan 1;25(1).

344. Meraz-Torres F, Niessner H, Plöger S, Riel S, Schörg B, Casadei N, et al. Augmenting MEK inhibitor efficacy in BRAF wild-type melanoma: synergistic effects of disulfiram combination therapy. Journal of Experimental and Clinical Cancer Research. 2024 Dec 1;43(1).

345. Falchook GS, Lewis KD, Infante JR, Gordon MS, Vogelzang NJ, DeMarini DJ, et al. Activity of the oral MEK inhibitor trametinib in patients with advanced melanoma: A phase 1 dose-escalation trial. Lancet Oncol. 2012 Aug;13(8):782–9.

346. Chatterjee A, Paul S, Bisht B, Bhattacharya S, Sivasubramaniam S, Paul MK. Advances in targeting the WNT/β-catenin signaling pathway in cancer. Drug Discov Today. 2022 Jan 1;27(1):82–101.

347. Gajos-Michniewicz A, Czyz M. Wnt signaling in melanoma. Vol. 21, International Journal of Molecular Sciences. MDPI AG; 2020. p. 1–31.

348. Koni M, Pinnarò V, Brizzi MF. The wnt signalling pathway: A tailored target in cancer. Vol. 21, International Journal of Molecular Sciences. MDPI AG; 2020. p. 1–26.

349. Spranger S, Bao R, Gajewski TF. Melanoma-intrinsic β-catenin signalling prevents anti-tumour immunity. Nature. 2015 Jul 9;523(7559):231–5.

350. Mattioli R, Ilari A, Colotti B, Mosca L, Fazi F, Colotti G. Doxorubicin and other anthracyclines in cancers: Activity, chemoresistance and its overcoming. Mol Aspects Med. 2023 Oct 1;93.

351. Christopher W. Schultz, Avinoam Nevler. Pyrvinium Pamoate: Past, Present, and Future as an Anti-Cancer Drug. Biomedicines. 2022;

352. Elmore S. Apoptosis: A Review of Programmed Cell Death. Toxicol Pathol. 2007;

353. Solano-Galvez SG, Abadi-Chiriti J, Gutierrez-Velez L, Rodriguez-Puente E, Konstat-Korzenny E, Alvarez-Hernandez DA, et al. Apoptosis: Activation and Inhibition in Health and Disease. Med Sci (Basel) [Internet]. 2018/07/06. 2018;6(3). Available from: https://www.ncbi.nlm.nih.gov/pubmed/29973578

354. Vitale C, Marzagalli M, Scaglione S, Dondero A, Bottino C, Castriconi R. Tumor Microenvironment and Hydrogel-Based 3D Cancer Models for In Vitro Testing Immunotherapies. Cancers (Basel). 2022 Feb 1;14(4).

355. Matias M, Pinho JO, Penetra MJ, Campos G, Reis CP, Gaspar MM. The challenging melanoma landscape: From early drug discovery to clinical approval. Vol. 10, Cells. MDPI; 2021.

356. Patton EE, Mueller KL, Adams DJ, Anandasabapathy N, Aplin AE, Bertolotto C, et al. Melanoma models for the next generation of therapies. Cancer Cell [Internet]. 2021 May;39(5):610–31. Available from: https://linkinghub.elsevier.com/retrieve/pii/S1535610821000556

357. Nomdedeu-Sancho G, Gorkun A, Mahajan N, Willson K, Schaaf CR, Votanopoulos KI, et al. In Vitro Three-Dimensional (3D) Models for Melanoma Immunotherapy. Vol. 15, Cancers. Multidisciplinary Digital Publishing Institute (MDPI); 2023.

358. Morales D, Vigneron P, Ferreira I, Hamitou W, Magnano M, Mahenthiran L, et al. Fibroblasts Influence Metastatic Melanoma Cell Sensitivity to Combined BRAF and MEK Inhibition. Cancers (Basel) [Internet]. 2021/10/14. 2021;13(19). Available from: https://www.ncbi.nlm.nih.gov/pubmed/34638245

359. Morales D, Lombart F, Truchot A, Maire P, Hussein M, Hamitou W, et al. 3D Coculture Models Underline Metastatic Melanoma Cell Sensitivity to Vemurafenib. Tissue Eng Part A [Internet]. 2018/12/07. 2019;25(15–16):1116–26. Available from: https://www.ncbi.nlm.nih.gov/pubmed/30501565

360. Hashemi G, Dight J, Khosrotehrani K, Sormani L. Melanoma Tumour Vascularization and Tissue-Resident Endothelial Progenitor Cells. Vol. 14, Cancers. MDPI; 2022.

361. Cho WC, Jour G, Aung PP. Role of angiogenesis in melanoma progression: Update on key angiogenic mechanisms and other associated components. Vol. 59, Seminars in Cancer Biology. Academic Press; 2019. p. 175–86.

362. Caulfield JI, Kluger HM. Emerging Studies of Melanoma Brain Metastasis. Vol. 24, Current Oncology Reports. Springer; 2022. p. 585–94.

363. Hasanov M, Acikgoz Y, Davies MA. Melanoma Brain Metastasis. Hematol Oncol Clin North Am. 2024 Oct;38(5):1027–43.

364. Wang X, Ji Q, Yan X, Lian B, Si L, Chi Z, et al. The Impact of Liver Metastasis on Anti-PD-1 Monoclonal Antibody Monotherapy in Advanced Melanoma: Analysis of Five Clinical Studies. Front Oncol. 2020 Sep 29;10.

365. Novotny J, Strnadova K, Dvorankova B, Kocourkova S, Jaksa R, Dundr P, et al. Single-Cell RNA Sequencing Unravels Heterogeneity of the Stromal Niche in Cutaneous Melanoma Heterogeneous Spheroids. Cancers (Basel) [Internet]. 2020/11/14. 2020;12(11). Available from: https://www.ncbi.nlm.nih.gov/pubmed/33182777

366. Kaur A, Ecker BL, Douglass SM, Kugel 3rd CH, Webster MR, Almeida F V, et al. Remodeling of the Collagen Matrix in Aging Skin Promotes Melanoma Metastasis and Affects Immune Cell Motility. Cancer Discov [Internet]. 2018/10/04. 2019;9(1):64–81. Available from: https://www.ncbi.nlm.nih.gov/pubmed/30279173

367. Jobe NP, Zivicova V, Mifkova A, Rosel D, Dvorankova B, Kodet O, et al. Fibroblasts potentiate melanoma cells in vitro invasiveness induced by UV-irradiated keratinocytes. Histochem Cell Biol [Internet]. 2018/02/13. 2018;149(5):503–16. Available from: https://www.ncbi.nlm.nih.gov/pubmed/29435761

368. Loos B, Salas-Bastos A, Nordin A, Debbache J, Stierli S, Cheng PF, et al. TGFβ signaling sensitizes MEKi-resistant human melanoma to targeted therapy-induced apoptosis. Cell Death Dis [Internet]. 2024 Dec 21;15(12):925. Available from: https://www.nature.com/articles/s41419-024-07305-1

369. Kamm DR, McCommis KS. Hepatic stellate cells in physiology and pathology. Journal of Physiology. 2022 Apr 1;600(8):1825–37.

370. Fane ME, Chhabra Y, Alicea GM, Maranto DA, Douglass SM, Webster MR, et al. Stromal changes in the aged lung induce an emergence from melanoma dormancy. Nature. 2022 Jun 9;606(7913):396–405.

371. Kaur A, Webster MR, Marchbank K, Behera R, Ndoye A, Kugel CH, et al. SFRP2 in the aged microenvironment drives melanoma metastasis and therapy resistance. Nature. 2016 Apr 14;532(7598):250–4.

372. Piquet L, Dewit L, Schoonjans N, Millet M, Bérubé J, Gerges PRA, et al. Synergic interactions between hepatic stellate cells and uveal melanoma in metastatic growth. Cancers (Basel). 2019 Aug 1;11(8).

373. Olaso E, Salado C, Egilegor E, Gutierrez V, Santisteban A, Sancho-Bru P, et al. Proangiogenic role of tumor-activated hepatic stellate cells in experimental melanoma metastasis. Hepatology. 2003 Mar 1;37(3):674–85.

374. Franchi-Mendes T, Lopes N, Brito C. Heterotypic Tumor Spheroids in Agitation-Based Cultures: A Scaffold-Free Cell Model That Sustains Long-Term Survival of Endothelial Cells. Front Bioeng Biotechnol [Internet]. 2021/06/29. 2021;9:649949. Available from: https://www.ncbi.nlm.nih.gov/pubmed/34178955

375. Chiew GGY, Wei N, Sultania S, Lim S, Luo KQ. Bioengineered three-dimensional co-culture of cancer cells and endothelial cells: A model system for dual analysis of tumor growth and angiogenesis. Biotechnol Bioeng [Internet]. 2017/04/04. 2017;114(8):1865–77. Available from: https://www.ncbi.nlm.nih.gov/pubmed/28369747

376. Lazzari G, Nicolas V, Matsusaki M, Akashi M, Couvreur P, Mura S. Multicellular spheroid based on a triple co-culture: A novel 3D model to mimic pancreatic tumor complexity. Acta Biomater [Internet]. 2018/08/14. 2018;78:296–307. Available from: https://www.ncbi.nlm.nih.gov/pubmed/30099198

377. Shoval H, Karsch-Bluman A, Brill-Karniely Y, Stern T, Zamir G, Hubert A, et al. Tumor cells and their crosstalk with endothelial cells in 3D spheroids. Sci Rep [Internet]. 2017/09/07. 2017;7(1):10428. Available from: https://www.ncbi.nlm.nih.gov/pubmed/28874803

378. Rama-Esendagli D, Esendagli G, Yilmaz G, Guc D. Spheroid formation and invasion capacity are differentially influenced by co-cultures of fibroblast and macrophage cells in breast cancer. Mol Biol Rep. 2014;41(5):2885–92.

379. Saleh NA, Rode MP, Sierra JA, Silva AH, Miyake JA, Filippin-Monteiro FB, et al. Three-dimensional multicellular cell culture for anti-melanoma drug screening: focus on tumor microenvironment. Cytotechnology [Internet]. 2021/01/29. 2021;73(1):35–48. Available from: https://www.ncbi.nlm.nih.gov/pubmed/33505112

380. Cogliati B, Yashaswini CN, Wang S, Sia D, Friedman SL. Friend or foe? The elusive role of hepatic stellate cells in liver cancer. Vol. 20, Nature Reviews Gastroenterology and Hepatology. Nature Research; 2023. p. 647–61.

381. Raskov H, Orhan A, Christensen JP, Gögenur I. Cytotoxic CD8+ T cells in cancer and cancer immunotherapy. Vol. 124, British Journal of Cancer. Springer Nature; 2021. p. 359–67.

382. Tay RE, Richardson EK, Toh HC. Revisiting the role of CD4+ T cells in cancer immunotherapy—new insights into old paradigms. Vol. 28, Cancer Gene Therapy. Springer Nature; 2021. p. 5–17.

383. Dilshat R, Fock V, Kenny C, Gerritsen I, Lasseur RMJ, Travnickova J, et al. Mitf reprograms the extracellular matrix and focal adhesion in melanoma. Elife. 2021;10:1–59.

384. LeSavage BL, Suhar RA, Broguiere N, Lutolf MP, Heilshorn SC. Next-generation cancer organoids. Vol. 21, Nature Materials. Nature Research; 2022. p. 143–59.

385. Lutolf MP, Lauer-Fields JL, Schmoekel HG, Metters AT, Weber FE, Fields GB, et al. Synthetic matrix metalloproteinase-sensitive hydrogels for the conduction of tissue regeneration: Engineering cell-invasion characteristics [Internet]. Vol. 29, PNAS April. 2003. Available from: www.pnas.orgcgidoi10.1073pnas.0737381100

386. Chen W, Zhou Z, Chen D, Li Y, Zhang Q, Su J. Bone Regeneration Using MMP-Cleavable Peptides-Based Hydrogels. Gels. 2021 Nov 5;7(4):199.

387. Augustin RC, Luke JJ. Top advances of the year: Melanoma. Vol. 129, Cancer. John Wiley and Sons Inc; 2023. p. 822–8.

388. Salzmann M, Pawlowski J, Loquai C, Rafei-Shamsabadi DA, Meiss F, Ugurel S, et al. MEK inhibitors for pre-treated, NRAS-mutated metastatic melanoma: A multi-centre, retrospective study. Eur J Cancer. 2022 May 1;166:24–32.

389. Awada G, Dirven I, Schwarze JK, Tijtgat J, Fasolino G, Kockx M, et al. Phase II Clinical Trial of Trametinib and Low-Dose Dabrafenib in Advanced, Previously Treated BRAFV600 /NRASQ61 Wild-Type Melanoma (TraMel-WT). JCO Precis Oncol. 2024 Feb;(8).

390. Barbosa MAG, Xavier CPR, Pereira RF, Petrikaitė V, Vasconcelos MH. 3D Cell Culture Models as Recapitulators of the Tumor Microenvironment for the Screening of Anti-Cancer Drugs. Vol. 14, Cancers. MDPI; 2022.

391. Fröhlich E. Issues with Cancer Spheroid Models in Therapeutic Drug Screening. Curr Pharm Des. 2020 Jun 10;26(18):2137–48.

392. Wenzel C, Riefke B, Gründemann S, Krebs A, Christian S, Prinz F, et al. 3D high-content screening for the identification of compounds that target cells in dormant tumor spheroid regions. Exp Cell Res. 2014 Apr 15;323(1):131–43.

393. Mittler F, Obeïd P, Rulina A V., Haguet V, Gidrol X, Balakirev MY. High-content monitoring of drug effects in a 3D spheroid model. Front Oncol. 2017 Dec 11;7(DEC).

394. Li Q, Chen C, Kapadia A, Zhou Q, Harper MK, Schaack J, et al. 3D models of epithelial-mesenchymal transition in breast cancer metastasis: High-throughput screening assay development, validation, and pilot screen. J Biomol Screen. 2011 Feb;16(2):141–54.

395. Kessel S, Cribbes S, Déry O, Kuksin D, Sincoff E, Qiu J, et al. High-Throughput 3D Tumor Spheroid Screening Method for Cancer Drug Discovery Using Celigo Image Cytometry. SLAS Technol. 2017 Aug 1;22(4):454–65.

396. Ortiz Jordan LM, Vega VF, Shumate J, Peles A, Zeiger J, Scampavia L, et al. Protocol for high throughput 3D drug screening of patient derived melanoma and renal cell carcinoma. SLAS Discovery. 2024 Apr 1;29(3).

397. Sirenko O, Mitlo T, Hesley J, Luke S, Owens W, Cromwell EF. High-Content Assays for Characterizing the Viability and Morphology of 3D Cancer Spheroid Cultures. Assay Drug Dev Technol. 2015 Sep 1;13(7):402–14.

398. Simeonov A, Jadhav A, Thomas CJ, Wang Y, Huang R, Southall NT, et al. Fluorescence spectroscopic profiling of compound libraries. J Med Chem. 2008 Apr 24;51(8):2363–71.

399. Herman van Vlijmen, Jean-Yves Ortholand, Volkhart M.-J. Li, Jon S.B. de Vlieger. The European Lead Factory: An updated HTS compound library for innovative drug discovery. Drug Discov Today. 2021;

400. Herman van Vlijmen, Andrew D. Pannifer, Phil Cochrane, Steven P. van Helden, Jon S.B. de Vlieger, European Lead Factory Consortium. The European Lead Factory: Results from a decade of collaborative, public–private, drug discovery programs. Drug Discov Today. 2024;

401. Palve V, Liao Y, Remsing Rix LL, Rix U. Turning liabilities into opportunities: Off-target based drug repurposing in cancer. Vol. 68, Seminars in Cancer Biology. Academic Press; 2021. p. 209–29.

402. Zhang JH, Chung TDY, Oldenburg KR. A simple statistical parameter for use in evaluation and validation of high throughput screening assays. J Biomol Screen. 1999;4(2):67–73.

403. Posch C, Sanlorenzo M, Ma J, Kim ST, Zekhtser M, Ortiz-Urda S. MEK/CDK4,6 co-targeting is effective in a subset of NRAS, BRAF and “wild type” melanomas [Internet]. 2018. Available from: www.oncotarget.com

404. Garutti M, Targato G, Buriolla S, Palmero L, Minisini AM, Puglisi F. Cdk4/6 inhibitors in melanoma: A comprehensive review. Vol. 10, Cells. MDPI; 2021.

405. Gureghian V, Herbst H, Kozar I, Mihajlovic K, Malod-Dognin N, Ceddia G, et al. A multi-omics integrative approach unravels novel genes and pathways associated with senescence escape after targeted therapy in NRAS mutant melanoma. Cancer Gene Ther. 2023 Oct 1;30(10):1330–45.

406. Randic T, Magni S, Philippidou D, Margue C, Grzyb K, Preis JR, et al. Single-cell transcriptomics of NRAS-mutated melanoma transitioning to drug resistance reveals P2RX7 as an indicator of early drug response. Cell Rep. 2023 Jul;42(7):112696.

407. Maresca L, Stecca B, Carrassa L. Novel Therapeutic Approaches with DNA Damage Response Inhibitors for Melanoma Treatment. Vol. 11, Cells. MDPI; 2022.

408. Oo ZY, Stevenson AJ, Proctor M, Daignault SM, Walpole S, Lanagan C, et al. Endogenous replication stress marks melanomas sensitive to CHEK1 inhibitors in vivo. Clinical Cancer Research. 2018 Jun 15;24(12):2901–12.

409. Luo M, Liu Y, Liu N, Shao W, Ming L, Liu J, et al. Proscillaridin A inhibits hepatocellular carcinoma progression through inducing mitochondrial damage and autophagy. Acta Biochim Biophys Sin (Shanghai). 2021 Jan 1;53(1):19–28.

410. Huot M, Caron M, Richer C, Djibo R, Najmanovich R, St-Onge P, et al. Repurposing proscillaridin A in combination with decitabine against embryonal rhabdomyosarcoma RD cells. Cancer Chemother Pharmacol. 2021 Nov 1;88(5):845–56.

411. Semba M, Takamatsu S, Komazawa-Sakon S, Miyoshi E, Nishiyama C, Nakano H, et al. Proscillaridin A Sensitizes Human Colon Cancer Cells to TRAIL-Induced Cell Death. Int J Mol Sci. 2022 Jul 1;23(13).

412. Da Costa EM, Armaos G, McInnes G, Beaudry A, Moquin-Beaudry G, Bertrand-Lehouillier V, et al. Heart failure drug proscillaridin A targets MYC overexpressing leukemia through global loss of lysine acetylation. Journal of Experimental and Clinical Cancer Research. 2019 Jun 13;38(1).

413. Fang S, Tao H, Xia K, Guo W. Proscillaridin A induces apoptosis and inhibits the metastasis of osteosarcoma in vitro and in vivo. Biochem Biophys Res Commun. 2020 Jan 22;521(4):880–6.

414. Wang F, Liu L, Tong Y, Li L, Liu Y, Gao WQ. Proscillaridin A slows the prostate cancer progression through triggering the activation of endoplasmic reticulum stress. Cell Cycle. 2020 Mar 3;19(5):541–50.

415. Tsai JY, Weng CW, Lai YH, Tsai MF, Chen HY, Chen JJ. Proscillaridin A inhibits lung cancer cell growth and motility through downregulation of the EGFR-Src-associated pathway [Internet]. Vol. 13, Am J Cancer Res. 2023. Available from: www.ajcr.us/

416. Hou J, Kang N, Liu NN, Tan D, Zhang S, Liu J, et al. Proscillaridin A induces mitochondrial damage and autophagy in pancreatic cancer and reduces the stability of SMAD4 in Panc-1 cells. Ann Transl Med. 2022 Aug;10(15):820–820.

417. Saleem MZ, Alshwmi M, Zhang H, Din SRU, Nisar MA, Khan M, et al. Inhibition of JNK-Mediated Autophagy Promotes Proscillaridin A- Induced Apoptosis via ROS Generation, Intracellular Ca+2 Oscillation and Inhibiting STAT3 Signaling in Breast Cancer Cells. Front Pharmacol. 2020 Sep 4;11.

418. Ha DP, Tsai YL, Lee AS. Suppression of ER-stress induction of GRP78 as an anti-neoplastic mechanism of the cardiac glycoside Lanatoside C in pancreatic cancer: Lanatoside C suppresses GRP78 stress induction. Neoplasia (United States). 2021 Dec 1;23(12):1213–26.

419. Duan Y, Chen L, Shao J, Jiang C, Zhao Y, Li Y, et al. Lanatoside C inhibits human cervical cancer cell proliferation and induces cell apoptosis by a reduction of the JAK2/STAT6/SOCS2 signaling pathway. Oncol Lett. 2021 Aug 17;22(4).

420. Reddy D, Kumavath R, Ghosh P, Barh D. Lanatoside c induces g2/m cell cycle arrest and suppresses cancer cell growth by attenuating MAPK, wnt, JAK-STAT, and PI3K/AKT/mTOR signaling pathways. Biomolecules. 2019 Dec 1;9(12).

421. Hu Y, Yu K, Wang G, Zhang D, Shi C, Ding Y, et al. Lanatoside C inhibits cell proliferation and induces apoptosis through attenuating Wnt/β-catenin/c-Myc signaling pathway in human gastric cancer cell. Biochem Pharmacol. 2018 Apr 1;150:280–92.

422. Bejček J, Jurášek M, Spiwok V, Rimpelová S. Quo vadis cardiac glycoside research? Toxins (Basel). 2021;13(5).

423. Frankel AE, Eskiocak U, Gill JG, Yuan S, Ramesh V, Froehlich TW, et al. Digoxin Plus Trametinib Therapy Achieves Disease Control in BRAF Wild-Type Metastatic Melanoma Patients. Neoplasia (United States). 2017 Apr 1;19(4):255–60.

424. Kurzeder C, Nguyen-Sträuli BD, Krol I, Ring A, Castro-Giner F, Nüesch M, et al. Digoxin for reduction of circulating tumor cell cluster size in metastatic breast cancer: a proof-of-concept trial. Nat Med [Internet]. 2025 Jan 24; Available from: http://www.ncbi.nlm.nih.gov/pubmed/39856336

425. Maertens O, Kuzmickas R, Manchester HE, Emerson CE, Gavin AG, Guild CJ, et al. MAPK pathway suppression unmasks latent dna repair defects and confers a chemical synthetic vulnerability in BRAF-, NRAS-, and NF1 -mutant melanomas [Internet]. Vol. 9, Cancer Discovery. 2019. p. 526–45. Available from: https://cancerdiscovery.aacrjournals.org/content/candisc/9/4/526.full.pdf

426. Alqathama A. BRAF in malignant melanoma progression and metastasis: potentials and challenges [Internet]. Vol. 10, American journal of cancer research. 2020. p. 1103–14. Available from: https://www.ncbi.nlm.nih.gov/pmc/articles/PMC7191094/pdf/ajcr0010-1103.pdf

427. Eroglu Z, Chen A, Li J, Markowitz J, Brohl AS, Tetteh L, et al. Phase I study of vemurafenib (VEM) and cobimetinib (COB) with heat shock protein 90 (HSP90) inhibitor XL888 in advanced BRAFV600 mutant melanoma. Journal of Clinical Oncology. 2019 May 20;37(15_suppl):9553–9553.

428. Zhu L, Yang Q, Hu R, Li Y, Peng Y, Liu H, et al. Novel therapeutic strategy for melanoma based on albendazole and the CDK4/6 inhibitor palbociclib. Sci Rep. 2022 Apr 5;12(1):5706.

429. Aubel-Sadron G, Londos-Gagliardi D. Daunorubicin and doxorubicin, anthracycline antibiotics, a physicochemical and biological review. Vol. 66, BIOCHIMIE. 1984.

430. Wang H, Xiao X, Xiao Q, Lu Y, Wu Y. The efficacy and safety of daunorubicin versus idarubicin combined with cytarabine for induction therapy in acute myeloid leukemia: A meta-analysis of randomized clinical trials. Vol. 99, Medicine (United States). Lippincott Williams and Wilkins; 2020. p. E20094.

431. Evans-Roberts K, Maxwell A. DNA Topoisomerases. Lovett ST, editor. EcoSal Plus [Internet]. 2009 Dec 31;3(2). Available from: https://journals.asm.org/doi/10.1128/ecosalplus.4.4.9

432. Al-Aamri HM, Ku H, Irving HR, Tucci J, Meehan-Andrews T, Bradley C. Time dependent response of daunorubicin on cytotoxicity, cell cycle and DNA repair in acute lymphoblastic leukaemia. BMC Cancer. 2019 Feb 27;19(1).

433. Heestand GM, Schwaederle M, Gatalica Z, Arguello D, Kurzrock R. Topoisomerase expression and amplification in solid tumours: Analysis of 24,262 patients. Eur J Cancer. 2017 Sep;83:80–7.

434. Uusküla-Reimand L, Wilson MD. Untangling the roles of TOP2A and TOP2B in transcription and cancer [Internet]. Vol. 8. 2022. Available from: https://www.science.org

435. Cheng X, Wei Y, Deng L, Dong H, Wei H, Xie C, et al. Expression and biological significance of topoisomerase II α (TOP2A) in oral squamous cell carcinoma. Discover Oncology. 2024 Sep 10;15(1):423.

436. Mu XC, Tran TA, Ross JS, Carlson JA. Topoisomerase II-alpha expression in melanocytic nevi and malignant melanoma. J Cutan Pathol. 2000;27(5):242–8.

437. Roby P, Page M. Melanoma-specific cytotoxicity of a human MGSA/GRO alpha C-terminal peptide conjugated to daunorubicin. Oncol Rep. 1996 Jan 1;

438. Alrbyawi H, Poudel I, Annaji M, Boddu SHS, Arnold RD, Tiwari AK, et al. pH-Sensitive Liposomes for Enhanced Cellular Uptake and Cytotoxicity of Daunorubicin in Melanoma (B16-BL6) Cell Lines. Pharmaceutics. 2022 May 26;14(6):1128.

439. Tokarska K, Lamch Ł, Piechota B, Żukowski K, Chudy M, Wilk KA, et al. Co-delivery of IR-768 and daunorubicin using mPEG-b-PLGA micelles for synergistic enhancement of combination therapy of melanoma. J Photochem Photobiol B. 2020 Oct;211:111981.

440. Varatharajan S, Panetta JC, Abraham A, Karathedath S, Mohanan E, Lakshmi KM, et al. Population pharmacokinetics of Daunorubicin in adult patients with acute myeloid leukemia. Cancer Chemother Pharmacol. 2016 Nov 1;78(5):1051–8.

441. Latagliata R, Breccia M, Fazi P, Iacobelli S, Martinelli G, Di Raimondo F, et al. Liposomal daunorubicin versus standard daunorubicin: long-term follow-up of the GIMEMA GSI 103 AMLE randomized trial in patients older than 60 years with acute myelogenous leukemia. Br J Haematol. 2008 Dec 11;143(5):681–9.

442. Fassas A, Anagnostopoulos A. The use of liposomal daunorubicin (DaunoXome) in acute myeloid leukemia. Vol. 46, Leukemia and Lymphoma. 2005. p. 795–802.

443. Yang AS, Chapman PB. The History and Future of Chemotherapy for Melanoma. Vol. 23, Hematology/Oncology Clinics of North America. 2009. p. 583–97.

444. Tomitsuka E, Kita K, Esumi H. An anticancer agent, pyrvinium pamoate inhibits the NADH-fumarate reductase system-a unique mitochondrial energy metabolism in tumour microenvironments. J Biochem. 2012 Aug;152(2):171–83.

445. Schultz CW, McCarthy GA, Nerwal T, Nevler A, DuHadaway JB, McCoy MD, et al. The FDA-approved anthelmintic pyrvinium pamoate inhibits pancreatic cancer cells in nutrient-depleted conditions by targeting the mitochondria. Mol Cancer Ther. 2021 Nov 1;20(11):2166–76.

446. Aminzadeh-gohari S, Weber DD, Catalano L, Feichtinger RG, Kofler B, Lang R. Targeting mitochondria in melanoma. Biomolecules. 2020 Oct 1;10(10):1–21.

447. Fan J, Reid RR, He TC. Pyrvinium doubles against WNT-driven cancer. Vol. 298, Journal of Biological Chemistry. American Society for Biochemistry and Molecular Biology Inc.; 2022.

448. Zheng L, Liu Y, Pan J. Inhibitory effect of pyrvinium pamoate on uveal melanoma cells involves blocking of Wnt/β-catenin pathway. Acta Biochim Biophys Sin (Shanghai). 2017 Oct 1;49(10):890–8.

449. Cao X, Hou J, An Q, Assaraf YG, Wang X. Towards the overcoming of anticancer drug resistance mediated by p53 mutations. Vol. 49, Drug Resistance Updates. Churchill Livingstone; 2020.

450. Rudolf K, Cervinka M, Rudolf E. Dual inhibition of topoisomerases enhances apoptosis in melanoma cells. Neoplasma. 2010;57(4):316–24.

451. Lage, al. Modulation of DNA topoisomerase II activity and expression in melanoma cells with acquired drug resistance. 2000.

452. Kalal BS, Upadhya D, Pai VR. Chemotherapy resistance mechanisms in advanced skin cancer. Vol. 11, Oncology Reviews. Page Press Publications; 2017. p. 19–25.

453. Meier P, Legrand AJ, Adam D, Silke J. Immunogenic cell death in cancer: targeting necroptosis to induce antitumour immunity. Vol. 24, Nature Reviews Cancer. Nature Research; 2024. p. 299–315.

454. Galluzzi L, Vitale I, Aaronson SA, Abrams JM, Adam D, Agostinis P, et al. Molecular mechanisms of cell death: Recommendations of the Nomenclature Committee on Cell Death 2018. Vol. 25, Cell Death and Differentiation. Nature Publishing Group; 2018. p. 486–541.

455. Castaneda M, den Hollander P, Kuburich NA, Rosen JM, Mani SA. Mechanisms of cancer metastasis. Vol. 87, Seminars in Cancer Biology. Academic Press; 2022. p. 17–31.

456. Damsky WE, Rosenbaum LE, Bosenberg M. Decoding melanoma metastasis. Vol. 3, Cancers. 2011. p. 126–63.

457. Damsky WE, Theodosakis N, Bosenberg M. Melanoma metastasis: New concepts and evolving paradigms. Vol. 33, Oncogene. Nature Publishing Group; 2014. p. 2413–22.

458. Vultur A, Villanueva J, Krepler C, Rajan G, Chen Q, Xiao M, et al. MEK inhibition affects STAT3 signaling and invasion in human melanoma cell lines. Oncogene. 2014 Apr 3;33(14):1850–61.

459. Friedl P, Wolf K. Tumour-cell invasion and migration: Diversity and escape mechanisms. Vol. 3, Nature Reviews Cancer. 2003. p. 362–74.

460. Winkler J, Abisoye-Ogunniyan A, Metcalf KJ, Werb Z. Concepts of extracellular matrix remodelling in tumour progression and metastasis. Nat Commun. 2020 Dec 1;11(1).

461. Carrella D, Manni I, Tumaini B, Dattilo R, Papaccio F, Mutarelli M, et al. Computational drugs repositioning identifies inhibitors of oncogenic PI3K/AKT/P70S6K-dependent pathways among FDA-approved compounds. Oncotarget [Internet]. 2016;7(37). Available from: www.impactjournals.com/oncotarget/

462. Venerando A, Girardi C, Ruzzene M, Pinna LA. Pyrvinium pamoate does not activate protein kinase CK1, but promotes Akt/PKB down-regulation and GSK3 activation. Biochemical Journal. 2013 May 15;452(1):131–7.

463. Zheng W, Hu J, Lv Y, Bai B, Shan L, Chen K, et al. Pyrvinium pamoate inhibits cell proliferation through ROS-mediated AKT-dependent signaling pathway in colorectal cancer. Medical Oncology. 2021 Feb 1;38(2).

464. Momtazi-Borojeni AA, Abdollahi E, Ghasemi F, Caraglia M, Sahebkar A. The novel role of pyrvinium in cancer therapy. Vol. 233, Journal of Cellular Physiology. Wiley-Liss Inc.; 2018. p. 2871–81.

465. Liu R, Chen Y, Liu G, Li C, Song Y, Cao Z, et al. PI3K/AKT pathway as a key link modulates the multidrug resistance of cancers. Vol. 11, Cell Death and Disease. Springer Nature; 2020.

466. Mah LJ, El-Osta A, Karagiannis TC. γh2AX: A sensitive molecular marker of DNA damage and repair. Vol. 24, Leukemia. Nature Publishing Group; 2010. p. 679–86.

467. Pang B, Qiao X, Janssen L, Velds A, Groothuis T, Kerkhoven R, et al. Drug-induced histone eviction from open chromatin contributes to the chemotherapeutic effects of doxorubicin. Nat Commun. 2013;4.

468. Dugan MM, Perez MC, Karapetyan L, Zager JS. Combination Atezolizumab, Cobimetinib, and Vemurafenib as a Treatment Option in BRAF V600 Mutation–Positive Melanoma: Patient Selection and Perspectives. Vol. 16, Cancer Management and Research. Dove Medical Press Ltd; 2024. p. 933–9.

469. Adler NR, Wolfe R, Kelly JW, Haydon A, McArthur GA, McLean CA, et al. Tumour mutation status and sites of metastasis in patients with cutaneous melanoma. Br J Cancer. 2017 Sep 26;117(7):1026–35.

470. Forschner A, Nanz L, Maczey-Leber Y, Amaral T, Flatz L, Leiter U. Response and outcome of patients with melanoma skin metastases and immune checkpoint inhibition. Int J Cancer. 2024 Jan 1;

471. Wang X, Ji Q, Yan X, Lian B, Si L, Chi Z, et al. The Impact of Liver Metastasis on Anti-PD-1 Monoclonal Antibody Monotherapy in Advanced Melanoma: Analysis of Five Clinical Studies. Front Oncol. 2020 Sep 29;10.

472. Tumeh PC, Hellmann MD, Hamid O, Tsai KK, Loo KL, Gubens MA, et al. Liver metastasis and treatment outcome with anti-PD-1 monoclonal antibody in patients with melanoma and NSCLC. Cancer Immunol Res. 2017 May 1;5(5):417–24.

473. Lee JHJ, Lyle M, Menzies AM, Chan MMK, Lo S, Clements A, et al. Metastasis-specific patterns of response and progression with anti-PD-1 treatment in metastatic melanoma. Pigment Cell Melanoma Res. 2018 May 1;31(3):404–10.

474. Schmidt KM, Dietrich P, Hackl C, Guenzle J, Bronsert P, Wagner C, et al. Inhibition of mTORC2/RICTOR Impairs Melanoma Hepatic Metastasis. Neoplasia (United States). 2018 Dec 1;20(12):1198–208.

475. Johnson DB, Lovly CM, Flavin M, Panageas KS, Ayers GD, Zhao Z, et al. Impact of NRAS mutations for patients with advanced melanoma treated with immune therapies. Cancer Immunol Res. 2015 Mar 1;3(3):288–95.

476. Wolchok JD, Chiarion-Sileni V, Rutkowski P, Cowey CL, Schadendorf D, Wagstaff J, et al. Final, 10-Year Outcomes with Nivolumab plus Ipilimumab in Advanced Melanoma. New

England Journal of Medicine [Internet]. 2024 Sep 15; Available from: http://www.nejm.org/doi/10.1056/NEJMoa2407417

477. Zhang Z, Yu X, Wang Z, Wu P, Huang J. Anthracyclines potentiate anti-tumor immunity: A new opportunity for chemoimmunotherapy. Vol. 369, Cancer Letters. Elsevier Ireland Ltd; 2015. p. 331–5.

478. Haggerty TJ, Dunn IS, Rose LB, Newton EE, Martin S, Riley JL, et al. Topoisomerase inhibitors modulate expression of melanocytic antigens and enhance T cell recognition of tumor cells. Cancer Immunology, Immunotherapy. 2011 Jan;60(1):133–44.

479. Esumi H, Lu J, Kurashima Y, Hanaoka T. Antitumor activity of pyrvinium pamoate, 6-(dimethylamino)-2-[2-(2,5-dimethyl-1-phenyl-1 *H* -pyrrol-3-yl)ethenyl]-1-methyl-quinolinium pamoate salt, showing preferential cytotoxicity during glucose starvation. Cancer Sci. 2004 Aug 31;95(8):685–90.

480. Xu W, Lacerda L, Debeb BG, Atkinson RL, Solley TN, Li L, et al. The Antihelmintic Drug Pyrvinium Pamoate Targets Aggressive Breast Cancer. PLoS One. 2013 Aug 27;8(8).

481. Ponzini FM, Schultz CW, Leiby BE, Cannaday S, Yeo T, Posey J, et al. Repurposing the FDA-approved anthelmintic pyrvinium pamoate for pancreatic cancer treatment: Study protocol for a phase i clinical trial in early-stage pancreatic ductal adenocarcinoma. BMJ Open. 2023 Oct 17;13(10).

482. Murphy BM, Terrell EM, Chirasani VR, Weiss TJ, Lew RE, Holderbaum AM, et al. Enhanced BRAF engagement by NRAS mutants capable of promoting melanoma initiation. Nat Commun. 2022 Dec 1;13(1).

Appendix

1. Supplementary Figures

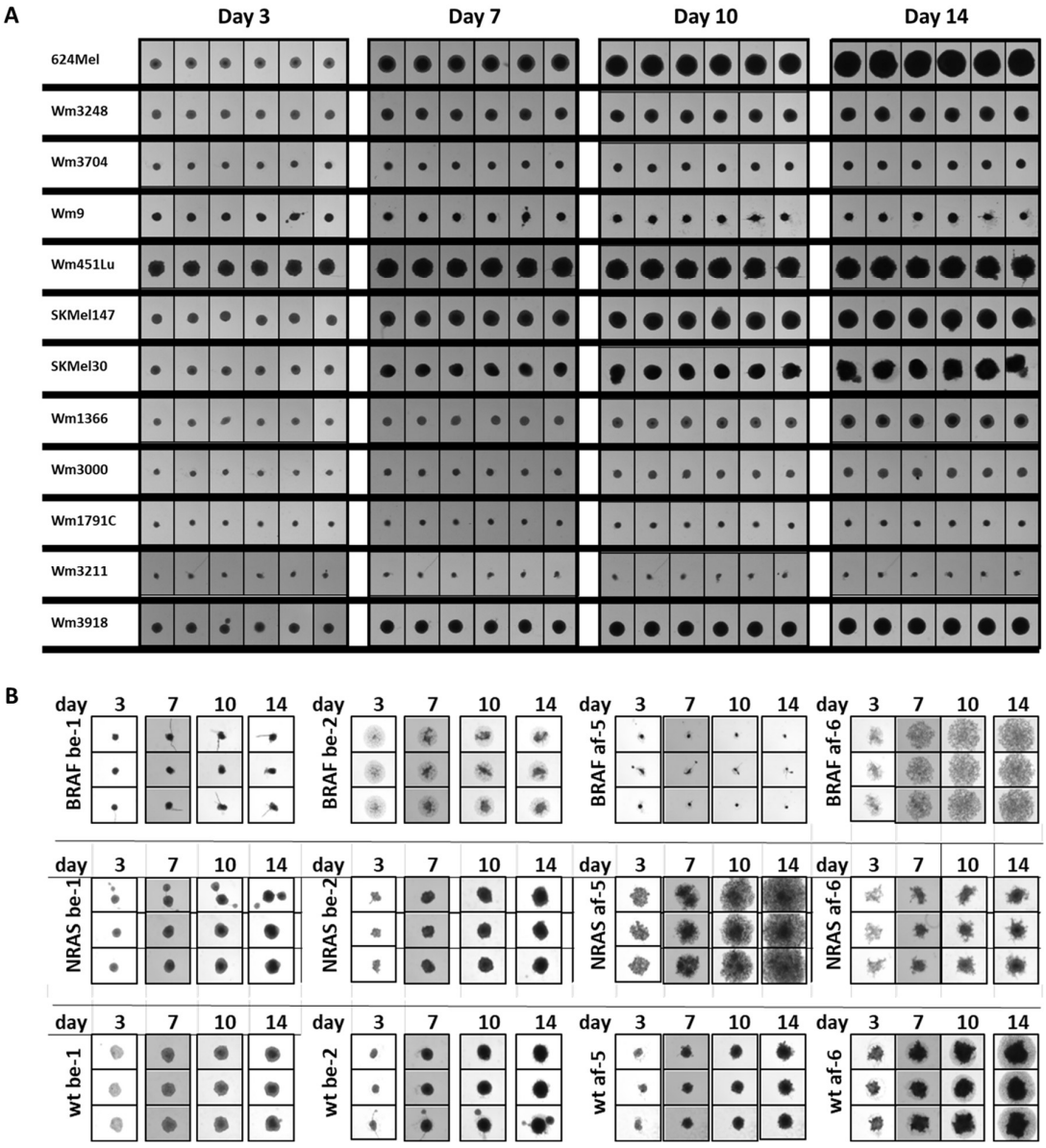

Suppl. Figure 1: A) Panel of BRAFmut, NRASmut, and WT commercially available melanoma cell lines tested for their sphere formation capacity and growth. Widefield pictures were acquired on days 3, 7, 10, and 14. B) Panel of BRAFmut, NRASmut, and WT primary metastatic melanoma cell lines tested for their sphere formation capacity and growth. Widefield pictures were acquired on days 3, 7, 10 and 14. NRAS be-1 is M160915, and NRAS be-2 is M161022.

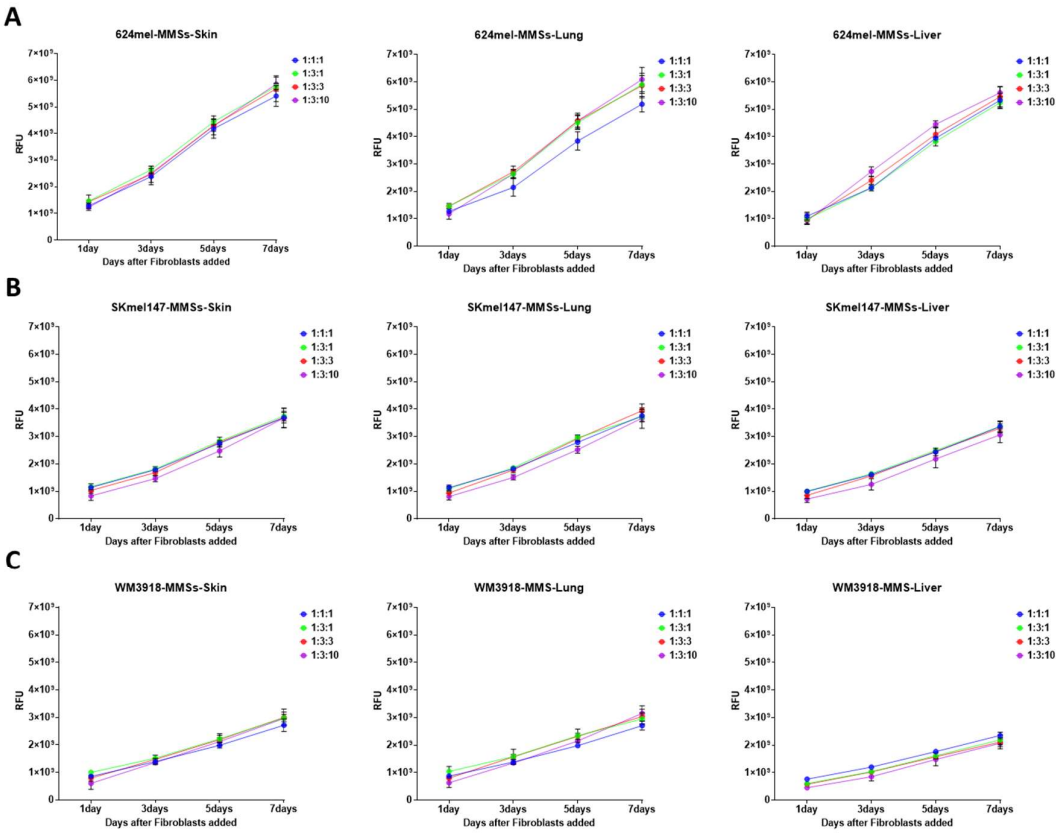

Suppl. Figure 2: Specific melanoma cell proliferation co-cultured with HMEC-1, and either NHDF (skin), MRC-5 (lung), or LX-2 (liver) at different cellular ratios. Melanoma cells were transduced to constitutively express fluorescent proteins, exploited to track their proliferation over time. A) 624mel, B) SKmel147, and C) WM3918.

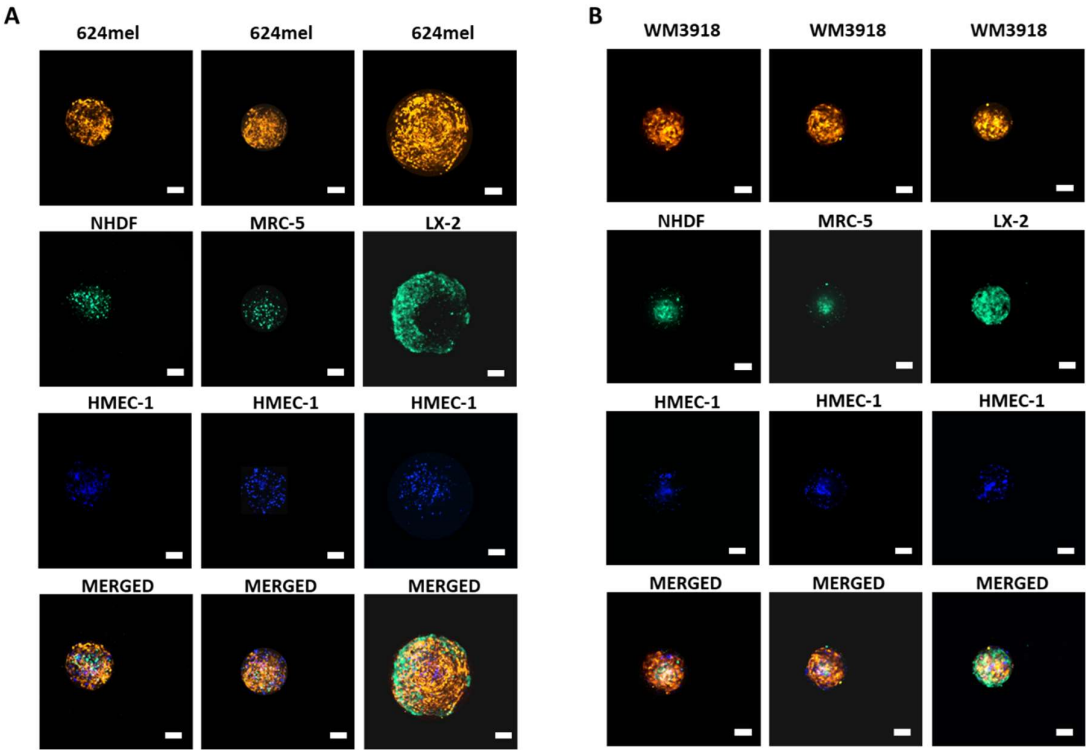

Suppl. Figure 3: Live-cell imaging of MMSs. (A) Cell lines constitutively expressing fluorescent proteins were used. Fluorescently labeled 624mel (orange-mCherry, (blue-BFP) HMEC-1, and either (green-GFP) NHDF, or MRC-5 or LX-2. Confocal images were taken at maximum intensity projections of multiple z-stacks. Objective 10x. Scale bar = 200 µm. (B) Cell lines constitutively expressing fluorescent proteins were used. Fluorescently labeled WM3918l (orange-mCherry, (blue-BFP) HMEC-1, and either (green-GFP) NHDF, or MRC-5 or LX-2. Confocal images were taken at maximum intensity projections of multiple z-stacks. Objective 10x. Scale bar = 200 µm.

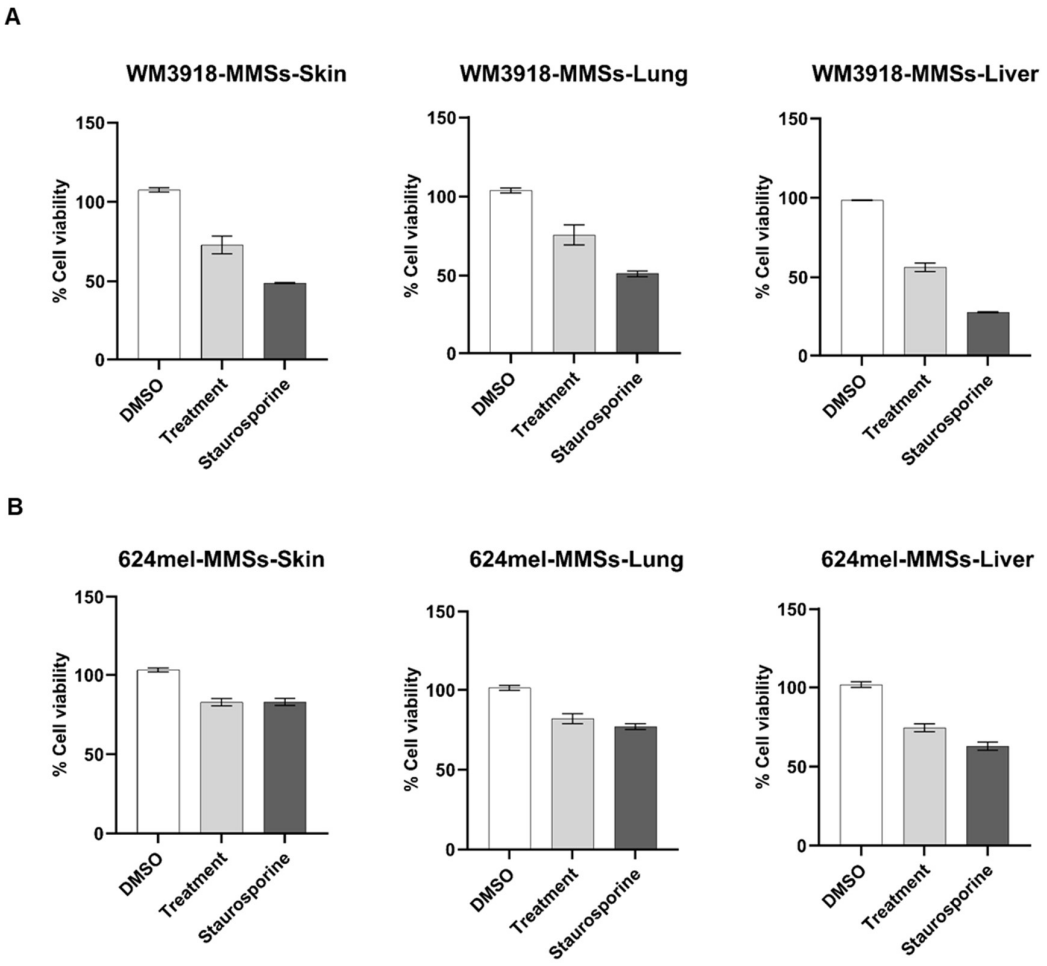

Suppl. Figure 4: MMSs viability measured after 96 hours from the beginning of the treatment. A) MMSs-Skin, -Lung, and –Liver using WM3918 as melanoma cells. B) MMSs-Skin, -Lung, and –Liver using 624mel as melanoma cells.

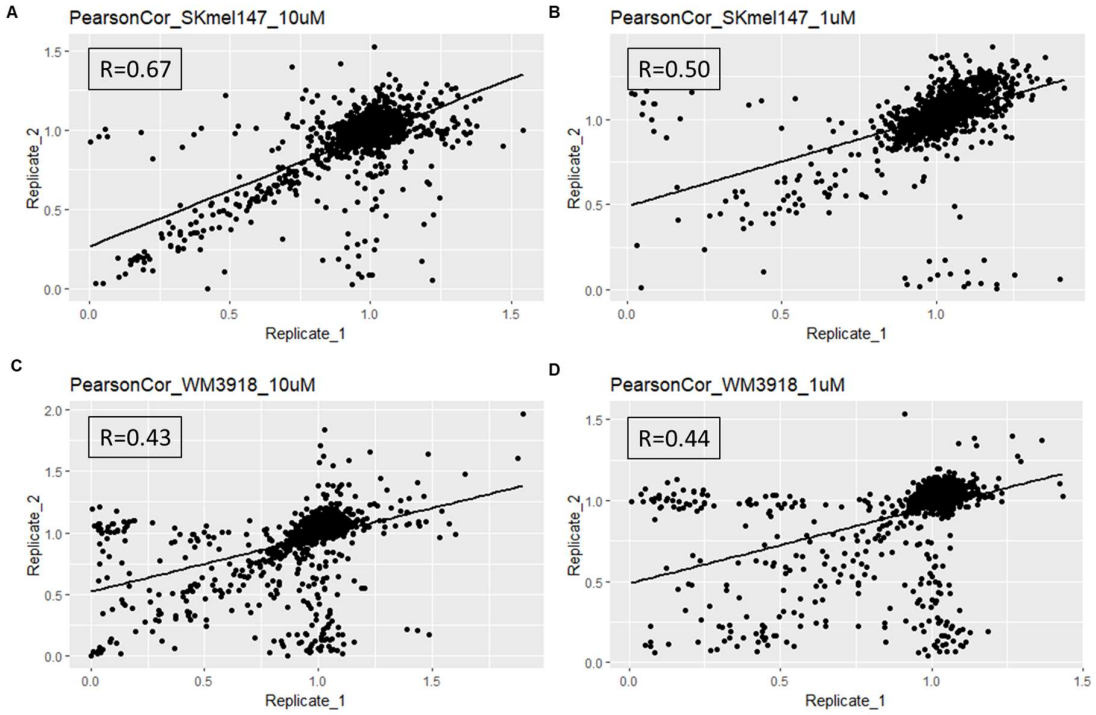

Suppl. Figure 5: Pearson's correlation between the two biological replicates for each condition results to be positively moderate-strong for SKmel147 and moderate for WM3918. A) libraries tested at 10 µM concentration and B) at 1 µM concentration, for SKmel147. A) libraries tested at 10 µM concentration and B) at 1 µM concentration, for WM3918.

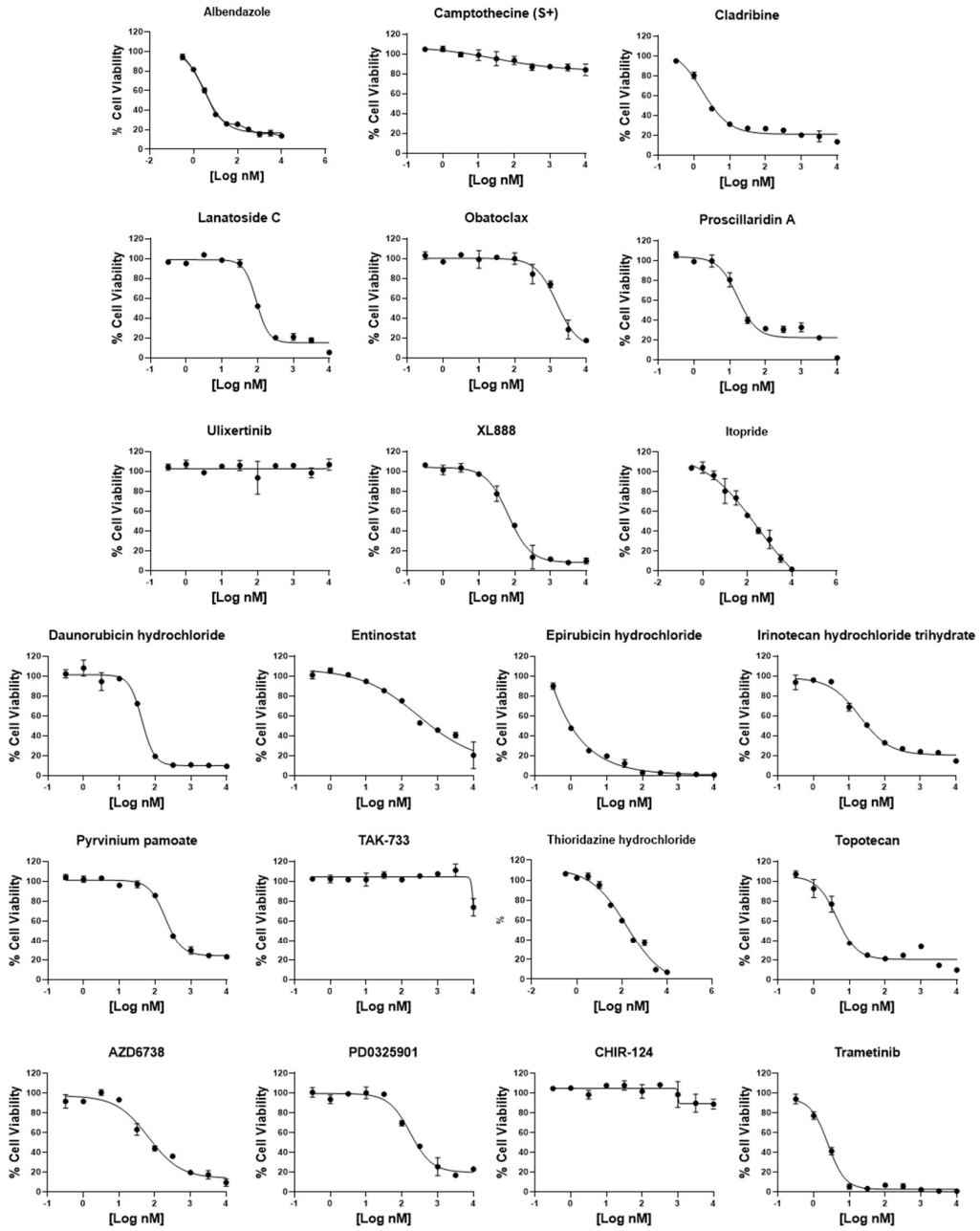

Suppl. Figure 6: Drug response curves of selected hit drugs validate on SKmel147 spheroids using DMSP platform.

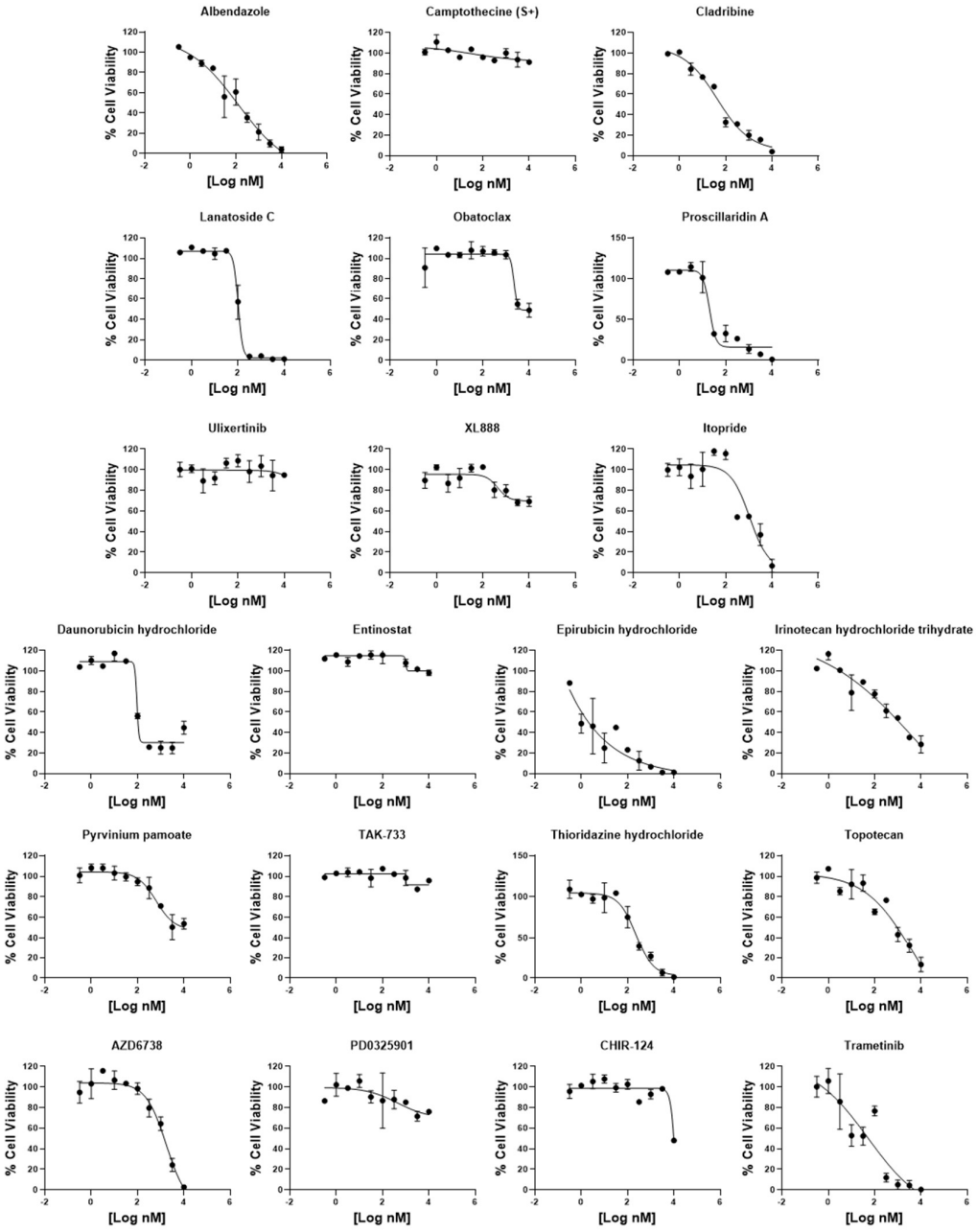

Suppl. Figure 7: Drug response curves of selected hit drugs validate on WM3918 spheroids using DMSP platform.

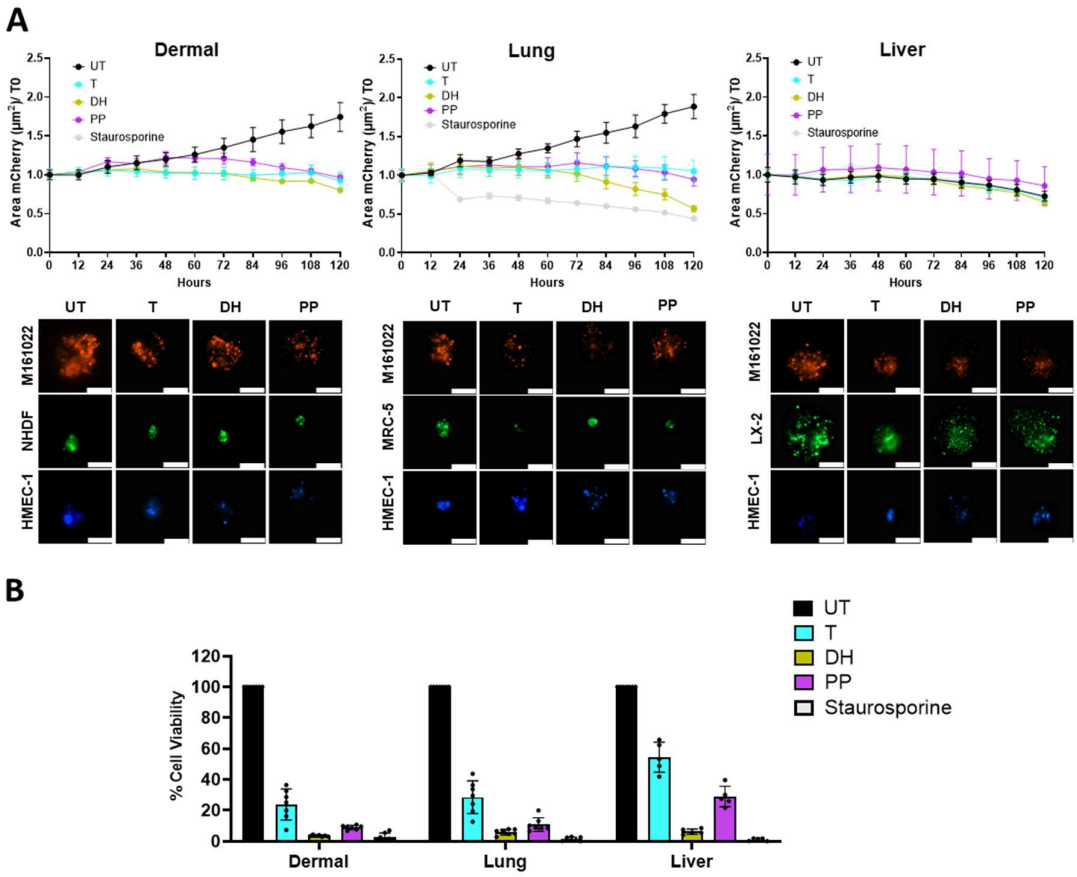

Suppl. Figure 8: Preliminary data (N=1) of the drug efficacy tested in M161022 cultured into the Melanoma Multicomponents Spheroid (MMS) models. A) Line graphs represent kinetic responses to 5-day drug of M161022-mCherry co-cultured into three Melanoma Multicomponent Spheroid (MMS) models: "Dermal", "Lung", and Liver". Fluorescent images exciting mCherry fluorescence were acquired every 12 hours. B) Bar plots represent the cell viability of the three M161022-MMS models after 5 days of drug treatment. Data are normalized by the untreated control. Staurosporine was used as positive control at 200 nM. Confocal pictures (objective 20x) of the different cell populations composing the different MMS models after 5 days of drug stimulations are shown; M161022-mCherry (red), NHDF/MRC-5/LX-2 (green), HMEC-1 (blue). Scale bar = 200 µm.

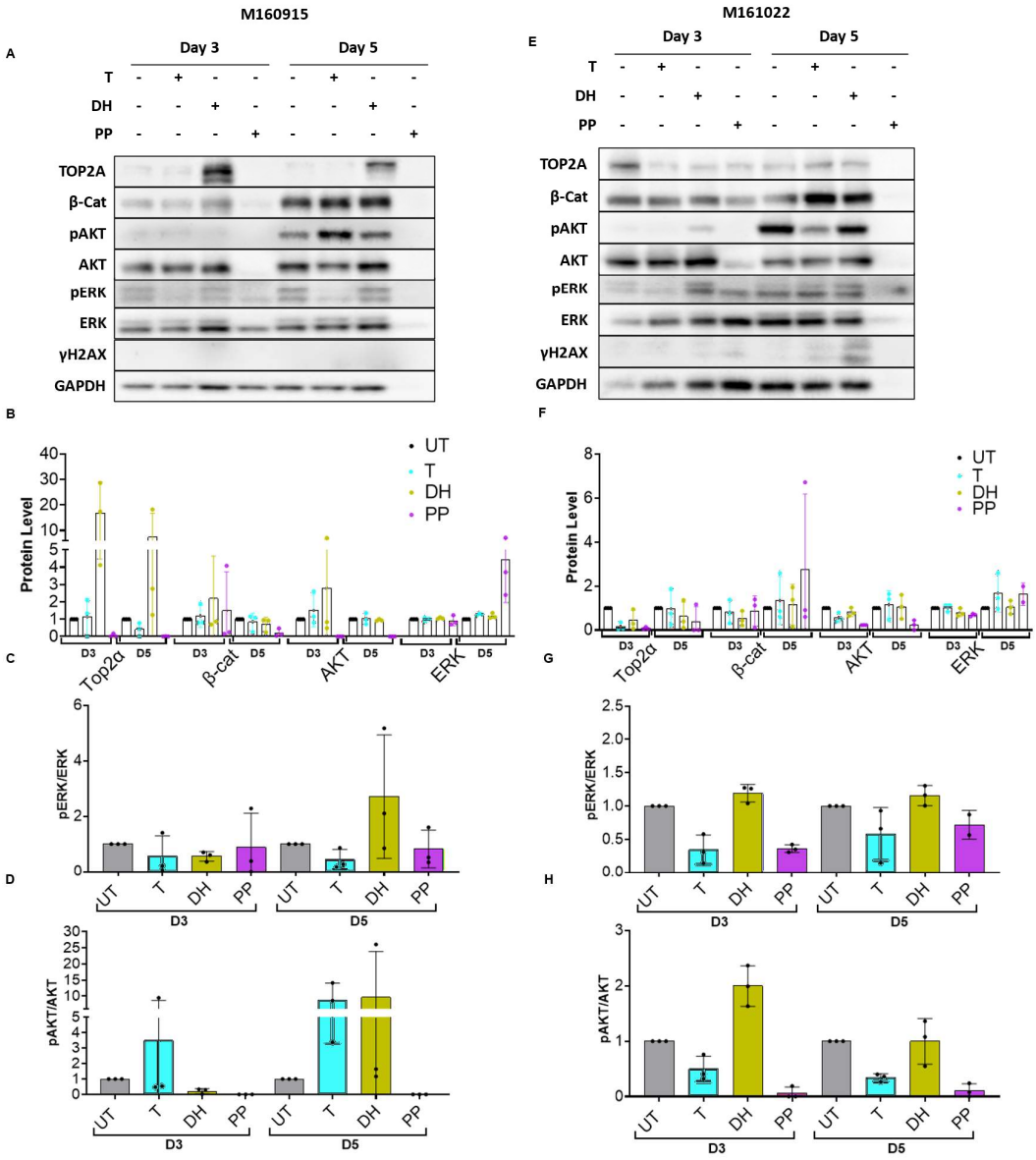

Suppl. Figure 9:Effect of Daunorubicin HCl and Pyrvinium Pamoate on drug-specific targets and key melanoma survival and proliferation kinases. A) Representative Western blots of M160915 treated for 3 and 5 days with cell-line specific IC50 values of T, DH, and PP. B) Quantification of the protein levels in M160915, normalized to the untreated control. C) pERK/ERK ratio analyzed as quotient of pERK versus ERK, in M160915. D) pAKT/AKT ratio analyzed as quotient of pAKT versus AKT, in M160915. E) Representative Western blots of M161022 treated for 3 and 5 days with cell-line specific IC50 values of T, DH, and PP. F) Quantification of the protein levels in M161022, normalized to the untreated control. G) pERK/ERK ratio analyzed as quotient of pERK versus ERK, in M161022. D) pAKT/AKT ratio analyzed as quotient of pAKT versus AKT, in M161022. γH2AX was excluded from the analysis. GAPDH was used as loading control; representative blots of three biological replicates are shown. (n=3. mean±SD).

2. Manuscript 1**: Protocol to generate scaffold-free, multicomponent 3D melanoma spheroid models for preclinical drug testing (DOI: 10.1016/j.xpro.2024.103058)**

STAR Protocols

CellPress
OPEN ACCESS

Protocol

Protocol to generate scaffold-free, multicomponent 3D melanoma spheroid models for preclinical drug testing

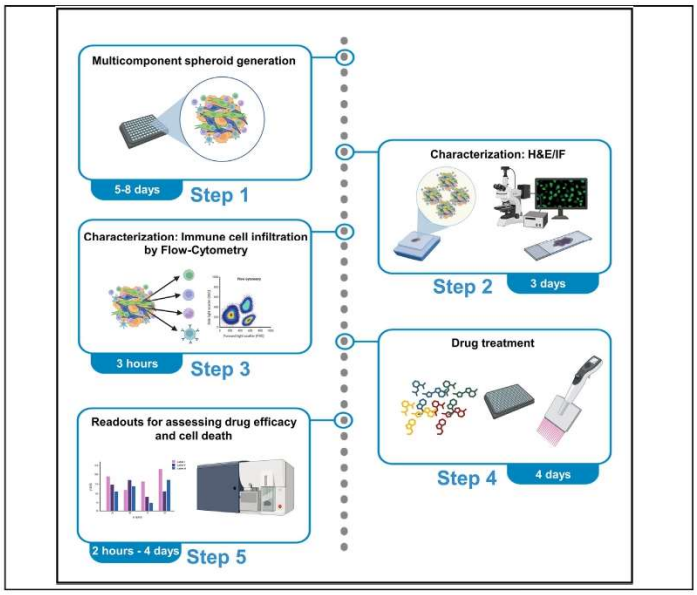

Three-dimensional (3D) models play an increasingly important role in preclinical drug testing as they faithfully mimic interactions between cancer cells and the tumor microenvironment (TME). Here, we present a protocol for generating scaffold-free 3D multicomponent human melanoma spheroids. We describe steps for characterizing models using live-cell imaging and histology, followed by drug testing and assessment of cell death through various techniques such as imaging, luminescence-based assays, and flow cytometry. Finally, we demonstrate the models' adaptability for co-cultures with immune cells.

Publisher's note: Undertaking any experimental protocol requires adherence to local institutional guidelines for laboratory safety and ethics.

Cristian Angeli, Joanna Patrycja Wroblewska, Eliane Klein, Christiane Margue, Stephanie Kreis

cristian.angeli@uni.lu (C.A.)
joanna.wroblewska@uni.lu (J.P.W.)
eliane.klein@uni.lu (E.K.)
stephanie.kreis@uni.lu (S.K.)

Highlights

Generation of a multicomponent 3D melanoma co-culture scaffold-free spheroid model

Functional co-culture of 3D melanoma spheroids with PBMCs

Characterization of multicomponent 3D model using immunofluorescence and flow cytometry

Assessment of drug efficacy in multicomponent 3D models using kinetic and endpoint assays

Angeli et al., STAR Protocols 5, 103058
June 21, 2024
https://doi.org/10.1016/j.xpro.2024.103058

STAR Protocols

CellPress
OPEN ACCESS

Protocol

Protocol to generate scaffold-free, multicomponent 3D melanoma spheroid models for preclinical drug testing

Cristian Angeli,[1,2,*] Joanna Patrycja Wroblewska,[1,2,*] Eliane Klein,[1,2,*] Christiane Margue,[1] and Stephanie Kreis[1,3,*]

[1]Department of Life Sciences and Medicine, University of Luxembourg, 4367 Belvaux, Luxembourg

[2]Technical contact

[3]Lead contact

*Correspondence: cristian.angeli@uni.lu (C.A.), joanna.wroblewska@uni.lu (J.P.W.), eliane.klein@uni.lu (E.K.), stephanie.kreis@uni.lu (S.K.)

https://doi.org/10.1016/j.xpro.2024.103058

SUMMARY

Three-dimensional (3D) models play an increasingly important role in preclinical drug testing as they faithfully mimic interactions between cancer cells and the tumor microenvironment (TME). Here, we present a protocol for generating scaffold-free 3D multicomponent human melanoma spheroids. We describe steps for characterizing models using live-cell imaging and histology, followed by drug testing and assessment of cell death through various techniques such as imaging, luminescence-based assays, and flow cytometry. Finally, we demonstrate the models' adaptability for co-cultures with immune cells.

BEFORE YOU BEGIN

In the past, two-dimensional (2D) cultures of cancer cells have been the main pre-clinical model for the evaluation of drug efficacy. However, the absence of a correct three-dimensional (3D) tumor architecture, which influences the complex interplay of different cell types and their exchange of nutrients and metabolites has resulted in gross misinterpretations of *in vivo* drug effects. 3D cultures better mimic physiological properties of tumor cells allowing for more reliable *in vitro* drug testing,[1,2] especially when different cell types of the tumor microenvironment (TME) are incorporated in multicomponent 3D spheroid models.[3,4] Their high reproducibility allows upscaling to high-throughput drug screening for drug discovery as well as studies investigating the mechanisms of drug responses.[5–11]

In this protocol, we describe the generation of scaffold-free 3D spheroid models in which melanoma cells are co-cultured with endothelial cells, and different types of fibroblasts derived from skin, lung, and liver, representing the sites of common melanoma metastasis. Furthermore, peripheral blood mononuclear cells (PBMCs) were introduced to mimic involvement of the immune system. Detailed sequential seeding protocols were adapted to melanoma cells (Figure 1) allowing for versatile combination of different cell types of choice as has previously been reported for other cancer types.[12] Our advanced Melanoma Multicomponent Spheroid (MMS) models support a more rational assessment of drug effectiveness than standard 2D tissue cultures on plastic surfaces resulting in strikingly different responses to certain drugs. Moreover, compatibility with histological staining methods (immunofluorescence, IF) and cellular assays such as flow cytometry makes these 3D models useful surrogates for the examination of cancer cells specific traits and drug pharmacodynamics. The use of either fluorescently labeled or unlabeled cell lines (Table 1) depends on the planned read-out assay and should be decided beforehand. We recommend using unlabeled cell lines for immunocytochemical staining and flow cytometry-based assays, while labeled cell lines are perfectly suited for microscopy-based imaging and fluorescence-based drug response assays.

CellPress
OPEN ACCESS

STAR Protocols
Protocol

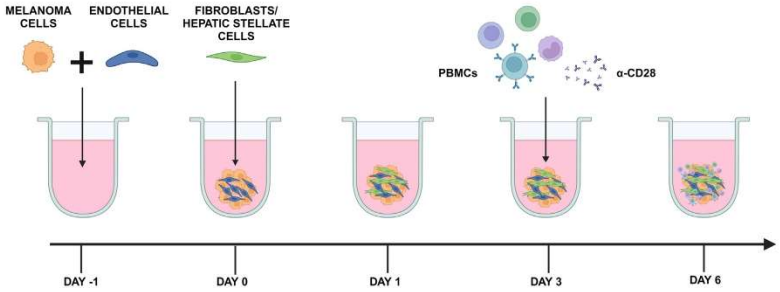

Figure 1. Sequential seeding protocol for Melanoma Multicomponent Spheroid (MMS) generation

Day −1, melanoma and endothelial cells are seeded at a 1:3 ratio in a U-bottom ULA microplate (384- or 96-wells). One day later (Day 0), 3 parts of fibroblasts or hepatic stellate cells are added atop (final ratio: 1:3:3). After 3 days of culture, MMSs can be co-cultured with PBMCs at a 1:10 ratio. Anti-CD28 antibody added for co-stimulatory signals for activation of immune cells. MMSs seeding can be performed in 384- or 96-well plates according to the chosen assays. Created with BioRender.com.

Institutional permissions

Appropriate precautions must be taken when handling human isolated PBMCs and cell lines transduced with lentiviral vectors (Table 1). All experiments involving the use of such material should be performed in accordance with biosafety level 2 (BSL2) guidelines, with dedicated class 2 biosafety cabinets and wearing appropriate protective equipment. Leukopaks for PBMC isolation were obtained from the Croix Rouge Luxembourg under the ethical agreement UNILUX-2023-001.

KEY RESOURCES TABLE

REAGENT or RESOURCE	SOURCE	IDENTIFIER
Antibodies		
Purified anti-human CD28 (mouse IgG1) 5 μg/mL	BioLegend	302902
Anti-human CD45 (mouse IgG1) 4 μL/100 μL of FACS buffer	BioLegend	368507
Anti-human CD8a (mouse IgG1) 1.7 μL/100 μL of FACS buffer	BioLegend	301014
Anti-human CD4 (mouse IgG1) 5 μL/100 μL of FACS buffer	BioLegend	300555
Anti-human CD56 (mouse IgG1) 5 μL/100 μL of FACS buffer	BioLegend	392409
Anti-human CD3 (mouse IgG1) 4 μL/100 μL of FACS buffer	BioLegend	300429
Anti-human CD11b (mouse IgG1) 5 μL/100 μL of FACS buffer	BioLegend	301345
Anti-human CD16 (mouse IgG1) 0.6 μL/100 μL of FACS buffer	BioLegend	302043
Anti-human CD14 (mouse IgG1) 5 μL/100 μL of FACS buffer	BioLegend	367111
Anti-human CD206 (mouse IgG1) 5 μL/100 μL of FACS buffer	BioLegend	321125
Anti-human CD163 (mouse IgG1) 5 μL/100 μL of FACS buffer	BioLegend	333605
Anti-Ki67 (rabbit IgG) 1:200	Abcam	ab16667
Anti-CD31 (mouse IgG1) 1:200	Cell Signaling Technology	3528S
Anti-αSMA (rabbit IgG) 1:200	Cell Signaling Technology	19245
Anti-S100A4 (rabbit IgG) 1:250	Cell Signaling Technology	13018S
Alexa Fluor 488, goat anti-mouse IgG, IgM, IgA (H + L) 1:1,000	Life Technologies	A-10667
Alexa Fluor 647, donkey anti-rabbit IgG, IgM, IgA (H + L) 1:1,000	Life Technologies	A-31573
Chemicals, peptides, and recombinant proteins		
RPMI 1640 + GlutaMAX	Gibco (Thermo Fisher Scientific)	61870036
FBS	Gibco (Thermo Fisher Scientific)	10270106
100× Penicillin/Streptomycin	Gibco (Thermo Fisher Scientific)	15140122

(Continued on next page)

STAR Protocols
Protocol

CellPress
OPEN ACCESS

Continued

REAGENT or RESOURCE	SOURCE	IDENTIFIER
DMEM + GlutaMAX	Gibco (Thermo Fisher Scientific)	31966021
MCDB131	Gibco (Thermo Fisher Scientific)	10372019
Hydrocortisone	Sigma-Aldrich (Merck)	H0888-1G
L-glutamine (200 mM)	Gibco (Thermo Fisher Scientific)	25030024
Animal-free recombinant human EGF	PeproTech	AF-100-15-100UG
PBS tablets	Life Technologies	18912014
Trypsin-EDTA (0.05%)	Gibco (Thermo Fisher Scientific)	25300054
Benzonase Nuclease	Merck	E1014-25KU
DAPI	Invitrogen (Thermo Fisher Scientific)	D1306
Mayer's hematoxylin	Merck	MHS32-1L
Eosin Y-solution 0.5% aqueous	Merck	1098441000
Acetic acid	Carl Roth	7332.1
NeoClear	Merck	109843
Eukitt Quick-hardening mounting medium	Merck	03989-100mL
Fluoromount-G mounting medium	Life Technologies	00-4958-02
ROTI Histofix	Carl Roth	P.087.3
Agarose	Carl Roth	2267.3
Trametinib	Selleckchem	S2673
Staurosporine	Cayman Chemical	81590-10
Propidium iodide	Sigma-Aldrich	81845-25MG
Triton X-100	Carl Roth	3051.3
Tris	Carl Roth	4855.3
EDTA	Carl Roth	8040.3
Tween 20	Carl Roth	9127.2
Citric acid monohydrate	Carl Roth	5110.5
Sodium hydroxide	Carl Roth	6771.1
TrypLE Express enzyme 1×, phenol red	Life Technologies	12605010
Accutase solution	Merck	A6964-500mL
Critical commercial assays		
CellEvent Caspase-3/7 detection reagent	Thermo Fisher Scientific	C10433
CellTiter-Glo 3D cell viability assay	Promega	G9682
LIVE/DEAD Fixable Near-IR Dead Cell Stain Kit	Invitrogen	L34975
Experimental models: Cell lines		
SKmel147 (human)	Prof. Dr. Jochen Utikal	N/A
NHDF (human)	PromoCell	C-12300
MRC-5 (human)	ATCC	CCL-171
LX-2 (human)	Merck	SCC064
HMEC-1 (human)	ATCC	CRL-3243
Buffy Coat of healthy human donors	Croix Rouge Luxembourg	N/A
Software and algorithms		
CellPathfinder software	Yokogawa	CellPathFinder
GraphPad Prism version 10.0.0	GraphPad Software	GraphPad Prism
Gen5	Agilent BioTek	N/A
BioRender	BioRender.com	BioRender
FlowJo version 10.10.0	BD Biosciences	FlowJo
Other		
CellVoyager CV8000	Yokogawa	N/A
Cytation 10	Agilent BioTek	N/A
BioSpa8 robotic arm and automated incubator	Agilent BioTek	N/A
Cytation 5	Agilent BioTek	N/A
96-well plate U bottom ULA clear faCellitate	faCellitate GmbH	F202003
384-well black/clear round bottom ultra-low attachment spheroid microplate	Corning	4516

(*Continued on next page*)

Continued

REAGENT or RESOURCE	SOURCE	IDENTIFIER
PrimeSurface Ultra-low attachment plates: 384 well, U bottom, clear plates	S-BIO	MS-9384UZ
Coverslips 24 × 60 mm	Carl Roth	H878.2
Epredia slides Superfrost PLUS	Fisher Scientific	11877802
Nunc Lab-Tek II Chamber Slide System	Thermo Fisher Scientific	154534PK
CellTrics 50 µm cell strainer	Sysmex	04-004-2327

MATERIALS AND EQUIPMENT

CellVoyager CV8000 (Yokogawa) configuration

The CellVoyager CV8000 high content imaging system with spinning disk technology was used to acquire confocal pictures of live MMSs over time. The instrument is equipped with solid lasers with the following excitation wavelengths: 405/488/561 nm and emission filters: 445/45 nm, 525/50 nm, 600/37 nm. Set the incubation temperature to 37°C.

Cytation 10 (Agilent BioTek) configuration

To robustly assess the efficacy of drugs, assays measurements are executed using automated microplate readers. The Cytation 10 confocal and wide-field microscopy with multimode plate reading with spinning disk technology for confocal images acquisition was used to acquire pictures of IF. The instrument is equipped with a 590 nm LED and Texas Red filter cube (Excitation 586/15 nm, Emission 647/57 nm) and was employed for tracking melanoma fluorescence changes over time. Moreover, the instrument is equipped with a laser combiner (spectral range 398–643 nm) and a DAPI filter cube (Excitation 390/40 nm, Emission 442/42 nm), a GFP filter cube (Excitation 472/30 nm, Emission 520/35 nm), and a TRITC filter cube (Excitation 556/20 nm, Emission 600/37 nm). The instrument is also equipped with a BioSpa8 robotic arm and automated incubator (Agilent BioTek).

Cytation 5 (Agilent BioTek) configuration

The Cytation 5 automated microplate reader is equipped with a luminescence detector and was used to acquire the luminescence signals emitted by 3D Cell Titer Glo.

BD LSRFortessa cell analyzer configuration

All flow cytometry-based assays were acquired on the 4-laser BD LSRFortessa cell analyzer with the BD FACSDiva software and analyzed using the FlowJo v10.10 software. The specific laser/detector setup is presented in the table below.

Laser	Filter	Dye
Violet (405 nm)	780/60	BV785
	710/50	BV711
	610/20	BV605
	450/50	BV421
Green (488 nm)	530/30	FITC
	670LP	PerCP Cy5.5
Yellow-Green (561 nm)	582/15	PE
	780/60	PE Cy7
	610/20	PE Dazzle 594
	582/15	PE
Red (640 nm)	670/20	APC
	780/60	APC Cy7

STAR Protocols
Protocol

CellPress
OPEN ACCESS

Table 1. Cell lines

Cell line	Source	Reporter
SKmel147[a]	Prof. Dr. Jochen Utikal[f]	unlabeled/mCherry[g]
NHDF[b]	PromoCell	unlabeled/GFP[g]
MRC-5[c]	ATCC (CCL-171)	unlabeled/GFP[g]
LX-2[d]	Merck	unlabeled/GFP[g]
HMEC-1[e]	ATCC (CRL-3243)	unlabeled/BFP[g]

[a]Metastatic Melanoma cell line.
[b]Normal Human Dermal Fibroblasts.
[c]Human Fetal Lung Fibroblasts.
[d]Hepatic Stellate Cells.
[e]Human Microvascular Endothelial Cells-1.
[f]University Medical Center Mannheim, Germany.
[g]Depending on the readout method for assay, either unlabeled or mCherry labeled cells were used. Please refer to description of cells lines used in particular steps of the protocol.

1% agarose solution

- Weigh 1 g of agarose and transfer to a bottle.
- Add 100 mL of PBS 1×.
- Boil in microwave to dissolve, the agarose should appear transparent.
- Store at 21°C–25°C up to 6 months.

CellEvent Caspase-3/7 detection reagent

- Reconstitute each vial of lyophilized reagent with 100 µL cell culture grade DMSO to obtain a 500 µM stock solution. Aliquoted solution can be stored in −20°C for several months.

Propidium iodide

- Reconstitute lyophilized powder with 25 mL of cell culture grade H_2O to obtain a 1 mg/mL stock solution. Aliquoted solution can be stored in 4°C for several months.

Melanoma cell medium

Reagent	Final concentration	Amount
RPMI 1640 + GlutaMax	N/A	500 mL
Fetal Bovine Serum	10%	50 mL
Penicillin/Streptomycin 100×	1%	5 mL

Note: Melanoma cell medium can be prepared in advance and can be stored for up to 1 month at 4°C.

Fibroblast/Hepatic Stellate Cell medium

Reagent	Final concentration	Amount
DMEM+ GlutaMax	N/A	500 mL
Fetal Bovine Serum	10%	50 mL
Penicillin/Streptomycin 100×	1%	5 mL

Note: Fibroblast/Hepatic Stellate Cell medium can be prepared in advance and can be stored for up to 1 month at 4°C.

Endothelial cell medium		
Reagent	Final concentration	Amount
MCDB131	N/A	500 mL
Fetal Bovine Serum	10%	50 mL
Penicillin/Streptomycin 100×	1%	5 mL
Hydrocortisone	1 μg/mL	10 mL
L-Glutamine (200 mM)	10 mM	25 mL
EGF	10 ng/mL	N/A

Note: Add EGF freshly and only for the required amount of medium used to culture endothelial cells in the flask of choice.

Note: Endothelial cell medium can be prepared in advance and can be stored for up to 1 month at 4°C.

PBMC thawing medium		
Reagent	Final concentration	Amount
RPMI 1640 + GlutaMax	N/A	500 mL
FBS	10%	50 mL
Penicillin/Streptomycin 100×	1%	5 mL
Benzonase Nuclease 25KU, >250 UI/μL	0.1 μL/mL	50 μL

Note: Add Benzonase Nuclease freshly and only for the required amount of medium.

Note: PBMC thawing medium can be prepared in advance and can be stored for up to 1 month at 4°C.

Note: PBMCs have been isolated from blood of healthy donors using Ficoll Paque Plus and a density gradient centrifugation protocol and stored in liquid nitrogen until used.

FACS Buffer		
Reagent	Final concentration	Amount
PBS 1×	1×	Up to 100 mL
Bovine Serum Albumin	1%	1 g

Antigen Retrieval solution		
Reagent	Final concentration	Amount
Sodium Citrate	10 mM	1.92 g
Tween-20	0.05%	0.5 mL
H_2O, Type II		1 L

TBST 0.1%		
Reagent	Final concentration	Amount
TBS 10×	1×	100 mL
Triton X-100	0.1%	1 mL
H_2O, Type II		900 mL

STAR Protocols
Protocol

CellPress
OPEN ACCESS

Blocking solution		
Reagent	Final concentration	Amount
TBST 0.1%	N/A	N/A[a]
FBS	10%	N/A[a]

[a]Total amount is prepared accordingly for the total number of slides. Use 200 µL to cover one full slide.

Staining Solution 1		
Reagent	Final concentration	Amount
CellEvent Caspase-3/7 Detection Reagent 500 µM	500 nM	2.5 µL
PBS 1×	1×	2.5 mL

Final volume depends on the number of analyzed samples. This example describes preparation of Staining Solution for 10 samples (250 µL per sample).

Staining Solution 2		
Reagent	Final concentration	Amount
Propidium Iodide 1 mg/mL	1 µg/mL	2.5 µL
PBS 1×	1×	2.5 mL

Final volume depends on the number of analyzed samples. This example describes preparation of Staining Solution for 10 samples (250 µL per sample).

STEP-BY-STEP METHOD DETAILS

Generation of melanoma multicomponent spheroids (MMSs)

Timing: 5–8 days

The first part of the protocol describes the generation of melanoma multicomponent spheroids (MMSs) by a sequential seeding method to ensure proper distribution of fibroblasts/hepatic stellate cells within the spheroids. In the first step, only melanoma and endothelial cells are seeded together, followed by addition of fibroblasts or hepatic stellate cells (HSCs) after 24 h (Figure 1). This protocol utilizes an optimized 1:3:3 ratio of melanoma cells: endothelial cells: fibroblasts or HSCs. Live cell imaging (if using fluorescently labeled cells) visualizes the cell type organization within the MMSs (Figures 2A–2D). Furthermore, this protocol allows the co-culture with PBMCs to recapitulate the immune microenvironment of a tumor.

Note: Before starting this procedure, all cell lines should be about 80% confluent in 2D culture flasks.

Alternatives: Seeding of melanoma, endothelial cells, fibroblasts or HSCs can be adapted to 96-well U bottom Ultra-Low Attachment (ULA) plates. Cellular ratios are fixed to 1:3:3 (melanoma cells: endothelial cells: fibroblasts or HSCs) with 2500 melanoma cells per well. Dispensed volume/well of cell suspension per step is 100 µL/well for a final total volume of 200 µL/well.

Day −1: Melanoma and endothelial cell seeding

Note: Pre-warm to 37°C Melanoma cell medium, Endothelial cell medium, PBS 1×, Trypsin-EDTA.

1. Harvest cells and create a single cell suspension for each cell line.

Note: Reported volumes correspond to a T75 flask.

a. Remove the culture medium.

CellPress
OPEN ACCESS

STAR Protocols
Protocol

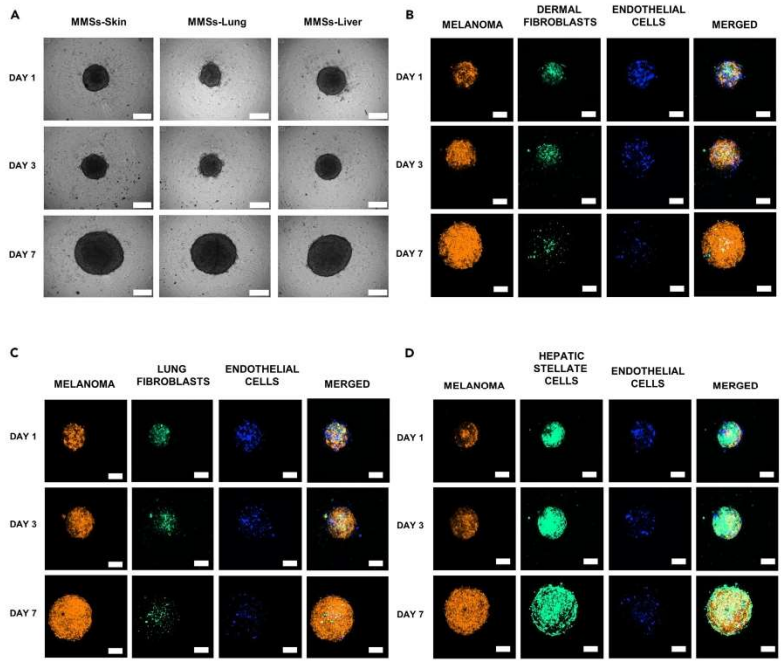

Figure 2. Live-cell images of MMSs

(A) Bright-field pictures of whole MMSs at day 1, 3 and 7 of culture.

(B–D) Cell lines constitutively expressing fluorescent proteins (see Table 1 "reporter") were used. Fluorescently labeled (orange-mCherry) melanoma cells, (blue-BFP) endothelial cells, and either (green-GFP) dermal fibroblasts (B), or lung fibroblasts (C) or hepatic stellate cells (D). In each condition, melanoma cells proliferate over time. Confocal images were taken at maximum intensity projections of multiple z-stacks. Objective 10×. Scale bar = 200 μm.

b. Wash with 5 mL of pre-warmed PBS 1×.
c. Incubate with 3 mL of Trypsin-EDTA for up to 5 min to detach the cells.
d. Visually monitor cell detachment by using a bench-top microscope.
e. Add 12 mL of medium to neutralize Trypsin-EDTA (medium to trypsin-EDTA ratio 4:1) and transfer the solution to a 50 mL conical tube.

Note: For Trypsin-EDTA neutralization, use the dedicated medium for each cell type.

f. Centrifuge cells for 3 min at 300 × *g*.
g. Remove supernatant, add 10 mL of pre-warmed culture medium and resuspend cells.
h. Count viable cells with trypan blue staining or an equivalent method.

2. Preparing the cell culture plates.

Note: To reduce evaporation of medium from wells, avoid using external rows and columns of plates for spheroid culture. Instead, fill them with PBS 1× to an equal or greater volume than the medium. Apply the same to all unused wells on the plate.

a. 384 well plates: Add 80–90 μL of PBS 1× in all external wells of the plate (columns 1, 24, and rows A, P).
b. 96 well plate: Add 200–250 μL of PBS 1× in all external wells of the plate (columns 1, 12, and rows A, H).

3. Seeding of melanoma and endothelial cells in 384-well U-bottom ULA plates.
   a. Prepare a cell suspension containing 500 melanoma cells/40 μL and 1500 endothelial cells/40 μL in a 50 mL conical tube in Melanoma cell medium.
   b. Centrifuge cells at 300 × *g* for 3 min and remove the supernatant.
   c. Resuspend the cell pellet in Melanoma cell medium and use appropriate volume for seeding in the desired number of wells.
   d. Pipet gently up and down 3–5 times until the cell pellet is fully resuspended.
   e. Seed 40 μL/well of cell suspension.
   f. Centrifuge the plate at 500 × *g* for 5 min.
   g. Incubate at 37°C and 5% CO_2 for 24 h.

Note: To facilitate the seeding and to avoid variability, a multichannel pipette can be used during the seeding steps.

Day 0: Fibroblast/HSC seeding

Note: Pre-warm to 37°C Melanoma cell medium, Fibroblast/Hepatic Stellate Cells (HSC) medium, PBS 1×, Trypsin-EDTA.

4. Perform enzymatic dissociation of Fibroblasts/HSCs as described for dissociation of melanoma and endothelial cells (step 1a–h).
5. Seeding of fibroblasts or HSCs in a 384-well U-bottom ULA plate on top of melanoma-endothelial cell spheres.
   a. Prepare a cell suspension in Fibroblast/HSC medium containing 1500 dermal fibroblasts or lung fibroblasts or HSCs/well in a 50 mL conical tube.
   b. Centrifuge cells at 300 × *g* for 3 min and remove the supernatant.
   c. Resuspend the cell pellet in Melanoma medium by gently pipetting up and down. The volume of medium is calculated by multiplying the number of well seeded by 40 μL, plus 20% as death volume.
   d. Add 40 μL/well of cell suspension to the of melanoma-endothelial cell spheres.

Note: To facilitate the seeding and to avoid variability a multichannel pipette can be used during the seeding steps.

   e. Centrifuge the plate at 500 × *g* for 5 min.
   f. Incubate at 37°C and 5% CO_2 for 3 days.

Note: Days of culture depend on many factors such as the type of cells, assay and readout. We decided to culture our MMS for 3 further days after fibroblast/HSC addition to have a final spheroid size of >250–300 μm diameter (Figure 2A), which mimics the proliferative (outer layer) and apoptotic/quiescent (inner layer) of the tumor *in vivo*,[13] as well as the perfusion of molecules and drugs.[5] If the spheroids are out of suggested range, we suggest testing different number of melanoma cells while maintaining the same cellular ratio.

6. Live cell imaging of MMSs over time with a high-resolution confocal microscope (CellVoyager CV8000).
   a. Select the 10× objective.
   b. Apply z-stack acquisition (ascending/descending distance and slicing intervals are set according to the spheroid sizes).

CellPress
OPEN ACCESS

STAR Protocols
Protocol

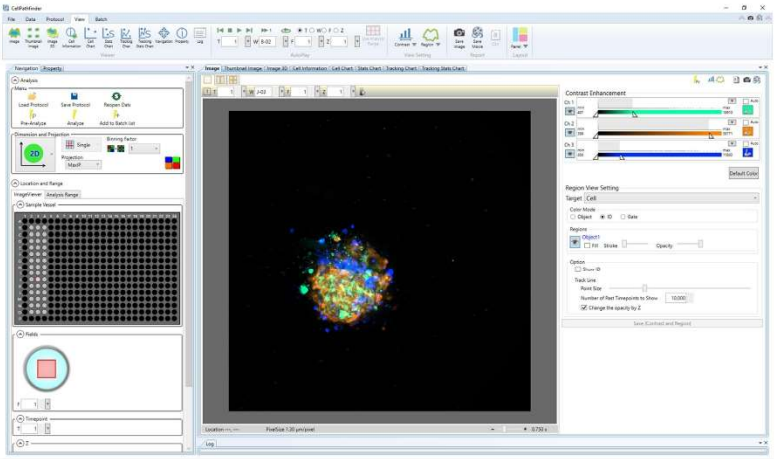

Figure 3. CellPathfinder Software

Overview of the main control board of the CellPathfinder software for visualization and analysis of MMSs pictures acquired using the CellVoyager CV8000 (Yokogawa) confocal microscope.

Note: We suggest applying slicing intervals ranging between 5 and 10 μm to have higher image resolution after Maximum Intensity Projection.

Note: Images are sequentially acquired using bright-field and fluorescence channels at predefined time points (see Figure 2).

c. Apply Maximum Intensity Projection (MIP) using the CellPathfinder Software (Figure 3).

Note: The generated MMSs can be used directly for histological characterization and drug testing or alternatively, co-culturing with PBMCs followed by flow-cytometry based characterization can be added.

Day 3: PBMC seeding

Note: PBMCs are added in a 1:10 ratio (1:10 ratio of MMSs to PBMCs) to pre-formed MMSs in 384-well or 96-well plates by adjusting the cell quantity and volume of the culture medium. For the subsequent steps, MMSs were generated in 96-well U-bottom ULA plates to facilitate subsequent flow cytometric analyses.

Note: Pre-warm to 37°C Melanoma cell medium and PBMC thawing medium.

7. Quickly thaw a cryotube containing PBMCs in a water bath at 37°C by gently swaying.
8. Add 500 μL of pre-warmed PBMC thawing medium dropwise into the cryovial.
9. Transfer the cell suspension dropwise to a 15 mL conical tube containing 5 mL of pre-warmed PBMC thawing medium.

10. Fill up the conical tube to 10 mL with PBMC thawing medium.
11. Centrifuge cells 300 × *g* for 8 min at 21°C–25°C.
12. Resuspend the cell pellet in 5 mL of PBMC thawing medium and incubate for 5–10 min at 37°C.

⚠ CRITICAL: Addition of Benzonase Nuclease to PBMC thawing medium will prevent clumping caused by DNA released from dead cells and increases PBMC recovery.

13. Add further 10 mL of PBMC thawing medium and centrifuge at 300 × *g* for 8 min at 21°C–25°C.
14. Remove the supernatant and resuspend the cell pellet in 10 mL Melanoma cell medium.
15. Adding PBMCs to a 96-well plate with pre-established melanoma-endothelial-fibroblast/HSC MMSs:
    a. Count the viable PBMCs using trypan blue staining or an equivalent method.
    b. Add the PBMC suspension to a 50 mL conical tube with a volume containing ten times the total cell number than that was used to generate MMSs (175000 PBMCs/well).
    c. Centrifuge cells 300 × *g* for 8 min at 21°C–25°C.
    d. Remove the supernatant and resuspend the cell pellet in an appropriate volume of Melanoma cell medium containing anti-CD28 antibody at final concentration of 5 μg/mL. The volume of medium is calculated by multiplying the number of well seeded by 100 μL, plus 20% as death volume.

    Note: Add anti-CD28 antibody to ensure necessary co-stimulatory signals for activation of immune cells.

    e. Remove 100 μL/well of medium from the 96-well plate.
    f. Add 100 μL/well of PBMC cell solution to reach a volume of 200 μL/well.
    g. Incubate at 37°C and 5% CO_2 for 3 days in an incubator.

Histological characterization of MMS

Timing: 3 days

Below, we describe the procedure for formalin-fixation and paraffin embedding (FFPE) of MMSs for histological analysis. We apply hematoxylin/eosin staining for structural evaluation, and immunofluorescence (IF) to visualize different cell populations by using antibodies listed in Table 2.

Note: MMSs were generated in a 96-well plate to augment the quantity of spheroids for downstream readouts.

16. MMSs collection.
    a. Begin from step 5f.

    ⚠ CRITICAL: To transfer spheroids without damaging them, use wide orifice tips.

    b. Using a multichannel pipet, collect the spheroids from the plates and transfer them to a reagent reservoir.

    ⚠ CRITICAL: Double-check the plate to ensure that all spheroids have been collected.

    c. Transfer the spheroids to a 15 mL conical tube and wait 5 min until spheroids sink to the bottom of the tube.
    d. Remove the supernatant and wash with 5 mL PBS 1×.

Table 2. Antibodies for immunofluorescence

Antibody	Source	Isotype	Dilution
Ki-67	Rabbit	IgG	1:200
PECAM-1/CD31	Mouse	IgG1	1:200
S100A4	Rabbit	IgG	1:200
a-SMA	Rabbit	IgG	1:250
Alexa 647	Rabbit	IgG	1:1000
Alexa 488	Mouse	IgG	1:1000

Note: Either aspirator with glass Pasteur pipet or plastic serological pipet can be used to remove the supernatant.

e. Add 5 mL of HISTOFIX and incubate for 30 min at 21°C–25°C.
f. Remove HISTOFIX and wash with 5 mL PBS 1×.
g. Repeat the wash once more.

Pause point: Fixed spheroids can be stored in PBS 1× at 4°C for several days. However, it is advisable to proceed with the next steps as soon as possible to minimize the loss of antigen signal.

17. Embedding and cutting.
    a. Heat the agarose 1% solution in a microwave until the melting point is reached and let it cool down for 5 min at 21°C–25°C.
    b. Remove PBS 1× from the conical tube completely by making sure not to touch the spheroids.
    c. Add 300 µL of agarose 1% solution to the spheroids.
    d. Transfer the spheroids in a chamber of a Lab-Tek II Chamber Slide.
    e. Place the µ-Slide 8 well on ice and let the agarose solidify for 5 min.
    f. Carefully transfer the agarose block into a 50 mL conical tube.
    g. Fix the agarose block by adding 15 mL HISTOFIX and incubate for 3–4 h at 21°C–25°C or ON at 4°C.

    Note: In one agarose block, up to 96 MMSs can be pooled together.

    h. Remove HISTOFIX solution and wash with 5 mL PBS 1×.
    i. Remove PBS 1× and add 20 mL of 70% Ethanol to the conical tube.

    Pause point: Agarose blocks can be stored at 4°C in 70% Ethanol for several weeks. However, it is recommended to proceed as soon as possible with paraffin embedding.

    j. Remove the 70% Ethanol.
    k. Transfer the block into an embedding cassette and transfer the cassette to a container with a magnetic stirrer.
    l. Add 500 mL 100% Ethanol and incubate for 2 h with continuous stirring.
    m. Repeat previous step once by removing and replacing with fresh 100% Ethanol.
    n. Add 500 mL NeoClear (Xylene substitute) solution and incubate for 1–2 h with continuous stirring.
    o. Remove NeoClear solution.
    p. Transfer the agarose block into an embedding mold, cover with liquid paraffin and incubate for 2 h at 60°C.
    q. Exchange the paraffin inside the embedding mold.
    r. Let the paraffin solidify on a cooling plate or on ice.

Note: Solidified FFPE blocks are stored at 21°C–25°C long term until needed for sectioning.

s. Cut 4–5 μm thick sections with a microtome slicer and place them on a microscope slide.

⚠ CRITICAL: If paraffin sections were cut more than a month before staining is performed, incubate the slides at 40°C–42°C from 16 to 20 h.

18. Rehydration of paraffin sections.

Note: Rehydration of paraffin sections steps must be performed inside r a fume hood or a ventilated staining table.

Note: Use Coplin jars for rehydration and dehydration steps. Prepare jars with appropriate volumes of descending percentages of Ethanol, TBST, hematoxylin and eosin solutions.

a. Place the slides in a slide holder and immerse the slides in NeoClear solution for 10 min, repeat once.
b. Transfer slide and immerse in 100% Ethanol for 5 min.
c. Transfer slide and immerse in 95% Ethanol for 5 min.
d. Transfer slide and immerse in 70% Ethanol for 5 min.
e. Transfer slide and immerse in 50% Ethanol for 5 min.
f. Transfer slide and rinse with TBST for 5 min

19. Hematoxylin and eosin staining.
a. Rinse with TBS.
b. Incubate in Mayer's hematoxylin for 30–40 s.
c. Rinse with TBS.
d. Incubate in Eosin solution for 30 s.
e. Rinse with TBS.
f. Immerse in 95% Ethanol for 2 min.
g. Immerse in 100% Ethanol for 2 min.
h. Immerse in NeoClear solution for 2 min.
i. Leave the slides to dry at 21°C–25°C .
j. Mount the slices by adding 1–2 drops of mounting medium (like Eukitt) per slide and cover with coverslips.

20. Immunofluorescence (IF): Begin from step 18f.
a. Wash with TBST in a coplin jar.
b. Transfer slides in a coplin jar filled with the appropriate antigen retrieval solution (ARS).

Note: Depending on the antibody used, different antigen retrieval solution (ARS) needs to be employed for heat-mediated antigen retrieval.

c. Perform heat-mediated antigen retrieval in a microwave. Start on 100% power until boiling point (up to several minutes). Assure that the slides are covered with the ARS.
d. Incubate in a microwave for a further 10–15 min on 10–20% power at sub-boiling temperature (95°C–98°C).

Alternatives: A water bath at 96°C–100°C can be used, place slides in a plastic jar with ARS and incubate for 30 min.

⚠ CRITICAL: During antigen retrieval the solution may evaporate. Make sure that the level of the solution is always above the level of the slides as the tissue may dry out. Keep a second coplin jar with the same antigen retrieval solution in the microwave or water bath in case the volume in the jar with the slides is dropping.

e. Leave at 21°C–25°C for 30 min to cool down.
f. Rinse 3 times with TBST in a coplin jar for 5 min each.
g. Place the slides in a staining tray and add 200 µL per slide of blocking solution and incubate at 21°C–25°C for 30 min.

⚠ CRITICAL: Place the slides in a humidified chamber to avoid evaporation during blocking, primary and secondary antibodies incubation steps.

h. Remove blocking solution by tilting the slides on paper towels and add 200 µL per slide of primary antibody, diluted in blocking solution.
i. Incubate at 4°C from 16 to 20 h in a humidified chamber.
j. Rinse 3 times with TBST in a coplin jar for 5 min each.
k. Add 200 µL per slide of conjugated secondary antibody solution and DAPI diluted in blocking solution and incubate at 21°C–25°C for 1 h.
l. Mount the slides by adding 2–3 drops of Fluoromount per slide and cover with coverslips.

Note: Use clear nail polish to seal the edges of the coverslip, to prevent dehydration. Mounted slides can be stored in the dark at 4°C for up to 1 month. It is recommended to image slides immediately due to the decay of fluorescent signals.

21. Image acquisition (Cytation 10).
    a. For imaging H&E staining, use a wide field 20× objective and colored bright field.
    b. For IF, use a confocal (spinning disk) microscope and a 20× objective.

MMS characterization: FACS analysis for PBMC interaction with MMSs

Timing: 3 h

This part of the protocol describes the detection of infiltrating and non-infiltrating immune cells co-cultured with MMSs by flow cytometry. To identify the subpopulations of immune cells (lymphocytes, monocytes, macrophages and Natural killer cells) we composed a panel of specific antibodies as listed in Table 3. MMSs are co-cultured with healthy donor PBMCs for 3 days with a ratio of 1:10 (1:10 ratio of MMSs to PBMCs). One 96-well plate of MMSs co-cultured with PBMCs is used for each specific composition of MMS (MMS-Skin, MMS-lung, MMS-Liver).

Note: MMSs were generated in a 96-well plate to augment the quantity of spheroids for the downstream readouts.

Table 3. Antibody panel for PBMCs

Antibody target	Conjugate	Volume (µL)[a]
CD45	FITC	4
CD8a	APC	1.7
CD4	BV605	5
CD56	PE-594	5
CD3	PerCP 5.5	4
CD11b	BV785	5
CD16	BV711	0.6
CD14	PE-Cy7	5
CD206	BV421	5
CD163	PE	5

[a]The specific volume of antibodies was validated per 1 million of PBMCs in 100 µL FACS buffer.

Note: It is necessary to generate a compensation matrix for all fluorophores used in the assay, to prevent fluorescent signals to spill over between channels. Compensation can be done using mono-stained compensation beads or cells.

22. Begin from step 15g.
23. Dissociation of MMSs co-cultured with PBMCs.
    a. Using a multichannel pipet, collect the spheroids and medium from 96-well plates and transfer them into a reagent reservoir.

    ⚠ CRITICAL: Collect all the medium in the wells to ensure the collection of all non-infiltrating PBMCs.

    b. Transfer all the reagent reservoir's content (spheroid and supernatant) in a 50 mL conical tube and wait approximately 5 min until spheroids sink to the bottom of the tube.
    c. Remove the supernatant, which contains non-infiltrating immune cells into another 50 mL conical tube and leave it at 21°C–25°C until further use.
    d. Wash MMSs with 10 mL PBS 1×.
    e. Centrifuge 300 × *g* for 3 min at 21°C–25°C.
    f. Transfer supernatant into the conical tube containing the non-infiltrating immune cells.
    g. Add 5 mL of a pre-warmed TrypLE Express and Accutase mix (1:1) to the MMSs.
    h. Mix well and incubate for 10 min at 37°C.

    ⚠ CRITICAL: To minimize dissociation-induced cell death, avoid prolonged incubation with the enzyme mix and vortexing MMSs. Proper dissociation of spheroids is ensured by the pipetting described below (Figure 4).

    i. To dissociate the MMSs, use a small tip (10 µL) on top of a bigger tip (1 mL) (Figure 4) and pipet up and down until a single cell solution is obtained.
    j. Add 10 mL PBS 1× to the dissociated MMSs.
    k. Centrifuge both infiltrated PBMCs (dissociated spheroids) and non-infiltrated cells at 300 × *g* for 8 min at 21°C–25°C.
    l. Remove supernatant and resuspend cells in 4 mL PBS 1×.
    m. Using a pipet, pass the whole volume of cell solution through a 50 µm strainer.
    n. Divide each sample into two and transfer to two FACS tubes: 1 mL (or: $^1/_4$ of the sample) for the unstained control and 3 mL (or: $^3/_4$ of the sample) for staining with antibodies.
    o. Centrifuge at 300 × *g* for 8 min at 4°C.
24. Flow cytometry staining and analysis.
    a. Prepare antibody mix in FACS buffer, keep on ice and in the dark until use.
    b. Remove supernatant from both tubes and add 100 µL of antibody panel for PBMCs (volumes per antibody reported in Table 2) to the cells. Add 100 µL FACS buffer for the unstained control tube.
    c. Incubate for 30 min at 4°C in the dark.
    d. Add 1 mL of FACS buffer to each tube and centrifuge at 300 × *g* for 8 min at 4°C.
    e. Remove supernatant and add 300 µL of FACS buffer.
    f. Keep on ice in the dark until acquisition.
    g. Run samples on BD LSRFortessa Cell Analyzer (or equivalent).
    h. Use a gating strategy as represented in Figure 5A.

Drug dispensation in MMSs

Timing: 4 days

CellPress
OPEN ACCESS

STAR Protocols
Protocol

Figure 4. Double plastic tip to enhance MMS dissociation
Using a 100–1000 µL micropipette, a 10 µL plastic tip is inserted on top of a 1000 µL plastic tip.

The fourth part of the protocol describes the drug testing procedure. Depending on the nature of the selected compound and targeted cell types, the drug concentration varies. Here, we use a MEK 1/2 inhibitor (Trametinib) at a concentration of 500 nM. For evaluating the drug effect, vehicle (DMSO 0.1%) and positive controls are included in each experiment. The selected positive control compound and its concentration may vary depending on the experimental criteria. In this protocol, Staurosporine is used as positive control.

Note: The following procedure reports volumes adapted for a 384-well U-bottom plate. However, the same protocol can be implemented in 96-well U-bottom plates by multiplying all volumes by a factor of 2.5.

Note: Pre-warm to 37°C Melanoma cell medium.

25. Begin from step 5f.
26. Check under the microscope that MMSs have an appropriate size (>250–300 µm) and a compact morphology (Figure 2A).
27. Prepare a 2× concentration of the compound to be tested and DMSO solution in Melanoma cell medium. The volume of medium is calculated by multiplying the number of well seeded by 40 µL, plus 20% as death volume.
28. Remove 40 µL/well of medium from the wells assigned to contain the vehicle control and tested compound.

STAR Protocols
Protocol

CellPress
OPEN ACCESS

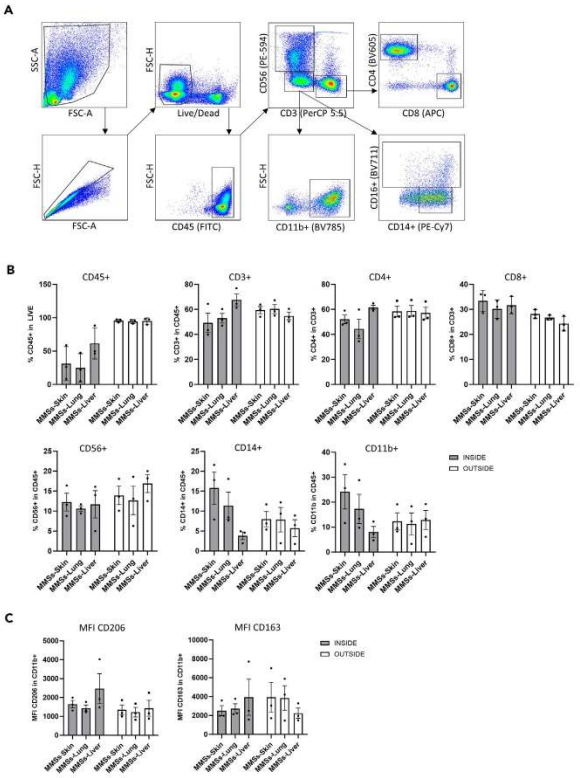

Figure 5. Flow-cytometry for identification of PBMC components

(A) Flow-cytometry gating strategy for identification of different immune cell populations using a specific panel of antibodies (Table 2). Arrows indicated in which order the gating was performed.

(B and C) Quantification of PBMC populations able to interact/infiltrate the MMSs (INSIDE, gray bars) or remaining in the supernatant (OUTSIDE, white bars). Data are mean ± SD of $n = 3$ independent biological replicates. The PBMC populations in the supernatant remain stable across the three MMS types (skin, lung and liver), while the interacting/infiltrating fractions show heterogeneity across the MMS types. (B) MMSs-liver present higher immunogenicity compared to -skin and -lung depicted by CD45+, with slightly higher lymphocyte infiltration (CD3+, CD8+, CD4+, CD56+) but lower monocyte infiltration (CD14+ and CD16+). (C) Median Fluorescence Intensity or MFI is depicted to assess tumor-associated macrophages (CD163 and CD206).

29. Add 40 µL/well of 2× concentrated compound and DMSO solution to the dedicated wells.

Note: Solutions are prepared 2× concentrated to be in a final volume of 80 µL/well.

30. Incubate at 37°C and 5% CO_2 for 3 days.

31. Prepare a 2× concentrated solution for the positive control. Calculate extra solution as dead volume.

Note: Given the strong apoptotic effect of Staurosporine, for endpoint assays (such as 3D Cell Titer Glo) 1 μM Staurosporine can be added 24 h before the end of the assay, while for kinetic assay (such as tracking fluorescence signal emitted by melanoma cells) 200 nM Staurosporine is dispensed at the same time with compound of interest and DMSO solution (step 29).

32. Remove 40 μL/well of medium only from wells assigned to positive controls.
33. Add 40 μL/well of positive control solution to these wells.
34. Incubate at 37°C and 5% CO_2 for 1 day.

Readout assays to evaluate drug efficacy

Timing: 2 h to 4 days

In the last section of the protocol, different assays are described for the evaluation of cell viability and cell death. Viability is assessed through two methods: kinetically, by following the fluorescence intensity of melanoma cells (Table 1) over time and by endpoint measurements using an assay (3D CellTiter-Glo) based on luciferin-ATP-luciferase. Alternatively, a combined staining with propidium iodide (PI) and a DEVD-conjugated dye (CellEvent Caspase-3/7) is applied to detect necrotic and apoptotic cells by flow cytometry.

35. Tracking melanoma fluorescence changes over time

Note: Melanoma cell proliferation in response to drugs is followed by kinetic measurements of the fluorescent signals emitted by fluorescently labeled melanoma cells (Table 1).

a. Begin from step 29.
b. Place the microplate in an automated microplate reader (Cytation 10) with a fluorescence signal acquisition option.

Note: Set the live-cell incubation (37°C) during the plate reading phase to maintain the plates' temperature and prevent water condensation on the lid.

c. Monitor intensity of the fluorescent signal every 4 h (Figures 6A–6C) assisted by an automated robotic station equipped with an integrated incubator (37°C and 5% CO_2).

Note: The detailed Cytation 10 configuration is reported in materials and equipment.

Note: Acquire bright-field pictures (wide field, 4× objective) as a quality control.

36. Cell viability assay: 3D Cell Titer Glo

Note: Reagent preparation is performed according to the manufacturer's guidelines (3D Cell Titer Glo_TechicalManual)

Note: The specified working volumes are intended for a 384-well plate, adjustments can be made to accommodate various types of multi-well plates while maintaining the same volume proportions. According to the manufacturer, a 1:1 ratio between medium and reagent is recommended.

a. Remove 40 μL/well of medium from all wells of a 384-well plate containing MMSs.

STAR Protocols
Protocol

CellPress
OPEN ACCESS

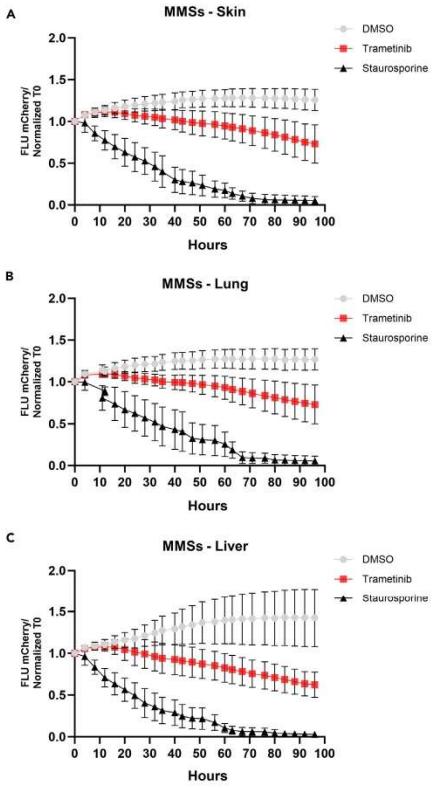

Figure 6. Kinetic assay

The fluorescent signal emitted by labeled melanoma cells is captured every 4 h for the kinetic evaluation of drug efficacy. Plotted is the kinetic profile of MMSs-skin (A), -lung (B) and -liver (C) treated for 96 h with Trametinib 500 nM, DMSO 0.1% and Staurosporine 200 nM. Data are mean ± SD of $n = 3$ independent biological replicates.

b. Remove the whole content of 3-6 wells containing PBS 1 × (edge wells) and add 40 µL/well of Melanoma cell medium (these wells will be dedicated to the Blank).

⚠ CRITICAL: Depending on the compound to be tested, cellular connections may be impaired, leading to the formation of fragmented MMSs that can be accidentally aspirated during pipetting. To avoid it remove the medium very slowly without disturbing the cells on the bottom of the wells.

c. Add 40 µL/well of 3D Cell Titer Glo.
d. Incubate at 37°C while shaking (orbital) at 400 rpm for 30 min.
e. Read luminescence signal.

37. Cell death assay: apoptosis and necrosis

This flow cytometry-based assay allows to determine the ratio of apoptotic and necrotic cells by double staining with a green fluorogenic substrate for activated Caspase 3/7 for apoptosis detection and propidium iodide for necrotic cell death.

Note: MMSs were generated in a 96-well plate to augment the quantity of spheroids for the downstream readouts.

Note: Reagent preparation is performed according to the manufacturer's guidelines. Staining Solutions 1 and 2 are prepared as described in materials and equipment.

⚠ CRITICAL: To minimize dissociation-induced cell death, avoid prolonged incubation with the enzyme mix and vortexing MMSs. Proper dissociation of MMSs is ensured by the pipetting described below.

Note: Pre-warm to 37°C PBS 1× and TrypLE Express and Accutase mix

a. Dissociation of MMSs.
   i. Using a multichannel pipet, collect the spheroids from 96-well plates and transfer them into a reagent reservoir.
   ii. Transfer the MMSs to a 50 mL conical tube and fill up to 50 mL with pre-warmed PBS 1×.
   iii. Centrifuge at 300 × *g* for 5 min at 21°C–25°C.
   iv. Remove supernatant carefully, avoid touching the pellet.
   v. Wash MMSs again with 10 mL PBS 1× and remove the supernatant.
   vi. Add 5 mL of a pre-warmed TrypLE Express and Accutase mix (1:1) to the pelleted MMSs.
   vii. Mix well by pipetting up and down and incubate for 10 min at 37°C.
   viii. To dissociate the MMS, use a small tip (10 µL) on top of a bigger tip (1 mL) (Figure 4) and pipet up and down until no cell clumps are visible anymore.
   ix. Fill up the tube with PBS 1× and centrifuge at 300 × *g* for 5 min at 21°C–25°C.
   x. Remove supernatant and resuspend cells in 2 mL PBS 1×.
   xi. Using a pipet pass the 2 mL cells suspension through a 50 µm strainer to obtain a single cell solution.
   xii. Divide each sample into two FACS tubes: 0.5 mL for unstained control and 1.5 mL for stained sample.
   xiii. Centrifuge at 300 × *g* for 5 min at 4°C.
b. Flow-cytometry staining and analysis.
   i. Prepare Staining Solution 1 (see Table Staining Solution 1) in PBS 1×, keep in the dark until use.
   ii. Remove supernatant and add 250 µL of Staining Solution 1 to the samples. Add 500 µL of PBS 1× to the unstained control tube.
   iii. Incubate for 30 min at 37°C in the dark.
   iv. Add 250 µL of Staining Solution 2 to the sample. Do not add anything to the unstained control tube.
   v. Immediately after adding Staining Solution 2 analyze samples on a BD LSRFortessa Cell Analyzer (or equivalent).
   vi. Use a gating strategy as represented in Figure 7A.

EXPECTED OUTCOMES

With the present protocol, we have established an *in vitro* 3D scaffold-free melanoma spheroid model that allows efficient evaluation of drugs in a physiologically meaningful context. These 3D spheroid models can be flexibly adapted to various microwell plate formats, ranging from low to medium-throughput (96-well plate) to high-throughput (several 384-well plates) drug screening.

STAR Protocols
Protocol

CellPress
OPEN ACCESS

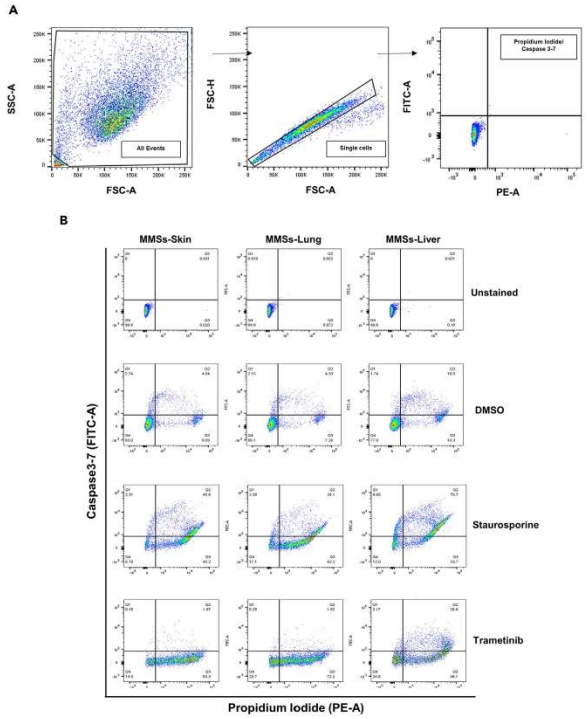

Figure 7. Flow-cytometry apoptosis assay

(A) Gating strategy for flow cytometry apoptosis assays, including a doublet discrimination step. Arrows indicated in which order the gating was performed.

(B) Representative dot plots of an apoptosis assay. Cells were treated with 500 nM Trametinib for 4 days or 1 μM Staurosporine (positive control) for 24 h. 0.1% DMSO was used as a vehicle control. Double staining with Caspase 3–7 and propidium iodide allows to determine the ratio of early apoptotic (positive for Caspase), late apoptotic (positive for both markers) and necrotic cells (positive for propidium iodide).

Sequential seeding (Figure 1) of different co-cultured cells results in 3D structures that far better resemble a tumor in its distinct microenvironment. Dermal and lung fibroblasts display similar growth behavior in MMSs with a tendency to migrate towards the core of the spheres (Figure 2B showing MMS-Skin and 2C showing MMS-lung), while HSCs remain on the outer layer of MMSs (Figure 2D). Histological assays are employed to determine proper cellular morphology and 3D architecture (Figure 8) together with staining of cell-specific markers (Figures 9A–9D). The inclusion of distinct cell types from metastatic target organs can mimic distinct TMEs while the different growth and migration behavior of certain cell types may give important clues to explain drug responses in 3D MMSs, which are more closely reflecting *in vivo* scenarios.

Establishment of co-cultures with PBMCs further increases the level of biological complexity of our model. A panel of antibodies (Table 2) permits the characterization of different PBMC populations

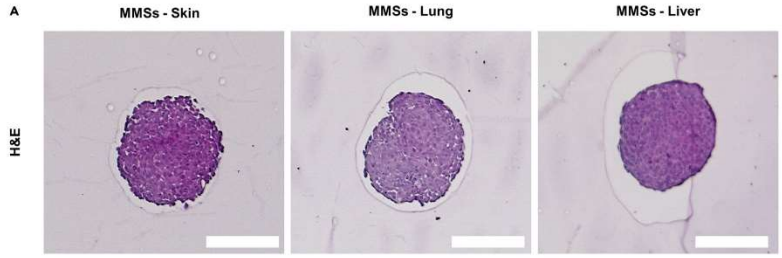

Figure 8. Hematoxylin & Eosin staining of MMSs fixed in formalin and embedded in paraffin (FFPE)
MMSs-skin, -lung, and -liver structure and cellular architecture by Hematoxylin and Eosin (H&E) staining. Objective 20×. Scale bar = 200 μm.

co-cultured with MMSs (Figure 5A). Infiltration of immune cells can be confirmed through flow cytometry of dissociated MMSs (Figures 5B and 5C) providing important information on the involvement of the immune compartment for specific drug responses, including combinations of targeted drugs with immune checkpoint inhibitors or other immune-modulating treatments.

To further increase the flexibility and usability of our models, we have set up several readout assays for kinetic (Figures 6A–6C) and endpoint analysis of cell viability (Figures 10A–10C) and the occurrence of both apoptosis and necrosis (Figure 7B), enabling a detailed evaluation of drug efficacy. Of note, all readout assays can also be applied to mono-component spheroids that only consist of melanoma cells from different genetic backgrounds (such as BRAFmut, NRASmut, and other genetic subtypes) if results need to be obtained faster and only in the cancer cell at hand without the influence of surrounding cell types. Furthermore, if the effect of extracellular matrix needs to be considered, MMSs can also be embedded in the appropriate matrix. We have successfully established protocols to embed multicomponent 3D models in hydrogel.

In conclusion, MMSs are a cost-effective and versatile 3D *in vitro* model for evaluating the efficacy of known or novel drugs or drug combinations. This model incorporates crucial cancer-TME interactions, which influence drug responses, better mirroring the physiological conditions found in early-stage and late-stage metastatic melanoma.

LIMITATIONS

While the application of multicomponent scaffold-free 3D spheroid *in vitro* models offers the opportunity to test novel or newly combined compounds for the treatment of melanoma patients in which cancer cells can interact with cells of the TME, some limitations apply.

For the establishment of this model, commercially available melanoma and stromal cell lines were used. These cell lines exhibit lower heterogeneity compared to patient-derived cells. Hence, the model requires further adaptation when melanoma cells isolated from patient-derived tumors are co-cultured with isolated stromal cells.

For specific readout assays, cells require fluorescent labeling. This might be more difficult to achieve in patient-derived primary melanoma cells compared to established cell lines.

The TME is composed of a vast variety of stromal and immune cells. As a proof of concept, this protocol includes only few stromal cell types such as endothelial cells, fibroblasts/HSCs and PBMCs. Other cell types of interest can be easily substituted paying attention to a potential need for cell type specific media. Immune cell compartments are here portrayed by PBMCs isolated from healthy

STAR Protocols
Protocol

CellPress
OPEN ACCESS

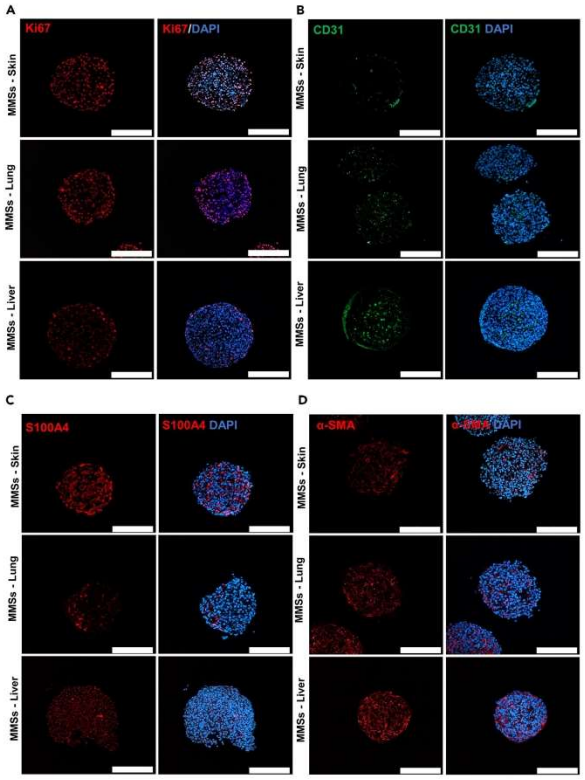

Figure 9. Immunofluorescence staining of MMSs fixed in formalin and embedded in paraffin (FFPE)
Immunofluorescence staining of skin-, lung- and liver-MMSs by (A) Ki67 for cell proliferation, (B) CD31/PECAM-1 for endothelial cell differentiation, (C) S100A4 for melanoma cells identification and (D) α-Smooth Muscle Actin (α-SMA) as a marker for fibroblasts/HSCs activation. Objective 20×. Scale bar = 200 μm.

donors, likely not exhibiting matching HLAs with the melanoma cells used for this protocol. When using patient-derived material, we recommend using PBMCs isolated directly from blood of the same patient, as this approach would provide matching HLAs, which might be relevant for a physiological immune response against the tumor cells when applying immunotherapy.

For this protocol, a single cellular ratio has been chosen for all three distinct melanoma metastasis models (1:3:3). However, depending on the stage of the tumor, the anatomical site, the proliferation rates of TME and cancer cells, these ratios can vary considerably and are expected to dynamically change over time. Therefore, a chosen ratio can only provide a snapshot of a given *in vivo* situation.

The above protocols evaluate the efficacy of tested compounds, primarily focusing on the effect on melanoma cells. Highly proliferative melanoma cells tend to overgrow fibroblasts and endothelial

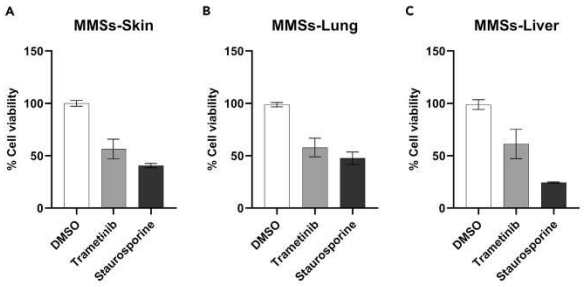

Figure 10. MMSs cell viability

MMS cell viability is assessed using an end-point luminescence-based assay (3D Cell Titer Glo) after 96 h. The tested compound (Trametinib 500 nM), vehicle (DMSO 0.1%) and positive control (Staurosporine 1 μM) are represented for MMSs-skin (A), -lung (B) and -liver (C). Data are mean ± SEM of $n = 3$ independent biological replicates.

cells over time, which reflects the physiological behavior of melanoma tumors. Further adaptations are required to evaluate the effects of test compounds on the TME cells, which would additionally provide an indication of the toxicity of the drug at hand.

TROUBLESHOOTING

Problem 1

Sphere formation issues (During steps 3–5).

Potential solutions

- Use U-bottom ultra-low attachment (ULA) microplates indicated in the Key Research Table. Batches of plates sometimes differ. Try a different batch or provider if problems persist. We recommend the use of U-bottom ULA microplates as outlined in the Key Research Table (KRT).
- Ensure correct and homogeneous mixing of cell solutions before seeding. This reduces the occurrence of incorrect melanoma and endothelial cell ratios per well.
- Ensure the correct centrifugation speed. Incorrect centrifugation speed can either impair cell viability or reduce cell aggregation.
- Melanoma cells (established cell lines and patient-derived cells) have various propensities to grow in 3D displaying lose aggregates to very compact round spheroids. Try different melanoma cells when 3D morphologies are not satisfactory.

Problem 2

PBMCs low viability after thawing (During steps 7–15).

Potential solutions

- Ensure a correct freezing process of PBMCs.
- Precise and quick thawing process reduces exposition time of PBMCs to freezing medium.
- Test PBMCs from a different donor.

Problem 3

PBMC hyperactivation (During step 15).

Potential solutions

- Use PBMCs isolated from a different donor.
- Use HLA-matched PBMCs that can be commercially purchased or use blood from same patient, if patient-derived melanoma cells are used.

Problem 4

A fraction of MMSs can be lost or damaged during the collection for histological and cellular analysis for two main reasons. First, spheroids can stick to the wall of the plastic tips and serological pipets during pipetting. Second, vigorous pipetting might damage the spheroids, which makes them unfit for histological assays (During steps 16, 23, and 37)

Potential solutions

- Pre-wash with PBS 1× the tips used for collecting and transferring the spheroids, which reduces the occurrence of sticky spheroids.
- Pre-coat the tips with pipetting up and down 1 mL of FBS. FBS coating minimizes adhesion of spheroids to plastic surfaces.
- Wash the tips with PBS 1× by pipetting up and down to remove sticky spheroids from the wall of the tips.
- Perform all pipetting steps carefully and with constant movements and treat 3D spheroids gently to avoid damage.

Problem 5

Several problems can be encountered during the embedding and cutting of MMSs. Specifically, breakage of agarose blocks might occur during transferring steps due to their soft consistency. Moreover, incorrect placement of spheroids in agarose and the embedding of agarose blocks into a paraffin cassette may result in unevenly sectioned MMSs (During step 17).

Potential solutions

- Adopt proper and standard procedures for histology staining practices.
- Gently transfer agarose blocks ensuring that all material is prepared and close by.
- Ensure an optimal positioning of spheres in the agarose by gently moving the MMSs with a fine needle.
- Ensure an optimal positioning of the agarose blocks into the paraffin cassettes.

Problem 6

Lack of signal from immunofluorescence staining (During steps 18, 20, and 21).

Potential solutions

- Ensure correct and complete deparaffinization using proper clearing solution. We recommend the use of xylene substitute (see KRT), which has a lower evaporation point than xylene and a less disturbing smell.
- Ensure to use the correct ARS specific for the antibodies used.
- Ensure antibodies have been stored correctly. Possibly, change primary antibodies trying another provider or a different antibody and/or lower dilutions.
- Using different cells and different antibodies, ensure that the antigens/markers of choice are present on the cells.
- Use the appropriate secondary conjugated antibodies ensuring the correct species-specificity and avoid overlapping the conjugate fluorophores emission wavelengths in case of multiplex immunofluorescence.

- Set up proper lasers and filters for confocal microscopy and ensure that settings match the chosen fluorophores.

Problem 7
Low MMS dissociation efficacy for the generation of single cell solutions for flow cytometry analysis (During steps 23 and 37).

Potential solutions

- Efficacy of spheroids dissociation into single cells is affected by cell types and experimental conditions. Under different conditions, cells might produce higher amounts of ECM, such as collagen. In that case, we suggest adding specific ECM-proteases (i.e., collagenase) to increase the efficacy of MMS dissociation or by optimizing the ratio of TrypLE Express and Accutase mix.
- Pay attention to excessive exposition of MMSs to dissociation solution, which might reduce cell viability.

Problem 8
Clogging of the flow cytometer's sample line due to poor dissociation of MMSs or low quantity of single cell events after the doublet exclusion step in data acquisition. (During steps 24 and 37).

Potential solutions

- Ensure proper dissociation of MMSs. In case of using cells producing large amounts of extracellular matrix, collagenase IV at a concentration of 1 mg/mL can be used to improve MMS dissociation.
- Do not skip the straining step, it is crucial to obtain a proper single cell suspension.

Problem 9
No signal detected from conjugated antibodies in FACS (During step 24).

Potential solutions

- Ensure use of proper, flow cytometry validated antibodies. Titration of antibodies is necessary in case of using different antibodies/flow cytometer than suggested in this protocol.
- Re-do the compensation matrix and adjust the lasers' voltage.

Problem 10
Spillover of 3D Cell Titer Glo and medium mix solution from the wells during orbital shaking (During step 36).

Potential solution

- Optimize a proper orbital shaking force for the type of plate, volume dispensed per well and type of MMSs to have optimal sphere lysis and to prevent solution spillover from well to well.

Problem 11
High background staining in confocal microscopy images (During step 21).

Potential solution

- Optimize antibody concentrations and incubation times.
- Use a negative control with only secondary antibody to detect unspecific binding and optimize the concentration of the secondary antibody.

STAR Protocols
Protocol

- Decrease the setting of the laser or/and the detector (laser power, gain).
- Extend the washing times or increase stringency of washing buffers by adding detergent (for instance Triton X-100, Tween 20).

RESOURCE AVAILABILITY

Lead contact

Further information and requests for resources and reagents should be directed to and will be fulfilled by the lead contact, Prof. Stephanie Kreis (stephanie.kreis@uni.lu).

Technical contact

Further technical information and requests should be directed to and will be fulfilled by the technical contacts, Cristian Angeli (cristian.angeli@uni.lu), Dr. Joanna Patrycja Wroblewska (joanna.wroblewska@uni.lu), and Eliane Klein (eliane.klein@uni.lu).

Materials availability

This study did not generate new unique reagents.

Data and code availability

This study did not generate/analyze [datasets/code].

ACKNOWLEDGMENTS

This work was supported by "MelCol" and "MultiMel" grants from the Vera Nijs & Jens Erik Rosborg Foundation (FVNER) under the aegis of the Fondation de Luxembourg and the "SecMelPro" grant from the Fondation Cancer, Luxembourg. We would like to thank the "Croix Rouge" in Luxembourg for providing Leukopak samples.

AUTHOR CONTRIBUTIONS

C.A. conceptualized and designed the MMSs model. C.A., J.P.W., and E.K. designed, performed the experiments, and analyzed the data. C.A., J.P.W., and E.K. wrote the manuscript. S.K. and C.M. edited the manuscript. S.K. acquired the fundings and supervised the whole study.

DECLARATION OF INTERESTS

The authors declare no competing interests.

REFERENCES

1. Eichhoff, O.M., Stoffel, C.I., Käsler, J., Briker, L., Turko, P., Karsai, G., Zila, N., Paulitschke, V., Cheng, P.F., Leitner, A., et al. (2023). ROS Induction Targets Persister Cancer Cells with Low Metabolic Activity in NRAS-Mutated Melanoma. Cancer Res. *83*, 1128–1146. https://doi.org/10.1158/0008547 2.CAN-22-1826.

2. Dunsche, L., Ivanisenko, N., Riemann, S., Schindler, S., Beissert, S., Angeli, C., Kreis, S., Tavassoli, M., Lavrik, I., and Kulms, D. (2023). A cytosolic mutp53(E285K) variant confers chemoresistance of malignant melanoma. Cell Death Dis. *14*, 831. https://doi.org/10.1038/s41419-023-06360-4.

3. Levesque, M.P., Cheng, P.F., Raaijmakers, M.I.G., Saltari, A., and Dummer, R. (2017). Metastatic melanoma moves on: translational science in the era of personalized medicine. Cancer Metastasis Rev. *36*, 7–21. https://doi.org/10.1007/s10555-017-9658-0.

4. Vörsmann, H., Groeber, F., Walles, H., Busch, S., Beissert, S., Walczak, H., and Kulms, D. (2013). Development of a human three-dimensional organotypic skin-melanoma spheroid model for in vitro drug testing. Cell. Death Dis. *4*, e719. https://doi.org/10.1038/cddis.2013.249.

5. Cui, X., Hartanto, Y., and Zhang, H. (2017). Advances in multicellular spheroids formation. J. R. Soc. Interface *14*, 20160877. https://doi.org/10.1098/rsif.2016.0877.

6. Han, S.J., Kwon, S., and Kim, K.S. (2021). Challenges of applying multicellular tumor spheroids in preclinical phase. Cancer Cell Int. *21*, 152. https://doi.org/10.1186/s12935-021-01853-8.

7. Mehta, G., Hsiao, A.Y., Ingram, M., Luker, G.D., and Takayama, S. (2012). Opportunities and challenges for use of tumor spheroids as models to test drug delivery and efficacy. J. Control. Release *164*, 192–204. https://doi.org/10.1016/j.jconrel.2012.04.045.

8. Nath, S., and Devi, G.R. (2016). Three-dimensional Culture Systems in Cancer Research: Focus on Tumor Spheroid Model. Pharmacol. Ther. *163*, 94–108. https://doi.org/10.1016/j.pharmthera.2016.03.013.

9. Lee, S.Y., Koo, I.S., Hwang, H.J., and Lee, D.W. (2023). In Vitro three-dimensional (3D) cell culture tools for spheroid and organoid models. SLAS Discov. *28*, 119–137. https://doi.org/10.1016/j.slasd.2023.03.006.

10. Manduca, N., Maccafeo, E., De Maria, R., Sistigu, A., and Musella, M. (2023). 3D Cancer Models: One Step Closer to in Vitro Human Studies. Front. Immunol. *14*, 1175503. https://doi.org/10.3389/fimmu.2023.1175503.

11. Brancato, V., Oliveira, J.M., Correlo, V.M., Reis, R.L., and Kundu, S.C. (2020). Could 3D Models of Cancer Enhance Drug Screening? Biomaterials *232*, 119744.

https://doi.org/10.1016/j.biomaterials.2019.119744.

12. Yakavets, I., Francois, A., Benoit, A., Merlin, J.L., Bezdetnaya, L., and Vogin, G. (2020). Advanced co-culture 3D breast cancer model for investigation of fibrosis induced by external stimuli: optimization study. Sci. Rep. *10*, 21273. https://doi.org/10.1038/s41598-020-78087-7.

13. Jarockyte, G., Dapkute, D., Karabanovas, V., Daugmaudis, J.V., Ivanauskas, F., and Rotomskis, R. (2018). 3D cellular spheroids as tools for understanding carboxylated quantum dot behavior in tumors. Biochim. Biophys. Acta. Gen. Subj. *1862*, 914–923. https://doi.org/10.1016/j.bbagen.2017.12.014.

3. Manuscript 2: A cytosolic mutp53 (E285K) variant confers chemoresistance of malignant melanoma (DOI: 10.1038/s41419-023-06360-4).

In this study, my contribution involved generating the data and the images presented in Figure 2D.

CDDpress

www.nature.com/cddis

ARTICLE OPEN

Check for updates

A cytosolic *mut*p53(E285K) variant confers chemoresistance of malignant melanoma

Luise Dunsche[1,2,6], Nikita Ivanisenko[3,6], Shamala Riemann[1,2], Sebastian Schindler[1,2], Stefan Beissert[1], Cristian Angeli[4], Stephanie Kreis[4], Mahvash Tavassoli[5], Inna Lavrik[3] and Dagmar Kulms[1,2]✉

Malignant melanoma (MM) is known to be intrinsically chemoresistant, even though only ~20% of MM carry mutations of the tumor suppressor p53. Despite improvement of systemic therapy the mortality rate of patients suffering from metastatic MM is still ~70%, highlighting the need for alternative treatment options or for the re-establishment of conventional therapeutic approaches, including chemotherapy. Screening the p53 mutation status in a cohort of 19 patient-derived melanoma samples, we identified one rarely described missense mutation of p53 leading to E285K amino acid exchange (*mut*p53(E285K)). Employing structural and computational analysis we revealed a major role of E285 residue in maintaining stable conformation of wild-type p53 (*wt*p53). E285K mutation was predicted to cause interruption of a salt-bridge network affecting the conformation of the C-terminal helix of the DNA-binding domain (DBD) thereby preventing DNA interaction. In this context, a cluster of frequently mutated amino acid residues in cancer was identified to putatively lead to similar structural effects as E285K substitution (E285 cluster). Functional analysis, including knockdown of endogenous p53 and reconstitution with diverse p53 missense mutants confirmed *mut*p53(E285K) to have lost transcriptional activity, to be localized in the cytosol of cancer cells, by both means conferring chemoresistance. Re-sensitization to cisplatin-induced cell death was achieved using clinically approved compounds aiming to restore p53 wild-type function (PRIMA1-Met), or inhibition of AKT-driven MAPK survival pathways (afuresertib), in both cases being partially due to ferroptosis induction. Consequently, active ferroptosis induction using the GPX4 inhibitor RSL3 proved superior in tumorselectively fighting MM cells. Due to high prevalence of the E285-cluster mutations in MM as well as in a variety of other tumor types, we conclude this cluster to serve an important function in tumor development and therapy and suggest new implications for ferroptosis induction in therapeutic applications fighting MM in particular and cancer in general.

Cell Death and Disease (2023)14:831 ; https://doi.org/10.1038/s41419-023-06360-4

INTRODUCTION

MM is considered to be widely chemoresistant due to multiple molecular mechanisms including modulation of the apoptotic machinery [1, 2]. Activating mutations of the serine-threonine kinases NRAS (*mut*NRAS) or BRAF (*mut*BRAF) are key drivers of uncontrolled MM growth through constitutive activation of Mitogen-Activated Protein Kinase (MAPK) pathways RAF-MEK-ERK and PI3K-AKT-mTOR [3–5]. Inhibitors targeting *mut*BRAF and/or downstream MEK have proven high response rates in patients [6, 7], however, the vast majority acquire resistance resulting in tumor relapse. Due to enhanced progression responses of relapsed metastases to immune checkpoint inhibition remain very low [8, 9]. Consequently, MM remains fatal, and demands for alternative treatment options or the reinvention of conventional treatment options, including chemotherapy [10, 11].

Mutation of the tumor suppressor p53 is found in ~50% of all human tumors leading to cancer cell resistance against p53-dependent cell cycle checkpoints and intrinsic apoptosis in response to chemotherapy [12]. In unstressed cells, *wt*p53 is kept at low expression due to MDM2-driven proteasomal turnover. Upon activation *wt*p53 initiates MDM2 transcription in a self-regulatory negative feedback loop [13]. Due to either loss-of-function or gain-of-function missense mutations, p53 remains strongly expressed in tumor cells, because mutants lose recognition of *wt*p53 transcription consensus sequences [14]. In particular missense mutations R175* (* = H), R248* (* = Q, W, G), R249* (* = T), R273* (* = C, L, H, G), R282* (* = W), and G245* (* = S, D) have been identified as hotspots for p53 gain-of-function. They encompass contact mutants that have lost the ability to bind DNA, and conformational mutants which are unable to fold properly showing significantly diminished and/or altered DNA-binding activity [15, 16], in both cases fostering tumor progression and therapy resistance [17]. Hence, restoration of *wt*p53 transcriptional activity [18–20] has become of major interest involving compounds that bind to and convert *mut*p53 into the native form of *wt*p53 (PRIMA1-Met/APR-246) [21], as well as compounds that act

[1]Experimental Dermatology, Department of Dermatology, TU-Dresden, 01307 Dresden, Germany. [2]National Center for Tumor Diseases, TU-Dresden, 01307 Dresden, Germany. [3]Translational Inflammation Research, Medical Faculty, Center of Dynamic Systems, Otto von Guericke University, 39106 Magdeburg, Germany. [4]Department of Life Science and Medicine, University of Luxembourg, Belvaux 4367, Luxembourg. [5]Molecular Oncology, Guy's Hospital, Kings College London, London SE1 1UL, UK. [6]These authors contributed equally: Luise Dunsche, Nikita Ivanisenko. ✉email: dagmar.kulms@ukdd.de

Edited by Professor Ivano Amelio

Received: 19 July 2023 Revised: 29 November 2023 Accepted: 30 November 2023
Published online: 14 December 2023

Official journal of CDDpress

SPRINGER NATURE
CDDpress

as Zn^{2+} chelators intending to inhibit misfolding of *mut*p53 (COTI-2, PEITC; [22, 23]).

Interestingly, only about 20% of MM carry p53 mutations [24], but still present with pronounced chemoresistance. We have recently identified a molecular mechanism by which MM cells that express functional *wt*p53 may escape DNA damage-induced and p53-driven cell death and undergo fast and extensive progression instead [25].

In the present study we screened the p53 mutation status of 19 patient-derived MM samples and identified one p53 missense mutation resulting in E285K conversion [26–28]. Investigating structural as well as functional properties of *mut*p53(E285K) we conclude that it serves a loss-of-function, as it lacks transcription of designated target genes, and confers chemoresistance. We provide evidence that sensitization of patient-derived *mut*-p53(E285K)-expressing MM cells to cisplatin via restoration of *wt*p53 function and MAPK inhibition, respectively, involves ferroptosis induction. Hence, we show ferroptosis induction through glutathione peroxidase 4 (GPX4) inhibition to tumorselectively eliminate *mut*p53- as well as *wt*p53-expressing MM cells, paving new avenues for improved MM treatment.

MATERIALS AND METHODS

Cells and reagents

Human melanoma cells were isolated from patients metastasis [M#10 = m (63); M#18/M#20 = m (87); M#31 = m (56); M#34 = m (70); M#35 = f (81); M#40 = m (75); M#45 = m (39); M#46/M#51_1/M#51_2/M#53 = m (72/73); M#47_1/M#47_2 = m (72); M#48 = m (52); M#54 = m (74); M#58 = m (82); M#59 = m (48); M#70 = m (51)], through incubation in HBBS (w/o Ca^{2+} and Mg^{2+}) containing 0.05% collagenase; 0.1% hyaluronidase; 1.25 U/ml dispase; 20 mM HEPES, 100 g/ml gentamycin; 100 U/ml penicillin and 100 g/ml streptomycin for 60 min at 37 °C in a humified atmosphere of 5% CO_2, and maintained in RPMI + 10% FCS (Invitrogen, Karlsruhe, Germany). The usage of patient-derived melanoma samples was approved by the ethics committee of the TU-Dresden (SR-EK230052020) and informed consent was obtained from all patients. Human melanoma cell lines WM1552C and SkMel29 were maintained in RPMI 1640 with 10% FCS. Primary human fibroblasts and melanocytes were purchased from Cell Systems (Troisdorf, Germany) and maintained in DMEM + 10% FCS or Melanocyte Growth Medium (M2, Promocell, Heidelberg, Germany).

All cell samples and cell lines were tested every other month to be mycoplasma-negative as judged by the MycoAlert Mycoplasma Detection Kit (LT-07, Lonza, Visp, Switzerland).

For stimulation of cells, Cisplatin (GRY-Pharma, Kirchzarten, Germany) was added at 15 µM, dabrafenib (#S2807; Selleckchem, Munich, Germany) at 10 µM, trametinib (#S2673; Selleckchem) at 10 nM, QVD (#IMI-2309-1; Novus Biologicals, Littleton, CO, USA) at 5 µM, Nec1s (#2236; BioVision, Hannover, Germany) at 15 µM, alpelisip (#HY-15244; MedChemExpress, Monmouth Junction, NJ, USA) at 10 µM, afuresertib (#S7521; Selleckchem) at 10 µM, PRIMA1-Met (#HY-19980; MedChemExpress) at 5–40 µM, COTI-2 (#HY-19896; MedChemExpress) at 0.5–10 µM, PEITC (#253731; Sigma-Aldrich, Taufkirchen, Germany) at 1–15 µM, MG132 (Merck Millipore, Darmstadt, Germany) at 10 µM, ferrostatin-1 at 15 µM, and RSL3 at 1.13 µM (kindly provided by Andreas Linkermann, TU-Dresden) to cell culture media.

RT-PCR, plasmids, cloning and transfection

RNA was extracted from 2×10^6 cells, reverse transcribed using First Strand cDNA Synthesis Kit (Thermo Scientific, Waltham, MA, USA) and subjected to PCR amplification using primers directed against p21 and MDM2 (#HP200369; #HP206085, OriGene Technologies, Inc. Rockville, MD, USA). GAPDH (forward: 5′-GCCTCCTGCACCACCAACTGC-3′ and reverse primer: 5′-CCCTCCGACGCCTGCTTCAC-3′) served as housekeeping expression control. For cloning and sequencing p53 was reverse transcribed and amplified via PCR using forward: 5′-CTAGCTAGCATGGAGGAGCCGCAG-3′ and reverse primer: 5′-GCATCTAGAGTCTGACTGAGGCCCTTC-3′. cDNA was cloned via NheI/XbaI restriction into pcDNA3.1(+) and subjected to sequence analysis (GATC, Konstanz, Germany) using pcDNA3.1-FP 5′-CTCTGGCTAACTAGAGAAC-3′ and pcDNA3.1-RP 5′-CAAACAACAGATGGCTGGC-3′ primer within the vector, and p53for 5′-ATGACGGAGGTTGTGAG-3′ and p53rev 5′-ACTCGGATAAGATGCTGAGG-3′ primers designed to match with the p53 cDNA. Sequences were subjected to BLAST analysis compared to *wt*p53 transcript variant 1 (https://www.ncbi.nlm.nih.gov/nuccore/NM_000546.4). pRetroSuper-blasto-p53i plasmid was used to stably knock down p53 in the presence of 5 µg/ml blasticidin (Thermo Scientific) [29]. Ectopic re-expression of p53 was facilitated by electroporating 6.5×10^6 cells with 25 µg of pCMV-neo-Bam-based p53 variants encoding plasmids containing silent mismatches [29] in 600 µl RPMI + 10% FCS + 1.25% DMSO. Based on the pCMV-neo-Bam-*wt*p53 plasmid site directed mutagenesis was performed to gain p53-E285K, p53-E285R, p53-K132E, p53-R175H, and p53-R248W mutants. Pfu-ultra polymerase (Promega, Madison, VC, USA) followed by *DpnI* digestion (Thermo Scientific) was used according to the manufacturer's instruction.

3D melanoma spheroids

M#31 and M#54 cells were transfected with pEGFP-N1 and stable clones selected by sorting (FACSAria III, BD-Biosciences, Heidelberg, Germany). Spheroids were generated using the "hanging drop" method as described before using 20×10^4 cells per drop [30]. After 12 days, individual spheroids were embedded into 30 µl of a dextran-based gel-matrices containing 4 nMol/L of thiol-reactive groups (3-D Life Dextran-CD Hydrogel SG, #G93-1; Cellendes, Reutlingen, Germany), according to the manufacturer's protocol [30] and incubated at 37 °C for 30 min. Subsequently, gels were covered with medium. Cell death of spheroids was visualized by addition of 6.7 µg/ml propidium iodide (PI, #3566, Thermo Scientific) in PBS for 20 min at RT. Confocal images were taken using an LSM 780/FCS inverse confocal fluorescence microscope (Zeiss, Marburg, Germany). Green fluorescence emission peak was 488 nm (emission filter 499–597 nm), 561 nm for red fluorescence (emission filter 606–686 nm).

Determination of cell death

Cell death was quantified in a 96-well format by determining PI (1 µg/ml) uptake every 4 h for 24 h using automated image-based IncuCyte® (Satorius, Goettingen, Germany) screening technology. High red intensity was quantified using the "cell-by-cell-module".

TUBE assay

Cells were lysed in TUBE lysis buffer (50 mM Tris-HCl, pH 7.5; 150 mM NaCl; 1% NP-40, 1 mM EDTA 10% glycerol) supplemented with Complete® (Roche, Mannheim, Germany), 10 µM PR-619 and 1 × 1,10-phenoanthroline. TUBE-Agarose pull down was performed according to the manufacturer's instructions (UM401, Life Sensors, Philadelphia, PN, USA), and protein extracts analyzed by Western-blotting.

Western-blot analysis

For whole cell lysates, cells were lysed in lysis buffer (50 mM HEPES, pH 7.5; 150 mM NaCl; 10% glycerol; 1% Triton-X-100; 1.5 mM $MgCl_2$; 1 mM EGTA; 100 mM NaF; 10 mM pyrophosphate; 0.01% NaN_3 (phosSTOP®; Complete®). For fractionation cytosolic (C: 10 mM HEPES, pH 7.5; 10 mM KCl; 100 µM EDTA; 0.5% NP-40) and nuclear (N: 20 mM HEPES, pH 7.5; 400 mM NaCl, 1 mM EDTA) extraction buffers were supplemented with phosSTOP®; Complete®; 1 mM DTT and 1 mM PMSF. Protein content was determined using DC Protein assay kit (BioRad, Hercules, USA). Protein extracts were subjected to SDS-PAGE (BioRad), blotted onto nitrocellulose membranes and incubated with antibodies directed against PARP, p53 (#551025, #554293, BD-Biosciences), caspase-3, cleaved caspase-3, γH2AX, H3, IκBα, MDM2, p21, p-p53(Ser15), PUMA, Tom20, and ubiquitin (#9665, #9661, #2577, #4499 #4814, #86934, #2947, #9284, #12450, #42406, #43124, Cell Signaling, Camebridge, UK), respectively. Equal loading was monitored by 0.1% Ponceau S (#5983.2, Roth, Karlsruhe, Germany) staining, and/or by re-probing membranes with an antibody against β-actin (#4970, Cell Signaling). HRP-conjugated secondary antibodies (mouse: #NA931; rabbit: #NA934) were purchased from GE-Healthcare (Buckinghamshire, UK). Bands were visualized with chemiluminescense SuperSignal® detection systems (Thermo Scientific).

Quantification and statistical analysis

Unless stated otherwise, results of cell death analysis are presented as mean ± SD of 3 independently performed experiments. PI intensity of respective control cells was subtracted from PI intensity in response cisplatin treatment to gain net increase in PI uptake, as shown in graphs. Western-blot analysis, RT-PCR, and immunofluorescent images represent one out of 3 independently performed experiments. Statistical analysis was

performed with unpaired Student *t-test* using GraphPad PRISM 6 software (https://www.graphpad.com). Quantification of tumor mass was performed calculating the area of the green fluorescent spheroid and the red PI stained cells using Fiji software (https://fiji.sc).

Bioinformatics and structural modeling

The ranking of solid cancers was deduced from https://gco.iarc.fr/today, excluding non-solid tumors (Non-Hodgkin lymphoma and leukemia) (Table S1). 10 pan-cancer studies from https://www.cbioportal.org were used to determine the frequency of p53 mutations in the selected cancer types. For analysis of p53-specific mutations in melanoma, data from https://www.cbioportal.org/study/summary?id=msk_met_2021 [31] were evaluated [32, 33]. The TP53 Database https://tp53.isb-cgc.org [34] was used to analyze the prevalence of p53 mutation in individual cancer types.

The structure of full-length *wt*p53 was derived from the AlphaFold Database [35]. The structure of *mut*p53 DNA-binding domain was predicted with ESMFold model [36]. The structural model of *mut*p53 bound to DNA was derived by structural alignment and replacing the *wt*p53 subunit from *wt*p53/DNA complex [37] by ESMFold-derived models using PyMOL software (https://pymol.org/2/). Stability changes were estimated as the per-residue difference in the pLDDT score derived from ESMFold models between wild-type and mutant proteins. Rosetta energy of interactions was predicted using RosettaDDG implemented within the PyRosetta framework [38] and ESMFold-derived model of p53 as an input. Stability changes using PoPMuSiC [39], PremPS [40], and MAESTRO [41] were predicted through corresponding web interfaces. The crystal structure of the p53 DNA-binding domain (PDB ID 2ADY) [42] was used for predictions.

RESULTS

Malignant melanoma comprises about 20% p53 mutations

MM was recently ranked among the top 15 most prevalent solid tumors worldwide (https://gco.iarc.fr/today; Fig. 1A; Table S1). While mutation of the tumor suppressor p53 presents with highest incidence among all cancers (48.3%), MM comprises only 21.5% p53 mutations (https://www.cbioportal.org; [32, 33] Fig. 1A; Table S2A, B), despite showing a highly progressive phenotype and chemoresistance. The spectrum of p53 mutations shows high diversity, predominantly truncations and missense mutations as deduced from https://www.cbioportal.org/study/summary?id=msk_met_2021 [31] (Fig. 1B). Most missense mutations as identified by *The TP53 Database* (https://tp53.isb-cgc.org; [34]) are located within the DBD of this transcription factor as indicated by spheres within the AlphaFold database-derived p53 protein structure model [35] (Fig. 1C).

p53 E285K mutation is localized close to the DNA-binding domain and renders melanoma cells resistant to cisplatin-induced cell death

To investigate the impact of *wt*p53 *versus mut*p53 on therapy responsiveness we sequenced p53 of 19 melanoma cell samples isolated from 14 patients with known BRAF/NRAS mutation status, and therapeutic record. In particular, from three primary tumors (Table 1, group 1 = light gray), seven systemic metastases (Table 1, group 2 = gray), and nine brain metastases (Table 1, group 3 = dark gray). In each group at least one p53 variant was identified: primary tumor-derived M#34 presented a c.237-238 deletion resulting in frame shift and premature stop at codon 147; skin metastasis-derived M#35 was identified to be a splice variant; brain metastasis-derived M#10 showed genomic loss of p53, all of which represent p53 loss-of-function. Brain metastasis-derived M#31 represented the only c.853G > A missense mutation, resulting in E285K amino acid exchange (Table 1).

To this end, our patient cohort convincingly represented the frequency (21.05%) and the heterogeneity of p53 mutations in MM. However, the p53 mutation status neither correlated with the BRAF/NRAS mutation status nor with MM localization (host tissue) or therapeutic stage, indicating that p53 mutation happens independently of these parameters. Moreover, six out of the remaining 15 MM samples expressed the p53 P72R point mutation (c.215C > G) considered to be a phenotypically silent single nucleotide polymorphism (SNP) [43]. Similar to M#10, M#34 and M#35 did not express the p53 protein, and hence p53 transcription-dependent MDM2 and p21 proteins remained absent in these loss-of-function variants (Fig. 2A). *Mut*p53(E285K) expression in M#31 appeared to be the strongest amongst all MM samples but also lacked MDM2 and p21 expression implying that *mut*p53(E285K) is not transcriptionally active [15, 16]. The structure of *wt*p53 bound to DNA suggested E285K mutation to be localized in a C-terminal helix of the DBD, which is in close proximity but not part of the DNA recognition site (Fig. 2B). More detailed structural analysis using Rosetta software [38] revealed E285K substitution to reduce conformational stability of the DBD, thereby putatively interfering with its function. Similar impact of E285K substitution was predicted by Polyphen2 [44], SIFT [45], and REVEL [46] tools (Table S3).

Responses of all MM samples to targeted *mut*BRAF inhibitor dabrafenib, downstream MEK1 inhibitor trametinib, or the clinically relevant co-inhibition remained very low, 10–20%, irrespective of the intrinsic BRAF/NRAS or p53 mutation status (Fig. S1). Upon treatment with the chemotherapeutic drug cisplatin, however, *wt*p53-expressing M#59, M#51_1/M51_2, M#46, M#48, M#53, M#54, M#58, and M#70 samples responded with 45–75% cell death, followed by p53(P72R-SNP)-expressing M#18, M#20, M#45, M#47_1/47_4, M#40 and M#48 cells (~50%). Surprisingly, M#10 cells featuring genomic p53 loss, remained quite sensitive to cisplatin-induced cell death (40%), whereas somatic p53 loss in M#34 and M#35 reduced cell death to 25–15%. M#31 stayed most resistant to cisplatin treatment (˂10%), suggesting *mut*p53(E285K) to serve a loss- or gain-of-function (Fig. 2C). To understand the role of *mut*p53(E285K) in cisplatin resistance we examined M#31 brain metastasis along with *wt*p53-expressing brain metastasis M#54. Cisplatin resistance of M#31 was confirmed comparing GFP-expressing M#31 and M#54 spheroids in an in vivo-mimicking 3D setting [30]. Three days after continuous cisplatin treatment, quantification of tumor mass (green) *versus* % PI-positive (PI^+, red) revealed significant cell death induction in M#54 spheroids but had only marginal effects on M#31 spheroid survival (Fig. 2D). Finally, RT-PCR confirmed expression of p53-responsive p21 and MDM2 genes to remain absent in *mut*p53(E285K)-expressing M#31 cells, while being present in *wt*p53-expressing M#54 cells (Fig. 2E). Conclusively, E285K missense mutation appears to interfere with DNA-binding.

Cytosolic localization of *mut*p53(E285K) protein is independent of K285 ubiquitination

According to the p53 structure, E285 takes part in formation of a salt-bridge network comprising electrostatic interactions of positively and negatively charged amino acid residues: E285, K132, E271, K164, and R273 (Fig. 3A). The amino acid exchange at position 285 from E to K causes a switch of charges leading to structural destabilization of this salt-bridge network entailing conformational changes of the p53 protein. For validation we computed the structural models of *wt*p53 and *mut*p53(E285K) using ESMFold [36], allowing to predict the tertiary structure of a target protein from amino acid sequence information alone, and providing the model quality metrics (pLDDT) for each amino acid residue. Indeed, ΔpLDDT analysis suggested E285K substitution to decrease stability of the aa281-294 region (Fig. 3A; Table S4), thereby affecting stability of the DBD itself (Table S3), and the area that connects the DBD to the tetramerization domain (TET) (compare Fig. 1C). Performing native-PAGE revealed complex formation of *mut*p53(E285K) in response to cisplatin treatment not to be altered compared to *wt*p53 (Fig. S2), implying that not tetramerization but rather DNA recognition is predominantly affected through destabilization of the salt-bridge network. Importantly, the salt-bridge network includes one hotspot for

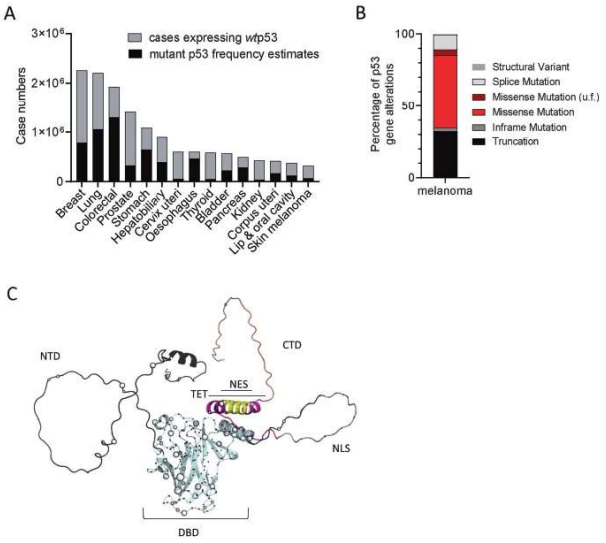

Fig. 1 Malignant melanoma comprises about 20% p53 mutations. A The frequency of p53 mutations taken from https://www.cbioportal.org was multiplied by the case number of the selected cancers https://gco.iarc.fr/today to get the estimated cases of mutant p53. **B** Percentage of different p53 alterations in melanoma analyzed from https://www.cbioportal.org/study/summary?id=msk_met_2021. **C** Full atom p53 structure with positions of mutations. NTD (1-93) = Intrinsically Disordered N-terminal Domain (gray); CTD (360-393) = C-terminal domain (brown); NES (340–351) = nuclear localization signal (yellow); TET (323–360) = tetramerization domain (purple); DBD (94–294) = DNA-binding domain (light blue). Spheres indicate the positions of missense mutations observed in tumor samples according to https://tp53.isb-cgc.org. The radii of spheres correspond to the mutation frequency in cancer.

Table 1. Overview of patient-derived tumor sample analysis.

M#	Mutation status	Localization	Therapy	p53 status
M#18	NRASQ61H	Primary tumor	None/surgery	wt (P72R)
M#34	NRASQ61L	Primary tumor	None	Truncated (cod. 147)
M#59	BRAFV600E	Primary tumor	None	wt
M#20	NRASQ61H	Lymph node metastasis	None/surgery	wt (P72R)
M#35	NRASQ61L	Skin metastasis	None	Splice mutation
M#45	BRAFV600E	Muscle metastasis	IFNα/ipilimumab/surgery	wt (P72R)
M#47_1	NRASQ61L	Skin metastasis	None	wt (P72R)
M#47_4	NRASQ61L	Skin metastasis	None	wt (P72R)
M#51_1	BRAFV600E	Lymph node metastasis	Dabrafenib/trametinib	wt
M#51_2	BRAFV600E	Intestine metastasis	Dabrafenib/trametinib	wt
M#10	BRAFV600E	Brain metastasis	IFNα/dabrafenib	Genomic loss
M#31	NRASQ61L	Brain metastasis	IFNα/pembrolizumab/bevazicumab/IFNα	E285K
M#40	wt	Brain metastasis	Nivolumab	wt (P72R)
M#46	BRAFV600E	Brain metastasis	None	wt
M#48	NRASQ61R	Brain metastasis	Ipilimumab/nivolumab	wt (P72R)
M#53	BRAFV600E	Brain metastasis	Dabrafenib/trametinib	wt
M#54	wt	Brain metastasis	Ipilimumab/nivolumab	wt (P72R)
M#58	wt	Brain metastasis	None	wt
M#70	BRAFV600K-NRASQ61R	Brain metastasis	Vemurafenib/cobimetinib	wt (P72R)

P53 mutations status of 19 human melanoma cell samples isolated from primary tumor (light gray), systemic metastases (gray), and brain metastases (dark gray) of known BRAF/NRAS mutation status, and therapeutic record are summarized.

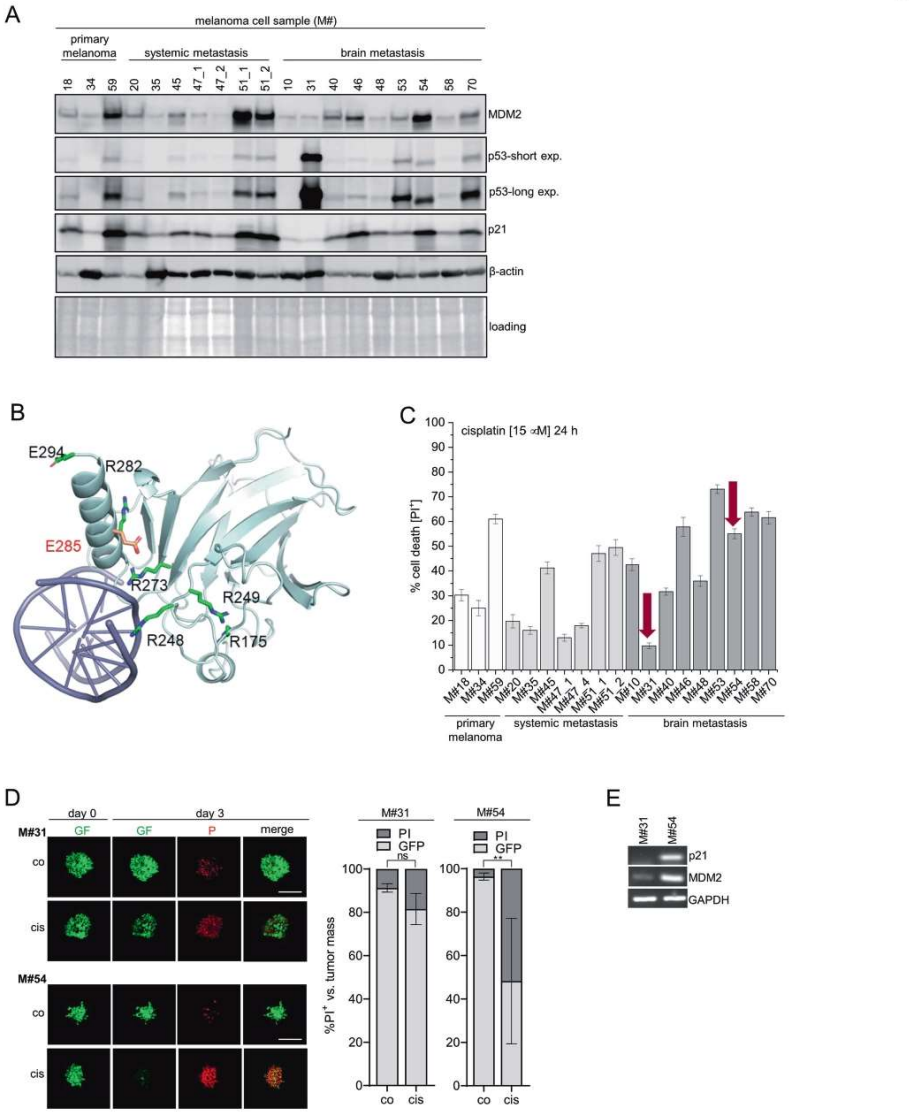

p53 gain-of-function mutation (R273), which directly interacts with DNA, and may be affected by structural changes due to E285K mutation thereby potentially serving an indirect gain-of-function.

To test if exposure of K285 within this less stable p53 protein conformation relies on K285 ubiquitination we performed TUBE assay. Addition of the proteasome inhibitor MG132 clearly caused overall accumulation of ubiquitinated proteins in the input lysates, however, *mut*p53(E285K) did not become ubiquitinated itself and, thus, remained unbound to the TUBE (Fig. 3B). In contrast, ubiquitinated *wt*p53 in M#54 cells became strongly accumulated

Fig. 2 p53-E285K mutation is localized close to the DNA-binding domain and renders melanoma cells resistant to cisplatin-induced cell death. A Expression of p53, MDM2, and p21 of unstimulated melanoma cell samples was assessed by Western-blot analysis with β-actin and Ponceau S staining as loading controls. **B** The DBD domain of p53 bound to DNA: The designated hotspot mutations of p53 are shown in green. E285 residue is depicted in red. **C** Cell death induction (PI^+) was monitored 24 h after stimulation of MM cell samples with cisplatin (15 µM) ($n = 3$; mean ± SD). Red arrows point at cell death responses of *mut*p53(E285K)-expressing M#31 and *wt*p53-expressing M#54 cells. **D** Individual GFP-expressing M#31 and M#54 spheroids were stimulated with cisplatin (15 µM) for 72 h. Cell death was visualized upon addition of PI (6.7 µg/ml). Confocal images of individual spheroids at day one and three as well as the quantification of tumor volume (green) *versus* tumor death (red) at day three are shown ($n = 3$; mean ± SD; $^{**}p \leq 0.01$; ns not significant). **E** Transcription of p21 and MDM2 in M#31 and M#54 cells, respectively, was assessed by RT-PCR. GAPDH served as housekeeping expression control.

and upon proteasomal inhibition and, hence, was captured by TUBE pull down (Fig. S3). These data imply that the switch of charge at position 285 alone is sufficient to cause conformational changes leading to a complete loss-of-function phenotype in *mut*p53(E285K) expressing cells. To confirm this concept, we reconstituted M#31 cells stably silenced for endogenous p53 with *wt*p53, as well as with E285K and a E285R p53 variant, which also provides the positive charge but is incapable of being ubiquitinated. Only *wt*p53 re-expressing M#31 cells responded to cisplatin with significant cell death induction, whereas both, *mut*p53(E285K) and *mut*p53(E285R) re-expression had no effect (Fig. 3C), confirming that destabilization of the salt-bridge network - independent of ubiquitination - is sufficient to cause cisplatin resistance in M#31 cells. Since E285 is in direct contact with K132 within this salt-bridge network (Fig. 3D), RosettaDDG software and ESMFold predicted K132E conversion to have a similar functional effect as E285K substitution (Fig. 3D; Table S5).

Accordingly, we investigated the effect of E285K along with K132E mutation in comparison to designated R175H and R248W gain-of-function p53 mutants on cisplatin-induced cell death in M#31 and M#54 cells stably silenced for endogenous p53. Intriguingly, silencing of *wt*p53 in M#54 only moderately but significantly reduced cisplatin-induced cell death, and was fully restored by re-expression of *wt*p53, implying that the presence and/or mutation status of p53 may not exclusively decide about cellular fate in response to DNA damage induction (Fig. 3E; Fig. S4A, B). Reconstitution of either E285K or K132E - just like R175H and R248W gain-of-function mutants - reduced cell death responses to the level of p53-silenced M#54 cells. As predicted, none of the p53 mutants but only ectopic expression of *wt*p53 slightly increased cell death in M#31 cells in response to cisplatin, supporting that affecting the salt-bridge network may phenotypically cause loss of p53 function. This becomes even more evident by showing that exclusively reconstitution of *wt*p53 but neither of E285K and K132E p53 variants, nor R175H and R248W gain-of-function p53 mutants re-gained p21 and MDM2 expression in M#31 cells (Fig. 3F). Following this line, only reconstitution of M#10 patient samples harboring genomic loss of p53 as well as M#34 samples presenting with somatic p53 loss with *wt*p53 but not with *mut*p53(E285K) re-gained expression of p21 and MDM2 RNA and proteins (Fig. S5A–D). To this end, data allow to conclude that E285 missense mutation causes complete failure of p53 to recognize responsive promoter elements.

Intriguingly, we found *mut*p53(E285K) to be exclusively localized in the cytosol of M#31 cells (Fig. 3G), with no significant recruitment to mitochondria (Fig. S6). While nuclear *wt*p53 in M#54 cells becomes upregulated and phosphorylated at Ser15 in response to cisplatin, cytosolic *mut*p53(E285K) also becomes phosphorylated but only a small fraction translocates into the nucleus, certainly contributing to the lack of transcriptional activity (MDM2, p21) of *mut*p53(E285K).

Mutations within the E285 cluster show high prevalence in melanoma and other cancer types

A more detailed model-based analysis revealed a whole cluster of amino acids frequently being mutated in p53-expressing cancers that may have a similar functional effect on the C-terminal helix of the DBD domain as E285K (E285 cluster) (Fig. 4A). Database analysis at https://www.cbioportal.org/study/summary?id=msk_met_2021 [31] revealed that the percentage of mutations within the E285 cluster (12%) is almost as high as of gain-of-function mutations at positions R175*, R248* and R273* (18%) (Fig. 4B). In particular, MM patients carrying missense mutations at positions S127*, E285*, and K132* within the E285 cluster present with elevated death rates comparable to patients with R175* or R273*, but clearly higher than R248* or G245* hotspot gain-of-function p53 mutations (Fig. 4C). Intriguingly, mutations within the E285 cluster and particularly E285K showed a high prevalence not only in MM but in a wide range of other cancer types, especially in those of endocrine glands (https://tp53.isb-cgc.org; [34]; Fig. 4D). Providing this global and pronounced prevalence of E285-cluster mutations, we aimed to identify a strategy to sensitize *mut*p53(E285K)-expressing cancer cells to chemotherapy.

*Mut*p53(E285K) gain-of-function expressing M#31 cells can be sensitized to cisplatin using PRIMA1-Met and AKT inhibition, respectively

Restoration of *wt*-function of *mut*p53 in human cancers has been a task for many years, however, most (pre-)clinical studies have been performed using p53 hotspot mutants [16]. We investigated p53-dependent (re-)sensitization of *mut*p53(E285K)-expressing M#31 cells to cisplatin-induced cell death using three compounds, COTI-2, PEITC, and PRIMA1-Met which have been included into multiple clinical trials (https://www.cancer.gov/about-cancer/treatment/clinical-trials/intervention/mutant-p53-activator-coti-2; https://clinicaltrials.gov/ct2/show/NCT00691132; https://aacrjournals.org/mct/article/12/11/2331/91591/PRIMA-1Met-APR-246-Displays-High-Antitumor; [16]). Low doses of COTI-2 and PEITC had only marginal effects on cisplatin-induced cell death, but displayed cisplatin-independent cytotoxicity at higher doses (Fig. 5A). Treatment with PRIMA1-Met instead pronouncedly enhanced cisplatin-induced cell death, with highest synergy at 20 µM (Fig. 5A). As expected, none of the respective drugs further enhanced cisplatin-induced cell death in *wt*p53-expressing M#54 cells (Fig. S7). In M#31 cells, however, sensitization to cisplatin by PRIMA1-Met co-treatment neither enhanced nuclear translocation of *mut*p53(E285K) compared to cisplatin alone, nor did it cause p53-dependent upregulation of pro-apoptotic PUMA (Fig. 5B). Hence, caspase-3 processing and pronounced PARP cleavage, being indicative for apoptotic cell death, remained absent (Fig. 5B), questioning whether restoration of p53 *wt*-function is the primary mode of action of PRIMA1-Met. Accordingly, cell death in response to co-treatment with PRIMA1-Met and cisplatin could partially be rescued by inhibitors for apoptosis (QVD), and also of ferroptosis (ferrostatin-1), but not necroptosis (Nec1s), indicating a mixed form of apoptotic and ferroptotic cell death to be induced (Fig. 5C).

An alternative strategy to enhance cell death in MM is concomitant inhibition of MAPK-dependent survival pathways [47]. Since inhibition of the MEK-dependent branch of MAPK signaling proved ineffective in MM samples (compare Fig. S1), we selected clinically relevant alpelisib (iPI3K) and afuresertib (iAKT) to inhibit PI3K and AKT signaling [30], respectively. Only iAKT but not iPI3K synergistically sensitized *mut*p53(E285K)-expressing M#31

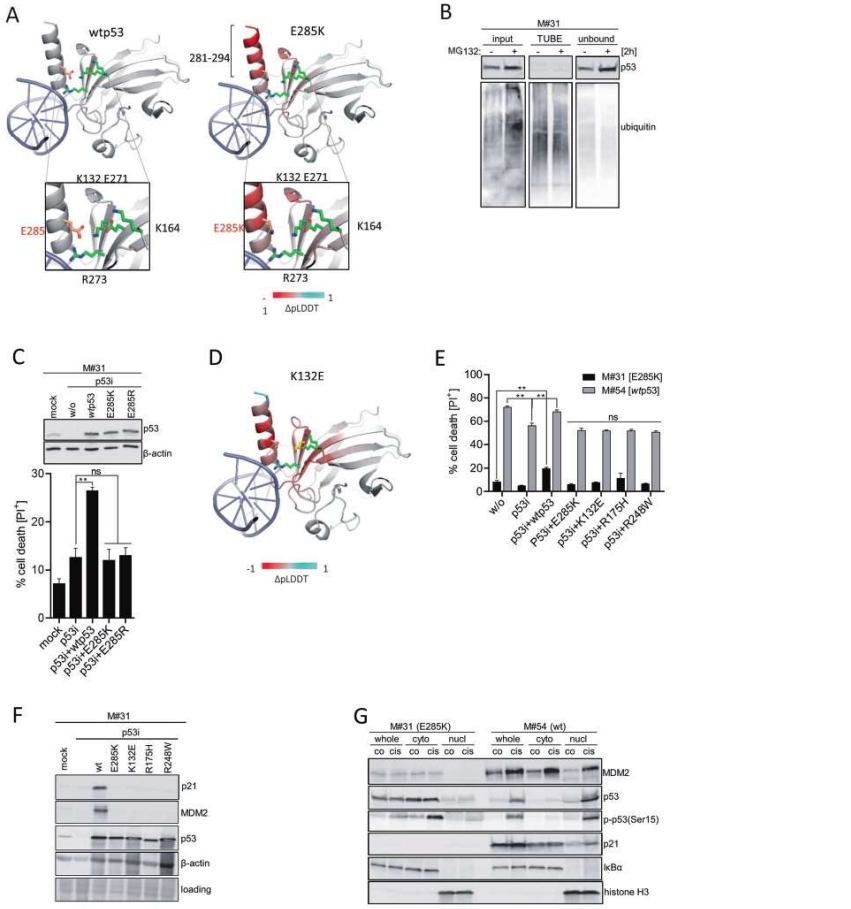

Fig. 3 Cytosolic expression of *mut*p53(E285K) protein is independent of putative K285 ubiquitination. A The effect of the E285K mutation on 281–294 helix stability was validated compared to *wt*p53 using ESMFold model. Red color indicates reduction in protein stability according to changes in pLDDT score from red (destabilizing) to cyan (stabilizing). *Mut*p53(E285K) is shown in red. Magnifications illustrate the molecular interaction network involving E285 (left) *versus* K285 (right). The key residues involved in this network: K132, E271, K164, and R273 are shown in green. The structure is colored according to changes in protein stability due to mutation as estimated by the ESMFold ΔpLDDT score from red (destabilizing) to cyan (stabilizing). **B** M#31 cells were pretreated or not with MG132 (10 μM) for 2 h and a TUBE assay performed. **C** M#31 cells silenced for endogens *mut*p53(E285K) were reconstituted with *wt*p53, *mut*p53(E285K), and *mut*p53(E285R), respectively, and cell death (PI^+) monitored 24 h after stimulation with cisplatin (15 μM) using IncuCyte® technology ($n = 3$; mean ± SD; $^{**}p \leq 0.01$; ns not significant). **D** Prediction of the effect of K132E mutation on the p53 DBD structure using ESMFold model. The structure is colored according to changes in protein stability due to mutation as estimated by the ESMFold ΔpLDDT score from red (destabilizing) to cyan (stabilizing). K132E and E285K mutations are depicted in yellow and red, respectively. The other residues involved in the salt-bridge network formation (K132, E271, K164, and R273) are shown in green. **E** M#31 and M#54 cells stably silenced for endogenous p53 were reconstituted with *wt*p53, and *mut*p53 variants E285K, K132E, R175H, and R248W, respectively, and cell death (PI^+) monitored 24 h after stimulation with cisplatin (15 μM) ($n = 3$; mean ± SD; $^{**}p \leq 0.01$; ns not significant). **F** The same M#31 transfectants were used to assess p21 and MDM2 expression by Western-blot analysis. β-actin served as loading control. **G** M#31 (E285K) and M#54 (*wt*) cells were stimulated with cisplatin (15 μM). After 24 h localization of MDM2, p53, p-p53(Ser15), and p21 was monitored in whole cell lysates as well as in cytosolic and nuclear fractions by Western-blot analysis. IκBα and histone H3 served as loading/fractionation controls.

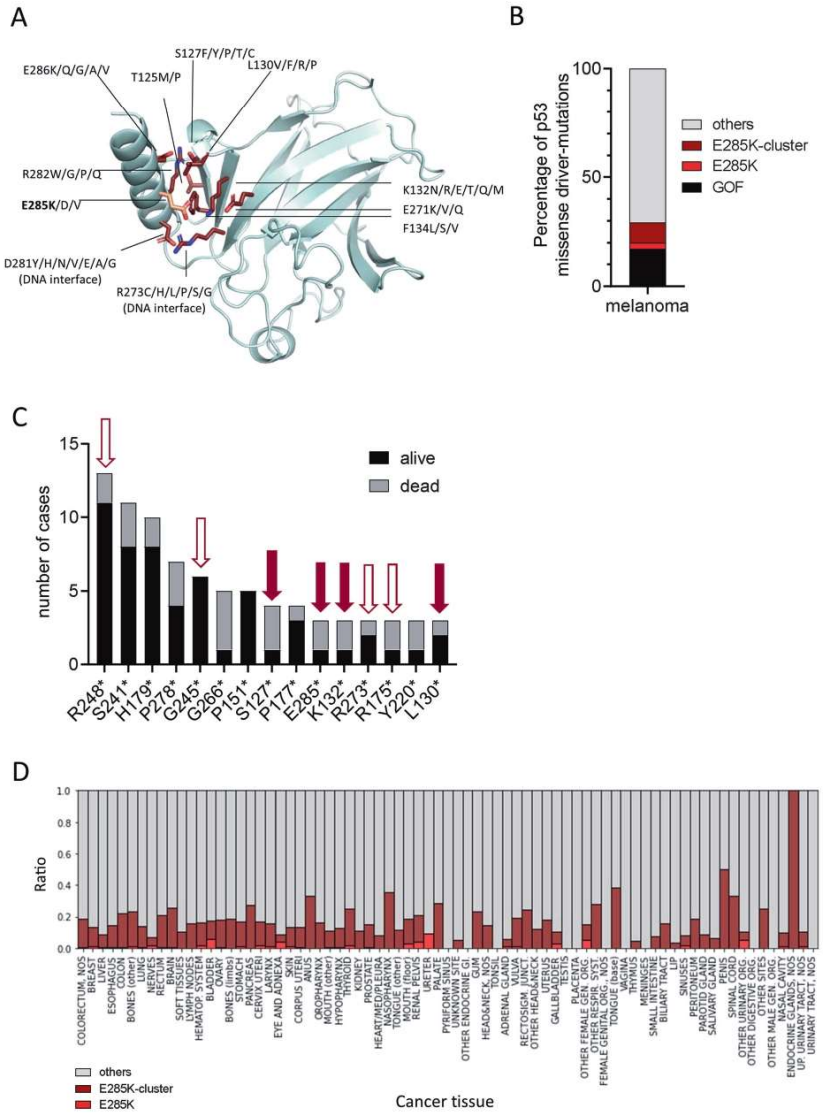

Fig. 4 Mutations within the E285 cluster show high prevalence in melanoma and other cancer types. A The cluster of amino acid mutations within p53 that can have a similar functional effect on the C-terminal helix of the DBD domain as E285K. The E285K mutation is shown in light red, all other mutations in dark red. Mutant residues forming contacts interacting with DNA in the DNA-bound p53 complex are indicated ("DNA interface"). **B** Prevalence of E285-cluster mutations and in particular E258K mutation compared to other p53 mutation variants in MM, and **C** the frequency of most common p53 mutation in MM was correlated with the patient outcome (alive vs death) https://www.cbioportal.org/study/summary?id=msk_met_2021. Filled red arrows point at mutations being present in the E285 cluster, open red arrows at designated gain-of-function mutations. **D** The frequency of p53 missense mutations in various cancer tissues. The ratio of E285* (light red), of mutations within the E285 cluster (dark red), and all other p53 mutations (gray) as derived from https://tp53.isb-cgc.org is shown.

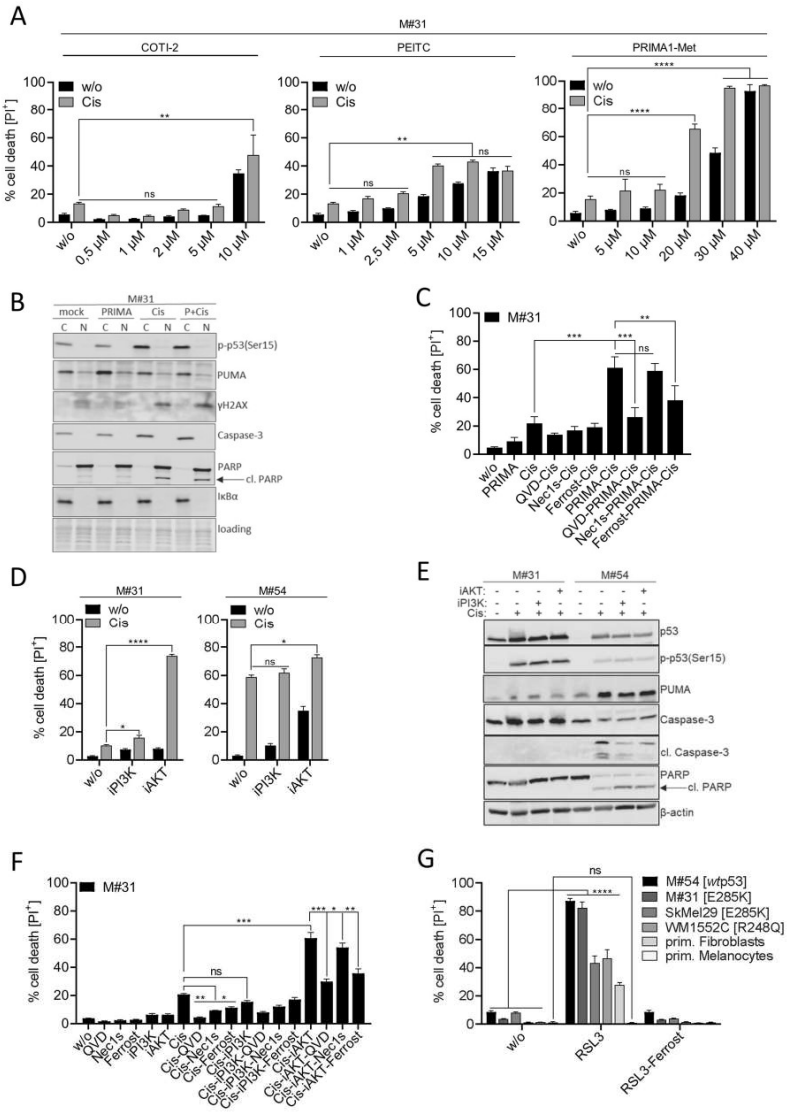

cells to cisplatin-induced cell death (70%) without showing cisplatin-independent cytotoxicity. In contrast, iAKT showed some toxicity in *wt*p53-expressing M#54 cells, but neither iAKT nor iPI3K pronouncedly enhanced cisplatin-dependent cell death (Fig. 5D). However, apoptosis induction was only evident in M#54 cells, due to upregulation and phosphorylation of *wt*p53, followed by p53-driven upregulation of PUMA and processing of caspase-3 and PARP, respectively. (Fig. 5E). In M#31 cells, phosphorylation of p53 did not result in transcriptional upregulation of PUMA, and consecutive apoptotic features, and hence, could only be partially

Fig. 5 *Mut*p53(E285K) gain-of-function expressing M#31 cells can be sensitized to cisplatin using PRIMA1-Met and AKT inhibition, respectively. A M#31 cells were pretreated for 1 h with COTI-2, PEITC, and PRIMA1-Met at the indicated concentrations and cell death (PI^+) monitored 24 h after stimulation with cisplatin (15 µM) ($n = 3$; mean ± SD; $^{****}p \le 0.0001$; $^{**}p \le 0.01$; ns not significant). **B** The effect of PRIMA1-Met treatment on the subcellular localization and expression of p53, p-p53(Ser15), γH2AX, Caspase-3, PUMA, and PARP was monitored in cytosolic/nuclear fractions by Western-blot analysis. Ponceau S staining and IκBα served as loading/fractionation controls. **C** M#31 cells were pre-stimulated with QVD (5 µM), Nec1s (15 µM), or ferrostatin-1 (15 µM) for 1 h followed by treatment with PRIMA1-Met (20 µM). 24 h after cisplatin (15 µM) treatment cell death (PI^+) was monitored ($n = 3$; mean ± SD; $^{***}p \le 0.001$; $^{**}p \le 0.01$; ns not significant). **D** M#31 and M#54 cells were pretreated with alpelisip (iPI3K, 10 µM) and afuresertib (iAKT, 10 µM), respectively, for 1 h and cell death (PI^+) in response to cisplatin (15 µM) determined after 24 h ($n = 3$; mean ± SD; $^{****}p \le 0.0001$; $^{*}p \le 0.05$; ns not significant). **E** Changes in expression of p53, p-p53(Ser15), PUMA, Caspase-3, cleaved Caspase-3 and PARP was assessed by Western-blot analysis with β-actin as loading control. **F** M#31 cells were pre-stimulated with QVD (5 µM), Nec1s (15 µM), or ferrostatin-1 (15 µM) for 1 h followed by treatment with either alpelisip (iPI3K, 10 µM) or afuresertib (iAKT, 10 µM), and cell death (PI^+) monitored after 24 h ($n = 3$; mean ± SD; $^{***}p \le 0.001$; $^{**}p \le 0.01$; $^{*}p \le 0.05$; ns not significant). **G** M#31 and M#54 cells, SkMel29 and WNM1552C MM cell lines, and primary human fibroblasts and melanocytes were pretreated or not with ferrostatin-1 (15 µM) for 1 h and cell death (PI^+) in response to RSL3 (1.13 µM) determined after 24 h ($n = 3$; mean ± SD; $^{****}p \le 0.000$; ns not significant).

inhibited with QVD (Fig. 5F). Similar to co-treatment with PRIMA1-Met, co-treatment with iAKT and cisplatin could partially be rescued by ferrostatin-1, confirming that M#31 cells were prone to ferroptosis induction (Fig. 5F). Conclusively, application of RSL3 a specific inhibitor of GPX4, induced extensive ferroptotic cell death (~90%) in *mut*p53(E285K)-expressing M#31, but also in *wt*p53-expressing M#54 cells. To estimate the clinical potential of RSL3 in treating MM we additionally investigated *mut*p53(E285K)-expressing SkMel29 and *mutp*53(R248Q) gain-of-function expressing WM1552C MM cell lines (https://p53.fr/tp53-database/the-tp53-cell-line-compendium), both being largely resistant to cisplatin as well as to re-sensitization with PRIMA1-Met (Fig. S8). Both cell lines responded with ~40–50% cell death to RSL3 treatment which was superior to 25% cell death being induced in primary fibroblasts. Most importantly, primary melanocytes fully resisted ferroptosis induction.

Taken together, we have identified an important cluster of p53 mutations, referred to as E285 cluster, being located close to the DBD indirectly interfering with DNA recognition and transcription of p53 target genes, presenting with high prevalence in MM but also in a wide range of other cancers. Our data furthermore challenge the concept of including ferroptosis-inducing agents into the treatment portfolio of MM, and most likely also for other cancer specimens.

DISCUSSION

To date, intervention strategies for the treatment of MM are exclusively based on the mutation status of the key drivers of metastatic progression, BRAF and NRAS oncogenes. Besides these genetic alterations other pathophysiological modifications, including the p53 mutation status, may contribute to therapy resistance [48].

Hotspot gain-of-function mutants account for ~28% of all missense mutations in p53 and have been investigated intensively [49, 50]. Much less information is available on residual ~72% missense mutations, most of which are also located within or adjacent to the DNA-binding domain [51].

Investigating the p53 mutation status in 19 patient-derived melanoma samples we have identified one p53 missense mutation E285K, previously described as a rare missense mutation being endowed with temperature-sensitive properties. At the permissive temperature of 32 °C this mutant was shown to regain wild-type properties allowing for profiling of p53-responsive genes [26]. Our data show *mut*p53(E285K) to be localized in the cytosol of M#31 cells and to only partially translocate into the nucleus in response to DNA damage, thereby conferring extensive chemoresistance. Cytosolic p53 cluster have recently gained increased attention, because they were found to correlate with poor prognosis in serous ovarian carcinoma [52], and to couple oncogene-driven metabolism to apoptosis in glioblastoma [53]. Restoration of *mut*p53(E285K), in M#31 and M#54 cells silenced for endogenous p53, as well as in M#10 and M#34 lacking endogenous p53 protein, prevented p53-driven transcription of p21, MDM2, and PUMA, and reduced cisplatin responses to the level of gain-of-function R175H and R248W re-expressing cells. Co-treatment with PRIMA1-Met (re)sensitized M#31 to cisplatin, however, this appeared to be independent of restoration of p53 *wt*-function. Multiple clinical trials have been conducted incorporating PRIMA1-Met (APR-246), showing some promising results when co-administered with conventional drugs in several hematologic malignancies and solid tumors. Unfortunately, a study on melanoma treatment was discontinued in 2019 (reviewed in [16]). All three drugs used in this study aiming to restore p53 *wt*-function (COTI-2, PEITC, PRIMA1-Met) have proven cytotoxic effects on various cancer types beyond p53 reactivation, mostly due to reactive oxygen (ROS) formation inducing oxidative stress [18, 54–56], which may contribute to lipid peroxidation, and thus, to ferroptosis [57]. This may explain partial ferroptosis induction upon PRIMA1-Met and cisplatin co-treatment. Moreover, AKT was recently shown to inhibit GPX4 degradation through creatine kinase B-dependent phosphorylation, thereby mitigating ferroptosis in hepatocellular carcinoma cell lines [58]. This in turn may explain how AKT inhibition may contribute to ferroptosis induction. Since clinical trials involving PI3K [59] or AKT [60] inhibition, alone or in combination with conventional *mut*BRAF or MEK targeting drugs have shown poor benefit for MM patients, direct ferroptosis induction may provide a promising alternative. We show GPX4 inhibition by RSL3 to tumorselectively induce extensive ferroptosis in wild-type and mutant p53-expressing MM cells while sparing primary cells of the skin, implying ferroptosis induction to be a viable alternative treatment option for MM irrespective of the intrinsic p53 mutation status. Accordingly, increasing effort is currently undertaken to implement ferroptotic marker identification into diagnostic measures as well as therapeutic strategies for the treatment of MM [61–63].

Our structural analysis revealed E285K to be part of a cluster of frequently occurring missense mutations (E285 cluster) in MM, but also in a wide range of other cancers. As a future task, small molecules that interfere with the destabilization of the C-terminal helix of the p53 DBD may represent a viable strategy to rescue the negative impact of E285-cluster mutations, thereby paving the way for alternative therapeutic options to fight cancer.

Reporting summary

Further information on research design is available in the Nature Research Reporting Summary linked to this article.

DATA AVAILABILITY

The datasets used and analyzed during the course of the current study are available from the corresponding author upon reasonable request. Uncropped Western Blots are available as Supplementary Data.

REFERENCES

1. Berthenet K, Castillo Ferrer C, Fanfone D, Popgeorgiev N, Neves D, Bertolino P, et al. Failed apoptosis enhances melanoma cancer cell aggressiveness. Cell Rep. 2020;31:107731.
2. Kalal BS, Upadhya D, Pai VR. Chemotherapy resistance mechanisms in advanced skin cancer. Oncol Rev. 2017;11:326.
3. Niessner H, Schmitz J, Tabatabai G, Schmid AM, Calaminus C, Sinnberg T, et al. PI3K pathway inhibition achieves potent antitumor activity in melanoma brain metastases in vitro and in vivo. Clin Cancer Res. 2016;22:5818–28.
4. Niessner H, Sinnberg T, Kosnopfel C, Smalley KSM, Beck D, Praetorius C, et al. BRAF Inhibitors amplify the proapoptotic activity of MEK inhibitors by inducing ER stress in NRAS-mutant melanoma. Clin Cancer Res. 2017;23:6203–14.
5. Paluncic J, Kovacevic Z, Jansson PJ, Kalinowski D, Merlot AM, Huang ML, et al. Roads to melanoma: key pathways and emerging players in melanoma progression and oncogenic signaling. Biochim Biophys Acta. 2016;1863:770–84.
6. Gotwals P, Cameron S, Cipolletta D, Cremasco V, Crystal A, Hewes B, et al. Prospects for combining targeted and conventional cancer therapy with immunotherapy. Nat Rev Cancer. 2017;17:286–301.
7. Long GV, Flaherty KT, Stroyakovskiy D, Gogas H, Levchenko E, de Braud F, et al. Dabrafenib plus trametinib versus dabrafenib monotherapy in patients with metastatic BRAF V600E/K-mutant melanoma: long-term survival and safety analysis of a phase 3 study. Ann Oncol. 2019;30:1848.
8. Dummer R, Lebbe C, Atkinson V, Mandala M, Nathan PD, Arance A, et al. Combined PD-1, BRAF and MEK inhibition in advanced BRAF-mutant melanoma: safety run-in and biomarker cohorts of COMBI-i. Nat Med. 2020;26:1557–63.
9. Luke JJ, Flaherty KT, Ribas A, Long GV. Targeted agents and immunotherapies: optimizing outcomes in melanoma. Nat Rev Clin Oncol. 2017;14:463–82.
10. Gupta A, Gomes F, Lorigan P. The role for chemotherapy in the modern management of melanoma. Melanoma Manag. 2017;4:125–36.
11. Luke JJ, Schwartz GK. Chemotherapy in the management of advanced cutaneous malignant melanoma. Clin Dermatol. 2013;31:290–7.
12. Vousden KH, Ryan KM. p53 and metabolism. Nat Rev Cancer. 2009;9:691–700.
13. Poyurovsky MV, Prives C. Unleashing the power of p53: lessons from mice and men. Genes Dev. 2006;20:125–31.
14. Oren M, Rotter V. Mutant p53 gain-of-function in cancer. Cold Spring Harb Perspect Biol. 2010;2:a001107.
15. Freed-Pastor WA, Prives C. Mutant p53: one name, many proteins. Genes Dev. 2012;26:1268–86.
16. Roszkowska KA, Piecuch A, Sady M, Gajewski Z, Flis S. Gain of function (GOF) mutant p53 in cancer-current therapeutic approaches. Int J Mol Sci. 2022;23:13287.
17. Tang Q, Su Z, Gu W, Rustgi AK. Mutant p53 on the path to metastasis. Trends Cancer. 2020;6:62–73.
18. Lindemann A, Patel AA, Silver NL, Tang L, Liu Z, Wang L, et al. COTI-2, a novel thiosemicarbazone derivative, exhibits antitumor activity in HNSCC through p53-dependent and -independent mechanisms. Clin Cancer Res. 2019;25:5650–62.
19. Liu S, Zhu Y, Yan S, Xiao H, Yi J, Li R, et al. Phenethyl isothiocyanate induces IPEC-J2 cells cytotoxicity and apoptosis via S-G(2)/M phase arrest and mitochondria-mediated Bax/Bcl-2 pathway. Comp Biochem Physiol C Toxicol Pharmacol. 2019;226:108574.
20. Synnott NC, O'Connell D, Crown J, Duffy MJ. COTI-2 reactivates mutant p53 and inhibits growth of triple-negative breast cancer cells. Breast Cancer Res Treat. 2020;179:47–56.
21. Mohell N, Alfredsson J, Fransson A, Uustalu M, Byström S, Gullbo J, et al. APR-246 overcomes resistance to cisplatin and doxorubicin in ovarian cancer cells. Cell Death Dis. 2015;6:e1794.
22. Aggarwal M, Saxena R, Asif N, Sinclair E, Tan J, Cruz I, et al. p53 mutant-type in human prostate cancer cells determines the sensitivity to phenethyl isothiocyanate induced growth inhibition. J Exp Clin Cancer Res. 2019;38:307.
23. Salim KY, Maleki Vareki S, Danter WR, Koropatnick J. COTI-2, a novel small molecule that is active against multiple human cancer cell lines in vitro and in vivo. Oncotarget. 2016;7:41363–79.
24. Zhang T, Dutton-Regester K, Brown KM, Hayward NK. The genomic landscape of cutaneous melanoma. Pigment Cell Melanoma Res. 2016;29:266–83.
25. Muller I, Strozyk E, Schindler S, Beissert S, Oo HZ, Sauter T, et al. Cancer cells employ nuclear caspase-8 to overcome the p53-dependent G2/M checkpoint through cleavage of USP28. Mol Cell. 2020;77:970–84.
26. Christgen M, Noskowicz M, Heil C, Schipper E, Christgen H, Geffers R, et al. IPH-926 lobular breast cancer cells harbor a p53 mutant with temperature-sensitive functional activity and allow for profiling of p53-responsive genes. Lab Invest. 2012;92:1635–47.
27. Jia LQ, Osada M, Ishioka C, Gamo M, Ikawa S, Suzuki T, et al. Screening the p53 status of human cell lines using a yeast functional assay. Mol Carcinog. 1997;19:243–53.
28. Muller P, Ceskova P, Vojtesek B. Hsp90 is essential for restoring cellular functions of temperature-sensitive p53 mutant protein but not for stabilization and activation of wild-type p53: implications for cancer therapy. J Biol Chem. 2005;280:6682–91.
29. Muller I, Beissert S, Kulms D. Anti-apoptotic NF-kappaB and "gain of function" mutp53 in concert act pro-apoptotic in response to UVB+IL-1 via enhanced TNF production. J Invest Dermatol. 2015;135:851–60.
30. Del Mistro G, Riemann S, Schindler S, Beissert S, Kontermann RE, Ginolhac A, et al. Focal adhesion kinase plays a dual role in TRAIL resistance and metastatic outgrowth of malignant melanoma. Cell Death Dis. 2022;13:54.
31. Nguyen B, Fong C, Luthra A, Smith SA, DiNatale RG, Nandakumar S, et al. Genomic characterization of metastatic patterns from prospective clinical sequencing of 25,000 patients. Cell. 2022;185:563–75.
32. Cerami E, Gao J, Dogrusoz U, Gross BE, Sumer SO, Aksoy BA, et al. The cBio cancer genomics portal: an open platform for exploring multidimensional cancer genomics data. Cancer Discov. 2012;2:401–4.
33. Gao J, Aksoy BA, Dogrusoz U, Dresdner G, Gross B, Sumer SO, et al. Integrative analysis of complex cancer genomics and clinical profiles using the cBioPortal. Sci Signal. 2013;6:pl1.
34. de Andrade KC, Lee EE, Tookmanian EM, Kesserwan CA, Manfredi JJ, Hatton JN, et al. The TP53 Database: transition from the International Agency for Research on Cancer to the US National Cancer Institute. Cell Death Differ. 2022;29:1071–3.
35. Varadi M, Anyango S, Deshpande M, Nair S, Natassia C, Yordanova G, et al. AlphaFold Protein Structure Database: massively expanding the structural coverage of protein-sequence space with high-accuracy models. Nucleic Acids Res. 2022;50:D439–44.
36. Lin Z, Akin H, Rao R, Hie B, Zhu Z, Lu W, et al. Evolutionary-scale prediction of atomic-level protein structure with a language model. Science. 2023;379:1123–30.
37. Suad O, Rozenberg H, Brosh R, Diskin-Posner Y, Kessler N, Shimon LJ, et al. Structural basis of restoring sequence-specific DNA binding and transactivation to mutant p53 by suppressor mutations. J Mol Biol. 2009;385:249–65.
38. Sora V, Laspiur AO, Degn K, Arnaudi M, Utichi M, Beltrame L, et al. RosettaDDGPrediction for high-throughput mutational scans: from stability to binding. Protein Sci. 2023;32:e4527.
39. Dehouck Y, Kwasigroch JM, Gilis D, Rooman M. PoPMuSiC 2.1: a web server for the estimation of protein stability changes upon mutation and sequence optimality. BMC Bioinform. 2011;12:151.
40. Chen Y, Lu H, Zhang N, Zhu Z, Wang S, Li M. PremPS: predicting the impact of missense mutations on protein stability. PLoS Comput Biol. 2020;16:e1008543.
41. Laimer J, Hofer H, Fritz M, Wegenkittl S, Lackner P. MAESTRO--multi agent stability prediction upon point mutations. BMC Bioinform. 2015;16:116.
42. Kitayner M, Rozenberg H, Kessler N, Rabinovich D, Shaulov L, Haran TE, et al. Structural basis of DNA recognition by p53 tetramers. Mol Cell. 2006;22:741–53.
43. Whibley C, Pharoah PD, Hollstein M. p53 polymorphisms: cancer implications. Nat Rev Cancer. 2009;9:95–107.
44. Adzhubei I, Jordan DM, Sunyaev SR. Predicting functional effect of human missense mutations using PolyPhen-2. Curr Protoc Hum Genet. 2013;7:20.
45. Ng PC, Henikoff S. SIFT: Predicting amino acid changes that affect protein function. Nucleic Acids Res. 2003;31:3812–4.
46. Ioannidis NM, Rothstein JH, Pejaver V, Middha S, McDonnell SK, Baheti S, et al. REVEL: an ensemble method for predicting the pathogenicity of rare missense variants. Am J Hum Genet. 2016;99:877–85.
47. Suvasini R, Somasundaram K. Essential role of PI3-kinase pathway in p53-mediated transcription: implications in cancer chemotherapy. Oncogene. 2010;29:3605–18.
48. Celesia A, Franzo M, Di Liberto D, Lauricella M, Carlisi D, D'Anneo A, et al. Oncogenic BRAF and p53 Interplay in melanoma cells and the effects of the HDAC inhibitor ITF2357 (Givinostat). Int J Mol Sci. 2023;24:9148.
49. Baugh EH, Ke H, Levine AJ, Bonneau RA, Chan CS. Why are there hotspot mutations in the TP53 gene in human cancers? Cell Death Differ. 2018;25:154–60.
50. Bouaoun L, Sonkin D, Ardin M, Hollstein M, Byrnes G, Zavadil J, et al. TP53 variations in human cancers: new lessons from the IARC TP53 database and genomics data. Hum Mutat. 2016;37:865–76.
51. Pitolli C, Wang Y, Mancini M, Shi Y, Melino G, Amelio I. Do mutations turn p53 into an Oncogene? Int J Mol Sci. 2019;20:6241.
52. Iwahashi N, Ikezaki M, Komohara Y, Fujiwara Y, Noguchi T, Nishioka K, et al. Cytoplasmic p53 aggregates accumulated in p53-mutated cancer correlate with poor prognosis. PNAS Nexus. 2022;1:pgac128.
53. Mai WX, Gosa L, Daniels VW, Ta L, Tsang JE, Higgins B, et al. Cytoplasmic p53 couples oncogene-driven glucose metabolism to apoptosis and is a therapeutic target in glioblastoma. Nat Med. 2017;23:1342–51.
54. Fujihara KM, Corrales Benitez M, Cabalag CS, Zhang BZ, Ko HS, Liu DS, et al. SLC7A11 Is a superior determinant of APR-246 (Eprenetapopt) response than TP53 mutation status. Mol Cancer Ther. 2021;20:1858–67.

55. Grellety T, Laroche-Clary A, Chaire V, Lagarde P, Chibon F, Neuville A, et al. PRIMA-1(MET) induces death in soft-tissue sarcomas cell independent of p53. BMC Cancer. 2015;15:684.
56. Liu J, Chen G, Pelicano H, Liao J, Huang J, Feng L, et al. Targeting p53-deficient chronic lymphocytic leukemia cells in vitro and in vivo by ROS-mediated mechanism. Oncotarget. 2016;7:71378–89.
57. Jiang X, Stockwell BR, Conrad M. Ferroptosis: mechanisms, biology and role in disease. Nat Rev Mol Cell Biol. 2021;22:266–82.
58. Wu K, Yan M, Liu T, Wang Z, Duan Y, Xia Y, et al. Creatine kinase B suppresses ferroptosis by phosphorylating GPX4 through a moonlighting function. Nat Cell Biol. 2023;25:714–25.
59. Algazi AP, Esteve-Puig R, Nosrati A, Hinds B, Hobbs-Muthukumar A, Nandoskar P, et al. Dual MEK/AKT inhibition with trametinib and GSK2141795 does not yield clinical benefit in metastatic NRAS-mutant and wild-type melanoma. Pigment Cell Melanoma Res. 2018;31:110–4.
60. Yam C, Xu X, Davies MA, Gimotty PA, Morrissette JJD, Tetzlaff MT, et al. A multicenter phase I study evaluating dual PI3K and BRAF inhibition with PX-866 and vemurafenib in patients with advanced BRAF V600-mutant solid tumors. Clin Cancer Res. 2018;24:22–32.
61. Guo W, Wang X, Zhang Y, Liu H, Ma S, Guan F. Construction and validation of a novel prognostic signature for cutaneous melanoma based on ferroptosis-related genes. Heliyon. 2023;9:e15725.
62. Jin B, Yang L, Ye Q, Pan J. Ferroptosis induced by DCPS depletion diminishes hepatic metastasis in uveal melanoma. Biochem Pharmacol. 2023;213:115625.
63. Manzari Tavakoli G, Mirzapour MH, Razi S, Rezaei N. Targeting ferroptosis as a cell death pathway in Melanoma: From molecular mechanisms to skin cancer treatment. Int Immunopharmacol. 2023;119:110215.

ACKNOWLEDGEMENTS

We thank Prof. Andreas Linkermann, TU-Dresden, for providing RSL3 and ferrostatin-1, as well as input on ferroptosis signaling. The present study was funded by the German Cancer Foundation (Deutsche Krebshilfe, 70114198) and the German Research Association (DFG, KU 1981/12-1).

AUTHOR CONTRIBUTIONS

LD, SR, CA, and SS conducted all cell-based experiments. NI performed p53 model analysis. DK, IL, and SK conceived the project and supervised research. MT and SB reviewed and edited the manuscript. All authors contributed to experimental design and manuscript writing.

FUNDING

Open Access funding enabled and organized by Projekt DEAL.

COMPETING INTERESTS

The authors declare no competing interests.

ETHICAL APPROVAL

The usage of patient-derived melanoma samples was approved by the ethics committee of the TU-Dresden (SR-EK230052020) and informed consent was obtained from all patients.

ADDITIONAL INFORMATION

Supplementary information The online version contains supplementary material available at https://doi.org/10.1038/s41419-023-06360-4.

Correspondence and requests for materials should be addressed to Dagmar Kulms.

Reprints and permission information is available at http://www.nature.com/reprints

Publisher's note Springer Nature remains neutral with regard to jurisdictional claims in published maps and institutional affiliations.

4. Manuscript 3: A multi-omics integrative approach unravels novel genes and pathways associated with senescence escape after targeted therapy in NRAS mutant melanoma (DOI: 10.1038/s41417-023-00640-z)

In this study, my contribution included the creation of Supplementary Figure 2 and support in data interpretation to elucidate the final mechanisms underlying the relationship between the senescent and resistant phenotypes involving ERK5.

www.nature.com/cgt Cancer Gene Therapy

ARTICLE OPEN Check for updates

A multi-omics integrative approach unravels novel genes and pathways associated with senescence escape after targeted therapy in NRAS mutant melanoma

Vincent Gureghian[1], Hailee Herbst[1], Ines Kozar[2], Katarina MihajIovic[3], Noël Malod-Dognin[3], Gaia Ceddia[3], Cristian Angeli[1], Christiane Margue[1], Tijana Randic[1], Demetra Philippidou[1], Milène Tetsi Nomigni[1], Ahmed Hemedan[4], Leon-Charles Tranchevent[4], Joseph Longworth[5], Mark Bauer[1], Apurva Badkas[1], Anthoula Gaigneaux[1], Arnaud Muller[6], Marek Ostaszewski[4], Fabrice Tolle[1], Nataša Pržulj[3,7,8,9] and Stephanie Kreis[1,9]✉

Therapy Induced Senescence (TIS) leads to sustained growth arrest of cancer cells. The associated cytostasis has been shown to be reversible and cells escaping senescence further enhance the aggressiveness of cancers. Chemicals specifically targeting senescent cells, so-called senolytics, constitute a promising avenue for improved cancer treatment in combination with targeted therapies. Understanding how cancer cells evade senescence is needed to optimise the clinical benefits of this therapeutic approach. Here we characterised the response of three different NRAS mutant melanoma cell lines to a combination of CDK4/6 and MEK inhibitors over 33 days. Transcriptomic data show that all cell lines trigger a senescence programme coupled with strong induction of interferons. Kinome profiling revealed the activation of Receptor Tyrosine Kinases (RTKs) and enriched downstream signaling of neurotrophin, ErbB and insulin pathways. Characterisation of the miRNA interactome associates miR-211-5p with resistant phenotypes. Finally, iCell-based integration of bulk and single-cell RNA-seq data identifies biological processes perturbed during senescence and predicts 90 new genes involved in its escape. Overall, our data associate insulin signaling with persistence of a senescent phenotype and suggest a new role for interferon gamma in senescence escape through the induction of EMT and the activation of ERK5 signaling.

Cancer Gene Therapy (2023) 30:1330–1345; https://doi.org/10.1038/s41417-023-00640-z

INTRODUCTION

Hayflick first observed in 1961 that fibroblasts stop proliferating after 50 passages and display an enlarged and flattened phenotype characteristic of senescence [1, 2]. This observation was later explained by the progressive shortening of telomeres upon replication, which ultimately triggers a DNA Damage Response (DDR) leading to cell cycle arrest [3, 4]. This process was called "replicative senescence". Several cellular events and environmental conditions induce senescence, and it now emerges as a generic stress response involved in central biological processes such as embryonic development, wound healing and aging [2, 4, 5].

Many stressors that induce senescence (e.g., oxidative stress, radiation), induce DNA damage and activate DDR. This leads to engagement of the Senescence Associated Secretory Phenotype (SASP), one of the characteristic features of senescence in which cells produce and secrete cytokines and growth factors. The SASP itself can trigger senescence in adjacent cells and contributes to the emergence of an inflammatory environment as the senescent cells, which are not eliminated by the immune system, accumulate in the organism [5]. This accumulation leads to the development of degenerative and hyperplastic pathologies and carcinogenesis, linking senescence to aging [6, 7]. Research in this field is challenging due to the heterogeneous and dynamic nature of the SASP and the lack of a universal marker for senescence.

Focusing on cancer, the activation of known oncogenes results in a constant proliferative signaling which causes replication forks to trigger DNA damage and drive primary cells to undergo Oncogene-Induced Senescence (OIS) [8]. Therefore, senescence may be considered as an early evolutionary mechanism of protection against cancer leading to cell cycle arrest of over-proliferating cells [9]. However, cells can escape this arrest and re-establish growth, ultimately leading to the development of cancer. Cancer cells can also undergo senescence when exposed to therapies, so called Therapy-Induced Senescence (TIS).

Thus, senescence appears as a natural barrier against cancer, but recent works suggest that senescence may be a reversible process

[1]Department of Life Sciences and Medicine, University of Luxembourg, 6, Avenue du Swing, L-4367 Belvaux, Luxembourg. [2]Laboratoire National de Santé, Dudelange, Luxembourg. [3]Barcelona Supercomputing Center, 08034 Barcelona, Spain. [4]Luxembourg Centre for Systems Biomedicine, University of Luxembourg, Esch-sur-Alzette, Luxembourg. [5]Experimental and Molecular Immunology, Department of Infection and Immunity, Luxembourg Institute of Health, Esch-sur-Alzette, Luxembourg. [6]LuxGen, TMOH and Bioinformatics platform, Data Integration and Analysis unit, Luxembourg Institute of Health, Esch-sur-Alzette, Luxembourg. [7]Department of Computer Science, University College London, London WC1E 6BT, UK. [8]ICREA, Pg. Lluís Companys 23, 08010 Barcelona, Spain. [9]These author contributed equally: Nataša Pržulj, Stephanie Kreis. ✉email: stephanie.kreis@uni.lu

Received: 24 March 2023 Revised: 19 May 2023 Accepted: 21 June 2023
Published online: 7 July 2023

SPRINGER NATURE

[10]. Exit from senescence has been recently linked with the stem-like properties of cancer cells, reinforcing the idea that aside from the SASP, senescence itself may be a transient state in carcinogenesis.

Melanoma arises from the deregulated proliferation of melanocytes representing the deadliest type of skin cancer accounting for about 75% of related deaths. Standard of care involves targeted therapies and immunotherapies [11]. For the BRAF mutated subtype, representing half of the cases, specific first line inhibitors targeting both MEK and BRAF have been developed. The NRAS mutated subtype, which accounts for a quarter of all melanoma cases, lacks such a targeted approach but ongoing clinical trials are assessing the effects of combined MEK and CDK4/6 inhibitors (NCT01781572; NCT02065063). However, tolerance or resistance to such targeted treatments inevitably develops.

MicroRNAs have been shown to be involved in resistance to treatment. miRNAs are 20–22 nucleotides short RNAs, which in complex with the Argonaute (AGO) protein, act as post-transcriptional regulators of gene expression [12]. Canonically, miRNAs destabilise mRNAs by binding to a complementary sequence within the 3′ UTR, this resulting in downregulation of the mRNA and the encoded protein [13]. Experimental methods based on immune-precipitation and sequencing have been developed to profile miRNA-mRNA interactions. The qCLASH method has the advantage of capturing direct physical interactions only, through an additional intermolecular ligation step linking mRNAs to their bound miRNAs [14].

To characterise the response of 3 NRAS mutant melanoma cell lines to a combination of MEK and CDK4/6 inhibitors, we treated the cells over 33 days and collected samples at multiple time points. Samples were analyzed by total RNA-seq, small RNA-seq, qCLASH and kinome profiling. Our results recapitulate several previous observations while displaying an unforeseen interplay between interferon signalling and senescence. Additionally, we uncover deregulated processes associated with the onset of senescence and its exit by adapting a non-negative matrix trifactorization (NMTF)-based methodology, "iCell" [15], to integrate bulk RNA-seq and single-cell data. Moreover, the dimensionality reduction and the clustering properties of the NMTF allowed us to associate novel genes to senescence escape.

RESULTS

Experimental design and description of the data sets

To study the effects of MEKi and CDK4/6i, 3 NRAS mutant melanoma cell-lines: MELJUSO, SKMEL30 and IPC298 were selected as they showed distinct cellular responses with spindle-shape (MELJUSO), augmented pigmentation (SKMEL30) and typical melanoma morphology (IPC298) phenotypes (Fig. 1). To further normalize the effect of treatment across cell lines, we determined the GI50 (drug concentration at which cell growth is reduced by half) and opted for a concentration of 110nM, 35nM, and 16nM of Binimetinib (MEKi) for MELJUSO, SKMEL30 and IPC298, respectively and 1 µM for Palbociclib (CDK4/6i) as this inhibitor led to incomplete dose-response curves (Supplementary Table 1). Upon treatment over 33 days, the 3 cell lines showed different behaviour with IPC298 suffering very little from the treatment showing constant proliferation and no morphological change. SKMEL30 on the other hand stopped proliferating and accumulated pigmentation before restoring proliferation after around 14 days. Finally, MELJUSO stopped dividing and started to stretch to acquire a spindle-shape phenotype after 4 days.

As distinct morphological changes were observed at these time points, we profiled the transcriptome of the cell lines at day 0, 4, 14 and 33 using total RNA-seq. Cellular signaling supporting the adaptation to the treatment was investigated by profiling the kinome of the senescent MELJUSO and adaptative SKMEL30 cell lines using PamGene technology. Next, we characterised the resistant miRNA interactome of the SKMEL30 and IPC298 at 33 days by combining small RNA-seq and the qCLASH method. Finally, by integrating bulk and single cell RNA-seq data, deregulated pathways and predicted genes associated with senescence escape were identified.

Cell lines display coherent transcriptomic profiles composed of interferons, EMT and senescent responses under prolonged CDK4/6i and MEKi treatment

Distinct cellular responses to treatment were reflected at the transcriptomic level where the cell lines clustered separately on the PCA (Fig. 2A). As MELJUSO displayed a different evolution over time, we decided to analyze each cell line individually. Differential expression analysis, comparing later time points to day 0, revealed a greater change in the MELJUSO transcriptome. MELJUSO corresponds to 9548, 11362 and 10126 significant ($p.adj <= 0.05$) differentially expressed genes at day 4, day 14 and day 33, respectively when compared to SKMEL30 and IPC298 (9208, 9749, 6509 and 5436, 7575 and 3217, respectively) (Supplementary Fig. 1). Interestingly, across all cell lines and for all time points, we noticed the deregulation of interferon-related genes such as STAT1, IRF7, MX1, OAS2 and IFI44.

Gene Set Enrichment Analysis (GSEA) was performed on differentially expressed genes using the "hallmarks" from MSigDB, which revealed the downregulation of pathways related to proliferation such as "MYC TARGETS V1", "E2F TARGETS", and "G2M CHECKPOINT" (Fig. 2B), all affected by our inhibitors. The clustering of samples on top of the heatmap clearly separates proliferative samples (left part) comprising the IPC298 cell line and SKMEL30 day 33 from cytostatic samples (right part) with MELJUSO and early time points for SKMEL30. Interestingly, we noticed across all cell lines an enrichment in interferon responses and an enrichment in Epithelial-to-Mesenchymal Transition (EMT) for the cytostatic samples (Fig. 2B). CDK4/6 inhibitors have been shown to induce cellular senescence in different cell types [16, 17]. We therefore used a recently published classifier, "SENESCopedia", to predict the levels of senescence in our samples (Fig. 2C) [18]. On day 14, all cell lines display high senescence scores suggesting that they all engage in a related transcriptional programme. Of note, all samples with a high senescence score are also enriched in EMT which is coherent with previous observations of EMT in different epithelial cell types after induction of senescence (fibroblasts, colorectal and lung cancer) [19–21].

Altogether, these results suggest that all 3 cell lines trigger the same type of responses composed of an interferon response, a senescence and "EMT" programme but with a different intensity and temporality, which may explain the different phenotypes observed.

Kinome profiling of adapting cell lines shows reactivation of RTK pathways and suggests a key role of ERK5

To better understand how the cell lines adapt to the treatment, we acquired PamGene data (Supplementary Fig. 2) to profile the kinome of MELJUSO and SKMEL30 cells at day 0, 1, 4 and 33 as these two cell lines showed persistent cytostasis and adaptation to treatment. MELJUSO stops proliferating and changes morphology after about 4 days while SKMEL30 acquires a dark pigmentation before restoring growth. Kinase activities were inferred from the levels of peptide phosphorylation at different time points and compared to day 0 (summarised in Fig. 3A). A phylogenetic representation shows that these two cell lines react similarly to the treatment only at early time points (Supplementary Fig. 3).

To perform pathway enrichment on a reduced set of proteins such as kinases, we used a network-based approach and obtained coherent results for the two cell lines (Table 1). Indeed, pathways like RIG-I or Toll-like receptor signaling (related to innate immunity and interferon responses) were enriched at early time points for both SKMEL30 and MELJUSO. Among the enrichment results, RTK pathways involving ErbB, neurotrophin and insulin appear (Fig. 3B, C). Some pathways were enriched before the increase in receptor

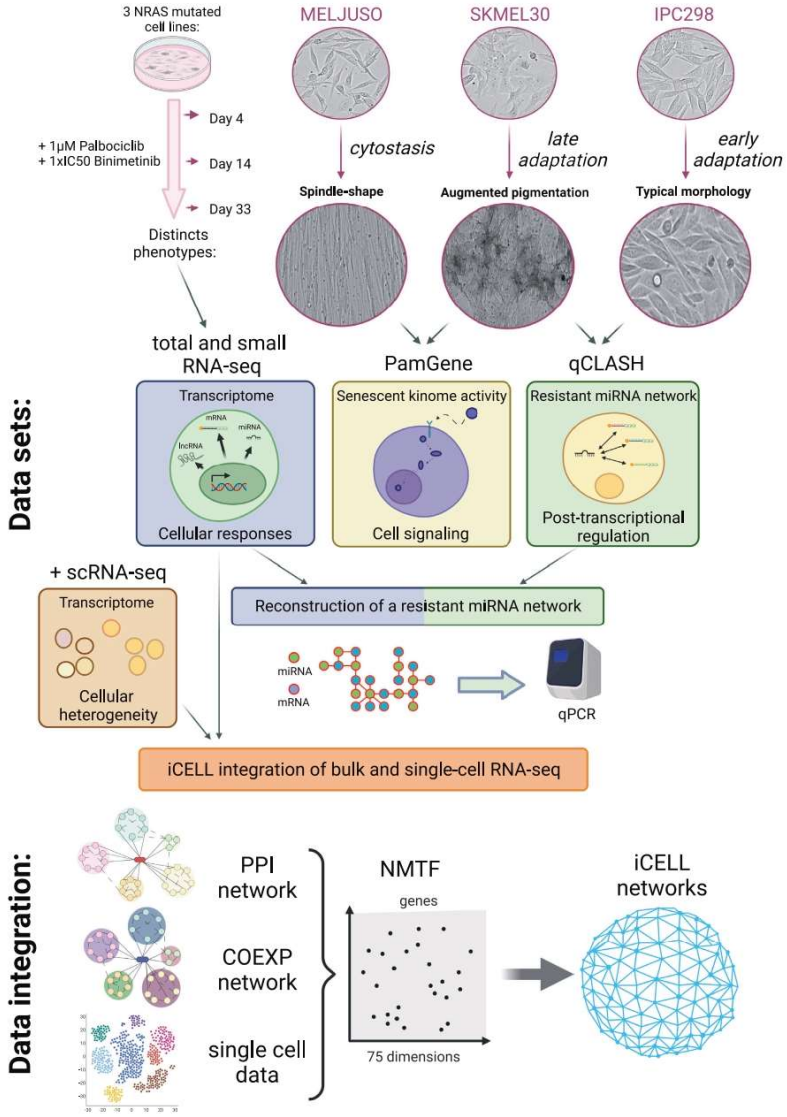

Fig. 1 Experimental setup, cellular phenotypes and omics characterization. IPC298, MELJUSO and SKMEL30 cell lines display different phenotypes upon CDK4/6i and MEKi. We characterised those using RNA-seq, kinome profiling and qCLASH method. RNA-seq and qCLASH data were further combined to construct a resistant miRNA network. Bulk and single-cell RNA-seq were finally integrated into "iCell" networks.

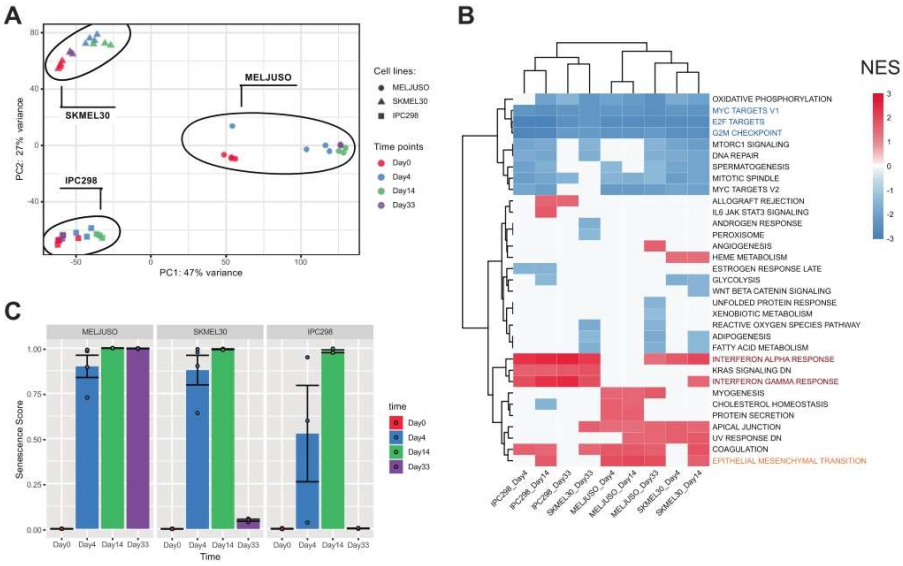

Fig. 2 NRAS mutant melanoma trigger IFN and EMT responses upon MEKi and CDK4/6i. A Principal component analysis clusters cell lines separately reflecting distinct observed phenotypes. **B** Gene Set Enrichment Analysis using the hallmarks gene sets from MSigDB. Color legends represent Normalised Enrichment Score (NES). All cell lines display an enrichment in interferons responses and at day 14 in EMT. **C** Senescence scores predicted by Cancer SENESCopedia. SENESCopedia webtool (https://ccb.nki.nl/publications/cancer-senescence) uses a gene expression classifier to predict senescence in cancer cell samples [18].

activity reached the significance threshold and those were therefore not represented on the phylogenetic tree (Supplementary Fig. 3). This signaling seems to persist after the receptor resumes normal activity (Table 1). It has previously been shown that the inhibition of ERK1/2 suppresses negative feedback on RTK expression, which can then be further activated to compensate for this inhibition [22] (Fig. 3B, Supplementary Fig. 3). Coherent with the enriched pathways, we observed in both cell lines a significant increase in the activity of RTKs such as HER3 and NTRK2 as well as insulin-related receptors (INSR, IGF1R and IRR). Noteworthy, downstream insulin signaling was enriched in the cytostatic MELJUSO only (detailed representation of pathways Supplementary Figs. 4–8). Other RTKs previously related to resistance such ALK, AXL or c-MET displayed an increased activity (complete list Supplementary Fig. 9) but those were not associated with enriched downstream signaling. Within the MAPK pathway, the decrease in ERK5 (*MAPK7*) activity was partially relieved in SKMEL30 but not in MELJUSO (Fig. 3B). Along these lines, Tubita et al. recently showed that knock-down by shRNA or inhibition of the kinase activity of ERK5 triggers senescence in melanoma [23].

Overall, the kinome data show the reactivation of ErbB, neurotrophin and insulin pathways and enrichment of their downstream signaling. Interestingly, ERK5 activity was strongly reduced in the cytostatic cell line MELJUSO (Fig. 3B).

Contribution of miRNAs to the resistant phenotype

To see if miRNAs could participate in the adaptation to treatment and the proliferative phenotypes, we profiled the miRNome of all three cell lines by small RNA-seq at day 0 and 33. In line with their phenotypes, IPC298 showed little deregulation of miRNAs compared to SKMEL30 and MELJUSO cell lines (Supplementary Fig. 10). Next, we performed qCLASH analysis for the two proliferative cell lines IPC298 (early adaptation) and SKMEL30 (late adaptation) (summarised in Fig. 4A).

Although qCLASH-based miRNA interactomes do not provide a complete picture of all interactions, PCA was able to discriminate between the different cell lines and conditions (Supplementary Fig. 11). Previous studies reported a correlation between the number of detected hybrids and the expression levels of its miRNA and mRNA components [14, 24]. These correlations hold true for our matching total and the small RNA-seq data when taking the total count across the replicates (Fig. 4B, left panels). Moreover, further summing up the hybrids for each miRNA or mRNA strengthens the correlation between RNA-seq and qCLASH data, especially for miRNAs (Fig. 4B, right panels). qCLASH data also contain transient interactions, which are unlikely to be functionally relevant for the cell and technical replicates are often used to further select most likely interactions. We explored how the detection of interactions in one, two or three replicates depends on their expression level and observed that interactions detected in triplicates were associated with a greater expression supporting the rationale of using such thresholds (Supplementary Fig. 12). To further select the most relevant miRNAs, we constructed a network with the interactions specific to the resistant phenotype. We first selected the interactions detected in triplicates, then ensured that they were present in both resistant IPC298 and SKMEL30 but absent from their untreated counterparts (Fig. 4C). Finally, we overlaid the log fold changes from the small and total RNA-seq for the corresponding miRNAs and mRNAs onto the resulting network (Fig. 4D). Based on those representations, we selected some interactions to confirm their deregulation by qPCR. We investigated if those observations could be extended to two BRAF mutant

A

Cell line	Time	Deregulated kinases	Total kinases
MelJuso	Day1	61	157
MelJuso	Day4	73	157
MelJuso	Day33	90	157
SKMel30	Day1	52	162
SKMel30	Day4	71	162
SKMel30	Day33	40	162

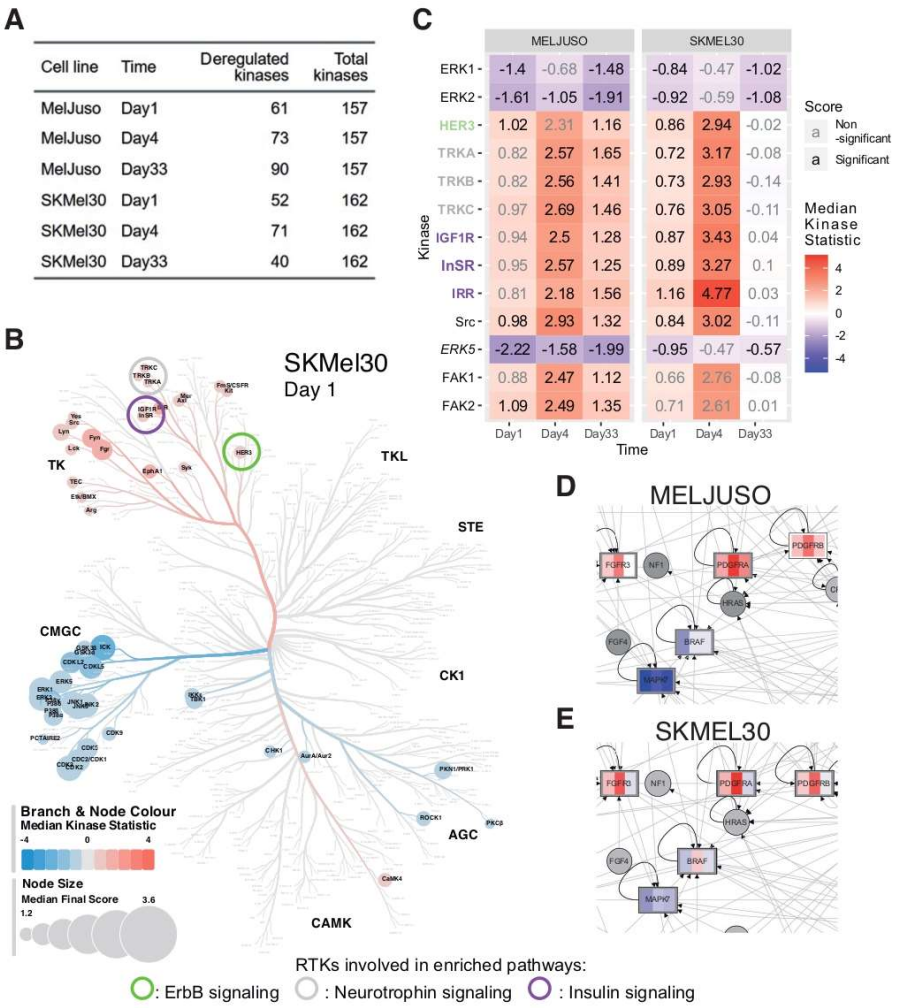

Fig. 3 MEKi and CDK4/6i lead to RTKs reactivation. A Summary of significantly deregulated kinases. **B** Kinase activities after MEKi and CDK4/6i. ERK1/2 inhibition leads to RTKs activation. Rreceptors names are colored according to the enriched pathways. **C** Phylogenetic tree for SKMEL30 on day 1. The size of the leafs represents the "Median Final Score", a score greater than 1.2 indicates a significant change between conditions. The color of the branches and leaves shows the "Median Kinase Statistic", which is the difference in kinase activity. Circles highlight RTKs contributing to enriched pathways. **D**, **E** Activity of ERK5 in the senescent and adaptative cell lines. **D** Zoom on the MAPK pathway showing the deregulation of ERK5 (*MAPK7*) in MELJUSO cell line. **E** same for the SKMEL30 cell line.

cell lines, A375 and 624Mel which underwent the same treatment and re-established growth (Supplementary Fig. 13). Most of the selected interactions did not exert a robust inverse expression between miRNA and mRNA (Supplementary Figs. 14, 15). Among mRNAs, we observed a robust upregulation of CCND1 which is a known resistance mechanism to CDK4/6i as well as a strong upregulation of IFN related gene IFI6 (Supplementary Fig. 13). Except for the amelanotic cell line A375, we observed the upregulation of LGALS3BP, TXNIP and TYRP1 (Fig. 4E). Among miRNAs, miR-211-5p was upregulated in all proliferative cell lines except the amelanotic A375, which is known not to express it (Fig. 4F) [25], and MELJUSO (Fig. 4G), which has very low levels.

Table 1. Enrichment results from PamGene data.

Pathway enrichment results for MELJUSO cell line

Day1			Day4			Day33		
Pathway Name	XD-score	*p*-adj	Pathway Name	XD-score	*p*-adj	Pathway Name	XD-score	*p*-adj
Shigellosis	1.83	6.12E-20	mTOR signaling pathway	1.13	1.33E-10	Type II diabetes mellitus	1.42	1.48E-09
NOD-like receptor signaling pathway	1.38	6.69E-14	Acute myeloid leukemia	1.05	1.50E-09	mTOR signaling pathway	1.08	2.57E-11
Epithelial cell signaling in Helicobacter pylori infection	1.12	3.49E-13	Type II diabetes mellitus	0.89	3.91E-06	**ErbB signaling pathway**	1.01	3.31E-12
Progesterone-mediated oocyte maturation	1.02	1.41E-14	Glioma	0.86	8.12E-08	Acute myeloid leukemia	1.00	3.13E-10
RIG-I-like receptor signaling pathway	1.00	1.99E-11	**ErbB signaling pathway**	0.86	2.02E-10	Fc epsilon RI signaling pathway	0.95	4.51E-12
ErbB signaling pathway	0.97	2.54E-13	Gap junction	0.77	3.34E-09	Progesterone-mediated oocyte maturation	0.95	4.23E-12
GnRH signaling pathway	0.93	1.47E-14	Prion diseases	0.75	2.78E-04	Glioma	0.95	1.69E-08
Type II diabetes mellitus	0.91	8.02E-07	Adherens junction	0.72	1.69E-07	Prion diseases	0.95	2.91E-05
Fc epsilon RI signaling pathway	0.90	6.70E-13	Fc gamma R-mediated phagocytosis	0.71	2.99E-10	Adipocytokine signaling pathway	0.87	2.60E-08
Neurotrophin signaling pathway	0.89	4.52E-17	VEGF signaling pathway	0.68	5.13E-08	VEGF signaling pathway	0.86	5.62E-10
Toll-like receptor signaling pathway	0.89	5.76E-14	Fc epsilon RI signaling pathway	0.65	7.58E-09	Shigellosis	0.86	1.53E-07
Pancreatic cancer	0.76	1.12E-08	Prostate cancer	0.65	5.45E-08	**Neurotrophin signaling pathway**	0.83	5.38E-13
Colorectal cancer	0.75	1.52E-07	Long-term potentiation	0.65	1.48E-06	Aldosterone-regulated sodium reabsorption	0.82	4.81E-05
T cell receptor signaling pathway	0.73	2.23E-12	Aldosterone-regulated sodium reabsorption	0.64	3.96E-04	Gap junction	0.82	7.28E-11
VEGF signaling pathway	0.69	6.13E-09	Tight junction	0.62	6.96E-11	Prostate cancer	0.80	1.21E-09
Acute myeloid leukemia	0.57	9.12E-08	Vascular smooth muscle contraction	0.60	4.24E-09	Adherens junction	0.79	3.65E-08
Prostate cancer	0.56	9.34E-08	Insulin signaling pathway	0.59	1.38E-10	GnRH signaling pathway	0.77	9.13E-11
Leishmaniasis	0.48	6.22E-06	**Neurotrophin signaling pathway**	0.59	2.88E-10	T cell receptor signaling pathway	0.75	3.13E-11
Dorso-ventral axis formation	0.48	1.13E-02	Progesterone-mediated oocyte maturation	0.58	8.17E-07	Long-term potentiation	0.72	2.77E-07
			GnRH signaling pathway	0.55	6.47E-08	NOD-like receptor signaling pathway	0.71	1.40E-06
			Adipocytokine signaling pathway	0.53	2.89E-05	Pancreatic cancer	0.69	2.77E-07
			Hedgehog signaling pathway	0.52	7.95E-05	Fc gamma R-mediated phagocytosis	0.65	1.68E-09
			Long-term depression	0.51	7.43E-07	Toll-like receptor signaling pathway	0.64	4.58E-09
			T cell receptor signaling pathway	0.47	2.18E-07	Epithelial cell signaling in Helicobacter pylori infection	0.63	2.77E-07
			Chemokine signaling pathway	0.44	4.38E-14	Long-term depression	0.59	1.26E-07
						Vascular smooth muscle contraction	0.55	2.33E-08
						Insulin signaling pathway	0.54	9.87E-10
						Colorectal cancer	0.54	3.31E-05

RTKs involved in enriched pathways: ○: ErbB signaling ○: Neurotrophin signaling ○: Insulin signaling

Pathway enrichment results for SKMEL30 cell line

Day1			Day4			Day33		
Pathway Name	XD-score	*p*-adj	Pathway Name	XD-score	*p*-adj	Pathway Name	XD-score	*p*-adj
Shigellosis	1.27	1.09E-13	Acute myeloid leukemia	1.27	8.19E-10	Shigellosis	1.17	1.64E-11
Fc epsilon RI signaling pathway	1.17	2.92E-16	Glioma	0.91	4.31E-08	NOD-like receptor signaling pathway	1.02	3.88E-10
NOD-like receptor signaling pathway	1.12	5.18E-11	mTOR signaling pathway	0.83	1.43E-09	Dorso-ventral axis formation	0.94	2.69E-04
Progesterone-mediated oocyte maturation	0.95	1.99E-13	**ErbB signaling pathway**	0.80	1.52E-09	Pancreatic cancer	0.85	1.06E-09
Type II diabetes mellitus	0.94	4.51E-07	Type II diabetes mellitus	0.74	4.02E-05	Type II diabetes mellitus	0.80	2.89E-06
RIG-I-like receptor signaling pathway	0.91	3.10E-10	Adipocytokine signaling pathway	0.71	1.06E-06	Epithelial cell signaling in Helicobacter pylori infection	0.79	1.70E-08
Epithelial cell signaling in Helicobacter pylori infection	0.88	2.11E-10	Long-term potentiation	0.69	7.97E-07	Progesterone-mediated oocyte maturation	0.78	4.11E-10
GnRH signaling pathway	0.87	2.04E-13	Fc gamma R-mediated phagocytosis	0.66	2.29E-09	Fc epsilon RI signaling pathway	0.75	1.53E-09
Neurotrophin signaling pathway	0.86	3.07E-16	Gap junction	0.60	3.74E-07	GnRH signaling pathway	0.74	1.54E-11
ErbB signaling pathway	0.80	9.43E-11	Prostate cancer	0.59	3.74E-07	**ErbB signaling pathway**	0.65	5.44E-09
Toll-like receptor signaling pathway	0.75	1.70E-11	Fc epsilon RI signaling pathway	0.58	6.98E-08	Toll-like receptor signaling pathway	0.62	1.04E-09
VEGF signaling pathway	0.73	2.85E-09	Vascular smooth muscle contraction	0.57	2.42E-08	RIG-I-like receptor signaling pathway	0.58	6.16E-07
Aldosterone-regulated sodium reabsorption	0.69	9.10E-05	Prion diseases	0.54	2.70E-03	T cell receptor signaling pathway	0.57	1.31E-09
T cell receptor signaling pathway	0.69	2.45E-11	Adherens junction	0.52	1.93E-05	Leishmaniasis	0.57	6.62E-07
Leishmaniasis	0.65	1.91E-07	**Neurotrophin signaling pathway**	0.49	2.15E-08	Colorectal cancer	0.54	9.30E-06
Adherens junction	0.65	2.25E-07	Apoptosis	0.49	4.20E-06	Endometrial cancer	0.51	9.97E-05
Colorectal cancer	0.64	1.78E-06	Tight junction	0.46	5.47E-08	**Neurotrophin signaling pathway**	0.47	3.13E-09
Prion diseases	0.54	1.08E-03	Non-small cell lung cancer	0.46	7.94E-05	VEGF signaling pathway	0.42	8.77E-06
Dorso-ventral axis formation	0.52	8.88E-03	Vibrio cholerae infection	0.46	7.74E-04			
Amyotrophic lateral sclerosis (ALS)	0.48	2.12E-04	Aldosterone-regulated sodium reabsorption	0.46	3.50E-03			
			Long-term depression	0.43	6.55E-06			
			Salivary secretion	0.42	6.05E-05			
			Progesterone-mediated oocyte maturation	0.41	6.05E-05			
			Gastric acid secretion	0.40	2.79E-04			
			VEGF signaling pathway	0.37	1.14E-04			

Network-based enrichment was performed on the significantly deregulated kinases at different time points.
MELJUSO and SKMEL30 cells show at all time points an enrichment in ErbB and neurotrophin pathway. Only MELJUSO cells show an enrichment in insulin pathway at day 4 and day 33.

Overall, the number of interactions detected by qCLASH method is influenced by the expression level of the corresponding miRNA and mRNA. Most of the detected interactions did not exert the expected inverse expression pattern between miRNA and mRNA. miRNAs and mRNAs displayed a more robust change in expression across cell lines. Except for the amelanotic A375, upregulation of miR-211-5p is associated with resistant and proliferative cell lines.

iCell integration of bulk and single-cell RNA-seq reveals perturbed pathways and predicts genes facilitating senescence escape

To gain further insights into NRAS mutant melanoma cells' adaptation to treatment, we integrated the bulk RNA-sequencing data with previous condition-matching single-cell data from our lab by adapting and applying a Non-negative Matrix Tri-Factorization (NMTF) approach called iCell [15]. We used the iCell methodology because it is a versatile data fusion framework, which has previously been used to perform integrative comparative analyses of disease and control tissue data, predicting new cancer and COVID-19 related genes [15, 26] and suggesting potential drug re-purposing candidates [26].

For each condition (treated cell line and time point), we constructed Protein-Protein Interaction (PPI) networks by overlaying the experimentally validated PPI network for *Homo Sapiens* from BioGRID [27] with the condition-specific bulk RNA-sequencing data. Also, we derived a condition-specific co-expression (COEXP) network from the corresponding bulk RNA-seq data (see Methods section). Next, we applied Non-negative Matrix Tri-Factorization (NMTF) on the corresponding adjacency matrices of the resulting PPI, COEXP and the single-cell expression data collectively, to ensure data fusion (Methods and [15]). This resulted in the creation of nine condition-specific iCell networks, by multiplying the G1 matrix resulting from the data fusion and its transpose (which is equivalent to computing

A

Cell line	Condition	Total hybrids	Distinct mRNA	Distinct miRNA
SKMEL30	sensitive	17,877	6,346	335
SKMEL30	resistant	37,476	8,776	392
IPC298	sensitive	24,623	7,462	350
IPC298	resistant	35,099	8,672	367

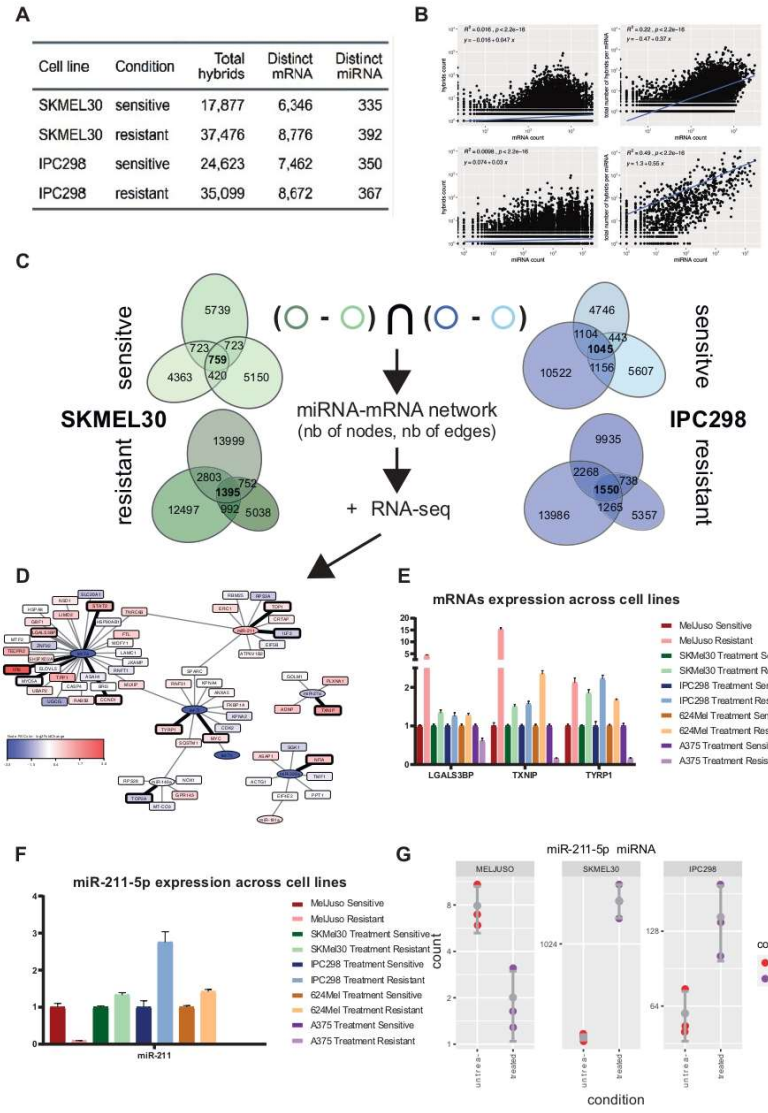

the dot product between gene pairs) and considering as interactions the 1% highest values in each row and column (Methods and [15]).

As illustrated in Supplementary Fig. 16, resulting condition-specific iCell networks were investigated by first comparing the global topology of all resulting iCell networks. Then, these topological changes were further characterised by identifying the genes that change or conserve their local topology between each pair of conditions. We related the identified most rewired genes and the least rewired ones to MSigDB hallmarks by performing an Over-Representation Analysis (ORA) (see Methods for details). Finally, for

Fig. 4 miRNA-mRNA interactions potentially contributing to resistance. A Summary of the interactions detected through the qCLASH method. **B** Top part, correlations between hybrid counts (qCLASH) and miRNA/mRNA counts (RNA-seq). Bottom part, summing hybrid counts per mRNA or miRNA (qCLASH) further strengthen the correlations with the RNA-seq. **C** To select candidates, we considered the interactions detected in three technical replicates (colored circles). Then for the two cell lines, interactions present in the resistant state but absent in the sensitive state were considered. Finally, interactions common to the two cell lines IPC298 and SKMEL30 were used. **D** RNA-seq data for SKMEL30 cell line as log fold changes overlayed onto the resistant miRNA network. Selected interactions for further validation by qPCR are represented with thick lines and the corresponding mRNAs and miRNAs with bolded borders. **E** Relative expression of LGALS3BP, TXNIP and TYRP1 mRNAs assessed by qPCR across three NRAS and two BRAF mutant melanoma cell lines. **F** Relative expression of miR-211-5p across the same cell lines as determined by qPCR. **G** Expression of miR-211-5p in the small RNA-seq.

each condition we clustered the genes based on their local topology in the iCell network and then found the MSigDB hallmarks enriched in the resulting clusters. We focused on two senescence-escape related hallmark pathways (IFN gamma and EMT) to predict novel genes potentially related based on their appearance in the clusters enriched across all conditions.

We compared the overall topology of iCell networks obtained for each condition by using thus far the most sensitive measure of global network topology, the "Graphlet Correlation Distance" (GCD-11) (see Methods and [28]). The lower the GCD-11 value, the closer the topologies of the networks [28]. We used Ward's hierarchical clustering to cluster the resulting heatmap of the GCD-11s between all iCell networks (all-to-all matrix). In line with our phenotypic observations, we showed on the heatmap (Fig. 5A) that for the resistant cell line IPC298, the conditions D4 and D33 have the lowest GCD-11 value (0.26) and hence clustered together, suggesting early adaptation to treatment of this cell line. For the two other cell lines, conditions D0 and D4 grouped together (GCD-11 values of 0.71 for SKMEL30 and 0.87 for MELJUSO), suggesting that these two cell lines adapt later.

Next, the local topology of genes in each condition-specific iCell networks was analysed to find out if some are rewired between conditions. To this end, we focused on genes that were expressed in both conditions (Venn diagrams in Fig. 5B and Supplementary Fig. 17). Within each iCell network, the local topology around a gene in the network was quantified by using its "Graphlet Degree Vector" (GDV). We then measure the rewiring of a gene between two conditions by comparing its GDVs in the two networks using "Graphlet Degree Vector Similarity" (GDVS) (detailed in Methods and in [29]). Between two conditions, genes with high GDVSs have conserved topologies and are called "stable", while the genes with low GDVSs are rewired and are called "perturbed". We related the top 10% of the most "stable" and the top 10% of the most "perturbed" genes to MSigDB hallmarks [30] by performing ORA. For each cell line, the condition-specific iCell networks were compared between time-points (i.e., D4 vs D0, D33 vs D4, and D33 vs D0). For all cell lines, we observed that the top 10% of the most "perturbed" genes were enriched at different contrasts in "ADIPOGENESIS" (also observed in senescent fibroblasts [31]) and "OXIDATIVE PHOSPHORYLATION" (OXPHOS) (a pathway commonly dysregulated in senescence which has been proposed as a targeting strategy [32]) (Fig. 5C). Then, condition-specific iCell networks were compared between cell lines at matching time points (e.g., MELJUSO_D0 vs SKMEL30_D0). Interestingly, the top 10% of the most "stable" genes were only found to be enriched when comparing IPC298 vs MELJUSO at day 0 and when comparing MELJUSO vs SKMEL30 at day 4, which suggests that these cell lines react coherently early on and diverge later (Supplementary Fig. 17). At day 0, and across all pairwise comparisons involving IPC298 cell line, the top 10% of the most "perturbed" genes were enriched for OXPHOS, suggesting a different initial metabolic state for IPC298. On day 4, when comparing IPC298 and SKMEL30 cells, the top 10% of the most "perturbed" genes were enriched in "INTERFERON ALPHA/GAMMA RESPONSE". At days 4 and 33, but not across all pairwise comparisons, we found that the top 10% of the most "perturbed" genes are enriched in "EPITHELIAL MESENCHYMAL TRANSITION", "ADIPOGENESIS" and "COAGULATION". Further information on the relevance of these enriched pathways can be found in the Discussion.

Finally, to predict novel genes which could contribute to senescence escape facilitated by interferons, genes were clustered based on their GDVs signatures in each condition-specific iCell network using "Ward's hierarchical clustering" and the "k-medoids" algorithms. For each condition, we performed ORA to associate the clusters to hallmarks from MSigDB (results of ORA on the clusters obtained by using k-medoids clustering in Fig. 5D). The results for the two algorithms showed limited agreement (Fig. 5E, left), as measured by Adjusted Rand Index for each condition: 0.31, 0.38 and 0.30 for MELJUSO at day 0, day 4 and day 33; 0.32, 0.30 and 0.26 for SKMEL30 at the same time points and 0.27, 0.31 and 0.45 for IPC298. Therefore, we considered the results from the two different clustering methods (hierarchical and k-medoids) separately. Enriched clusters were filtered to exclude genes that are already known to be associated with hallmarks in MSigDB. For the remaining genes, we counted the number of times a gene was found in the clusters enriched in one of the two senescence escape-related pathways, EMT and interferon gamma (Fig. 5E right). Then, based on the distributions of the number of times genes appeared in these enriched clusters, we predicted genes that appeared in two or more clusters as related to senescence escape. To obtain more robust predictions, we only considered genes predicted by both algorithms. This resulted in a set of 90 predicted genes, among which CCND1, a known regulator of G1 phase. Furthermore, many of our predictions are known to interact with TP53, further supporting their connection to senescence (Fig. 5F, Supplementary Table 2).

To conclude, the integrated analysis of bulk and single-cell data by using the iCell methodology further confirms our phenotypic observations and uncovers the most dysregulated processes ("OXIDATIVE PHOSPHORYLATION", "ADIPOGENESIS", "COAGULATION" and "EPITHELIAL MESENCHYMAL TRANSITION") during adaptation to the treatment. Furthermore, it allowed us to predict 90 new genes involved in senescence escape.

DISCUSSION

Most cancer cells inevitably develop resistance to targeted therapies. Anticipating the development of such resistance to a newly tested combination of CDK4/6i and MEKi, we characterised the transcriptomic responses in 3 NRAS mutant melanoma cell lines over an extended treatment duration of 33 days. Our RNA-seq data exhibited a strong enrichment in interferon responses, coherent with previous observations by Goel et al. [33] following CDK4/6 inhibition. This study showed that CDK4/6 inhibitors downregulate E2F2 and DNMT1, subsequently leading to a hypomethylation of the genome (Supplementary Fig. 18). The works of Chiappinelli et al. [34] and Roulois et al. [35] first showed that hypomethylation brought about by DNMT inhibitors induce the expression of otherwise silenced endogenous retroviruses (ERVs). These ERVs then form dsRNAs in the cytoplasm and trigger an anti-viral immune response associated with interferon production. Alternatively, ERVs can be reverse transcribed and produce ssDNA and dsDNA triggering the cGAS-STING pathway leading to similar responses [36]. The

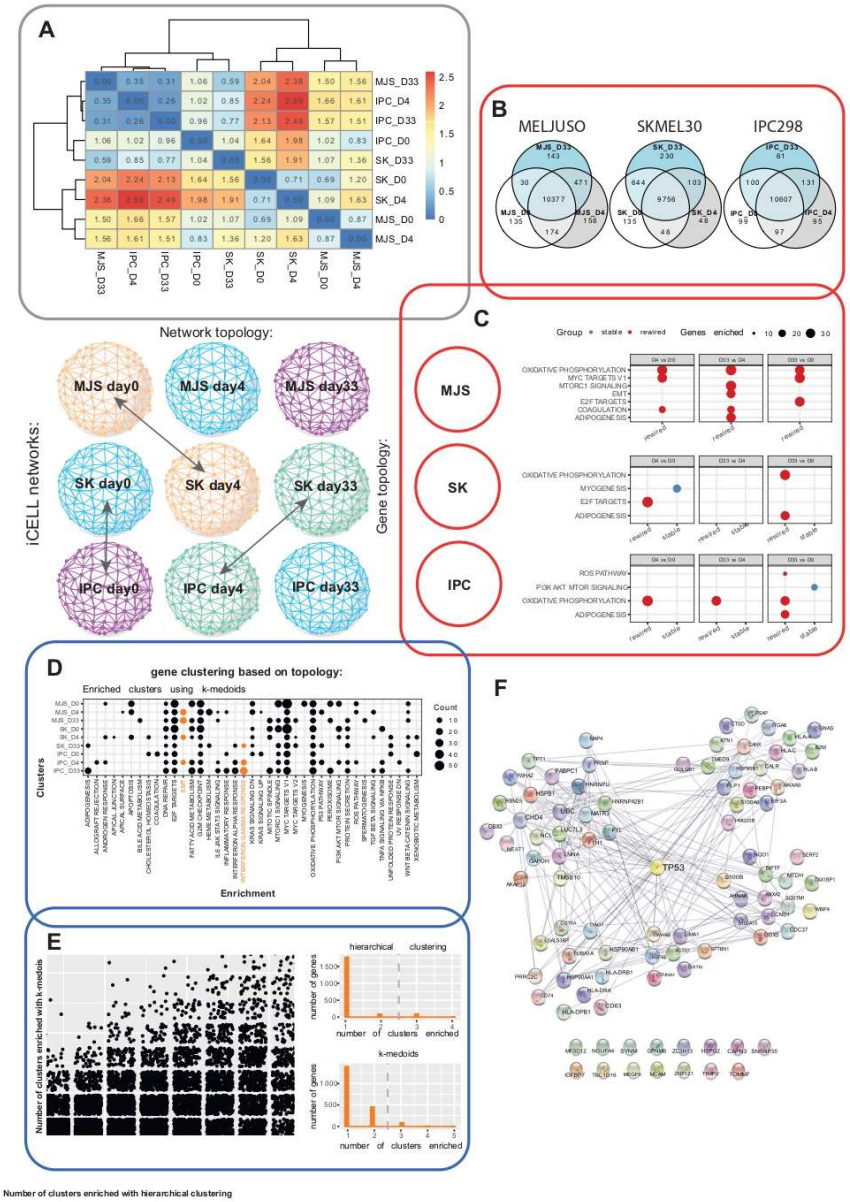

Number of clusters enriched with hierarchical clustering

Fig. 5 "iCell" integration of bulk and single-cell RNA-seq. A Comparison of iCell networks topology using Graphlet Correlation Distances (GCD). iCELL networks recapitulate phenotypic observations and early adaptation of IPC298. **B** Venn diagrams representing genes overlap between conditions. **C** Comparison of gene local topology using Graphlet Degree Signature Similarity (GDSS). Within all cell lines, the different time points were compared. ORA was performed on the top 10% most "stable" or "perturbated" genes. **D** Genes were clustered according to their Graphlets Degree Signatures. ORA was performed to associate gene clusters with biological function. **E** Left panel: number of enriched clusters detected for each gene across all conditions. Right panel, Number of detected clusters for the EMT and iFN gamma pathways (related to senescence escape) for the two algorithms. **F** Protein-protein interactions (BioGRID) between P53 and the genes associated with EMT and IFN gamma.

activation of these two pathways can be concomitant and their relative importance may be cell-type specific. This phenomenon, termed "viral mimicry", has been extended to other types of retroelements and it has been proposed to be integral part of carcinogenesis in a rheostat model [37]. It has been reported in different cancer types and in response to different epigenetic perturbations (DNMTi, HDACi, HMTi). Brägelmann et al. [38] also reported the activation of viral mimicry in the case of BRAF mutant melanoma and MAPK inhibitors (BRAFi + MEKi) further supporting the E2F2-DNMT1 axis as a mechanism of action. Melanoma cells are considered very immunogenic [39] and this partially explains why melanoma respond better to immunotherapy than other cancer types. IFN signaling is known to upregulate PD-L1, explaining why many treatments activating viral mimicry have been shown to synergise with immune checkpoint inhibitors. Here, we confirm the appearance of an IFN signature following CDK4/6 and MEK inhibition suggesting a potential induction of viral mimicry.

A "senescence score" predicted from our data with SENESCopedia [18] suggested induction of a senescent transcriptional programme in all cell lines. Cytokines composing the SASP can induce features of EMT [40] and EMT has been recently proposed to inhibit senescence in HeLa cells treated with Doxorubicin [41]. TIS and EMT share common transcription factors with opposite effects on both processes (Supplementary Fig. 19) [42] and cancer cells escaping from TIS have been associated with a mesenchymal phenotype [43]. IFN gamma, by promoting EMT [44–46], could further support escape from senescence (Supplementary Fig. 20A). To understand the relationship between IFN gamma and EMT gene sets (from the hallmarks) and a recent gene set characterizing senescence in cancer cell lines [47], we looked at changes in expression (log2 fold change) between those gene sets at day 14 where all cell lines display high senescence scores. IFN gamma shows an opposite trend in expression to the EMT and senescence gene sets (Supplementary Fig. 20B), suggesting that IFN may accelerate the EMT process and thereby repress senescence. Albeit interferon signaling has earlier on been linked with senescence [48], only later Katlinskaya and Yu et al. showed a role of IFNAR1 in the induction of senescence [49]. Recently, the accumulation of double stranded RNA was proposed to also contribute to the onset of senescence [50, 51]. These findings suggest a link between senescence and viral mimicry, which can engage autocrine and paracrine secretion of interferons. Embryonic stem cells (ESCs) are another cellular model where transposable elements play an important role, where they are profoundly repressed during embryogenesis and leakage in their expression may impair developmental processes. Recent work by Asimi et al. in mesenchymal ESCs suggests that ERV transcription participates in the remodeling of epigenetic landscapes by competing with super-enhancers for the formation of transcriptional condensates, which may explain the phenomenon of onco-exaptation (oncogene activation by a TE-derived promoter) [52]. Also recently, Liu et al. demonstrated a role of ERV expression in the induction of senescence and attributed the observed paracrine effects to the production of retrovirus like particles [53]. We propose here that the IFN gamma signalling programme activated after induction of viral mimicry may contribute to senescence escape by inducing EMT. This might represent a general cellular mechanism to cope with different extrinsic and intrinsic stressors.

To identify targetable proteins, which could explain the senescent phenotype, we profiled the kinase activities of SKMEL30 and MELJUSO cells upon CDK4/6 and MEK inhibition. We observed the reactivation of different RTKs due to ERK1/2 inhibition as previously reported by others [22, 54]. Some of the corresponding pathways such as ErbB, neurotrophin and insulin were found enriched through network-based enrichment hinting at an active downstream signalling. Interestingly, all those pathways have been shown to activate ERK5. In breast cancer, ERK5 contributes to the response to EGF stimulation [55] and is involved in the resistance to ErbB-2 (HER2) inhibitors by facilitating G1-S transition [56]. In BRAF mutant melanoma resistant to BRAFi and MEKi, IGF1R activation induces ERK5 phosphorylation [57]. In senescent fibroblasts, BDNF-TrkB has been shown to activate ERK5 and was proposed to form an autocrine loop further enhancing senescent cell viability [58]. ERK5 activation has also been linked to PDGFR signalling in NRAS mutant melanoma treated with MEK and ERK1/2 inhibitors [59, 60] (Fig. 3B, D, E). In other cell types, Src is also known to activate ERK5 and Focal Adhesion Kinases (FAK1 and FAK2) [61, 62]. Other Src Family Kinases (SFKs) display an increased activity (Supplementary Fig. 21) and have been previously linked with EMT [63]. Finally, IFN gamma was reported to activate ERK5 and its activation is necessary for the full expression of interferon stimulated genes [64]. Linking this observation with our RNA-seq data (Supplementary Fig. 22) further supports the idea that IFN gamma could facilitate senescence escape by activating ERK5.

Investigating the contribution of miRNAs to the establishment of resistance, we noticed the upregulation of mir-211-5p in all proliferative cell lines but the amelanotic A375. miR-211-5p is highly expressed in the melanocytic lineage as well as in the nervous tissue, as reported by the TissueAtlas2 [65]. Both cell types derive from the neurectoderm. Interestingly, miR-211-5p is known to derive from the TRPM1 transcript and both are very lowly expressed in the senescent cell line MELJUSO (Supplementary Fig. 23). miR-211-5p inhibits DUSP6, which regulates ERK5 kinase activity, and this axis has been shown to be relevant in vivo in genetic variants of A375 overexpressing mir-211 or DUSP6 and treated with BRAF/MEKi [66]. In qPCR validation experiments, mRNAs displayed a more robust change in expression with LGALS3BP, TXNIP and TYRP1 being upregulated in four out of five cell lines. LGALS3BP and TXNIP are interferon-inducible and interestingly, LGALS3BP has been reported to promote EMT.

Integrating single-cell and bulk RNA-seq data, we observed the perturbation of OXPHOS in all cell lines. This is in line with previous works demonstrating metabolic adaptation after MAPK inhibition or CDK4/6i in BRAF mutant and uveal melanoma [67, 68]. Moreover, OXPHOS metabolism has been previously reported as a generic drug resistance mechanism and as a key decision point between cell death and survival [69, 70]. Upon comparison of different treatment time points, differences in processes such as "ADIPOGENESIS" and "COAGULATION" were observed. Interestingly, those have recently been associated with replicative senescence [31], cell cycle arrest caused by CDK4/6i [71] and escape from OIS [72]. EMT has been reported to inhibit senescence [19, 41]. We therefore clustered the genes in the networks and enriched those clusters to report novel associations between genes and the processes of EMT and IFN gamma response, which could support senescence escape. Our

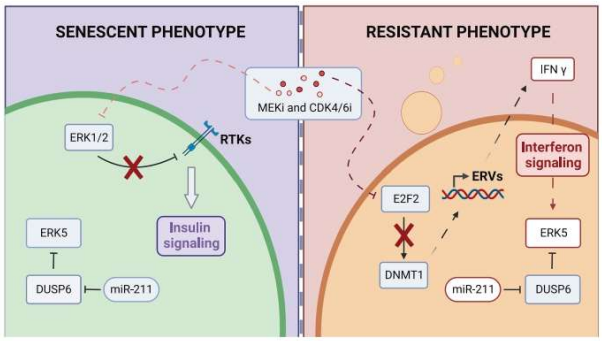

Fig. 6 Graphical summary. The phenotypes observed across three different NRAS mutant melanoma cell lines can be summarised as "senescent" (left) and "resistant" (right). Insulin signalling is associated with the "senescent" phenotype and can be explained by the mechanism of action of MEKi, which downregulates ERK1/2, suppressing negative feedback on RTKs. Interferon signaling can be explained by CDK4/6i, which downregulates DNMT1 leading and lead to hypomethylation of the genome and expression of Endogenous Retroviruses (ERVs). Induced expression of intracellular ERVs trigger an innate immune response and production of interferons. IFN γ can activate ERK5, inducing EMT. This phenotype is moreover associated with upregulation of miR-211-5p, which indirectly regulates ERK5.

predicted genes are coherent with the results of a genetic screen aiming to identify genes contributing to senescence bypass after p16 overexpression in melanoma [73]. Interestingly, the IFN-inducible gene LGALS3BP, previously reported to contribute to EMT and identified in our miRNA resistant network, was predicted by our approach to be associated with senescence escape. On the other hand, TXNIP, another IFN-inducible gene from the miRNA network, recently shown to participate in the induction of senescence upon IGF1 stimulation, was found associated only once and therefore not selected [74]. This further suggests that our approach can relate genes to function beyond their expression pattern, providing a list of 90 potential targets to overcome senescence escape in cancer cells (Fig. 5.F). For example, our top-prediction NEAT1 was shown to be important for the viability of lung cancer cells [75] while its knock-down triggered interferon signaling and impaired tumor growth in vivo. Finally, NEAT1 was shown to physically interact with DNMT1 to epigenetically inhibit TP53, STING and cGAS. Among the predictions with the lowest scores, MTDH has been shown to epigenetically regulate TWIST1 and promote stemness in breast cancer [76] while AKAP12 has been suggested to protect ERK5 from PKCζ phosphorylation on residue S486A which inhibits its transcriptional activity [77].

Taken together, our data describe how NRAS mutant melanoma adapt to CDK4/6 and MEK inhibition by triggering an EMT programme. This is reminiscent of the Neural Crest Stem Cell (NCSC)-like state identified in single cell RNA-seq of patient samples after MAPKi by Rambow and colleagues [78]. This state was later characterised by FAK-dependent AKT activation [79], associated with slow or no proliferation and the expression of EMT-related transcription factors.

In sum, our work sheds new light on the intimate relationships between three interacting pathways, senescence, interferon and insulin signalling, with the EMT process (Fig. 6). Our data suggest a new role of interferon gamma, which, by triggering EMT, can facilitate senescence escape while insulin signaling is associated with a robust cytostasis and senescent transcriptome.

METHODS

Cell culture

NRAS-mutant MELJUSO, SKMEL30 and IPC298 (ACC-74, DSMZ; ACC-151, DSMZ; ACC-74, DSMZ) and BRAF-mutant A375 and 624MEL (CRCL-1619, ATCC; kindly provided by Dr. Ruth Halaban, Yale School of Medicine) melanoma cell lines were grown in RPMI-1640 medium supplemented with 10% heat-inactivated fetal bovine serum, L-glutamine (2 mM), streptomycin (100 µg/mL) and penicillin (100 units/mL). The cells were kept at 37 °C, in a humidified atmosphere with 5% CO2 and sub-cultivated twice a week. Resistance of MELJUSO, SKMEL30, and IPC298 cells to the MEK and CDK4 inhibitors was induced by treatment with 110nM, 35nM or 16nM of Binimetinib, respectively, and 1µM of Palbociclib for 33 days.

Total RNAseq

Transcriptome sequencing was performed using total RNA. Libraries were prepared using "TruSeq Stranded Total RNA Library Prep Gold" Kit (Illumina, USA) and sequenced as 2x75bp on a NextSeq 550 (Illumina, USA). The sequencing was carried out at Luxgen platform, LNS. Data were aligned to the reference genome (hg38) using STAR (v 2.7.9a) and differential expression analysis was performed using R (v 4.2.2) and DESeq2 (v 1.34.0). This analysis was automated in a snakemake workflow (v 0.3.2) [80] (https://gitlab.lcsb.uni.lu/aurelien.ginolhac/snakemake-rna-seq) using docker file (v0.6) (https://hub.docker.com/r/ginolhac/snake-rna-seq/tags). Mixing all cell lines into one analysis masked the differences of each time course. Therefore, a subset per cell line was created and the differential gene expression was performed independently. To predict senescence scores with SENESCopedia [18], data were reprocessed and aligned to GENCODE (v 34) using kallisto (v 0.46.2) according to the recommendations of the authors.

Gene-list based pathway enrichment

Over-Representation Analysis (ORA) and Gene Set Enrichment Analysis (GSEA) were performed using R (v 4.2.2) and the package "clusterProfiler" (v 4.0.5). The Hallmark Gene Set Collection from MSigDB were used as reference. Differentially expressed genes used for GSEA were ranked according to the π value, which takes into consideration both the statistical significance and the biological relevance through the product of the *p*-value and the fold change [81]. The results were represented using the package "pheatmap" (v 1.0.12) using the default "Ward.D2" clustering algorithm. ORA results were displayed using the "ggplot2" (v 3.3.6) package.

Kinase activity (PamGene)

To assess the kinase activity within the NRAS mutant melanoma cell lines MELJUSO and SKMEL30 to a combination of CDK4/6 and MEK inhibitors, cell samples were collected at day 0, 1, 4 and 33. Cell pellets were lysed in Mper (78501, Thermo Fisher) supplemented with Halt Phosphatase Inhibitor Cocktail (78428, Thermo Fisher) and Halt Protease Inhibitor Cocktail, EDTA free (78437, Thermo Fisher), for 15 min on ice. The lysate was clarified (10000g, 15 min, 4 °C) before aliquoting and freezing at −80 °C. Adopting a balanced design, three replicates for each condition and cell line were

assessed for both tyrosine kinase activity on PTK chips (86402, PamGene International B.V., 's-Hertogenbosch, the Netherlands) and serine threonine kinase activity on STK chips (87102, PamGene International B.V., 's-Hertogenbosch, the Netherlands) using the manufacturer's protocol. Each chip contains a panel of 196 (PTK) and 144 (STK) phorylatable peptides. The phosphorylation of these peptides by native kinases in the applied lysate was quantified by sequence agnostic fluorescently coupled anti phosphorylation antibodies (Suppl. Fig. 4). Image processing was achieved using the instrument manufacturer's Bionavigator software before applying COMBAT normalization and performing Upstream Kinases Analysis (UKA) using a multiple hypothesis testing approach. This identified responsible kinases for the observed phosphorylation status with a median final score for the likelihood of the kinase being responsible for observed phosphorylation to which a cutoff of 1.2 was applied and a median kinase statistic indicating the degree of and direction of kinase activity change between compared conditions. The results were compiled to construct representative kinome trees with an adaptation of the CORAL tool [82] in R (v 4.2.0).

Network-based pathway enrichment

To identify biological pathways enriched in a protein list, we applied a network-based protein set enrichment analysis approach using EnrichNet [83]. The inputs are a list of the PamGene protein identifiers and the database of interest from which reference protein sets will be extracted. The databases include (KEGG, BioCarta, WikiPathways, Reactome, PID, and GO. Using a genome-scale molecular interaction network, we map the target and reference datasets and then perform a network analysis, which involves two steps: i) the use of a random walk with restart (RWR) algorithm to score the distance between the mapped target protein set and reference datasets in the network. ii) the comparison of the calculated scores against a background model. Extensive information on how the RWR method for node relevance scoring was developed is found in [83]. A network similarity score (XD-score) measures how close the protein set of the PamGene data is to the pathways in the databases. The XD score is compared to a classical enrichment analysis score (*p*-values) which measure the significance of the overlap between pathways and the protein set. A similarity ranking table of the reference datasets is generated, including their network-based association scores (measured using the XD-score). The table ranks the pathways from a chosen database to the protein set of the PamGene data. Using an interactive graph-based visualization, we generate interoperable interaction networks for each pathway. This network (XML-based) highlights the proteins that overlap in pathways, illustrating their interactions.

Small RNAseq

Small RNAseq was performed on the same samples used for total RNAseq. Libraries were prepared using "QIASeq miRNA Library kit" (Qiagen, Germany) and sequenced as 1x75bp on a NextSeq 550 (Illumina, USA). The sequencing was carried out at Luxgen platform, LNS. Data were aligned to the miRBase (v 2.2.2.1) and piRBase (regulatoryrna.org, v 2.0) using bowtie2 (v 2.3.4.1) and differential expression analysis was performed using R (v 4.2.2) and DESeq2 (v 1.34.0). This analysis was performed using a snakemake workflow adapted from a previous workflow designed by https://github.com/jounikuj/ for this library preparation. Briefly, the snakemake workflow applies 4 passes of trimming (including UMIs) and map the obtained reads on miRBase using bowtie2 with the parameter –very-sensitive-local. Next, the corresponding un-mapped reads are aligned to piRBase and the successfully mapped read coming from these 2 passes of alignment are merged in a unique BAM file per sample. Finally reads are counted, after UMI collapsing (UMI_tools v. 1.0.0) using a combination of samtools (v 1.9) and bash commands.

qCLASH

qCLASH sample preparations were performed exactly as previously described by Kozar et al. [16] Briefly, 50 million cells were UV cross-linked at a wavelength of 250nm and 600J/cm2. AGO protein immunoprecipitation was performed using Protein G Dynabeads (Invitrogen), and 10µl 2A8 anti-Ago antibody (Millipore) per sample. qCLASH libraries were sequenced on a NextSeq500 instrument with a read length of 85bp. The raw sequences were pre-processed and analyzed as previously described [16] using the bioinformatics pipeline *hyb* [84], and custom scripts available at GitHub (https://github.com/RenneLab/qCLASH-Analysis).

miRNA network construction and representation

qCLASH data were analysed using R (v 4.2.2) and the "tidyverse" package. Interaction lists were converted to "igraph" objects with the corresponding package (v 1.3.4) and further exported to cytoscape using "RCy3" (v 2.12.4). Final representations were made using Cytoscape (v 3.8.2) and the plugin "Legend Creator" (v 1.1.6).

RT-qPCR

RNA was extracted from cell lysates using the Quick-RNA MiniPrep kit with on-column DNase I treatment (Zymo Research, USA) according to the manufacturer's protocol. RNA purity and quality were assessed using the NanoDrop2000 Spectrophotometer (Thermo Scientific, USA). 500ng of RNA were used to perform reverse transcription using the miScript RT II Kit and HiFlex Buffer Reverse Transcription (Qiagen, Netherlands). Quantitative polymerase chain reaction (qPCR) was performed in technical triplicates using the CFX384 Detection System (BioRad, USA) using 5ng and 50ng of cDNA as a template for subsequent miRNA and mRNA expression detection, respectively. Primers were purchased from Qiagen (miScript Primer Assay range) and from Eurogentec (primer list Supplementary Table 4) to respectively amplify miRNA and mRNA. Amplification curves were analyzed using CFX software (BioRad, USA) and expression was normalised using three housekeeping genes (RNU1A, RNU5A, SCARNA17 for miRNA and HPRT, PPIA, TBP for mRNA). Statistical significance was calculated for each condition considering biological replicates ($n = 3$) using multiple welch's t-test and an FDR of 0.01.

Single cell RNA-seq analysis

Single cell RNA-seq data from [Randic et al., in revision] were reprocessed using Seurat (v 4.2.0) and SeuratObject (v 4.1.2). Reads were aligned to human genome hg38 using STAR aligner. Transcripts were filtered to be detected in at least 3 cells and to totalise at least 100 counts across cells. Cells were filtered based on mitochondrial transcripts (<=25%), ribosomal transcripts (<= 1%), and a cell complexity (log10GenesPerUMI >=80%). Thresholds for Unique Molecular Identifiers (UMI), genes detected were different between cells lines (for MELJUSO and SKMEL30: 150 and 100, for IPC298: 350 and 150). Finally, mitochondrial, ribosomal and hemoglobin genes were removed, and genes were filtered to have at least 10 counts across the filtered cells.

iCell data-fusion framework

iCell methodology [15] was applied separately to each of the three cell lines (MELJUSO, SKMEL30 and IPC298) at day 0, day 4 and day 33, to obtain integrated networks that encompass the condition-specific (i.e., defined by a cell line and day) PPI, COEX, and single-cell RNA-seq data from our lab [Randic et al., unpublished]. We used the iCell methodology because it is an intermediate data integration method that uses Non-negative Matrix Tri-factorization (NMTF) to simultaneously decompose multiple relational matrices through the inference of a single joint model [15, 85]. Therefore, it does not suffer from information loss of early integration approaches that combine all datasets into a single dataset before integration, or late integration methods that first build models for each dataset and then combine them into an integrated model. Additionally, NMTF-based methods are co-clustering methods that encode the high-dimensional input data into three low-dimensional matrix factors [86]. The clustering information is contained in the so-called cluster indicator matrices that are easily interpretable (unlike the resulting matrices of other artificial intelligence algorithms), making them ideal for mining biological data.

For each condition (treated cell lines and time points), we constructed condition-specific Protein-Protein Interaction (PPI) and gene co-expression (COEXP) networks as follows. We collected the experimentally validated protein-protein interactions of *Homo sapiens* from BioGRID (v 4.3.195) [32], from which we excluded genes (nodes in the network) that are not expressed in our condition-specific bulk RNA-seq data (zFPKM < -3, [87]). To generate the condition-specific COEXP networks, we applied Spearman's correlation between the gene expression profiles from the condition-specific bulk RNA-seq data, using a 0.9 correlation threshold with a $p\text{-value} \leq 0.01$. These two condition-specific networks were further filtered to exclude genes (nodes in the networks) that are not expressed in any single cell according to the corresponding condition-specific single cell RNA-seq data.

For each condition, we followed the iCell methodology [15] to integrate the condition-specific PPI, COEXP, and single-cell expression data together. To this aim, we used Non-negative Matrix Tri-Factorization to simultaneously

decompose the adjacency matrices of the PPI and COEXP networks, A_1 and A_2, respectively, and the single cell RNA-seq expression data, E. More precisely, the two adjacency matrices, A_1 and A_2, are simultaneously decomposed as the products of three matrix factors each, A_1 as the product of matrix factors G_1, S_1 and G_1^T, and A_2 as the product of matrix factors G_1, S_2 and G_1^T, i.e.: $A_1 \approx G_1 S_1 G_1^T$ and $A_2 \approx G_1 S_2 G_1^T$, where G_1 is interpreted as the cluster indicator matrix of the genes and matrices S_1 and S_2 are interpreted as the compressed representations of the PPI and COEXP networks, respectively. The condition-specific single-cell RNA-seq expression matrix, E, is decomposed into the product of three matrix factors G_1, S_3 and G_2^T as: $E \approx G_1 S_3 G_2^T$, where S_3 is interpreted as the compressed representation of the single-cell expression data, G_2 is the cluster indicator matrix of single cells, and G_1 is the cluster indicator matrix of the genes that is shared across the decompositions of all input matrices, which facilitates the information flow and allows for learning from all data.

Furthermore, to ease interpretability, we constrain all matrix factors to be non-negative. We also impose orthogonality constraint to the G_2 matrix factor to obtain less ambiguous functional organization captured by the clusters [86].

This decomposition is done by minimizing the following objective function, F:

$$\min_{G_1,G_2,S_1,S_2,S_3\geq 0} F(G_1,G_2,S_1,S_2,S_3) = \min_{G_1,G_2,S_1,S_2,S_3\geq 0} \left[\sum_{i=1}^{2} \left\|A_i - G_1 S_i G_1^T\right\|_F^2 + \left\|E - G_1 S_3 G_2^T\right\|_F^2\right],\ G_2 G_2^T = I$$

where $\| \ \|_F$ denotes the Frobenius norm and I is the identity matrix.

Because minimizing this objective function is an NP-hard continuous optimization problem [88], we heuristically solve it by using a fixed point method that, starting from an initial solution, iteratively applies multiplicative update rules [86] to converge towards a locally optimal solution (described in the next section).

After minimizing F, we used the obtained matrix factors to create an integrated network that encompasses the condition-specific PPI, COEXP, and single cell RNA-seq data, which we call iCell network. Following the iCell methodology [15], we created this network by computing $G_1 \cdot G_1^T$ and thresholding the resulting matrix to preserve only the top 1% of the strongest relationships in each row and column.

We apply this methodology for each condition separately, resulting in nine condition-specific iCell networks.

Fixed point solver

Following the iCell methodology [15], first we derive the Karush-Kuhn-Tucker (KKT) conditions, which are necessary for a solution to be optimal [88]:

$$\frac{\partial F}{\partial G_1} = \sum_{i=1}^{2}\left(-A_i^T G_1 S_i + A_i G_1 S_i^T + G_1 S_i G_1^T G_1 S_i^T + G_1 S_i^T G_1^T G_1 S_i\right) - E G_2 S_3^T + G_1 S_3 G_2^T G_2 S_3^T - \eta_1 = 0,$$

$$\frac{\partial F}{\partial G_2} = -E^T G_1 S_3 + G_2 S_3^T G_1^T G_1 S_3 - \eta_2 = 0,$$

$$\frac{\partial F}{\partial S_1} = -G_1^T A_1 G_1 + G_1^T G_1 S_1 G_1^T G_1 = 0,$$

$$\frac{\partial F}{\partial S_2} = -G_1^T A_2 G_1 + G_1^T G_1 S_2 G_1^T G_1 = 0,$$

$$\frac{\partial F}{\partial S_3} = -G_1^T E G_2 + G_1^T G_1 S_3 G_2^T G_2 = 0,$$

$$\eta_1, \eta_2, G_1, G_2 \geq 0,$$

$$\eta_1 \odot G_1 = 0,$$

$$\eta_2 \odot G_2 = 0,$$

$$G_2 G_2^T = I,$$

where $\odot$ is the Hadamard (elementwise) product, I is the identity matrix, and matrices, η_1 and η_2, are the dual variables for the primal constraints $G_1 \geq 0$ and $G_2 \geq 0$, respectively.

Then, we derive the following multiplicative update rules for all matrix factors, G_1, G_2, S_1, S_2 and S_3, to solve the KKT conditions presented above:

$$G_1 = G_1 \sqrt{\frac{\sum_{i=1}^{2}\left(A_i G_1 S_i^T\right) + E G_2 S_3^T}{\sum_{i=1}^{2}\left(G_1 S_i G_1^T G_1 S_i^T\right) + G_1 G_1^T E G_2 S_3^T}},$$

$$G_2 = G_2 \sqrt{\frac{E^T G_1 S_3}{G_2 G_2^T E^T G_1 S_3}},$$

$$S_1 = S_1 \sqrt{\frac{G_1^T A_1 G_1}{G_1^T G_1 S_1 G_1^T G_1}},$$

$$S_2 = S_2 \sqrt{\frac{G_1^T A_2 G_1}{G_1^T G_1 S_2 G_1^T G_1}},$$

$$S_3 = S_3 \sqrt{\frac{G_1^T E G_2}{G_1^T G_1 S_3 G_2^T G_2}}.$$

In our fixed point approach, we start from initial solutions of the matrix factors, which we compute using singular value decomposition (SVD) of the original input matrices [88], and iteratively use the derived update rules to compute new matrix factors, G_1, G_2, S_1, S_2 and S_3, until convergence. Initializing the matrix factors with SVD reduces the number of iterations that are needed to achieve convergence and makes our solver deterministic [89]. To satisfy the non-negativity constraint of NMTF, we generate the initial solutions by taking the absolute values of the entries from the matrices computed using SVD.

The iterative process ends when the objective function does not decrease anymore, which we measure every ten iterations with: $\left|\frac{F^{-1}-F^{i}}{F^{0}}\right| \leq 10^{-3}$, where F^0 is the value of the objective function at the current iteration, i, and F^{-1} is the value computed at iteration *i-10*.

Analyzing the topology of iCells

To mine the biological knowledge hidden in the iCell networks, we applied graphlet-based methods because they are the most sensitive measures of network topology to date [28, 29]. Graphlets are small, connected, nonisomorphic, induced subgraphs of a large network that appear at any frequencies in the network [88]. Within a graphlet, the symmetries between groups of nodes are called automorphism orbits and are used to characterise the different topological positions that a node participates in [90]. These orbits are used to generalise the notion of the node degree (the number of edges that the node touches in the network): for each orbit, the "graphlet degree of the node" in the network is the number of times the node touches (is found at the position of) the particular orbit [28]. Following the methodology of Yaveroğlu et al. (2014), we characterised the topology of each node in a network by using the 11 nonredundant orbits of 2- to 4-node graphlets. Therefore, the topology of every node is captured by an 11-dimensional vector called "Graphlet Degree Vector" (GDV).

We compared the global topological dissimilarity between two condition-specific iCell networks by using "Graphlet Correlation Distance" (GCD-11), because it is the most sensitive network distance measure [28]. To do this, first we characterised the global topology of a network with its "Graphlet Correlation Matrix" (GCM), which is an 11×11 symmetric matrix that contains the Spearman's correlations between GDVs over all nodes of the network. Then, the GCD-11 between two networks is the Euclidean distance between the upper triangle values of their GCMs. The lower the GCD-11 value, the closer the topologies of the networks [28].

Additionally, we measure the change in the wiring of a gene between two condition-specific iCell networks by using the "Graphlet Degree Vector Similarity" (GDVS) between the GDVs of the node in the two networks, which is computed as follows. Given the GDV vector of a gene (node) in one network, $\boldsymbol{a}$, and the GDV vector of the same gene (node) in another network, $\boldsymbol{b}$, the distance between the i^{th} coordinates of vectors $\boldsymbol{a}$ and $\boldsymbol{b}$ is defined as:

$$D_i(\boldsymbol{a},\boldsymbol{b}) = w_i \frac{|log(\boldsymbol{a}_i+1) - log(\boldsymbol{b}_i+1)|}{log(max\{\boldsymbol{a}_i,\boldsymbol{b}_i\}+2)},$$

where w_i is the weight of orbit i that accounts for dependencies between the orbits [29]. Then, GDVS between vectors $\boldsymbol{a}$ and $\boldsymbol{b}$ is defined as:

$$GDVS(\boldsymbol{a}, \boldsymbol{b}) = 1 - \frac{\sum_{i=1}^{11} D_i(\boldsymbol{a}, \boldsymbol{b})}{\sum_{i=1}^{11} w_i}.$$

GDVS is the similarity measure in (0,1] range, such that the similarity equal to 1 means that the two GDV vectors are identical, and thus, that the gene has the same local topology in both networks. We use GDVS to identify the genes whose topology changed between two condition-specific iCell networks, which we termed "perturbed" (i.e., whose GDVSs were close to 0), as well as the genes whose local topology did not change, which we termed "stable" (i.e., whose GDVSs were close to 1). These comparisons were made between different time points for the same cell line, as well as between different cell lines for the same time point.

Clustering

For each cell line and each time point, we performed clustering of the Graphlet Degree Vectors (GDVs). Prior to clustering, the features were weighted by using previously defined weights [29] and then log-transformed. In addition, both the NMTF and GCM matrices were scaled to a 0 mean and unit variance. For each input matrix, we first computed the Hopkins statistics to estimate cluster tendency. Then, to identify the numbers of clusters, we estimate the cluster validity of potential solutions reporting between 50 and 150 clusters, using 21 different metrics. We rank all clustering solutions for each metric. Then, for each input matrix, the number of clusters is selected based on the solution associated with the minimal median rank across all 21 metrics. We then performed hierarchical and k-medoids clustering using a Pearson correlation-based distance and validated the obtained repartitions using silhouette width and the between/within average distance ratio. All scripts are available on the associated Git repository.

Network representation of gene predictions

Protein-Protein interactions between TP53, a known regulator of senescence, and genes associated with "EMT" and "INTERFERON GAMMA RESPONSE" which have been linked with senescence escape were extracted from BioGRID (v 4.4.217). A network representation was created by using Cytoscape (v 3.9.1). The representation was further refined by using stringApp (v 2.0.0) and clusterMaker2 app (v 2.3.2) and modified by using Inkscape (v 1.2.1).

DATA AVAILABILITY

Raw data together with processed files were deposited to: PRJEB59603. Code to reproduce the results in this manuscript are available via GitLab repository (https://gitlab.com/Ahmed7emdan/integrative-multi-omics-analysis).

REFERENCES

1. Hayflick L, Moorhead PS. The serial cultivation of human diploid cell strains. Exp Cell Res. 1961;25:585–21.
2. Kumari R, Jat P. Mechanisms of cellular senescence: cell cycle arrest and senescence associated secretory phenotype. Front Cell Dev Biol. 2021;9:645593.
3. Ou HL, Hoffmann R, González-López C, Doherty GJ, Korkola JE, Muñoz-Espin D. Cellular senescence in cancer: From mechanisms to detection. Mol Oncol. 2021;15:2634–71.
4. Liao C, Xiao Y, Liu L. The dynamic process and its dual effects on tumors of therapy-induced senescence. Cancer Manag Res. 2020;12:13553.
5. Wang L, Lankhorst L, Bernards R. Exploiting senescence for the treatment of cancer. Nature Rev Cancer. 2022;22:340–55.
6. Campisi J. Aging, cellular senescence, and cancer. Annu Rev Physiol. 2013;75:685.
7. Campisi J, Robert L. Cell senescence: role in aging and age-related diseases. Aging. 2014;39:45–61.
8. Zhu H, Blake S, Kusuma FK, Pearson RB, Kang J, Chan KT. Oncogene-induced senescence: From biology to therapy. Mech Ageing Dev. 2020;187:111229.
9. Prieur A, Peeper DS. Cellular senescence in vivo: a barrier to tumorigenesis. Curr Opin Cell Biol. 2008;20:150–5.
10. Roger L, Tomas F, Gire V. Mechanisms and regulation of cellular senescence. Int J Mol Sci. 2021;22:13173.
11. Caksa S, Baqai U, Aplin AE. The future of targeted kinase inhibitors in melanoma. Pharmacol Therap. 2022;239:108200.
12. Naeli P, Winter T, Hackett AP, Alboushi L, Jafarnejad SM. The intricate balance between microRNA-induced mRNA decay and translational repression. FEBS J. 2022;290:2508–2524.
13. Bartel DP. Metazoan micrornas. Cell. 2018;173:20–51.
14. Kozar I, Philippidou D, Margue C, Gay LA, Renne R, Kreis S. Cross-linking ligation and sequencing of hybrids (qCLASH) reveals an unpredicted miRNA Targetome in melanoma cells. Cancers. 2021;13:1096.
15. Malod-Dognin N, Petschnigg J, Windels SF, Povh J, Hemingway H, Ketteler R, et al. Towards a data-integrated cell. Nature Commun. 2019;10:805.
16. Klein ME, Kovatcheva M, Davis LE, Tap WD, Koff A. CDK4/6 inhibitors: the mechanism of action may not be as simple as once thought. Cancer Cell. 2018;34:9–20.
17. Goel S, Bergholz JS, Zhao JJ. Targeting CDK4 and CDK6 in cancer. Nature Rev Cancer. 2022;22:356.
18. Jochems F, Thijssen B, De Conti G, Jansen R, Pogacar Z, Groot K, et al. The Cancer SENESCopedia: A delineation of cancer cell senescence. Cell Rep. 2021;36:109441.
19. Laberge RM, Awad P, Campisi J, Desprez PY. Epithelial-mesenchymal transition induced by senescent fibroblasts. Cancer Microenviron. 2012;5:39–44.
20. Tato-Costa J, Casimiro S, Pacheco T, Pires R, Fernandes A, Alho I, et al. Therapy-induced cellular senescence induces epithelial-to-mesenchymal transition and increases invasiveness in rectal cancer. Clinical Colorectal Cancer. 2016;15:170–8.
21. Morales-Valencia J, Lau L, Martí-Nin T, Ozerdem U, David G. Therapy-induced senescence promotes breast cancer cells plasticity by inducing Lipocalin-2 expression. Oncogene. 2022;41:4361–4370.
22. Rosell R, Karachaliou N, Morales-Espinosa D, Costa C, Molina MA, Sansano I, et al. Adaptive resistance to targeted therapies in cancer. Transl Lung Cancer Res. 2013;2:152.
23. Tubita A, Lombardi Z, Tusa I, Lazzeretti A, Sgrignani G, Papini D, et al. Inhibition of ERK5 elicits cellular senescence in melanoma via the cyclin-dependent kinase inhibitor p21. Cancer Res. 2022;82:447–57.
24. Fields CJ, Li L, Hiers NM, Li T, Sheng P, Huda T, et al. Sequencing of Argonaute-bound microRNA/mRNA hybrids reveals regulation of the unfolded protein response by microRNA-320a. PLoS Genet. 2021;17:e1009934.
25. Margue C, Philippidou D, Reinsbach SE, Schmitt M, Behrmann I, Kreis S. New target genes of MITF-induced microRNA-211 contribute to melanoma cell invasion. PloS One. 2013;8:e73473.
26. Xenos A, Malod-Dognin N, Zambrana C, Pržulj N. Integrated Data Analysis Uncovers New COVID-19 Related Genes and Potential Drug Re-Purposing Candidates. Int J Mol Sci. 2023;24:1431.
27. Oughtred R, Stark C, Breitkreutz BJ, Rust J, Boucher L, Chang C, et al. The BioGRID interaction database: 2019 update. Nucleic Acids Res. 2019;47:D529–41.
28. Yaveroğlu ÖN, Malod-Dognin N, Davis D, Levnajic Z, Janjic V, Karapandza R, et al. Revealing the hidden language of complex networks. Sci Rep. 2014;4:4547.
29. Milenković T, Pržulj N. Uncovering biological network function via graphlet degree signatures. Cancer Inform. 2008;6:CIN-S680.
30. Liberzon A, Birger C, Thorvaldsdóttir H, Ghandi M, Mesirov JP, Tamayo P. The molecular signatures database hallmark gene set collection. Cell Syst. 2015;1:417–25.
31. Chan M, Yuan H, Soifer I, Maile TM, Wang RY, Ireland A, et al. Novel insights from a multiomics dissection of the Hayflick limit. Elife. 2022;11:e70283.
32. Lee YH, Park JY, Lee H, Song ES, Kuk MU, Joo J, et al. Targeting mitochondrial metabolism as a strategy to treat senescence. Cells. 2021;10:3003.
33. Goel S, DeCristo MJ, Watt AC, BrinJones H, Sceneay J, Li BB, et al. CDK4/6 inhibition triggers anti-tumour immunity. Nature. 2017;548:471.
34. Chiappinelli KB, Strissel PL, Desrichard A, Li H, Henke C, Akman B, et al. Inhibiting DNA methylation causes an interferon response in cancer via dsRNA including endogenous retroviruses. Cell. 2015;162:974–86.
35. Roulois D, Yau HL, Singhania R, Wang Y, Danesh A, Shen SY, et al. DNA-demethylating agents target colorectal cancer cells by inducing viral mimicry by endogenous transcripts. Cell. 2015;162:961–73.
36. Chen R, Ishak CA, De Carvalho DD. Endogenous Retroelements and the Viral Mimicry Response in Cancer Therapy and Cellular Homeostasis. Cancer Discov. 2021;11:2707–25.
37. Kermi C, Lau L, Asadi Shahmirzadi A, Classon M. Disrupting mechanisms that regulate genomic repeat elements to combat cancer and drug resistance. Front Cell Dev Biol. 2022;10:838.
38. Brägelmann J, Lorenz C, Borchmann S, Nishii K, Wegner J, Meder L, et al. MAPK-pathway inhibition mediates inflammatory reprogramming and sensitizes tumors to targeted activation of innate immunity sensor RIG-I. Nature Commun. 2021;12:1–15.
39. Huang AC, Zappasodi R. A decade of checkpoint blockade immunotherapy in melanoma: understanding the molecular basis for immune sensitivity and resistance. Nature Immunol. 2022;23:660–70.
40. Takasugi M, Yoshida Y, Hara E, Ohtani N. The role of cellular senescence and SASP in tumour microenvironment. FEBS J. 2023;290:1348–61.

41. Hu X, Zhang H. Doxorubicin-induced cancer cell senescence shows a time delay effect and is inhibited by epithelial-mesenchymal transition (EMT). Med Sci Monit. 2019;25:3617.
42. Faheem MM, Seligson ND, Ahmad SM, Rasool RU, Gandhi SG, Bhagat M, et al. Convergence of therapy-induced senescence (TIS) and EMT in multistep carcinogenesis: Current opinions and emerging perspectives. Cell Death Discov. 2020;6:51.
43. De Blander H, Morel AP, Senaratne AP, Ouzounova M, Puisieux A. Cellular plasticity: a route to senescence exit and tumorigenesis. Cancers. 2021;13:4561.
44. Imai D, Yoshizumi T, Okano S, Itoh S, Ikegami T, Harada N, et al. IFN-γ promotes epithelial-mesenchymal transition and the expression of PD-L1 in pancreatic cancer. J Surg Res. 2019;240:115–23.
45. Lo UG, Bao J, Cen J, Yeh HC, Luo J, Tan W, et al. Interferon-induced IFIT5 promotes epithelial-to-mesenchymal transition leading to renal cancer invasion. Am J Clin Exp Urol. 2019;7:31.
46. Lee M, Kim DW, Khalmuratova R, Shin SH, Kim YM, Han DH, et al. The IFN-γ–p38, ERK kinase axis exacerbates neutrophilic chronic rhinosinusitis by inducing the epithelial-to-mesenchymal transition. Mucosal Immunol. 2019;12:601–11.
47. Saul D, Kosinsky RL, Atkinson EJ, Doolittle ML, Zhang X, LeBrasseur NK, et al. A new gene set identifies senescent cells and predicts senescence-associated pathways across tissues. Nature Commun. 2022;13:4827.
48. Fridman AL, Tainsky MA. Critical pathways in cellular senescence and immortalization revealed by gene expression profiling. Oncogene. 2008;27:5975–87.
49. Katlinskaya YV, Katlinski KV, Yu Q, Ortiz A, Beiting DP, Brice A, et al. Suppression of type I interferon signaling overcomes oncogene-induced senescence and mediates melanoma development and progression. Cell Rep. 2016;15:171–80.
50. Mullani N, Porozhan Y, Mangelinck A, Rachez C, Costallat M, Batsche E, et al. Reduced RNA turnover as a driver of cellular senescence. Life Sci Alliance. 2021;4:3.
51. Harries LW. Dysregulated RNA processing and metabolism: a new hallmark of ageing and provocation for cellular senescence. FEBS J. 2023;290:1221–34.
52. Asimi V, Sampath Kumar A, Niskanen H, Riemenschneider C, Hetzel S, Naderi J, et al. Hijacking of transcriptional condensates by endogenous retroviruses. Nature Genet. 2022;54:1238–47.
53. Liu X, Liu Z, Wu Z, Ren J, Fan Y, Sun L, et al. Resurrection of endogenous retroviruses during aging reinforces senescence. Cell. 2023;186:287–304.
54. Chen CH, Hsia TC, Yeh MH, Chen TW, Chen YJ, Chen JT, et al. MEK inhibitors induce Akt activation and drug resistance by suppressing negative feedback ERK-mediated HER 2 phosphorylation at Thr701. Mol Oncol. 2017;11:1273–87.
55. Ortega-Muelas M, Roche O, Fernández-Aroca DM, Encinar JA, Albandea-Rodríguez D, Arconada-Luque E, et al. ERK5 signalling pathway is a novel target of sorafenib: Implication in EGF biology. J Cell Mol Med. 2021;25:10591–603.
56. Zhang J, Pearson AJ, Sabherwal N, Telfer BA, Ali N, Kan K, et al. Inhibiting ERK5 overcomes breast cancer resistance to anti-HER2 therapy by targeting the G1–S cell-cycle transition. Cancer Res Commun. 2022;2:131–45.
57. Benito-Jardón L, Díaz-Martínez M, Arellano-Sánchez N, Vaquero-Morales P, Esparís-Ogando A, Teixidó J. Resistance to MAPK Inhibitors in Melanoma Involves Activation of the IGF1R–MEK5–Erk5 Pathway. Cancer Res. 2019;79:2244–56.
58. Anerillas C, Herman AB, Munk R, Garrido A, Lam KWG, Payea MJ, et al. A BDNF-TrkB autocrine loop enhances senescent cell viability. Nature Commun. 2022;13:6228.
59. Adam C, Fusi L, Weiss N, Goller SG, Meder K, Frings VG, et al. Efficient suppression of NRAS-driven melanoma by co-inhibition of ERK1/2 and ERK5 MAPK pathways. J Investig Dermatol. 2020;140:2455–65.
60. Randic T, Kozar I, Margue C, Utikal J, Kreis S. NRAS mutant melanoma: Towards better therapies. Cancer Treat Rev. 2021;99:102238.
61. Cook SJ, Lochhead PA. ERK5 Signalling and Resistance to ERK1/2 Pathway Therapeutics: The Path Less Travelled?. Front Cell Dev Biol. 2022;10:839997.
62. Jiang W, Cai F, Xu H, Lu Y, Chen J, Liu J, et al. Extracellular signal regulated kinase 5 promotes cell migration, invasion and lung metastasis in a FAK-dependent manner. Protein Cell. 2020;11:825–45.
63. Ortiz MA, Mikhailova T, Li X, Porter BA, Bah A, Kotula L. Src family kinases, adaptor proteins and the actin cytoskeleton in epithelial-to-mesenchymal transition. Cell Commun Signal. 2021;19:1–19.
64. Saleiro D, Blyth GT, Kosciuczuk EM, Ozark PA, Majchrzak-Kita B, Arslan AD, et al. IFN-γ–inducible antiviral responses require ULK1-mediated activation of MLK3 and ERK5. Sci Signal. 2018;11:eaap9921.
65. Keller A, Gröger L, Tschernig T, Solomon J, Laham O, Schaum N, et al. miRNATissueAtlas2: an update to the human miRNA tissue atlas. Nucleic Acids Res. 2022;50:D211–21.
66. Lee B, Sahoo A, Sawada J, Marchica J, Sahoo S, Layng FI, et al. MicroRNA-211 modulates the DUSP6-ERK5 signaling axis to promote BRAFV600E-driven melanoma growth in vivo and BRAF/MEK inhibitor resistance. J Investig Dermatol. 2021;141:385–94.
67. Santiappillai NT, Abuhammad S, Slater A, Kirby L, McArthur GA, Sheppard KE, et al. CDK4/6 inhibition reprograms mitochondrial metabolism in BRAFV600 melanoma via a p53 dependent pathway. Cancers. 2021;13:524.
68. Teh JLF, Purwin T J, Han A, Chua V, Patel P, Baqai U. et al. Metabolic Adaptations to MEK and CDK4/6 Cotargeting in Uveal MelanomaMetabolic Adaptations to Inhibitors in Ocular Melanoma. Mol Cancer Ther. 2020;19.8:1719–26.
69. Lee JS, Lee H, Jang H, Woo SM, Park JB, Lee SH, et al. Targeting oxidative phosphorylation reverses drug resistance in cancer cells by blocking autophagy recycling. Cells. 2020;9:2013.
70. Corazao-Rozas P, Guerreschi P, André F, Gabert PE, Lancel S, Dekiouk S, et al. Mitochondrial oxidative phosphorylation controls cancer cell's life and death decisions upon exposure to MAPK inhibitors. Oncotarget. 2016;7:39473.
71. Carpintero-Fernández P, Borghesan M, Eleftheriadou O, Pan-Castillo B, Fafián-Labora JA, Mitchell TP, et al. Genome wide CRISPR/Cas9 screen identifies the coagulation factor IX (F9) as a regulator of senescence. Cell Death Dis. 2022;13:163.
72. Martínez-Zamudio RI, Stefa A, Freitas JANLF, Vasilopoulos T, Simpson M, Doré G, et al. Escape from oncogene-induced senescence is controlled by POU2F2 and memorized by chromatin scars. Cell Genom. 2023;3:4.
73. Lee WJ, Škalamera D, Dahmer-Heath M, Shakhbazov K, Ranall MV, Fox C, et al. Genome-wide overexpression screen identifies genes able to bypass p16-mediated senescence in melanoma. SLAS DISCOV. 2017;22:298–308.
74. Nagaraj K. Long-Term IGF1 Stimulation Leads to Cellular Senescence via Functional Interaction with the Thioredoxin-Interacting Protein, TXNIP. Cells. 2022;11.20:3260
75. Ma F, Lei YY, Ding MG, Luo LH, Xie YC, Liu XL. LncRNA NEAT1 interacted with DNMT1 to regulate malignant phenotype of cancer cell and cytotoxic T cell infiltration via epigenetic inhibition of p53, cGAS, and STING in lung cancer. Front Genet. 2020;11:250.
76. Liang Y, Hu J, Li J, Liu Y, Yu J, Zhuang X, et al. Epigenetic activation of TWIST1 by MTDH promotes cancer stem–like cell traits in breast cancer. Cancer Res. 2015;75:3672–80.
77. Li Z, Hu J, Guo J, Fan L, Wang S, Dou N. et al. SSeCKS/Gravin/AKAP12 inhibits pkcζ-mediated reduction of ERK5 transactivation to prevent endotoxin-induced vascular dysfunction. Cardiovasc Toxicol. 2019;19:372–81.
78. Rambow F, Rogiers A, Marin-Bejar O, Aibar S, Femel J, Dewaele M, et al. Toward minimal residual disease-directed therapy in melanoma. Cell. 2018;174:843–55.
79. Marin-Bejar O, Rogiers A, Dewaele M, Femel J, Karras P, Pozniak J, et al. Evolutionary predictability of genetic versus nongenetic resistance to anticancer drugs in melanoma. Cancer Cell. 2021;39:1135–49.
80. Mölder F, Jablonski KP, Letcher B, Hall MB, Tomkins-Tinch CH, Sochat V, et al. Sustainable data analysis with Snakemake. F1000Research. 2021;10:33.
81. Xiao Y, Hsiao TH, Suresh U, Chen HIH, Wu X, Wolf SE, et al. A novel significance score for gene selection and ranking. Bioinformatics. 2014;30:801–7.
82. Metz KS, Deoudes EM, Berginski ME, Jimenez-Ruiz I, Aksoy BA, Hammerbacher J. Coral: clear and customizable visualization of human kinome data. Cell Syst. 2018;7:347–50.
83. Glaab E, Baudot A, Krasnogor N, Schneider R, Valencia A. EnrichNet: network-based gene set enrichment analysis. Bioinformatics. 2012;28:i451–7.
84. Travis AJ, Moody J, Helwak A, Tollervey D, Kudla G. Hyb: a bioinformatics pipeline for the analysis of CLASH (crosslinking, ligation and sequencing of hybrids) data. Methods. 2014;65:263–73.
85. Gligorijević V, Malod-Dognin N, Pržulj N. Patient-specific data fusion for cancer stratification and personalised treatment. In Biocomputing 2016: Proceedings of the Pacific Symposium. World Scientific Publishing Company; Hackensack, NJ, USA. 2016. pp. 321–332.
86. Ding C, Li T, Peng W, Park H. Orthogonal nonnegative matrix t-factorizations for clustering. In Proceedings of the 12th ACM SIGKDD international conference on Knowledge discovery and data mining. Association for Computing Machinery. New York, NY, United States. 2006. pp. 126–135.
87. Hart T, Komori HK, LaMere S, Podshivalova K, Salomon DR. Finding the active genes in deep RNA-seq gene expression studies. BMC Genom. 2013;14:1–7.
88. Pržulj N. Analyzing Network Data in Biology and Medicine: An Interdisciplinary Textbook for Biological, Medical and Computational Scientists. Cambridge University Press; Cambridge, England. 2019.
89. Qiao H. New SVD based initialization strategy for non-negative matrix factorization. Pattern Recog Lett. 2015;63:71–77.
90. Pržulj N, Corneil DG, Jurisica I. Modeling interactome: scale-free or geometric? Bioinformatics. 2004;20:3508–15.

ACKNOWLEDGEMENTS

The authors want to thank L. Sinkonnen for his suggestions regarding the qCLASH method and its extended applications, J.P. Wroblewska for her feedback and her insights regarding the biology of amelanotic melanoma, A. Ginolhac for his help in the analysis of our RNA-seq data and his tips regarding R language. Several in silico experiments presented in this paper were carried out using the HPC facilities of the University of Luxembourg, Varrette et al. 2022, https://hpc.uni.lu.

AUTHOR CONTRIBUTIONS

SK conceived the study. SK, FT, DP, MT, TR and VG contributed to the experimental design. VG, FT, and DP acquired total RNA-seq and small RNA-seq data and AM, AG and VG processed, analysed and interpreted the data. TR, DP and CM acquired PamGene data, JL processed the data and performed Upstream Kinase Analysis. MO and AH performed network-based pathway enrichment and created xml models to overlay the inferred kinase activities; VG and CA interpreted the results. IK and HH performed qCLASH method, IK processed the data and AG, VG and HH analysed the hybrids and constructed the miRNA network. HH performed qPCR validations. MB processed the scRNA-seq data. NP, NMD, GC and KM conceived the data integration. KM, GC, and VG performed it and analysed the results under the supervision of NMD and NP. LT performed the gene clustering; AB, MB, and VG analyzed the gene clusters. VG, HH, AH, CA, AB and FT contributed to the figures. VG and SK drafted the manuscript with input from all authors. NP, NMD and MO reviewed the manuscript. All authors read and approved the final manuscript.

FUNDING

VG is supported by the Luxembourg National Research Fond (FNR) PRIDE DTU CanBIO [grant reference: 21/16763386]. TR is supported by the FNR PRIDE DTU CriTiCS [grant reference: 10907093]. Project-related work performed by VG, HH, CM, DP, MTN, MB, AG, FT and SK were also supported by the University of Luxembourg and the Fondation Cancer, Luxembourg (grant "SecMelPro"). KM and NP are supported by funding from the European Union's EU Framework Programme for Research and Innovation Horizon 2020, Innovative Training Networks (MSCA-ITN-2019), funded under EXCELLENT SCIENCE - Marie Skłodowska-Curie Actions, Grant Agreement No 860895. KM, NMD, GC and NP are supported by funding from the European Research Council (ERC) Consolidator Grant 770827. NP is also supported by funding from the Spanish State Research Agency AEI 10.13039/501100011033 grant number PID2019-105500GB-I00.

COMPETING INTERESTS

The authors declare no competing interests.

ADDITIONAL INFORMATION

Supplementary information The online version contains supplementary material available at https://doi.org/10.1038/s41417-023-00640-z.

Correspondence and requests for materials should be addressed to Stephanie Kreis.

Reprints and permission information is available at http://www.nature.com/reprints

Publisher's note Springer Nature remains neutral with regard to jurisdictional claims in published maps and institutional affiliations.

5. Prestwick Chemical Library ® (PCL)

Chemical name	CAS number	Therapeutic class	Therapeutic effect	FDA approved
(-) -Levobunolol hydrochloride	27912-14-7	Ophthalmology	Antiglaucoma	Yes
(-)-Emtricitabine	143491-57-0	Infectiology	Antiviral	Yes
(-)-Eseroline fumarate salt	104015-29-4	Central Nervous System	Analgesic	
(-)-MK 801 hydrogen maleate	77086-19-2	Central Nervous System	Anticonvulsant	
(+) -Levobunolol hydrochloride	47141-41-3	Ophthalmology	Antiglaucoma	Yes
(+)-Isoproterenol (+)-bitartrate salt	14638-70-1	Respiratory	Antiasthmatic	Yes
(+,-)-Octopamine hydrochloride	770-05-8	Cardiovascular		
(+,-)-Synephrine	94-07-5	Cardiovascular	Vasoconstrictor	
(R) -Naproxen sodium salt	23979-41-1	Metabolism	Anti-inflammatory	Yes
(R)-(+)-Atenolol	56715-13-0	Cardiovascular	Antianginal	Yes
(R)-Duloxetine hydrochloride	116539-60-7			Yes
(R)-Propranolol hydrochloride	13071-11-9	Cardiovascular	Antianginal	Yes
(S)-(-)-Atenolol	93379-54-5	Cardiovascular	Antianginal	Yes
(S)-(-)-Cycloserine	339-72-0	Infectiology	Antibacterial	Yes
(S)-propranolol hydrochloride	4199-10-4	Cardiovascular	Antianginal	Yes
1,8-Dihydroxyanthraquinone	117-10-2	Gastroenterology	Laxative	
2-Aminobenzenesulfonamide	3306-62-5	Metabolism	Diuretic	
3-alpha-Hydroxy-5-beta-androstan-17-one	53-42-9	Endocrinology		
5-fluorouracil	51-21-8	Oncology	Antineoplastic	Yes
6-Furfurylaminopurine	525-79-1	Dermatology		
Abacavir Sulfate	188062-50-2	Infectiology	Antiviral	Yes
Acamprosate calcium	77337-73-6	Central Nervous System		Yes
Acarbose	56180-94-0	Endocrinology	Antidiabetic	Yes
Acebutolol hydrochloride	34381-68-5	Cardiovascular	Antianginal	Yes
Aceclidine Hydrochloride	6109-70-2	Ophthalmology	Antiglaucoma	
Aceclofenac	89796-99-6	Central Nervous System	Analgesic	
Acefylline	652-37-9	Central Nervous System	CNS Stimulant	
Acemetacin	53164-05-9	Metabolism	Anti-inflammatory	

Acenocoumarol	152-72-7	Hematology	Anticoagulant	
Acetaminophen	103-90-2	Central Nervous System	Analgesic	Yes
Acetazolamide	59-66-5	Metabolism	Anticonvulsant	Yes
Acetohexamide	968-81-0	Endocrinology	Antidiabetic	Yes
Acetopromazine maleate salt	3598-37-6	Central Nervous System	Antiemetic	
Acetylcysteine	616-91-1	Metabolism	Mucolytic	Yes
Acetylsalicylic acid	50-78-2	Central Nervous System	Analgesic	Yes
Acetylsalicylsalicylic acid	530-75-6	Central Nervous System	Analgesic	
Acipimox	51037-30-0	Metabolism	Antilipemic	
Acitretin	55079-83-9	Dermatology	Antipsoriatic	Yes
Actarit	18699-02-0	Immunology	Anti-inflammatory	
Acyclovir	59277-89-3	Metabolism	Antiviral	Yes
Adamantamine fumarate	80789-67-9	Infectiology	Antiviral	Yes
Adapalene	106685-40-9	Dermatology	Keratolytic	Yes
Adenosine 5'-monophosphate monohydrate	18422-05-4	Cardiovascular	Antiarrhythmic	
Adiphenine hydrochloride	50-42-0	Neuromuscular	Antispastic	
Adrenosterone	382-45-6	Endocrinology		
Albendazole	54965-21-8	Metabolism	Antihelmintic	Yes
Alclometasone dipropionate	66734-13-2	Metabolism	Anti-inflammatory	Yes
Alcuronium chloride	15180-03-7	Neuromuscular	Muscle relaxant	
Alendronate sodium	121268-17-5	Metabolism	Antiosteoporetic	Yes
Alexidine dihydrochloride	22573-93-9	Infectiology	Antibacterial	
Alfacalcidol	41294-56-8	Metabolism	Antiosteoporetic	Yes
Alfadolone acetate	23930-37-2	Central Nervous System	Anesthetic	
Alfaxalone	23930-19-0	Central Nervous System	Anesthetic	
Alfuzosin hydrochloride	81403-68-1	Cardiovascular	Vasodilator	Yes
Algestone acetophenide	24356-94-3	Endocrinology	Contraceptive	
Alizapride hydrochloride	59338-87-3	Central Nervous System	Antiemetic	
Allantoin	97-59-6	Dermatology	Antipsoriatic	

Allopurinol	315-30-0	Metabolism		Yes
Alosetron hydrochloride	122852-69-1	Central Nervous System	Antidiarrheal	Yes
Alprenolol hydrochloride	13707-88-5	Cardiovascular	Antianginal	
Alprostadil	745-65-3	Cardiovascular	Erectile dysfunction treatment	Yes
Althiazide	5588-16-9	Metabolism	Antihypertensive	
Altrenogest	850-52-2	Endocrinology	Progestogen	
Altretamine	645-05-6	Oncology	Antineoplastic	Yes
Alverine citrate salt	5560-59-8	Neuromuscular	Antispastic	
Ambrisentan	177036-94-1	Cardiovascular	Antihypertensive	Yes
Ambroxol hydrochloride	23828-92-4	Respiratory	Expectorant	
Amcinonide	51022-69-6	Metabolism	Anti-inflammatory	Yes
Amethopterin (R,S)	60388-53-6	Immunology	Anti-inflammatory	
Amfepramone hydrochloride	90-84-6	Central Nervous System		
Amidopyrine	58-15-1	Central Nervous System	Analgesic	
Amifostine	20537-88-6	Diagnostic		Yes
Amikacin hydrate	37517-28-5	Infectiology	Antibacterial	Yes
Amiloride hydrochloride dihydrate	17440-83-4	Metabolism	Antihypertensive	Yes
Aminacrine	90-45-9	Infectiology	Antiseptic	
Aminocaproic acid	60-32-2	Allergology	Antifibrinolytic	Yes
Aminohippuric acid	61-78-9	Diagnostic		
Aminophylline	317-34-0	Cardiovascular	Bronchodilator	Yes
Aminopurine, 6-benzyl	1214-39-7	Endocrinology		
Amiodarone hydrochloride	19774-82-4	Cardiovascular	Antianginal	Yes
Amiprilose hydrochloride	60414-06-4	Immunology	Immunomodulator	
Amisulpride	71675-85-9	Central Nervous System	Antipsychotic	
Amitryptiline hydrochloride	549-18-8	Central Nervous System	Antidepressant	Yes
Amlexanox	68302-57-8	Allergology	Anti-inflammatory	Yes
Amlodipine	88150-42-9	Cardiovascular	Antihypertensive	Yes
Amodiaquin dihydrochloride dihydrate	6398-98-7	Infectiology	Anti-inflammatory	Yes
Amorolfine hydrochloride	78613-38-4	Infectiology	Antifungal	Yes

Amoxapine	14028-44-5	Central Nervous System	Antidepressant	Yes
Amoxicillin	26787-78-0	Metabolism	Antibacterial	Yes
Amphotericin B	1397-89-3	Infectiology	Antibacterial	Yes
Ampicillin trihydrate	7177-48-2	Infectiology	Antibacterial	Yes
Ampiroxicam	99464-64-9	Immunology	Anti-inflammatory	
Amprolium hydrochloride	137-88-2	Infectiology	Anticoccidial	
Ampyrone	83-07-8	Central Nervous System	Analgesic	
Amrinone	60719-84-8	Cardiovascular		Yes
Amyleine hydrochloride	532-59-2	Neuromuscular	Local anesthetic	
Anagrelide	68475-42-3	Hematology	Thrombolytic	Yes
Anastrozole	120511-73-1	Oncology	Antineoplastic	Yes
Androsterone	53-41-8	Endocrinology	Anabolic	
Anethole-trithione	532-11-6	Metabolism	Choleretic	
Aniracetam	72432-10-1	Central Nervous System	Anti-Alzheimer	
Antazoline hydrochloride	2508-72-7	Allergology	Antihistaminic	Yes
Anthralin	1143-38-0	Dermatology	Antipsoriatic	
Antimycin A	1397-94-0	Infectiology	Antibacterial	
Antipyrine	60-80-0	Central Nervous System	Analgesic	
Antipyrine, 4-hydroxy	1672-63-5	Metabolism		
Apramycin	37321-09-8	Metabolism	Antibacterial	
Aprepitant	170729-80-3	Metabolism	Antiemetic	Yes
Arbutin	497-76-7	Metabolism	Antibacterial	
Argatroban	74863-84-6	Hematology	Anticoagulant	Yes
Aripiprazole	129722-12-9	Central Nervous System	Antipsychotic	Yes
Artemisinin	63968-64-9	Infectiology	Antimalarial	
Articaine hydrochloride	23964-57-0	Central Nervous System	Anesthetic	Yes
Ascorbic acid	50-81-7	Metabolism	Anti-oxidant	Yes
Asenapine maleate	85650-56-2	Central Nervous System	Antipsychotic	Yes
Astemizole	68844-77-9	Allergology	Antihistaminic	
Atorvastatin	134523-00-5	Metabolism		Yes

Atovaquone	95233-18-4	Infectiology	Antimalarial	Yes
Atracurium besylate	64228-81-5	Neuromuscular	Curarizing	Yes
Atropine sulfate monohydrate	5908-99-6	Ophthalmology	Antispastic	Yes
Auranofin	34031-32-8	Metabolism	Analgesic	Yes
Avermectin B1	71751-41-2	Infectiology	Antihelmintic	
Avobenzone	70356-09-1	Dermatology	Cytoprotectant	Yes
Azacyclonol	115-46-8	Central Nervous System	Antipsychotic	
Azacytidine-5	320-67-2	Oncology	Antineoplastic	
Azaguanine-8	134-58-7	Oncology	Antineoplastic	
Azaperone	1649-18-9	Central Nervous System	Antipsychotic	
Azapropazone	13539-59-8	Central Nervous System	Analgesic	
Azatadine maleate	3978-86-7	Allergology	Antihistaminic	Yes
Azathioprine	446-86-6	Oncology	Antineoplastic	Yes
Azelastine hydrochloride	79307-93-0	Immunology	Antihistaminic	Yes
Azithromycin	83905-01-5	Infectiology	Antibacterial	Yes
Azlocillin sodium salt	37091-65-9	Metabolism	Antibacterial	Yes
Aztreonam	78110-38-0	Infectiology	Antibacterial	Yes
Bacampicillin hydrochloride	37661-08-8	Infectiology	Antibacterial	Yes
Bacitracin	1405-87-4	Metabolism	Antibacterial	Yes
Baclofen (R,S)	1134-47-0	Central Nervous System	Antispastic	Yes
Balsalazide Sodium	80573-04-2	Gastroenterology	Anti-inflammatory	Yes
Bambuterol hydrochloride	81732-46-9	Neuromuscular	Bronchodilator	Yes
Beclomethasone dipropionate	5534-09-8	Metabolism	Anti-inflammatory	Yes
Bemegride	64-65-3	Central Nervous System	CNS stimulant	
Benazepril hydrochloride	86541-74-4	Cardiovascular	Antihypertensive	Yes
Bendroflumethiazide	73-48-3	Cardiovascular	Antihypertensive	Yes
Benfluorex	23602-78-0	Central Nervous System	Anorectic	
Benfotiamine	22457-89-2	Metabolism		
Benidipine hydrochloride	91599-74-5	Cardiovascular	Antihypertensive	
Benoxinate hydrochloride	5987-82-6	Neuromuscular	Local anesthetic	Yes

Benperidol	2062-84-2	Central Nervous System	Antipsychotic	
Benserazide hydrochloride	14919-77-8	Central Nervous System	Antiparkinsonian	
Benzamil hydrochloride	2898-76-2	Metabolism	Antihypertensive	
Benzathine benzylpenicillin	5928-84-7	Metabolism	Antibacterial	Yes
Benzbromarone	3562-84-3	Cardiovascular	Antianginal	
Benzethonium chloride	121-54-0	Infectiology	Antibacterial	
Benzocaine	94-09-7	Neuromuscular	Local anesthetic	
Benzonatate	104-31-4	Neuromuscular	Antitussive	Yes
Benzoxiquine	86-75-9	Infectiology	Antiseptic	
Benzthiazide	91-33-8	Cardiovascular	Antihypertensive	Yes
Benztropine mesylate	132-17-2	Central Nervous System	Antiparkinsonian	Yes
Benzydamine hydrochloride	132-69-4	Central Nervous System	Analgesic	
Benzylpenicillin sodium	69-57-8	Infectiology	Antibacterial	Yes
Bephenium hydroxynaphthoate	3818-50-6	Metabolism		
Bepridil hydrochloride	74764-40-2	Cardiovascular	Antianginal	Yes
Besifloxacin hydrochloride	141388-76-3	Ophthalmology	Antibacterial	Yes
Beta-Escin	11072-93-8	Metabolism	Antineoplastic	
Betahistine mesylate	54856-23-4	Allergology	Vasodilator	
Betamethasone	378-44-9	Endocrinology	Anti-inflammatory	Yes
Betaxolol hydrochloride	63659-19-8	Cardiovascular	Antiglaucoma	Yes
Betazole hydrochloride	138-92-1	Gastroenterology	Diagnostic	Yes
Bethanechol chloride	590-63-6	Metabolism		Yes
Bezafibrate	41859-67-0	Metabolism	Antilipemic	
Bicalutamide	90357-06-5	Endocrinology	Antineoplastic	Yes
Bifonazole	60628-96-8	Infectiology	Antifungal	
Biotin	58-85-5	Metabolism		Yes
Biperiden hydrochloride	1235-82-1	Central Nervous System	Antiparkinsonian	Yes
Bisacodyl	603-50-9	Gastroenterology	Laxative	Yes
Bisoprolol fumarate	104344-23-2	Cardiovascular	Antianginal	Yes
Bosentan	147536-97-8	Cardiovascular	Vasodilator	Yes

Bretylium tosylate	61-75-6	Cardiovascular	Anesthetic	Yes
Brimonidine L-Tartrate	70359-46-5	Ophthalmology	Antiglaucoma	Yes
Brinzolamide	138890-62-7	Metabolism	Antiglaucoma	Yes
Bromhexine hydrochloride	611-75-6	Respiratory	Expectorant	
Bromocryptine mesylate	22260-51-1	Central Nervous System	Antiparkinsonian	Yes
Bromopride	4093-35-0	Central Nervous System	Antiemetic	
Bromperidol	10457-90-6	Central Nervous System	Antipsychotic	
Brompheniramine maleate	980-71-2	Allergology	Antihistaminic	Yes
Bucladesine sodium salt	16980-89-5	Cardiovascular		
Budesonide	51333-22-3	Endocrinology	Anti-inflammatory	Yes
Bufexamac	2438-72-4	Central Nervous System	Analgesic	
Buflomedil hydrochloride	35543-24-9	Cardiovascular	Vasodilator	
Bumetanide	28395-03-1	Metabolism	Diuretic	Yes
Bupivacaine hydrochloride	18010-40-7	Neuromuscular	Local anesthetic	Yes
Bupropion hydrochloride	31677-93-7	Central Nervous System	Antidepressant	Yes
Buspirone hydrochloride	33386-08-2	Central Nervous System		Yes
Busulfan	55-98-1	Oncology	Antineoplastic	Yes
Butacaine	149-16-6	Dermatology	Anesthetic	
Butalbital	77-26-9	Central Nervous System	Hypnotic	Yes
Butamben	94-25-7	Central Nervous System	Anesthetic	
Butenafine Hydrochloride	101828-21-1	Infectiology	Antifungal	Yes
Butoconazole nitrate	32872-77-1	Infectiology	Antibacterial	Yes
Butylparaben	94-26-8	Metabolism	Antifungal	
Butylscopolammonium (n-) bromide	149-64-4	Central Nervous System	Antispastic	
Caffeine	58-08-2	Central Nervous System	CNS Stimulant	Yes
Calcipotriene	112965-21-6	Dermatology	Antipsoriatic	Yes
Camptothecine (S,+)	7689-03-4	Oncology	Antineoplastic	
Camylofine chlorhydrate	54-30-8			
Candesartan	139481-59-7	Cardiovascular	Antihypertensive	Yes
Canrenoic acid potassium salt	2181-04-6	Endocrinology	Antihypertensive	

Canrenone	976-71-6	Endocrinology	Diuretic	
Captopril	62571-86-2	Cardiovascular	Antihypertensive	Yes
Carbachol	51-83-2	Cardiovascular	Antihypertensive	Yes
Carbadox	6804-07-5	Infectiology	Antibacterial	
Carbamazepine	298-46-4	Central Nervous System	Analgesic	Yes
Carbarsone	121-59-5	Infectiology	Antiamebic	
Carbenoxolone disodium salt	7421-40-1	Metabolism	Antiulcer	
Carbetapentane citrate	23142-01-0	Central Nervous System	Antispastic	
Carbidopa	28860-95-9	Central Nervous System	Antiparkinsonian	Yes
Carbimazole	22232-54-8	Metabolism	Antihyperthyroid	
Carbinoxamine maleate salt	3505-38-2	Allergology	Antihistaminic	Yes
Carisoprodol	78-44-4	Central Nervous System	Analgesic	Yes
Carmofur	61422-45-5	Metabolism	Antineoplastic	
Carprofen	53716-49-7	Metabolism	Anti-inflammatory	Yes
Carteolol hydrochloride	51781-21-6	Cardiovascular	Antiglaucoma	Yes
Carvedilol	72956-09-3	Cardiovascular	Antihypertensive	Yes
Catharanthine	2468-21-5	Oncology	Antineoplastic	
Cefaclor hydrate	70356-03-5	Infectiology	Antibacterial	Yes
Cefadroxil	50370-12-2	Infectiology	Antibacterial	Yes
Cefazolin sodium salt	27164-46-1	Metabolism	Antibacterial	Yes
Cefdinir	91832-40-5	Infectiology	Antibacterial	Yes
Cefepime hydrochloride	123171-59-5	Infectiology	Antibacterial	Yes
Cefixime	79350-37-1	Infectiology	Antibacterial	Yes
Cefmetazole sodium salt	56796-39-5	Infectiology	Antibacterial	Yes
Cefoperazone dihydrate	not available	Infectiology	Antibacterial	Yes
Ceforanide	60925-61-3	Infectiology	Antibacterial	Yes
Cefotaxime sodium salt	64485-93-4	Infectiology	Antibacterial	Yes
Cefotetan	69712-56-7	Infectiology	Antibacterial	Yes
Cefotiam hydrochloride	61622-34-2	Infectiology	Antibacterial	Yes
Cefoxitin sodium salt	33564-30-6	Metabolism	Antibacterial	Yes

Cefpiramide	70797-11-4	Infectiology	Antibacterial	Yes
Cefpodoxime proxetil	87239-81-4	Infectiology	Antibacterial	Yes
Cefprozil	121123-17-9	Infectiology	Antibacterial	Yes
Cefsulodin sodium salt	52152-93-9	Metabolism	Antibacterial	
Ceftazidime pentahydrate	78439-06-2	Infectiology	Antibacterial	Yes
Ceftibuten	97519-39-6	Infectiology	Antibacterial	Yes
Cefuroxime axetil	64544-07-6	Infectiology	Antibacterial	Yes
Cefuroxime sodium salt	56238-63-2	Infectiology	Antibacterial	Yes
Celecoxib	169590-42-5	Metabolism	Anti-inflammatory	Yes
Celiprolol hydrochloride	57470-78-7	Cardiovascular	Antianginal	
Cephalosporanic acid, 7-amino	957-68-6	Infectiology	Antibacterial	
Cephalothin sodium salt	58-71-9	Infectiology	Antibacterial	Yes
Cetirizine dihydrochloride	83881-52-1	Allergology	Antihistaminic	Yes
Chenodiol	474-25-9	Gastroenterology	Cholagogue	Yes
Chicago sky blue 6B	2610-05-1	Central Nervous System		
Chloramphenicol	56-75-7	Infectiology	Antibacterial	Yes
Chlorcyclizine hydrochloride	1620-21-9	Allergology	Antiemetic	
Chlorhexidine	55-56-1	Infectiology	Antibacterial	Yes
Chlormadinone acetate	302-22-7	Endocrinology	Antineoplastic	
Chlormezanone	80-77-3	Central Nervous System	Anxiolytic	Yes
Chloropyramine hydrochloride	6170-42-9	Allergology	Antihistaminic	
Chloroquine diphosphate	50-63-5	Metabolism	Anti-inflammatory	Yes
Chlorothiazide	58-94-6	Metabolism	Antihypertensive	Yes
Chlorotrianisene	569-57-3	Endocrinology	Antineoplastic	Yes
Chloroxine	773-76-2	Dermatology		Yes
Chlorpheniramine maleate	113-92-8	Allergology	Antihistaminic	Yes
Chlorphensin carbamate	886-74-8	Central Nervous System	Muscle relaxant	Yes
Chlorpromazine hydrochloride	69-09-0	Cardiovascular	Antiemetic	Yes
Chlorpropamide	94-20-2	Endocrinology	Antidiabetic	Yes
Chlorprothixene hydrochloride	6469-93-8	Central Nervous System	Antiemetic	Yes

Chlortetracycline hydrochloride	64-72-2	Infectiology	Antiamebic	Yes
Chlorthalidone	77-36-1	Metabolism	Antihypertensive	Yes
Chlorzoxazone	95-25-0	Central Nervous System	Anticonvulsant	Yes
Ciclesonide	126544-47-6	Respiratory		Yes
Ciclopirox ethanolamine	41621-49-2	Infectiology	Antibacterial	Yes
Cilnidipine	132203-70-4	Cardiovascular	Antihypertensive	
Cilostazol	73963-72-1	Hematology	Anticoagulant	Yes
Cimetidine	51481-61-9	Gastroenterology	Antiulcer	Yes
Cinnarizine	298-57-7	Allergology	Antihistaminic	
Cinoxacin	28657-80-9	Metabolism	Antibacterial	Yes
Ciprofibrate	52214-84-3	Metabolism	Hypocholesterolemic	
Ciprofloxacin hydrochloride monohydrate	93107-08-5	Infectiology	Antibacterial	Yes
Cisapride	81098-60-4	Gastroenterology	Gastroprokinetic	Yes
Cisatracurium besylate	64228-79-1	Neuromuscular	Muscle relaxant	Yes
Citalopram Hydrobromide	59729-32-7	Central Nervous System	Antidepressant	Yes
Cladribine	4291-63-8	Oncology	Antineoplastic	Yes
Clarithromycin	81103-11-9	Infectiology	Antibacterial	Yes
Clavulanate potassium salt	58001-44-8	Infectiology	Antibacterial	Yes
Clebopride maleate	84370-95-6	Central Nervous System	Antiemetic	
Clemastine fumarate	14976-57-9	Allergology	Antiemetic	Yes
Clemizole hydrochloride	1163-36-6	Allergology	Antibacterial	
Clenbuterol hydrochloride	21898-19-1	Neuromuscular	Antiasthmatic	
Clidinium bromide	3485-62-9	Neuromuscular	Antispastic	Yes
Clinafloxacin	105956-97-6	Infectiology	Antibacterial	
Clindamycin hydrochloride	21462-39-5	Infectiology	Antibacterial	Yes
Clioquinol	130-26-7	Metabolism	Antiamebic	Yes
Clobetasol propionate	25122-46-7	Metabolism	Anti-inflammatory	Yes
Clobutinol hydrochloride	1215-83-4	Central Nervous System	Antitussive	
Clocortolone pivalate	34097-16-0	Endocrinology	Anti-inflammatory	Yes

Clofazimine	2030-63-9	Infectiology	Antibacterial	Yes
Clofibrate	637-07-0	Metabolism	Antilipemic	Yes
Clofibric acid	882-09-7	Metabolism	Antilipemic	Yes
Clofilium tosylate	92953-10-1	Cardiovascular	Antiarrhythmic	
Clomiphene citrate (Z,E)	50-41-9	Endocrinology		Yes
Clomipramine hydrochloride	17321-77-6	Central Nervous System	Antidepressant	Yes
Clonidine hydrochloride	4205-91-8	Cardiovascular	Analgesic	Yes
Clopamide	636-54-4	Metabolism	Antihypertensive	
Cloperastine hydrochloride	14984-68-0	Respiratory	Antitussive	
Clopidogrel	113665-84-2	Cardiovascular	Antiplatelet	Yes
Clorgyline hydrochloride	17780-75-5	Central Nervous System	Antidepressant	
Clorsulon	60200-06-8	Infectiology	Antihelmintic	
Closantel	57808-65-8	Infectiology	Antihelmintic	
Clotrimazole	23593-75-1	Infectiology	Antibacterial	Yes
Cloxacillin sodium salt	642-78-4	Infectiology	Antibacterial	Yes
Clozapine	5786-21-0	Central Nervous System	Antiparkinsonian	Yes
Colchicine	64-86-8	Metabolism	Antigout	Yes
Colistin sulfate	1264-72-8	Infectiology	Antibacterial	Yes
Corticosterone	50-22-6	Endocrinology	Anti-inflammatory	
Cortisol acetate	50-03-3	Metabolism	Anti-inflammatory	Yes
Cortisone	53-06-5	Endocrinology	Anti-inflammatory	Yes
Cromolyn disodium salt	15826-37-6	Allergology	Antiasthmatic	Yes
Crotamiton	483-63-6	Dermatology	Antipruritic	Yes
Cyanocobalamin	68-19-9	Metabolism	Analgesic	Yes
Cyclizine hydrochloride	303-25-3	Allergology	Antiemetic	Yes
Cyclobenzaprine hydrochloride	6202-23-9	Neuromuscular	Muscle relaxant	Yes
Cycloheximide	66-81-9	Infectiology	Antibacterial	
Cyclopenthiazide	742-20-1	Cardiovascular	Antihypertensive	
Cyclopentolate hydrochloride	5870-29-1	Metabolism		Yes
Cyclophosphamide	50-18-0	Immunology	Antineoplastic	Yes

Cyclosporin A	59865-13-3	Immunology	Immunosuppressant	Yes
Cyproheptadine hydrochloride	969-33-5	Allergology	Antihistaminic	Yes
Cyproterone acetate	427-51-0	Endocrinology	Antineoplastic	
Cytarabine	147-94-4	Oncology	Antineoplastic	Yes
D,L-Penicillamine	52-66-4	Central Nervous System	Analgesic	Yes
Dacarbazine	4342-03-4	Oncology	Antineoplastic	Yes
Danazol	17230-88-5	Endocrinology	Anabolic	Yes
Dantrolene sodium salt	14663-23-1	Neuromuscular	Muscle relaxant	Yes
Dapsone	80-08-0	Infectiology	Antibacterial	Yes
Darifenacin hydrobromide	133099-07-7	Neuromuscular		Yes
Darunavir	635728-49-3	Infectiology		Yes
Daunorubicin hydrochloride	23541-50-6	Infectiology	Antibacterial	Yes
D-cycloserine	68-41-7	Infectiology	Antibacterial	Yes
Debrisoquin sulfate	581-88-4	Cardiovascular	Antihypertensive	
Decamethonium bromide	541-22-0	Neuromuscular	Muscle relaxant	Yes
Deferoxamine mesylate	138-14-7	Diagnostic	Chelating	Yes
Deflazacort	14484-47-0	Immunology	Anti-inflammatory	
Dehydrocholic acid	81-23-2	Gastroenterology	Choleretic	
Dehydroisoandosterone 3-acetate	853-23-6	Endocrinology		
Delavirdine	136817-59-9	Infectiology		Yes
Demecarium bromide	56-94-0	Ophthalmology	Antiglaucoma	Yes
Demeclocycline hydrochloride	64-73-3	Metabolism	Antibacterial	Yes
Denatonium benzoate	3734-33-6	Neuromuscular		
Deoxycorticosterone	64-85-7	Endocrinology	Anti-inflammatory	
Deptropine citrate	2169-75-7	Allergology	Antihistaminic	
Dequalinium dichloride	522-51-0	Infectiology	Antibacterial	
Desipramine hydrochloride	58-28-6	Central Nervous System	Antidepressant	Yes
Desloratadine	100643-71-8	Allergology	Antihistaminic	Yes
Desonide	638-94-8	Dermatology	Antipsoriatic	Yes
Dexamethasone acetate	1177-87-3	Endocrinology	Anti-inflammatory	Yes

Dexfenfluramine hydrochloride	3239-45-0	Central Nervous System	Anorectic	
Dextromethorphan hydrobromide monohydrate	6700-34-1	Central Nervous System	Antitussive	Yes
Diacerein	13739-02-1	Immunology	Antiarthritic	
Diatrizoic acid dihydrate	50978-11-5	Diagnostic	Contrastant	Yes
Diazoxide	364-98-7	Cardiovascular	Antidiuretic	Yes
Dibenzepine hydrochloride	315-80-0	Central Nervous System	Antidepressant	
Dibucaine	85-79-0	Neuromuscular	Local anesthetic	Yes
Dichlorphenamide	120-97-8	Ophthalmology	Antiglaucoma	Yes
Diclazuril	101831-37-2	Metabolism		
Diclofenac sodium	15307-79-6	Central Nervous System	Anti-inflammatory	Yes
Dicloxacillin sodium salt hydrate	13412-64-1	Infectiology	Antibacterial	Yes
Dicumarol	66-76-2	Hematology	Anticoagulant	Yes
Dicyclomine hydrochloride	67-92-5	Gastroenterology	Antispastic	Yes
Didanosine	69655-05-6	Infectiology	Antiviral	Yes
Dienestrol	84-17-3	Endocrinology		Yes
Diethylcarbamazine citrate	1642-54-2	Infectiology	Antihelmintic	Yes
Diethylstilbestrol	56-53-1	Endocrinology		Yes
Diflorasone Diacetate	33564-31-7	Endocrinology	Anti-inflammatory	
Diflunisal	22494-42-4	Central Nervous System	Analgesic	Yes
Digitoxigenin	143-62-4	Cardiovascular	Cardiotonic	
Digoxigenin	1672-46-4	Diagnostic		
Digoxin	20830-75-5	Cardiovascular	Cardiotonic	Yes
Dihydroergotamine tartrate	5989-77-5	Central Nervous System	Antimigraine	Yes
Dihydrostreptomycin sulfate	5490-27-7	Infectiology	Antibacterial	Yes
Dilazep dihydrochloride	20153-98-4	Cardiovascular	Antiplatelet	
Diloxanide furoate	3736-81-0	Metabolism	Antiamebic	
Diltiazem hydrochloride	33286-22-5	Cardiovascular	Antianginal	Yes
Dimaprit dihydrochloride	23256-33-9	Metabolism		
Dimenhydrinate	523-87-5	Allergology	Antiemetic	Yes

Dimethadione	695-53-4	Central Nervous System	Anticonvulsant	
Dimethisoquin hydrochloride	2773-92-4	Neuromuscular	Antipruritic	
Dinoprost trometamol	38362-01-5	Endocrinology	Oxytocic	Yes
Diosmin	520-27-4	Cardiovascular		
Dioxybenzone	131-53-3	Dermatology		
Diperodon hydrochloride	537-12-2	Neuromuscular	Local anesthetic	
Diphemanil methylsulfate	62-97-5	Gastroenterology	Antispastic	Yes
Diphenhydramine hydrochloride	147-24-0	Allergology	Antiemetic	Yes
Diphenidol hydrochloride	3254-89-5	Central Nervous System	Antiemetic	Yes
Diphenylpyraline hydrochloride	132-18-3	Allergology	Antihistaminic	
Dipivefrin hydrochloride	64019-93-8	Ophthalmology	Antiglaucoma	Yes
Diprophylline	479-18-5	Cardiovascular	Analeptic	
Dipyridamole	58-32-2	Cardiovascular	Anticoagulant	Yes
Dipyrone	5907-38-0	Central Nervous System	Analgesic	
Dirithromycin	62013-04-1	Infectiology	Antibacterial	Yes
Disopyramide	3737-09-5	Cardiovascular	Antiarrhythmic	Yes
Disulfiram	97-77-8	Metabolism	Antabuse effect	Yes
Dizocilpine maleate	77086-22-7	Central Nervous System	Anticonvulsant	
DO 897/99	not available	Central Nervous System	Antidepressant	
Dobutamine hydrochloride	49745-95-1	Cardiovascular	Analeptic	Yes
Docetaxel	114977-28-5	Oncology	Antineoplastic	Yes
Dofetilide	115256-11-6	Cardiovascular	Antiarrhythmic	Yes
Dolasetron mesilate	115956-13-3	Central Nervous System	Antiemetic	Yes
Domperidone	57808-66-9	Central Nervous System	Antiemetic	
Donepezil hydrochloride	120011-70-3	Central Nervous System	Anti-Alzheimer	Yes
Dopamine hydrochloride	62-31-7	Cardiovascular	Antihypertensive	Yes
Dorzolamide hydrochloride	130693-82-2	Cardiovascular	Antiglaucoma	Yes
Dosulepin hydrochloride	897-15-4	Central Nervous System	Antidepressant	
Doxapram hydrochloride	7081-53-0	Respiratory	Analeptic	Yes
Doxazosin mesylate	77883-43-3	Cardiovascular	Antihypertensive	Yes

Doxepin hydrochloride	1229-29-4	Allergology	Anticonvulsant	Yes
Doxofylline	69975-86-6	Respiratory	Bronchodilator	
Doxorubicin hydrochloride	25316-40-9	Infectiology	Antibacterial	Yes
Doxycycline hydrochloride	10592-13-9	Metabolism	Antibacterial	Yes
Doxylamine succinate	562-10-7	Allergology	Anti-anorectic	Yes
Drofenine hydrochloride	548-66-3	Neuromuscular	Antispastic	
Droperidol	548-73-2	Central Nervous System	Antipsychotic	Yes
Dropropizine (R,S)	17692-31-8	Respiratory	Antitussive	
Dyclonine hydrochloride	536-43-6	Neuromuscular	Local anesthetic	Yes
Dydrogesterone	152-62-5	Endocrinology	Progestogen	Yes
Ebselen	60940-34-3	Metabolism	Anti-inflammatory	
Eburnamonine (-)	4880-88-0	Central Nervous System	Vasodilator	
Econazole nitrate	24169-02-6	Infectiology	Antifungal	Yes
Edrophonium chloride	116-38-1	Diagnostic	Anti-fatigue	Yes
Efavirenz	154598-52-4	Infectiology	Antiviral	Yes
Emedastine	87233-61-2	Allergology	Antihistaminic	Yes
Enalapril maleate	76095-16-4	Cardiovascular	Antihypertensive	Yes
Enalaprilat dihydrate	84680-54-6	Cardiovascular	Antihypertensive	Yes
Enilconazole	35554-44-0	Metabolism	Antifungal	Yes
Enoxacin	84294-96-2	Infectiology	Antibacterial	Yes
Enrofloxacin	93106-60-6	Infectiology	Antibacterial	
Entacapone	130929-57-6	Central Nervous System	Antiparkinsonian	Yes
Epiandrosterone	481-29-8	Endocrinology	Anabolic	
Epirizole	18694-40-1	Central Nervous System	Analgesic	Japan approved
Epirubicin hydrochloride	56390-09-1	Oncology	Antineoplastic	Yes
Equilin	474-86-2	Endocrinology		
Erlotinib	183321-74-6	Oncology	Antineoplastic	Yes
Erythromycin	114-07-8	Infectiology	Antibacterial	Yes
Escitalopram oxalate	128196-01-0	Central Nervous System	Antidepressant	Yes
Eserine hemisulfate salt	64-47-1	Central Nervous System	Antiglaucoma	

Esmolol hydrochloride	81161-17-3	Cardiovascular	Antiarrhythmic	Yes
Estradiol Valerate	979-32-8	Endocrinology	Contraceptive	Yes
Estradiol-17 beta	50-28-2	Endocrinology	Antigonadotropin	Yes
Estramustine	2998-57-4	Oncology	Antineoplastic	Yes
Estrone	53-16-7	Endocrinology		Yes
Estropipate	7280-37-7	Endocrinology		Yes
Etanidazole	22668-01-5	Oncology	Antineoplastic	
Ethacrynic acid	58-54-8	Metabolism	Diuretic	Yes
Ethambutol dihydrochloride	1070-11-7	Infectiology	Antibacterial	Yes
Ethamivan	304-84-7	Central Nervous System	Analeptic	
Ethamsylate	2624-44-4	Cardiovascular	Antiplatelet	
Ethaverine hydrochloride	985-13-7	Central Nervous System	Antispastic	
Ethinylestradiol	57-63-6	Endocrinology	Contraceptive	Yes
Ethionamide	536-33-4	Infectiology	Antibacterial	Yes
Ethisterone	434-03-7	Endocrinology	Contraceptive	
Ethopropazine hydrochloride	1094-08-2	Central Nervous System	Antiparkinsonian	Yes
Ethosuximide	77-67-8	Central Nervous System	Anticonvulsant	Yes
Ethotoin	86-35-1	Central Nervous System	Anticonvulsant	Yes
Ethoxyquin	91-53-2	Metabolism	Antifungal	
Ethoxzolamide	452-35-7	Ophthalmology	Antiglaucoma	Yes
Ethynodiol diacetate	297-76-7	Endocrinology	Contraceptive	Yes
Ethynylestradiol 3-methyl ether	72-33-3	Endocrinology		Yes
Etifenin	63245-28-3	Diagnostic	Chemosensitizer	
Etilefrine hydrochloride	534-87-2	Cardiovascular	Vasoconstrictor	
Etodolac	41340-25-4	Central Nervous System	Analgesic	Yes
Etofenamate	30544-47-9	Metabolism	Anti-inflammatory	
Etofylline	519-37-9	Cardiovascular	Antispastic	
Etomidate	33125-97-2	Central Nervous System	Anesthetic	Yes
Etoposide	33419-42-0	Oncology	Antineoplastic	Yes
Etoricoxib	202409-33-4	Central Nervous System	Analgesic	

Etretinate	54350-48-0	Dermatology	Antipsoriatic	Yes
Eucatropine hydrochloride	536-93-6	Neuromuscular	Antiglaucoma	
Exemestane	107868-30-4	Endocrinology	Antineoplastic	Yes
Ezetimibe	163222-33-1	Metabolism	Hypocholesterolemic	Yes
Famciclovir	104227-87-4	Infectiology	Antiviral	Yes
Famotidine	76824-35-6	Gastroenterology	Antiulcer	Yes
Famprofazone	22881-35-2	Central Nervous System	Analgesic	
Felbamate	25451-15-4	Central Nervous System	Antiepileptic	Yes
Felbinac	5728-52-9	Central Nervous System	Analgesic	
Felodipine	72509-76-3	Neuromuscular	Antianginal	Yes
Fenbendazole	43210-67-9	Infectiology	Antihelmintic	
Fenbufen	36330-85-5	Central Nervous System	Analgesic	
Fendiline hydrochloride	13636-18-5	Cardiovascular	Antianginal	
Fenipentol	583-03-9	Metabolism	Choleretic	
Fenofibrate	49562-28-9	Metabolism	Hypocholesterolemic	Yes
Fenoldopam	67227-56-9	Cardiovascular	Antihypertensive	Yes
Fenoprofen calcium salt dihydrate	53746-45-5	Metabolism	Anti-inflammatory	Yes
Fenoterol hydrobromide	1944-12-3	Neuromuscular	Bronchodilator	
Fenspiride hydrochloride	5053-08-7	Respiratory	Antitussive	
Fentiazac	18046-21-4	Metabolism	Anti-inflammatory	
Finasteride	98319-26-7	Endocrinology	Anti-alopecia	Yes
Fipexide hydrochloride	34161-23-4	Central Nervous System	Anti-fatigue	
Flavoxate hydrochloride	3717-88-2	Metabolism	Antispastic	Yes
Flecainide acetate	54143-56-5	Cardiovascular	Antiarrhythmic	Yes
Fleroxacin	79660-72-3	Infectiology	Antibacterial	
Florfenicol	73231-34-2	Metabolism	Antibacterial	
Floxuridine	50-91-9	Oncology	Antineoplastic	Yes
Flubendazol	31430-15-6	Metabolism		
Flucloxacillin sodium	1847-24-1	Metabolism	Antibacterial	
Fluconazole	86386-73-4	Metabolism	Antifungal	Yes

Flucytosine	2022-85-7	Metabolism	Antifungal	Yes
Fludarabine	21679-14-1	Oncology	Antineoplastic	Yes
Fludrocortisone acetate	514-36-3	Dermatology	Anti-inflammatory	Yes
Flufenamic acid	530-78-9	Central Nervous System	Analgesic	
Flumequine	42835-25-6	Infectiology	Antibacterial	
Flumethasone	2135-17-3	Metabolism	Anti-inflammatory	Yes
Flumethasone pivalate	2002-29-1	Dermatology	Anti-inflammatory	Yes
Flunarizine dihydrochloride	30484-77-6	Central Nervous System	Anticonvulsant	
Flunisolide	3385-03-3	Endocrinology	Anti-inflammatory	Yes
Flunixin meglumine	42461-84-7	Central Nervous System	Analgesic	
Fluocinolone acetonide	67-73-2	Metabolism	Anti-inflammatory	Yes
Fluocinonide	356-12-7	Metabolism	Anti-inflammatory	Yes
Fluorometholone	426-13-1	Endocrinology	Anti-inflammatory	Yes
Fluoxetine hydrochloride	59333-67-4	Central Nervous System	Antidepressant	Yes
Fluphenazine dihydrochloride	146-56-5	Central Nervous System	Antipsychotic	Yes
Flurandrenolide	1524-88-5	Dermatology	Anti-inflammatory	Yes
Flurbiprofen	5104-49-4	Central Nervous System	Analgesic	Yes
Fluspirilen	1841-19-6	Central Nervous System	Antipsychotic	
Flutamide	13311-84-7	Oncology	Antineoplastic	Yes
Fluticasone propionate	80474-14-2	Cardiovascular	Anti-inflammatory	Yes
Fluvastatin sodium salt	93957-55-2	Cardiovascular	Antilipemic	Yes
Fluvoxamine maleate	61718-82-9	Central Nervous System	Antidepressant	Yes
Folic acid	59-30-3	Metabolism		Yes
Folinic acid calcium salt	6035-45-6	Hematology	Antianemic	Yes
Fomepizole	7554-65-6	Metabolism		Yes
Formestane	566-48-3	Endocrinology	Antineoplastic	
Formoterol fumarate	43229-80-7	Respiratory	Antiasthmatic	Yes
Fosfosal	6064-83-1	Central Nervous System	Analgesic	
Fosinopril	98048-97-6	Cardiovascular	Antihypertensive	Yes
Fulvestrant	129453-61-8	Endocrinology	Antineoplastic	Yes

Furaltadone hydrochloride	3759-92-0	Infectiology	Antibacterial	Yes
Furazolidone	67-45-8	Metabolism		Yes
Furosemide	54-31-9	Metabolism	Antihypertensive	Yes
Fursultiamine Hydrochloride	2105-43-3	Metabolism	Anti-Alzheimer	
Fusidic acid sodium salt	751-94-0	Infectiology	Antibacterial	
Gabapentin	60142-96-3	Central Nervous System	Anticonvulsant	Yes
Gabazine bromide	105538-73-6	Central Nervous System	CNS Stimulant	
Gabexate mesilate	56974-61-9	Hematology	Anticoagulant	
Galanthamine hydrobromide	1953-04-4	Central Nervous System	Analgesic	Yes
Gallamine triethiodide	65-29-2	Neuromuscular	Muscle relaxant	Yes
Ganciclovir	82410-32-0	Metabolism	Antiviral	Yes
Gatifloxacin	112811-59-3	Infectiology	Antibacterial	Yes
GBR 12909 dihydrochloride	67469-78-7	Central Nervous System	Antidepressant	
Gefitinib	184475-35-2	Oncology	Antineoplastic	Yes
Gemcitabine	95058-81-4	Oncology	Antineoplastic	Yes
Gemfibrozil	25812-30-0	Metabolism	Hypocholesterolemic	Yes
Gentamicine sulfate	1405-41-0	Infectiology	Antibacterial	Yes
Gestrinone	16320-04-0	Endocrinology	Contraceptive	
Glafenine hydrochloride	65513-72-6	Metabolism	Analgesic	
Glibenclamide	10238-21-8	Endocrinology	Antidiabetic	Yes
Gliclazide	21187-98-4	Metabolism	Anticoagulant	
Glimepiride	93479-97-1	Endocrinology	Antidiabetic	Yes
Glipizide	29094-61-9	Endocrinology	Antidiabetic	Yes
Gliquidone	33342-05-1	Endocrinology	Antidiabetic	
Glutethimide, para-amino	125-84-8	Oncology	Antineoplastic	Yes
Glycopyrrolate	596-51-0	Gastroenterology	Antispastic	Yes
Granisetron	109889-09-0	Endocrinology	Antiemetic	Yes
Grepafloxacin	146863-02-7	Infectiology		Yes
Griseofulvin	126-07-8	Infectiology	Antifungal	Yes
Guaiacol	90-05-1	Respiratory	Expectorant	

Guaifenesin	93-14-1	Respiratory	Bronchodilator	Yes
Guanabenz acetate	23256-50-0	Central Nervous System	Antihypertensive	Yes
Guanadrel sulfate	22195-34-2	Cardiovascular	Antihypertensive	Yes
Guanethidine sulfate	60-02-6	Central Nervous System	Antihypertensive	Yes
Guanfacine hydrochloride	29110-48-3	Cardiovascular	Antihypertensive	Yes
Halcinonide	3093-35-4	Dermatology	Anti-inflammatory	Yes
Halofantrine hydrochloride	36167-63-2	Metabolism	Antimalarial	Yes
Haloperidol	52-86-8	Central Nervous System	Antiemetic	Yes
Haloprogin	777-11-7	Infectiology	Antifungal	Yes
Hemicholinium bromide	312-45-8	Neuromuscular	Curarizing	
Heptaminol hydrochloride	543-15-7	Cardiovascular	Analeptic	
Hesperidin	520-26-3	Oncology	Anti-haemorrhoids	
Hexachlorophene	70-30-4	Infectiology	Antiseptic	Yes
Hexamethonium dibromide dihydrate	55-97-0	Cardiovascular	Antihypertensive	
Hexestrol	84-16-2	Endocrinology	Antineoplastic	
Hexetidine	141-94-6	Infectiology	Antifungal	
Hexylcaine hydrochloride	532-76-3	Dermatology	Anesthetic	Yes
Histamine dihydrochloride	56-92-8	Oncology	Antineoplastic	Yes
Homatropine hydrobromide (R,S)	51-56-9	Diagnostic	Antispastic	Yes
Homochlorcyclizine dihydrochloride	1982-36-1	Allergology	Antihistaminic	
Homosalate	118-56-9	Dermatology	Radioprotectant	
Homoveratrylamine	120-20-7	Cardiovascular	Antihypertensive	
Hycanthone	3105-97-3	Infectiology	Antihelmintic	
Hydralazine hydrochloride	304-20-1	Cardiovascular	Antihypertensive	Yes
Hydrochlorothiazide	58-93-5	Metabolism	Antihypertensive	Yes
Hydrocortisone base	50-23-7	Endocrinology	Anti-inflammatory	Yes
Hydroflumethiazide	135-09-1	Metabolism	Antihypertensive	Yes
Hydroxychloroquine sulfate	747-36-4	Metabolism	Antimalarial	Yes
Hydroxytacrine maleate (R,S)	118909-22-1	Central Nervous System	Anti-Alzheimer	
Hydroxyzine dihydrochloride	2192-20-3	Allergology	Antiemetic	Yes

Hymecromone	90-33-5	Metabolism	Muscle relaxant	
Hyoscyamine (L)	101-31-5	Central Nervous System	Antiemetic	
Ibandronate sodium	114084-78-5	Metabolism	Antiosteoporetic	Yes
Ibudilast	50847-11-5	Metabolism	Anti-inflammatory	Japan approved
Ibutilide fumarate	122647-32-9	Cardiovascular	Antiarrhythmic	Yes
Idazoxan hydrochloride	79944-56-2	Central Nervous System	Antiparkinsonian	
Idebenone	58186-27-9	Oncology	Antineoplastic	
Idoxuridine	54-42-2	Infectiology	Antiviral	Yes
Ifenprodil tartrate	23210-58-4	Cardiovascular	Vasodilator	
Ifosfamide	3778-73-2	Oncology	Antineoplastic	Yes
Imatinib	152459-95-5	Oncology	Antineoplastic	Yes
Imidurea	39236-46-9	Infectiology	Antifungal	
Imipenem	74431-23-5	Infectiology	Antibacterial	Yes
Imipramine hydrochloride	113-52-0	Central Nervous System	Antidepressant	Yes
Imiquimod	99011-02-6	Dermatology	Antiviral	Yes
Indapamide	26807-65-8	Metabolism	Antihypertensive	Yes
Indatraline hydrochloride	86939-10-8	Central Nervous System	Antidepressant	
Indinavir sulfate	157810-81-6	Infectiology	Antiviral	Yes
Indomethacin	53-86-1	Central Nervous System	Analgesic	Yes
Indoprofen	31842-01-0	Central Nervous System	Analgesic	
Iobenguane sulfate	103346-16-3	Oncology	Antineoplastic	Yes
Iocetamic acid	16034-77-8	Diagnostic	Contrastant	Yes
Iodipamide	606-17-7	Diagnostic	Contrastant	Yes
Iodixanol	92339-11-2	Diagnostic	Contrastant	Yes
Iohexol	66108-95-0	Diagnostic	Contrastant	Yes
Iopamidol	60166-93-0	Diagnostic	Contrastant	Yes
Iopanoic acid	96-83-3	Diagnostic	Contrastant	Yes
Iopromide	73334-07-3	Diagnostic	Contrastant	Yes
Ioversol	87771-40-2	Diagnostic	Contrastant	Yes
Ioxaglic acid	59017-64-0	Diagnostic	Contrastant	Yes

Ipriflavone	35212-22-7	Metabolism	Antiosteoporetic	
Iproniazide phosphate	305-33-9	Cardiovascular	Antidepressant	
Ipsapirone	95847-70-4	Central Nervous System		
Irbesartan	138402-11-6	Cardiovascular	Antihypertensive	Yes
Irinotecan hydrochloride trihydrate	136572-09-3	Oncology	Antineoplastic	Yes
Irsogladine maleate	84504-69-8	Metabolism	Antiulcer	
Isocarboxazid	59-63-2	Central Nervous System	Antidepressant	Yes
Isoconazole	27523-40-6	Infectiology	Antibacterial	
Isoetharine mesylate salt	7279-75-6	Respiratory	Bronchodilator	Yes
Isoflupredone acetate	338-98-7	Endocrinology	Anti-inflammatory	
Isometheptene mucate	7492-31-1	Cardiovascular	Antimigraine	
Isoniazid	54-85-3	Infectiology	Antibacterial	Yes
Isopropamide iodide	71-81-8	Metabolism	Antiulcer	Yes
Isopyrin hydrochloride	18342-39-7	Central Nervous System	Analgesic	
Isosorbide dinitrate	87-33-2	Cardiovascular	Antianginal	Yes
Isosorbide mononitrate	16051-77-7	Cardiovascular	Antianginal	Yes
Isotretinoin	4759-48-2	Dermatology	Keratolytic	Yes
Isoxicam	34552-84-6	Central Nervous System	Analgesic	
Isoxsuprine hydrochloride	579-56-6	Cardiovascular	Vasodilator	
Isradipine	75695-93-1	Cardiovascular	Antianginal	Yes
Itopride	122898-67-3	Metabolism		
Itraconazole	84625-61-6	Infectiology	Antifungal	Yes
Ivermectin	70288-86-7	Infectiology	Antihelmintic	Yes
Josamycin	16846-24-5	Infectiology	Antibacterial	
Kanamycin A sulfate	25389-94-0	Infectiology	Antibacterial	Yes
Ketanserin tartrate hydrate	83846-83-7	Cardiovascular	Antihypertensive	
Ketoconazole	65277-42-1	Infectiology	Antifungal	Yes
Ketoprofen	22071-15-4	Central Nervous System	Analgesic	Yes
Ketorolac tromethamine	74103-07-4	Central Nervous System	Analgesic	Yes
Ketotifen fumarate	34580-14-8	Allergology	Antihistaminic	Yes

Khellin	82-02-0	Cardiovascular	Antispastic	
L(-)-vesamicol hydrochloride	112709-59-8	Neuromuscular		
Labetalol hydrochloride	32780-64-6	Cardiovascular	Antihypotensive	Yes
Lacidipine	103890-78-4	Cardiovascular	Antihypertensive	
Lamivudine	134678-17-4	Infectiology	Antiviral	Yes
Lamotrigine	84057-84-1	Central Nervous System	Anticonvulsant	Yes
Lanatoside C	17575-22-3	Cardiovascular	Cardiotonic	
Lansoprazole	103577-45-3	Metabolism	Antiulcer	Yes
Latanoprost	145773-22-4	Ophthalmology	Antiglaucoma	Yes
Leflunomide	75706-12-6	Immunology	Immunosuppressant	Yes
Letrozole	112809-51-5	Oncology	Antineoplastic	Yes
Levalbuterol hydrochloride	50293-90-8	Respiratory	Antiasthmatic	Yes
Levamisole hydrochloride	16595-80-5	Immunology	Antihelmintic	Yes
Levetiracetam	102767-28-2	Central Nervous System	Anticonvulsant	Yes
Levocabastine hydrochloride	79547-78-7	Allergology	Antihistaminic	Yes
Levodopa	59-92-7	Central Nervous System	Antiparkinsonian	Yes
Levonordefrin	829-74-3	Cardiovascular	Vasoconstrictor	Yes
Levopropoxyphene napsylate	5714-90-9	Central Nervous System	Analgesic	Yes
Lidocaine hydrochloride	73-78-9	Cardiovascular	Antiarrhythmic	Yes
Lidoflazine	3416-26-0	Cardiovascular	Antianginal	
Lincomycin hydrochloride	859-18-7	Infectiology	Antibacterial	Yes
Linezolid	165800-03-3	Infectiology	Antibacterial	Yes
Liothyronine	6893-02-3	Endocrinology		Yes
Liranaftate	88678-31-3	Infectiology	Antifungal	
Lisinopril	83915-83-7	Cardiovascular	Antihypertensive	Yes
Lithocholic acid	434-13-9	Metabolism	Cholagogue	
Lodoxamide	53882-12-5	Allergology	Antihistaminic	Yes
Lofepramine	23047-25-8	Central Nervous System	Antidepressant	
Lofexidine	31036-80-3	Cardiovascular	Antihypertensive	
Lomefloxacin hydrochloride	98079-52-8	Infectiology	Antibacterial	Yes

Lomerizine hydrochloride	101477-54-7	Central Nervous System	Antimigraine	
Loperamide hydrochloride	34552-83-5	Gastroenterology	Antidiarrheal	Yes
Loracarbef	121961-22-6	Infectiology	Antibacterial	Yes
Loratadine	79794-75-5	Allergology	Antihistaminic	Yes
Lorglumide sodium salt	97964-56-2	Metabolism	Antiulcer	
Losartan	114798-26-4	Cardiovascular	Antihypertensive	Yes
Loteprednol etabonate	82034-46-6	Ophthalmology	Anti-inflammatory	Yes
Lovastatin	75330-75-5	Metabolism	Hypocholesterolemic	Yes
Loxapine succinate	27833-64-3	Central Nervous System	Antipsychotic	Yes
Luteolin	491-70-3	Respiratory	Expectorant	
Lymecycline	992-21-2	Metabolism	Antibacterial	
Lynestrenol	52-76-6	Endocrinology	Contraceptive	
Mafenide hydrochloride	138-37-4	Infectiology	Antibacterial	Yes
Maprotiline hydrochloride	10347-81-6	Central Nervous System	Antidepressant	Yes
Mebendazole	31431-39-7	Infectiology	Antihelmintic	Yes
Mebeverine hydrochloride	2753-45-9	Neuromuscular	Antispastic	
Mebhydroline 1,5-naphtalenedisulfonate	6153-33-9	Allergology	Antihistaminic	
Mecamylamine hydrochloride	826-39-1	Cardiovascular	Antihypertensive	Yes
Meclocycline sulfosalicylate	73816-42-9	Infectiology	Antibacterial	Yes
Meclofenamic acid sodium salt monohydrate	6385-02-0	Central Nervous System	Anti-inflammatory	Yes
Meclofenoxate hydrochloride	3685-84-5	Central Nervous System	CNS Stimulant	Yes
Meclozine dihydrochloride	1104-22-9	Allergology	Antiemetic	Yes
Medrysone	2668-66-8	Metabolism	Anti-inflammatory	Yes
Mefenamic acid	61-68-7	Central Nervous System	Analgesic	Yes
Mefexamide hydrochloride	3413-64-7	Central Nervous System	CNS Stimulant	
Mefloquine hydrochloride	51773-92-3	Infectiology	Antimalarial	Yes
Megestrol acetate	595-33-5	Endocrinology	Antineoplastic	Yes
Meglumine	6284-40-8	Metabolism	Antileishmanial	Yes
Melatonin	73-31-4	Central Nervous System	Anticonvulsant	
Melengestrol acetate	2919-66-6	Endocrinology		

Meloxicam	71125-38-7	Metabolism	Anti-inflammatory	Yes
Memantine Hydrochloride	41100-52-1	Central Nervous System	Anti-Alzheimer	Yes
Mepenzolate bromide	76-90-4	Neuromuscular	Antispastic	Yes
Mephenesin	59-47-2	Central Nervous System	Anticonvulsant	
Mephentermine hemisulfate	1212-72-2	Cardiovascular	Antihypotensive	Yes
Mepivacaine hydrochloride	1722-62-9	Neuromuscular	Local anesthetic	Yes
Meprylcaine hydrochloride	956-03-6	Neuromuscular	Local anesthetic	
Meptazinol hydrochloride	59263-76-2	Central Nervous System	Analgesic	
Merbromin	129-16-8	Infectiology	Antibacterial	
Mercaptopurine	50-44-2	Immunology	Immunosuppressant	Yes
Meropenem	96036-03-2	Infectiology	Antibacterial	Yes
Mesalamine	89-57-6	Metabolism	Anti-inflammatory	Yes
Mesna	19767-45-4	Oncology	Chemoprotectant	Yes
Mesoridazine besylate	32672-69-8	Central Nervous System	Antipsychotic	Yes
Metaproterenol sulfate, orciprenaline sulfate	5874-97-5	Respiratory	Bronchodilator	Yes
Metaraminol bitartrate	33402-03-8	Cardiovascular	Antihypotensive	Yes
Metergoline	17692-51-2	Central Nervous System	Antiprolactin	
Metformin hydrochloride	1115-70-4	Endocrinology	Anorectic	Yes
Methacholine chloride	62-51-1	Diagnostic		Yes
Methacycline hydrochloride	3963-95-9	Metabolism	Antibacterial	Yes
Methantheline bromide	53-46-3	Neuromuscular	Antispastic	Yes
Methapyrilene hydrochloride	135-23-9	Allergology	Antihistaminic	
Methazolamide	554-57-4	Metabolism	Antiglaucoma	Yes
Methenamine	100-97-0	Infectiology	Antibacterial	Yes
Methiazole	108579-67-5	Infectiology	Antihelmintic	
Methicillin sodium	7246-14-2	Oncology		Yes
Methimazole	60-56-0	Endocrinology		Yes
Methiothepin maleate	19728-88-2	Central Nervous System	Antipsychotic	
Methocarbamol	532-03-6	Central Nervous System	Analgesic	Yes
Methotrexate	59-05-2	Oncology	Antineoplastic	Yes

Methotrimeprazine maleat salt	7104-38-3	Central Nervous System	Analgesic	Yes
Methoxamine hydrochloride	61-16-5	Cardiovascular	Antihypotensive	Yes
Methyl benzethonium chloride	25155-18-4	Infectiology	Antibacterial	
Methylatropine nitrate	52-88-0	Neuromuscular	Antispastic	
Methyldopa (L,-)	555-30-6	Cardiovascular	Antihypertensive	Yes
Methyldopate hydrochloride	2508-79-4	Cardiovascular	Antihypertensive	Yes
Methylergometrine maleate	57432-61-8	Neuromuscular	Hemostatic	
Methylhydantoin-5-(D)	55147-68-7			
Methylhydantoin-5-(L)	40856-73-3	Central Nervous System	Anticonvulsant	
Methylprednisolone, 6-alpha	83-43-2	Endocrinology	Anti-inflammatory	Yes
Meticrane	1084-65-7	Metabolism	Antihypertensive	
Metixene hydrochloride	1553-34-0	Central Nervous System	Antiparkinsonian	
Metoclopramide monohydrochloride	7232-21-5	Central Nervous System	Antiemetic	Yes
Metolazone	17560-51-9	Cardiovascular	Antihypertensive	Yes
Metoprolol-(+,-) (+)-tartrate salt	56392-17-7	Cardiovascular	Antiarrhythmic	Yes
Metrizamide	31112-62-6	Diagnostic	Contrastant	Yes
Metronidazole	443-48-1	Infectiology	Antiamebic	Yes
Metyrapone	54-36-4	Endocrinology		Yes
Mevalonic-D, L acid lactone	674-26-0	Cardiovascular	Antilipemic	
Mevastatin	73573-88-3	Cardiovascular	Hypocholesterolemic	
Mexiletine hydrochloride	5370-01-4	Cardiovascular	Antiarrhythmic	Yes
Mianserine hydrochloride	21535-47-7	Cardiovascular	Antidepressant	
Miconazole	22916-47-8	Infectiology	Antifungal	Yes
Midodrine hydrochloride	3092-17-9	Cardiovascular	Antihypertensive	Yes
Mifepristone	84371-65-3	Endocrinology	Abortifacient	Yes
Miglitol	72432-03-2	Endocrinology	Antidiabetic	Yes
Milnacipran hydrochloride	101152-94-7	Central Nervous System	Antidepressant	Yes
Milrinone	78415-72-2	Cardiovascular	Vasodilator	Yes
Minaprine dihydrochloride	25953-17-7	Central Nervous System	Anti-Alzheimer	
Minocycline hydrochloride	13614-98-7	Infectiology	Antibacterial	Yes

Minoxidil	38304-91-5	Cardiovascular	Anti-alopecia	Yes
Mirabegron	223673-61-8	Neuromuscular		Yes
Mirtazapine	61337-67-5	Central Nervous System	Antidepressant	Yes
Misoprostol	59122-46-2	Metabolism	Antiulcer	Yes
Mitotane	53-19-0	Endocrinology	Antineoplastic	Yes
Mitoxantrone dihydrochloride	70476-82-3	Oncology	Antineoplastic	Yes
Mizolastine	108612-45-9	Allergology		
Moclobemide	71320-77-9	Central Nervous System	Antidepressant	
Modafinil	68693-11-8	Central Nervous System	CNS Stimulant	Yes
Molindone hydrochloride	15622-65-8	Central Nervous System	Antipsychotic	Yes
Molsidomine	25717-80-0	Cardiovascular	Antianginal	
Mometasone furoate	83919-23-7	Endocrinology	Anti-inflammatory	Yes
Monensin sodium salt	22373-78-0	Infectiology	Antibacterial	
Monobenzone	103-16-2	Dermatology		Yes
Montelukast	158966-92-8	Respiratory	Antiasthmatic	Yes
Morantel tartrate	26155-31-7	Infectiology	Antihelmintic	
Moricizine hydrochloride	31883-05-3	Cardiovascular	Antiarrhythmic	Yes
Moroxidine hydrochloride	3160-91-6	Infectiology	Antiviral	
Moxalactam disodium salt	64953-12-4	Metabolism	Antibacterial	Yes
Moxifloxacin	151096-09-2	Infectiology	Antibacterial	Yes
Moxisylyte hydrochoride	964-52-3	Cardiovascular	Erectile dysfunction treatment	
Moxonidine	75438-57-2	Cardiovascular	Antihypertensive	
Mupirocin	12650-69-0	Infectiology		Yes
N6-methyladenosine	1867-73-8	Oncology	Antineoplastic	
Nabumetone	42924-53-8	Central Nervous System	Analgesic	Yes
N-Acetyl-DL-homocysteine Thiolactone	1195-16-0	Respiratory	Expectorant	
N-Acetyl-L-leucine	1188-21-2	Central Nervous System	Antivertigo	
Nadide	53-84-9	Metabolism		
Nadifloxacin	124858-35-1	Infectiology	Antibacterial	

Nadolol	42200-33-9	Cardiovascular	Antianginal	Yes
Nafcillin sodium salt monohydrate	7177-50-6	Metabolism	Antibacterial	Yes
Nafronyl oxalate	3200-06-4	Cardiovascular	Anti-ischemic	
Naftifine hydrochloride	65473-14-5	Infectiology	Antifungal	Yes
Naftopidil dihydrochloride	57149-08-3	Cardiovascular	Antihypertensive	
Nalbuphine hydrochloride	23277-43-2	Central Nervous System	Analgesic	Yes
Nalidixic acid sodium salt	3374-05-8	Infectiology	Antibacterial	Yes
Nalmefene hydrochloride	58895-64-0	Central Nervous System		Yes
Naloxone hydrochloride	357-08-4	Central Nervous System	Opioate antidote	Yes
Naltrexone hydrochloride dihydrate	16676-29-2	Central Nervous System	Analgesic	Yes
Nandrolone	434-22-0	Endocrinology	Antianemic	Yes
Naphazoline hydrochloride	550-99-2	Cardiovascular	Nasal Decongestant	Yes
Naproxen	22204-53-1	Central Nervous System	Analgesic	Yes
Nateglinide	105816-04-4	Endocrinology	Antidiabetic	Yes
Nefazodone hydrochloride	82752-99-6	Central Nervous System	Antidepressant	Yes
Nefopam hydrochloride	23327-57-3	Central Nervous System	Analgesic	
Nelarabine	121032-29-9	Infectiology		Yes
Nelfinavir mesylate	159989-65-8	Infectiology	Antiviral	Yes
Neomycin sulfate	1405-10-3	Infectiology	Antibacterial	Yes
Neostigmine bromide	114-80-7	Diagnostic	Anti-fatigue	Yes
Nevirapine	129618-40-2	Infectiology	Antiviral	Yes
Niacin	59-67-6	Cardiovascular	Antilipemic	Yes
Nicardipine hydrochloride	54527-84-3	Cardiovascular	Antianginal	Yes
Nicergoline	not available	Cardiovascular	Anti-ischemic	
Niclosamide	50-65-7	Infectiology	Antihelmintic	Yes
Nicorandil	65141-46-0	Cardiovascular	Antianginal	
Nicotinamide	98-92-0	Dermatology		
Nifedipine	21829-25-4	Cardiovascular	Antianginal	Yes
Nifekalant	130636-43-0	Cardiovascular	Antiarrhythmic	
Nifenazone	2139-47-1	Central Nervous System	Analgesic	

Niflumic acid	4394-00-7	Central Nervous System	Analgesic	
Nifuroxazide	965-52-6	Infectiology	Antibacterial	
Nifurtimox	23256-30-6	Metabolism		
Nilutamide	63612-50-0	Oncology	Antineoplastic	Yes
Nilvadipine	75530-68-6	Cardiovascular	Antianginal	
Nimesulide	51803-78-2	Metabolism	Anti-inflammatory	
Nimodipine	66085-59-4	Cardiovascular	Vasodilator	Yes
Niridazole	61-57-4	Infectiology	Antihelmintic	
Nisoldipine	63675-72-9	Cardiovascular	Antianginal	Yes
Nisoxetine hydrochloride	57754-86-6	Central Nervous System	Antidepressant	
Nitazoxanide	55981-09-4	Infectiology	Antiprotozoal	Yes
Nitrendipine	39562-70-4	Cardiovascular	Antihypertensive	
Nitrocaramiphen hydrochloride	98636-73-8	Central Nervous System		
Nitrofural	59-87-0	Infectiology	Antibacterial	
Nitrofurantoin	67-20-9	Infectiology	Antibacterial	Yes
Nizatidine	76963-41-2	Metabolism	Antiulcer	Yes
Nocodazole	31430-18-9	Oncology	Antineoplastic	
Nomegestrol acetate	58652-20-3	Endocrinology	Contraceptive	
Nomifensine maleate	32795-47-4	Central Nervous System	Antidepressant	
Norcyclobenzaprine	303-50-4	Gastroenterology	Antiulcer	
Norethindrone	68-22-4	Endocrinology	Contraceptive	Yes
Norethynodrel	68-23-5	Endocrinology	Contraceptive	Yes
Norfloxacin	70458-96-7	Infectiology	Antibacterial	Yes
Norgestimate	35189-28-7	Endocrinology		Yes
Norgestrel-(-)-D	797-63-7	Endocrinology	Contraceptive	Yes
Nortriptyline hydrochloride	894-71-3	Central Nervous System	Antidepressant	Yes
Novobiocin sodium salt	1476-53-5	Metabolism	Antibacterial	Yes
Nylidrin	447-41-6	Cardiovascular	Vasodilator	
Nystatine	1400-61-9	Infectiology	Antifungal	Yes
Ofloxacin	82419-36-1	Infectiology	Antibacterial	Yes

Olanzapine	132539-06-1	Central Nervous System	Antipsychotic	Yes
Olmesartan	144689-63-4	Cardiovascular	Antihypertensive	Yes
Olopatadine hydrochloride	140462-76-6	Allergology	Antihistaminic	Yes
Omeprazole	73590-58-6	Gastroenterology	Antiulcer	Yes
Ondansetron Hydrochloride	103639-04-9	Central Nervous System	Antianemic	Yes
Opipramol dihydrochloride	909-39-7	Central Nervous System	Antidepressant	
Ornidazole	16773-42-5	Infectiology	Antibacterial	
Orphenadrine hydrochloride	341-69-5	Allergology	Antihistaminic	Yes
Oxacillin sodium	1173-88-2	Infectiology	Antibacterial	Yes
Oxalamine citrate salt	1949-20-8	Central Nervous System	Anti-inflammatory	
Oxandrolone	53-39-4	Endocrinology		Yes
Oxantel pamoate	68813-55-8	Infectiology	Antihelmintic	
Oxaprozin	21256-18-8	Central Nervous System	Analgesic	Yes
Oxcarbazepine	28721-07-5	Central Nervous System	Anticonvulsant	Yes
Oxethazaine	126-27-2	Neuromuscular	Local anesthetic	
Oxfendazol	53716-50-0	Metabolism		
Oxibendazol	20559-55-1	Metabolism		
Oxiconazole Nitrate	64211-46-7	Infectiology	Antifungal	Yes
Oxolinic acid	14698-29-4	Metabolism	Antibacterial	
Oxprenolol hydrochloride	6452-73-9	Cardiovascular	Antianginal	Yes
Oxybenzone	131-57-7	Dermatology		Yes
Oxybutynin chloride	1508-65-2	Neuromuscular	Antispastic	Yes
Oxymetazoline hydrochloride	2315-02-8	Respiratory	Nasal Decongestant	Yes
Oxymetholone	434-07-1	Endocrinology	Anabolic	Yes
Oxyphenbutazone	129-20-4	Metabolism	Anti-inflammatory	Yes
Oxytetracycline dihydrate	6153-64-6	Infectiology	Antibacterial	Yes
Ozagrel hydrochloride	78712-43-3	Cardiovascular	Antianginal	
Paclitaxel	33069-62-4	Oncology	Antineoplastic	Yes
Palonosetron hydrochloride	135729-62-3	Central Nervous System	Antiemetic	Yes
Pancuronium bromide	15500-66-0	Neuromuscular	Muscle relaxant	Yes

Panthenol (D)	81-13-0	Metabolism	Anti-alopecia	Yes
Pantoprazole sodium	138786-67-1	Metabolism	Antiulcer	Yes
Papaverine hydrochloride	61-25-6	Cardiovascular	Antispastic	
Parbendazole	14255-87-9	Infectiology		
Pargyline hydrochloride	306-07-0	Cardiovascular	Antidepressant	Yes
Paromomycin sulfate	1263-89-4	Metabolism	Antiamebic	Yes
Paroxetine Hydrochloride	110429-35-1	Central Nervous System	Antidepressant	Yes
Parthenolide	20554-84-1	Metabolism	Anti-inflammatory	
Pefloxacine	70458-92-3	Infectiology	Antibacterial	
Pemetrexed disodium	357166-30-4	Oncology	Antineoplastic	Yes
Pemirolast potassium	100299-08-9	Ophthalmology	Anti-inflammatory	Yes
Pempidine tartrate	546-48-5	Cardiovascular	Antihypotensive	
Penbutolol sulfate	38363-32-5	Cardiovascular	Antianginal	Yes
Penciclovir	39809-25-1	Infectiology	Antiviral	Yes
Pentamidine isethionate	140-64-7	Infectiology	Antifungal	Yes
Pentetic acid	67-43-6	Oncology	Chelating	Yes
Pentobarbital	76-74-4	Central Nervous System	Anesthetic	Yes
Pentolinium bitartrate	52-62-0	Cardiovascular	Antihypertensive	Yes
Pentoxifylline	6493-05-6	Cardiovascular	Bronchodilator	Yes
Pentylenetetrazole	54-95-5	Central Nervous System	Analeptic	
Pepstatin A	26305-03-3	Infectiology	Antiviral	
Pergolide mesylate	66104-23-2	Central Nervous System	Antiparkinsonian	Yes
Perhexiline maleate	6724-53-4	Cardiovascular	Antianginal	
Perospirone	150915-41-6	Central Nervous System	Antipsychotic	
Perphenazine	58-39-9	Central Nervous System	Antiemetic	Yes
Phenacetin	62-44-2	Central Nervous System	Analgesic	
Phenazopyridine hydrochloride	136-40-3	Central Nervous System	Analgesic	Yes
Phenelzine sulfate	156-51-4	Central Nervous System	Antidepressant	Yes
Phenethicillin potassium salt	132-93-4	Infectiology	Antibacterial	
Phenformin hydrochloride	834-28-6	Endocrinology	Antidiabetic	

Phenindione	83-12-5	Hematology	Anticoagulant	Yes
Pheniramine maleate	132-20-7	Allergology	Antihistaminic	Yes
Phenothiazine	92-84-2	Central Nervous System	Antipsychotic	
Phenoxybenzamine hydrochloride	63-92-3	Cardiovascular	Antihypertensive	Yes
Phenprobamate	673-31-4	Central Nervous System	Muscle relaxant	
Phensuximide	86-34-0	Central Nervous System	Anticonvulsant	Yes
Phentermine hydrochloride	1197-21-3	Central Nervous System		Yes
Phentolamine hydrochloride	73-05-2	Cardiovascular	Antihypertensive	Yes
Phenylbutazone	50-33-9	Metabolism	Anti-inflammatory	Yes
Phenylpropanolamine hydrochloride	154-41-6	Respiratory	Antihypotensive	Yes
Phthalylsulfathiazole	85-73-4	Metabolism	Antibacterial	
Picotamide monohydrate	80530-63-8	Hematology	Anticoagulant	
Picrotoxinin	17617-45-7	Central Nervous System	Analeptic	
Pidotimod	121808-62-6	Immunology	Immunostimulant	
Pilocarpine nitrate	148-72-1	Ophthalmology	Antiglaucoma	Yes
Pimethixene maleate	13187-06-9	Allergology	Antihistaminic	
Pimozide	2062-78-4	Central Nervous System	Antipsychotic	Yes
Pinacidil	85371-64-8	Cardiovascular	Antihypertensive	Yes
Pinaverium bromide	53251-94-8	Neuromuscular	Antispastic	
Pindolol	13523-86-9	Cardiovascular	Antianginal	Yes
Pioglitazone	111025-46-8	Endocrinology		Yes
Pipemidic acid	51940-44-4	Metabolism	Antibacterial	
Pipenzolate bromide	125-51-9	Gastroenterology	Antispastic	
Piperacetazine	3819-00-9	Central Nervous System	Antipsychotic	Yes
Piperacillin sodium salt	59703-84-3	Metabolism	Antibacterial	Yes
Piperidolate hydrochloride	129-77-1	Neuromuscular	Antispastic	
Piracetam	7491-74-9	Central Nervous System	CNS Stimulant	
Pirenperone	75444-65-4	Central Nervous System		
Pirenzepine dihydrochloride	29868-97-1	Gastroenterology	Antiulcer	
Piretanide	55837-27-9	Cardiovascular	Antihypertensive	

Piribedil hydrochloride	78213-63-5	Cardiovascular	Antiparkinsonian	
Pirlindole mesylate	60762-57-4	Central Nervous System	Antidepressant	
Piromidic acid	19562-30-2	Metabolism	Antibacterial	
Piroxicam	36322-90-4	Central Nervous System	Analgesic	Yes
Pivampicillin	33817-20-8	Metabolism	Antibacterial	
Pizotifen malate	5189-11-7	Allergology	Antihistaminic	
Podophyllotoxin	518-28-5	Metabolism	Antiviral	
Practolol	6673-35-4	Cardiovascular	Antianginal	
Pralidoxime chloride	51-15-0	Neuromuscular		Yes
Pramipexole dihydrochloride	104632-25-9	Central Nervous System	Antiparkinsonian	Yes
Pramoxine hydrochloride	637-58-1	Neuromuscular	Local anesthetic	Yes
Pranlukast	103177-37-3	Respiratory	Antiasthmatic	
Pranoprofen	52549-17-4	Metabolism	Anti-inflammatory	
Pravastatin	81093-37-0	Metabolism	Antilipemic	Yes
Praziquantel	55268-74-1	Infectiology	Antihelmintic	Yes
Prazosin hydrochloride	19237-84-4	Cardiovascular	Antihypertensive	Yes
Prednicarbate	73771-04-7	Metabolism	Anti-Inflammatory	Yes
Prednisolone	50-24-8	Endocrinology	Anti-inflammatory	Yes
Prednisone	53-03-2	Dermatology	Anti-inflammatory	Yes
Pregabalin	148553-50-8	Central Nervous System	Anticonvulsant	Yes
Pregnenolone	145-13-1	Endocrinology	Anabolic	
Prenylamine lactate	69-43-2	Cardiovascular	Antianginal	
Pridinol methanesulfonate salt	6856-31-1	Central Nervous System	Antiparkinsonian	
Prilocaine hydrochloride	1786-81-8	Neuromuscular	Local anesthetic	Yes
Primaquine diphosphate	63-45-6	Infectiology	Antimalarial	Yes
Primidone	125-33-7	Central Nervous System	Anticonvulsant	Yes
Proadifen hydrochloride	62-68-0	Neuromuscular	Local anesthetic	
Probenecid	57-66-9	Metabolism	Antigout	Yes
Probucol	23288-49-5	Metabolism	Antilipemic	Yes
Procainamide hydrochloride	614-39-1	Cardiovascular	Antiarrhythmic	Yes

Procaine hydrochloride	51-05-8	Neuromuscular	Local anesthetic	Yes
Procarbazine hydrochloride	366-70-1	Oncology	Antineoplastic	Yes
Prochlorperazine dimaleate	84-02-6	Central Nervous System	Antiemetic	Yes
Procyclidine hydrochloride	1508-76-5	Central Nervous System	Antiparkinsonian	Yes
Progesterone	57-83-0	Endocrinology	Progestogen	Yes
Proglumide	6620-60-6	Gastroenterology	Antiulcer	
Proguanil hydrochloride	637-32-1	Metabolism	Antimalarial	Yes
Promazine hydrochloride	53-60-1	Central Nervous System	Antipsychotic	Yes
Promethazine hydrochloride	58-33-3	Allergology	Antihistaminic	Yes
Pronethalol hydrochloride	51-02-5	Cardiovascular	Antianginal	
Propafenone hydrochloride	34183-22-7	Cardiovascular	Antiarrhythmic	Yes
Propantheline bromide	50-34-0	Neuromuscular	Antispastic	Yes
Proparacaine hydrochloride	5875-06-9	Central Nervous System	Anesthetic	Yes
Propidium iodide	25535-16-4	Infectiology	Antibacterial	
Propofol	2078-54-8	Central Nervous System	Anesthetic	Yes
Propoxycaine hydrochloride	550-83-4	Central Nervous System	Anesthetic	Yes
Propylthiouracil	51-52-5	Metabolism	Antihyperthyroid	Yes
Proscillaridin A	466-06-8	Cardiovascular		
Prothionamide	14222-60-7	Infectiology	Antibacterial	
Protriptyline hydrochloride	1225-55-4	Central Nervous System	Antidepressant	Yes
Pyrantel tartrate	33401-94-4	Infectiology	Antihelmintic	
Pyrazinamide	98-96-4	Infectiology	Antibacterial	Yes
Pyridostigmine iodide	4685-03-4	Central Nervous System		Yes
Pyridoxine hydrochloride	58-56-0	Metabolism		Yes
Pyrilamine maleate	59-33-6	Allergology	Antihistaminic	Yes
Pyrimethamine	58-14-0	Infectiology	Antimalarial	Yes
Pyrithyldione	77-04-3	Central Nervous System	Hypnotic	
Pyrvinium pamoate	3546-41-6	Metabolism		Yes
Quetiapine hemifumarate	111974-72-2	Central Nervous System	Antipsychotic	Yes
Quinacrine dihydrochloride hydrate	69-05-6	Infectiology	Antihelmintic	

Quinapril hydrochloride	82586-55-8	Cardiovascular	Antihypertensive	Yes
Quinethazone	73-49-4	Cardiovascular	Antihypertensive	Yes
Quinidine hydrochloride monohydrate	6151-40-2	Cardiovascular	Antiarrhythmic	Yes
Quipazine dimaleate salt	150323-78-7	Central Nervous System	Antiemetic	
R(-) Apomorphine hydrochloride hemihydrate	41372-20-7	Central Nervous System	Antiparkinsonian	Yes
Rabeprazole Sodium salt	117976-89-3	Metabolism	Antiulcer	Yes
Racecadotril	81110-73-8	Gastroenterology	Antidiarrheal	
Racepinephrine hydrochloride	329-63-5	Cardiovascular	Bronchodilator	Yes
Raclopride	84225-95-6	Central Nervous System		
Raloxifene hydrochloride	82640-04-8	Endocrinology		Yes
Raltitrexed	112887-68-0	Oncology	Antineoplastic	
Ranitidine hydrochloride	66357-59-3	Gastroenterology	Antiulcer	Yes
Ranolazine	95635-55-5	Cardiovascular	Antianginal	Yes
Rasagiline	136236-51-6	Central Nervous System	Antiparkinsonian	Yes
Rebamipide	90098-04-7	Metabolism	Antiulcer	
Reboxetine mesylate	98769-81-4	Central Nervous System	Antidepressant	
Remoxipride Hydrochloride	73220-03-8	Central Nervous System	Antipsychotic	
Repaglinide	135062-02-1	Endocrinology	Antidiabetic	Yes
Reserpine	50-55-5	Central Nervous System	Antipsychotic	Yes
Retinoic acid	302-79-4	Dermatology	Keratolytic	
Ribavirin	36791-04-5	Metabolism	Antiviral	Yes
Ribostamycin sulfate salt	53797-35-6	Metabolism	Antibacterial	
Rifabutin	72559-06-9	Infectiology	Antibacterial	Yes
Rifampicin	13292-46-1	Infectiology	Antibacterial	Yes
Rifapentine	61379-65-5	Infectiology	Antibacterial	Yes
Rifaximin	80621-81-4	Infectiology	Antibacterial	Yes
Riluzole hydrochloride	not available	Central Nervous System	Antispastic	Yes
Rimantadine Hydrochloride	13392-28-4	Infectiology	Antiviral	Yes
Rimexolone	49697-38-3	Metabolism	Anti-inflammatory	Yes

Risedronic acid monohydrate	105462-24-6	Metabolism	Antiosteoporetic	Yes
Risperidone	106266-06-2	Central Nervous System	Antipsychotic	Yes
Ritodrine hydrochloride	23239-51-2	Neuromuscular	Tocolytic	Yes
Ritonavir	155213-67-5	Infectiology	Antiviral	Yes
Rivastigmine	123441-03-2	Central Nervous System		Yes
Rizatriptan benzoate	145202-66-0	Central Nervous System	Antimigraine	Yes
Rofecoxib	162011-90-7	Metabolism	Anti-inflammatory	Yes
Rolipram	61413-54-5	Central Nervous System	Antidepressant	
Ronidazole	7681-76-7	Infectiology	Antibacterial	
Ropinirole hydrochloride	91374-20-8	Central Nervous System	Antiparkinsonian	Yes
Rosiglitazone Hydrochloride	122320-73-4	Metabolism	Antidiabetic	Yes
Roxatidine Acetate hydrochloride	93793-83-0	Gastroenterology	Antiulcer	
Roxithromycin	80214-83-1	Metabolism	Antibacterial	
Rufloxacin	101363-10-4	Infectiology	Antibacterial	
S(-)Eticlopride hydrochloride	97612-24-3	Central Nervous System		
S-(+)-ibuprofen	51146-56-6	Central Nervous System	Analgesic	Yes
Salbutamol	18559-94-9	Neuromuscular	Bronchodilator	
Salmeterol	89365-50-4	Respiratory	Bronchodilator	Yes
Saquinavir mesylate	149845-06-7	Immunology	Antiviral	Yes
Scopolamine hydrochloride	55-16-3	Central Nervous System	Antiemetic	Yes
Scopolamin-N-oxide hydrobromide	6106-81-6	Neuromuscular	Antispastic	Yes
Secnidazole	3366-95-8	Infectiology	Antiamebic	
Selegiline hydrochloride	14611-52-0	Central Nervous System	Antiparkinsonian	Yes
Serotonin hydrochloride	153-98-0	Central Nervous System	CNS Stimulant	
Sertaconazole nitrate	99592-39-9	Metabolism	Antibacterial	Yes
Sertindole	106516-24-9	Central Nervous System	Antipsychotic	
Sertraline	79617-96-2	Central Nervous System	Antidepressant	Yes
Sibutramine hydrochloride	125494-59-9	Central Nervous System		Yes
Sildenafil	139755-83-2	Cardiovascular	Antihypertensive	Yes
Silodosin	160970-54-7	Cardiovascular	Antihypertensive	Yes

Simvastatin	79902-63-9	Cardiovascular	Antilipemic	Yes
Sisomicin sulfate	53179-09-2	Infectiology	Antibacterial	
Sotalol hydrochloride	959-24-0	Cardiovascular	Antianginal	Yes
Spaglumic acid	4910-46-7	Allergology	Antiallergic	
Sparfloxacin	110871-86-8	Infectiology	Antibacterial	Yes
Spectinomycin dihydrochloride	21736-83-4	Metabolism	Antibacterial	Yes
Spiperone	749-02-0	Central Nervous System	Antipsychotic	Japan approved
Spiramycin	8025-81-8	Metabolism	Antibacterial	
Spironolactone	52-01-7	Endocrinology	Diuretic	Yes
Stanozolol	10418-03-8	Endocrinology		Yes
Stavudine	3056-17-5	Infectiology	Antiviral	Yes
Streptomycin sulfate	3810-74-0	Infectiology	Antibacterial	Yes
Streptozotocin	18883-66-4	Oncology	Antineoplastic	Yes
Succinylsulfathiazole	116-43-8	Infectiology	Antibacterial	
Sulbactam	68373-14-8	Infectiology	Antibacterial	Yes
Sulconazole nitrate	61318-91-0	Metabolism	Antifungal	Yes
Sulfabenzamide	127-71-9	Infectiology	Antibacterial	Yes
Sulfacetamide sodic hydrate	6209-17-2	Dermatology	Antibacterial	Yes
Sulfachloropyridazine	80-32-0	Infectiology	Antibacterial	
Sulfadiazine	68-35-9	Infectiology	Antibacterial	Yes
Sulfadimethoxine	122-11-2	Infectiology	Antibacterial	
Sulfadoxine	2447-57-6	Infectiology	Antibacterial	Yes
Sulfaguanidine	57-67-0	Infectiology	Antibacterial	
Sulfamerazine	127-79-7	Infectiology	Antibacterial	Yes
Sulfameter	651-06-9	Metabolism	Antibacterial	Yes
Sulfamethazine sodium salt	1981-58-4	Metabolism	Antibacterial	Yes
Sulfamethizole	144-82-1	Metabolism	Antibacterial	Yes
Sulfamethoxazole	723-46-6	Infectiology	Antibacterial	Yes
Sulfamethoxypyridazine	80-35-3	Infectiology	Antibacterial	
Sulfamonomethoxine	1220-83-3	Metabolism	Antibacterial	

Sulfanilamide	63-74-1	Infectiology	Antibacterial	Yes
Sulfaphenazole	526-08-9	Infectiology	Antibacterial	Yes
Sulfapyridine	144-83-2	Metabolism	Antibacterial	Yes
Sulfaquinoxaline sodium salt	967-80-6	Infectiology	Antibacterial	
Sulfasalazine	599-79-1	Infectiology	Antibacterial	Yes
Sulfathiazole	72-14-0	Infectiology	Antibacterial	Yes
Sulfinpyrazone	57-96-5	Hematology	Antiplatelet	Yes
Sulfisoxazole	127-69-5	Infectiology	Antibacterial	Yes
Sulindac	38194-50-2	Central Nervous System	Analgesic	Yes
Sulmazole	73384-60-8	Cardiovascular	Cardiotonic	
Suloctidil	54063-56-8	Neuromuscular	Antiplatelet	
Sulpiride	15676-16-1	Central Nervous System	Antidepressant	
Sumatriptan succinate	103628-48-4	Central Nervous System	Antimigraine	Yes
Suprofen	40828-46-4	Central Nervous System	Analgesic	Yes
Suxibuzone	27470-51-5	Central Nervous System	Analgesic	
Tacrine hydrochloride	1684-40-8	Central Nervous System	CNS Stimulant	Yes
Tamoxifen citrate	54965-24-1	Endocrinology	Antineoplastic	Yes
Tazobactam	89786-04-9	Infectiology	Antibacterial	Yes
Tegafur	17902-23-7	Oncology	Antineoplastic	
Tegaserod maleate	189188-57-6	Gastroenterology	Gastroprokinetic	Yes
Telenzepine dihydrochloride	147416-96-4	Gastroenterology	Antiulcer	
Telmisartan	144701-48-4	Cardiovascular	Antihypertensive	Yes
Temozolomide	85622-93-1	Oncology	Antineoplastic	Yes
Tenatoprazole	113712-98-4	Metabolism	Antiulcer	
Tenoxicam	59804-37-4	Central Nervous System	Analgesic	
Terazosin hydrochloride	63590-64-7	Cardiovascular	Antihypertensive	Yes
Terbinafine	91161-71-6	Infectiology	Antifungal	Yes
Terbutaline hemisulfate	23031-32-5	Respiratory	Antiasthmatic	Yes
Terconazole	67915-31-5	Infectiology	Antifungal	Yes
Terfenadine	50679-08-8	Allergology	Antihistaminic	

Testosterone propionate	57-85-2	Endocrinology	Anabolic	Yes
Tetracaïne hydrochloride	136-47-0	Neuromuscular		Yes
Tetracycline hydrochloride	64-75-5	Infectiology	Antibacterial	Yes
Tetraethylenepentamine pentahydrochloride	4961-41-5	Metabolism	Antilipemic	
Tetrahydrozoline hydrochloride	522-48-5	Cardiovascular	Nasal Decongestant	Yes
Tetramisole hydrochloride	5086-74-8	Immunology	Antihelmintic	
Thalidomide	50-35-1	Central Nervous System	Hypnotic	Yes
Theobromine	83-67-0	Cardiovascular	Bronchodilator	
Theophylline monohydrate	5967-84-0	Cardiovascular	Bronchodilator	Yes
Thiamine hydrochloride	67-03-8	Immunology	Immunostimulant	Yes
Thiamphenicol	15318-45-3	Infectiology	Antibacterial	
Thiethylperazine dimalate	52239-63-1	Central Nervous System	Antiemetic	Yes
Thiocolchicoside	602-41-5	Central Nervous System	Antispastic	
Thioguanosine	85-31-4	Metabolism	Antineoplastic	
Thioperamide maleate	106243-16-7	Central Nervous System	Antiemetic	
Thioproperazine dimesylate	2347-80-0	Central Nervous System	Antiemetic	
Thioridazine hydrochloride	130-61-0	Central Nervous System	Antipsychotic	Yes
Thiorphan	76721-89-6	Gastroenterology	Antidiarrheal	
Thiostrepton	1393-48-2	Infectiology	Antibacterial	
THIP Hydrochloride	85118-33-8	Central Nervous System	Sedative	
Thonzonium bromide	553-08-2	Dermatology	Antiseptic	Yes
Thyroxine (L)	51-48-9	Endocrinology	Antihypothyroid	Yes
Tiabendazole	148-79-8	Infectiology	Antifungal	
Tiapride hydrochloride	51012-33-0	Central Nervous System	Antiemetic	
Tiaprofenic acid	33005-95-7	Central Nervous System	Analgesic	
Tibolone	5630-53-5	Endocrinology		
Ticarcillin sodium	74682-62-5	Infectiology	Antibacterial	Yes
Ticlopidine hydrochloride	53885-35-1	Hematology	Anticoagulant	Yes
Tigecycline	220620-09-7	Infectiology		Yes
Timolol maleate salt	26921-17-5	Cardiovascular	Antianginal	Yes

Tinidazole	19387-91-8	Infectiology	Antiamebic	Yes
Tioconazole	65899-73-2	Infectiology	Antifungal	Yes
Tiratricol, 3,3',5-triiodothyroacetic acid	51-24-1	Endocrinology	Antihypothyroid	
Tizanidine hydrochloride	51322-75-9	Metabolism	Muscle relaxant	Yes
Tobramycin	32986-56-4	Infectiology	Antibacterial	Yes
Tocainide hydrochloride	71395-14-7	Cardiovascular	Anesthetic	Yes
Todralazine hydrochloride	3778-76-5	Cardiovascular	Antihypertensive	
Tolazamide	1156-19-0	Metabolism	Antidiabetic	Yes
Tolazoline hydrochloride	59-97-2	Cardiovascular	Vasodilator	Yes
Tolbutamide	64-77-7	Endocrinology	Antidiabetic	Yes
Tolcapone	134308-13-7	Central Nervous System	Antiparkinsonian	Yes
Tolfenamic acid	13710-19-5	Central Nervous System	Analgesic	
Tolmetin sodium salt dihydrate	64490-92-2	Metabolism	Anti-inflammatory	Yes
Tolnaftate	2398-96-1	Infectiology	Antifungal	
Tolterodine tartrate	209747-05-7	Neuromuscular	Muscle relaxant	Yes
Tomoxetine hydrochloride	82248-59-7	Central Nervous System		Yes
Topiramate	97240-79-4	Central Nervous System	Anticonvulsant	Yes
Topotecan	123948-87-8	Oncology	Antineoplastic	Yes
Toremifene	89778-26-7	Endocrinology	Antineoplastic	Yes
Torsemide	56211-40-6	Cardiovascular	Antihypertensive	Yes
Tosufloxacin hydrochloride	100490-36-6	Infectiology	Antibacterial	
Tracazolate hydrochloride	41094-88-6	Central Nervous System	Anticonvulsant	
Tramadol hydrochloride	27203-92-5	Central Nervous System	Analgesic	Yes
Tranexamic acid	1197-18-8	Hematology	Hemostatic	Yes
Tranilast	53902-12-8	Allergology	Antiallergic	
Tranylcypromine hydrochloride	1986-47-6	Central Nervous System	Antidepressant	Yes
Trapidil	15421-84-8	Cardiovascular	Vasodilator	
Trazodone hydrochloride	25332-39-2	Central Nervous System	Antidepressant	Yes
Tremorine dihydrochloride	51-73-0	Central Nervous System	CNS Stimulant	
Triamcinolone	124-94-7	Endocrinology	Anti-inflammatory	Yes

Triamterene	396-01-0	Metabolism	Antihypertensive	Yes
Tribenoside	10310-32-4	Cardiovascular		
Trichlormethiazide	133-67-5	Cardiovascular	Antihypertensive	Yes
Triclabendazole	68786-66-3	Infectiology	Antihelmintic	
Triclosan	3380-34-5	Infectiology	Antibacterial	Yes
Tridihexethyl chloride	4310-35-4	Neuromuscular	Antispastic	Yes
Trifluoperazine dihydrochloride	440-17-5	Central Nervous System	Antiemetic	Yes
Triflupromazine hydrochloride	1098-60-8	Central Nervous System	Antiemetic	Yes
Trifluridine	70-00-8	Metabolism	Antiviral	Yes
Triflusal	322-79-2	Hematology	Anticoagulant	
Trihexyphenidyl-D,L Hydrochloride	58947-95-8	Central Nervous System	Antiparkinsonian	Yes
Trimebutine	39133-31-8	Neuromuscular	Antispastic	
Trimeprazine tartrate	4330-99-8	Allergology	Antihistaminic	Yes
Trimetazidine dihydrochloride	13171-25-0	Cardiovascular	Antianginal	
Trimethadione	127-48-0	Central Nervous System	Anticonvulsant	Yes
Trimethobenzamide hydrochloride	554-92-7	Central Nervous System	Antiemetic	Yes
Trimethoprim	738-70-5	Infectiology	Antibacterial	Yes
Trimetozine	635-41-6	Central Nervous System	Sedative	
Trimipramine maleate salt	521-78-8	Central Nervous System	Antidepressant	Yes
Trioxsalen	3902-71-4	Dermatology		Yes
Tripelennamine hydrochloride	154-69-8	Allergology	Antihistaminic	Yes
Triprolidine hydrochloride	550-70-9	Allergology	Antihistaminic	Yes
Troglitazone	97322-87-7	Metabolism	Antidiabetic	Yes
Troleandomycin	2751-09-9	Infectiology	Antibacterial	Yes
Trolox	53188-07-1	Metabolism	Anti-oxidant	
Tropicamide	1508-75-4	Neuromuscular	Mydriatic	Yes
Tropisetron hydrochloride	105826-92-4	Central Nervous System	Antiemetic	
Troxipide	99777-81-8	Metabolism	Antiulcer	
Tulobuterol	41570-61-0	Respiratory	Bronchodilator	
Tylosin	1401-69-0	Infectiology	Antibacterial	

Tyloxapol	25301-02-4	Respiratory	Mucolytic	Yes
Ubenimex	58970-76-6	Oncology	Antineoplastic	
Urapidil hydrochloride	64887-14-5	Cardiovascular	Antihypertensive	
Urosiol	128-13-2	Metabolism		
Valacyclovir hydrochloride	124832-27-5	Infectiology	Antiviral	Yes
Valdecoxib	181695-72-7	Metabolism	Antiarthritic	Yes
Valproic acid	99-66-1	Central Nervous System	Anticonvulsant	Yes
Valsartan	137862-53-4	Cardiovascular	Vasodilator	Yes
Vancomycin hydrochloride	1404-93-9	Infectiology	Antibacterial	Yes
Vardenafil	224785-90-4	Cardiovascular	Erectile dysfunction treatment	Yes
Vatalanib	212141-54-3	Oncology	Antineoplastic	
Vecuronium bromide	50700-72-6	Metabolism	Muscle relaxant	Yes
Venlafaxine	93413-69-5	Central Nervous System	Antidepressant	Yes
Verapamil hydrochloride	152-11-4	Cardiovascular	Antihypertensive	Yes
Vidarabine	5536-17-4	Metabolism	Antiviral	Yes
Vigabatrin hydrochloride	1391054-02-6	Central Nervous System	Anticonvulsant	Yes
Viloxazine hydrochloride	35604-67-2	Central Nervous System	Antidepressant	
Vincamine	1617-90-9	Central Nervous System	CNS Stimulant	
Vinpocetine	42971-09-5	Cardiovascular	CNS Stimulant	
Viomycin sulfate	37883-00-4	Infectiology	Antibacterial	Yes
Voriconazole	137234-62-9	Infectiology	Antifungal	Yes
Vorinostat	149647-78-9	Oncology	Antineoplastic	Yes
Warfarin	81-81-2	Hematology	Anticoagulant	Yes
Xamoterol hemifumarate	73210-73-8	Cardiovascular		
Xylazine	7361-61-7	Central Nervous System	Analgesic	
Xylometazoline hydrochloride	1218-35-5	Cardiovascular	Nasal Decongestant	
Yohimbine hydrochloride	65-19-0	Cardiovascular	Erectile dysfunction treatment	
Zafirlukast	107753-78-6	Respiratory	Antiasthmatic	Yes
Zalcitabine	7481-89-2	Metabolism	Antiviral	Yes
Zaleplon	151319-34-5	Central Nervous System	Hypnotic	Yes

Zaprinast	37762-06-4	Cardiovascular	Erectile dysfunction treatment	
Zardaverine	101975-10-4	Respiratory	Bronchodilator	
Zidovudine, AZT	30516-87-1	Infectiology	Antiviral	Yes
Zileuton	111406-87-2	Respiratory	Antiasthmatic	Yes
Zimelidine dihydrochloride monohydrate	61129-30-4	Central Nervous System	Antidepressant	
Ziprasidone Hydrochloride	138982-67-9	Central Nervous System	Antipsychotic	Yes
Zoledronic acid hydrate	165800-06-6	Oncology	Antiosteoporetic	Yes
Zolmitriptan	139264-17-8	Central Nervous System		Yes
Zomepirac sodium salt	64092-48-4	Metabolism	Anti-inflammatory	
Zonisamide	68291-97-4	Central Nervous System	Anticonvulsant	Yes
Zopiclone	43200-80-2	Central Nervous System	Hypnotic	Yes
Zotepine	26615-21-4	Central Nervous System	Antipsychotic	
Zoxazolamine	61-80-3	Metabolism	Antigout	
Zuclopenthixol dihydrochloride	633-59-0	Central Nervous System	Antipsychotic	

6. Melanoma Drug Library (MDL)

Name	Target	Pathway
Selumetinib (AZD6244)	MEK	MAPK
Panobinostat (LBH589)	HDAC	Epigenetics
PD0325901	MEK	MAPK
Vorinostat (SAHA, MK0683)	Autophagy,HDAC	Epigenetics
Entinostat (MS-275)	HDAC	Epigenetics
Crizotinib (PF-02341066)	ALK,c-Met	Protein Tyrosine Kinase
Belinostat (PXD101)	HDAC	Epigenetics
Danusertib (PHA-739358)	Aurora Kinase,Bcr-Abl,c-RET,FGFR	Cell Cycle
Mocetinostat (MGCD0103)	HDAC	Epigenetics
PLX-4720	Raf	MAPK
BX-795	IκB/IKK,PDK	PI3K/Akt/mTOR
Ruxolitinib (INCB018424)	JAK	JAK/STAT
Adavosertib （MK-1775）	Wee1	Cell Cycle
AZD7762	Chk	Cell Cycle
Fasudil (HA-1077) HCl	Autophagy,ROCK	Cell Cycle
Verteporfin	VDA,Hippo pathway	Angiogenesis
RAF265 (CHIR-265)	Raf,VEGFR	MAPK
BGJ398 (NVP-BGJ398|Infigratinib)	FGFR	Angiogenesis
Volasertib (BI 6727)	PLK	Cell Cycle
Buparlisib (BKM120, NVP-BKM120)	PI3K	PI3K/Akt/mTOR
Imatinib (STI571)	PDGFR	Protein Tyrosine Kinase
TAK-733	MEK	MAPK
CHIR-124	Chk	Cell Cycle
Tofacitinib (CP-690550,Tasocitinib)	JAK	JAK/STAT
TAE226 (NVP-TAE226)	FAK	Angiogenesis
PF-562271	FAK	Angiogenesis
Abemaciclib	CDK	Cell Cycle
Ceritinib (LDK378)	ALK	Protein Tyrosine Kinase
(+)-JQ1	Epigenetic Reader Domain	Epigenetics
MLN2480	Raf	MAPK
XL888	HSP (e.g. HSP90)	Cytoskeletal Signaling
TAK-632	Raf	MAPK
EHop-016	Rho	Cell Cycle
OTX015	Epigenetic Reader Domain	Epigenetics
Sorafenib	Raf	MAPK
Ribociclib (LEE011)	CDK	Cell Cycle
EHT 1864 2HCl	Rho	Cell Cycle
Uprosertib (GSK2141795)	Akt	PI3K/Akt/mTOR
GSK269962A HCl	ROCK	Cell Cycle

AZD6738	ATM/ATR	PI3K/Akt/mTOR
CCT196969	Raf,Src	MAPK
Itacitinib (INCB39110)	JAK	JAK/STAT
Ulixertinib (BVD-523, VRT752271)	ERK	MAPK
Entrectinib (RXDX-101)	Trk receptor,ALK	Protein Tyrosine Kinase
NSC 23766	Rho	Cell Cycle
ASP3026	ALK	Protein Tyrosine Kinase
Tucidinostat (Chidamide)	HDAC	Epigenetics
LXH254	Raf	MAPK
Belvarafenib(GDC5573, HM95573, RG6185)	Raf	MAPK
CCG-222740	Rho	Cell Cycle
9-ing-41	GSK-3	PI3K/Akt/mTOR
UNC2025	FLT3	Protein Tyrosine Kinase
Larotrectinib	Trk receptor	Protein Tyrosine Kinase
Obatoclax (GX15-070)	Bcl-2	Apoptosis